Aalto University
School of Engineering
Department of Material Engineering

Mikko Kuitunen

Comparison of the material modelling performing characterization of weld microstructure of S355N steel and defining of residual stresses

Thesis submitted in partial fulfilment of the requirements for the degree of Master of Science in Technology
Espoo, 30.5.2016
Supervisor: Professor Hannu Hänninen
Instructors: Professor Veli Kujanpää and Ph.D. Pekka Nevasmaa

AALTO UNIVERSITY
SCHOOLS OF TECHNOLOGY
PO Box 12100, FI-00076 AALTO
http://www.aalto.fi

ABSTRACT OF THE MASTER'S THESIS

Author: Mikko Kuitunen

Title: Comparison of the material modelling performing characterization of weld microstructure of S355N steel and defining of residual stresses

School: School of Engineering

Department: Department of Material Engineering

Professorship: Engineering Materials | Code: Kon-67

Supervisor: Professor Hannu Hänninen
Instructor(s): Professor Veli Kujanpää and Ph.D. Pekka Nevasmaa

The objective of this Master thesis was to answer the following questions. Do the characterized microstructures of VTT S355N samples with their mechanical properties and the experimental results of TIG welds of the Voss's doctoral thesis correspond to the modelled material results? Do X-ray diffraction measured residual stresses of S355N butt weld samples correspond with the measured residual stresses of Contour method? Is the mixing of the investigated weld samples of LAHW and MAG welds even? The purpose of these comparisons is to support validation of simulation processes which will be carried out in future. Additionally this thesis discussed if the maximum grain size of coarse-grained zone can be determined by measuring the grain size distribution with micrographs and Matlab.

Charasterisation of microstructures of bead-on-plate VTT samples was focused on coarse-grained zones near fusion lines because there are the weakest parts of the welds. Hardness distributions and measuring of dimensions of HAZ (*Heat Affected Zone*) and weld metal were measured for all bead-on-plate welds of VTT. Recognition of phases of microstructures was carried out with the help of micrographs, hardnesses and recognition micrographs of IIW (International Institute of Welding). Cooling times were measured for all bead-on-plate welds with thermoelements. Values of $t_{8/5}$ were determined for cooling times of measured, simulated, and of Voss's doctoral thesis if possible. Determined $t_{8/5}$ values, measured dimensions of HAZ and weld metals were compared between measured values of VTT samples, simulated values of FLOW-3D and measured values of Voss's doctoral thesis. Residual stresses were measured for base material, two MAG and LAHW butt welds with Contour method and X-ray diffraction and the measured residual stresses were compared. Mixing of MAG and LAHW S355N samples of VTT were clarified with mixing calculations and with chromium, nickel and iron distributions of stainless weld metal. Distributions of chromium, nickel and iron were measured with EDS (Energy-dispersive X-ray Spectroscopy). Contents of chromium, nickel and iron were measured for one MAG sample with OES (Optical Emission Spectrometry). Mixing of one dissimilar MAG sample was clarified with etching, Schaeffler and WRC-92 diagrams. Reason of high variation of hardness near fusion line was investigated with one dissimilar MAG sample. Maximum grain sizes of coarse-grained zones were measured with optical microscopy and grain size distributions from base material to weld metal were determined with the help of micrographs, image processing and Matlab for all bead-on-plate welds of VTT.

Most characterized microstructures of VTT samples with their mechanical properties and the experimental results of TIG welds of the Voss's doctoral thesis were near the modelling results. X-ray diffraction measured residual stresses of weld samples correlate with the measured residual stresses of Contour method. Mixing of investigated LAHW and MAG welds are even. Measuring of maximum grain size of prior austenite from coarse-grained zone with the grain size distribution was not possible because Matlab software measures dimensions of martensite blocks inside prior austenite.

Date:30.5.2016 | Language: English | Number of pages: 96 + 18 Appendix

Keywords: Metallography, residual stresses, X-ray diffraction, Contour method, mixing, grain size, grain size distribution

AALTO-YLIOPISTO TEKNIIKAN KORKEAKOULUT PL 12100, 00076 Aalto http://www.aalto.fi	DIPLOMITYÖN TIIVISTELMÄ

Tekijä: Mikko Kuitunen

Työn nimi: Teräksen S355N hitsausliitoksien materiaalimallinnustulosten vertailu mikrorakenteen karakterisoinnin ja jäännösjännitysten avulla

Korkeakoulu: Insinööritieteiden korkeakoulu

Laitos: Koneenrakennustekniikan laitos

Professuuri: Koneenrakennuksen materiaalitekniikka	Koodi: Kon-67

Työn valvoja: Professori Hannu Hänninen
Työn ohjaaja(t): Professori Veli Kujanpää ja TkT Pekka Nevasmaa

Tämän diplomityön tavoitteena oli vastata seuraaviin kysymyksiin. Vastaako VTT S355N näytteiden karakterisoidut mikrorakenteet ja niiden mekaaniset ominaisuudet ja kokeellisesti määritetyt Vossin tohtorityön TIG hitsien tulokset materiaalimallinnuksen tuloksia? Vastaako röntgendiffraktiolla mitatut S355N päittäisliitosten jäännösjännitykset Contour menetelmällä mitattuja jäännösjännityksiä? Onko tutkittujen LAHW ja MAG hitsien sekoittuminen tasaista? Tämän vertailun tavoite on tukea tulevaisuudessa tehtäviä simulointiprosessien validointeja. Lisäksi tässä päättötyössä mietittiin voidaanko karkearakeisen vyöhykkeen maksimiraekoko määrittää mittaamalla raekokojakauma mikrorakennekuvien ja Matlabin avulla.

VTT:n päällehitsien mikrorakenteiden karakterisoinnit kohdistettiin karkearakeisille vyöhykkeille lähelle sularajoja, koska ne ovat hitsien heikoin kohta. Kaikille VTT:n päällehitseille mitattiin kovuusjakaumat sekä HAZ:ien (*Heat Affected Zone*) ja hitsien mitat. Mikrorakenteiden faasien tunnistus tehtiin kaikille VTT:n päällehitseille mikrorakennekuvien, kovuuksien ja IIW:n (*International Institute of Welding*) tunnistuskuvien avulla. Jäähtymisajat mitattiin kaikille VTT:n päällehitseille lämpöelementtien avulla. Simuloiduille, mitatuille ja Vossin työn jäähtymisajoille määritettiin $t_{8/5}$ arvot, jos mahdollista. Määritettyjä $t_{8/5}$ arvoja sekä mitattuja HAZ:ien ja hitsien mittoja verrattiin keskenään VTT:n mitattujen arvojen, VTT:n FLOW-3D simulaatioiden ja Vossin tohtorityön mitattujen arvojen kesken. Perusmateriaalin, kahden MAG näytteen ja LAHW näytteen päittäisliitoksien jäännösjännityksiä mitattiin Contour menetelmän ja röntgendiffraktion avulla sekä mitattuja jäännösjännityksiä verrattiin keskenään. VTT:n MAG ja LAHW hitsattujen S355N näytteiden sekoittumista selvitettiin sekoittumislaskelmilla ja ruostumattoman hitsiaineen kromi-, nikkeli- ja rautajakaumien avulla. Kromi-, nikkeli- ja rautajakaumat mitattiin EDS:n (*Energy-dispersive X-ray Spectroscopy)* avulla. Rauta, nikkeli ja kromipitoisuudet mitattiin yhdelle MAG näytteelle OES:n (*Optical Emission Spectrometry*) avulla. MAG "eripari" näytteen sekoittumista selvitettiin syövytyksen, Schaeffler ja WRC-92 diagrammien avulla. Suuren kovuusvaihtelun syytä lähellä sularajaa selvitettiin yhdellä MAG eripari hitsillä. Karkearakeisten vyöhykkeiden maksimiraekoko mitattiin valomikroskoopilla ja raekokojakaumat määritettiin perusmateriaalista hitsiin mikrorakennekuvien, kuvan käsittelyn ja Matlabin avulla kaikille VTT:n päällehitseille.

Suurin osa VTT:n näytteiden karakterisoiduista mikrorakenteista ja niiden mekaanisista ominaisuuksista ja Vossin tohtorityön mitatuista tuloksista ovat lähellä FLOW-3D simulaatioiden tuloksia. Röntgendiffraktiolla mitatut hitsien jäännösjännitykset korreloivat Contour menetelmällä mitattujen jäännösjännitysten kanssa. LAHW ja MAG hitsien sekoittuminen on tasaista. Karkearakeisen vyöhykkeen maksimiraekoon määrittäminen raekokojakauman avulla ei ole mahdollista, koska Matlab ohjelma mittasi martensiittipakettien mittoja perinnäisen austeniitin rakeiden sisällä.

Päivämäärä: 30.5.2016	Kieli: Englanti	Sivumäärä: 96 + 18 liitettä

Avainsanat: metallografia, jäännösjännitykset, röntgendiffraktio, Contour menetelmä, sekoittuminen, raekoko, raekokojakauma

Acknowledgement

This Master thesis is part of the Project "Digital materials engineering and modelling of mass and heat flow for optimisation of joining materials" (FIDIPRONA) in cooperation project with VTT (Technical Research Centre of Finland), KAIST (Korea Advanced Institute of Science and Technology), a university in South Korea and Finnish industrial companies.

Cost saving, safety and eco-friendliness were improved with the help of validation of material modelling. The target of this Master thesis was to improve these benefits by comparing ready modelling results of LAHW, LASER, MAG and TIG welds for 5 and 15 mm thick S355N samples of bead-on-plate and butt welds with the help of microstructure characterisation and measuring of residual stresses.

I would like to thank my supervising professor Hannu Hänninen and my instructors Pekka Nevasmaa and Veli Kujanpää for their guidance and valuable comments during Master thesis. I thank Mika Siren for valuable instructions and simulations of cooling time and dimensions of HAZ and weld metals. I am thankful to Iikka Virkkunen for guidance and calculations of Contour method. I am very thankful to Timo Kiesi who gave me valuable instructions and measured residual stresses of sample with X-ray diffraction. I thank Pedro Vilaca for his supporting. I would like to thank Pauli Lehto for the good instructions and determination of grain size distributions with Matlab. I am thankful to Teemu Sarikka for EDS analysis and Jouni Penttilä for the results of OES.

I am thankful to Marketta Mattila, Taru Lehtikuusi and Seija Kivi for their guidance and helping in material laboratory in VTT. I thank Laura Tiainen and Kim Widell their help in material laboratory of Aalto University. I would like to thank Seppo Nurmi for wire cutting of samples and Iikka Palosuo and Pasi Laukkanen for coordination measuring of samples topography. I thank Åsa Åvall and Cristina Vähävaara for their help and instructions of writing.

I would like to thank Jari Hartikainen for language checking.

I am very thankful to VTT Oy for the opportunity to do my Master thesis.

I would like to thank all my friends who supported me. Special thanks go to my wife Satu Kuitunen and my children Anni, Roosa, Suvi, Henrik, Aaro and Erno for their patience and understanding during this period of my life.

Espoo 30.5.2016

Mikko Kuitunen

Table of contents

Units of measurements

T_m	[K]	Melting point temperature
C	-	Specific heat of the workpiece
CE	[%]	Carbon Equivalent
CET	[%]	Carbon Equivalent
d	[mm]	Material thickness
d	[m]	Distance between points of lattices
d_0	[m]	Distance between stressed material
d_{hkl}	[m]	Distance between lattice planes with non-stressed material
Mixing1	[%]	Mixing of bead-on-plate weld
Mixing2	[%]	Mixing of butt weld
E	[kJ/mm]	Welding energy
E	[N/mm^2]	Elastic modulus
F2	-	Joint factor for two-dimensional thermal conduction
F3	-	Joint factor for three-dimensional thermal conduction
g	[mm]	Thickness of workpiece
h	-	Miller's index
HB	[HB]	Brinell hardness
HD	[ml/100g]	Hydogen content
HV	[HV]	Vickers hardness
I	[A]	Current
k	-	Thermal efficiency
k	-	Partition ratio
k	[J/msK]	Thermal conductivity
k	-	Thermal diffusivity
k	-	Miller's index
K_0	-	Modified Bessel function
L	[mm^2]	Cross-section area of filler metal
l	-	Miller's index
m	[wt%]	Weight percent
n	-	Multiple of wave length
P	[mm^2]	Diluted cross-section area of weld
P1	[mm^2]	Diluted cross-section area of weld
P2	[mm^2]	Diluted cross-section area of weld
Q	[kJ/mm]	Heat input
r	[m]	Radial distance in origin
T	[˚C]	Temperature
T_0	[˚C]	Temperature before welding
T_0	[˚C]	Working temperature
$t_{8/5}$	[s]	Cooling time between 800 ˚C and 500 ˚C
U	[V]	Voltage
v	[mm/min]	Welding speed
P_{cm}	[%]	Carbon Equivalent

T_P	[˚C]	Preheat temperature
ϕ	[˚]	Angle of RXD
$\Delta\ \theta$	[˚]	Change of angle of Bragg's law
ψ	[˚]	Angle of RXD
σ_y	[m^2/s]	Thermal diffuctivity
Θ	[˚]	Angle of incoming X-ray
θ_0	[˚]	Angle of Bragg's law
λ	[m]	Wave length of radiation
ρ	[kg/m^3]	Density
ρC	[J/m^3K]	Volume thermal capacity
ε	[mm]	Strain
σ	[N/mm^2]	Stress
σ	[N/mm^2]	Biaxial stress
σ	[N/mm^2]	Entire stress tensor
σ_x	[N/mm^2]	Stress on x direction
τ_{xy}	[N/mm^2]	Shear stress for xy planes
τ_{xz}	[N/mm^2]	Shear stress for xz planes
Φ	[˚]	Angle of RXD

Abbreviations

VTT	Technical Research Centre of Finland
(A)	Fully austenitic solidification
(A-F)	Austenite – Ferrite solidification
(F)	Fully ferrite solidification
(F-A)	Ferrite – Austenite solidification
(F-A-F)	Ferrite – Austenite – Ferrite solidification
AF	Coarse acicular ferrite
BCC	Body-centered cubic
CCT	Continuous Cooling Transformation
CFD	Computational Fluid Dynamics
DMW	Dissimilar Metal Welding
EBSD	Electron Backscatter Diffraction
EDS	Energy-dispersive X-ray Spectroscopy
F	Ferrite
FCC	Face-centered cubicle
FEM	Finite Element Method
FiDiPro	Finland Distinguished Professor Programme
FZ	Fusion zone
GTAW	Gas-Tungsten Arc Welding
HAZ	Heat Affected Zone
HV	Vicker Hardness
KAIST	Korea Advanced Institute of Science and Technology
LAHW	Laser Arc Hybrid Welding
LB	Lower bainite
LBW	Laser Beam Welding
M	Martensite
MAG	Metal Active Gas
MIG	Metal Inert Gas
OES	Optical Emission Spectrometry
OU	Osaka University
PMZ	Partially melted zone
Pv	Chemical composition of VTT / OU method
SEM	Scanning Electron Microscope
TIG	Tungsten Inert Gas
TP	Peak temperature time
UB	Upper bainite
WM	Weld metal
VTT / OU	Calculation method for HV hardness developed by VTT and OU
XRD	X-ray diffraction

1 Introduction

Material modelling has been in the key position in exporting welded structures in Finland. Cost saving, safety and eco-friendliness has been improved with the help of comparison between test welds and material modelling.

Project "Digital materials engineering and modelling of mass and heat flow for optimisation of joining materials" (FIDIPRONA) is a cooperation project of VTT (*Technical Research Centre of Finland*), KAIST (*Korea Advanced Institute of Science and Technology*), a university in South Korea and Finnish industrial companies. Welding simulations, techniques and methods were developed with four topics. The first topic was dependency of metallurgical phenomena and material properties. The second was quality optimization of welds in aspect of production and service. The third was industrial proof, validation and implementation. The fourth was to do three theses about previous topics.

The target of this thesis is to answer the following questions. Do the characterized microstructures of VTT samples with their mechanical properties and the experimental results of TIG welds of the Voss's doctoral thesis correspond to the material modelling results? Do XRD (*X-ray diffraction*) measured residual stresses of weld samples correspond with the measured residual stresses of Contour method? Is the mixing of the investigated weld samples of LAHW and MAG welds even? Additionally this thesis discusses if the maximum grain size can be determined by measuring the grain size distribution. The purpose of these targets is to support validation of simulation processes which will be carried out in future.

The weakest part of the weld is usual in coarse-grained zone near the fusion line. The microstructures of bead-on-plate samples are characterized and mechanical properties of coarse-grained zones of VTT samples are defined. Hardness distributions and dimensions of HAZ (*Heat Affected Zone*) are also measured. Recognition of phases of microstructures is carried out with the help of micrographs, hardnesses and recognition micrographs of IIW (*International Institute of Welding*). Different microstructures are consequence of different cooling times. Cooling times for bead-on-plate samples of VTT are measured for all bead-on-plate welds with thermoelements and their $t_{8/5}$ values are determined.

The second objective is to measure residual stresses for base material, two MAG and LAHW butt welds with Contour method and X-ray diffraction, find out if the measured residual stresses correlated.

Mixing base material and filler metal affects the properties of weld. Mixing of MAG and LAHW samples of VTT whose base material is structural steel are studied with mixing calculations and with chromium, nickel and iron distributions of stainless weld metal. These distributions are determined with EDS (*Energy-dispersive X-ray Spectroscopy*). Contents of chromium, nickel and iron are determined for one MAG sample with OES (*Optical Emission Spectrometry*). Mixing of one dissimilar MAG sample is studied with etching, Schaeffler and WRC-92 diagrams. Reason of high variation of hardness near fusion line is investigated with one dissimilar MAG sample.

The grain size affects the properties of weld. The purpose is to clarify if it is possible to determine the maximum grain size of coarse-grained zone with the measured grain size distribution. The maximum grain sizes of coarse-grained zones are measured with optical microscopy. The grain size distributions from base material to weld metal are determined with the help of micrographs, image processing and Matlab for all bead-on-plate welds of VTT.

Characterization of microstructures concentrates on coarse-grained zones and weld metals of all samples of bead-on-plate welds of VTT. Residual stresses are defined for all butt weld samples of VTT. Tensile and Charpy tests are not made in this Master's thesis.

2 State of the art

2.1 Structure and properties of welded joint

During welding the peak temperature of the weld varies between the temperature of the molten steel and ambient temperature in a narrow area. Zones which have different microstructures are created as a consequence of the temperature gradient. The welded joint can be roughly divided into two zones which are weld metal and HAZ (Heat Affected Zone). Figure 1 shows different regions of the welded joint which are: (1) (2)

1. Weld metal (WM), FZ (Fusion zone)
2. Fusion line, PMZ (partially melted zone)
3. Coarse-grained zone
4. Fine-grained zone
5. Partially austenitized and tempered zone
6. Tempered zone

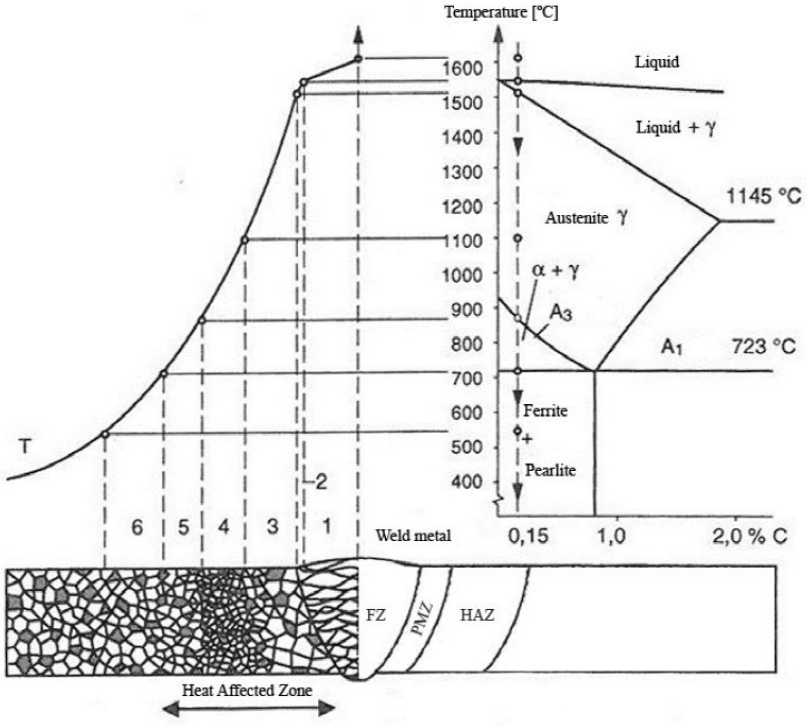

Figure 1: Schematic presentation of different regions in the welded joints (edited picture). (3) (1)

The temperature curve describes the distribution of peak temperatures caused by welding in various sections of welded joint. The microstructures which correspond to the distribution of temperature of the whole weld can be seen from the phase diagram. The vertical dot line represents the carbon content of steel which is 0.15 wt%. (1)

Partially melted zone and coarse-grained zone are the weakest points of weld. Impact ductility of the weld is poorest in the coarse-grained zone due to brittle phases which have formed as the consequence of fast cooling rate. The weld metal affects critically the mechanical properties with high welding energy. (1)

Fine-grained zone, partially austenitized and tempered zone and tempered zone have better mechanical properties than partially melted zone and coarse-grained zone have. The microstructure of the fine-grained zone is fine-grained pearlite or fine-grained ferrite and pearlite in hypoeutectic carbon steel. Fine-grained zone has good impact ductility and the hardness is usually less than the hardness of the base material. The formation of brittle phases in partially austenitized and tempered zone is rare but possible. Properties of tempered zone are usually similar with the properties of the base material. Welding stresses can cause plastic deformation after welding. This can lead to strain aging in this zone. (1)

Microstructure and mechanical properties of HAZ depend on peak temperature, peak temperature time (TP), cooling rate, mixing, chemical composition of the weld metal (WM) and the base material. (1)

2.2 Welding energy and heat input

Arc energy means the welding energy per unit of length. The arc energy can be calculated according to equation (1): (1)

$$E = \frac{60 \times U \times I}{1000 \times v}, \quad \textbf{(1)}$$

where
E = welding energy [kJ/mm]
U = voltage [V]
I = current [A]
v = welding speed [mm/min]

Heat input means the heat amount which has moved to the weld per unit of length during the welding process. The heat input is dependent on the thermal efficiency ratio of the welding process according to equation (2) (1) (4). Table 1 shows thermal efficiency factors for most common welding methods. (4)

$$Q = k * E = k * \frac{U * I}{\left(\frac{v}{60}\right)} * 10^{-3}, \quad \textbf{(2)}$$

where
Q = heat input [kJ/mm]
k = thermal efficiency

Thermal efficiency of heat source can be measured with a calorimeter (2). Thermal efficiency k for arc welding methods is shown in Table 1. k is between 0.3 % and 0.9 % with LAHW and LASER-welding (5).

Table 1: Thermal efficiency factor of arc welding process (4)

Process No.	Welding process	*k*
12	Submerged arc welding	1,0
111	Manual metal arc welding	0,8
131	MIG welding	0,8
135	MAG welding	0,8
114	Self-shielded tubular-cored arc welding	0,8
136	Tubular-cored wire metal arc welding with active gas shield	0,8
137	Tubular-cored wire metal arc welding with inert gas shield	0,8
141	TIG welding	0,6
15	Plasma arc welding	0,6

2.3 Solidification

2.3.1 Solute redistribution during solidification

When liquid metal alloy solidifies, the resultant solid is seldom uniform in composition. The solute atoms of liquid are redistributed during solidification. This depends on thermo-dynamics and kinetics phenomena which are phase transformation, diffusion, undercooling and fluid flow. (2)

Figure 2 shows part of phase diagram. Melting point T_m, solid phase S, and liquid L are marked in the figure. Initial solidification of alloy C_0 intersects the liquidus line at the liquidus temperature T_L and the solidus line at the solidus temperature T_S. Phase diagram assumes that undercooling is negligible so that the solidification begins when the liquid cools to T_L according to the equilibrium. (2)

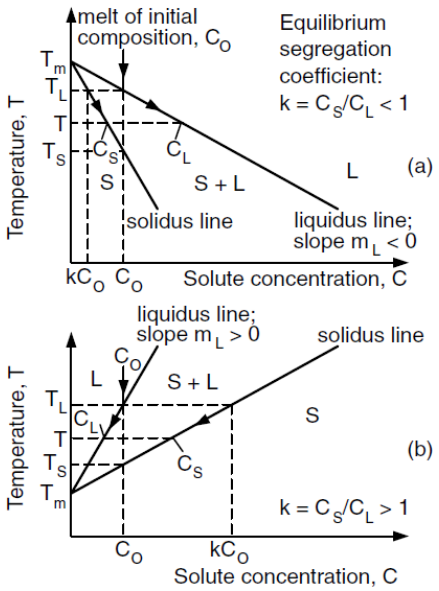

Figure 2 Part of phase diagram shows the equilibrium partition ratio k. (2)

In reality solidification takes place according to equilibrium partition ratio. This ratio can be calculated according to equation (3). (2)

$$k = \frac{C_S}{C_L} \tag{3}$$

C_S and C_L are the compositions of the solid and liquid at the S/L interface. Equilibrium partition ratio k is assumed to be constant. This means that solidus and liquidus lines are assumed to be straight lines according to Figure 2.

When k is less than 1 the solid cannot accommodate as much solute as the liquid does according to Figure 2 a. Solid rejects the solute to the liquid during solidification. This means that the solute content of liquid starts to rise during solidification.

When k is more than 1 solid can accommodate more solute than liquid does according to Figure 2 (b). Solid absorbs the solute from the liquid during solidification. This leads that solute content of liquid starts to drop during solidification.

2.3.2 Solidification and epitaxial growth

Solidification starts in weld pool on S/L interface usually planar with pure metal (2) (6). In the constitutional super cooling the temperature of the liquid is less than its melting point (6). Four different solidification modes are shown in Figure 3. These modes are planar, cellular, columnar dendritic and equal axial dendritic solidification modes (2) (6). The rate of constitutional supercooling affects solidification modes according to Figure 4 (2).

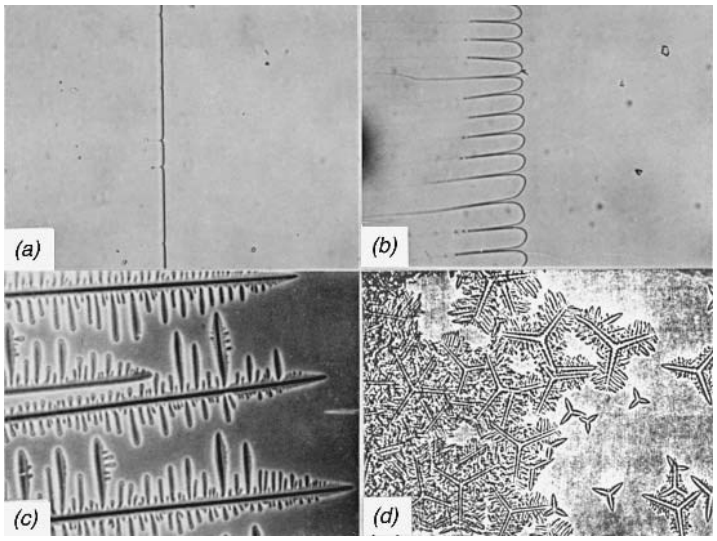

Figure 3 Solidification modes are shown with 67X magnification: (a) Planar solidification of carbon tetra bromide. (b) Cellular solidification of carbon tetra bromide with small amount impurity. (c) Same (b) but more impurities cause columnar dendritic solidification. (2)

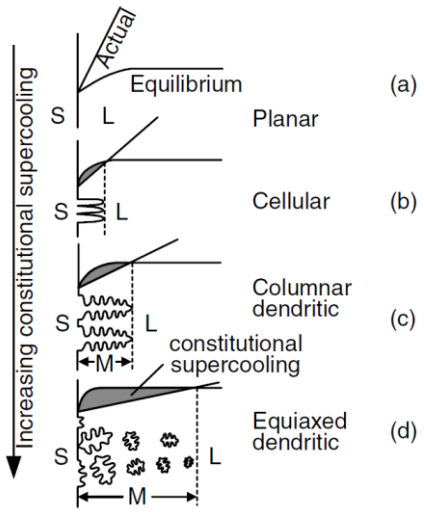

Figure 4 Effect of the constitutional super cooling on solidification modes. (2)

Temperature gradient G and the growth rate R affect the solidification of microstructure as shown in Figure 5. The mode of solidification and the size of solidification structure depend on the ratio G/R. (2)

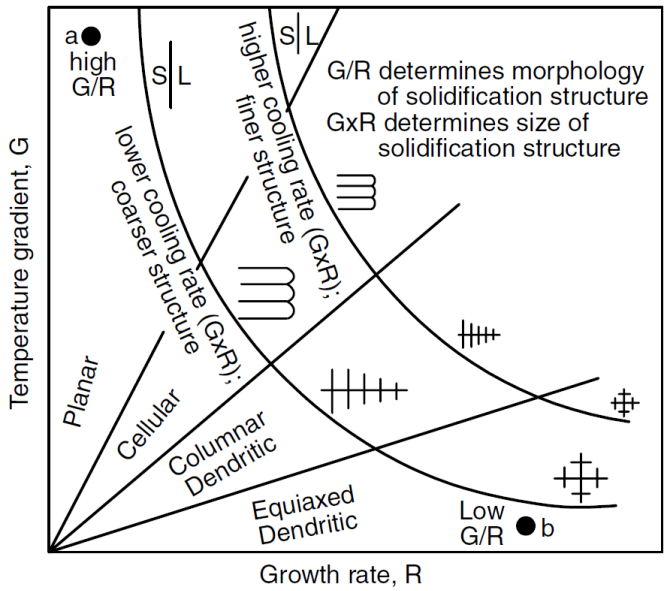

Figure 5 Effect of temperature gradient G and growth rate R on the morphology and size of solidification microstructure. (2)

Figure 6 shows that solidification modes may change from planar to cellular, columnar dendritic and equiaxed dendritic in the middle of weld and fusion line according to ratio G/R. (2)

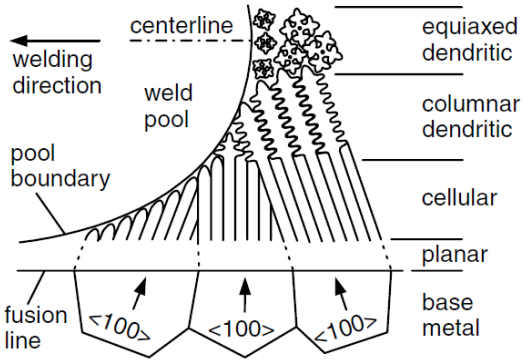

Figure 6 Solidification of weld. (2)

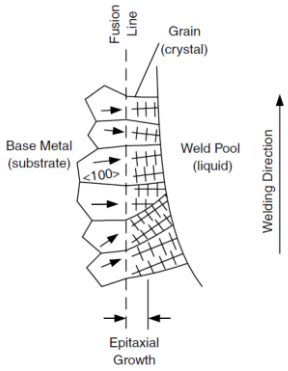

Figure 7 Epitaxial growth. (2)

Figure 7 shows normal epitaxial grain growth when grains are oriented roughly perpendicularly to the fusion boundary during solidification. Epitaxial growth occurs when welding takes place without a filler metal. Epitaxial growth is not valid if different filler metal is used or two different base materials are welded together. (2)

2.3.3 Solidification modes of austenitic stainless steel

In austenitic stainless steel a lot of delta ferrite occurs in the beginning of solidification. The austenitic stainless steel includes less delta ferrite after solidification because delta ferrite is a phase which changes according to equilibrium at high temperatures. Infiltration affects the amount of ferrite. Ferrite is equilibrium phase at room temperature. Diffusion equalizes difference of compositions which are created during solidification and cooling. This take places in the transformation from ferrite to austenite.

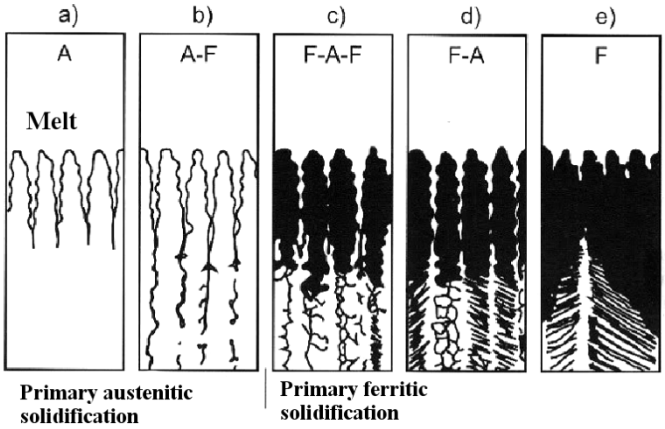

Figure 8 Solidification modes of austenitic stainless steel. (6)

Sequence of solidification of stainless steel weld is affected by the properties of weld. 5 types of sequence of solidification of austenitic stainless steel are shown in Figure 8. These solidification modes are mentioned below. (6) (7)

1. Fully austenitic solidification (A)
2. Austenite – Ferrite solidification (A-F)
3. Ferrite – Austenite – Ferrite solidification (F-A-F)
4. Ferrite – Austenite solidification (F-A)
5. Fully ferritic solidification (F)

The relationships of solidification types to pseudo-binary phase diagram are shown in Figure 9. Amount of ferrite can be approximated with the help of Schaeffler and WRC 1992 diagram. These diagrams are explained later.

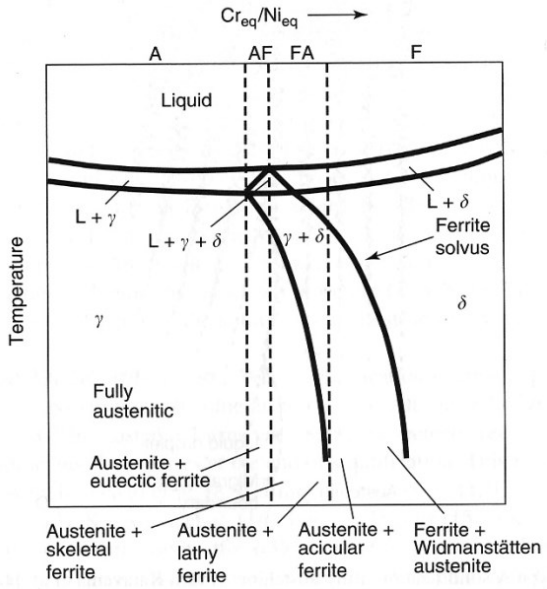

Figure 9 Relationship between solidification and pseudo-binary phase diagram. (8)

2.4 Heat flow in welding

When a weld cools down, the heat will conduct away from the base metal and radiate to the environment. Heat conductivity, dimension of part and especially material thickness affect the cooling rate. The welding parameters such as welding current, arc voltage and welding speed affect the cooling rate of the weld. (6)

2.4.1 Rosenthal's equations

Rosenthal's equations can be used to calculate temperature distribution in the workpiece during welding. T-x curves can be converted into temperature time plots which are called thermal cycles according to Figure 11 and 12. Rosenthal's equations take the following simplifications into consideration for heat flow during welding (2):

1. Steady state heat flow
2. Point heat source
3. Negligible heat of fusion
4. Constant thermal properties
5. No heat losses from the workpiece surface
6. No convection in the weld pool

Two-dimensional heat flow is shown by equation (4) and schematic presentation of thin sheet in Figure 11.

$$\frac{2\pi(T-T_0)kg}{Q} = \exp\left(\frac{Vx}{2\alpha}\right)K_0\left(\frac{Vr}{2\alpha}\right), \quad \textbf{(4)}$$

where
T = temperature (with structure steel 1530 ˚C)
T_0 = workpiece temperature before welding
k = thermal conductivity of workpiece (See Table 2)
g = thickness of workpiece
Q = heat transferred
V = travel speed
α = workpiece thermal diffusivity, k/(ρC), where ρ is density and C specific heat of the workpiece (See Table 2)
K_0 = modified Bessel function of second kind and zero order as shown in Figure 10
r = radial distance from origin, namely $(x^2+y^2)^{1/2}$

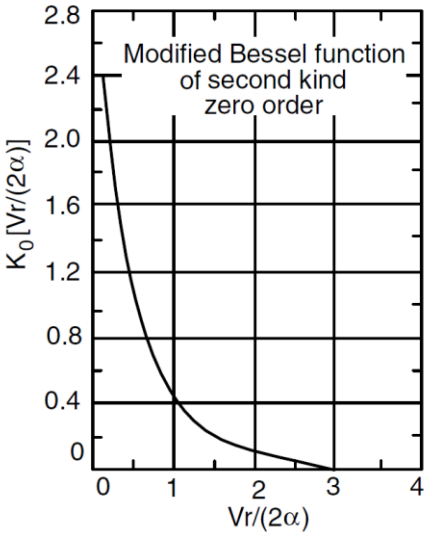

Figure 10 Modified Bessel function of second kind and zero order. (2)

Table 2 Thermal material properties. (2)

Material	Thermal Diffusivity, α (m^2/s)	Volume Thermal Capacity, ρC_s (J/m^3K)	Thermal Conductivity, k (J/ms K)	Melting Point (K)
Aluminum	8.5×10^{-5}	2.7×10^6	229.0	933
Carbon steel	9.1×10^{-6}	4.5×10^6	41.0	1800
9% Ni steel	1.1×10^{-5}	3.2×10^6	35.2	1673
Austenitic stainless steel	5.3×10^{-6}	4.7×10^6	24.9	1773
Inconel 600	4.7×10^{-6}	3.9×10^6	18.3	1673
Ti alloy	9.0×10^{-6}	3.0×10^6	27.0	1923
Copper	9.6×10^{-5}	4.0×10^6	384.0	1336
Monel 400	8.0×10^{-6}	4.4×10^6	35.2	1573

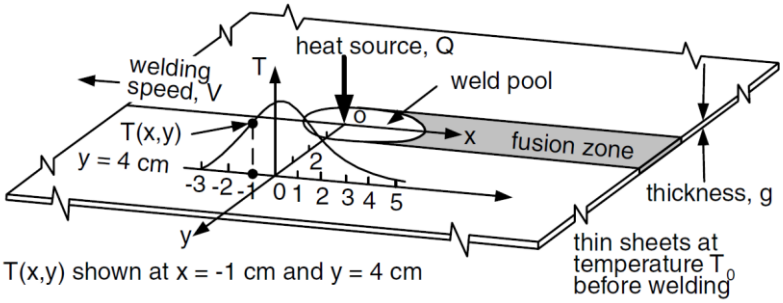

Figure 11 Two-dimensional heat flow of thin workpiece during welding. (2)

Three-dimensional heat flow is shown by equation (4) and schematic presentation of thick sheet in Figure 12.

$$\frac{2\pi(T-T_0)kR}{Q} = \exp\left[\frac{-V(R-x)}{2\alpha}\right] \quad \textbf{(5)}$$

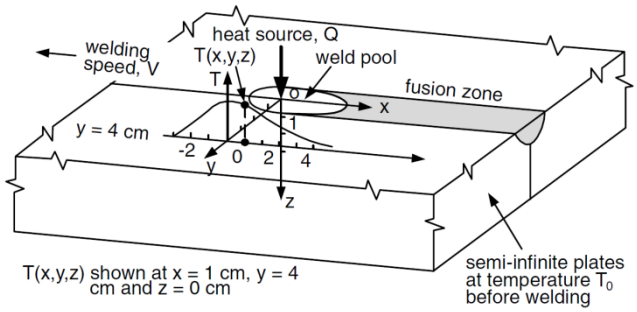

Figure 12 Three-dimensional heat flow of thick workpiece during welding. (2)

Figure 13 shows results which have been calculated with Rosenthal's three-dimensional heat flow equation.

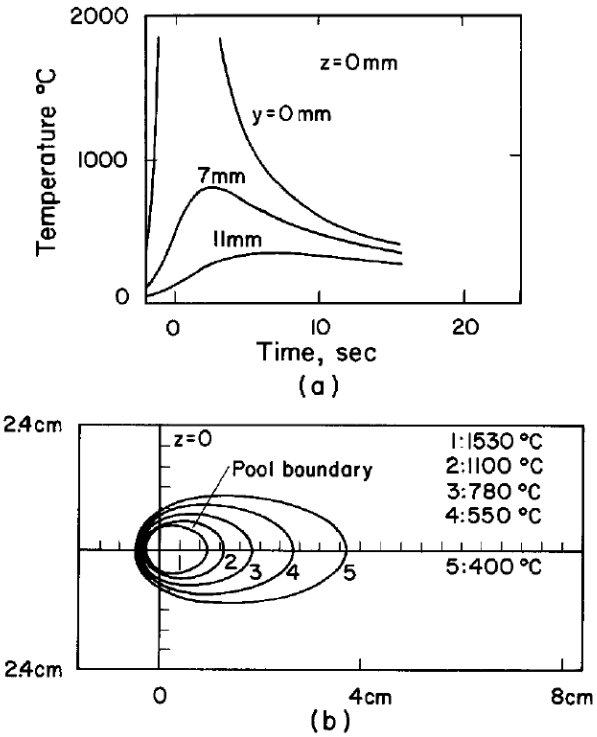

Figure 13 Results of (a) thermal cycles and (b) isotherms which have been calculated with Rosenthal's three-dimensional heat flow equation. Welding speed is 2.4 mm/s and heat input 3200 W. Test material is 1018 steel. (2)

2.4.2 Cooling time $t_{8/5}$

The properties of the welded joint depend on the cooling rate. The thickness of material, joint form, working temperature and welding energy affect the cooling rate. Most significant solid phase transformations of microstructures in HAZ happen between temperatures 800 and 500 ˚C. $t_{8/5}$ describes cooling time for the passing of this temperature range. (1)

Figure 14 shows the effect of the cooling time on the hardness and transition temperature of the impact toughness. The hardness increases with the short cooling time due to the hardening. This kind of martensite structure is brittle. The transition temperature increases and the hardness decreases with the long cooling time. Optimal mechanical properties are reached in area 2. (1)

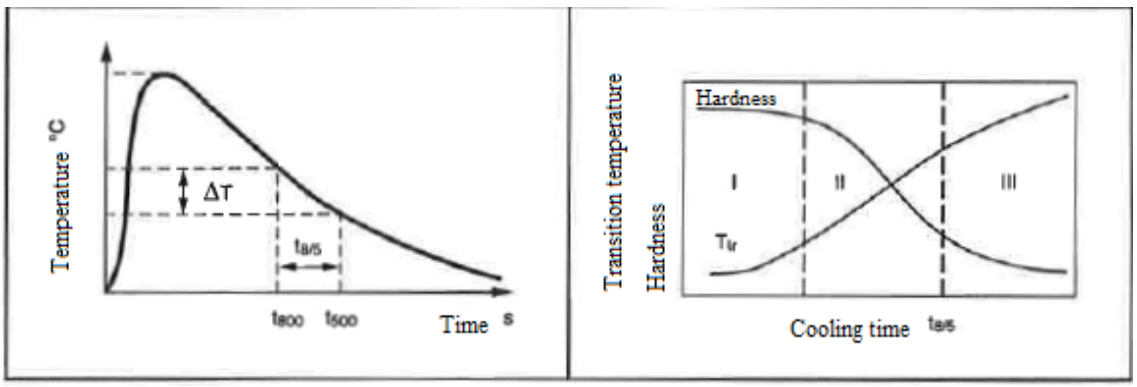

Figure 14: Cooling time $t_{8/5}$ and its effect on hardness and transition temperature of impact toughness of the welded joint. (1)

Working temperature (T_0) means temperature of workpiece in the beginning of the welding process and it will affect the cooling rate of the welded joint significantly. The higher

working temperature causes longer cooling time $t_{8/5}$. The working temperature can be raised with a pre-heating or interpass temperature of multi-run welding. Cooling time $t_{8/5}$ can be calculated for thin plates with two-dimensional cooling according to equation (6) and for thick three-dimensional plates according to equation (7) (1) (9). These equations include simplifications and they can be obtained with the help of Rosenthal's equations.

Two-dimensional cooling for thin plates:

$$t_{8/5} = (4300 - 4{,}3T_0)10^5 \frac{k^2E^2}{d^2}\left[\left(\frac{1}{500 - T_0}\right)^2 - \left(\frac{1}{800 - T_0}\right)^2\right]F_2 \quad (6)$$

Three-dimensional cooling for thick plates:

$$t_{8/5} = (6700 - 5T_0)kE\left[\left(\frac{1}{500 - T_0}\right)^2 - \left(\frac{1}{800 - T_0}\right)^2\right]F_3 \quad (7)$$

where
d = material thickness [mm]
$t_{8/5}$ = cooling time between 800 ˚C and 500 ˚C [s]
T_0 = working temperature [˚C]
k = thermal efficiency (See Table 1)
E = welding energy [kJ/mm]
F_2 = type of joint factor for two-dimensional thermal conduction (See Table 3)
F_3 = type of joint factor for three-dimensional thermal conduction (See Table 3)

Table 3 Effect of the joint type for the coefficient joint form. F_2 means two-dimensional heat conductivity and F_3 three-dimensional conductivity. (1) (9) (Modified table)

Joint type	F_2	F_3
Bead-on-plate welds	1.0	1.0
Square groove with two welding beads	0.9-1.0	1.0

Figure 15 shows transition plate thickness d_t from three-dimensional to two-dimensional heat flow as a function of heat input for different preheat temperatures (9). The d_t means plate thickness at which the transition from three-dimensional to two-dimensional heat flow takes place. (9) Correct equation can be chosen between 2- and 3-dimensional formulas by this figure.

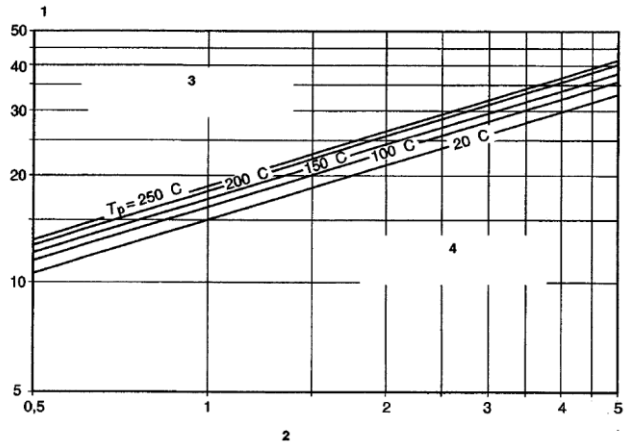

Figure 15 Key: 1 means axis of transition thickness d_t (mm), 2 means axis of heat input (kJ/mm), 3 is area of three-dimensional heat flow and 4 is area of two-dimensional heat flow. (9)

Cooling time $t_{8/5}$ can also be defined with the help of Figure 16, based on plate thickness and working temperature.

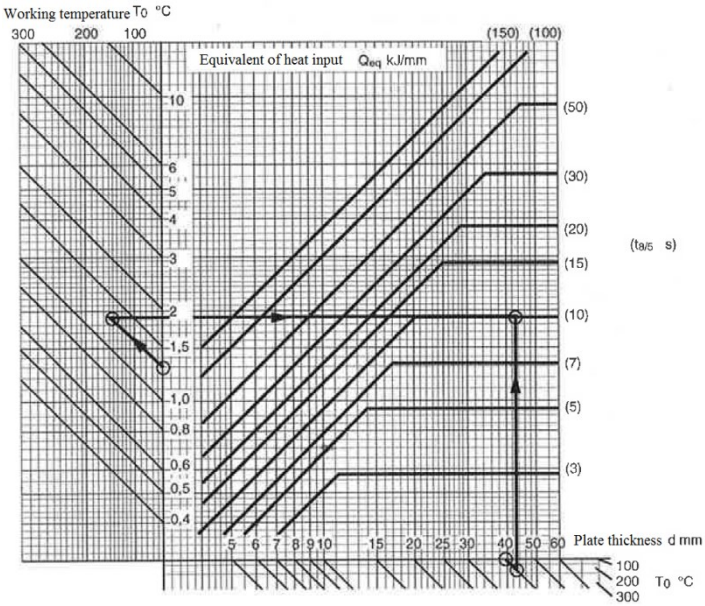

Figure 16 Cooling time dependency on heat input, equivalent working temperature and plate thickness. Equivalent heat input (Q_{eq}=F*k*E) is determined with the help of Table 3. (1)

2.4.3 CCT diagram

Cooling rate affects decomposition of austenite essentially. CCT-diagrams (*Continuous Cooling Transformation*) were developed for heat treatment of alloy steel. Traditional alloy steels are hardened strongly with relatively slow cooling rate. This means that they are not sensitive to cooling time. CCT-diagrams may describe sensitivity to cold cracking when austenitizing temperature is 1350 °C. Hardenability of HAZ of modern strong low-carbon steels depends more on grain size of prior austenite than alloying. The thermal processes during the welding and heat treating of carbon steel differ from each other significantly. The first is temperature peak during welding in HAZ which can approach 1500 °C. The maximum temperature of heat treating is around 900 °C which is less than the peak temperature of welding in HAZ. The second thing is that the heating and cooling rate is high and retention time above A_3 is short during welding process. In heat treating the heating and cooling rate is much slower and retention time above A_3 is much longer. Grain size of welded joint after welding is coarser than corresponding normalized steel structure due to the previous circumstances. Grain size of prior austenite depends on the type of steel, welding energy and nucleation conditions of ferrite. CCT-diagrams do not take into account these circumstances sufficiently. CCT-diagrams were created with the help of small test samples. Microstructures of these small samples do not correspond to real welded joints. Grain size of prior austenite is coarser with small test samples than larger welded joints. Dependency between microstructure and cooling time can be approximated with the help of CCT in many practical cases although CCTs are not commonly valid. (1) (2) (10) (11)

The microstructure of the welded joint and the mechanical properties can be predicted roughly with CCT-diagram which is shown in Figure 17. Worst properties of microstructure are usually created in the fusion line and in the coarse-grained zone of weld. Only the

properties of the fusion line and coarse-grained zone are needed to study for this reason. Properties of weld metal can be critical if welding energy is high. (1)

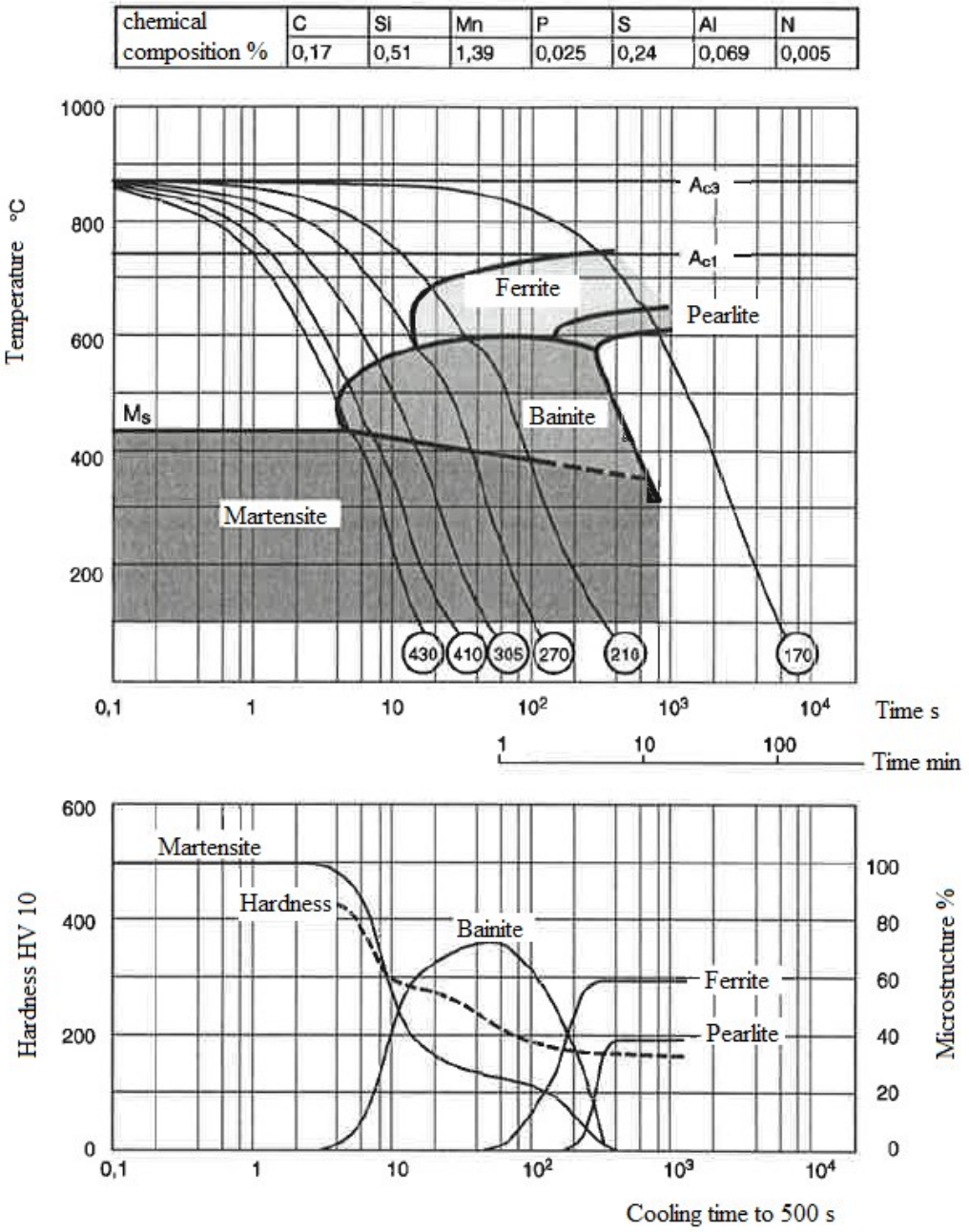

Figure 17 CCT-diagram and microstructure for S355N steels. (1)

2.5 Phases of hypoeutectic carbon steel in coarse-grained zone

Different phases of hypoeutectic carbon steel are the consequence of solid phase transformation. Allotropy of iron crystal makes possible different solution of carbon in iron. Steel whose carbon content is less than 0.8 wt% is hypoeutectic steel. Structural steel like S355N is this kind of steel. Result of very slow cooling rate of S355N is ferrite and pearlite according to Figure 1 and Figure 17. These phases are in equilibrium and solid phase transformation happens with the help of diffusion. Cooling rate of weld is high. Due to the fast cooling phases of microstructures of weld and HAZ are not in equilibrium. Result of high

cooling rate of steel can be martensite or bainite. This chapter is concentrated on microstructures of coarse-grained zone of hypoeutectic carbon steel.

Austenite is stable over 723 ˚C and its crystal structure is face-centred cubic. Austenite is ductile and soft at room temperature. Hardness of austenite can be raised and stabilized with 1.5 wt% carbon content and rapid cooling in room temperature so that maximum hardness 150 HB can be reached. (12)

Ferrite is magnetic, ductile and easy to form at normal temperature and its crystal structure is body-centred cubic. Hardness of ferrite varies between 60 HB and 90 HB according to grain size, but with the help of 4 wt% silicon it can reach over 200 HB. (12)

Cementite, iron carbide Fe_3C, contains 6.68 wt% carbon. Cementite is brittle and its hardness is 820 HB. Cementite is unstable and it is decomposed to austenite and carbon in 1300 ˚C. (12)

Pearlite is a lamellar phase combination of cementite and ferrite according to Figure 19. Precipitations of cementite or ferrite start in grain boundaries of austenite according to Figure 18 (a). The precipitation grows in width and length direction. When the precipitation phase is cementite balance of concentration between carbon and ferrite is small. Carbon content of austenite is decreased when width of adjacent precipitation of cementite grows more. Due to this new core of precipitation is formed according to Figure 18 (b). Ferrite is balanced with the austenite which carbon content is high. Figure 18 (c) shows that growing ferrite push carbon to austenite until core of cementite is created. Same alternation continues and result of this is lamellar structure according to Figure 18 (d). Direction of lamellar growing can vary according to Figure 18 (e). (13)

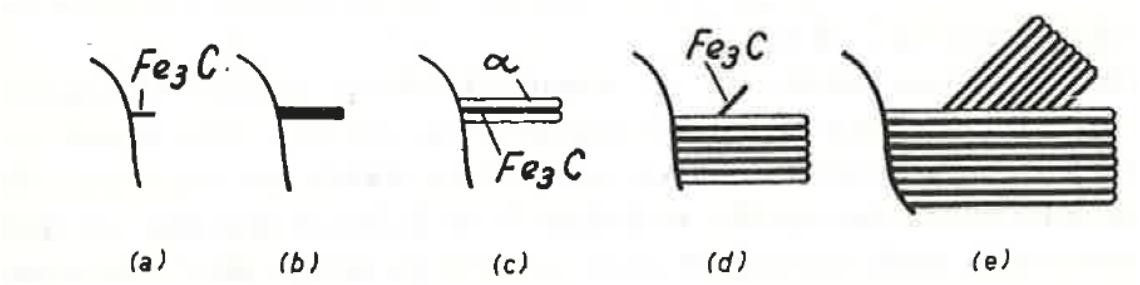

Figure 18 Formation of pearlite. (13)

Interlamellar spacing means distance between cementite and ferrite in pearlite and it can vary according to the temperature. Interlamellar distance is high (0.4 µm) in high temperature. Hardness of this kind of structure is 200 HB. If interlamellar spacing is small (0.1 µm) hardness of pearlite is 400 HB. Formation temperature of pearlite can be controlled by cooling rate. (13)

Figure 1 includes an iron-carbon equilibrium diagram. The equilibrium diagram represents the metastable equilibrium between iron and carbon. Steel with carbon content 0.15 wt% in temperature 1100 ˚C is austenitic. The decomposition of austenite starts when austenite cools and reaches A_3 limit. The steel starts decompose from austenite to ferrite after this limit. When the steel reaches A_1 limit structure is ferrite and austenite. Figure 19 (a) shows 100% lamellar pearlite which is formed when the carbon content has been 0.8 wt%. Figure 19 (b) shows microstructure of ferrite and pearlite which is formed when carbon content is less than 0.8 wt%. The darker areas of this microstructure are pearlite and white areas are ferrite.

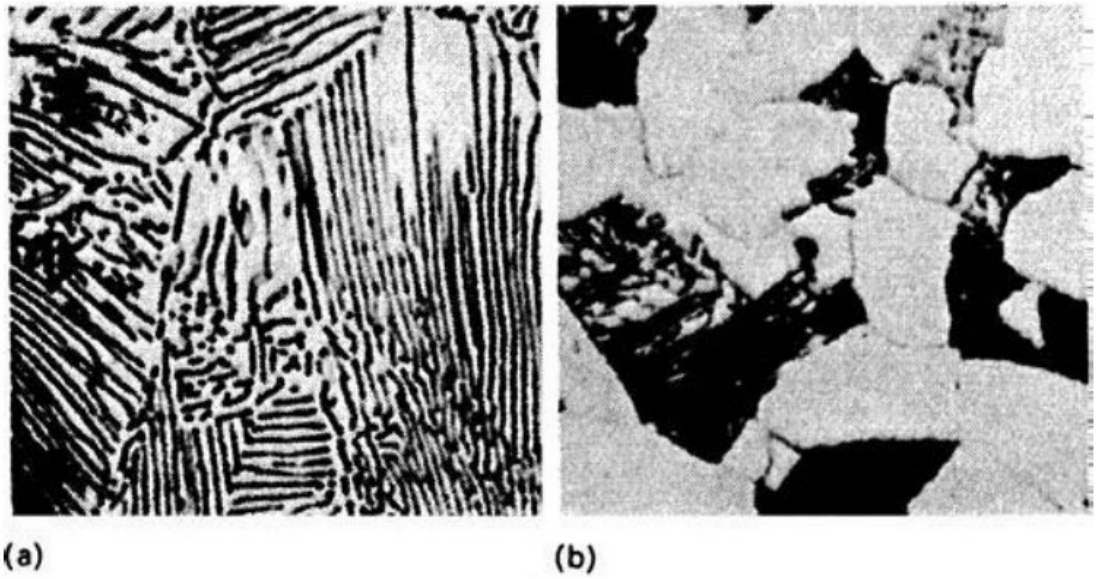

Figure 19 (a) 0.8 wt% C pearlitic steel. Optical micrograph x1000, (b) 0.4 wt% C steel structure ferrite and pearlite. Optical micrograph x1000. (14)

Decomposition happens from austenite to cementite and ferrite by diffusion. Diffusion requires sufficient temperature and enough time. Prevention of diffusion and decomposition of austenite can be made by rapid cooling.

Formation of metastable austenite (which is called also retained austenite) or martensite is formed during rapid cooling without diffusion. Formation of martensite occurs by shear transformation. Crystal structure transforms from austenite (fcc) to martensite (bcc) with shear transformation according to Figure 20.

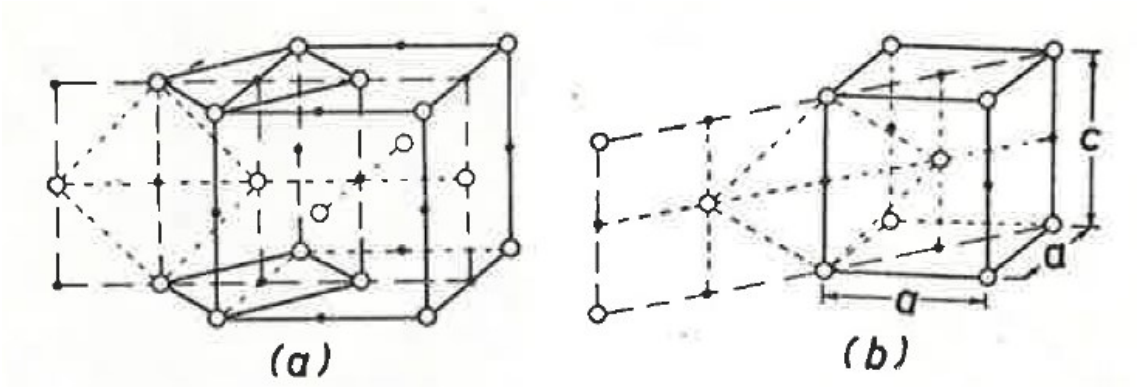

Figure 20 Possible positions of carbon atoms (black points) are shown in unit cells of austenite (a) and martensite (b). (13)

Lath martensite is formed by shear slip and plate martensite is formed by twining shear according to Figure 21. Figure 22 shows that lath and plate martensite are formed according to carbon content. Steels which carbon content is less than 0.6 wt% can form only lath martensite. Lath and plate martensite occur if carbon content is between 0.6 wt% and 1.0 wt%. Steels which carbon content is more than 1.0 wt% form only plate martensite.

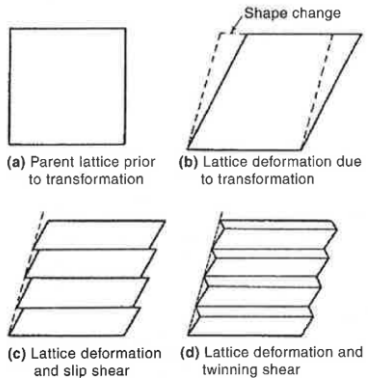

Figure 21 Twining shear and shear slip formation mechanisms of martensite. (15)

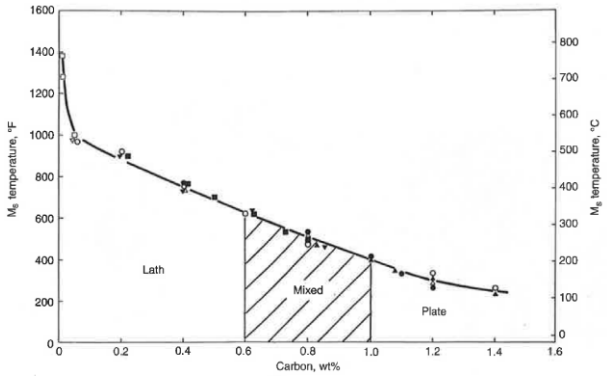

Figure 22 Martensite transformation start temperature versus carbon content. Hardness and type of martensite are shown. (15)

Two different morphologies of ferrous martensite microstructure are shown in Figure 25. The temperature peak in austenitic region and the time determine the grain size of prior austenite. The grain size of prior austenite determines the packet size of martensite. Martensite packets grow inside boundaries of prior austenite. Small size of prior austenite means smaller martensite packets. Strength and ductility are higher with smaller martensite packets. Lath or acicular (meaning needle-like) martensite is shown in Figure 25 (a) and Figure 24. Plate or lenticular (lens-shaped) martensite crystals are shown in Figure 25 (b) and Figure 23. (15)

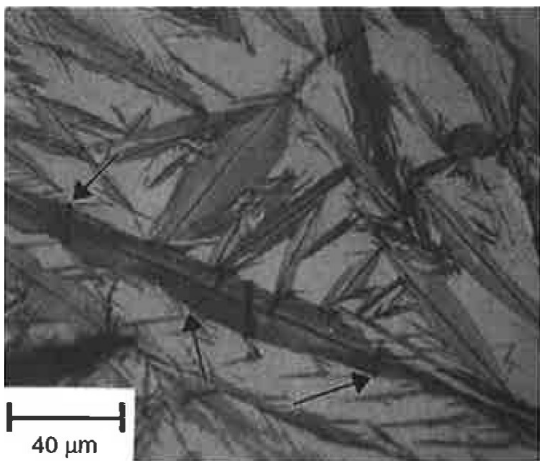

Figure 23 Plate martensite forms in Fe-1.86C steel. Arrows indicate micro-cracks. (15)

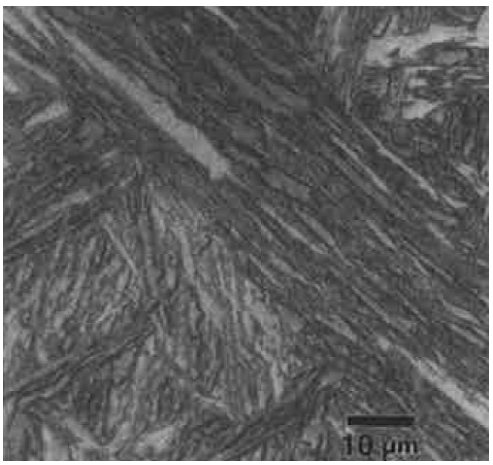

Figure 24 Water-quenched Fe-0.2C steel which has lath martensite crystal structure. (15)

The high hardness and brittleness of martensite are consequence of rapid cooling. Figure 27 shows effect of carbon content on the hardness of martensite compared with relatively small effect of retained austenite in room temperature by the addition of nickel. (14)

Hardness of martensite depends only of carbon content. Other alloying elements and structure of martensite do not affect to hardness of martensite (13). Carbon addition increases hardness according to Figure 27.

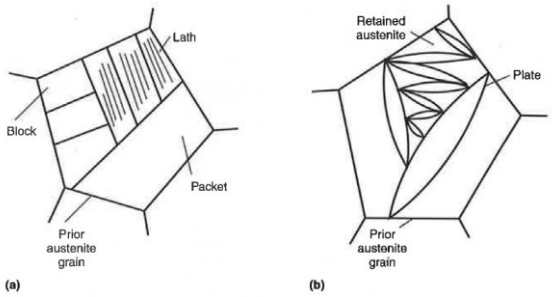

Figure 25 Lath and plate martensite. (15)

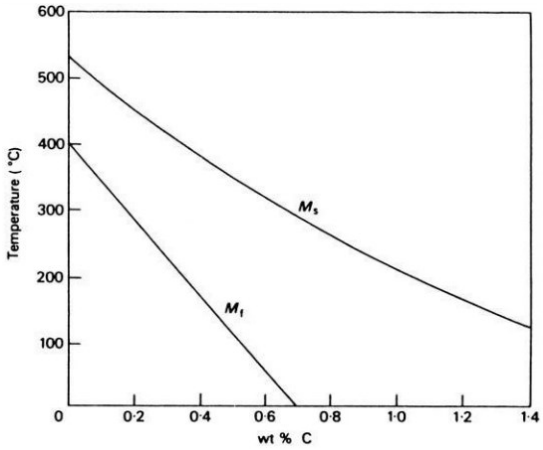

Figure 26 Effect of carbon on M_s and M_f. (14)

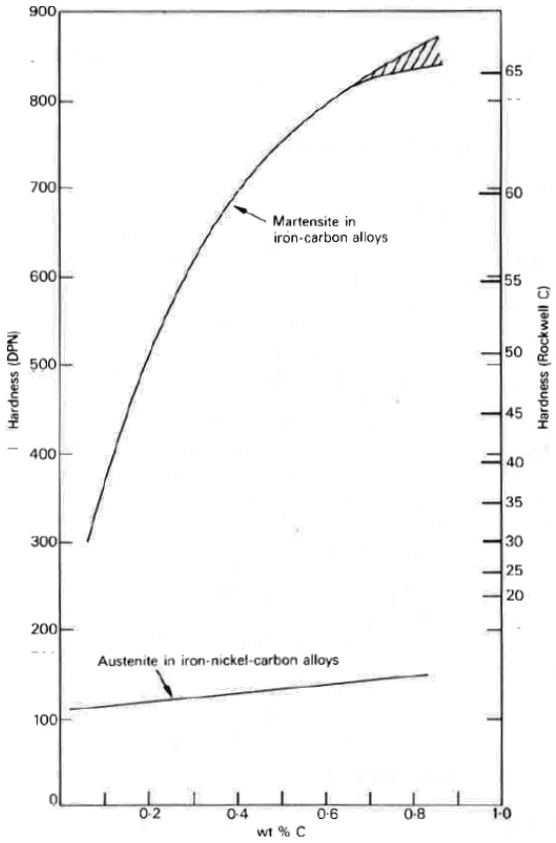

Figure 27 Effect of carbon content on the hardness of martensite and austenite. (14)

M_s means martensite start and M_f means martensite finish temperature. Figure 26 shows the effect of carbon content on M_s and M_f. Retained austenite is formed if structure cools to room temperature, but does not reach M_f limit with 0.7C wt%. (14)

The bainite reaction of eutectoid carbon steel happens in temperatures between 250 ˚C and 550 ˚C with the help of time and carbon diffusion according to Figure 28. Cooling rate is between rate of martensite and ferrite according to CCT diagram of Figure 17 (14). Main forms of bainite are lower and upper bainite (13) (14).

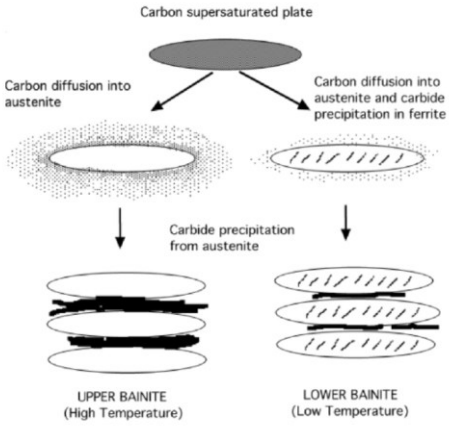

Figure 28 Transition from austenite to upper and / or lower bainite. (14) (15)

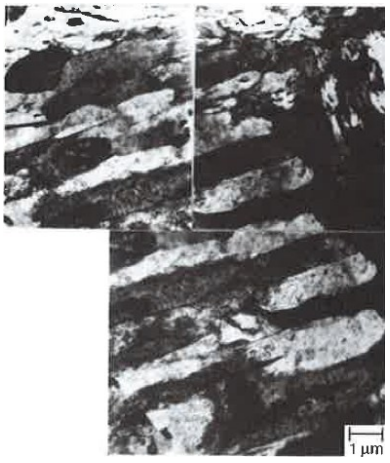

Figure 29 TEM micrograph illustrates substructure of upper bainite in a 2340 steel, austenitized at 1095 ˚C and isothermally transformed at 540 ˚C for 15 h. (15)

The microstructure of upper bainite includes fine plates of ferrite which are about 0.2 µm thick and 10 mm long. These ferrite plates of upper bainite nucleate at the grain boundaries

of austenite according to Figure 28 with the help of carbon diffusion in temperatures between 550 ˚C and 400 ˚C. Figure 29 shows that carbon diffusion happens only in austenite but not in ferrite. Plates grow in clusters which are called sheaves. Sheaves orientate parallel and identical crystallographic orientation. The individual plates are usually separated by low-misorientation boundaries or by cementite particles according to Figure 30 (a) (14) (13). Figure 30 (b) shows bainite without cementite.

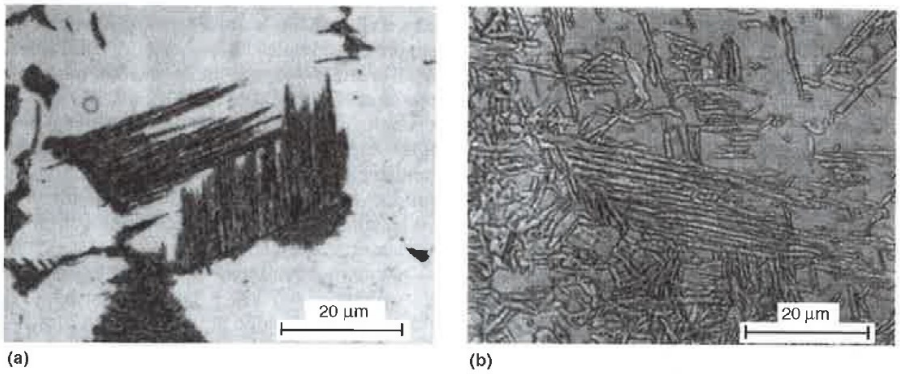

Figure 30 Upper bainite: Optical micrographs of the microstructures produced at 400˚C. (a) Bainite with cementite in Fe-0.478C-4.87Ni wt% steel. (b) Bainite without cementite in Fe-0.485C-4.82Ni-1.55Si wt% steel. (15)

Crystallographic features and a microstructure of lower bainite are similar with upper bainite with the exception of carbide precipitation in ferrite. Cementite precipitations of lower bainite are nucleated at the grain boundaries and inside the plates of ferrite according to Figure 28 with the help of carbon diffusion in temperatures between 400 ˚C and 250 ˚C. (13) (14)

Formation of lower bainite occurs at lower temperature than formation of upper bainite. Lower bainite is much tougher and usually stronger than upper bainite because only a fraction of the carbon partitions into the austenite and the inter-plate carbides are much smaller than corresponding carbides in upper bainite. (14)

Hardness of upper bainite which resembles lath martensite with light optical microscope is 400 HB. Hardness of lower bainite which resembles plate martensite with optical light microscope can reach 600 HB. (13)

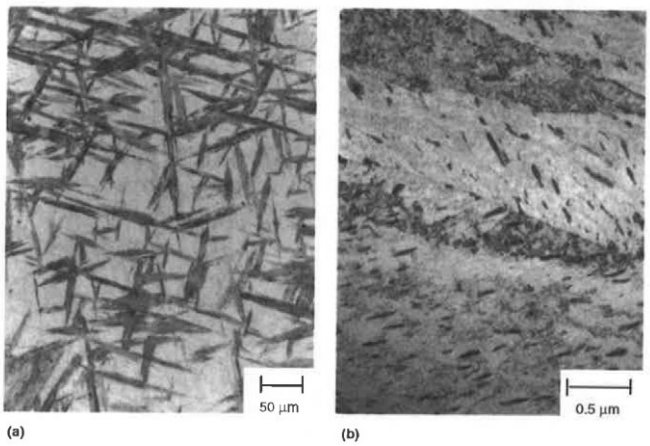

Figure 31 Lower bainite. (a) Light micrograph illustrating sheaves of lower bainite in Fe-0.3C-4Cr wt% steel. The light matrix phase is martensite. TEM micrograph illustrates subunits of lower bainite. (15)

HV hardnesses of previous phases of microstructures are collected in Table 4.

Table 4 HV hardnesses of the phases forming the microstructures.

Phase	HV Hardness
Austenite	136
Ferrite	90
Ferrite with 4 wt% silicon	190 (max)
Pearlite (inter lamellar spacing 0.4 µm)	190
Pearlite (inter lamellar spacing 0.1 µm)	380
Lower Bainite	630
Upper Bainite	420
Martensite (Carbon content of structural steel 0.15-0.16 wt% according Figure 27)	440

2.6 Recognition of phases in coarse-grained area

Phases of microstructure in coarse-grained zone can be recognized according to Table 5. Microstructures and their comments were loaded from internet page of IIW (*International Institute of Welding*) and collected to this table. (16)

Table 5 Classification of microstructures in HAZ. (16) Modified.

Phases of microstructure	Definition	Microstructure
• Coarse acicular ferrite (AF) • Ferrite F • Upper bainite (UB)	AF has nonpolyhedric constituents of ferrite laths with boundaries having a small angle. The pseudo pearlite (carbide) islands use to segregate along laths. AF has relatively low toughness.	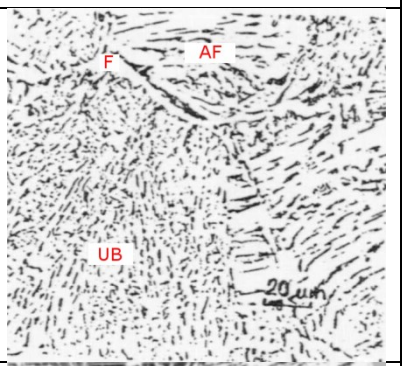
• Upper bainite I (UB) • Martensite (M)	Upper bainite I is composed by a complex of parallel ferrite laths with M-A micro-structure between them which can be partially decomposed to mixture of ferrite and carbides.	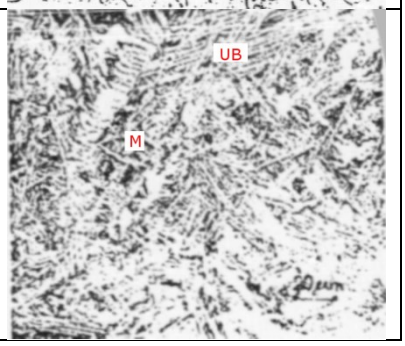

• Upper bainite I (UB)	Upper bainite I is composed by a complex of parallel ferrite laths with M-A micro-structure between them which can be partially decomposed to mixture of ferrite and carbides.	
• Upper bainite II (UB)	Upper bainite II is composed by a complex of parallel ferrite laths along which cementite in form of continuous film or single particles.	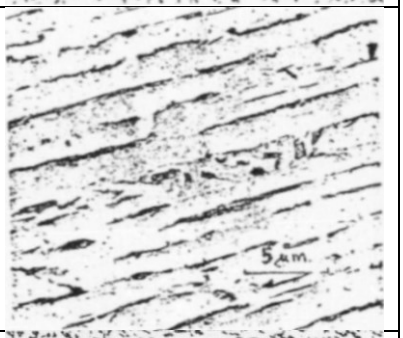
• Lower bainite (LB)	Lower bainite is formed of ferrite laths with interphases of carbide particles. It is composed consequence of high cooling rate as upper bainite.	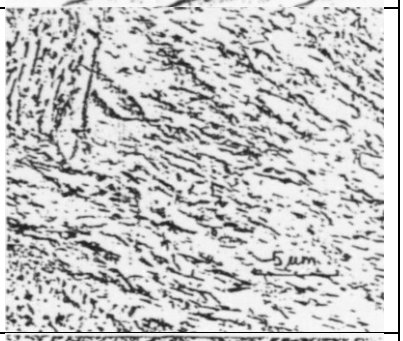
• Martensite (M)	Martensite has acicular structure. In welded joints of low-carbon and low-alloy steels it is present as self-tempered martensite.	

2.7 Determination of hardness by VTT/OU method

VTT/OU method was developed to avoid hydrogen cracking of welds with collaboration of VTT (Research Centre of Finland) and OU (Osaka University) in the mid-1980's. (17)

Determination of hardness with VTT/OU method is based on calculation of $t_{8/5}$, carbon content and chemical composition of base material. P_v can be calculated according to equation (8). (17)

$$P_v = C + \frac{Mn}{3} + \frac{Ni}{8} + \frac{Cr}{12} + \frac{Mo}{2} + \frac{Cu}{5} \quad (8)$$

Maximum Vickers hardness of the coarse-grained zone can be calculated by equation (9) where C is carbon content. (17)

$$HV = (922C - 230P_v + 250)\exp\left(\frac{-3\Delta t_{8/5}}{310^{Pv}}\right) + 188P_v + 80 \quad (9)$$

2.8 Mixing

Rate of mixing means proportion of base material in weld metal. Mixing affects mechanical properties and contents of alloying elements of weld. Welded metal consists of filler metal and melted base material. Mixing of weld metal depends on the welding process, groove form and welding parameters. Typical rate of mixing is with MAG welding 20-40 %. The mixing can be counted for butt welds or to bead-on-plate welds according to

Figure 32 and according to equations (10) and (11). (1) (18)

$$Dilution_1 = \frac{P}{L+P} \times 100\ (\%) \quad (10)$$

$$Dilution_2 = \frac{P_1+P_2}{L+P_1+P_2} \times 100\ (\%) \quad (11)$$

where
P = diluted cross-section area of weld [mm^2]
P1 = diluted cross-section area of weld [mm^2]
P2 = diluted cross-section area of weld [mm^2]
L = cross-section area of weld metal [mm^2]

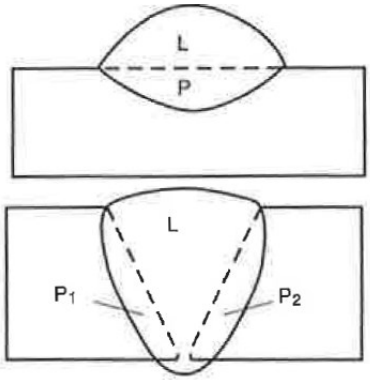

Figure 32 Mixing for bead-on-plate and butt welds (edited picture). (1)

2.9 Determining weld metal constitution with Schaeffler and WRC 1992 diagram

The Schaeffler and the WRC-1992 diagrams can be used to predict the microstructure which is a combination of filler metal and stainless steel. Microstructure of dissimilar weld joints can be predicted with the help of these diagrams. The best known benefit of high ferrite content is preventing hot cracking. The best known disadvantages of high ferrite content are worse mechanical properties and corrosion tolerance. Composition of molten weld pool strongly affects the ferrite content. Mixing of base metal and filler metal affects composition of molten weld pool. Shielding gas and cooling rate affect composition of molten weld pool also. Schaeffer diagram takes into account these circumstances. Ferrite content of austenitic stainless steel can be predicted with the help of Schaeffer diagram.

Figure 33 shows Schaeffer diagram which presents relationships between composition and ferrite content. Ferrite content is calculated with the help of diagram, nickel and chromium equivalents. (2) (19)

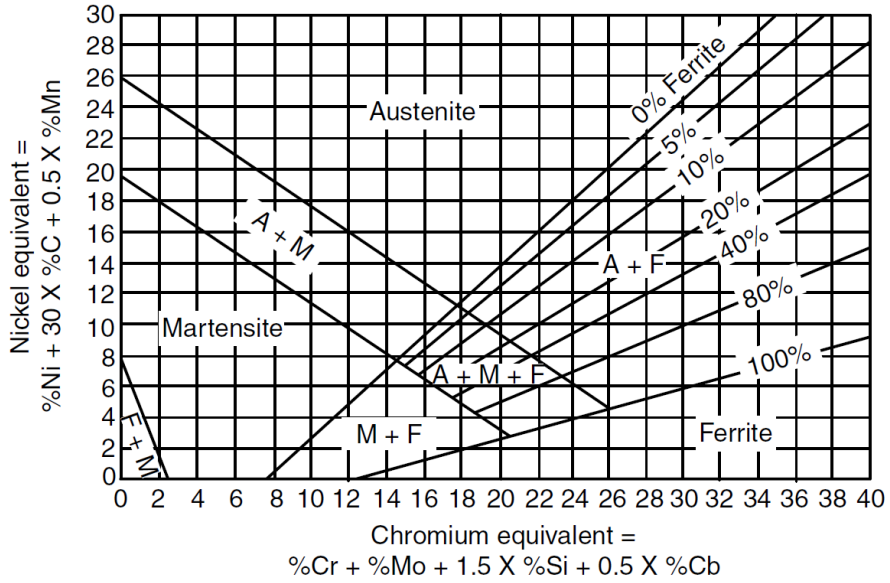

Figure 33 Schaeffler diagram. (2)

There are many similar diagrams which are used to predict ferrite content. The latest diagram is the WRC-92 diagram according to Figure 34. Prediction of ferrite content of WRC-92 is more accurate than with the other diagrams. Hot cracking risk is smallest with type of FA solidification. (2) (19)

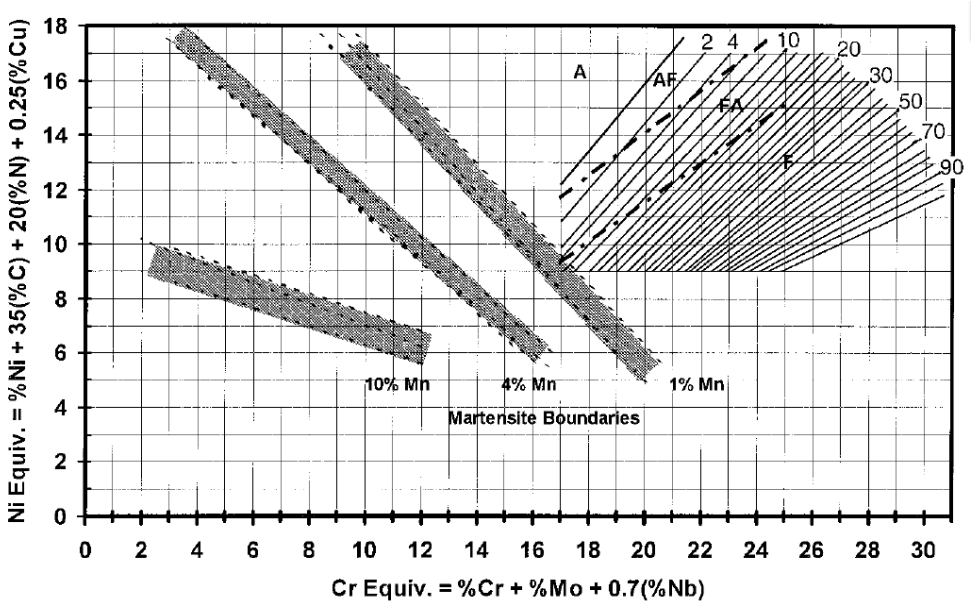

Figure 34 WRC-1992 diagram with martensite boundaries. (2)

2.10 Phase prediction of dissimilar metal welding

Dissimilar metal welding (DMW) is used to join stainless steel to other materials. Phases of dissimilar metal joint with austenitic stainless steel, low alloy steel and carbon steel can be predicted with the help of Schaeffler diagram and WRC-1992 diagram in weld metal

and transition region microstructure (8). Using these diagrams based on that microstructure of weld depends more on composition than welding parameters or cooling time (6).

Tie lines are used with prediction of amount the phases with binary phase diagrams and lever rule. Tie-line can be used to also predict the microstructure in the transition region at the fusion boundary of dissimilar weld. Tie-lines are drawn in Schaeffler diagram of Figure 110 and WRC-1992 diagram of Figure 111. Tie-line is drawn between the composition of filler metal and the base metal. Phases of microstructures can be evaluated with the help of these tie-lines and calculated rates of dilutions according to the Figures. The microstructures are usually in a narrow about 1 mm thick region between base metal and HAZ. (6) (8) (20)

Figure 35 shows types of fusion boundaries of dissimilar metal welding. Type 1 means fusion boundary which grows with normal epitaxial growth when grains are oriented roughly perpendicularly to the fusion boundary. When the base metal is ferritic and at temperatures near melting point and weld metal is austenitic, normal epitaxial growth may be supressed. The result of this kind of growing is called type 2 boundaries, which run roughly parallel to the fusion boundary according to the Figure 36. (8) (19)

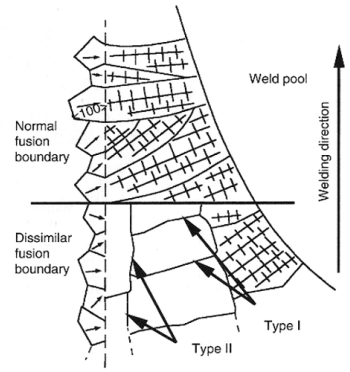

Figure 35 Formation of Type 1 and 2 boundaries. (8) (19)

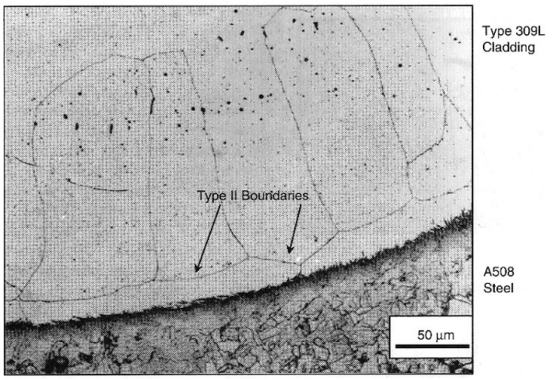

Figure 36 Fusion boundary region of A508 pressure vessel steel clad with Type 309L weld cladding. (8)

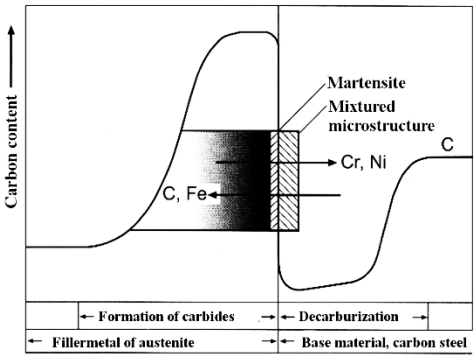

Figure 37 Carbon diffusion in dissimilar metal joint. (6)

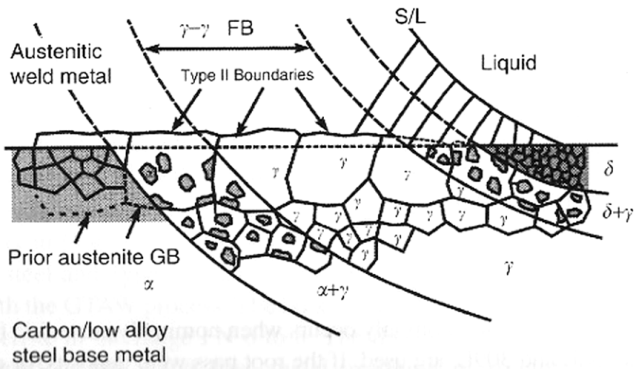

Figure 38 Mechanism of Type 2 boudary formation during dissimilar metal welding between an austenitic weld metal and carbon steel. (8) (19)

Carbon diffusion can take place near the fusion line when temperature is more than 300 or 400 °C due to different composition of base material and weld metal according to Figure 37. Carbon diffuses from the higher carbon content area to the lower carbon content area. This leads to narrow zones which include low and high amount of carbon near fusion line according to Figure 38. High carbon content causes narrow martensitic region which is

called carbon pile-up at the fusion boundary in stainless weld metal side by carbon migration. Hardness of this zone is high and brittle according to Figure 39. Figure 38 shows mechanisms of Type 2 boundaries which are typical of DMW-welding. Decarburization is a phenomenon which is caused by decreasing carbon content due to carbon diffusion which is called also carbon migration. Hardness of decarburization zone which is called also carbon-depleted zone is low due to small carbon content. Figure 39 shows zones of tie-line. Small indentations near the fusion line in Figure 39 (b) indicate higher hardness due to martensite. (6) (8)

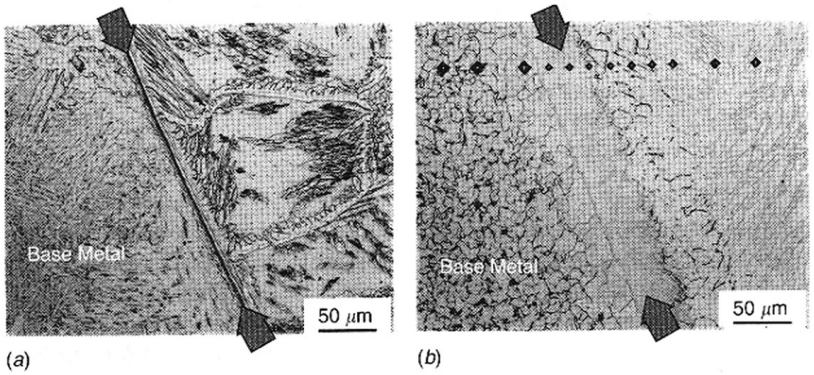

Figure 39 Microstructure between A36 structural steel and 2209 filler metal: (a) top; (b) bottom. Note the traverse of Vickers hardness impressions across the fusion boundary in the bottom of weld. The smaller impressions indicate higher hardness due to martensite, in the transition region. (8)

2.11 Weldability of structural steels

On the basis of the chemical composition of steel the tendency of hardening and cold cracking with CE (*Carbon Equivalent*) can be evaluated according to SFS EN 1011-2 equation (12) (2). This equation suits best for HAZ of steels which is not hardened totally in consequence of welding. CE is suitable for non-alloyed, fine-grained and low-alloy steels, like S355N structural steel. If CE is between $0.41 \leq CE \leq 0.45$ the weldability will be good when dry and basic filler metal is used (1) (9). Limitations of CE are shown in Table 6.

$$CE = C + \frac{Mn}{6} + \frac{Cr + Mo + V}{5} + \frac{Cu + Ni}{15} \quad (12)$$

The influence of the chemical composition on the cold cracking behaviour can be evaluated also with the help of CET according to SFS EN 1011-2 according to equation (13). Limitations of CET are shown in Table 6. This equation is suitable for carbon steels, carbon-manganese steels and micro-alloying of fine-grain steels. (1) (9)

$$CET = C + \frac{Mn + Mo}{10} + \frac{Cr + Cu}{20} + \frac{Ni}{40}\ [\%] \quad (13)$$

Table 5 Limitations of CE and CET according to SFS-EN 1011-2. (9)

Wt% contents		
Element	CE	CET
C	0.05...0.25	0.05...0.32
Si	max 0,8	max 0,8
Mn	max 1.7	0.5...1.9
Cr	max 0.9	max 1.5
Cu	max 1.0	max 0.7
Mo	max 0.75	max 0.75
N	-	max 0.06
Ni	max 2.5	max 2.5
Ti	-	max 0.12
V	max 0.20	max 0.18
B	-	max 0.005

The weldability index can be calculated with the P_{cm} according to equation (14). This equation is recommended to use for high-strength tempered steels which carbon content is no more than 0.22% and it is suitable for HAZ which microstructure is fully martensitic as consequence of rapid cooling. (1)

$$P_{cm} = C + \frac{Si}{30} + \frac{Mn + Cu + Cr}{20} + \frac{Ni}{60} + \frac{Mo}{15} + \frac{V}{10} + 5B \quad (14)$$

The hydrogen cracking can be avoided with preheating. Need of preheating is evaluated with CE and CET. Preheat temperature is possible to calculate with the help of CET, plate thickness d, the hydrogen content of the weld metal HD and the heat input according to SFS EN 1011-2 using equation (15). (9)

$$T_P = 697 \text{ x } CET + 160 \text{ x } \tanh(d/35) + 62 \text{ x } HD^{0,35} + (53 \text{ x } CET - 32) \text{ x } Q - 328 \; [^{\circ}C] \quad (15)$$

This relationship is valid for structural steel which yield strength is less than 1000 N/mm^2. The variables of the equation have following limits: CE = 0.2 to 0.5 %, d = 10 to 90 mm, HD = 1 to 20 ml/100 g and Q = 0.5 to 4.0 kJ/mm.

2.12 Welding procedures

Test samples were welded with MAG (*Metal Active Gas Welding*), TIG (*Tungsten Inert Gas Arc Welding*), LBW (*Laser Beam Welding*) and LAHW (*Laser Arc Hybrid Welding*). The purpose of this chapter is to introduce main principles of the welding procedures which have been used in this diploma work.

In the arc welding the electric energy is changed to heat with the help of the arc. The temperature of the arc which has been created is so high that it is possible to melt all metals with it. The arc is an electric discharge in gas between welding electrode and base material which requires enough particles in gas which are electrically charged. Formation of the arc requires the air gap which is small enough, ionized gas and enough high voltage. (20)

The electrons go towards the anode and the ions towards the cathode according to Figure 40. The electrons crash to the gas molecules. Due to this the electronic balance is disturbed

and gas molecules decompose into atoms. This decomposition of gas is called dissociation. The kinetic energy of ions and electrons are changed to heat with the help of crash. (20)

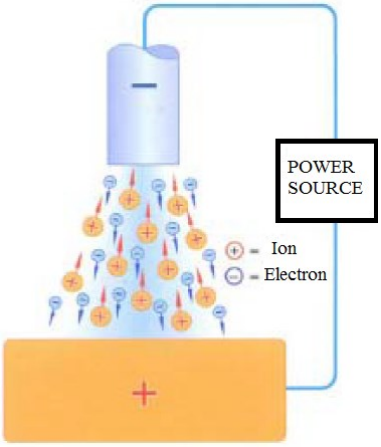

Figure 40 Current in arc. (20) Modified.

GMAW (Gas Metal Arc Welding) is process that melts and joins metal by heating with the help of an arc according to Figure 41. The arc is formed between base metal and filler wire electrode. As shielding gas of the molten weld pool is used inert gases such as argon or helium or some active gas like CO_2 or their mixtures (Ar-CO_2 and Ar-O_2). The name of GMAW process is MIG (Metal Inert Gas) when inert gas is used. When active gas is used the name of the welding process is MAG (Metal Active Gas). (2)

The welding gun wire drive control system pulls filler wire from wire reel and leads it through welding gun to workpiece, as shown in Figure 41 (a). The shielding gas goes from shielding gas cylinder trough the torch body to shielding gas nozzle which is directed to weld pool to protect it from the air according to Figure 41 (a) and (b). Figure 41 (b) shows that the wire electrode is connected to copper contact tube which is connected to the welding cable 1 which comes from the power source. The cable 2 is connected from the power source to the weld metal. (2)

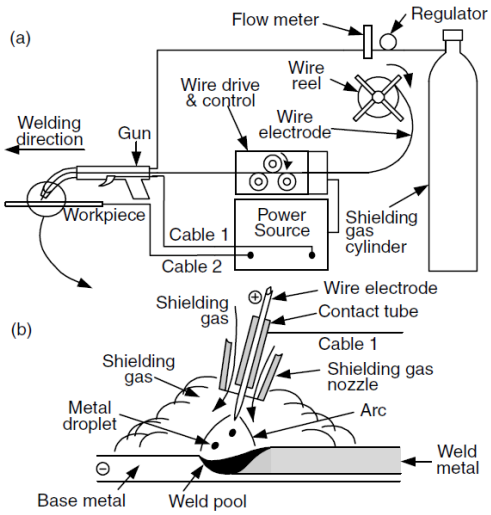

Figure 41 Schematic presentation of GMAW (2).

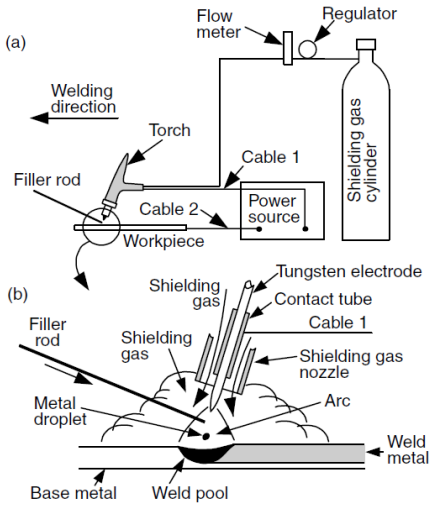

Figure 42 Schematic presentation of GTAW (2).

GTAW (Gas-Tungsten Arc Welding) is a process that melts and joins metals with the help of an arc according to Figure 42. Tungsten electrode is nonconsumable and shielding gas is used. Figure 42 (a) shows torch holding the tungsten electrode which is connected to a shielding gas cylinder and power source. The tungsten electrode is often cooled with contact tube by water according to Figure 42 (b). This copper contact tube is connected to the welding cable 1 from the power source. Welding current and heating water use same cable.

Cable 2 is connected to the workpiece. The shielding gas goes from shielding gas cylinder trough the torch body to shielding gas nozzle which is directed to weld pool to protect it from the air. Used shielding gas of GTAW is usually argon or helium. For this reason, GTAW is also called TIG (Tungsten Inert Gas) welding. Filler metal is used if needed. (2)

Laser is brought with stimulated emission with the help of an electrical power source by optical pumping. This kind of monochromatic and coherent light is called LASER (Light Amplification by the Stimulated Emission). Laser beam is focused by optical lenses to smaller area which increases energy intensity. (21) (2) (22)

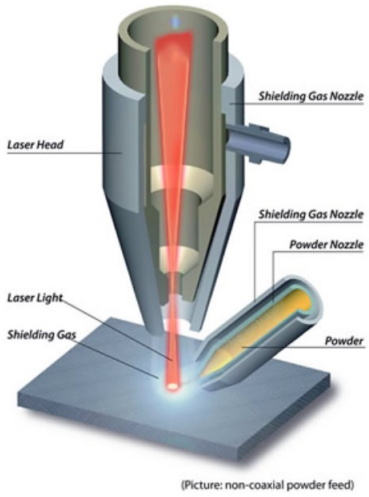

Figure 43 Schematic presentation of LBW. (23)

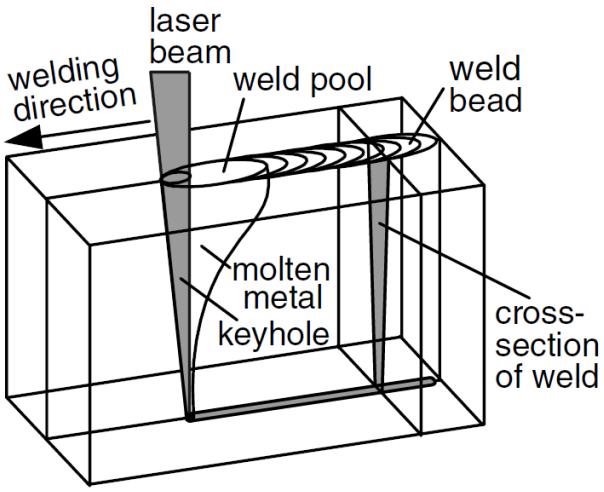

Figure 44 Principle of LBW (2).

LBW (Laser Beam Welding) is a welding process that melts and joins metals by heating them with a laser beam. The laser beam is produced by solid state laser or gas laser. Figure 43 and 44 show principle of laser welding. Shielding gas and filler metal are used according to Figure 43. (2) (22)

Plasma which is produced during LBW can absorb and scatter the laser beam and reduce penetration. The shielding gas to protect the molten metal can be directed to blow the plasma away from weld pool. Most used shielding gases of LBW are argon, helium and their mixtures. (2)

Some advantages of LBW are deep and narrow welds with high welding speed because LBW has high energy intensity. Narrow HAZ also means little distortions with small heat input and small distortions (2) (24). Disadvantage of LBW is hardening of HAZ with thick plates. Heat input is low due to high energy intensity. This leads to the quick solidification and cooling of the weld. Due to this weld can become hard and more brittle structure of martensite (25). On the other hand hardening depends on carbon content and other alloying elements. Martensite which is formed during laser welding has fine-grained microstructure. That is why this kind of microstructure is less brittle. (5)

Penetration of GMAW-weld is smaller than that of LBW and heat input of GMAW is greater than in LBW which leads greater distortions. Due to the greater heat input GMAW welded microstructure is more ductile than LBW welded microstructure.

LAHW (Laser Arc Hybrid Welding) is a combination of LBW and arc welding which principle is shown in Figure 45. Laser-MAG welding is combination of advantages of LBW and MAG. In the hybrid welding the heat input is bigger than in LBW. This leads to

the slower cooling rate which causes tough and soft structure of weld. On the other hand penetration is deeper than in MAG-welding (2).

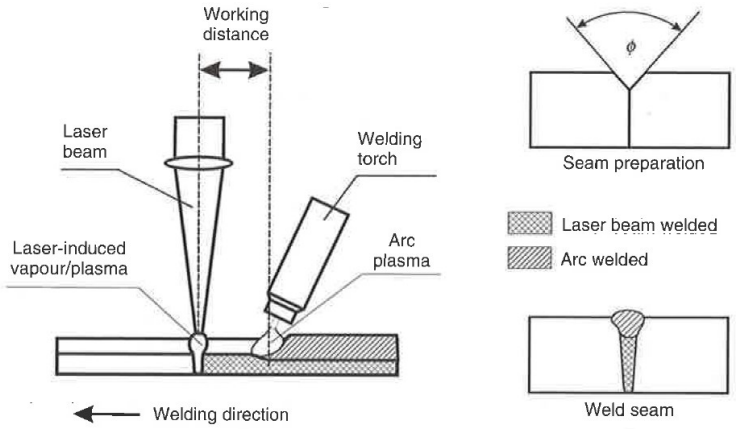

Figure 45 Schematic presentation of LAHW. (26)

2.13 Material modelling

The material modelling can be divided into CFD (*Computational Fluid Dynamics*) and FEM (*Finite Element Method*) analysis. CFD analysis is modelling of behaviour of fluids. Cooling time and dimensions of HAZ and weld can be determined with the help of CFD analysis. CFD analysis is possible to make with the help of 3D Flow software.

FEM analysis is investigation of behaviour of solids. Residual stresses can be determined with the help of CFD and FEM analyses. FEM analysis can be made with the help of Sysweld or Elmer software.

2.14 Residual stresses and distortions

Welded structure can contain external and internal stresses. External stresses disappear when external loads are removed, but not internal stresses. The internal stresses are called residual stresses. (27) (2)

There are two kinds of internal stresses. The first kind of stress is macroscopic stress. Macroscopic stress is influenced over many grains of microstructure and it can be measured easily by destructive mechanical means. Thermal treatments, mechanical operations, chemical processes and combinations of these can cause macroscopic stresses (28) (27). The second kind of residual stress is called structural micro-stress. Structural micro-stress is influenced in the area of one grain. Difference in mechanical properties of different phases or by yield anisotropy between individual grains may generate structural micro-stresses. (27) (28) The role of macroscopic stresses is well known and taken into account by design engineers but not the structural micro-stresses (27).

Three identical metal bars were connected to two rigid blogs at room temperature according to Figure 46 (a). If the middle bar is heated up, its thermal expansion causes expansion and compression stress until yield strength is reached. Figure 46 (b) shows how the middle bar cools down and its thermal contraction causes tensile stress until yield stress is reached. (2)

The weld metal and adjacent base metal are analogous to the middle bar according to Figure 46 (c). Residual stresses are the consequence of the cooling due to thermal expansion and contraction. (2)

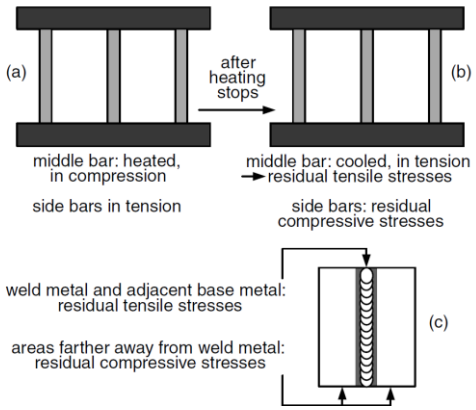

Figure 46 Thermally induced stresses: (a) during heating; (b) during cooling; (c) residual stresses in weld. (2)

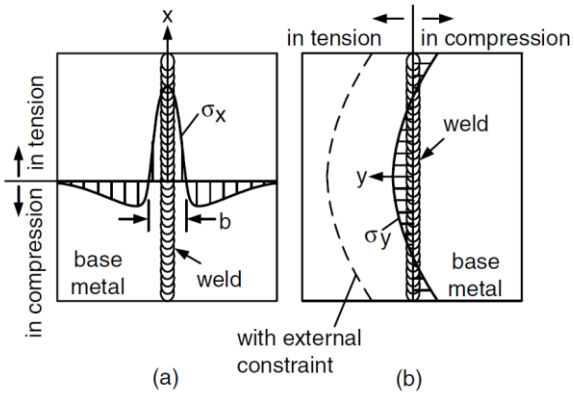

Figure 47 Distributions of longitudinal (σ_x) and transverse (σ_y) residual stresses in butt weld. (2)

Figure 47 (a) and (b) show the distribution of residual stresses in butt weld (2). Residual stresses can be measured by different methods like X-ray diffraction and contour method which are presented later.

The workpiece has a tendency to distort due to solidification shrinkage and thermal contraction. The main types of weld distortions are illustrated in Figure 48. The welded part can shrink in the transverse direction according to Figure 48 (a) or in longitudinal direction according to Figure 48 (b). Figure 48 (c) shows that angular distortions usually occur if the weld is done on top of the workpiece only. The weld is wider at the top side than at bottom. This causes more solidification shrinkage and thermal contraction at the top of the weld than at the bottom. Due to this the resultant of angular distortion is upward. Fillet weld between vertical and horizontal plates pull the horizontal sheet toward vertical sheet. This causes angular distortion in the horizontal sheet according to Figure 48 (d). (2)

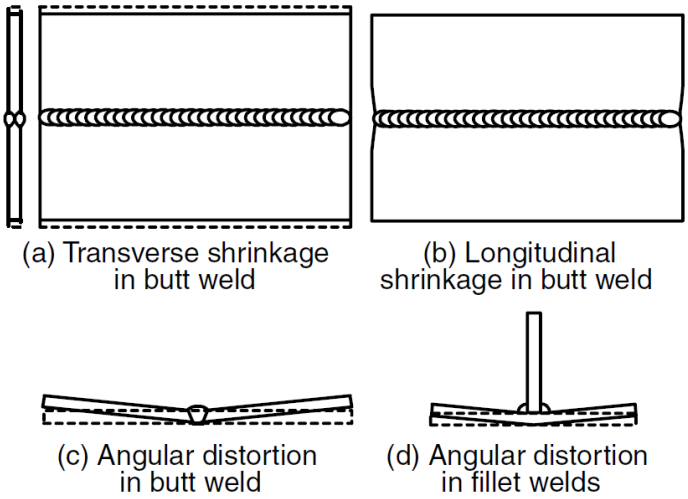

Figure 48 Distortions in welded parts (2).

Distortions of thin plates are larger than those in thicker plates with the same heat input, but residual stresses are higher with thicker plates. Distortions can be avoided by stiffeners. Stiffness of the structure is due to added residual stresses because free shrinkage is prevented. (29)

2.15 X-ray diffraction

X-ray diffraction (XDR) is one of most used measuring method of residual stresses. Benefits of this method are fast and non-destructive measuring. The biggest restriction of this method is ability to measure stresses only 7-15 μm deep. (30)

The accelerated electrons give a part of their energy when hitting to the cathode material. Atoms of material are gotten excited state due to electrons which have extracted from electron atmosphere. Discharge of excited state causes moving of electron from one shell to another shell. This electron moving causes X-radiation. The X-radiation causes strong intensity peak in spectrum of X-radiation. CrK_{α}-radiation is most used with analysis of steel. (30)

The distance between points of lattice is constant in non-stressed materials. If stressed material is exposed to X-rays, to moving of intensity peak of x-radiation due to change of distance between lattice levels can be detected. (30)

The mean lattice spacing is changed by elastic strain. Because of this only elastic strains can be measured by X-ray diffraction. If elastic limit is exceeded, all residual stresses are only elastic after deformation. (28)

Determination of residual stress of material is based on law of Bragg which is shown in equation (16) (28). d is distance between points of lattices, Θ is angle of incoming X-ray, n is multiple of wave length and λ is wave length of radiation. Principle of this equation is shown in Figure 49. (30) (31) (32) (33)

$$2d \sin\theta = n\lambda \tag{16}$$

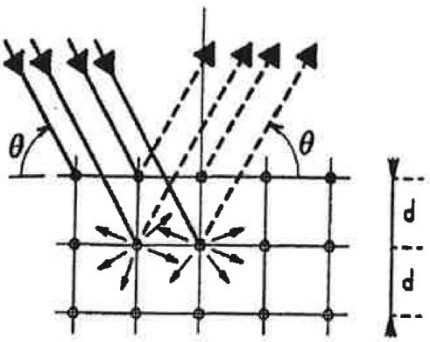

Figure 49 Principle of Bragg's law. (34)

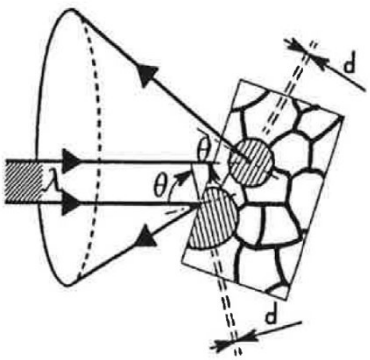

Figure 50 X-ray is reflected as pattern of cone in polycrystalline material. (34)

If X-ray hits lattice planes only in right angle, scattering will happen. Polycrystalline metals have some amount grains which have right angles. This makes scattering possible. Reflected X-rays form pattern of cone according to Figure 50. (30)

Under tension load distance of lattice planes grows in tension direction and decreases transverse of load according to Poisson's phenomenon. Distance between lattice planes with non-stressed material d_{hkl} can be calculated according to equation (17), where a is lattice constant and h, k and l are Miller's indices. (30)

$$d_{hkl}=\frac{a}{\sqrt{h^2+k^2+l^2}} \quad (17)$$

Strain is possible to calculate with the help of information of distance between unstressed material d_0 and angle of Bragg's law θ_0 according to equation (18). (33)

$$\varepsilon_y = \frac{d-d_0}{d_0} = \frac{\Delta d}{d_0} - (\theta - \theta_0)\cot\theta_0 = -\Delta\theta cot\theta_0 \quad (18)$$

Stress σ_y can be calculated according to Hooke's equation (19) where E is elastic modulus. (33)

$$\sigma_y = E\,\varepsilon_y \quad (19)$$

In the determination of the stress of the sample the displacement of peak of diffraction $\Delta\theta$ must be as large as possible so that the accuracy of measurement would be good. Large displacement is reached by using as large 2θ angle as possible. Previous condition is reached by using suitable wave length and lattice planes. This condition means with ferritic and martensitic steels that lattice plane is {211} and wave length is 2.2911 Å. Displacement of peak of diffraction must be sufficiently large because defects exist in lattice and X-rays are not fully monochromatic. Large displacement of peak of diffraction is changed to a bell-shaped curve for this reason. Accuracy of analysis demands sufficient displacements. (30)

Reliable defining of displacement demands measuring with many different angles. Measuring is made least from 6 directions for stress calculation. Figure 51 shows change of diffraction peaks when detector angle changes. (30)

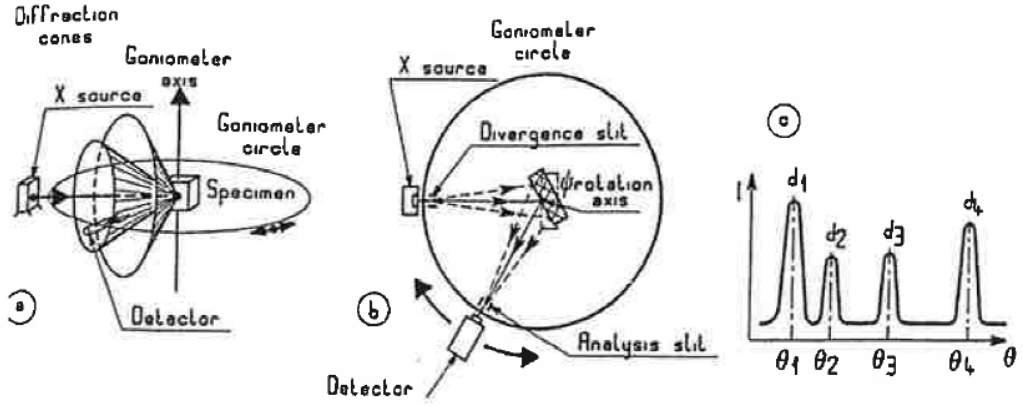

Figure 51 Tilting of sample from two direction (a and b) and measured diffraction peaks with different angles (c). (34)

Because the x-ray penetration is extremely shallow (<10 μm), a condition of plane stress is assumed to exist in the diffracting surface layer. Coordinate system during measuring of X-ray diffraction is according to Figure 52.
The strain in the sample surface at an angle ϕ from the principal stress σ_{11} is given by:

$$\varepsilon_{\phi\psi} = \frac{1+v}{E}\,\sigma_\phi sin^2\psi - \frac{v}{E}(\sigma_{11} + \sigma_{22}) \quad (20)$$

If $d_{\phi\Psi}$ is the spacing between the lattice planes measured in the direction defined by ϕ and Ψ, the strain can be expressed in terms of changes in the spacing of the crystal lattice.

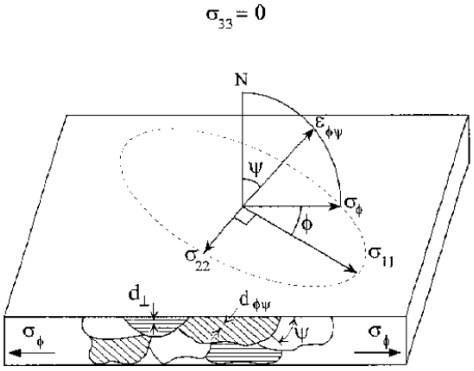

Figure 52 Coordinate systems which are used with X-ray diffraction. (35)

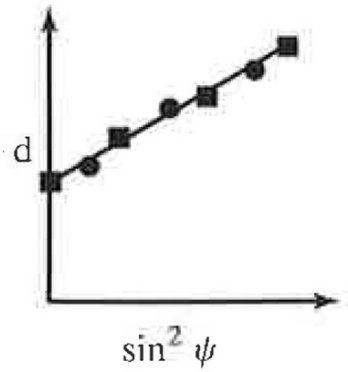

Figure 53 Different types of d vs. $\sin^2 \psi$ plots.

Strains of Figure 51 can be determined according equation (21) when distance between lattice levels $d_{\phi\Psi}$ and unstressed distance d_0 are known (35):

$$\varepsilon_{\phi\psi} = \frac{\Delta d}{d_0} = \frac{d_{\phi\psi} - d_0}{d_0} \tag{21}$$

If $d_{\psi\phi}$ is measured with many ψ-angles, it is possible to plot curve of $\sin^2\psi$ according to Figure 53. State of stress can be evaluated with the help of plot in Figure 53. In Figure 53 ε_{13} and ε_{23} are 0 when plot is straight. (35)

Hooke's law is utilized for defining residual stresses. State of stress is assumed plane stress state with this kind of calculations because perpendicular component of stress is 0 near surface of sample. (35)

Handling of measuring data, restriction of X-ray equipment and measurer influence the result. Most significant factors which cause inaccurate results with measuring residual stresses are large gradients of residual stresses on the surface of sample due to, for example, hardening. Hardening causes usually triaxial stresses and plane stress conditions are not met. (35)

Coarse grains cause problems with X-ray diffraction. This usually is problem with coarse-grained zone of weld due to small amount of measured grains. Small amount of measuring points make measurement cause dispersion of measuring which may cause difficulties or impossible. (30)

Strong texture or deformation of material cause also difficulties with measuring of X-ray diffraction because d-$\sin^2\psi$ chart becomes indeterminate. Materials which include many phases are problematic. This is because measuring of x-ray diffraction is focused only on one phase. Surface of the sample has to be smooth and in vertical position with measuring equipment when ψ-angle is zero. (30)

Typical portable measuring devices are usually safe to use and their safe distance is usually enough. Equipment is calibrated before using by sample of powder because its state of is zero. Sample is measured by several values of angle ψ. Software of this equipment calculates the plot and distribution of stress. (30)

2.16 Contour method

The contour method is based on deformation of cross-section surface of cut parts due to residual stress redistribution. The test sample under stress is first cut into two pieces with the EDM (*Electric Discharge Machine).* The releasing of stresses causes deformation on surface normal to the cross-section. The deformation can be measured by CMM (*Coordinate Measuring Machine*) and white light interferometer. Coordinates of measured points of surface topography are possible to combine as three dimensional surface height map of cross-section. The distribution of residual stress on normal cut surface is possible to calculate with the help of the deformation of the surface height map by FEM (*Finite Element Model*). (36)

Figure 54 shows principle of EDM. CNC aided EDM machine puts impulse voltage between electrode wire and workpiece through impulse source under deionized water. Numerous tiny holes appear due to erosion of impulse spark discharging during cutting. (37)

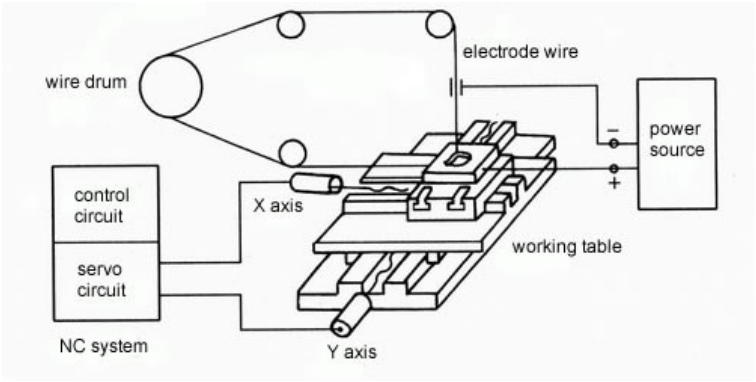

Figure 54 Principle of wire cut EDM (37)**.**

Electrode wire is connected to cathode of impulse power source and workpiece is connected to anode of impulse power source. The eroded workpiece is cooled down swiftly and cutting particles are flushed away under deionized water. (37)

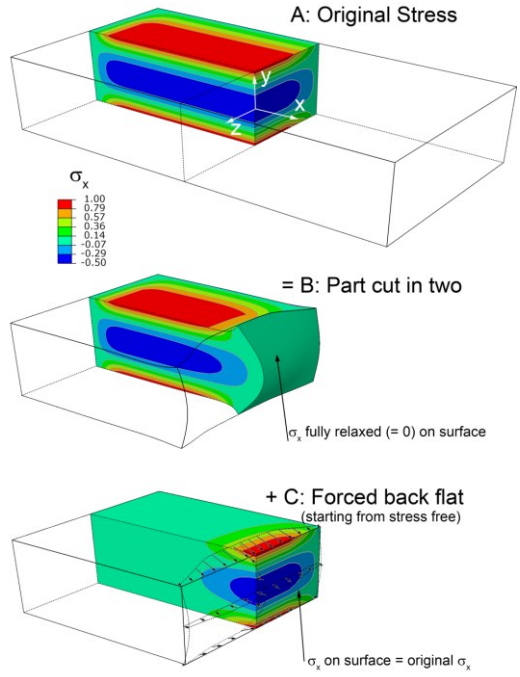

Figure 55 Principle of superposition for the contour method. Stresses are plotted on one quarter of the original body. (36)

Figure 55 (a) shows original sample which includes residual stresses that one wishes to determine. Figure 55 (b) shows that part has been cut in two pieces. Shear planes have deformed because of the residual stresses released by cut. Figure 55 (C) shows how deformed cut surface is forced back to its original shape. Change of stress is possible to determine with the help of displacement. (36)

$$\sigma^A(x,y,z) = \sigma^B(x,y,z) + \sigma^C(x,y,z), \qquad (22)$$

where σ is entire stress tensor and superscripts are various steps of Figure 55 because σ_x, τ_{xy} and τ_{xz} are 0 on the free surface in B. The described superposition principle uniquely determines the original distribution of the residual stresses on the plane of the cut. (36)

The superposition principle assumes that the material behaves elastically during releasing of residual stresses. Both sides of measured sample are supported strongly during EDM cut and rising of temperature is avoided with deionized cooling water because these both influence change of dimensions. (36) Surface height map of cross-section plane is possible to measure with coordinate measuring machine and white light interferometer measuring. (36)

3 Comparison of measurements and simulations

The results of characterized microstructure of VTT samples, measured residual stresses of VTT samples, modelling results and results of Voss's doctoral thesis were compared according to Figure 56.

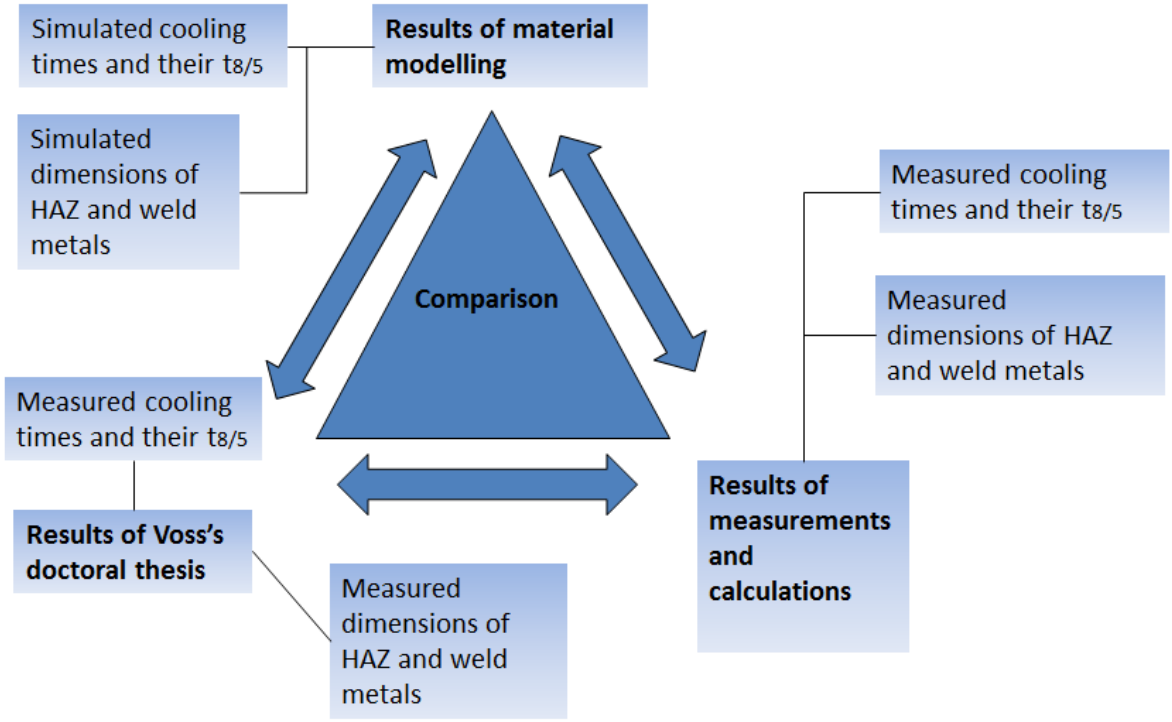

Figure 56 Comparison between results of material modelling, Voss's doctoral thesis and measurements and calculations for weld samples.

Before discussing the measurements, material modelling and the doctoral thesis the test samples, making microsections, measuring hardness distributions, calculating $t_{8/5}$ and hardnesses and recognizing phases of microstructure are described.

3.1 Bead-on-plate welds and their welding parameters

Bead-on-plate samples of VTT were welded by LUT and all their investigations were made by VTT. Table 6 shows used welding methods of bead-on-plate welds, their welding parameters and other information. All sample materials of bead-on-plate welds were S355N. Test plate information and chemical compositions for 5 mm and 15 mm plate samples are in Appendix 1 and Appendix 2. Dimensions of the plates were 200x150x5 mm and 200x150x15 mm. Photographs of the samples are in Appendix 3.

Table 6 Dimensions of bead-on-plate welds and their welding parameters.

Welding method	Sample number	s	I	U	P	v	Filler metal	Shielding gas
		Plate thickness (mm)	(A)	(V)	(kW)	Welding speed (m/min)		
LAHW	3.5.2-3	5	180	28.9	8.2	1.20	ESAB OK 308LSi d=1 mm	MISON 2 He
LAHW	3.15.2-9	15	185	29.4	10.4	1.20	ESAB OK 308LSi d=1 mm	MISON 2 He
LASER	3.5.2-7	5	-	-	3.0	1.20	none	Ar
LASER	3.15.2-5	15	-	-	5.0	1.20	none	Ar
MAG	3.5.2-2	5	196	29.5	5.8	0.55	ESAB OK 308LSi d=1 mm	MISON 2 He
MAG	3.15.2-4	15	196	29.5	5.8	0.35	ESAB OK 308LSi d=1 mm	MISON 2 He
TIG	3.5.2-4	5	243	11.4	2.8	0.43	none	Ar
TIG	3.5.2-8	5	250	11.2	2.8	0.13	none	Ar
TIG	3.5.2-9	5	260	11.4	3.0	0.28	none	Ar
TIG	3.15.2-6	15	250	11.2	2.8	0.13	none	Ar
TIG	3.15.2-7	15	260	11.4	3.0	0.28	none	Ar
TIG	3.15.2-8	15	243	11.4	2.8	0.43	none	Ar

Visual inspections were made for all bead-on-plate welds according to SFS-EN 13018 and partially ISO 5817:2014(E) without tools by naked eye. All detected imperfections and defects are documented in Table 7. Some faults were observed with the help of optical microscope.

Results of visual and microscope inspections are collected in Table 7. (X) means defect in the beginning or end of the weld. [X] means defect in the middle of weld metal. E means external defects which are detected without microsections with naked eye. I means internal defects which are detected from microsections with naked eye or optical light microscope and - means no defects.

Table 7 Results of visual and microscope inspection of bead-on-plate welds.

Visual and microscope inspection of bead-on-plate welds								
Welding method	**Sample number**	**Spatter**	**Crater pipe**	**Cracks**	**Gas bore**	**Undercut**	**Overlap in root side**	**Incomplete joint penetration**
LAHW	3.5.2-3	E	-	-	[II]	-	-	-
LAHW	3.15.2-9	E	-	[III]	[III]	-	-	-
LASER	3.5.2-7	-	-	-	[III]	E	-	-
LASER	3.15.2-5	-	-	[I]	[I]	-	-	-
MAG	3.5.2-2	E	-	-	-	-	-	-
MAG	3.15.2-4	E	-	[I]	I	-	-	-
TIG	3.5.2-4	-	-	-	-	-	-	E
TIG	3.5.2-8	-	-	-	-	-	E	E
TIG	3.5.2-9	-	E	-	-	-	-	E
TIG	3.15.2-6	-	-	-		-	-	(E)
TIG	3.15.2-7	-	-	-	-	-	-	-
TIG	3.15.2-8	-	-	-	-	-	(E)	(E)

Both sides of bead-on-plate and butt weld samples were photographed with Olympus digital camera of model number E-30 with 35 mm macro objective. All welded joints and their positions of cut parts were photographed. The photos of bead-on plate welds are collected in Appendix 3 and the photos of butt welds are collected in Appendix 4.

3.2 Making microsections

The test samples were sawed to smaller slices with a cooled band saw after the visual inspection and photography. The slices were cut to smaller parts with a cutting-off machine Struers Distoton 50. The cross-sections of weld samples were ground with water and sandpapers of micro-section machine from 320 to 1200 grit so that HAZ areas were detected with naked eye. HAZ area of some samples was difficult to detect by naked eye. These samples were polished with 3 µm to 1 µm suspension of diamond with polishing machine and etched with 2% Nital so that HAZ was displayed. Nikon Ephipot 200 light optical microscope and small magnifications was used for detecting of HAZ in difficult cases.

The samples were cut to smaller parts with the cutting-off machine, so that HAZ was not damaged. The information of the cut parts was carved to every piece immediately after the cutting. All samples were washed ultrasonically with an ultrasonic washing device with alcohol for 5 min.

All test samples were compressed in Polyfast plastic which is conductive and compatible with SEM microscope. Casting machine was Struers ProntoPress-20. Polyfast was compressed with peak value of 30 MPa for 9 min. Water cooling was used during compression.

Microsections were ground and polished with Struers Tergamin 30. Grinding was made with sandpapers of silicon carbide (SiC) and water at first 220 grit for 4 min, then 500 grit for 2 min and eventually 1200 grit for 2 min. Microsections were polished with same machine with diamond suspensions first at 3 µm for 4 min, then 1 µm for 3 min and eventually 0.25 µm for 1.5 min.

Nital 3% etch was used to reveal the microstructure of HAZ of 355N. Nital contains 3 % by volume nitric acid (HNO_3) and 97 % by volume ethanol (C_2H_5OH). Nitro hydrochloric

acid etch was used to reveal the microstructure of AISI 308 LSi weld metal. Nitro hydrochloric acid contains 3 parts HCl, 2 parts glycerol and 1 part HNO_3. (15)

3.3 Measured hardness distributions

The primary goal of hardness testing was determination of hardness distribution for welds and to find positions of hardest points of coarse-grained zones by measuring of HV1. Hardness distributions of laser welds were measured by HV01 due to small size of weld. Secondary goal was to measure hardness distribution of MAG welded sample 3.15.2-4 more accurately near fusion line with the help of HV01 due to investigations of tie-line. HV01 hardnesses were measured also near fusion line and in coarse-grained zone of MAG welded sample 3.5.2-2.

HV1 and HV01 hardness were measured partially according to standard SFS-EN ISO 6507-1 and SFS-EN ISO 9015-2 with the help of Zwick / Roell BZ2.5 / TS1P, Buehler 1600-6400 and Durascan of Struers. Used force with HV1 was 9.8 N and waiting time at the point of load application was 10 s. (38)

Hardness was measured along horizontal lines from base material across HAZ and weld to base material with 0.5 mm spacing according to recommendation of SFS-EN ISO 9015-2 and according to SFS-EN ISO 6507-1 (39). Measuring lines were positioned at the depth where the most coarsened grain areas existed.

Positions of hardest points from coarse-grained zones were searched after automatic hardness measuring. Additional hardness measurements were made near measured maximum hardness positions by Buehler 1600-6400.

Two following principles were followed in measuring according to SFS-EN ISO 6507-2. The distance between centres of adjacent indentations must be at least three times the mean diagonal length of the indentation with steels. The distance between the centre of indentation and edge of the sample must be 2.5 times the mean diagonal length of the indentation (39). Hardness distributions and maximum hardnesses were measured for all bead-on-plate samples in the similar way.

Figure 57(a) shows horizontal indentations of measured HV1 hardness distribution for MAG sample 3.5.2-2. Additional HV1 hardnesses were measured around measured hardness maximum according to Figure 57 (b).

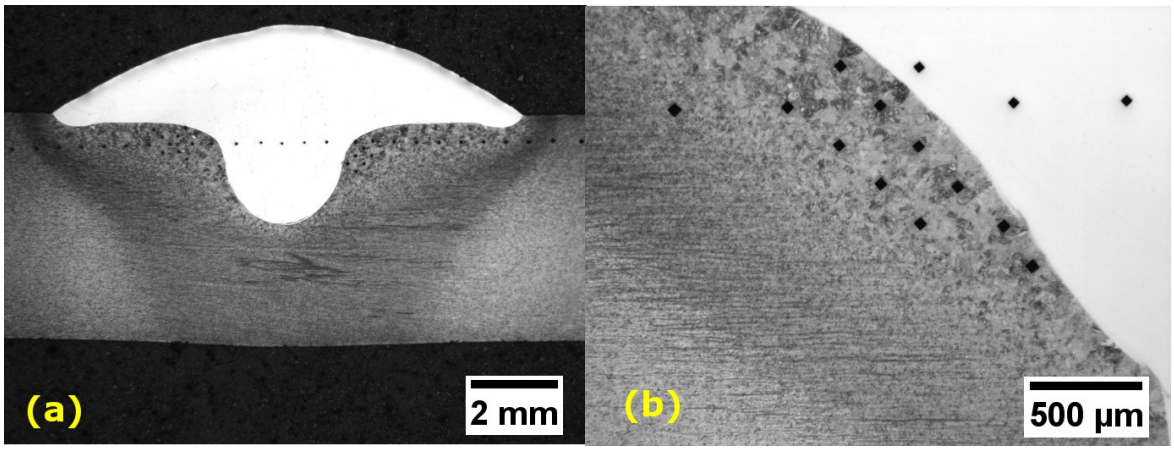

Figure 57 Figure (a) and (b) show HV01 indentations of MAG welded sample 3.5.2-2. (a) Measured hardness distribution of microsections of welds measured by automatic Zwick / Roell BZ2.5 / TS1P. Additional measurements are made by Buehler 1600-6400. This micrograph was taken with Leica

MEF 4M light optical microscope, 10X ocular and 1X objective. (b) Additional measurements are made from near maximum hardness peak from coarse-grained zone by Buehler 1600-6400. This micrograph was taken with Leica MEF 4M light optical microscope, 10X ocular and 5X objective.

Figure 58 shows distribution of hardness which positions correspond to hardnesses of Figure 57(a). Fusion lines, limits of coarse-grained and fine-grained zone are shown in this picture.

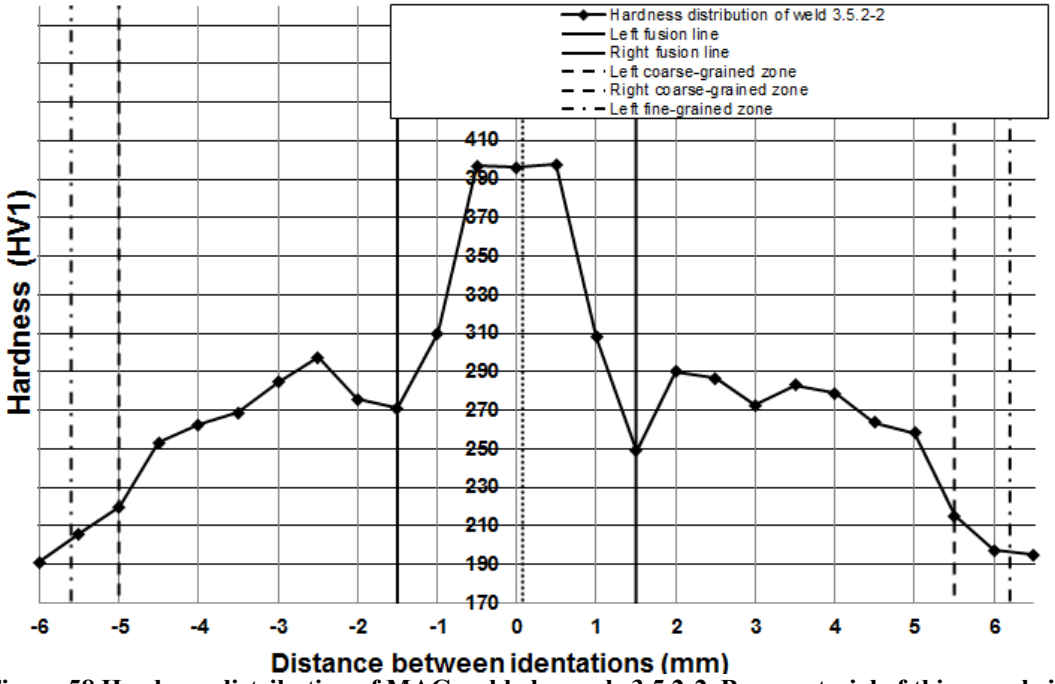

Figure 58 Hardness distribution of MAG welded sample 3.5.2-2. Base material of this sample is S355N and filler metal AISI 308 LSi.

Measured additional hardness and their positons are show in Figure 57 (b) and 59. Additional hardnesses were measured from fusion line near measured maximum hardness of coarse-grained zone. Distances of Figure 59 are measured from fusion line.

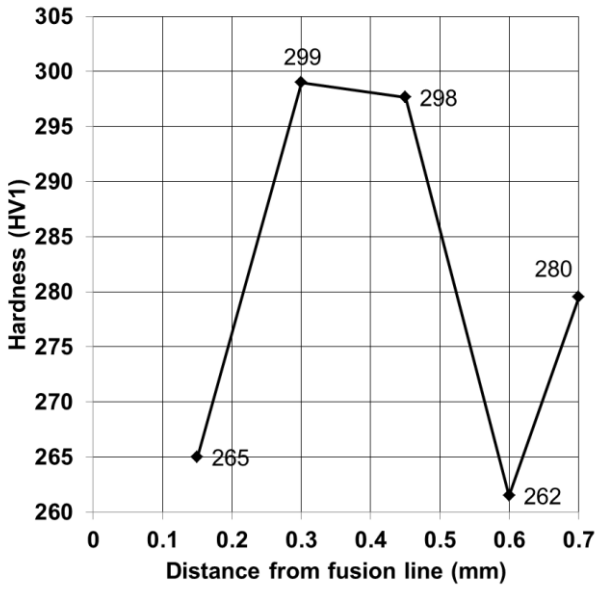

Figure 59 Additional hardness distribution of MAG welded sample 3.5.2-2. Distances of the measuring points are measured from fusion line.

Table 8 Measured maximum HV1 and HV01 hardnesses of bead-on-plate wels from coarse-grained zone.

Welding method	Number of samples	HV max of coarse-grained zone
LAHW	3.5.2-3	354 HV1
LAHW	3.15.2-9	455 HV1
LASER	3.5.2-7	448 HV01
LASER	3.15.2-5	450 HV01
MAG	3.5.2-2	299 HV1
MAG	3.15.2-4	416 HV1
TIG	3.5.2-4	376 HV1
TIG	3.5.2-8	232 HV1
TIG	3.5.2-9	294 HV1
TIG	3.15.2-6	423 HV1
TIG	3.15.2-7	421 HV1
TIG	3.15.2-8	447 HV1

The measured hardness distributions of welds, maximum hardnesses of coarse-grained zones and micrographs of their indentations are collected in Appendix 6. Table 9 includes measured HV1 and HV01 hardnesses from coarse-grained zone.

Figure 60 (a-b) and 61 (a-b) show extra HV01 hardness distributions of MAG welded sample 3.15.2-4 which are measured over fusion line.

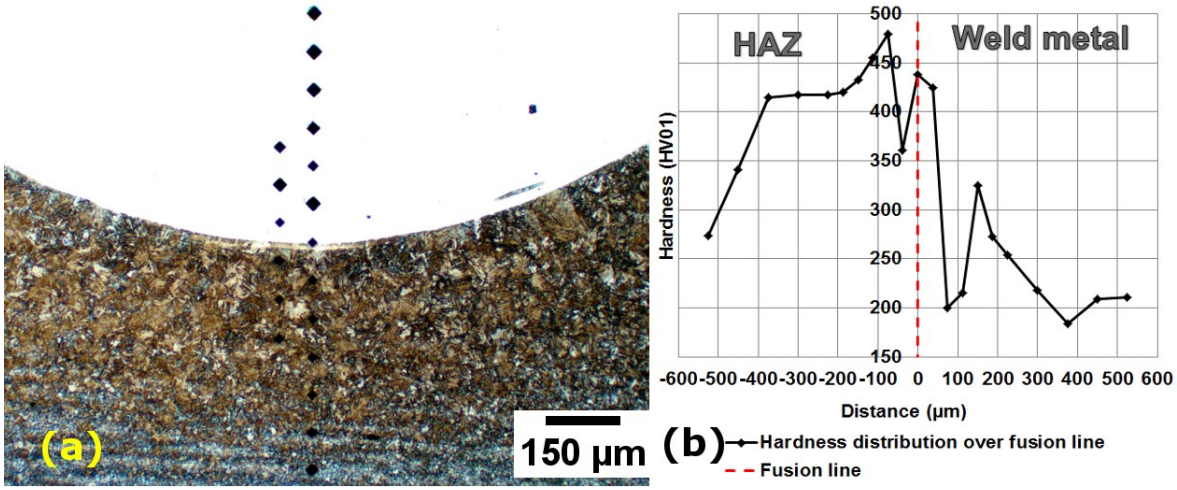

Figure 60 (a) Root side of weld 3.15.2-4 and indentations of HV01. (b) Measured hardness distribution of root side of weld 3.15.2-4.

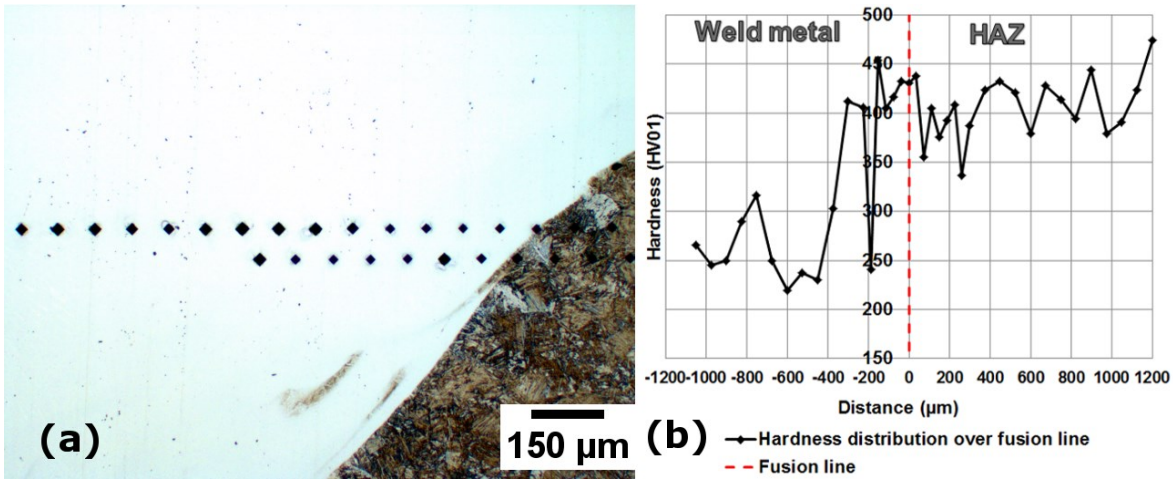

Figure 61 (a) Side of weld 3.15.2-4 and indentations of HV01. (b) Measured hardness distribution of side of weld 3.15.2-4.

In MAG welded sample 3.15.2-4 three HV01 hardnesses in the middle of weld near crack were measured. Values of these hardnesses were 386 HV01, 386 HV01 and 367 HV01. Mean value of these hardnesses is 386 HV01. Three hardness values were measured also on top side of MAG welded sample 3.15-2-4. Values of these hardnesses were 377 HV01, 395 HV01 and 373 HV01. Mean value of these hardnesses is 572 HV01.

Additional HV01 measurements were made also for MAG sample 3.5.2-2 according to Figure 62.

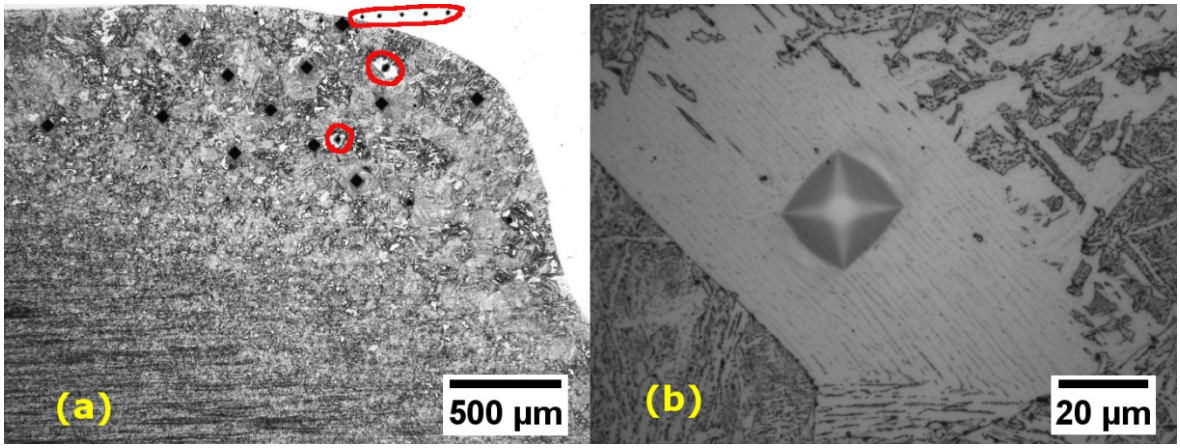

Figure 62 (a) Micrograph of MAG welded sample 3.5.2-2. Indentations of HV01 hardnesses are circled. (b) This micrograph is partial magnification of middle circled area of micrograph (a).

Table 9 shows measured hardnesses from coarse-grained zone and Table 10 measured hardnesses from weld metal near fusion line of MAG welded sample 3.5.2-2. Indentations of these measured hardnesses can be found in Figure 62 (a) and (b).

Table 9: HV01 hardnesses of white areas from coarse-grained zone of MAG welded sample 3.5.2-2.

Hardness measurements from white areas of HAZ.	HV01
1 (Upper circled area from HAZ)	274
2 (Lower circled area from HAZ)	219
3 (From coarse-grained zone)	247
4 (From coarse-grained zone)	266
5 (From coarse-grained zone)	268
6 (From coarse-grained zone)	256
Average	255

Table 10: 5 HV01 hardnesses from left to right from weld metal near fusion zone of MAG welded sample 3.5.2-2.

Hardness measurements from weld metal from left to right.	HV01
1	472
2	396
3	387
4	350
5	351
Average	391

Two HV01 hardness distributions were measured from coarse-grained zone to weld metal over fusion line for MAG welded sample 3.15.2-4. Variations of hardnesses are detected on both sides of fusion line. This kind of variation is typical for dissimilar metal weld. Measured hardnesses refers that reason of variation of hardnesses is variation of carbon content in one millimetre length which is caused by carbon diffusion. MAG welded sample 3.15.2-4 is solidified from base material to weld metal. Growth type of the weld is Type 2 according to previous theory. The one millimetre length includes narrow zones which have different hardness. Carbon depleted zone which hardness is lower than other areas of coarse-grained zone is found from coarse-grained zone near fusion line. Carbon depleted zone is consequence of decarburization. Another zone is detected in weld metal side near fusion line which hardness is higher than hardness of weld metal. This causes carbon pile-up zone where carbon content is high. Both zones are consequence of carbon migration due to carbon diffusion. Unmixed and non-fusible base material bands were found from weld metal side near fusion line.

At first HV01 hardness distribution of Figure 60 (a) were measured on root side of the weld. Hardness peak of 479 HV01 was measured from HAZ side about 75 µm from fusion line according to Figure 60 (b). This kind of hardness means fully martensitic zone. Hardness decreases when approaching the fusion line so that minimum hardness of coarse-grained zone is 361 HV01 when the distance is 38 µm from fusion line in HAZ side due to decarburization. This kind of structure may include martensite and upper bainite due to hardness. Recognized phases of microstructure of coarse-grained zone support also the

previous deduction according to Table 12. Hardness is 438 HV01 which corresponds hardness of martensite in fusion line. Hardness of weld metal is high near fusion line which is consequence of high carbon content due to migration of carbon. Hardness decreases when going from fusion line to weld metal side until hardness is 200 HV01 and distance is 75 µm from fusion line. Smaller amount of carbon causes that hardness decreases further from fusion line in weld metal side. Hardness of weld metal is increased so that 325 HV01 is reached when distance is 150 µm from fusion line. Hardness decreases again from the previous point to 184 HV01 when distance from fusion line is 375 µm and after this hardness level varies less. This second lower hardness peak can be consequence of different local phase or some other reason which causes hardness variation.

HV01 hardness distribution of Figure 61 (a) and (b) were measured on side of weld. Hardness of coarse-grained zone is 412 HV01 from 300 µm from fusion line. Hardness of coarse-grained zone is dropped to 241 HV01 when distance from fusion line is 188 µm due to decarburization. Measured peak of coarse-grained zone is 454 HV01 from 150 µm from fusion line which indicates that microstructure of thin zone in HAZ side is martensitic due to high carbon content. Hardness of coarse-grained zone decreases from 454 HV01 to 405 HV01 when distance is 113 µm from fusion line due to decarburization. Hardness 438 HV01 is reached in weld metal side 38 µm from fusion line which is consequence high carbon content which is caused carbon migration. Hardness drops to 355 HV01 when distance is 75 µm from fusion line in weld metal side due to lower carbon content. Hardness varies deeper in weld metal side.

Both measured hardness distributions look similar. Small differences like width of zones and their positions between side of weld and root side of weld are probably consequence of cooling and mixing differences.

Three HV01 hardnesses were measured in the middle of MAG welded sample 3.15.2-4 near solidification crack in the middle of weld according Figure 64. Mean value of these hardnesses is 386 HV01. Most of microstructure is martensite and partially austenite in the middle of weld metal according to measured hardnesses, Schaeffler diagram of Figure 110 and WRC92 diagram of Figure 111.

Three HV01 hardnesses were measured also on top side of MAG welded sample 3.15.2-4. Figure 65 shows microstructure of this area. Mean value of these hardnesses is 572 HV01. This kind of structure is fully martensite due to hardness. Schaeffler diagram of Figure 110 and WRC92 diagram of Figure 111 support also that microstructure is partially or fully martensitic.

Figure 60 (a) and 61 (b) show non-fusible and unmixed base material near fusion line. Figure 63 shows light microscope micrograph of MAG welded sample of 3.15.2-4 from root side from fusion line. Position 1 of this micrograph is S355N base material which is out of focus due to etching of nitrohydrochloric acid. Positions 2, 5, 8 and 9 are austenite or mixture of austenite and delta ferrite. White areas of positions 3, 4, and 7 are delta ferrite. Position 6 is unmixed and non-fusible base material.

According to measured hardness distributions of Figure 60 and 61 and positions of microstructures of Figure 63 which are near fusion line are detected zones which hardnesses vary very much. Position 1 includes zone which carbon content and hardness is high and another zone which carbon content and hardness are low near fusion line in HAZ. Hardness of HAZ is increased with ferritic structural steel due to hardening. Microstructure of these zones includes bainite and martensite according to Table 12. Hardness of coarse-grained zone decreases near fusion line due to decarburization and result of this is carbon-depleted

zone. Hardness of austenitic weld metal is higher near fusion line due to carbon migration from ferritic steel to austenitic weld metal in position 2. This causes carbon pile-up zone where carbon content is high. Hardness of this zone is high due to hardening. Position 2 shows zone which hardness of weld metal decrease because carbon content decreases when going to the middle of weld metal. Mentioned zones form 1 mm wide area which is called tie-line. Zones which hardness is high or low are consequence of carbon diffusion according to previous theory.

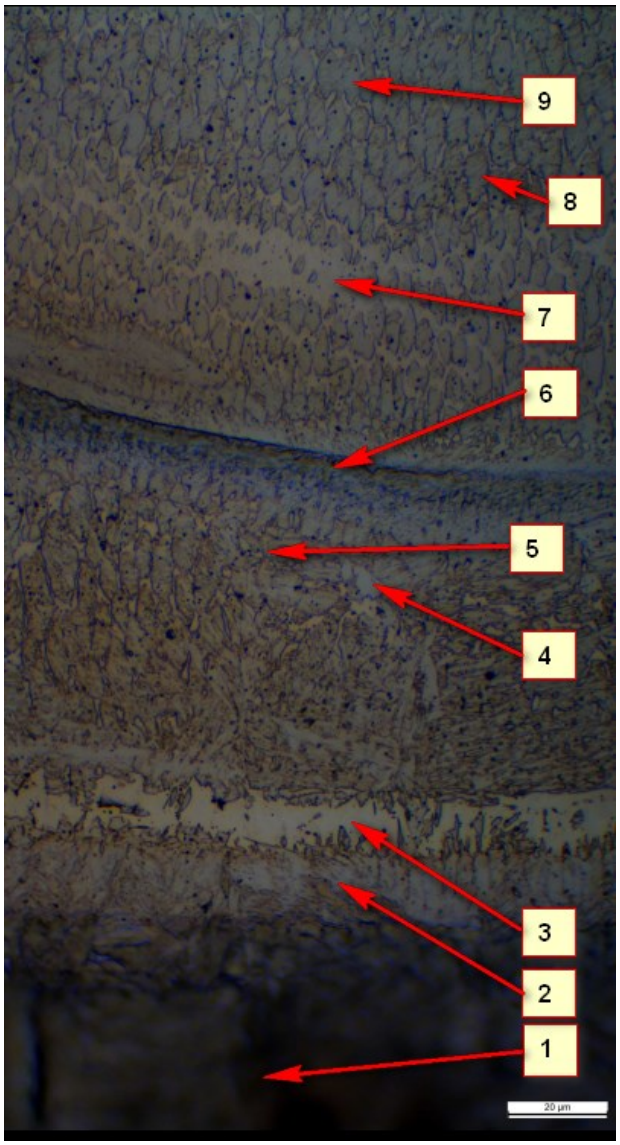

Figure 63 Micrograph of root side of MAG welded sample.

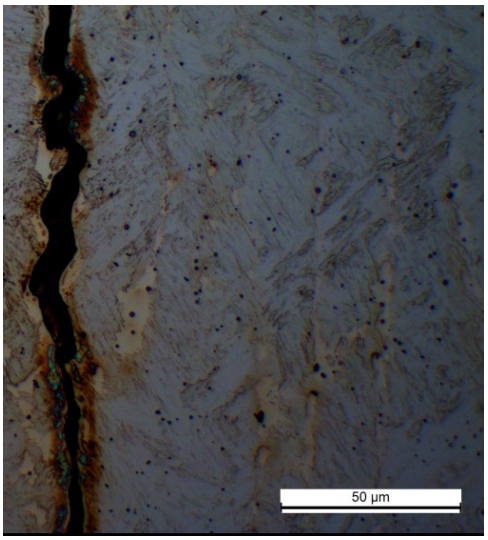

Figure 64 Crack in the middle of weld metal.

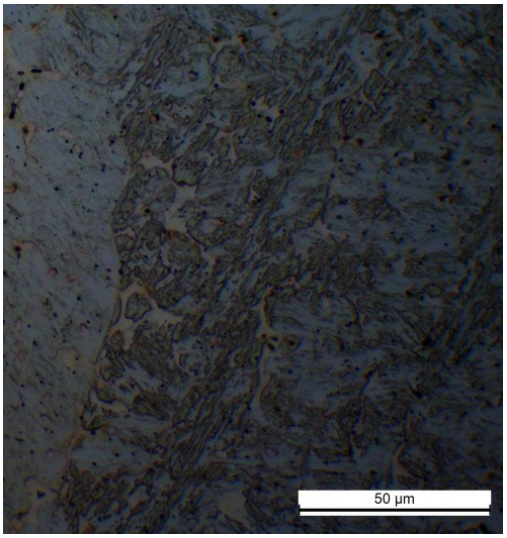

Figure 65 Top side of weld.

Additional HV01 hardnesses were measured for thinner MAG welded sample of 3.5.2-2. According to additional HV01 hardness measuring values of Table 9 and micrograph of lamellar structure of Figure 62 (b) “white areas” in HAZ of Figure 62 (b) are upper bainite. Table 10 and Figure 62 (a) refer that near fusion line in weld metal side is hardened carbon pile-up zone near fusion line.

The thicker MAG welded bead-on-plate weld sample 3.15.2-4 represents typical hardness distribution of dissimilar metal weld. Figure 37 illustrates reason of hardness variation which is diffusion in fusion line in dissimilar metal welded joint. It is possible to recognize different zones with the help of hardness and micrographs. Normal epitaxial growth is su-

pressed in the case of MAG welded sample 3.15.2-4. According to micrographs, Figure 36 and Figure 38 growth type of this case is Type 2 according to previous theory.

3.4 Calculated $t_{8/5}$ and hardnesses

Two-dimensional calculation of TIG welded sample 3.5.2-4 and three-dimensional calculation of TIG welded sample 3.15.2-6 is made for $\Delta t_{8/5}$ cooling and HV01 hardness according to the equations (1), (2), (6), (7), (8) and (9). These calculations were made for all bead-on-plate welds with Excel. Two-dimensional calculation for TIG welded sample 3.5.2-4 is shown below.

S = 5 mm
I = 243 A
U = 11.4 V
k = 0.6
V = 0.427 m/min = 427 mm/min

$$E = \frac{60 \times U \times I}{1000 \times v} = \frac{60 * 11{,}4\ V * 243\ A}{1000 * 427\ \text{mm/min}} = 0{,}389\ kJ/mm$$

$$Q = kE = 0{,}6 * 0{,}389\ kJ/mm = 0{,}234\ kJ/mm$$

In two-dimensional cooling for thin plates joint factor for this case is $F_2 = 1$ and working temperature $T_0 = 20$ ˚C

$$\Delta t_{8/5} = (4300 - 4.3T_0)10^5 \frac{k^2E^2}{d^2}\left[\left(\frac{1}{500 - T_0}\right)^2 - \left(\frac{1}{800 - T_0}\right)^2\right]F_2$$

$$= (4300 - 4.3 * 20\text{˚C})10^5 \frac{0{,}6^2 * (0.389\ kJ/mm)^2}{5^2}\left[\left(\frac{1}{500 - 20\text{˚C}}\right)^2 - \left(\frac{1}{800 - 20\text{˚C}}\right)^2\right] * 1 = 2.476\ \text{s}$$

$$P_v = C + \frac{Mn}{3} + \frac{Ni}{8} + \frac{Cr}{12} + \frac{Mo}{2} + \frac{Cu}{5}$$

$$= 0.154 + \frac{1.42}{3} + \frac{0.04}{8} + \frac{0.05}{12} + \frac{0.010}{2} + \frac{0.017}{5} = 0.6449$$

$$HV = (922C - 230P_v + 250)\exp\left(\frac{-3\Delta t_{8/5}}{310^{Pv}}\right) + 188P_v + 80 = (922 * 0.154 - 230 * 0.6449 + 250)\exp\left(\frac{-3*2.476\ \text{˚C/s}}{310^{0.6449}}\right) + 188 * 0.6449 + 80 = 404\ \text{HV}$$

Three-dimensional calculation for TIG welded sample 3.15.2-6 is shown below.

S = 15 mm
I = 250 A
U = 11.2 V
k = 0.6
V = 0,134 m/min = 134mm/min

$$E = \frac{60 \times U \times I}{1000 \times v} = \frac{60 * 11{,}2\ V * 250\ A}{1000 * 134\ \text{mm/min}} = 1.254\ kJ/mm$$

$$Q = kE = 0.6 * 1.254\ kJ/mm = 0.752\ kJ/mm$$

In three-dimensional cooling for thick plates joint factor for this case is $F_3 = 1$ and working temperature $T_0 = 20$ ˚C

$$\Delta t_{8/5} = (6700 - 5T_0)kE\left[\left(\frac{1}{500 - T_0}\right) - \left(\frac{1}{800 - T_0}\right)\right]F_3 = (6700 - 5 * 20°\text{C}) * 0.6 * 1.254\frac{\text{kJ}}{\text{mm}} * \left[\left(\frac{1}{500 - 20°\text{C}}\right) - \left(\frac{1}{800 - 20°\text{C}}\right)\right] * 1 = 4.0\ \text{s}$$

$$P_v = C + \frac{Mn}{3} + \frac{Ni}{8} + \frac{Cr}{12} + \frac{Mo}{2} + \frac{Cu}{5} = 0.161 + \frac{1.40}{3} + \frac{0.04}{8} + \frac{0.05}{12} + \frac{0.006}{2} + \frac{0.015}{5} = 0.642$$

$$HV = (922C - 230P_v + 250)\exp\left(\frac{-3\Delta t_{8/5}}{310^{Pv}}\right) + 188P_v + 80 = (922 * 0.161 - 230 * 0.642 + 250)\exp\left(\frac{-3 * 4}{310^{0.642}}\right) + 188 * 0.642 + 80 = 387\ HV$$

According to previous calculations maximum hardness of TIG welded sample 3.5.2-4 is 404 HV and maximum hardness of TIG welded sample of 3.15.2-6 is 387 HV. These calculated maximum hardness values are near the measured maximum values of hardness. All $t_{8/5}$ and maximum hardnesses of bead-on-plate welds are calculated by Excel in a similar way and the results are in Table 11. The calculations use thermal efficiency factors of Table 1 and welding parameters of Table 6.

Table 11 Cooling and hardness calculations which are calculated with the help of welding parameters of Table 6.

Welding method	Sample number	Q (kJ/mm)	Thickness (mm)	Two-dimensional $t_{8/5}$ (s)	Three-dimensional $t_{8/5}$ (s)	Selected value of $t_{8/5}$ (s)	Two-dimensional hardness from coarse-grained zone (HV)	Three-dimensional hardness from coarse-grained zone (HV)	Selected hardness from coarse-grained zone (HV)
LAHW	**3.5.2-3**	0.2	5	2.0	1.1	**2.0**	412	426	**412**
LAHW	**3.15.2-9**	0.2	15	0.2	1.2	**1.2**	447	431	**431**
LASER	**3.5.2-7**	0.1	5	0.7	0.6	**0.7**	433	434	**433**
LASER	**3.15.2-5**	0.2	15	0.2	1.1	**1.1**	448	432	**432**
MAG	**3.5.2-2**	0.5	5	11.6	2.7	**11.6**	304	401	**304**
MAG	**3.15.2-4**	0.8	15	3.2	4.2	**4.2**	398	384	**384**
TIG	**3.5.2-4**	0.2	5	2.5	1.2	**2.5**	404	424	**404**
TIG	**3.5.2-8**	0.8	5	25.7	4.0	**25.7**	237	383	**237**
TIG	**3.5.2-9**	0.4	5	6.6	2.0	**6.6**	351	411	**351**
TIG	**3.15.2-6**	0.8	15	2.9	4.0	**4.0**	403	387	**387**
TIG	**3.15.2-7**	0.4	15	0.7	2.0	**2.0**	438	416	**416**
TIG	**3.15.2-8**	0.2	15	0.3	1.2	**1.2**	446	429	**429**

The equations of two-dimensional $t_{8/5}$ cooling times are suitable for thin plates and the equation of three-dimensional for thick plates. Two- and three-dimensional $t_{8/5}$ values were calculated for the all weld samples according to Table 11. Easiest choice between two- and three-dimensional cooling can be made by choosing longer $t_{8/5}$ value. It is also possible to

solve it according to Figure 15 of SFS-EN 1011-2. Limit of material thickness where heat transfer is changed from two-dimensional to three-dimensional is possible to solve by to set two- and three-dimensional equations and solve the thickness.

It is good to remember that measured maximum grain sizes of coarse-grained zone and measured $t_{8/5}$ values affect results which are calculated by VTT / OU method which is validated for arc welding.

3.5 Recognizing phases of microstructures

Phases of microstructures of bead-on-plate welds were recognized with the help of the measured hardnesses and micrographs. Examination of microstructures were done with the help of micrographs which were taken with Leica MEF 4M light optical microscope. Figure 66, 67, 68 and 69 show some micrographs of LASER welded sample 3.5.2-7. Micrographs of all bead-on-plate welds are collected in Appendix 7.

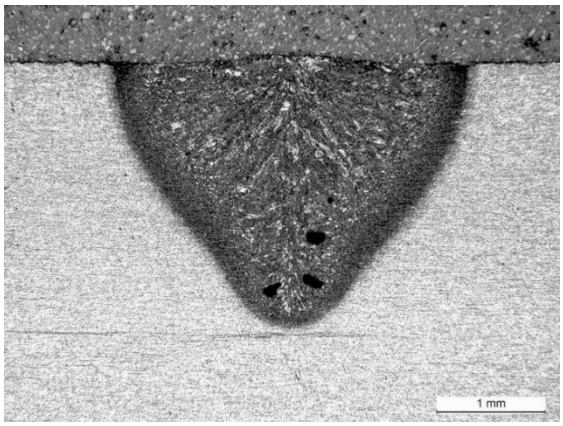

Figure 66 This micrograph of LASER welded sample 3.5.2-7 is taken with 10X ocular and 2.5X objective with Leica MEF 4M light microscope.

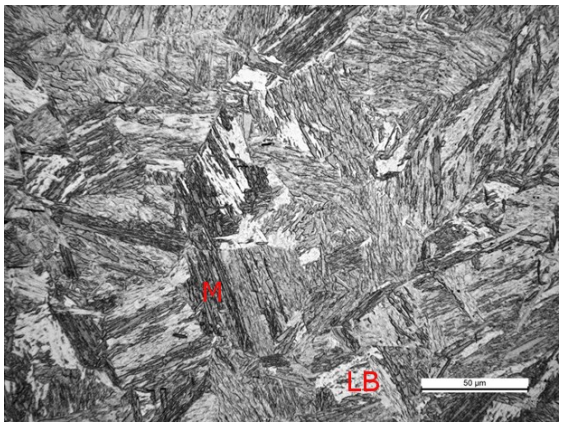

Figure 67 This micrograph of LASER welded sample 3.5.2-7 is taken with 10X ocular and 50X objective from coarse-grained zone with Leica MEF 4M light microscope

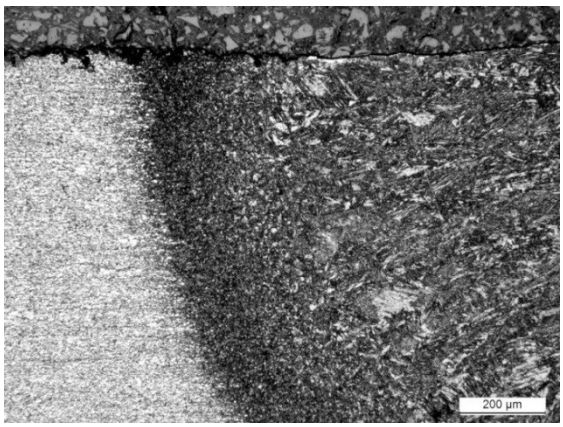

Figure 68 This micrograph of LASER welded sample 3.5.2-7 is taken with 10X ocular and 10X objective with Leica MEF 4M light microscope.

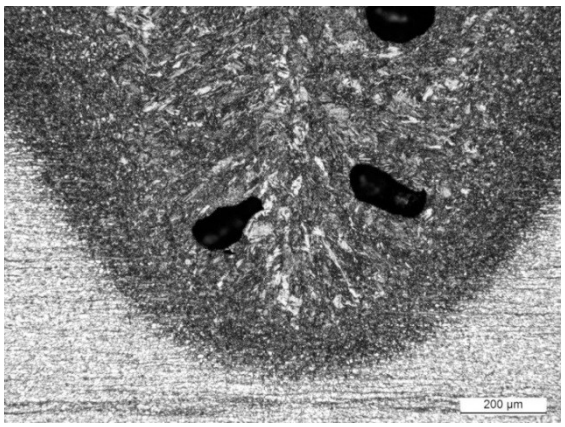

Figure 69 This micrograph of LASER welded sample 3.5.2-7 is taken with 10X ocular and 10X objective with Leica MEF 4M light microscope. Porosity was founded in weld metal.

Different microstructures of weld and HAZ are consequence of cooling time and chemical composition. Dependency between microstructure and cooling time can be approximated with the help of CCT in many practical cases despite CCT are not commonly valid. Figure 17 shows CCT diagram of investigated base material S355N and its chemical composition.

The CCT diagram shows hardnesses, microstructure of phases and their portions which are consequence of cooling time.

Cooling speed differs from near the weld to areas away from the fusion line. Cooling time and temperature peaks change from middle of weld to base material during welding. The cooling time gradient causes gradient of different phases of microstructure. This can be proved with measured hardness distributions and different microstructures of phases. Hardness distributions are shown in Appendix 6 and phases of microstructures are shown in Appendix 7.

There is a difference between hardnesses with 15 mm and 5 mm thick VTT samples. Measured hardnesses are more than 400 HV with all samples which thickness are 15 mm. The 15 mm thick plates are cooled more rapidly than 5 mm thick plates which hardnesses are lower. Measurement by thermoelements of Appendix 11 supports that thicker 15 mm plates cool more rapidly than thinner 5 mm plates. Heat input affects cooling rate also. The higher is the heat input the smaller is cooling rate which affects coming phases of micro-structure.

Phases of coarse-grained zone were recognized with the help of measured hardnesses and Table 5, which includes phase recognition microstructures according to IIW (*International Institute of Welding*) (16).

Figure 70 shows microstructure of LASER welded sample 3.5.2-7 whose hardness is 484 HV. Recognised phases are martensite (M) and lower bainite (LB). The rest of recognized phases of bead-on-plate welds are show in Table 12. Other micrographs and their phase recognitions are in Appendix 6.

Table 12 Phase recognition. M = martensite, LB = lower bainite, UB =upper bainite, F = ferrite and AF = coarse acicular ferrite.

Weld-ing method	Number of samples	Recognized phases
LAHW	3.5.2-3	M + LB
LAHW	3.15.2-9	M + LB +UB
LASER	3.5.2-7	M + LB
LASER	3.15.2-5	M + LB
MAG	3.5.2-2	F + UB
MAG	3.15.2-4	M + LB
TIG	3.5.2-4	M + LB +UB
TIG	3.5.2-8	AF + F + UB
TIG	3.5.2-9	AF + UB
TIG	3.15.2-6	M + LB
TIG	3.15.2-7	M + LB
TIG	3.15.2-8	M + LB

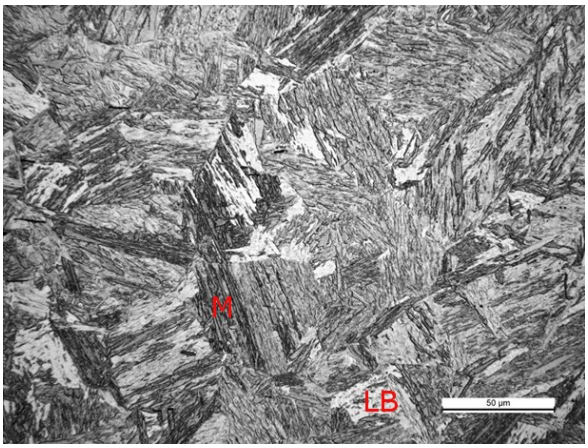

Figure 70 This micrograph of LASER welded sample 3.5.2-7 is taken with 10X ocular and 50X objective from coarse-grained zone with Leica MEF 4M light microscope. Measured maximum hardness of this microstructure is 484 HV01. Phases of this microstructure are martensite (M) and lower bainite (LB).

3.6 Measurements and calculations of bead-on-plate welds

3.6.1 Measured cooling times and their $t_{8/5}$

All bead-on-plate welds were made by University of Lappeenranta. Cooling times were measured for all bead-on-plate welds with thermoelements by VTT. Figure 71 shows positions of thermoelements of LAHW and TIG welded bead-on-plate welds. Cooling times were measured also for LASER and TIG welds.

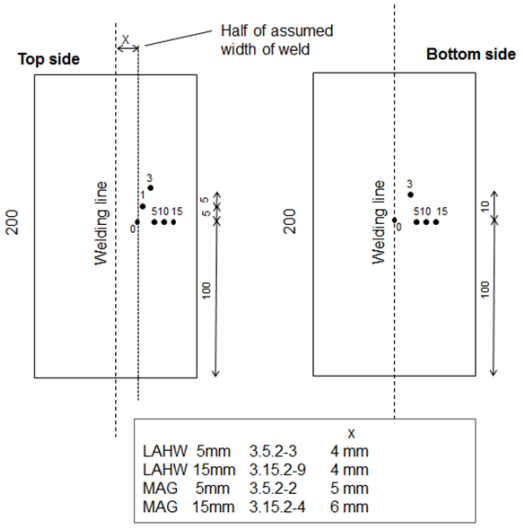

Figure 71 Position of thermoelements for bead-on-plate LAHW and MAG welded samples.

The welding line of Figure 71 means in the middle of weld, dimension x is half of assumed width of weld and numbers of marked points indicate distance between assumed fusion line and thermoelements according to Figure 71. Thermoelements were positioned to both sides of test samples.

Figure 72 shows data points of measured cooling curves for all positioned thermoelements of MAG welded sample 3.15.2-4 from face side of weld. Number of thermoelements means approximated distance between fusion line and thermoelements.

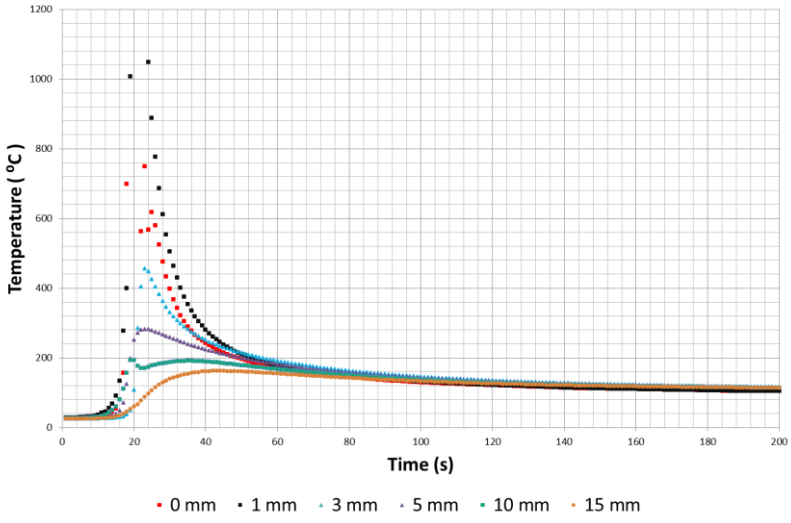

Figure 72 Face side of MAG-weld sample 3.15.2-4. Six cooling curves are measured with the help of six thermoelements which numbers in this picture describe the distance between approximated fusion line and the thermoelements.

The figure includes only one curve which temperature peak is sufficient for determination of $t_{8/5}$. Figure 73 shows determination of $t_{8/5}$ values of this cooling curve. Values of $t_{8/5}$ were determined with the help of interpolation of Excel for all cases near fusion line if possible. Positioning of all thermoelements, their measured cooling curves and their determined $t_{8/5}$ values are documented in Appendix 12.

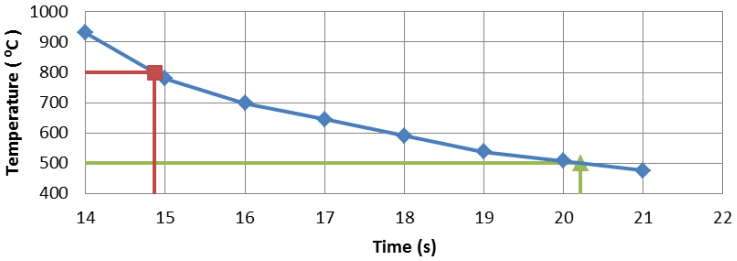

Figure 73 Measured $t_{8/5}$ is 5.4 s on face side of MAG welded VTT sample 3.15.2-2 from fusion line.

3.6.2 Measured dimensions of HAZ and weld metals

Optical microscope examination was made after etching of microsections with Leica MEF 4M light optical microscope and Leica MZ12 stereo microscope. Both microscopes were used with DFC450 digital camera and software of LAS Core V4.6.1.

Vertical and horizontal maximum dimensions of HAZ and weld metal of bead-on-plate welds were measured by Leica MZ12 stereo microscope and software of LAS Core V4.6.1. Areas of weld metals of LAHW and MAG welds were measured with Leica MZ12 stereo microscope and the same software.

Microstructures and macrostructures of bead-on-plate welds were examined with Leica MEF 4M optical light microscope. Objectives 1X, 2.5X, 10X, 20X and 50X were used with 10X ocular. Micrographs were taken from most coarsened areas of coarse-grained zone for all bead-on-plate welds with the help of with Leica MEF 4M optical light microscope.

Width and height of all bead-on-plate welds and HAZ were measured by stereomicroscope. Horisontal and vertical dimensions of bead-on-plate welds according to Figure 74 are collected in Table 13. The table of results, macrophotos of stereomicroscope and their dimensions are in Appendix 5.

Table 13 Dimensions of HAZ and weld metal according to Figure 74.

Welding process	Number of sample	Dimensions (mm)			
		Weld		HAZ	
		A	B	C	D
LAHW	3.15.2-9	10.1	5.9	11.2	5.9
LAHW	3.5.2-3	9.4	3.7	10.3	4
LASER	3.15.2-5	3.2	4.8	4.8	4.9
LASER	3.5.2-7	2.7	2.5	3.7	2.7
MAG	3.15.2-4	12.9	2.6	15.4	3.9
MAG	3.5.2-2	11.1	2.7	12.7	trough
TIG	3.15.2-6	9	3.3	12.5	5.2
TIG	3.15.2-7	8.1	2.5	10.8	3.8
TIG	3.15.2-8	7.2	1.4	9.5	2.7
TIG	3.5.2-4	7.6	1.7	9.6	3.7
TIG	3.5.2-8	10.6	3.2	19.3	trough
TIG	3.5.2-9	9.3	1.7	11.3	trough

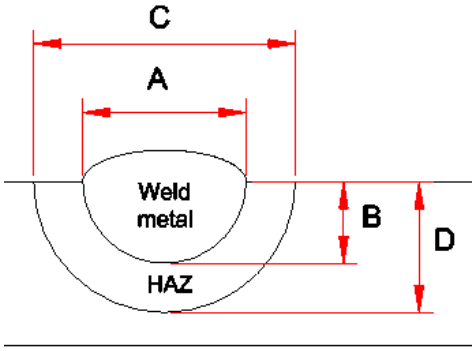

Figure 74 Dimensions of HAZ and weld metal.

3.7 Modelling of bead-on-plate welds

3.7.1 Simulated dimensions of HAZ and welds

Dimensions of HAZ and welds for TIG and MAG welds were simulated by CFD of FLOW-3D software by VTT. Welding and modelling parameters of this parallel work for TIG and MAG simulation are shown in Table 15. These welding parameters use similar parameters with Voss's doctoral thesis. All simulated dimensions of HAZs and welds of bead-on-plate welds are collected in Table 14.

Table 14 Penetrations and widths of bead-on-plate welds and HAZ.

Welding process	Simulation	Dimensions (mm)			
		Penetration		Widths	
		Fusion	HAZ	Fusion	HAZ
LAHW 3.15.2-9	-	-	-	-	-
LAHW 3.5.2-3	-	-	-	-	-
LASER 3.15.2-5	-	-	-	-	-
LASER 3.5.2-7	-	-	-	-	-
MAG 3.15.2-4	MAG-BOP-2_151201	1.4	3.4	9.6	13.6
MAG 3.5.2-2	MAG-BOP-1_151201	1.0	5.0	8.0	12.4
TIG 3.15.2-6	BOP-6_150715	2.6	4.6	10.0	13.6
TIG 3.15.2-7	BOP-7_151015	1.8	3.8	6.0	9.2
TIG 3.15.2-8	BOP-81_150602	1.4	3.4	8.0	10.4
TIG 3.5.2-4	BOP-5_150709	1.0	3.8	6.4	9.2
TIG 3.5.2-8 (1)	BOP-1_150709	1.8	5.0	11.4	14.0
TIG 3.5.2-8 (2)	BOP-14_151015	4.6	5.0	10.0	12.8
TIG 3.5.2-9 (1)	BOP-2_150709	1.4	5.0	8.2	11.0
TIG 3.5.2-9 (2)	BOP-21_151016	1.8	5.0	8.0	11.2
TIG 3.5.2-9 (3)	BOP-3b_151015	1.2	5.0	9.0	11.6

3.7.2 Simulated cooling times and their $t_{8/5}$

Cooling times for TIG and MAG welds were simulated by CFD of FLOW-3D software by VTT. Welding and modelling parameters of this parallel work for TIG and MAG simulation are shown in Table 15. These welding parameters are similar with Voss's doctoral thesis.

Table 15 Welding parameters for simulation of bead-on-plate welds.

Sample number	Simulation	Welding								Measures (cm)			
		s	I	U	P	k / η	v	E	Q	L	Mesh	Symmetry	X
		(mm)	(A)	(V)	(W)		(mm/min	(kJ/mm)	(kJ/cm)				
TIG 3.5.2-8 (1)	BOP-1_150709	5	250	10.52	2630	0.8	130	1.21	0.97	4	0.02	on	2.0
TIG 3.5.2-8 (2)	BOP-14_151015	5	250	10.52	2630	0.8	130	1.21	0.97	4	0.04	on	1.4
TIG 3.5.2-9 (1)	BOP-2_150709	5	250	10.92	2730	0.8	280	0.59	0.47	5	0.04	off	3.0
TIG 3.5.2-9 (2)	BOP-21_151016	5	250	10.92	2730	0.8	280	0.59	0.47	5	0.04	on	2.5
TIG 3.5.2-9 (3)	BOP-3b_151015	5	250	10.92	2730	0.8	280	0.59	0.47	5	0.02	on	2.4
TIG 3.5.2-4	BOP-5_150709	5	250	10.24	2560	0.8	430	0.36	0.29	6	0.04	on	2.0
TIG 3.15.2-6	BOP-6_150715	15	250	10.24	2560	1	130	1.18	1.18	4	0.04	on	1.8
TIG 3.15.2-7	BOP-7_151015	15	250	10.00	2500	1	280	0.54	0.54	5	0.04	on	2.5
TIG 3.15.2-8	BOP-81_150602	15	250	10.00	2500	1	430	0.35	0.35	6	0.04	on	2.6
MAG 3.5.2-2	MAG-BOP-1_151201	5	196	29.5	5782	0.8	550	0.63	0.50	11	0.04	on	5.5
MAG 3.15.2-4	MAG-BOP-2_151201	15	196	29.5	5782	0.8	350	0.99	0.79	9	0.04	on	4.5

LASER and LAHW welds were not simulated. Influence of mesh size was investigated between TIG 3.5.2-8 (1) and TIG 3.5.2-8 (2). Influence of mesh size and used calculation symmetry were investigated between TIG 3.5.2-9 (1), TIG 3.5.2-9 (2) and TIG 3.5.2-9 (3). L means length of simulated part and X means position of investigated cross-section of FLOW-3D.

Figure 75 and 76 were created by the FLOW-3D software. These figures describe dimensions of HAZ and weld metal when the fusion is largest. Red color describes weld metal, yellow color the fusion line, green color HAZ areas and blue color base material.

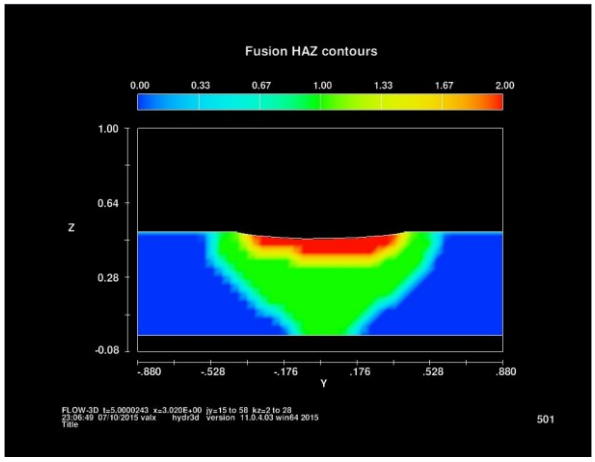

Figure 75 CFD analyses of bead-on-plate welds with FLOW-3D.

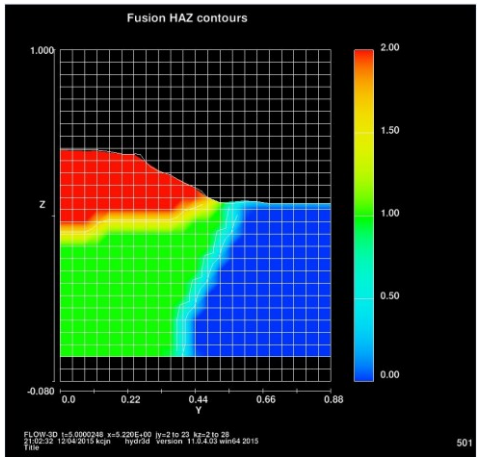

Figure 76 CFD analyses of bead-on-plate welds with FLOW-3D.

Cooling curves were simulated with the help of FLOW-3D for all bead-on-plate welds according to Figure 77. Results of cooling curves and their $t_{8/5}$ values are collected in Appendix 13 excepted LAHW welds.

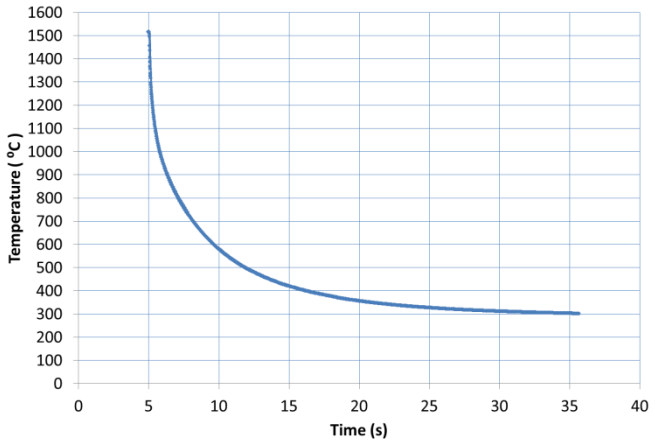

Figure 77 Cooling curve of TIG welded sample. This curve is simulated near to fusion line.

Simulated cooling curves and their $t_{8/5}$ values were determined for all cases for fusion line and for position of measured maximum hardness of coarse-grained zone, with the exception of TIG welded sample 3.15.2-8 due to measured insufficient temperature area. Values of simulated $t_{8/5}$ are determined in similar way as with case of the thermoelements of VTT samples. Determined $t_{8/5}$ values for all simulated cooling curves of bead-on-plate welds are in Appendix 13 except TIG welded sample 3.15.2-8.

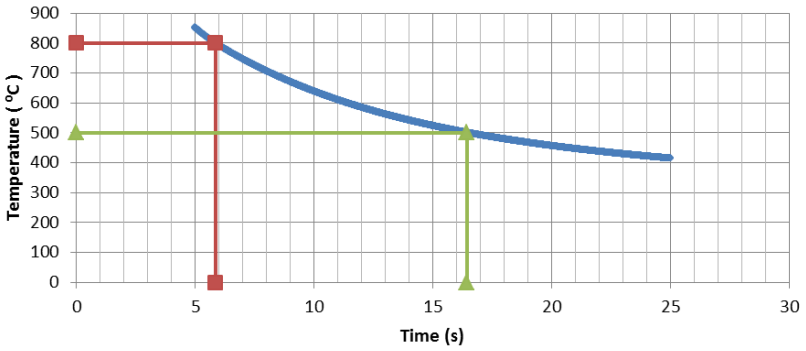

Figure 78 FLOW-3D simulated $t_{8/5}$ is 5.9 s on top side of MAG welded VTT sample 3.15.2-2 for fusion line.

Figure 78 shows determination of $t_{8/5}$ for fusion line and Figure 79 shows determination of $t_{8/5}$ in position of maximum hardness of coarse-grained zone for MAG welded sample 3.15.2-4. Determined $t_{8/5}$ values show only small difference between Figure 78 and 79.

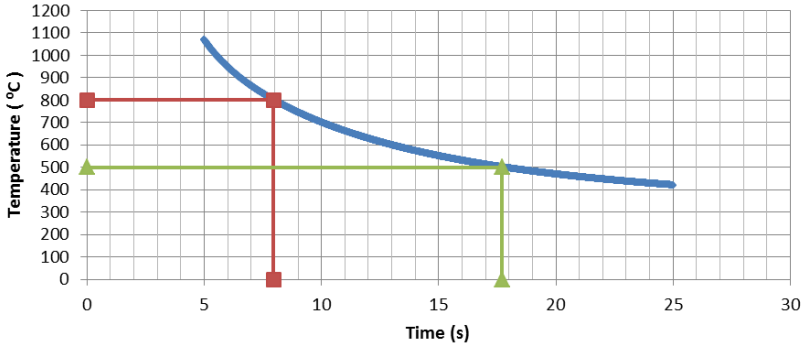

Figure 79 Figure 80 FLOW-3D simulated $t_{8/5}$ is 8.0 s on top side of MAG welded VTT sample 3.15.2-2 for coarse-grained zone 1 mm from fusion line.

3.8 Results of Voss's doctoral thesis

Cooling times, their $t_{8/5}$ values, dimensions of HAZ and weld metal and hardness distributions of TIG welded bead-on-plate samples which are results of Voss's doctoral thesis are collected in Appendix 14 (40). The results of Voss's doctoral thesis support results of the dimensions of HAZ and weld metals and the hardness distributions of this master thesis. Only one value of $t_{8/5}$ of Voss's doctoral thesis was determined because other measured ranges of cooling curves were insufficient.

Voss's doctoral thesis used same welding parameters with material modelling which are shown in Table 15. There are small differences between welding parameters of the Voss's doctoral thesis and welding parameters of the bead-on-plate weld samples of VTT.

The comparison between the results of the bead-on-plate samples of VTT, Voss's doctoral thesis and FLOW-3D simulations are in chapter 7.

4 Defining residual stresses with Contour and XRD methods

Another purpose of this master thesis was to find out if XRD and Contour measured residual stresses of butt weld samples corresponded. Distribution of residual stresses in butt weld samples was measured with X-ray diffraction on surface. Distributions of residual stresses normal to the cut surfaces are measured with the help of contour method.

4.1 Butt welds and their welding parameters

Butt weld samples of VTT were welded by LUT and all their investigations were made by VTT. Figure 81 shows section of but weld of MAG and Figure 82 shows section of butt weld of LAHW, their dimensions and welding sequence.

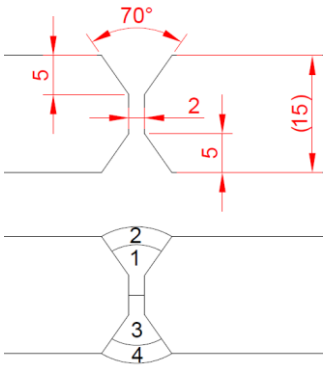

Figure 81 Section of MAG weld.

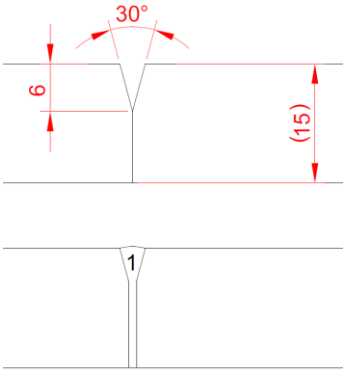

Figure 82 Section of LAHW. (LASER-MAG)

Table 16 shows used welding methods for butt welds, their welding parameters and other information. All sample materials of butt welds were S355N. Test plate information for 15 mm plates of samples is in Appendix 2. One sample of base material which dimensions were 400x150x15 mm was also examined. All butt welds of Table 16 were assembled this kind of plates. Photographs of these samples can be found in Appendix 4.

Table 16 Information of butt welds and their welding parameters.

Welding method & Sample number		Code	s	I	U	P	v	v	Filler metal	Shielding gas
			Plate thickness (mm)	(A)	(V)	(kW)	Filler metal (m/min)	Welding speed (mm/min)		
MAG 1	root pass	3.15.4V-17 & 3.15.4V-4	15	201	25.6	5.1	9.6	300.00	Aristorod 12.50 1mm	Awomix 8% CO2, Argon, 16 l/min
	final pass			229	29.2	6.7	10.6			
MAG 2	root pass	3.15.4V-1 & 3.15.4V-16	15	201	25.6	5.1	9.6	300.00	Aristorod 12.50 1mm	Awomix 8% CO2, Argon, 16 l/min
	final pass			229	29.2	6.7	10.6			
Base plate 3		-	15	-	-	-	-	-	-	-
LAHW 5		-	15	339	25.2	8.5	10.5	?	18mm free wire	Awomix 8% CO2, Argon, 16 l/min

4.2 Macrographs and micrographs of butt-welded LAHW and MAG samples

Optical micrographs of butt welds were taken in similar way as bead-on-plate welds by VTT. Macrographs of MAG welded sample 1 and LAHW welded sample 5 were taken with Leica MZ12 stereo microscope. Micrographs of MAG welded sample 1 and LAHW welded sample 5 were taken with Leica MEF 4M light optical microscope.

Figure 83 shows macrograph of MAG welded sample and Figure 84 shows macrograph of LAHW welded sample. Macrographs and micrographs are collected in Appendix 18.

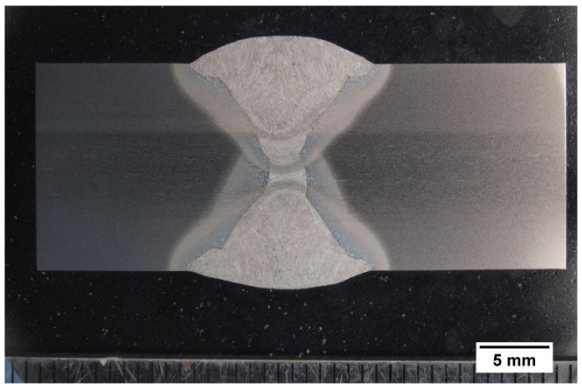

Figure 83 MAG welded sample 1.

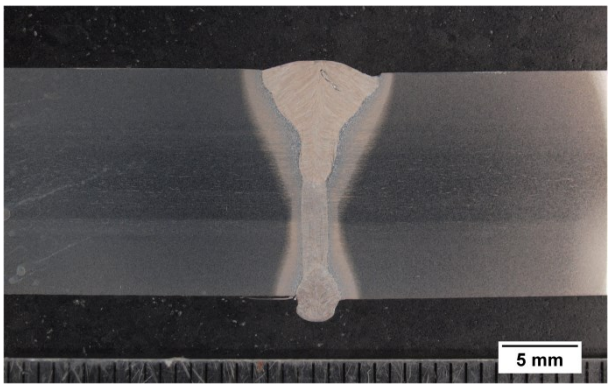

Figure 84 LAHW welded sample 5.

4.3 Hardness distributions of butt welds

Hardnesses of butt welds were measured in similar way with bead-on-plate welds excepted following by VTT. Hardnesses were measured along horizontal lines from base material across HAZ and weld to base material with 1 mm spacing according to recommendation of SFS-EN ISO 9015-2 and according to SFS-EN ISO 6507-1 (39). Measuring lines were positioned at the depth where the most coarse grain areas existed.

Measured hardness distributions for MAG welded sample 1 which is measured from 0.9 mm deep and LAHW welded sample 5 which is measured from 1.5 mm deep are collected in Appendix 17.

Maximum measured hardness of coarse-grained zone of MAG welded sample 1 was 306 HV1 which was measured from 1.4 mm deep and 0.58 mm from fusion line. Maximum measured hardness of coarse-grained zone of LAHW welded sample 5 was 295 HV1 which was measured from 1.0 mm deep and 0.12 mm from fusion line.

4.4 Implementation of X-ray diffraction

All samples which are shown in Table 16 were measured with XRD in Aalto University. Impurities were removed before marking measuring points of XRD. Roll scale and rust was etched away from surface of samples with the help of cleaner of fracture surface (6-n $HCl+C_6H_{12}N_4$). Benefit of this acid it is that is etching away rust, roll scale and other impurities, but not base material. Figure 85 shows etched area and marked XRD measuring points of one sample.

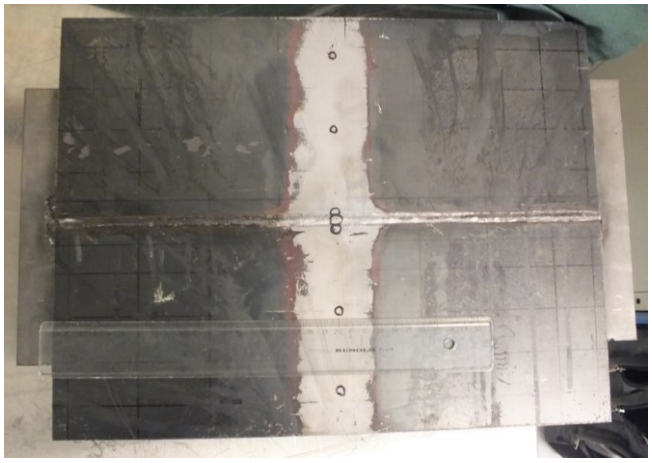

Figure 85 Etched surface of weld sample and some marks of XRD measuring points.

Blue measuring points of XRD and EDM cutting lines are marked for base material in Figure 86 and one side of butt weld samples in Figure 87. Positions of all measuring points for other samples are shown similarly in Appendix 10.

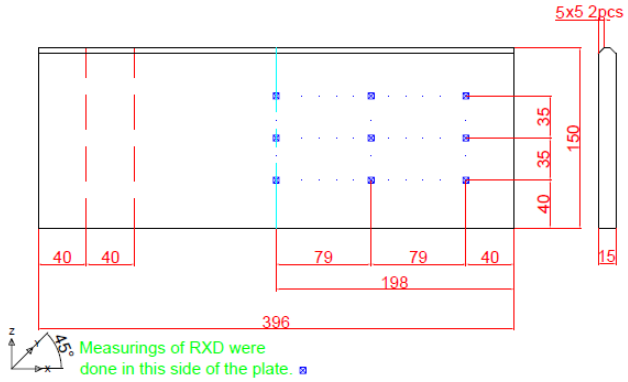

Figure 86 Dimension of base material plate, its X-ray difraction measuring points (blue) and EDM cutting dotlines.

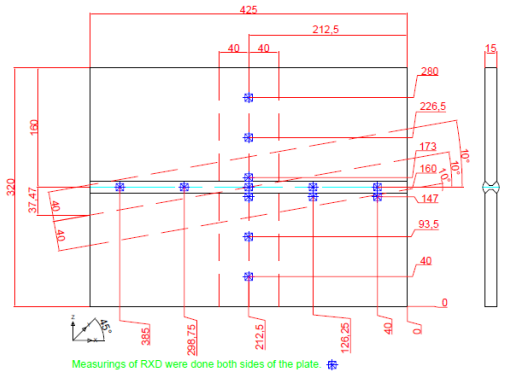

Figure 87 Dimension of MAG and LAHW welds, some X-ray difraction measuring points (blue points) and EDM cutting dotlines.

Measuring of X-ray diffraction was made by X-Stress 3000 according to Figure 88 CrK∝ of X-ray tube and collimator which diameter was 5 mm were used. Figure 88 shows unit which includes goniometer, X-ray tube and detectors. Cover of diffractometer was removed during photographing. This X-ray measuring device includes central processing unit which creates high voltage for X-ray tube and computer with software of measuring which guides the measuring device. Used parameters of X-ray diffraction measurings are in Table 17.

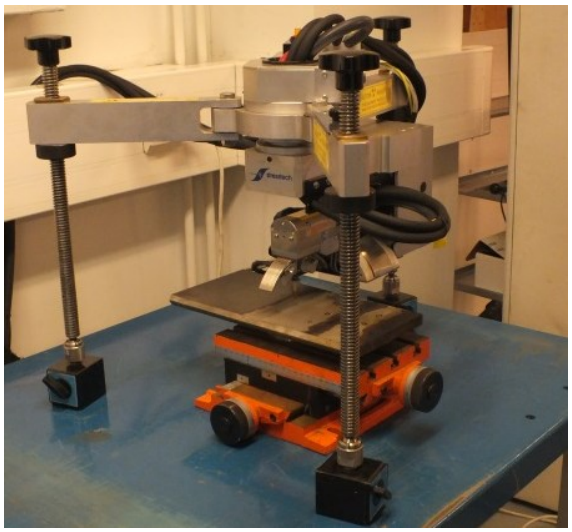

Figure 88 XRD diffractometer and sample.

Table 17 Parameters of measuring of X-ray diffraction.

Cr-tube:	CrKα	Inclination:	45°
I:	6.7 mA	Oscillation:	0
U/I:	30 kV	Rotation:	0° / 45° / 90°
Exp time:	8 s	phi oscillation:	0
Calibration:	10.07 mm	nro oscillation:	0
Pulver material:	α - Fe	Material information:	x - Fe
Collimator D:	3 mm	hkl:	211
Measuring method:	psi	Poisson's ratio:	0.3
psi tilt:	6 / 6	E:	211 GPa

Figure 89 (a) shows positions of XRD measuring points and Figure 89 (b) shows XRD measured distributions of residual stresses on surface of MAG welded sample 1. Measured distributions of residual stresses for base material, MAG welded samples and LAHW sample are collected in Appendix 10.

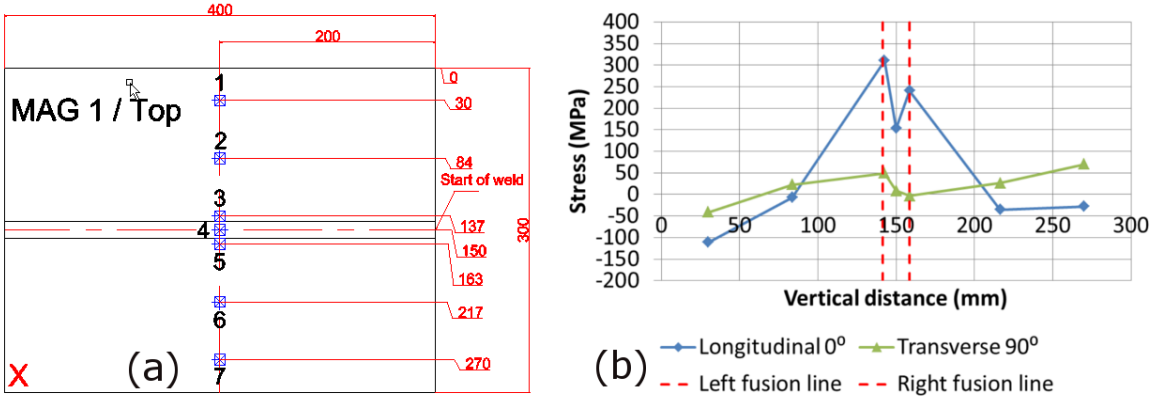

Figure 89 (a) Positions of XRD measuring points of MAG welded sample 1 are introduced in this picture. (b) Distributions of residual stresses of MAG welded sample 1.

4.5 Implementation of Contour measurement

Residual stress normal to the cut plane was measured with the help of contour method. Base material plate was cut before measuring of XRD diffraction. Other butt weld samples were measured by XRD before cutting and measuring with contour method.

Figure 90 and 91 show EDM cutting device which was used for the cutting of samples. Diameter of Ni and Zn coated brass cutting wire was 0.25 mm which caused 0.33-0.32 mm width cutaway. Cutting voltage was 85 V and cutting speed 2.5 mm/min.

Figure 90 EDM cutting device.

Figure 91 EDM cutting in deionized water.

Figure 92 shows rigid support of base material on rigid frame. Base material was cut with EDM cutting along the red dashed line according to Figure 93.

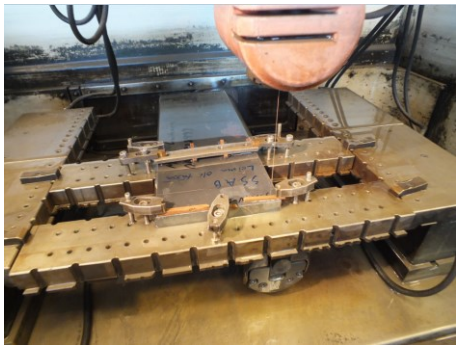

Figure 92 Supporting of base material plate (Sample 3).

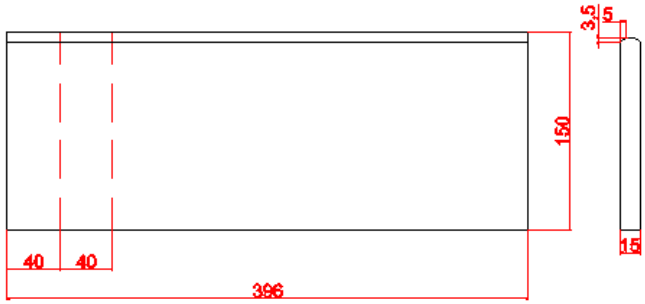

Figure 93 Dimensions and cutting lines (red dot lines) of base material (Sample 3).

Figure 94 shows rigid support of MAG welded sample 1 on rigid frame. MAG welded sample 1 was cut with EDM cutting along the red dashed line according to Figure 95

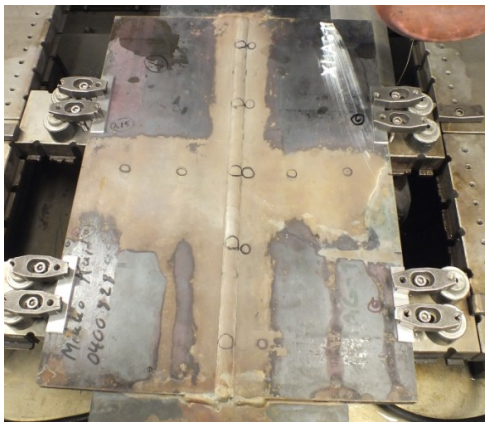

Figure 94 Supporting of base MAG welded sample 1.

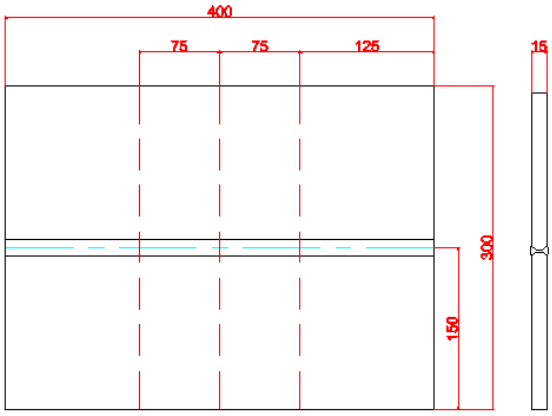

Figure 95 Cutting of MAG welded sample 1.

Figure 96 shows rigid support of MAG welded sample 2 on rigid frame. MAG welded sample 2 was cut with EDM cutting along the red dashed line according to Figure 97.

Figure 96 Supporting of MAG welded sample 2.

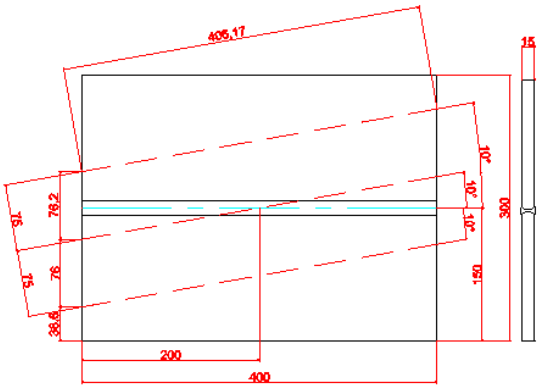

Figure 97 Cutting of MAG welded sample 2

Figure 98 shows rigid support of LAHW welded sample 5 on rigid frame. LAHW welded sample 5 was cut with EDM cutting along the red dashed line according to Figure 99.

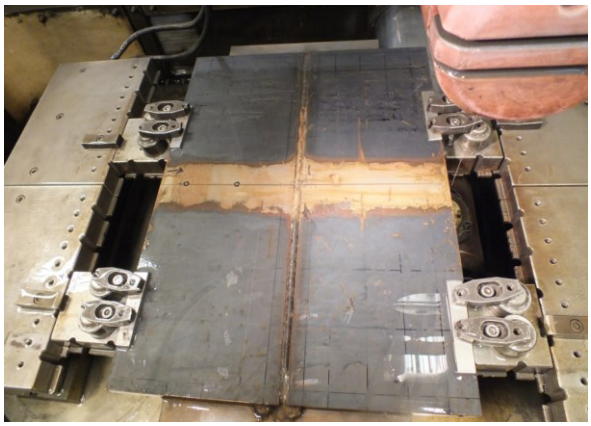

Figure 98 Supporting of LAHW welded sample 5.

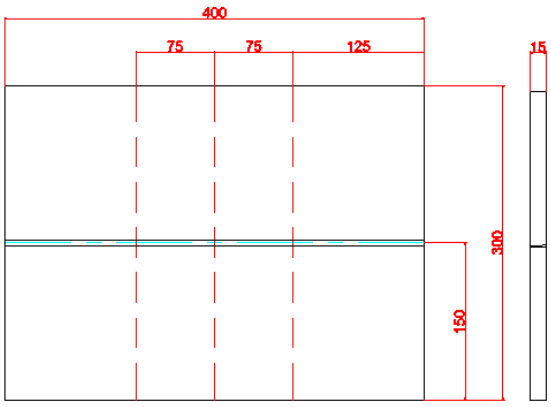

Figure 99 Cutting of LAHW welded sample 5.

Most of shear surfaces of investigated samples were cleaned smoothly with cleaner of fracture surface (6-n HCl+$C_6H_{12}N_4$) due to rust and impurities. Benefit of this cleaner is that it does not etch topography of investigated shear surface. Cutting surfaces and their origins were marked for all samples.

Investigated shear surfaces were measured with the help of Mitutoyo Legex 9106 coordination measuring machine by VTT. The CCM measuring machine, measuring tip and supporting of sample are shown in Figure 100, 101 and 102.

Figure 100 Coordination measuring machine (CMM).

Figure 101Measuring ball tip of CMM which diameter is 3 mm.

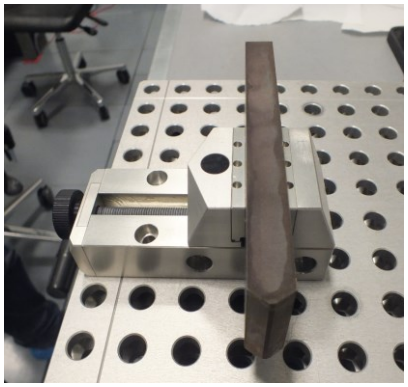

Figure 102 All samples were supported similarly according to this picture.

Measuring accuracy follows standard ISO 10360-2. Maximum error for length is (0.35+L/1000) µm when L = mm. Maximum deviation for 3D touch is 0.35 µm and maximum error for scanning is 1.4 µm. Measuring force is between 0.03 N and 0.09 N and diameters of measuring tips between 0.5 and 30 mm. Diameter of used measuring tips was 3 mm.

Flatness of samples was determined with the method of least square with the help of 6 measuring points at first. Results of determined flatness are points in measuring coordination which file format are dxf. Dxf-files were opened with Vertex G4 design software and 3D planes were created with the help of Vertex G4 by extruding. 3D planes were exported to IGES because this makes possible creating net over surfaces of welds. Software of the CMM is CAT 1000PS MCOMOS-3V35.R6 which can open IGES-files. Measuring area, measuring sequence and densities of measuring points were determined. Measurings were started after simulations and results of the measurings are topographies of measured surfaces in GWS-format.

The distributions of residual stresses on normal cut surface were calculated with the help of the deformation of the surface height map with FEM. Deformed cut surface was forced back to its original shape. Changes of stress were determined with the help of displacements. Used FEM software was Elmer which is an open source simulation software which mainly was developed by IT Center for Science (CSC).

The results of Contour method are two-dimensional maps of residual stresses normal to the measurement plane. Maps of both cutting surfaces for base material are shown in Figure 103 (a) and (b). Results of two-dimensional map of base material, two MAG welded samples and LAHW samples are shown in Appendix 11.

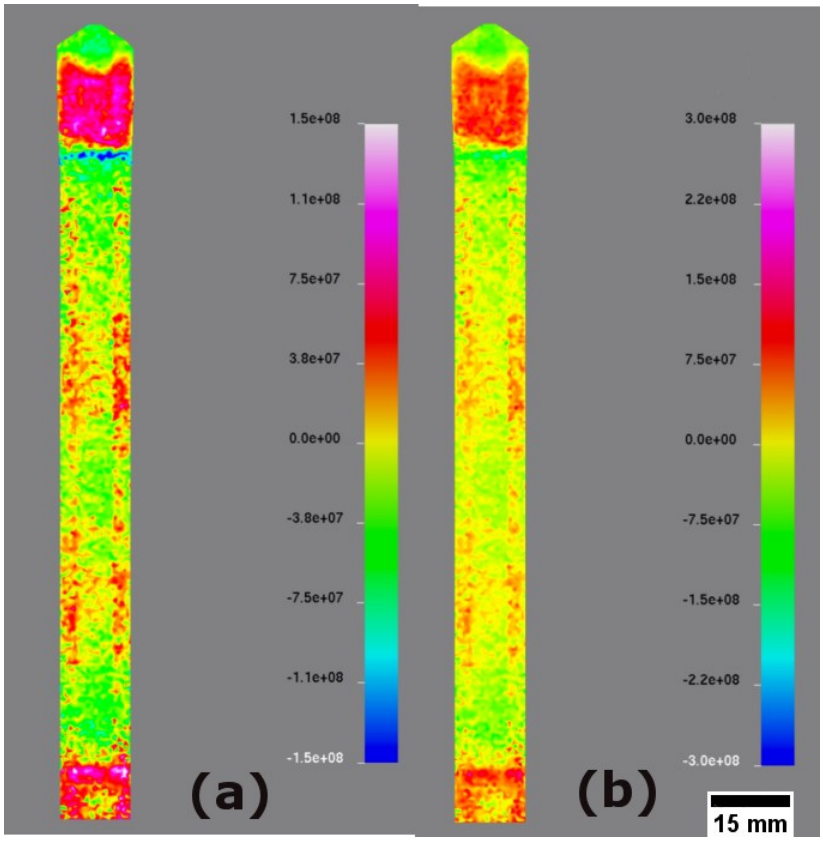

Figure 103 (a) Two-dimensional map of residual stresses normal to the measurement plane of base material. (b) Two-dimensional map of residual stresses normal to the measurement plane of base material. Scale of stresses is different for opposite plane for (a).

5 Measuring and calculating of mixing of MAG and LAHW welds

Mixing of MAG and LAHW welds were determined with calculated Cr, Ni and Fe contents of weld samples, Schaeffler diagram, WRC-92 diagram and EDS measured Cr, Ni and Fe distributions of bead-on-plate welds. Additional investigation of MAG welded sample 3.15.2-4 was done with etched microstructure of stainless weld metal and optical spectroscopy.

Microstructures of MAG and LAHW samples are different from other bead-on-plate welds due to mixture of stainless filler metal and carbon steel base material. Base metal of these samples was S355N and filler metal ESSAB OK AUTROD AISI 308 LSi which contains 20 wt% chromium and 10 wt% nickel (41). Mixing of stainless filler metal is clarified with the help of distributions of chromium, nickel and iron.

Distribution of chromium, nickel and iron was measured for weld samples 3.15.2-9 (LAHW), 3.5.2-3 (LAHW), 3.15.2-4 (MAG) and 3.5.2-2 (MAG) by EDS (*Energy-Dispersive X-ray Spectroscopy*) in Aalto University. Filler metal of these welds was stainless OK AUTROD 308 LSi. EDS-analyses were made with Zeiss Ultra 55 SEM-microscope (*Scanning Electron Microscope*) before etching of microsections.

Figure 104 (a) shows root side of MAG welded sample and measuring line of EDS where measured chromium and nickel distributions are shown in Figure 104 (b) and measured iron distribution in Figure 104 (d). Average distributions of chromium and nickel are shown in Figure 104 (c). It is easier to examine average distribution because variation of measured distributions makes examination too difficult.

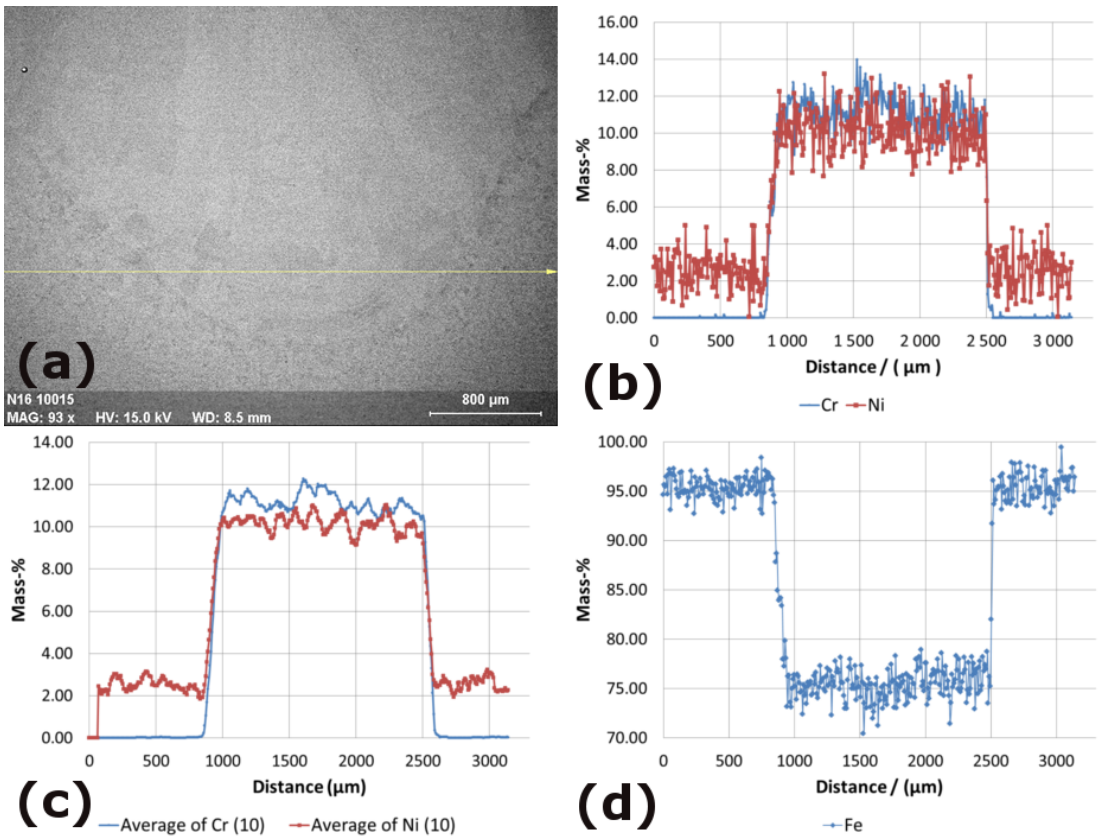

Figure 104 (a) Position and direction of measuring line 1 (EDS 1) for MAG welded sample 3.15.2-4. (b) Measured Cr and Ni distributions of measuring line 1. (c) Moving average of Cr and Ni distributions of measuring line 1 (n=10). (d) Measured Fe distribution of measuring line 1.

Figure 104 (c) shows that contents of chromium and nickel increase from base material to weld metal side. The increase of chromium and nickel is very steep in fusion line. Average content of chromium is 11 wt% and nickel 10 wt% in weld metal side according to Figure 104 (c). Iron content seems to be 75 wt% according to Figure 104 (d). This means that content of other elements is 4 wt%.

Five chromium and five nickel distributions were measured for each LAHW and MAG welds by EDS. Average of distributions was determined for all measured distributions of weld metal. The distributions and their average distributions are collected in Appendix 8.

Chromium and nickel contents of MAG welded sample 3.15.2-4 were measured with the optical emission spectrometry by VTT. Face side of MAG welded sample 3.15.2-4 was warmed up and forged because measuring area needed to be extended. Face side of sample was grinded before measuring of optical emission spectroscopy according to picture of Appendix 9. Measured content of chromium was 12.8 wt% and content of nickel was 6.8 wt%. All measured chemical contents are collected in Appendix 9.

Etching of MAG welded sample 3.15.2-4 was investigated. Figure 105 shows microstructures of HAZ and weld metal which is combination of Nital etched HAZ and nitrohydrochloric acid etched weld metal which were combined with the help of Gimp 2. Figure 105 shows that etching is even in weld metal. Even etching supports that mixing is even.

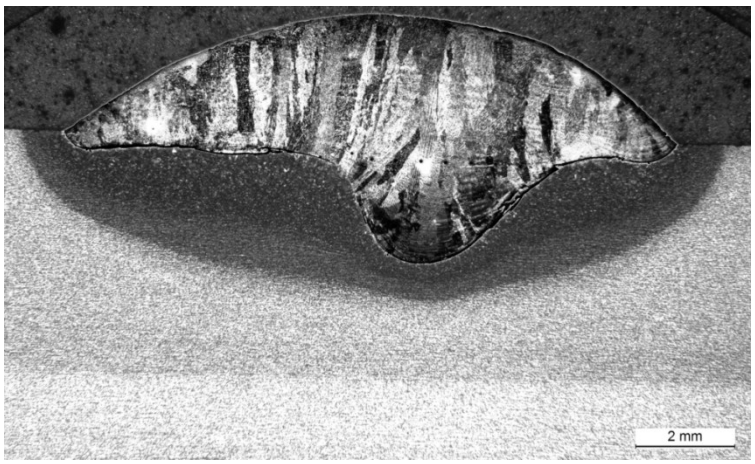

Figure 105 Microstructure of MAG welded sample 3.15.2-4.

Cr- and Ni-contents of MAG and LAHW samples are calculated with the help of mixing calculations which based on geometry of weld metals and even mixing which are detected with EDS and etching of MAG welded 15 mm thick sample 3.15.2-4. Mixing is not typically so even with thicker plates. It can be assumed that mixing of thinner 5 mm thick 3.5.2-2 sample is even for this reason. Mixing of arc welded samples is usually more even than mixing of LASER welded samples and mixing of LAHW welds are between these welds. Calculated mixings of MAG welds are typical MAG welds. (18) (1) (5). Mixing of LAHW welding are typically smaller (5).

Figure 106, 107, 108 and 109 show macro-sections of welds and measured areas of these weld metals. Filler metals of the welds were AISI 308 LSi which contains 20% chromium and 10% nickel. The areas of the weld metals were measured with Leica stereo optical microscope MZ12 and its software of LAS Core V4.6.1. Mixing was calculated for all the weld samples with the help of equation (10). Mixing of MAG welded sample 3.5.2-2 is calculated below.

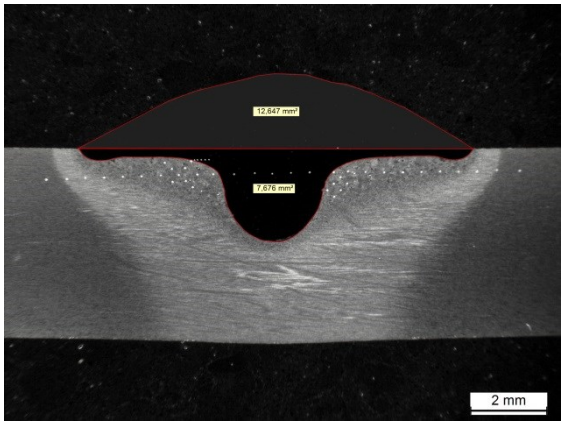

Figure 106 MAG welded sample 3.5.2-2.

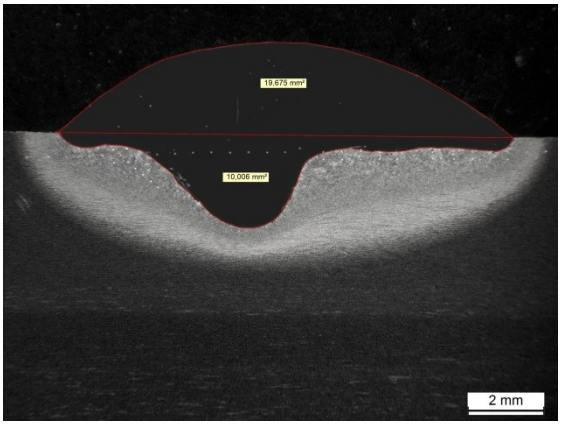

Figure 107 MAG welded sample 3.15.2-4.

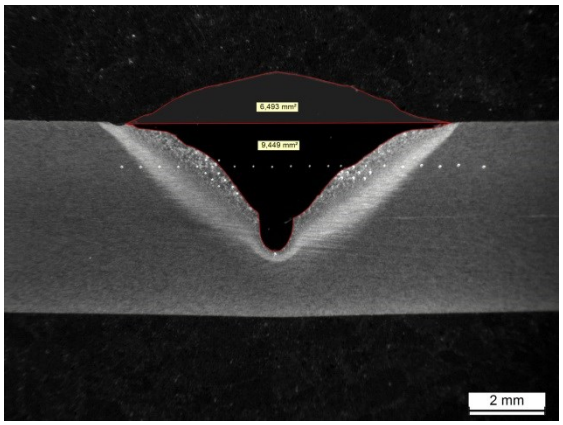

Figure 108 LAHW welded sample 3.5.2-3.

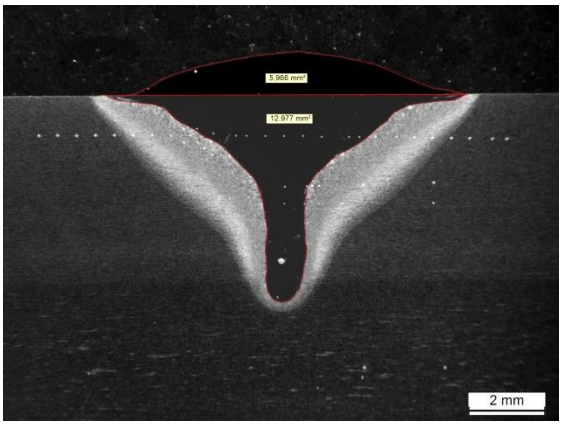

Figure 109 LAHW welded sample 3.5.2-9.

$$Mixing = \frac{P}{(L+P)} * 100\% = \frac{7.676}{(7.676 + 12.647)} = 37.8\%$$

Calculated mixing 37.8% means content of base material. Content of filler metal is 100% - 37.8% = 62.2%. Cr- and Ni contents of 3.5.2-4 in weld metal are calculated as follows. Amount of chromium is $62.2\% * 0.20 = 12.4\%$ and amount of nickel is $62.2\% * 0.10 = 6.2\%$.

Mixing, chromium and nickel contents are calculated for samples 3.5.2-4, 3.15-2-4, 3.5.2-3 and 3.15.2-9. Results of these calculations are collected in Table 18. Calculation of mixing shows that all MAG welds are mixed evenly because relation of contents of Cr and Ni are near contents of filler metal. The rates of mixing are typical for MAG and LHAW welding (5).

Table 18 Calculated Cr and Ni contents and mixing of MAG and LAHW welds.

Sample number	L (mm^2)	P (mm^2)	Mixing of base material (wt %)	Mixing of weld metal (wt %)	Cr content (w t%)	Ni content (wt %)
MAG 3.5.2-2	12.6	7.7	37.8	62.2	12.4	6.2
MAG 3.15.2-4	19.7	10.0	33.7	66.3	13.3	6.6
LAHW 3.5.2-3	6.5	9.4	59.3	40.7	8.1	4.1
LAHW 3.15.2-9	6.0	13.0	68.5	31.5	6.3	3.1

Microstructure of weld metal is fully martensitic according equivalents of filler metal, equivalents of base material and WRC-92 diagram. On the other hand microstructure of weld metal is mostly martensitic which includes little austenite according to equivalents of filler metal, equivalents of base material and Schaeffler diagram. Microstructure is similar according the diagrams and equivalents which are calculated for weld metal according to contents of optical emission spectroscopy.

Phases of microstructure of MAG welded sample 3.15.2-4 are evaluated with the help of the Schaeffer diagram according to Figure 110 and equivalents of Table 19. Calculated chromium and nickel equivalents of OK Autrod AISI 308 LSi and S355N are shown in Table 19. Composition of S355N is used according to Appendix 2. Composition of filler metal according to filler metal book of ESAB is included in same table (41). This book does not tell amount of Nb and Mo. Amount of these metals are evaluated (5). Composition of MAG welded sample 3.15.2-4 which is measured with optical emission spectrometer is included in Table 19. Measured compositions of optical emission spectrometer of weld metal are in Appendix 9.

Table 19 Calculated chromium and nickel equivalent of MAG welded sample 3.15.2-4 according to Cr- and Ni-equivalents of Schaeffler diagram. Equivalents were calculated for S355N and filler metal of OK Autrod 308 LSi.

S355N				OK Autrod 308Lsi (ESAB)				OK Autrod 308Lsi (OES)			
Cromium equivqlent		Nickel equivalent		Cromium equivalent		Nickel equivalent		Cromium equivalent		Nickel equivalent	
Element	Composition (wt%)	Element	Composition (wt%)	Element	Composition (wt%)	Element	Composition (wt%)	Element	Composition (wt%)	Element	Composition (wt%)
Cr	0.05	Ni	0.04	Cr	20.00	Ni	10.00	Cr	12.80	Ni	6.81
Mo	0.01	C	0.161	Mo	0.10	C	0.025	Mo	0.03	C	0.067
Si	0.20	Mn	1.40	Si	0.80	Mn	1.80	Si	0.60	Mn	1.59
Nb	0.03	**Ni-ekv**	**5.57**	Nb	0.04	**Ni-ekv**	**11.65**	Nb	0.04	**Ni-ekv**	**9.62**
Cr-ekv	**0.37**			**Cr-ekv**	**21.32**			**Cr-ekv**	**13.75**		

Dots of Figure 110 which intercept blue line are used with evaluation of included phases according to contents of filler metal of manufacturer (ESAB) and base material. Microstructure is mainly martensite and a little amount of austenite with mixing of 33.7 % according to marked blue dot inside which is small yellow dot.

Chromium and nickel equivalent were calculated with the help of results of OES according Table 19 and it is positioned in Schaeffler-diagram of Figure 110. This position describes red dot which shows microstructure of welded sample which is measured with optical spectroscopy. The red dot is positioned near a yellow dot. The yellow dot describes microstructure which is determined with the help of calculated Cr- and Ni-equivalents of the Table 19 and dilution calculation. Microstructure is mainly martensite and a little amount of austenite with the result of OES of welded sample and calculated equivalents of S355 and OK Autrod 308Lsi. Schaeffler diagram supports the measured contents of OES which are measured for sample 3.15.2-4.

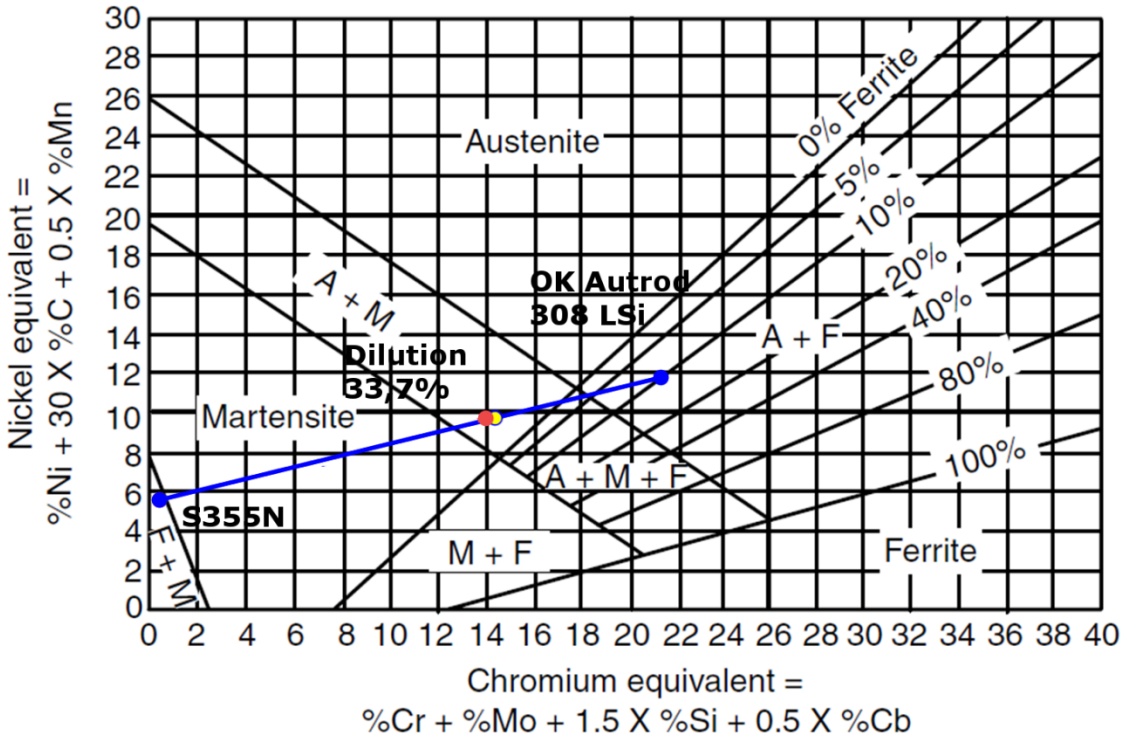

Figure 110 Schaeffler-diagram.

Phases of microstructure of MAG welded sample 3.15.2-4 are evaluated with the help of the WRC-92 diagram according to Figure 111 and equivalents of Table 20. Calculated Cr- and Ni-equivalents of OK Autrod AISI 308 LSi and S355N are shown in Table 20. Compositions of S355N are used according to Appendix 2. Compositions of filler metal are used according to filler metal book of ESAB which is included in same table (41). This book not shows amount of N, Cu, Nb and Mo. Amount of these metals are evaluated (5). Compositions of weld metal of MAG welded sample 3.15.2-4 are measured with optical emission spectrometer which results are included in Table 19. Measured compositions of optical emission spectrometer are in Appendix 9.

Table 20 Calculated chromium and nickel equivalent of sample MAG 3.15.2-4 according to equations of WRC 92 diagram. Equivalents were calculated for S355N and filler metal of OK Autrod 308 LSi.

S355N				OK Autrod 308Lsi (ESAB)				OK Autrod 308Lsi (OES)			
Cromium		Nickel equivalent		Cromium		Nickel equivalent		Cromium		Nickel equivalent	
Element	Composition (wt%)	Element	Composition (wt%)	Element	Composition (wt%)	Element	Composition (wt%)	Element	Composition (wt%)	Element	Composition (wt%)
Ni	0.04	Cr	0.05	Ni	10.00	Cr	20.00	Ni	6.81	Cr	12.80
C (max)	0.161	Mo	0.01	C	0.025	Mo	0.10	C	0.067	Mo	0.03
N	0.01	Nb	0.03	N	0.06	Nb	0.04	N	0.06	Nb	0.04
Cu	0.02	**Cr-ekv**	**0.08**	Cu	0.06	**Cr-ekv**	**20.13**	Cu	0.06	**Cr-ekv**	**12.86**
Ni-ekv	**5.78**			**Ni-ekv**	**12.09**			**Ni-ekv**	**10.37**		

Dots of Figure 111 which intercept blue line are used with evaluation of included phases according to contents of filler metal of manufacturer (ESAB) and base material. Microstructure is pure martensite with mixing of 33.7 % according to marked blue dot inside which is small yellow dot.

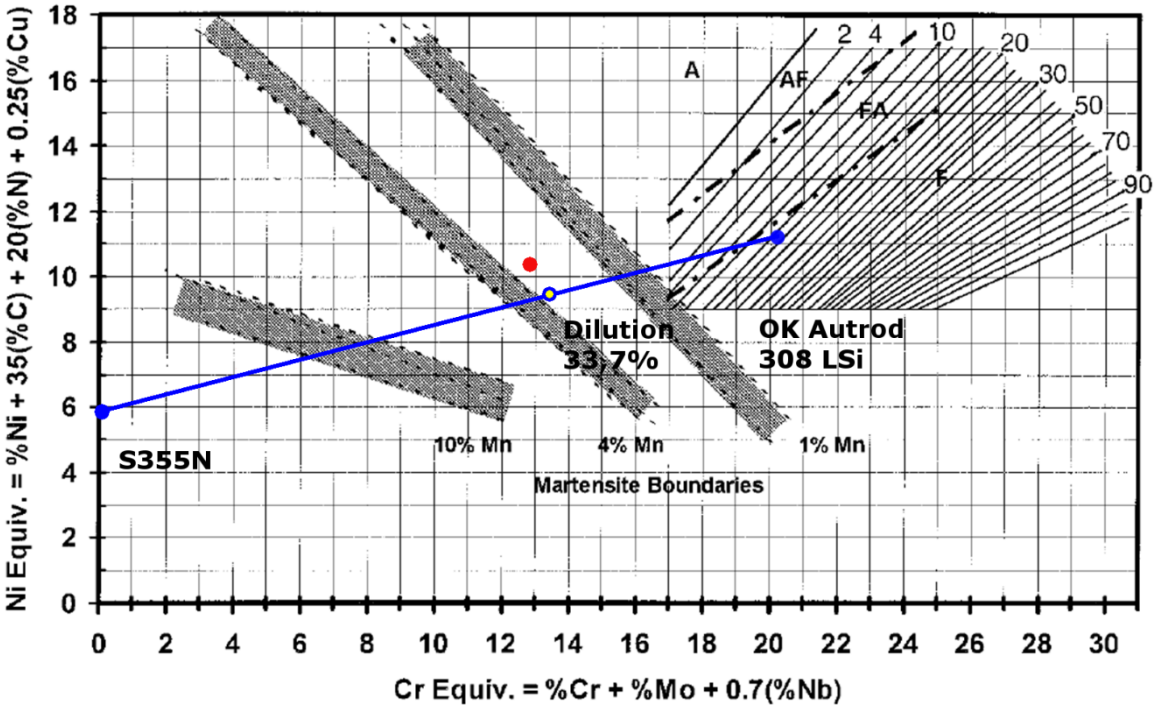

Figure 111 WRC-92 diagram.

Chromium and nickel equivalents were calculated with the help of the OES of the welded metal according Table 20 and it is positioned in Figure 111. This position describes red dot which shows microstructure of OES for weld metal. The red dot is positioned near yellow dot. Microstructure is pure martensite according contents of OES which is same result as mixing of S355 and OK Autrod 308Lsi. WRC-92 diagram supports the measured contents of OES which are measured for sample 3.15.2-4.

6 Determining maximum grain sizes and grain size distributions

Variation of grain size influences the mechanical properties of the welded joint. Determination of grain size distribution for a weld is more useful than determination of grain size because it gives a more realistic description of the variation of the grain size. Grain size distributions were measured for coarse-grained zone of all bead-on-plate welds over weld according to Appendix 15. Grain-size distributions of weld metal were determined for all TIG- and LASER-welds.

Determination of grain size distribution was based on average grain intercept method which is explained in standard ASTM E112-13 (42). Grain size distributions for bead-on-plate welds were determined with the help of micrographs, image processing and Pauli Lehto's Matlab code which is based on standard ASTM E1382 (43). Micrographs were processed with Photoshop software. Wikipedia of Aalto University was utilized with determination of grain size distribution. The Wikipedia includes Matlab grain size measurement code, theory and instructions for grain size determination. (44)

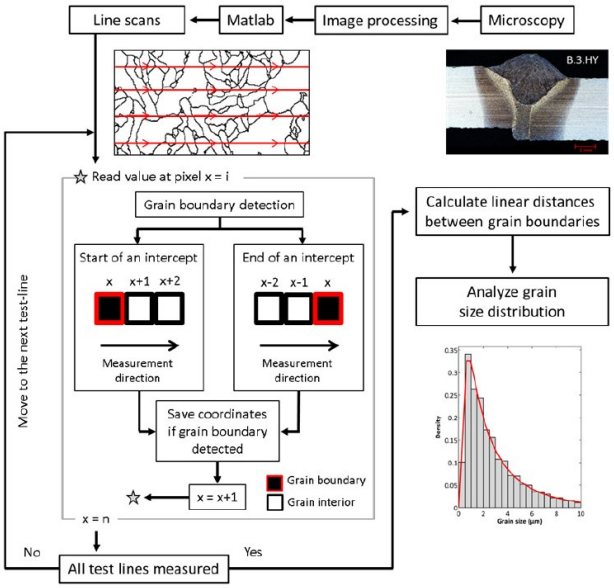

Figure 112 Defining of grain size distribution with the help of microscopy, image processing and Matlab according to ASTM E1382. (45)

Microsections were ground, polished and etched with Nital in the same way as before. Image processing of grain boundary maps was done according to Figure 112.

Mosaic micrographs were taken with 10X ocular and 50X objective with optical microscope and were collected automatically together with the software of the microscope. One micrograph was taken with same magnification so that it included scale bars due to clarification of scale. Scale of mosaic micrograph was settled with the help of scale bar. Scale bars were not included in mosaic micrographs because these disturbed determination of grain size distribution. Mosaic micrographs with scale bars for all bead-on-plate welds can be found in Appendix 15. Mosaic micrographs were taken over weld or less over coarse-grained zone from most coarsened area in horizontal direction according to Appendix 15.

Figure 113 shows partially original mosaic micrograph of LASER welded sample 3.5.2-7 which are taken with Leica MEF 4M light optical microscope with DFC450 digital camera, computer aided table and software of LAS Core V4.6.1. All mosaic micrographs of bead-on-plate welds are taken in similar way.

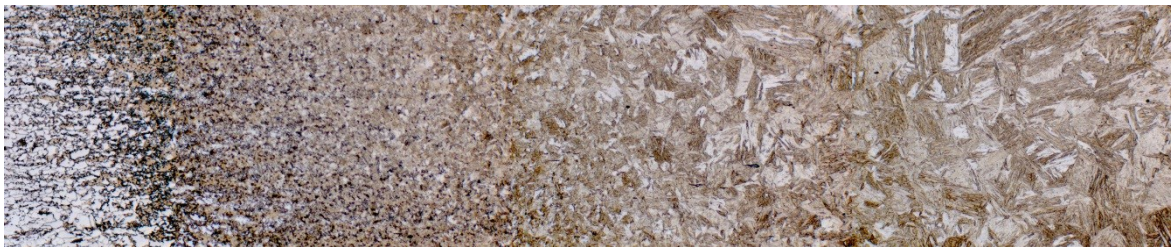

Figure 113 Part of original mosaic micrograph of LASER welded 3.5.2-7 without scale bar.

Image processing was done for all mosaic micrographs of bead-on-plate welds by Photoshop. Contrast and color range selection of boundaries of micrographs, sharpness and contrast were enhanced according to Figure 114. Grain boundary map definition required manual tracing and enhancing the grain boundaries in some cases. Binary conversion of micrograph was done. Figure 115 shows grain boundary map of the enhanced sample. Holes in the grain interiors were filled if needed. Color range selection and grain boundaries were enhanced in some cases.

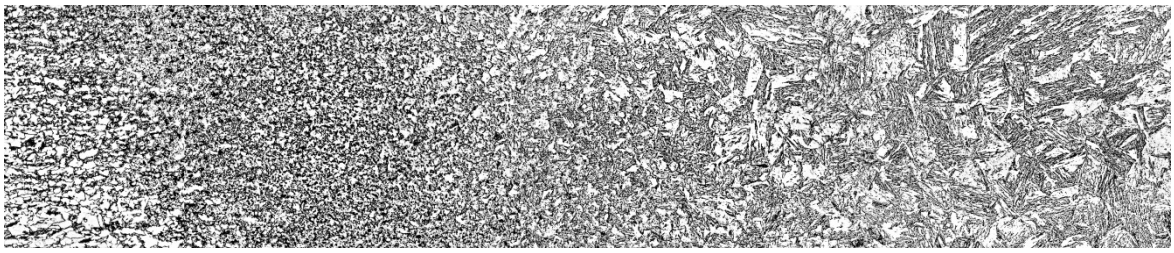

Figure 114 Part of micrograph of LASER welded sample 3.5.2-7 without scale bar which contrast and sharpness were enhanced.

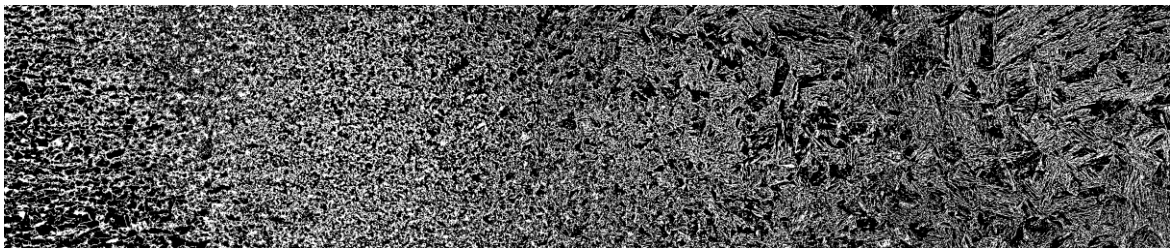

Figure 115 Part of grain boundary map of LASER welded sample 3.5.2-7 without scale bar.

Grain size distribution was calculated with Matlab. Positions of calculations for grain size measurement were determined randomly and measuring line angles (0˚, 45˚, 90˚and 135˚) were determined for each grain. Grain size determination was based on amount of interceptions of measuring lines and grain boundaries. Unit of determined grain size distribution was $d^{-0.5}$ ($\mu m^{-0.5}$). Maximum and minimum grain sizes were taken as the 99% and 1% probability level grain sizes. (44)

Four different grain-size distribution curves were determined per sample. Figure 116 shows grain size distribution of LASER welded sample 3.2.2-7 which was determined with the help of Matlab and grain boundary map of Figure 115. Upper grey curve is moving average which is determined from 50 pixel wide strip with full highness of the micrograph. Amount of the measurings are between 500-1000 which mean values were calculated between 5 pixels in X direction. At the second smoothed red curve was similar as at first curve but it was smoothed so that moving average was 50. Grey curve which name is largest measurements is similar with mean curve excepted that mean curve was determined only directions of maximum grain size. Largest measurements-smoothed red curve was similar as red curve of largest measurement but it was smoothed so that moving average was 50.

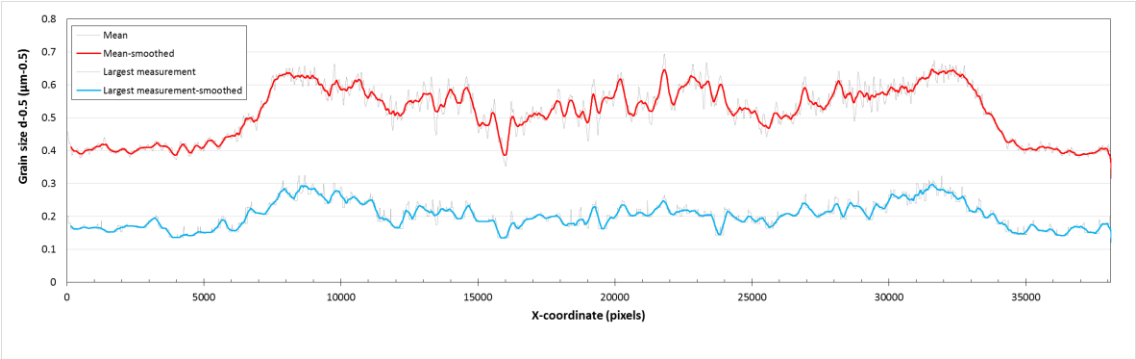

Figure 116 Grain size distributions of LASER welded sample 3.5.2-7 were calculated by Matlab.

Results of measured grain size distributions and their maximum grain sizes are collected in Appendix 15. Unit of Hall-Petch of determined grain size distribution is $d^{-0.5}$ ($\mu m^{-0.5}$). Diameter of a grain is got to raise this value to the power -2 and unit of this result is µm. Distances of X-axis are pixels. Units of pixels are possible to convert to µm units when pixels

are divided scale. Figure 117 shows grain size distribution of LASER welded sample 3.5.2-7.

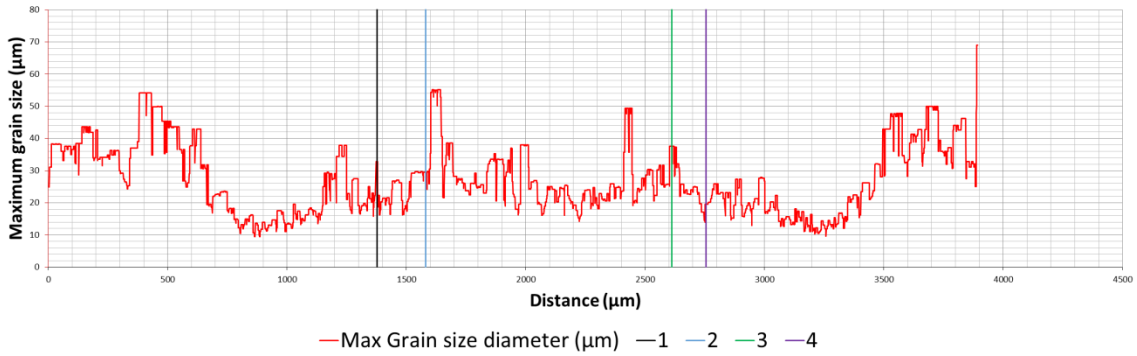

Figure 117 Grain size distribution over LASER welded sample 3.5.2-7. Left fusion line is between lines 1 and 2 and right fusion line of is between lines 3 and 4. Limit of fusion line is not accurate because according to Figure 113 fusion lines are not vertical.

Distances of X-axis of Figure 117 are measured from scale bar of mosaic micrograph of LASER welded sample 3.5.2-7. Fusion lines are marked between vertical lines of the figure. Distribution of the figure not represents typical grain size distribution of weld. Highest values of grain size distribution seem to be in base material and some high peak in weld metal side. Lowest values of grain size distribution are in HAZ in fine-grained zone. It is true that smallest grain sizes are in fine-grained zone, but in coarse-grained zone or in weld metal should be the higher grain size values than in fine-grained zone and base material.

Maximum grain sizes of measured distributions from base material, coarse-grained zone and weld metal are shown in Table 21. Determined grain size distributions for all bead-on-plate welds are shown in Appendix 15.

Table 21 Maximum grain size of base material, coarse-grained zone and weld metal for bead-on-plate welds.

Method and number of sample	Max distribution size from BM (µm)	Max distribution size from coarse-grained zone (µm)	Max distribution size from weld metal (µm)
LAHW 3.5.2-3	12	17	-
LAHW 3.15.2-9	28	15	-
LASER 3.5.2-7	69	38	55
LASER 3.15.2-5	31	19	14
MAG 3.5.2-2	12	32	-
MAG 3.15.2-4	20	12	-
TIG 3.5.2-4	12	19	13
TIG 3.5.2-8	13	19	18
TIG 3.5.2-9	9	8	13
TIG 3.15.2-6	17	9	10
TIG 3.15.2-7	29	10	14
TIG 3.15.2-8	23	12	17

Metallographic determination of the average grain size for steels can be made according to standards SFS-EN ISO 643 and ASTM E112-12 on many ways. In this investigation these standards were not followed. Maximum grain sizes were determined for MAG-welded sample 3.5.2-2 by looking for largest grains from 5 places in coarse-grained zones with the help of Leica MEF 4M light microscope according to Figure 118 (a). Largest measured diameter of measured grains was 201 µm according to Figure 118 (b).

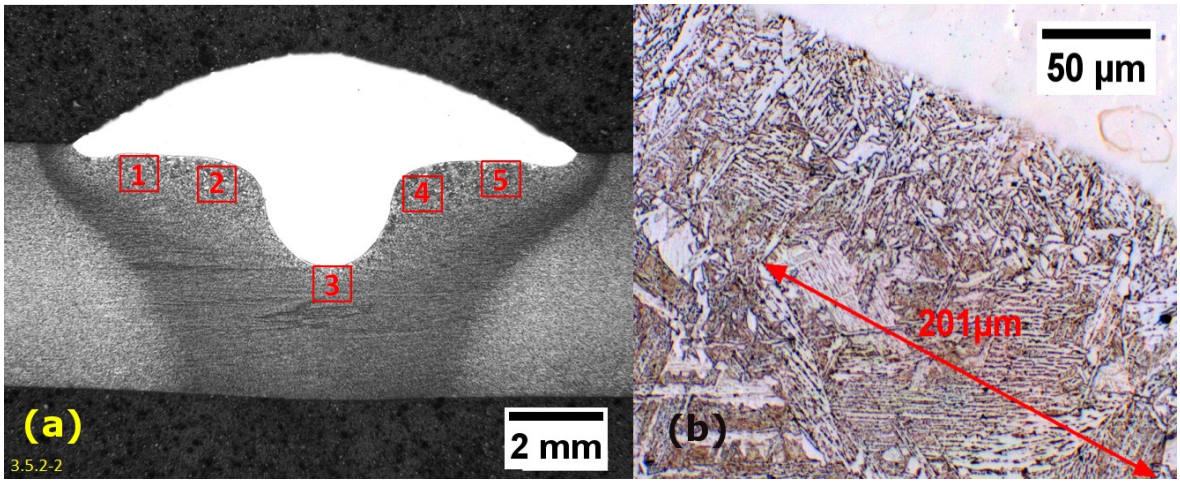

Figure 118 (a) Positions of measured maximum grain size diameter of MAG welded sample 3.5.2-2 were numbered (10X ocular & 1 objective). (b) Maximum diameter of grain was 201 µm.

Maximum grain sizes were measured from coarse-grained zone with the help of optical micrograph and ImageJ for all bead-on-plate welds according to Appendix 16. Maximum measured grain sizes of coarse-grained zones and amount of measured micrographs for all bead-on-plate welds are collected in
Table 22.

Table 22 Maximum grain sizes were measured from coarse-grained zone.

Number of sample	Amount of measured micrographs	Max measured size (µm)
LAHW 3.5.2-3	5	102
LAHW 3.15.2-9	5	107
LASER 3.5.2-7	5	124
LASER 3.15.2-5	5	136
MAG 3.5.2-2	11	201
MAG 3.15.2-4	5	162
TIG 3.5.2-4	3	173
TIG 3.5.2-8	5	180
TIG 3.5.2-9	3	220
TIG 3.15.2-6	4	135
TIG 3.15.2-7	3	138
TIG 3.15.2-8	3	144

7 The results

Maximum hardnesses of coarsegrained zone, $t_{8/5}$ values and dimensions of HAZ and weld metals are compared between results of the bead-on-plate samples of VTT, Voss's doctoral thesis and FLOW-3D simulations in this chapter. Residual stresses of butt welds of VTT which were measured with XRD and contour method are compared. Contents of chromium and nickel are compared between results of EDS, OES and calculated contents. Maximum grain size of the determined grain size distribution and the maximum grain size which were measured with optical microscope are compared.

7.1 Comparison of simulations, measurements and Voss's doctoral thesis

7.1.1 Comparisons of maximum hardnesses in coarse-grained zones

Strong correlations between all these hardnesses are detected according to Figure 119. Hardness comparisons of maximum hardnesses in coarse-grained zones are done between calculated hardnesses of VTT samples of Table 11, measured hardnesses of VTT samples of Table 8 and experimental determined hardnesses of Voss's doctoral thesis for TIG welds which based on values of Appendix 14. The values of measured maximum hardnesses of coarse-grained zones are near calculated hardnesses and hardnesses of Voss's doctoral thesis.

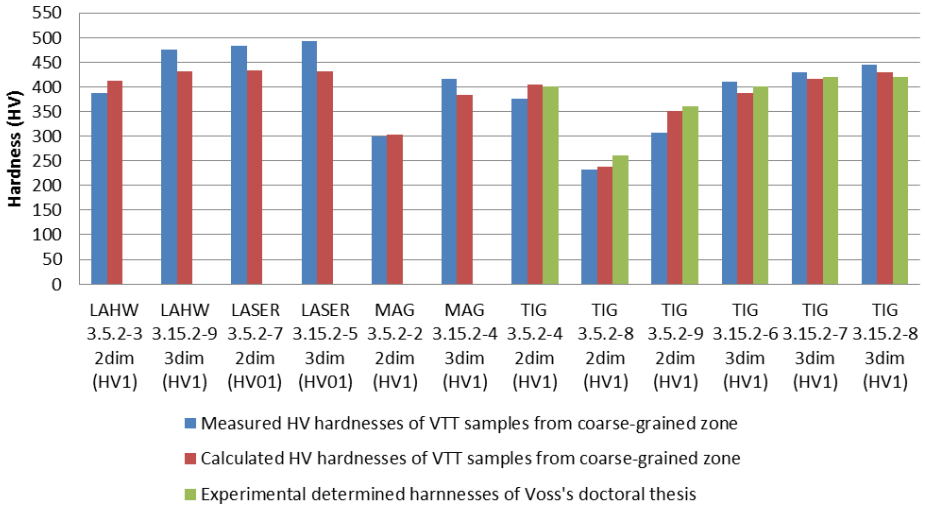

Figure 119 Comparison of HV-hardnesses from coarse-grained zone. 2dim and 3dim means that hardnesses are calculated with the help of two- or three-dimensional cooling.

The maximum hardnesses of coarse-grained zones were measured by HV1 except laser welds which were measured by HV01 due to smaller size of welds. The largest differences between measured and calculated hardnesses were measured with laser welds which hardnesses are measured with small pyramidal diamond indenter of HV01. The small diamond intender caused small indentations which hit locally small area of one or some grains or phase. This can cause large variation of measured hardnesses. Uniform hardness values can be measured with HV1 because indentation area is larger. This means that larger indentation area can hit several grains and phases and cause uniform measured result of hardness.

Equations (8) and (9) are meant for arc welds but not LASER and LAHW welds. This can be seen in larger variation with LAHW and LASER welds than arc welds in Figure 119 but difference is small.

HV hardnesses of Voss's doctoral thesis are collected to Figure 119 with the help of hardness maps and micrographs of Appendix 12 and ruler. HV1 hardnesses from coarse-grained zone can vary due to large steps of hardness map which are 40 HV1.

7.1.2 Comparison of $t_{8/5}$

Correlations are detected between measured $t_{8/5}$ values of bead-on-plate samples of VTT, simulated FLOW-3D $t_{8/5}$ values of bead-on-plate samples of VTT and calculated samples

$t_{8/5}$ values of bead-on-plate samples of VTT with most of samples. Cooling times were measured for all bead-on-plate welds with thermoelements and $t_{8/5}$ values were determined with the help of cooling curves. Hardnesses were calculated with the help of VVT / OU equations (8) and (9). Calculated hardnesses were correlated with measured hardnesses and hardnesses of Voss's doctoral thesis. Because VTT / OU use measured $t_{8/5}$ values with these hardness calculations, VVT / OU method supports correlation of cooling curves and their $t_{8/5}$ values with the exception of LASER and LAHW welds.

Figure 120 shows comparison between measured $t_{8/5}$ of VTT samples (blue beam), calculated $t_{8/5}$ for VTT samples (red beam), FLOW-3D simulated $t_{8/5}$ values from coarse-grained zone (purple beam), FLOW-3D simulated $t_{8/5}$ from fusion line (green beam) and experimental determined $t_{8/5}$ value of Voss's doctoral thesis (black beam). Correlations between arc welded samples are detected between measured, calculated and simulated values with the exception of welded samples of 3.5.2-8, 3.15.2-8 and 3.5.2-7 according to Figure 120.

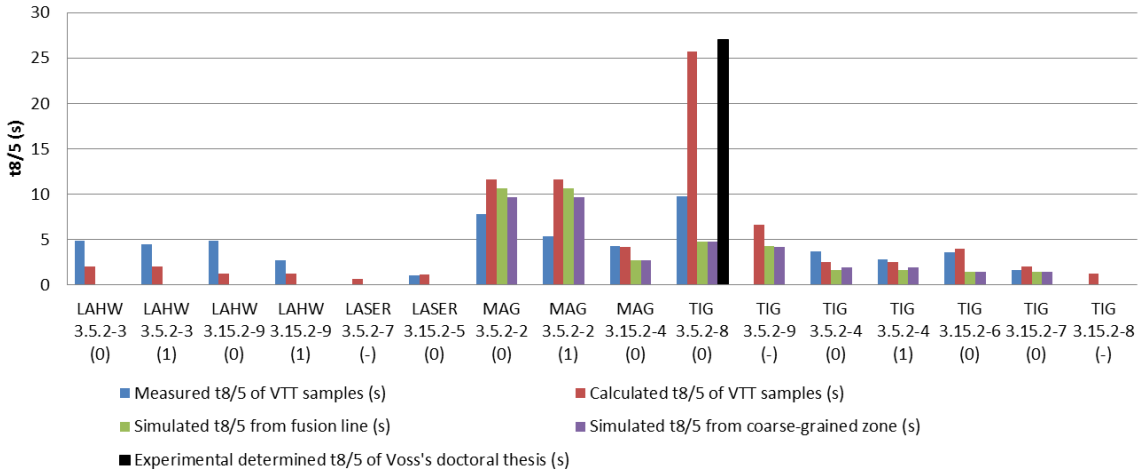

Figure 120 Comparison of $t_{8/5}$ between measured, calculated and simulated values. Numbers in brackets mean distance between approximated fusion line and the thermoelements in coarse-grained zone.

Only one value of $t_{8/5}$ of Voss's doctoral thesis was determined and some other values of $t_{8/5}$ could not be determined according to Figure 120 due to insufficient range of measured cooling curves. This can be seen in Appendix 12, 13 and 14. Numbers in brackets after welding methods are thermoelements numbers which describe distance (mm) between thermoelements and fusion line on HAZ side. Thermoelements numbers are chosen according nearest measured cooling curves which temperature ranges are sufficient for $t_{8/5}$ determination and as near measured maximum hardness as possible. Measured $t_{8/5}$ values of Figure 120 show that cooling is faster in further in HAZ than in fusion line due to cooling of base material according to measured values of thermoelements.

Values of $t_{8/5}$ were calculated for all samples according to equations (1), (2), (8) and (9) which are based on standard SFS-EN 1011-2. The standard was validated for arc welding, but not for LASER or LAHW welding. Figure 120 shows the difference between calculated and measured $t_{8/5}$ values. Higher difference can be detected between calculated and measured values between LAHW and LASER welds for this reason. Arc welded values of $t_{8/5}$ which are calculated according to standard SFS-EN 1011-2 are closer measured values than LAHW and LASER welded samples.

Difference between calculated and measured $t_{8/5}$ values with TIG welded sample 3.5.2-8 is highest in arc welded samples. The calculated value of $t_{8/5}$ of VTT sample is 25.7 s. This value is two-dimensional according to Table 11 and Figure 15 because TIG welded 5 mm VTT sample 3.5.2-8 which Q is 0.8 kJ/mm hits area of two-dimensional heat flow.

Experimental value of $t_{8/5}$ of Voss's doctoral thesis for sample 3.5.2-8 is 27 s and both FLOW-3D simulated values of $t_{8/5}$ is 4.8 s in fusion line and in position of maximum hardness area of coarse-grained zone. The FLOW-3D simulated values should lead fully martensitic microstructure which hardness is over 400 HV according to CCT of Figure 17. Measured $t_{8/5}$ of VTT sample is 9.8 s which should lead martensitic microstructure which includes a little bainite and hardness of this microstructure is over 400 HV according to CCT of Figure 17.

Recognized phases of microstructures of Table 12 for VTT sample 3.5.2-8 are acicular ferrite (AF), ferrite (F) and upper bainite (UB). The recognized phases and determined hardnesses support higher calculated cooling time $t_{8/5}$ of the VTT sample and the experimental $t_{8/5}$ value of Voss's doctoral thesis. Calculated hardnesses of TIG welded sample 3.5.2-8 of VTT in Figure 119 is 237 HV1. This is near the experimentaly determined maximum hardness of coarse-grained zone of Voss's doctoral thesis which is 260 HV1 according to Figure 119. Calculated two-dimensional value of $t_{8/5}$ which is 25.7 s and value of $t_{8/5}$ of Voss's doctoral thesis is 27 s correspond hardnesses and phases of microstructure of CCT of Figure 17. Values of $t_{8/5}$ are nearer reality with Voss's doctoral thesis and calculated values than measured and simulated values for this reason. It is good to remember that CCT approximations are not accurate.

Measured, calculated and simulated $t_{8/5}$ values are close to each other with others TIG welded samples and MAG welded sample 3.15.2-4. Calculated $t_{8/5}$ is little higher than measured $t_{8/5}$ with MAG welded sample 3.5.2-2.

Figure 120 shows that thicker plates cool more rapidly than thin plates. Faster cooling can lead to martensitic structure whose hardness is higher with thicker plates due to more rapid cooling according to CCT of Figure 17, Figure 119 and recognized phases of Table 12. VTT / OU method use measured $t_{8/5}$ values of VTT samples with hardness calculations of VTT samples which correlation is shown in Figure 119. For this reason VVT / OU method supports measured cooling curves of VTT samples and their $t_{8/5}$ values with the exception of LASER and LAHW welds.

Hardness is more than 400 HV with all 15 mm thick plates and $t_{8/5}$ time less than 5 s. This refers that all 15 mm thick samples have martensitic microstructure which includes a little bainite according to CCT of Figure 17 and Table 12. Hardness is less than 400 HV with all 5 mm thick plates and $t_{8/5}$ time is usually longer than the thicker plates with the exception of LASER welded sample 3.5.2-7. Recognized microstructures of these samples include less or no martensite, upper bainite, ferrite and acicular ferrite.

7.1.3 Comparison of dimensions of HAZ and weld metals

Most of measured dimensions of HAZ and weld metals of VTT samples, material modelling simulation of FLOW-3D of VTT and measured dimensions of Voss's doctoral thesis are near each other and they correlated. Horizontal and vertical dimensions of HAZ and weld metals of VTT samples were measured with stereomicroscope for all bead-on-plate welds. These dimensions are in Table 13 and in Appendix 5. Welding parameters for these bead-on-plate welds are in Table 6. Dimensions of HAZ and weld metal for bead-on-plate TIG welds are investigated by Voss's doctoral thesis (40). The parameters and dimensions of HAZ and welds are shown in Appendix 12.

Penetration comparisons of HAZ are done between material modelling simulation of FLOW-3D and measured penetrations for VTT samples of bead-on-plate TIG welds according to Figure 121.

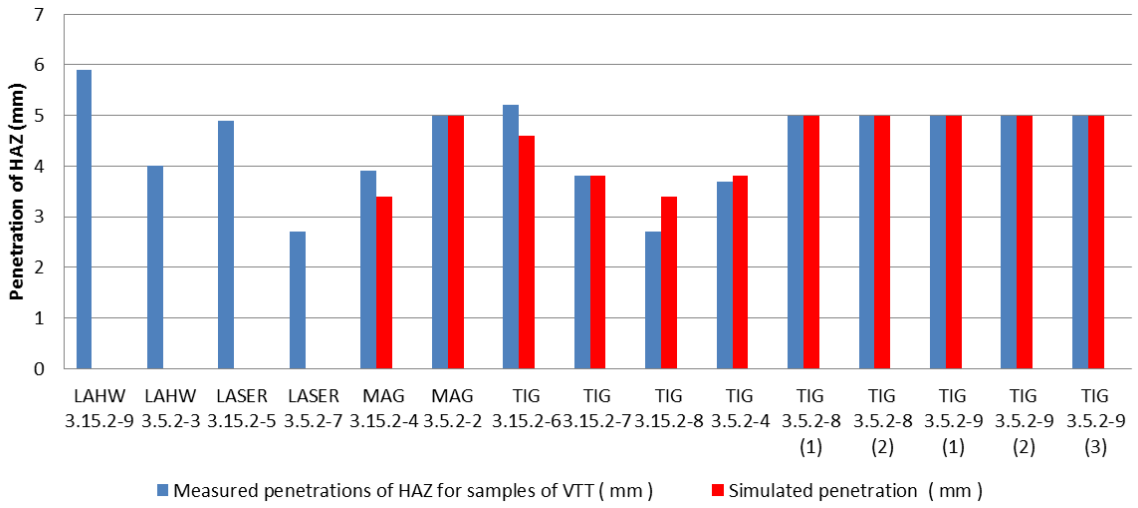

Figure 121 Comparison of penetrations between measured dimensions of VTT samples, simulations of VTT and Voss's doctoral thesis of HAZ.

Correlations of penetrations of TIG and MAG welds between measured samples of VTT and FLOW-3D simulated samples of VTT are detected according to Figure 121. Simulated and measured penetrations are equal with MAG 3.5.2-2 and TIG 3.15.2-6 and other penetration are near each other.

Influence of mesh size using calculation symmetry with penetration of HAZ was investigated between TIG 3.5.2-8 and TIG 3.5.2-9 according to Table 15 in Figure 121. There is no difference between measured and simulated penetration of HAZ with thin plates. The reason is that penetration is trough 5 mm thick plates.

Comparison of widths of HAZ for bead-on-plate welds was done between material modelling simulations of FLOW-3D, measured widths of samples and measured dimensions of Voss's doctoral thesis for TIG welds which are shown in Figure 122.

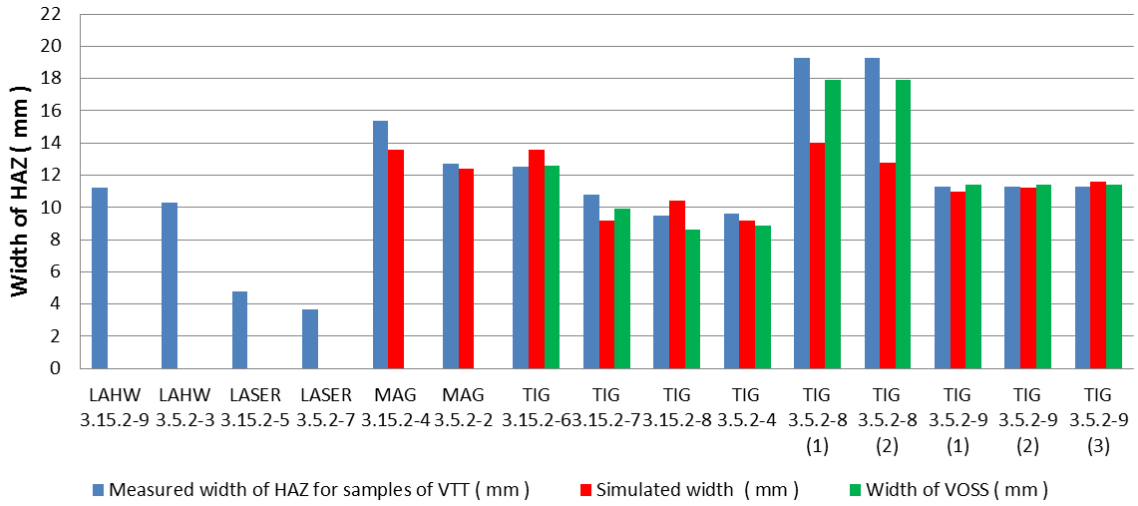

Figure 122 Comparison of widths between measured dimensions of VTT samples, simulations of VTT and Voss's doctoral thesis of HAZ.

Correlations of penetrations of TIG and MAG welds between measured samples of VTT, FLOW-3D simulated samples of VTT and measured penetrations of Voss's doctoral thesis are detected according to Figure 122. Both simulated widths for TIG 3.5.2-8 are lower than corresponded measured widths of VTT samples and widths of Voss's doctoral thesis. Highest differences with TIG welded sample 3.5.2-8 are detected. Reason for this can be different welding parameters. Overlap and incomplete joint penetration in weld according to Table 7 refers that something may have gone wrong with welding parameters. Other widths of TIG samples are near each other.

Influence of mesh size and using calculation symmetry with width of HAZ were investigated with samples 3.5.2-8 and 3.5.2-9 according to Table 15. Effect of changing mesh size and using calculation symmetry can be seen in Figure 122. Difference between TIG welded sample 3.5.2-8 (1) and 3.5.2-8 (2) is small.

Comparisons of penetration for weld metal of bead-on-plate welds were made between material modelling simulations of FLOW-3D, measured penetrations of VTT samples and measured dimensions of Voss's doctoral thesis for TIG welds which are shown in Figure 123.

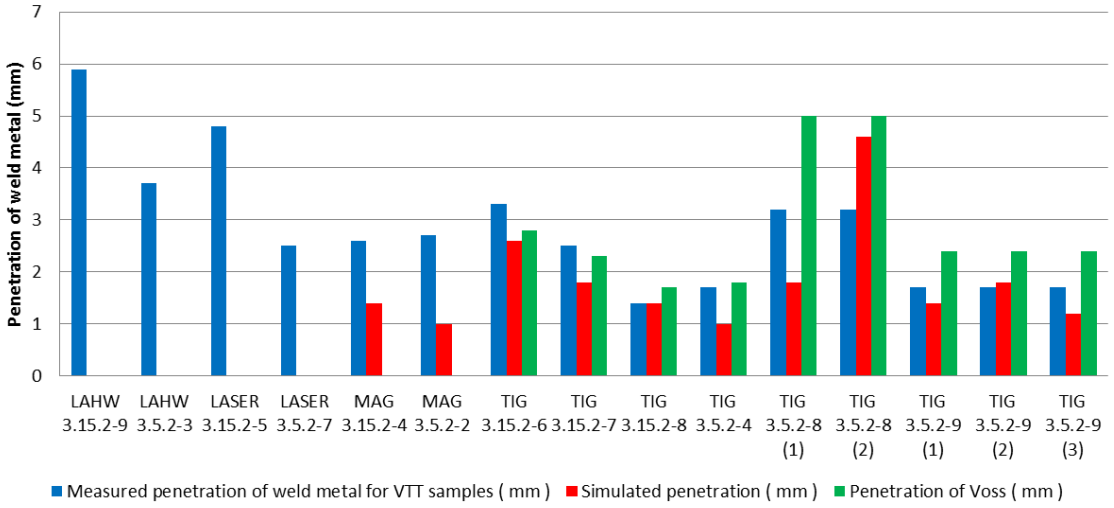

Figure 123 Comparison of penetrations between measured dimensions of VTT samples, simulations of VTT and Voss's doctoral thesis of welds.

Correlations of penetrations of TIG and MAG welds between measured samples of VTT, FLOW-3D simulated samples of VTT and measured penetrations of Voss's doctoral thesis are detected according to Figure 123. Measured penetrations are approximately two times higher than simulated penetrations with MAG samples. Reason for this can be different welding parameters like too high current or moisture with MAG welds which refers detected spatters in weld according to Table 7.

Influence of mesh size and using calculation symmetry with penetration of weld metal were investigated with samples 3.5.2-8 and 3.5.2-9 according to Table 15. Effect of changing mesh size and using calculation symmetry can be seen in Figure 123. Differences between TIG welded sample 3.5.2-8 (1) and 3.5.2-8 (2) are detected.

Comparisons of widths for weld metal of bead-on-plate welds are done between material modelling simulations of FLOW-3D, measured widths of VTT samples and measured dimensions of Voss's doctoral thesis for TIG welds which are shown in Figure 124.

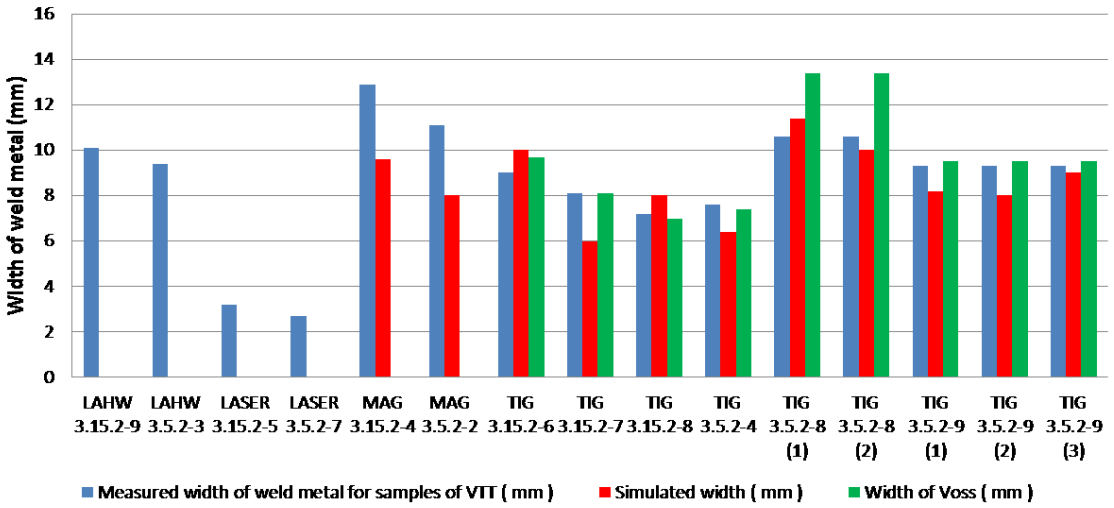

Figure 124 Comparison of widths between measured dimensions of VTT samples, simulations of VTT and Voss's doctoral thesis of welds.

Correlations of penetrations of TIG and MAG welds between measured samples of VTT, FLOW-3D simulated samples of VTT and measured penetrations of Voss's doctoral thesis are detected according to Figure 124. Measured widths are approximately higher than simulated penetrations with MAG samples.

Influence of mesh size and using calculation symmetry with width of weld metal were investigated with samples 3.5.2-8 and 3.5.2-9 according to Table 15. Effect of changing mesh size and using calculation symmetry can be seen in Figure 124. Small differences between these TIG welded samples are detected.

Welding parameters of Voss's doctoral thesis and parameters of material modelling simulation are corresponded. Welding parameters of material modelling simulations are shown in Table 15. Welding parameters differ little from those of TIG samples of VTT which are shown in Table 6. Welding voltage and current were higher with weld samples of VTT than they are in Voss's doctoral thesis and FLOW-3D simulation. The consequence of this is that welding energy and heat input are higher. This affects dimensions of HAZ and weld metal so that all measured dimensions for samples of VTT should be a little bit larger. Parameters of welding speeds are similar with all compared welds. Welding parameters of MAG welds are the same between samples of VTT and FLOW-3D simulated welds. Table 7 shows results of visual and microscope investigation which shows defects of welds. Defects are possible consequence of something going wrong with welding parameters. Example spatters of LAHW welded sample refer too high welding current. On the other hand only welding parameters not affect weld. Example moisture can cause spattering also.

Thermal efficiency differs between theory of this work and FLOW-3D simulation. Table 15 shows that the simulation uses thermal efficiency 1 with 15 mm thick TIG samples and 0.8 with other samples. Thermal efficiency is 0.6 with TIG welds and 0.8 with MAG welds according to Table 1. Higher thermal efficiency of TIG welds increases simulated dimensions of HAZ and weld metal. This affects comparison of dimensions of HAZ and weld metal between simulation and measured dimensions. Higher thermal efficiency factors increase dimensions of simulation. Surface active elements like nitrogen and oxygen can cause variation of penetration (5).

Dimensions of HAZ and weld metal for LAHW and LASER welds were not simulated because LAHW, LASER and MAG welds were not examined in Voss's doctoral thesis. These welds are not compared in Figure 121, 122, 123 and 124 for this reason. Another

reason is that LAHW and LASER welds of VTT are welded too high heat input because HAZ and weld metal are wider according Appendices 5 and 7. Properties and shapes of LAHW and LASER welds are nearer arc weld due to probably higher heat input.

7.2 Comparison between XRD and Contour residual stresses

Residual stresses were measured by XRD and Contour method for MAG and LAHW welded butt weld samples. Correlations are detected between XRD and Contour measured residual stresses with all butt weld samples, but correlation of sample 2 is weaker. Planar tensile stresses were detected in the middle of cutting surface of sample 2. These tensile stresses deep in the material probably formed before welding. This kind of finding is possible to do with Contour method but not with XRD. Machining and welding sequence affects residual stresses. XRD measured residual stresses and their positions and directions are in Appendix 10 and results of contour method are in Appendix 11 for all investigated butt samples and base materials.

0.5 mm width unmeasured zones affect comparison between XRD measured and Contour measured stresses due to restriction of CCM. Residual stresses should be measured also on edges of cutting surfaces because it makes comparison of Contour measured and XRD measured residual stresses more reliable.

It is possible to extrapolate the internal stresses to surface of investigated samples, but two-dimensional maps of residual stresses normal to the measurement was not enough accurate. Correct locally Contour measured extrapolated stress values are needed below XRD measured points for more accurate comparison. On the other hand, extrapolated values are only approximation. Assumption is also that residual stress distributions correspond on surfaces of welded samples. More accurate and reliable comparison is possible to reach with all measured topography of cutting surface with white light interferometry which was not available during this master thesis.

Benefit of contour method is possibility to measure normal stresses of cross-section from trough investigated sample. If residual stresses need to be measured in depth Contour method can recommended. During EDM cutting some cut surfaces were rusted a little due to water and rust had to be removed by etching. This may affect results of CMM and contour method a little.

7.2.1 Base material sample 3

Maps of both cutting surfaces for base material are shown in Figure 103 (a) and (b) and in Appendix 11. Peak of tension stresses to upper and lower edge are caused by machining. Stresses on surfaces were measured for base plate by XRD only one side of the plate.

Average of XRD measured compression stresses from surface of base material is -19 MPa and average of Contour measured compression stresses is -11 MPa. More accurate values with their positions can be found in Appendix 10. Measured Contour stresses are lower because these stresses are measured 0.5 mm deep due to restriction of measuring ball of coordinate measuring machine.

7.2.2 MAG welded sample 1

Figure 125 and 126 show comparison between XRD and Contour measured normal residual stresses of cross-section of MAG welded sample 1. XRD residual stresses were measured on top and bottom surface of MAG welded sample 1. Residual stresses of Contour method are measured from 0.5 mm depth from both sides of the plate. Tensile stresses are typically higher in surface in fusion line surface in the middle of the weld, which can be detected by XRD measured distributions of residual stresses from both sides of the weld. Change of shape in fusion line, shrinkage and thermal expansion cause peak of tensile stress in fusion line. Properties of filler metal affect also residual stresses in the middle of weld.

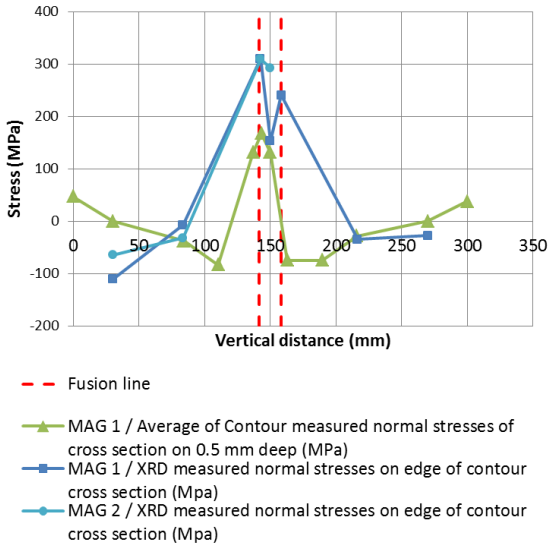

Figure 125 Comparison of XRD and Contour measured residual stresses on top side of MAG welded sample 1.

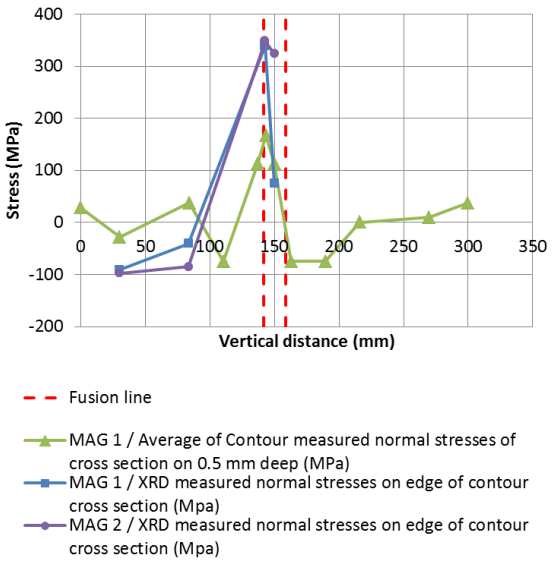

Figure 126 Comparison of XRD and Contour measured residual stresses on bottom side of MAG welded sample 1.

XRD measured residual stresses of MAG welded samples 1 and 2 are comparable because these samples are identical. Figure 125 and 126 show comparison of residual stresses between Contour and XRD measured values with both sides of the MAG welded sample 1. Corresponding XRD measured residual stress distributions of MAG welded sample 2 are added to these figures. All XRD measured stresses of these figures are near to each other. Correlation is detected between XRD and Contour measured stresses, but residual stresses of XRD are measured from surface of sample and Contour stresses 0.5 mm deeper. For this reason XRD measured stresses differ from Contour measured values according to Figure 125 and 126.

Figure 83 shows MAG welded sample 1. It can detect that highest pass are welded after lowest pass because upper heat-affected zone covers lower heat-affected zone. Welding sequence affects residual stresses so that the first pass is tempered during temperature peak of the second pass and so on. The pass which is welded last has usually higher hardness, different microstructure and higher residual stresses than previous passes. Consequence of this is that the last pass has usually worse mechanical properties than previous passes. For this reason residual stresses are different on top side and bottom side of samples also with MAG welded sample 2 and LAHW sample 5.

7.2.3 MAG welded sample 2

Figure 127 and 128 show comparison between XRD and Contour measured normal residual stresses of cross-section of MAG welded sample 2. XRD residual stresses are measured on top and bottom surface of MAG welded sample 2. Residual stresses of Contour method are measured from 0.5 mm depth on both sides of plate. Peaks of tensile stresses are not detected near fusion line with contour measured distributions of residual stresses which is unusual. Measured XRD peaks of Figure 127 and 128 cannot be detected because measured curve does not include measuring points in fusion line. XRD measured residual stresses reveal that in fusion line there should be higher contour measured residual stresses.

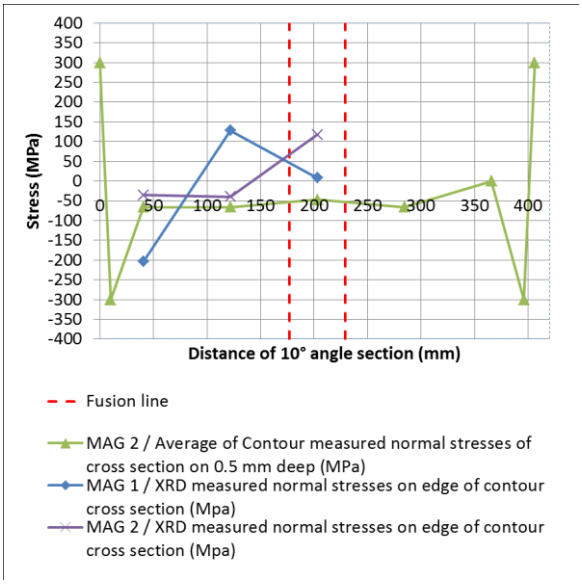

Figure 127 Comparison of XRD and Contour measured residual stresses on top side of MAG welded sample 2.

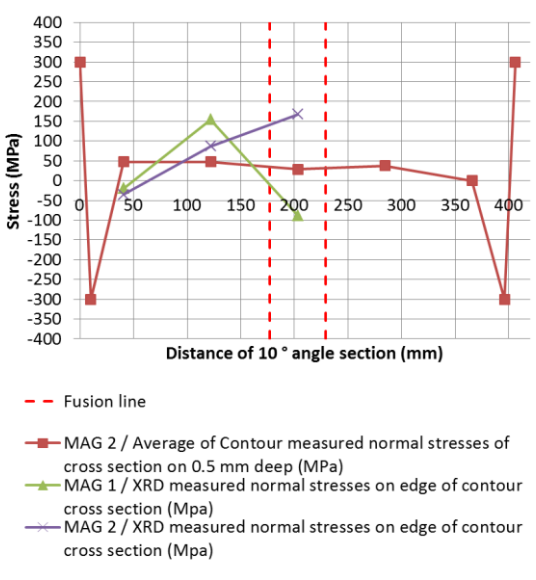

Figure 128 Comparison of XRD and Contour measured residual stresses on bottom side of MAG welded sample 2.

XRD measured residual stresses of MAG welded samples 1 and 2 are comparable because these samples are identical. Corresponding XRD measured residual stress points of MAG welded sample 1 are added on figures of MAG welded sample 2. XRD measured residual stresses of sample 1 are not near XRD measured residual stresses of sample 2 for some reason. XRD measured residual stresses on top and bottom side of sample 2 are near to each other but residual stresses on bottom side are a little higher. Residual stresses of Contour method are higher on bottom side of the sample than on top side in the middle of weld according to figures. Reason for this can be welding sequence of passes. Weak correlation is detected between XRD and Contour measured stresses. Highest difference between XRD and Contour measured residual stresses is that Contour is measured 0.5 mm deeper than XRD.

One interesting finding was Contour measured stresses in the middle of MAG welded sample 2 which have existed in base material before welding. Longitudinal highlight colors in the middle of welded sample are tensile stresses according to Figure 6 and 7 of Appendix 11. These planar tensile stresses were probably in the material before welding. It is possible that these stresses are consequence of manufacturing. This kind of stresses can make welded structure weaker. For this reason is good to check the source of this kind of stress and remove it.

7.2.4 LAHW welded sample 5

Figure 129 and 130 show comparison between Contour and XRD measured normal residual stresses of cross-section for both sides of the LAHW 5 sample. Tensile stresses are typically higher in surface in fusion line than in surface in the middle of the weld which can be detected by XRD measured distributions of residual stresses on both sides of weld. One reason of this is change of shape in fusion line which causes peak of tensile stress in fusion line. Properties of filler metal affect also the residual stresses in the middle of weld.

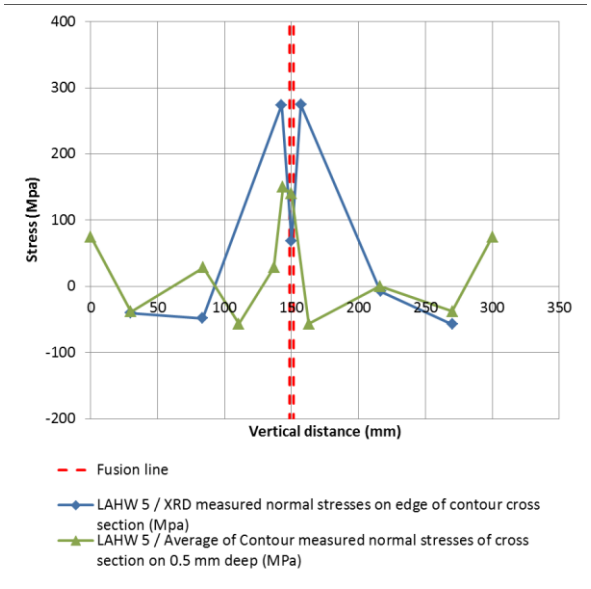

Figure 129 Comparison between Contour and XRD measured normal residual stresses on face side of the LAHW 5 sample.

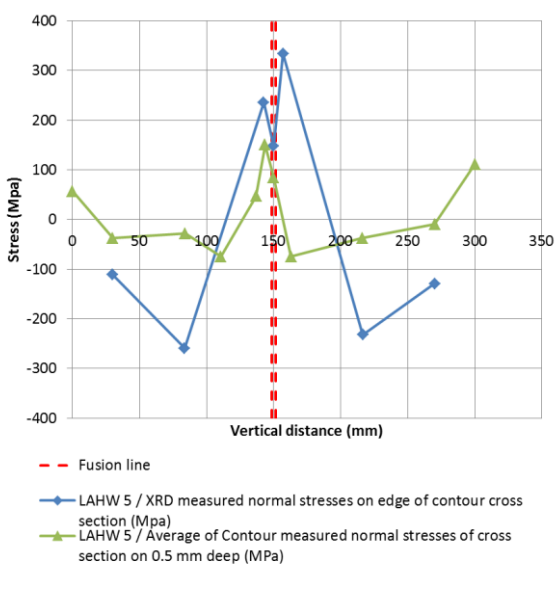

Figure 130 Comparison between Contour and XRD measured normal residual stresses on root side of the LAHW 5 sample.

Correlation is detected between measured residual stresses of XRD and Contour method. Residual stresses of XRD are measured from surface of sample and Contour stresses 0.5 mm deeper. For this reason XRD measured residual stresses differ from Contour measured values according to the figures. Incomplete penetration and excessive penetration were detected with LAHW 5 weld which can be seen from Appendix 4. It is possible that bad quality of LAHW 5 weld affects residual stresses. Anyway correlation seems to be good according Figure 163 and 164.

7.3 Inspection of mixing of MAG and LAHW welds

Mixing of filler metal and base metal are detected even with the help of EDS measured distribution of iron, chromium and nickel of weld metals with all MAG and LAHW welds. According to Figure 105 etching of MAG welded sample 3.15.2-4 is even in weld metal which means even mixing.

Microstructure of MAG welded sample 3.15.2-4 which was determined with the help Schaeffler and WRC-92 diagrams according Figure 110 and Figure 111 are near recognized microstructure of Table 12. Schaeffler and WRC-92 diagrams support results of OES. It is good to remember that Schaeffler and WRC-92 diagrams do not take into account influence of cooling rate which affects phase formations. The measured proportional amount of chromium and nickel differ between EDS and OES for some reason.

Figure 131 shows EDS measured average contents of chromium and nickel and their range for MAG welded sample 3.15.2-4. Average contents are measured on 5 different positions in weld metal side. Measuring position of EDS 1 is shown in Figure 104 (c) and other positions are shown in Appendix 8.

Two beams of Figure 131 show chromium and nickel contents which were measured with OES. All measured contents of spectroscopy are shown in Appendix 9. Measured chromium contents are higher and nickel contents are lower than EDS measured chromium contents according to Figure 131. On the other hand values of spectroscopy are near calculated values of Table 18 in Figure 131.

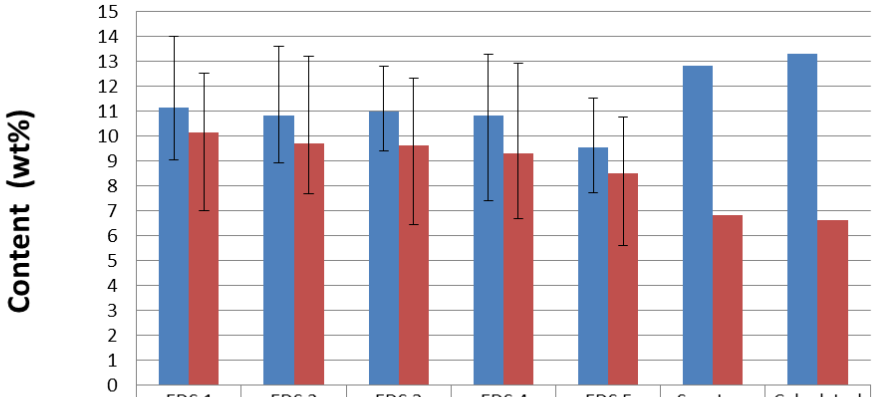

	EDS 1 (n=154)	EDS 2 (n=222)	EDS 3 (n=54)	EDS 4 (n=92)	EDS 5 (n=54)	Spectros copy	Calculated content
Average contetn of Cr (wt%)	11.15	10.83	10.99	10.82	9.55	12.8	13.3
Average contetn of Ni (wt%)	10.15	9.70	9.63	9.29	8.51	6.81	6.6

Figure 131 Average of Cr and Ni contents from weld metal and their range of MAG welded sample 3.15.2-4.

Ratio between chromium and nickel should be the same although amount of them is smaller with even mixing. Proportional amount of chromium in the weld metal was smaller with values of EDS analysis than it is with original filler metal. One reason of this can be evaporation of chromium during welding, but it does not explain so high difference between results of EDS and optical spectroscopy. OES supports calculated contents of Table 18, because they are near each other according to Figure 131.

It is good question why chromium and nickel contents between results of EDS and spectroscopy are not matched. Contents of optical spectroscopy, calculated values and relative amounts of chromium and nickel in filler metal are near to each other. On the other hand, EDS analysis is done for test stainless steel sample and result was matched with this stainless steel sample after EDS measurement.

Positions of EDS measurements were deeper in weld than measuring of optical emission spectrometer which was measured on face side of the weld according to figure of Appendix 9. One explanation of difference of measured contents of chromium and nickel between EDS analysis and OES cannot be that mixing is different on face side of the weld than deeper in the weld where EDS analyses were made. Reason for this is that mixing is detected even with etching and EDS.

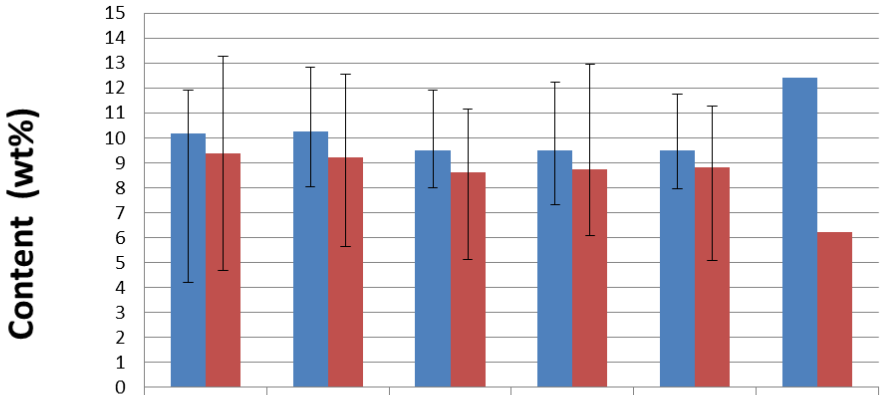

	EDS 1 (n=128)	EDS 2 (n=233)	EDS 3 (n=47)	EDS 4 (n=78)	EDS 5 (n=38)	Calculated content
Average contetn of Cr (wt%)	10.16	10.25	9.51	9.51	9.48	12.40
Average contetn of Ni (wt%)	9.38	9.20	8.60	8.72	8.82	6.20

Figure 132 Average of Cr and Ni contents and their range from weld metal of MAG welded sample 3.5.2-2.

A little lower chromium and nickel contents are detected on root side of MAG welded sample 3.5.2-2 in Figure 132. Reason of this can be faster cooling of root and which may reduce a little mixing in root side. Calculated amount of chromium is higher and nickel is lower than values of EDS with all samples. Correlations are detected between EDS measured values.

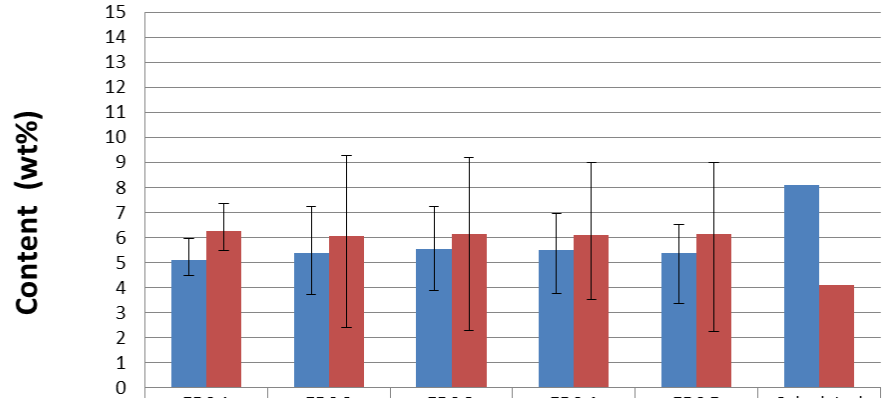

	EDS 1 (n=75)	EDS 2 (n=220)	EDS 3 (n=138)	EDS 4 (n=112)	EDS 5 (n=126)	Calculated content
Average contetn of Cr (wt%)	5.10	5.38	5.56	5.49	5.38	8.10
Average contetn of Ni (wt%)	6.27	6.06	6.12	6.10	6.14	4.10

Figure 133 Average of Cr and Ni contents from weld metal and their range of LAHW welded sample 3.5.2-3.

Mixing is even with LAHW 3.5.2-3, LAHW 3.15.2-9, MAG 3.15.2-4 and MAG 3.5.2-2 due to correlations of Figure 131, 132, 133 and 134. Difference between calculated contents and EDS measured contents with these figures are shown. All measured chromium, nickel and iron distributions by EDS, their positions and average of chromium and nickel contents are shown in Appendix 8.

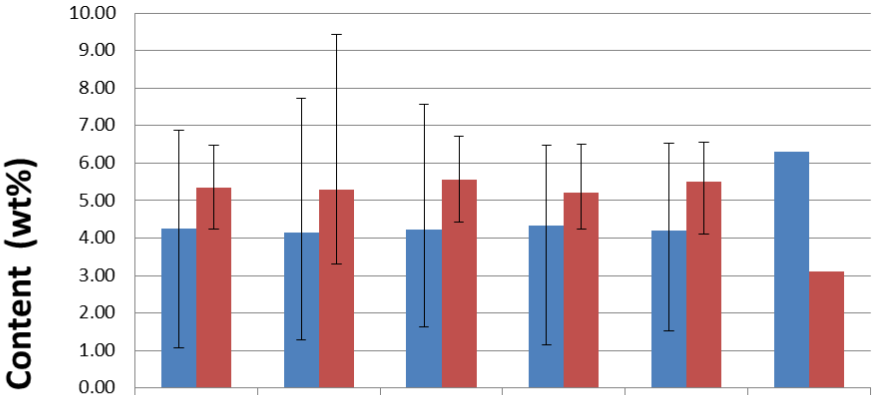

	EDS 1 (n=53)	EDS 2 (n=85)	EDS 3 (n=131)	EDS 4 (n=137)	EDS 5 (n=94)	Calculated content
Average contetn of Cr (wt%)	4.26	4.16	4.23	4.34	4.19	6.30
Average contetn of Ni (wt%)	5.33	5.29	5.56	5.21	5.51	3.10

Figure 134 Average of Cr and Ni contents from weld metal and their range of LAHW welded sample 3.15.2-9.

7.4 Inspection of grain size distribution and maximum grain size of coarse-grained zones

Figure 135 shows comparison between maximum values of grain size distribution and measured maximum grain sizes of optical micrographs which can be found in Appendix 16. Maximum peaks of grain size distributions for coarse-grained zone is significantly lower than measured maximum grain sizes of coarse-grained zones according to the figure. Letter n means amount of micrographs which were taken from coarse-grained zones for measuring the maximum grain size.

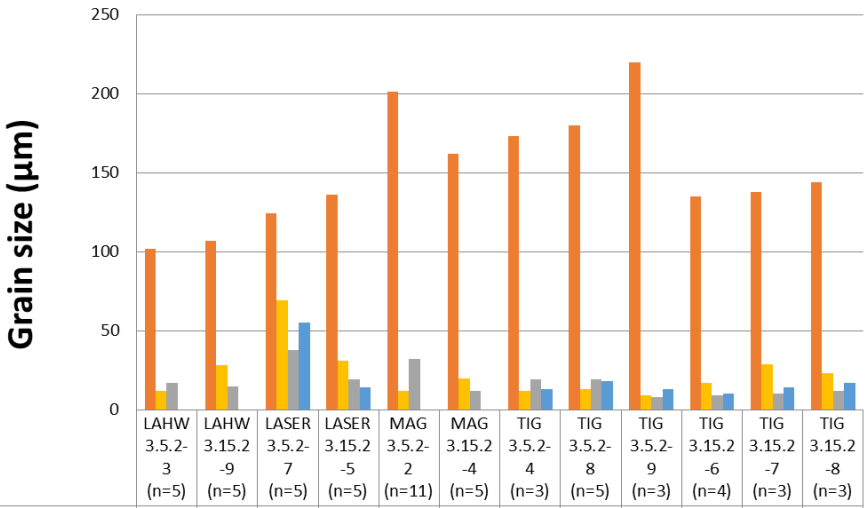

	LAHW 3.5.2-3 (n=5)	LAHW 3.15.2-9 (n=5)	LASER 3.5.2-7 (n=5)	LASER 3.15.2-5 (n=5)	MAG 3.5.2-2 (n=11)	MAG 3.15.2-4 (n=5)	TIG 3.5.2-4 (n=3)	TIG 3.5.2-8 (n=5)	TIG 3.5.2-9 (n=3)	TIG 3.15.2-6 (n=4)	TIG 3.15.2-7 (n=3)	TIG 3.15.2-8 (n=3)
Max measured grain size from coarse-grained zone with optical microscope (µm)	102	107	124	136	201	162	173	180	220	135	138	144
Max distribution size from base material (µm)	12	28	69	31	12	20	12	13	9	17	29	23
Max distribution size from coarse-grained-zone (µm)	17	15	38	19	32	12	19	19	8	9	10	12
Max distribution size from weld metal (µm)			55	14			13	18	13	10	14	17

Figure 135 Comparison between maximum values of grain size distribution and measured grain sizes of optical micrographs.

Martensite blocks are detected inside grains boundaries of prior austenite in coarse-grained zone of bead-on-plate welds according to Figure 25 and micrographs of Appendix 16. Measuring maximum grain size of prior austenite with the help of grain size distribution is

not possible because Matlab software measures dimensions of martensite blocks inside prior austenite. Investigations support also that no clear granular structure can be defined for martensite (46).

Figure 136 shows base material of LASER welded sample 3.15.2-5. Maximum measured grain size of base material of the picture is 34 µm. The measured grain size is near corresponding maximum grain size of distribution which is 31 µm. This supports that maximum grain size distribution of base material is near, but validation of this case demands a lot more measured micrographs of base material and more measured grain-size distributions.

Figure 137 is micrograph which is taken from weld metal of LASER welded sample 3.15.2-5. Oriented dendrites are detected from the micrograph which maximum grain size is significantly higher than corresponding maximum grain size of distribution which is 14 µm. Possible smaller details inside of oriented grains are measured like martensite, lower bainite or other phases.

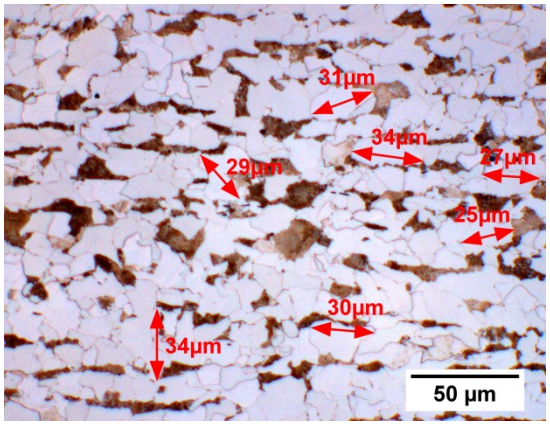

Figure 136 Base material of LASER welded sample 3.15.2-5.

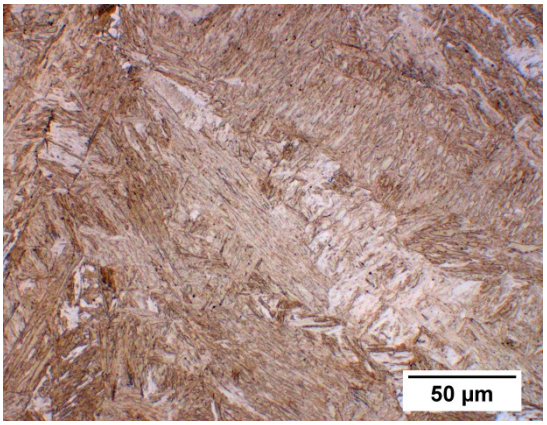

Figure 137 Weld metal of LASER welded sample 3.15.2-5.

The fault was detected in step motor of computer aided table of light microscope during taking mosaic micrographs. A step motor adjusted focus insufficiently from time to time. Lens of 50X objective was focused sharply in the middle of investigated microstructure but corner areas were a little unsharp. Shading adjusting was in some cases difficult due to uneven halogen light which is better to substitute with led light in future if possible. These circumstances caused difficulties in quality of mosaic micrographs for some cases. Small differences of shading and brightness were detected. Sharpness which varies inside of one micrograph, overexposure, underexposure and etching affected reliability of results of grain size distributions for some cases.

Quality of some micrographs is possible to improve taking micrographs manually again and combining them manually, but it does not bring additional value for determination of grain size distribution of coarse-grained zone because quality of micrographs is sufficient for most of cases.

8 Discussion

The weakest part of the weld is in coarse-grained zone where peak of grain size and hardness are. Maximum hardnesses and grain size determinations, recognition of phases and determinations of $t_{8/5}$ were allocated for this area. Most characterized microstructures of VTT samples with their mechanical properties and the experimental results of TIG welds of the Voss‘s doctoral thesis were near the modelled material results. The residual stresses of the butt weld samples which were measured with XRD and Contour method were corre-

lated. Mixing of investigated LAHW and MAG welds were even. Measuring of maximum grain size of prior austenite from coarse-grained zone with the help of the grain size distribution is not possible because Matlab software measured dimensions of martensite blocks inside of prior austenite.

Most of the compared $t_{8/5}$ values were correlated between measured, calculated and simulated values with MAG and TIG welded samples except few TIG welded samples of bead-on-plate welds. The correction between calculated hardnesses of VTT / OU method, measured hardnesses of VTT samples and measured hardnesses of Voss's doctoral thesis supported comparison of $t_{8/5}$. Recognized phases of microstructures support comparison of $t_{8/5}$ values because cooling time affects the microstructure. VTT / OU method was validated for arc welding, but not for LASER or LAHW welding. Higher difference can be detected between calculated and measured values between LAHW and LASER welds for this reason.

Correlations are detected between dimensions of HAZ and weld metals of TIG and MAG welds between measured samples of VTT, FLOW-3D simulated dimensions of parallel VTT work and measured dimensions of Voss's doctoral thesis with the few exceptions. Differences of welding parameters and thermal efficiency factors are affected little to the comparison. Consequence of different welding parameters is that welding energy and heat input are higher with VTT samples. Higher thermal efficiency factors increase dimensions of HAZ and welds with VTT samples. Dimensions of HAZ and weld metal for LAHW and LASER welds were not simulated because LAHW, LASER and MAG welds were not examined in Voss's doctoral thesis. Another reason is that LAHW and LASER welds of VTT are welded with too high heat input because HAZ and weld metal are wider. Properties and shapes of LAHW and LASER welds are nearer to arc weld due to probably higher heat input.

Contour and XRD measured residual stresses correlate with MAG welded sample 1 and LAHW welded sample 5, but correlation of sample 2 is weaker. Residual stresses were measured from surface with XRD and with Contour method from 0.5 mm depth due to restriction of used measuring ball of CCM. More reliable comparison between XRD and Contour method can be reached, when the whole topography of cutting edge is measured. Whole topography of cutting surface can be measured with white light interferometer, but it was not available during this master thesis.

One alternative is to extrapolate the internal stresses to surface of investigated samples, but two-dimensional maps of residual stresses normal to the measurement was not enough accurate. Correct locally Contour measured extrapolated stress values are needed in XRD measured points for more accurate comparison. On the other hand, extrapolated values are only approximation. Assumption is also that residual stress distributions correspond on surfaces of welded samples. It is better to measure all topography of cutting surface with white light interferometry.

Mixing affects properties of weld. Mixing is even according the etched microstructure of stainless MAG weld sample, calculated Cr, Ni and Fe contents of weld samples, Schaeffler diagram, WRC-92 diagram and EDS measured Cr, Ni and Fe distributions of bead-on-plate welds. Calculated contents of Cr and Ni which are calculated with the help of equation (10) are near results of OES. Microstructure which is determined with the help of contents of base material and weld metal is similar to microstructure which is determined with optical emission spectroscopy according Schaeffler and WRC-92 diagram. This means that Schaeffler and WRC-92 diagram support results of OES. On the other hand, measured

relative amount of chromium which was measured with OES is lower than corresponding content of chromium which was measured with EDS for some reason.

Although mixing is found to be even, different zones were detected on both sides of fusion line of one MAG welded sample. Hardness of martensite in coarse-grained zone depends mostly on carbon content. The difference between base material and filler metal carbon content tends to stabilize due to diffusion. Reason of high hardness variation of dissimilar MAG welded bead-on-plate weld near fusion line was variation of carbon content on both sides of a fusion line due to carbon diffusion. Consequence of carbon diffusion was decarburization zone in coarse-grained zone near fusion line which are called carbon-depleted zone. Hardness of carbon-depleted zone is lower than other areas of coarse-grained zone. Another zone is detected in weld metal side near the fusion line which hardness is higher than hardness of weld metal. Carbon migration causes carbon pile-up zone in weld metal side where carbon content is high. Mentioned zones form 1 mm wide area which is called tie-line. Bands of unmixed and non-fusible base material were detected near fusion line on weld metal side. Similar kind of hardness variation can be detected also with other welds, if carbon content difference is between base material and filler metal.

The maximum grain sizes of coarse-grained zones which were determined by optical microscope were compared to the maximum grain sizes of coarse-grained zones of the determined grain size distribution. Compared maximum grain sizes were not matched by. Measuring maximum grain size of prior austenite is not possible with grain size distribution because Matlab software measures dimensions of martensite blocks inside of prior austenite. Investigations supports that no clear granular structure can be defined for martensite (46).

Most of the compared properties of microstructures and residual stresses can be utilized in validation of simulation processes because most of compared results correlated. Cost saving, safety and eco-friendliness can be improved with the help of the validations of simulations which are goals of FIDIPRONA project.

Benefit of contour method is possibility to measure normal residual stresses from whole cross-section area. One interesting finding was Contour measured residual stresses in the middle of MAG welded sample 2 which have been in base material before welding. These planar residual stresses are probably consequence of manufacturing. This kind of residual stresses can make welded structure weaker. For this reason it is good to find the source of this kind of residual stress and remove it.

Machining causes peaks of tensile stresses in base material. Welding sequence affects the residual stresses so that the last pass has usually higher hardness, different microstructure and higher residual stresses than the previous passes.

Results of mixing can be utilized with validation prosess of simulation of mixing. Mixing of investigated MAG and LAHW butt welds were even.

Measuring maximum grain size of prior austenite is not possible with the help of determination of grain size distribution because Matlab software measures dimensions of martensite blocks inside of prior austenite.

9 Future plan and recommendations

Compared dimensions of HAZ and weld, $t_{8/5}$ values and hardnesses between VTT samples, simulations of parallel work and Voss's doctoral thesis correlated. This supports validation

of the material modelling with the help of characterization of weld microstructure of S355N which will be done in future. The validation of material modelling of hardness dimensions of HAZ and weld metal, defining microstructures with the help of $t_{8/5}$ values and mixing of weld are needed for statistical comparison. Statistical comparison needs more measurements per sample which means that reliable validation needs more investigated samples. This is because difference may include single cases of real weld samples and simulations.

It seems that compared XRD measured and Contour measured residual stresses correlate with investigated butt weld samples except correlation of sample 2 which was weaker. The correlation supports validation of simulated results of residual stresses of weld samples which will be done in future. Residual stresses were measured from surface with XRD and with Contour method from 0.5 mm deeper due to restriction of used measuring ball of CCM. More reliable comparison between XRD and Contour method is possible when whole topography of cutting edge is measured for Contour method. Whole topography of cutting surfaces can be measured with white light interferometer. When residual stresses are measured from same position on surface with XRD and Contour method comparison is easier and more reliable. Validation of simulated results of residual stresses needs more investigated samples. Simulation results are possible to validate with the help of these measured residual stresses after this if good correlation is detected.

Measuring of maximum grain size of prior austenite is not possible because Matlab software measures dimensions of martensite blocks inside prior austenite. It would be interesting to etch grain boundaries more visible with some other etchant if possible, hoping that martensite blocks are not visible and try again determination of grain size distribution for coarse-grained zone.

Better visibility of grain boundaries can be reached with EBSD (*Electron backscatter diffraction*) but it does not help the case of the grain boundaries of prior austenite where internal martensite blocks make the measuring of grain size distribution with Matlab difficult due to internal grain boundaries of martensite blocks. Grain boundaries are more visible with EBSD than with an optical microscope. Maximum grain sizes of coarse-grained zone are easier to measure with EBSD than with an optical microscope for this reason.

List of references

1. **Vähäkainu, O.** *Hitsaajan opas.* Keuruu : Otavan Kirjapaino Oy, 2003. ISBN 952-5010-35-X.
2. **Kou, S.** *Welding Metallurgy.* New Jersey : A John Wiley & Sons, Inc., Publication, 2003. ISBN 0-471-43491-4.
3. **Peltonen, M.** *Weldability of high-strenght steel using conventional welding methods.* Espoo : Aalto University, 2014.
4. **1011-1, SFS-EN.** *Welding – Recommendations for welding of metallic materials.* Helsinki : SFS, 2009. Finnish Standards Association SFS.
5. **Kujanpää, V.** Doctor of welding. *Personal interview.* Lappeenranta : VTT, Advanced Manufacturing Technologies, 15. October 2015.
6. **Kyröläinen A. ja Lukkari, J.** *Ruostumattomat teräkset ja niiden hitsaus.* Tampere : Metalliteollisuuden keskusliitto, MET, 2002. ISBN 951-817-794-5.
7. Ferrite number control in Austenitic Stainless Steel Welding. *Weldpedia.com.* [Online] 2013. http://www.weldpedia.com/2014/05/ferritenumber-control-in-austenitic.html.
8. **Lippold J, Kotecki D.** *Welding metallurgy and weldability of stainless steels.* New Jersey : John Wiley & Sons, 2005. ISBN 0-471-47379-0.
9. **1011-2, SFS-EN.** *Welding – Recommendations for welding of metallic materials. Part 2: Arc welding of ferritic steels.* Helsinki : Finnish Standards Association SFS, 2000.
10. **Nevasmaa, P. and Karppi, R.** *Energian säästö lujien terästen hitsauksen esikuumennuksessa.* Espoo : VTT. VTT Tiedotteita 1268, 1991.
11. **Nevasmaa P., Toyoda M., Vilpas M. and Karppi R.** *Uudet termomekaanisesti valssatut teräkset - edut ja rajoitukset.* Espoo : VTT. VTT Tiedotteita 760, 1987.
12. **Meskanen S, Toivonen P.** Metallurgian perusteita, Valimotekniikan perusteet. *http://www.valuatlas.fi/.* [Online] Teknillinen korkeakoulu. http://www.valuatlas.fi/tietomat/docs/vtp_sulatus_metallurgia.pdf.
13. **Lindroos, V., Sulonen, M. and Veistinen, M.** *Uudistettu Miekk-ojan metallioppi.* Helsinki : Otava, 1986. ISBN 951-666-216-1.
14. **Bhadesia, H. K. D. H. and Honeycombe R. W. K.** *Steels: Microstructure and Properties.* London : Edward Arnold, A Division of Hodder Headlinec PLC, 1995. ISBN 0-340-58946-9.
15. **ASM International Handbook.** *Metallograbhy and Microstructures.* Ohio : The Materials Information Society, 2004. ISBN: 0-87170-706-3.
16. **Bosansky, J. and Mraz, L.** International Institute of Welding. *Classification of welded joint structures.* [Online] www.iiwelding.org. IX 1533-88.
17. **Nevasmaa, P. and Karppi, R. A. J.** *Contribution to comparison of methods for determining welding prosedures for the avoidance of hydrogen cracking.* Espoo : VTT Technical Research Centre of Finland, 1992. ISBN 951-38-4225-8.
18. Hitsaustekniikka 4/2011. *Musta/ruostumaton-eripari liitosten hitsaus ja kuumahalkeamia TIG-eriparihitsauksessa.* [Online] 1. 4 2016. www.shy-hitsaus.net.
19. **Lippold, John C.** *Welding Metallurgy and Weldability of Nickel-Base Alloys.* New Jersey : Wiley, 2009. ISBN9780470500217.
20. Kaarihitsauksen perusteet. *http://mandata.pp.fi.* [Online] SHY (Suomen Hitsaus Yhdistys). http://mandata.pp.fi/Hitsaus/Artikkelit/A1.pdf.
21. **Kujanpää, V. and Salminen, A.** *Suuritehoisen Nd:YAG-laserin käyttö konepajateollisuudessa.* Helsinki : Hakapaino Oy, 1998. ISBN 951-817-686-8.
22. **Hirn, J.** *Suitability of resistance spot welding and laser welding for the production of all steel sandwhich panels with ultra high-strenght thin faces and high-strenght core.* Espoo : Aalto University, 2010.
23. **165 10th Street, Suite 50, San Francisco, CA 94103.** https://radiation5.wikispaces.com. *Wikispaces.* [Online] https://radiation5.wikispaces.com/Laser+Welding.

24. **Callister, W. M., Jr. and Rethwisch, D. G.** *Materials Science and Engineering: an Introduction.* USA : John Wiley & Sons, Inc., 2010. ISBN 978-0-470-41997-7.
25. **Johnson D, Penn W, Bushik S.** Application Experiences with Laser Beam Welding. [Online] Alabama Laser. [Viitattu: 22. 11 2015.] http://www.alspi.com/lsrweld.htm.
26. **Olsen, O.** *Hybrid laser-arc welding.* Oxford : Woodhead Puplishing, 2009. ISBN 978-1-84569-370-1.
27. **Finch, D. M.** *A rewiew of non-destructive residual stress measurement techniques.* s.l. : ERA, 1994.
28. **Prevey, Paul S.** Current applications of X-ray diffraction residual stress measurement. *www.lambdatechs.com.* [Online] Lambda Technologies, 1996. www.lambdatechs.com.
29. **SHY, Suomen Hitsausteknillinen Yhdistys.** Hitsauksen teoriaopetus. *B4 Kutistuminen, jäännösjännitykset ja muodonmuutokset.* [Online] 2012. http://mandata.pp.fi/Hitsaus/Artikkelit/B4.pdf.
30. **Mulli, E.** *Terästermotelan sisäisten jännitysjakaumien kokeellinen tutkiminen ja selvitys.* Espoo : Aalto University, 2008.
31. **Masubuchi, K.** *Analysis of Welded Structures.* London : Pergamon Press, 1980. ISBN 0-08-022714-7.
32. **Lou, L.-F.** *Introduction to Phonons and Electrons.* London : World Scientific Publishing, 2003. ISBN 981-238-439-1.
33. **Cullity, B. D. and Stock S. R.** *Elements of X-ray Diffraction.* New Jersey : Pearson Education, 2001. ISBN 0-13-178818-3.
34. **Lu, J.** *Handbook of Measurement of Residual Stresses.* Liburn (GA) : Fairmont Press, 1996. ISBN 0-88173-229-X.
35. **Preváy, Paul S.** www.lambdatechs.com. *Current aplications of xray difraction residual stress measurement.* [Online] 1996. www.lambdatechs.com.
36. **Prime, M. B., and DeWald, A.T.** *The Contour Method.* s.l. : Los Alamos, 2013.
37. http://www.kingedms.com. *Principle of wire cut EDM.* [Online] Kingred Electrical And Mechanical Technology Co., Ltd. http://www.kingedms.com/blog/index.php/2011/11/principle-of-wire-cut-edm/.
38. **6507-1, SFS-EN ISO.** *Part 1: Test method.* Helsinki : SFS, 2005. Finnish Standards Association SFS.
39. **9015-2, SFS-EN ISO.** *Part 2: Micro hardness testing on welded joints.* Helsinki : SFS, 2011. SFS, Finnish Standards Association.
40. **Voß, O.** *Untersuchung relevanter Einflußgrößen auf die numerische Schweißsimulation.* Shaker Verlag : Shaker Verlag GmbH, 2001. ISBN 3-8265-9119-4.
41. *ESAB hitsauslisäaineet.* Helsinki : OY ESAB, 2000.
42. **E112-13, ASTM.** *Standard Test Methods for Determining Average Grain Size.* West Conshohocken : ASTM International, 2010.
43. **E1382, ASTM.** *Standard Test Methods for Determining Average Grain Size Using Semiautomatic.* West Conshohocken : ASTM International, 2004.
44. **Lehto, P.** Grain size measurement using Matlab. *https://wiki.aalto.fi.* [Online] 7. 1 2015. https://wiki.aalto.fi/display/GSMUM/Grain+size+measurement+using+Matlab.
45. **Lehto, P.** *Influence of grain size distribution on strength of welded shipbuilding structural steel.* Espoo : Aalto University, 2012.
46. **Lehto, P.** *Influence of grain size distribution on the Hall-Petch relationship of welded structural steel.* Espoo : Aalto University, 2014.

Appendix 1 / Test plate information for 5 mm plate

SSAB

TEST PLATE INFORMATION

73209K-001 A

06.02.2015

Tilaaja Purchaser
SSAB EUROPE OY
RAAHE STEEL WORKS

Vastaanottaja Consignee
SSAB EUROPE OY
RAAHE STEEL WORKS

Päivämäärä Date
06.02.2015

Valmistajan merkki
Mark of the Manufacturer

Tilaus nro Order No.
TEST SAMPLES

Tilausvahvistus Order Confirmation

Asiakkaan merkki Shipping mark
TEST SAMPLES

Todistus Certificate

Laivaus Shipping

Laatuleimaus Quality Stamping

Tarkastajan leima
Stamp of Inspector

Vastaanottajan leima
Stamp of Surveyor

Muut leimaukset
Other Stamps

Toimitustyyppi Delivery type

Sulatus nro levy nro Cast No. Plate No.
XXXXX XXX XX XXX

Tuote Product

Toleranssit Tolerances

Tekniset vaatimukset ja/tai viralliset määräykset Technical terms of Delivery and/or Official Regulations

Laji Grade
MULTISTEEL/S355K2+N

Laatuselvitys Quality Specifications

Positio Item	Levypaksuus mm Plate thickness mm	Merkki Marke	Kpl Pcs	Paino kg Weight kg	Sulatus levy nro Cast plate No	SP nro SP No	UT UT	MT MT
	5.00				25011 031			

Raahe Steel Works

Testaus ja tarkastus Testing and Inspection

MINNA VALKAMA
Valtuutettu tarkastaja Authorized inspection representative

RTXPS
Yhtiön nimi Company Name: SSAB Europe Oy
Kotipaikka Registered Office: HELSINKI
Osoite Address: PL 93, P.O Box 93
FIN-92101 RAAHE, FINLAND
Puhelin Telephone: 020 5911
+358 20 5911
Telekopio Telefax: 020 592 2736
+358 20 592 2736
Y-tunnus Business ID: 2389445-7

SSAB

TEST PLATE INFORMATION
TEST REPORT

73209K-001 A

06.02.2015

Tilaaja Purchaser
SSAB EUROPE OY
RAAHE STEEL WORKS

Tilaus nro Order No.
TEST SAMPLES

Laji Grade
MULTISTEEL/S355K2+N

Laatuselvitys Quality Specifications

Vastaanottaja Consignee
SSAB EUROPE OY
RAAHE STEEL WORKS

Asiakkaan merkki Shipping mark
TEST SAMPLES

Lisävaatimukset Additional requirements

Päivämäärä Date
06.02.2015 MHR

Valmistajan merkki
Mark of the Manufacturer

Jatkuvavalettua happiterästä
Oxygen steel, continuous casting

Fully killed, Fine grain practiced

Pos. Item	Sulatus, k.erä nro Cast. test No	T-tila Cond	Vetokoe Tensile test															Taivutuskoe Bend test		Huom Nb	Päästö Tempering °C
			K2	°C	RP02 MPa	RT05 MPa	REL MPa	REH MPa	RM MPa 1	RM MPa 2	RM MPa 3	A % 50	A % 80	A % 200	REH / RM	RM * A5	RAZ % 1	RAZ % 2	RAZ % 3	Keskiarvo Average	K5	D = X t		
	25011 031	NR	31		413				524			23											

K2: 31=CENTRE, TRANSVERSE

NR=NORMALIZING ROLLING

Pos. Item	Sulatus k.erä nro Cast. test No	Iskukoe Impact test						Sitkeämurtuma Ductile fracture				Erikoiskokeet Special tests					Huom Nb	Päästö Tempering °C
		K3	°C	1	2	3	Keskiarvo Average	1	2	3	Keskiarvo Average	K4	°C	1	2	Keskiarvo Average		
	25011 031	137	-020	82	59	65	69											

K3: 137=CH-V/ISO-V(J),TX10,CENTRE,LONGIT,KV600

Raahe Steel Works

Testaus ja tarkastus Testing and Inspection

MINNA VALKAMA
Valtuutettu tarkastaja Authorized inspection representative

RTXPS
Yhtiön nimi Company Name: SSAB Europe Oy
Kotipaikka Registered Office: HELSINKI
Osoite Address: PL 93, P.O Box 93, FIN-92101 RAAHE, FINLAND
Puhelin Telephone: 020 5911, +358 20 5911
Telekopio Telefax: 020 592 2736, +358 20 592 2736
Y-tunnus Business ID: 2389445-7

SSAB

TEST PLATE INFORMATION
ANALYSIS

73209K-001 A
06.02.2015

Sulatus nro Cast No Schmelzen Nr. No de coulén № Плавки	Koe nro Test No Prüf Nr. Essai No № Пробы	Positio Item Pos. Poste Поз.	Cekv Ceq Cäq Cég Сеkv	Analyysi % Chemical composition % Chemisch Zusammensetzung % Composition Chimique % Анализ плавки % (*=ppm)											
				C	SI	MN	P	S	AL	NB	V	CU	CR	NI	MO
25011			.41	.154	.21	1.42	.011	.009	.038	.015	.007	.017	0.05	0.04	.010

Päivämäärä Date Datum Date Дата
06.02.2015 MHR

CEQ=C+MN/6+(CR+MO+V)/5+(NI+CU)/15

Raahe Steel Works

Testaus ja tarkastus / Prüfung und Kontrolle — Testing and Inspection / Essais et Contrôle — Испытание и контроль качества

Steel manufactured and supplied by Raahe Steel Works is free from radiation.
Производимая на металлургическом комбинате «Raahe Steel Works» и поставляемая заказчику сталь не излучают радиации.

MINNA VALKAMA
Valtuutettu tarkastaja / Sachverständiger — Authorized inspection representative / Inspector autorisé — Уполномоченный инспектор

Yhtiön nimi Company Name: SSAB Europe Oy
Kotipaikka Registered Office: HELSINKI
Osoite Address: PL 93, P.O Box 93, FIN-92101 RAAHE, FINLAND
Puhelin Telephone: 020 5911, +358 20 5911
Telekopio Tlefax: 020 592 2736, +358 20 592 2736
Y-tunnus Business ID: 2389445-7

Appendix 2/ Test plate information for 15 mm plate

SSAB

TEST PLATE INFORMATION

A 39603 -001 A
11.02.2015

Tilaaja Purchaser
SSAB EUROPE OY
RAAHE STEEL WORKS

Vastaanottaja Consignee
SSAB EUROPE OY
RAAHE STEEL WORKS

Päivämäärä Date
13.02.2015

Tilaus nro Order No.
TEST SAMPLES

Tilausvahvistus Order Confirmation

Asiakkaan merkki Shipping mark
TEST SAMPLES

Valmistajan merkki
Mark of the Manufacturer

Todistus Certificate

Laivaus Shipping

Laatuleimaus Quality Stamping

Tarkastajan leima
Stamp of Inspector

Vastaanottajan leima
Stamp of Surveyor

Muut leimaukset
Other Stamps

Toimitustyyppi Delivery type

Sulatus nro levy nro Cast No. Plate No.
XXXXX XXX XX XXX

Tuote Product

Toleranssit Tolerances

Tekniset vaatimukset ja/tai viralliset määräykset Technical terms of Delivery and/or Official Regulations

Laji Grade
S355J2+N

Laatuselvitys Quality Specifications

Positio Item	Levypaksuus mm Plate thickness mm	Merkki Marke	Kpl Pcs	Paino kg Weight kg	Sulatus levy nro Cast plate No	SP nro SP No	UT UT	MT MT
	15.00				24778 013			

Raahe Steel Works

Testaus ja tarkastus Testing and Inspection

MINNA VALKAMA
Valtuutettu tarkastaja Authorized inspection representative

RTXPS
Yhtiön nimi Company Name: SSAB Europe Oy
Kotipaikka Registered Office: HELSINKI
Osoite Address: PL 93, P.O Box 93
FIN-92101 RAAHE, FINLAND
Puhelin Telephone: 020 5911
+358 20 5911
Telekopio Telefax: 020 592 2736
+358 20 592 2736
Y-tunnus Business ID: 2389445-7

SSAB

TEST PLATE INFORMATION
TEST REPORT

A 39603 -001 A

11.02.2015

Tilaaja Purchaser
SSAB EUROPE OY
RAAHE STEEL WORKS

Tilaus nro Order No.
TEST SAMPLES

Laji Grade
S355J2+N

Laatuselvitys Quality Specifications

Vastaanottaja Consignee
SSAB EUROPE OY
RAAHE STEEL WORKS

Asiakkaan merkki Shipping mark
TEST SAMPLES

Lisävaatimukset Additional requirements

Päivämäärä Date
13.02.2015 MHR

Valmistajan merkki
Mark of the Manufacturer

Jatkuvavalettua happiterästä
Oxygen steel, continuous casting

Fully killed, Fine grain practiced

Pos. Item	Sulatus, k.erä nro Cast. test No	T-tila Cond	Vetokoe Tensile test																Taivutuskoe Bend test		Huom Nb	Päästö Tempering °C
			K2	°C	RP02 MPa	RT05 MPa	REL MPa	REH MPa	RM MPa 1	RM MPa 2	RM MPa 3	A % 50	A % 80	A % 200	REH / RM	RM * A5	RAZ % 1	RAZ % 2	RAZ % 3	Keskiarvo Average	K5	D = X t		
	24778 013	NR	11					443	554			25											

K2: 11=TOP,TRANSV.

NR=NORMALIZING ROLLING

Pos. Item	Sulatus k.erä nro Cast. test No	Iskukoe Impact test						Sitkeämurtuma Ductile fracture				Erikoiskokeet Special tests					Huom Nb	Päästö Tempering °C
		K3	°C	1	2	3	Keskiarvo Average	1	2	3	Keskiarvo Average	K4	°C	1	2	Keskiarvo Average		
	24778 013	111	-020	153	198	174	175											

K3: 111=CH-V/ISO-V(J),10X10,TOP,LONGIT,KV600

Raahe Steel Works

Testaus ja tarkastus Testing and Inspection

MINNA VALKAMA
Valtuutettu tarkastaja Authorized inspection representative

RTXPS
Yhtiön nimi Company Name: SSAB Europe Oy
Kotipaikka Registered Office: HELSINKI
Osoite Address: PL 93, P.O Box 93
FIN-92101 RAAHE, FINLAND
Puhelin Telephone: 020 5911
+358 20 5911
Telekopio Telefax: 020 592 2736
+358 20 592 2736
Y-tunnus Business ID: 2389445-7

SSAB

TEST PLATE INFORMATION
ANALYSIS

A 39603 -001 A
11.02.2015

Sulatus nro Cast No Schmelzen Nr. No de coulén № Плавки	Koe nro Test No Prüf Nr. Essai No № Пробы	Positio Item Pos. Poste Поз.	Cekv Ceq Cäq Cég Сеkv	Analyysi % Chemical composition % Chemisch Zusammensetzung % Composition Chimique % Анализ плавки % (*=ppm) C	SI	MN	P	S	AL	NB	V	TI	CU	CR	NI	MO	N	B
24778			.41	.161	.20	1.40	.011	.009	.035	.034	.008	.003	.015	0.05	0.04	.006	.005	.0002

Päivämäärä Date Datum Date Дата
13.02.2015 MHR

CEQ=C+MN/6+(CR+MO+V)/5+(NI+CU)/15

Raahe Steel Works

Testaus ja tarkastus Testing and Inspection Испытание и контроль качества
Prüfung und Kontrolle Essais et Contrôle

Steel manufactured and supplied by Raahe Steel Works is free from radiation.
Производимая на металлургическом комбинате «Raahe Steel Works» и поставляемая заказчику сталь не излучают радиации.

MINNA VALKAMA
Valtuutettu tarkastaja Authorized inspection representative Уполномоченный инспектор
Sachverständiger Inspector autorisé

Yhtiön nimi Company Name: SSAB Europe Oy
Kotipaikka Registered Office: HELSINKI
Osoite Address: PL 93, P.O Box 93, FIN-92101 RAAHE, FINLAND
Puhelin Telephone: 020 5911, +358 20 5911
Telekopio Tlefax: 020 592 2736, +358 20 592 2736
Y-tunnus Business ID: 2389445-7

Appendix 3 / Photographs of bead-on-plate welds and position of their microsections

Contents

Appendix 3

TIG 3.5.2-8

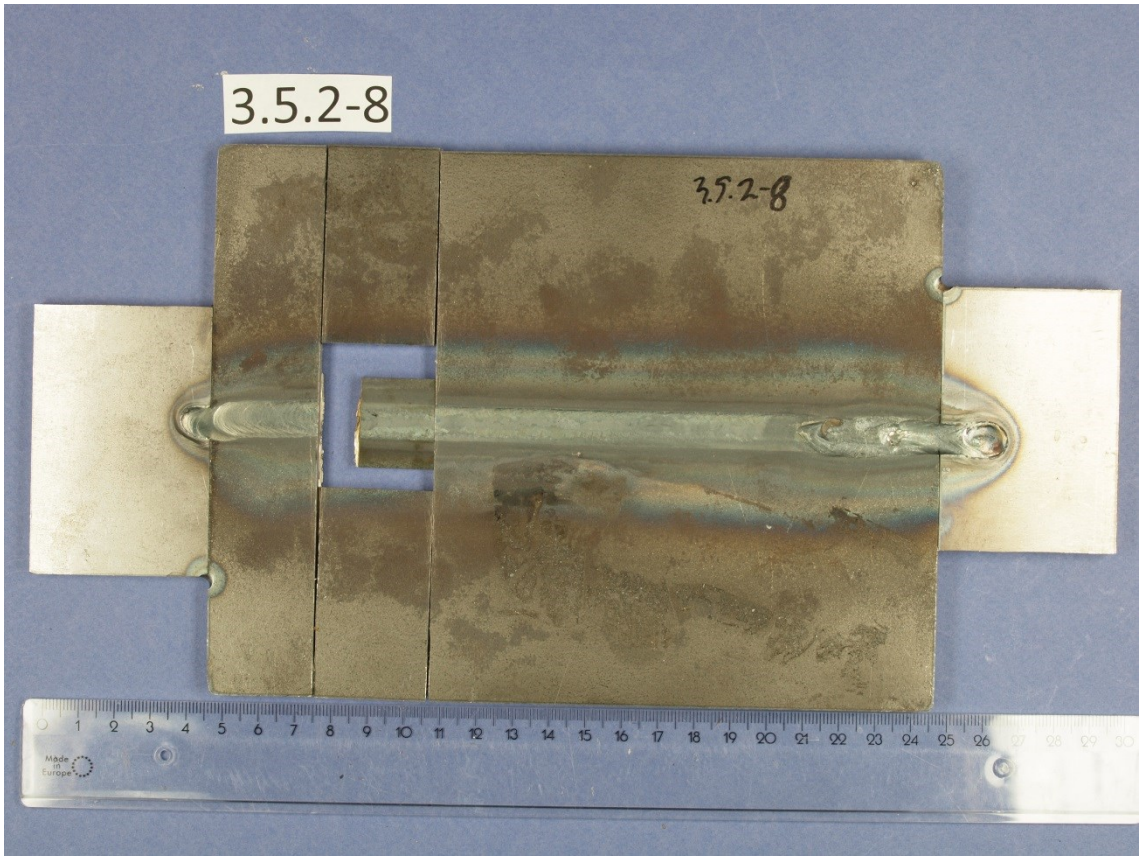

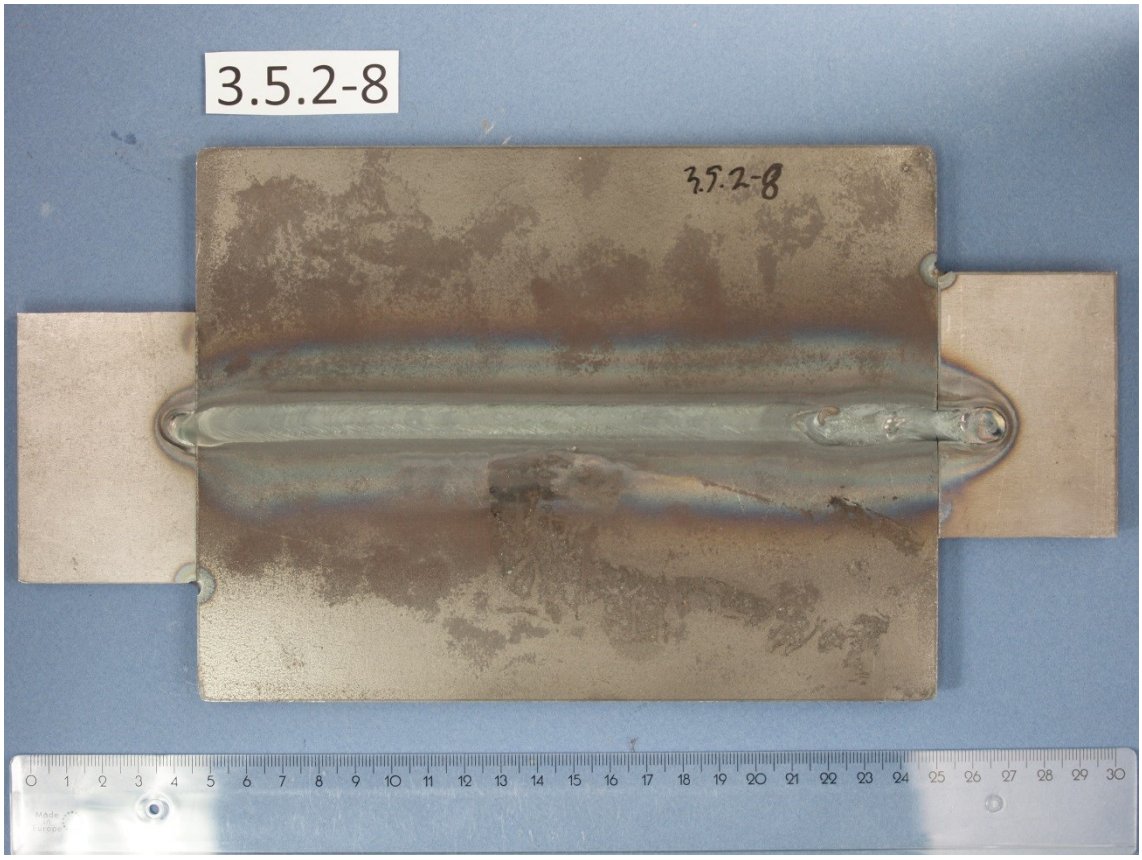

Appendix 3

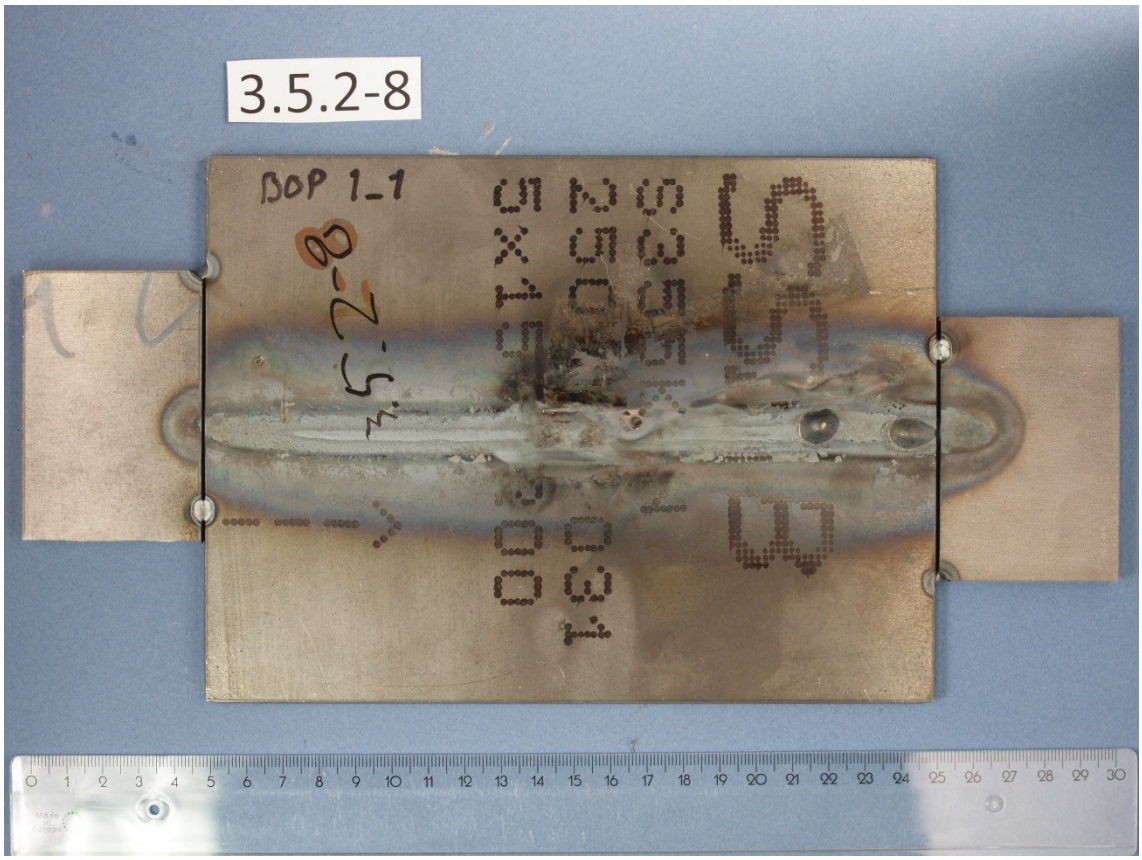

TIG 3.15.2-6

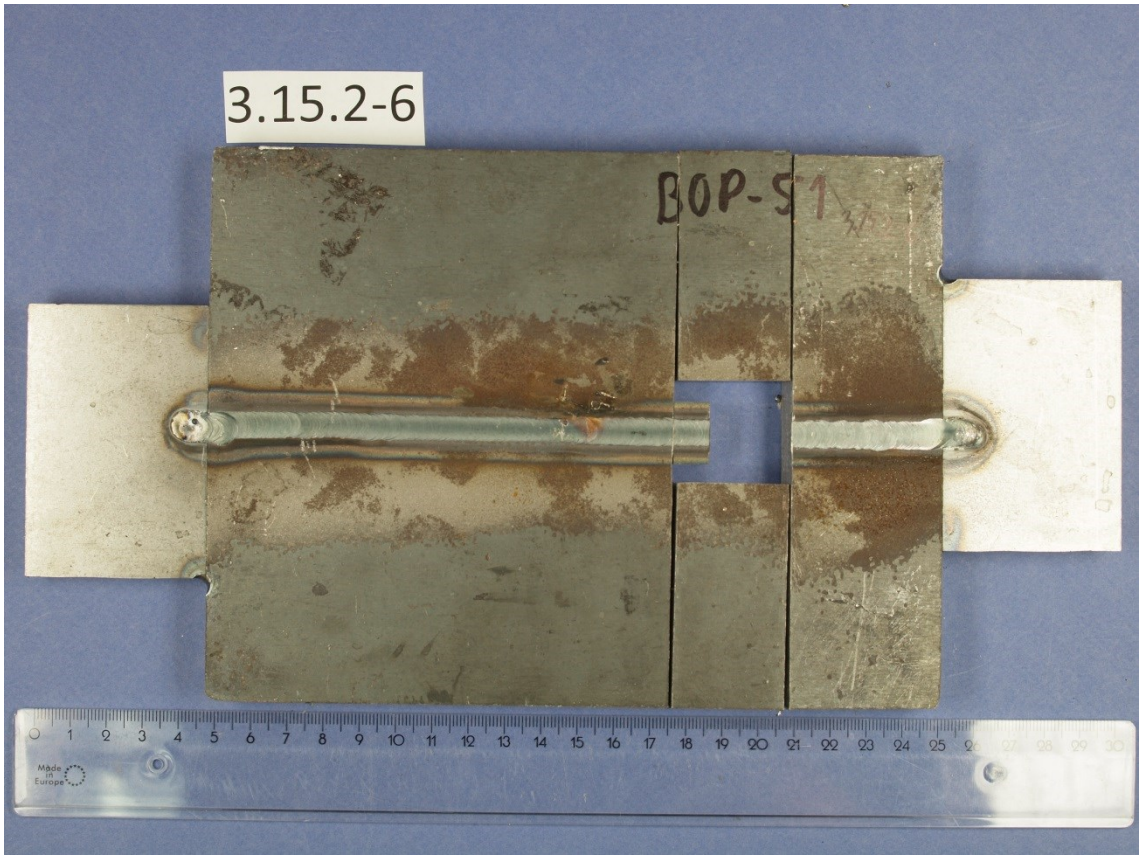

Appendix 3

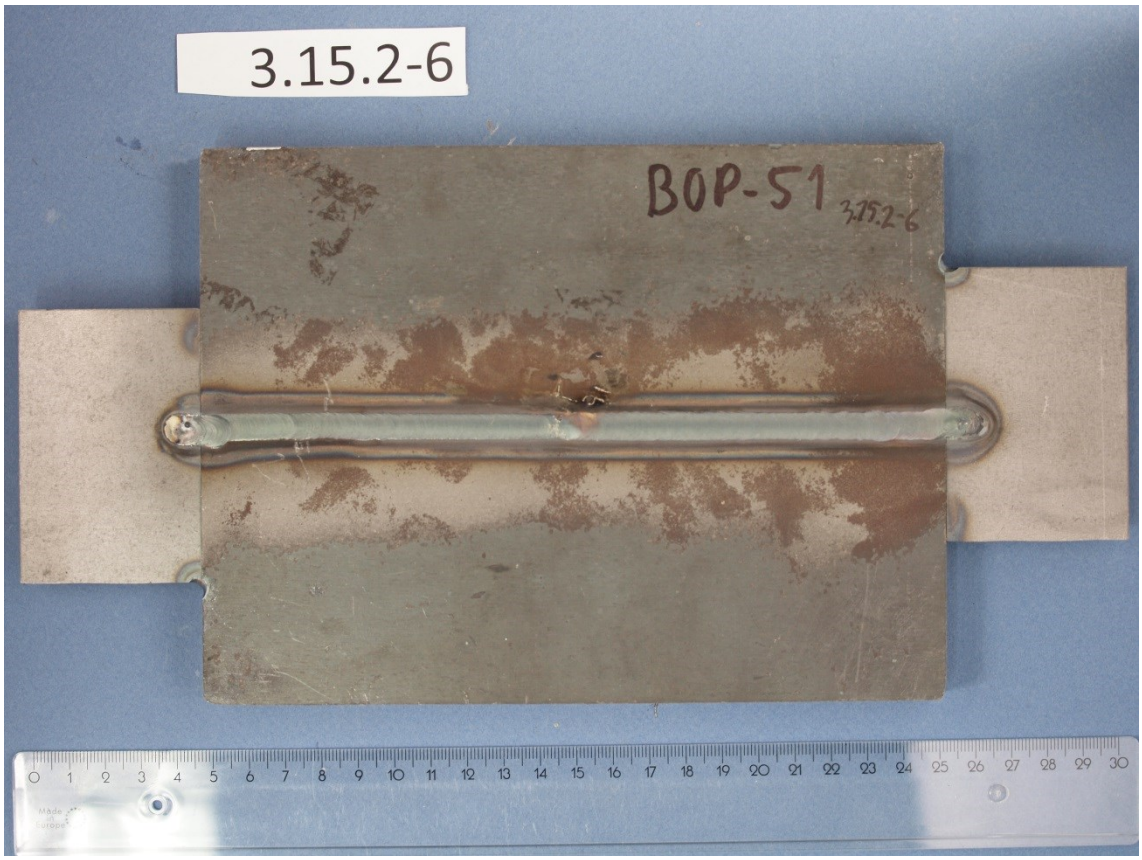

Appendix 3

TIG 3.15.2-7

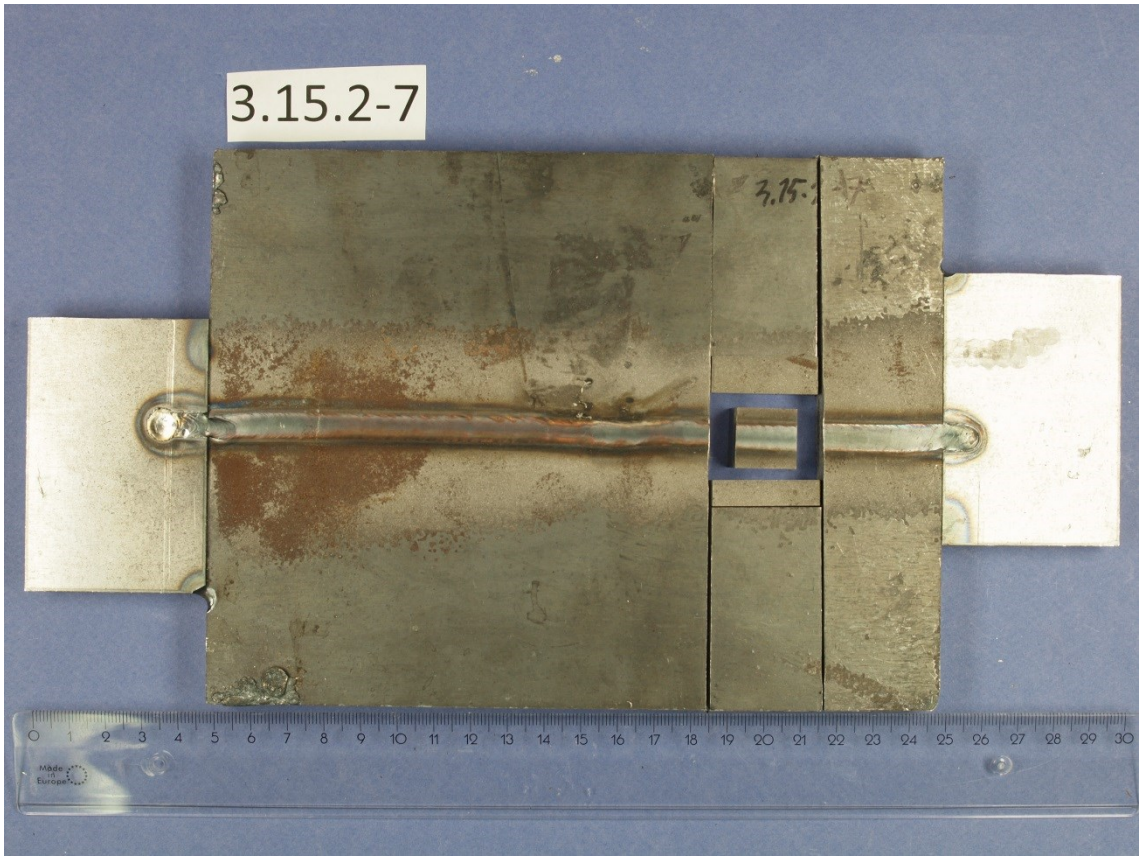

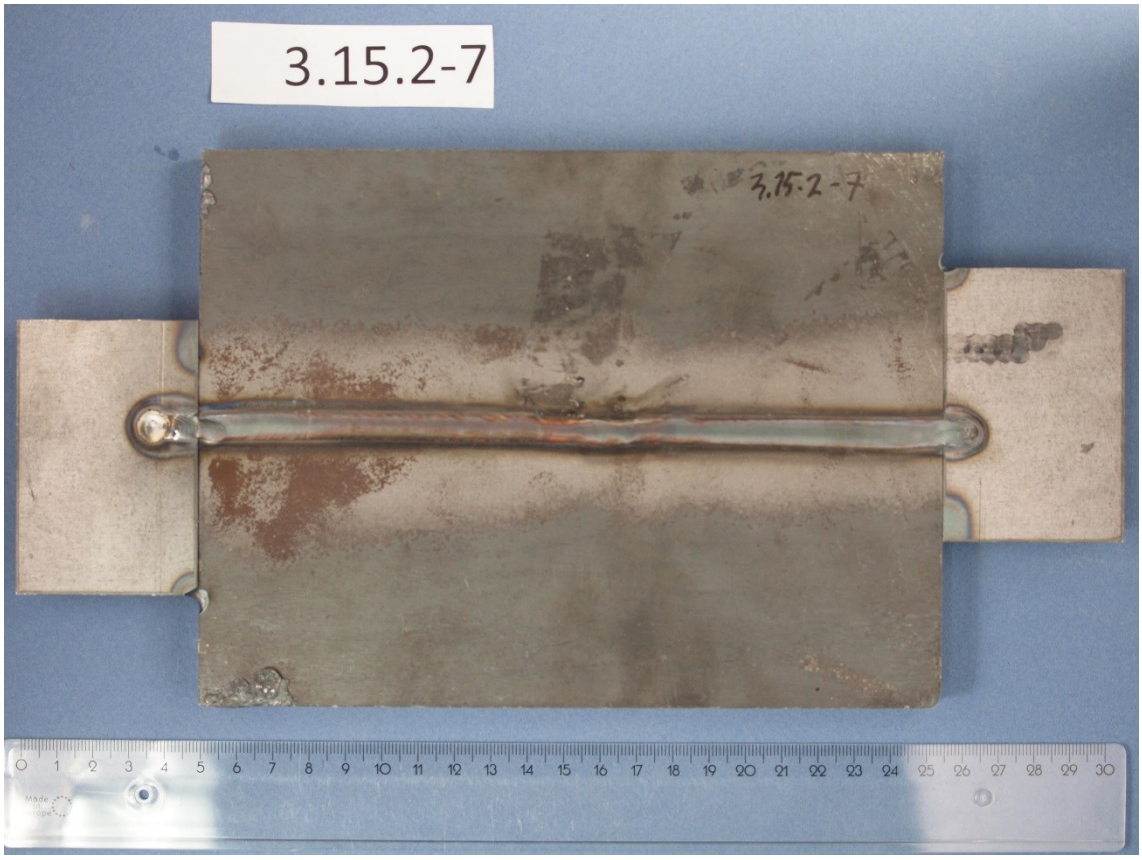

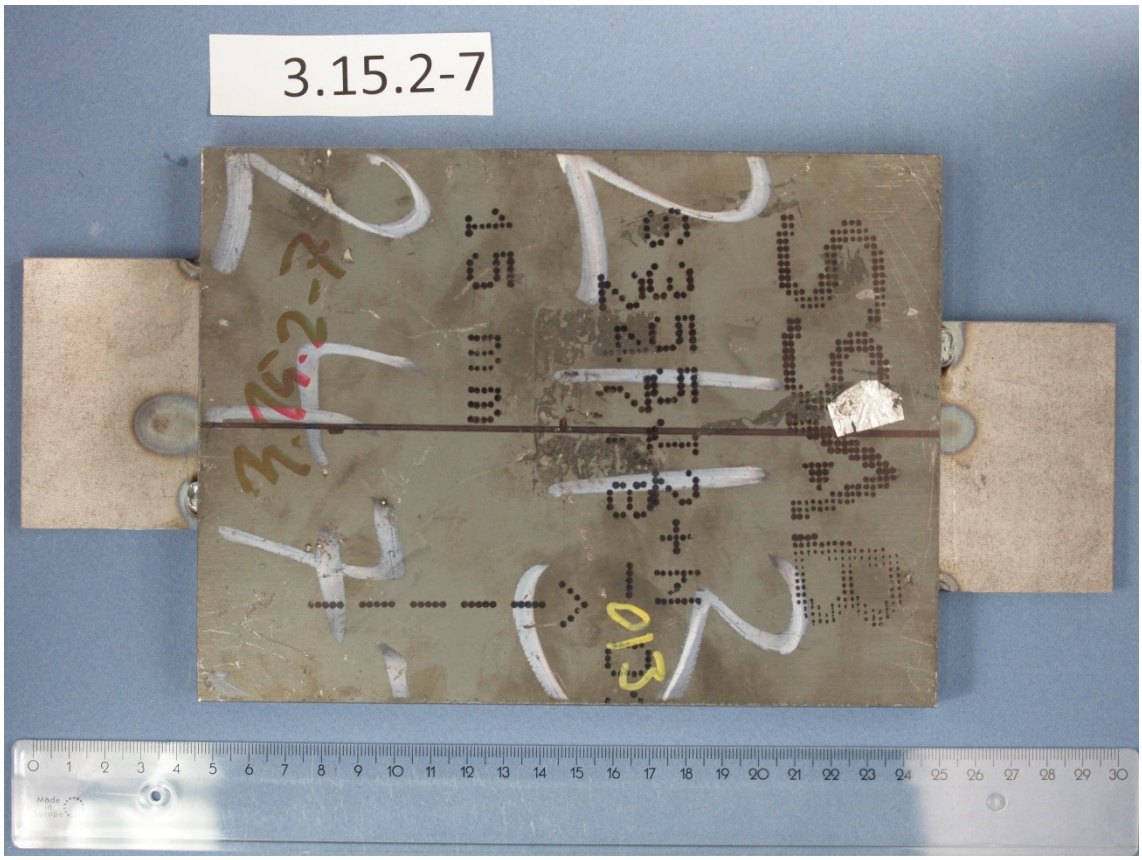

TIG 3.15.2-8

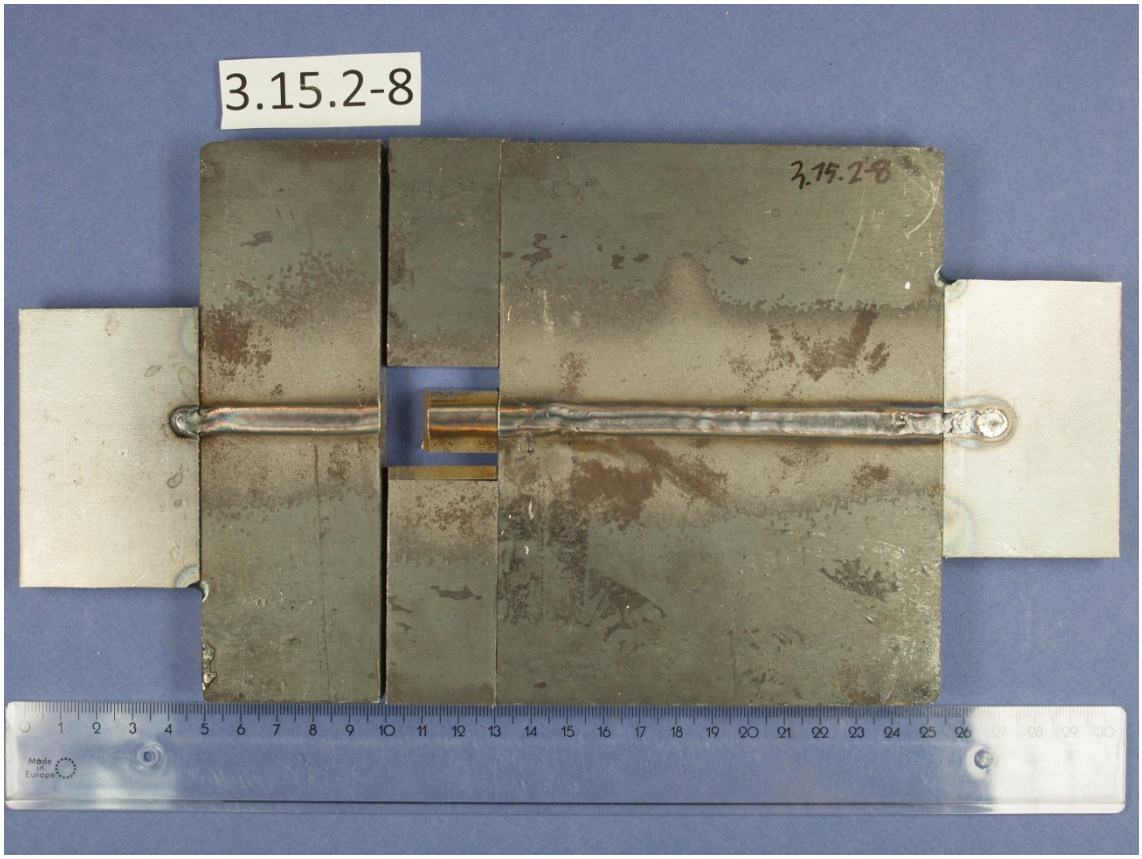

Appendix 3

Appendix 3

TIG 3.5.2-4

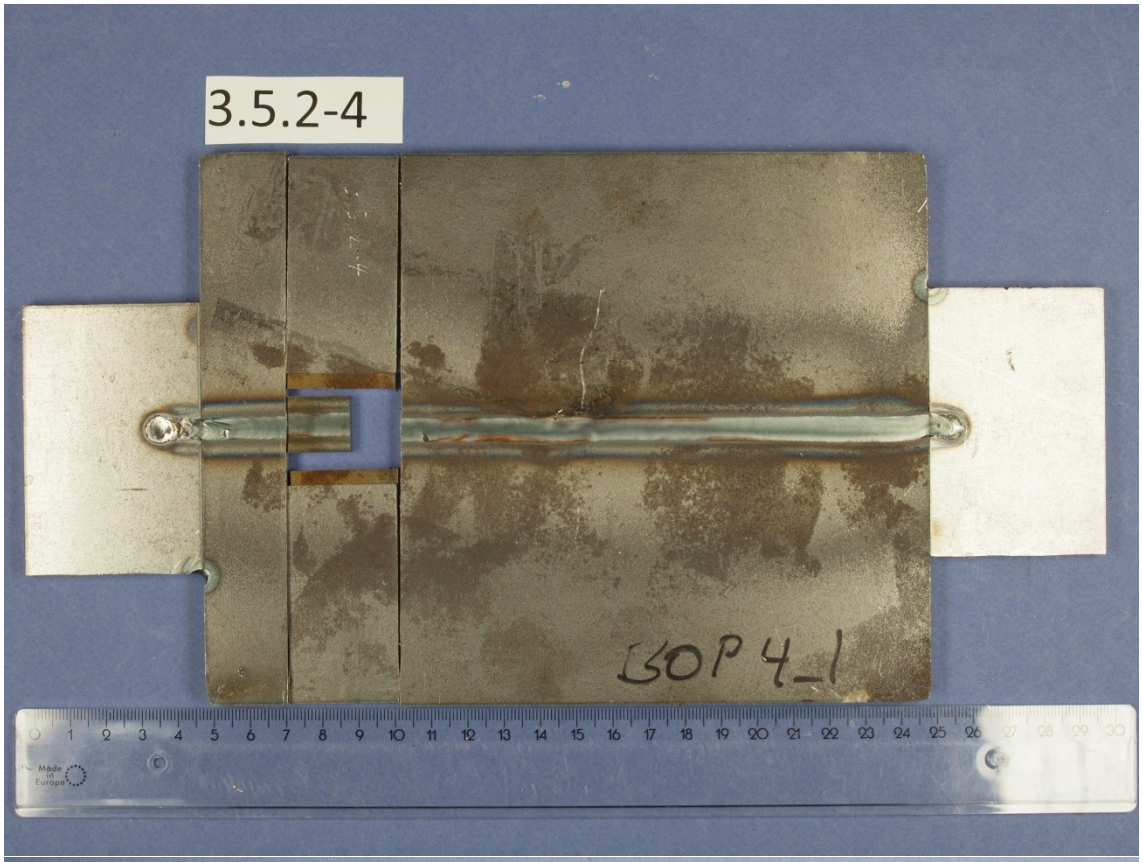

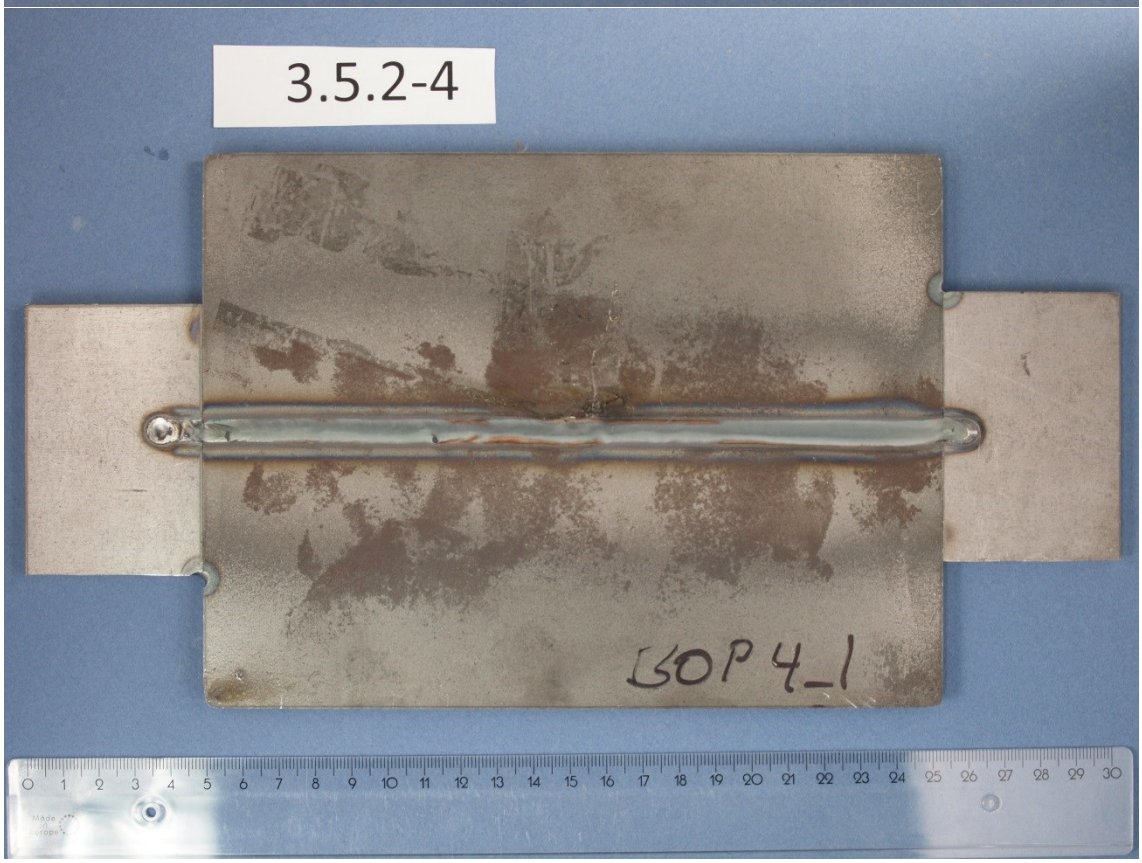

Appendix 3

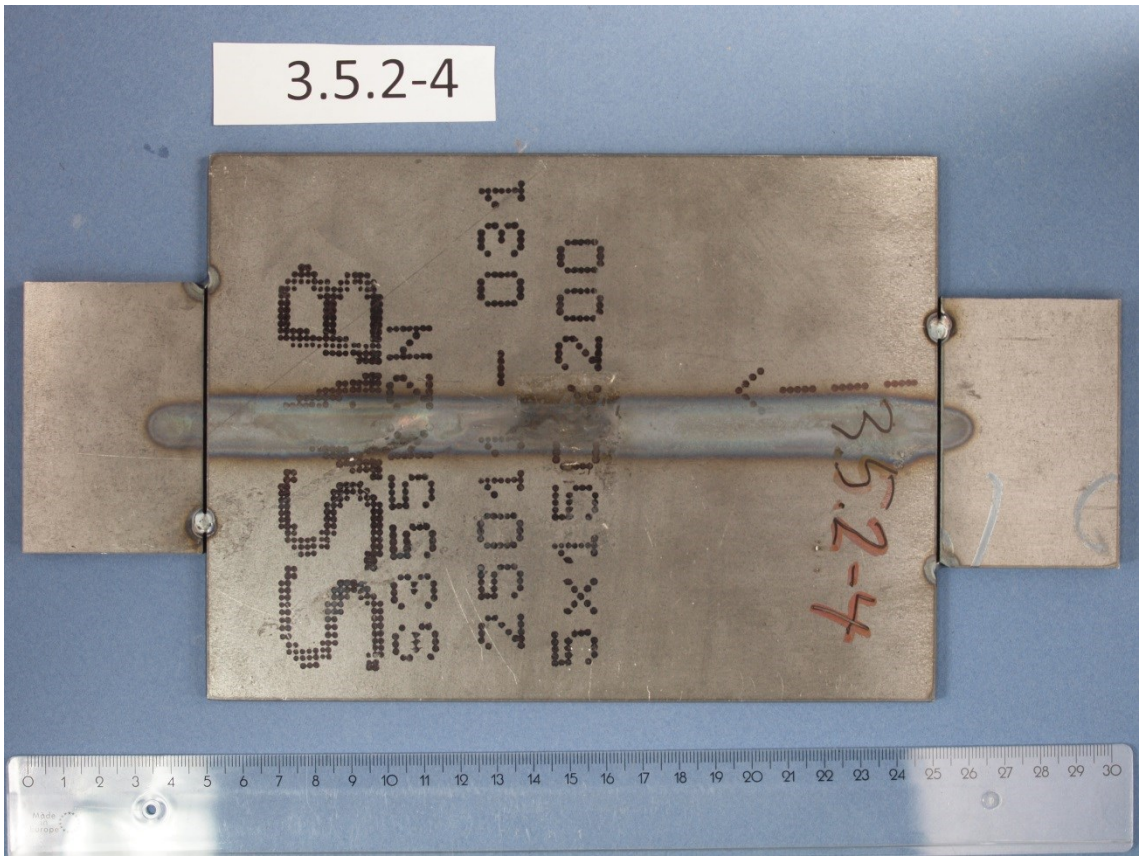

TIG 3.5.2-9

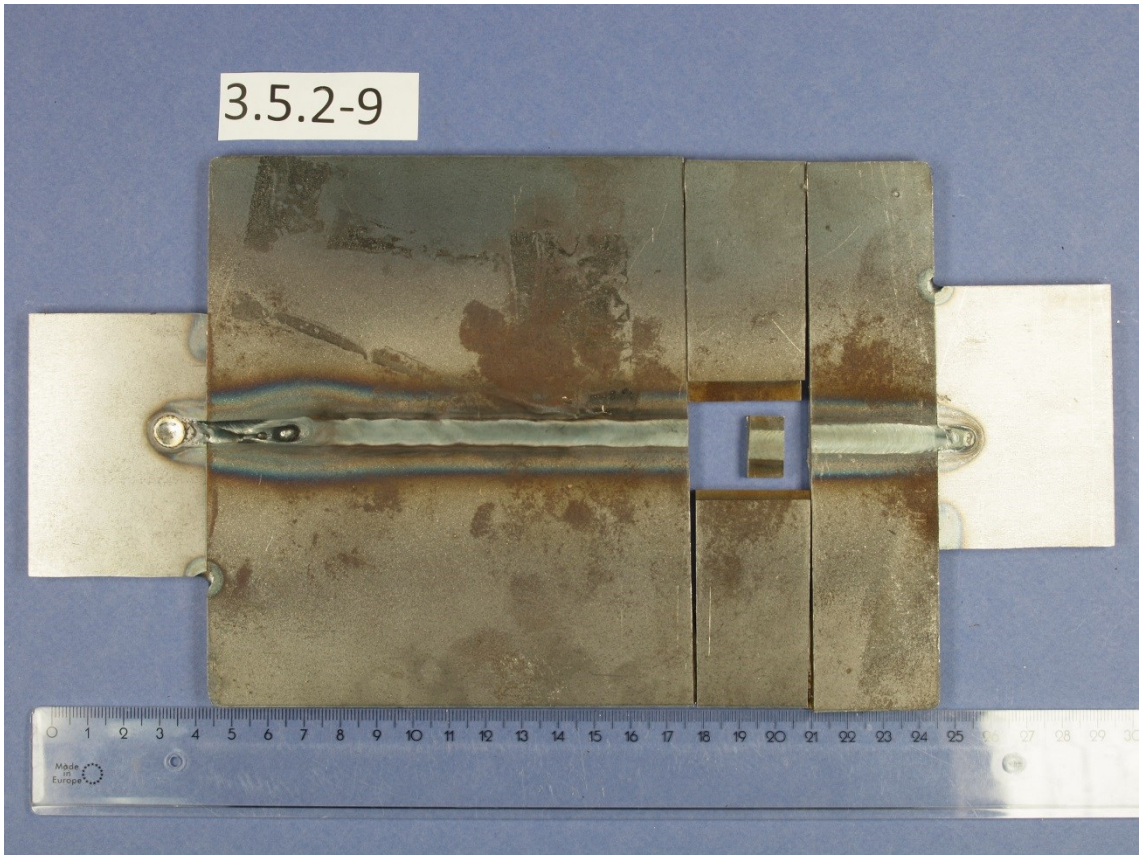

Appendix 3

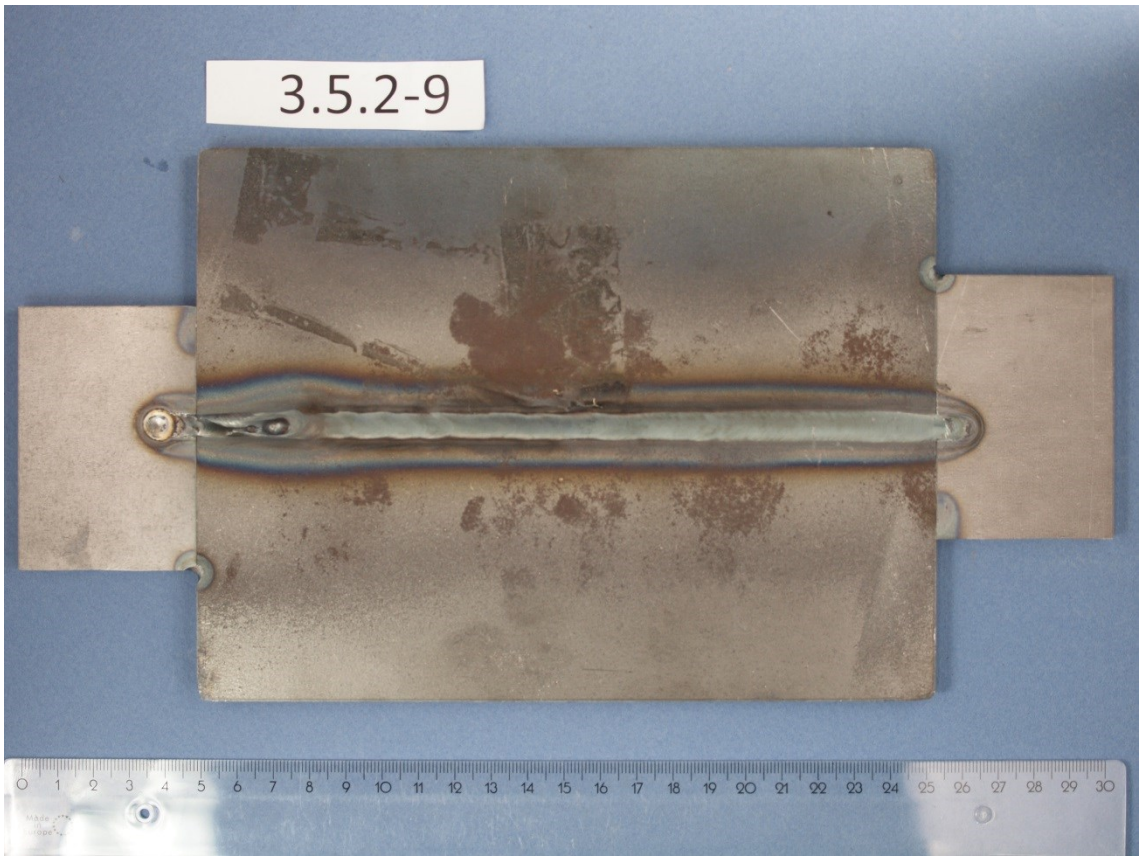

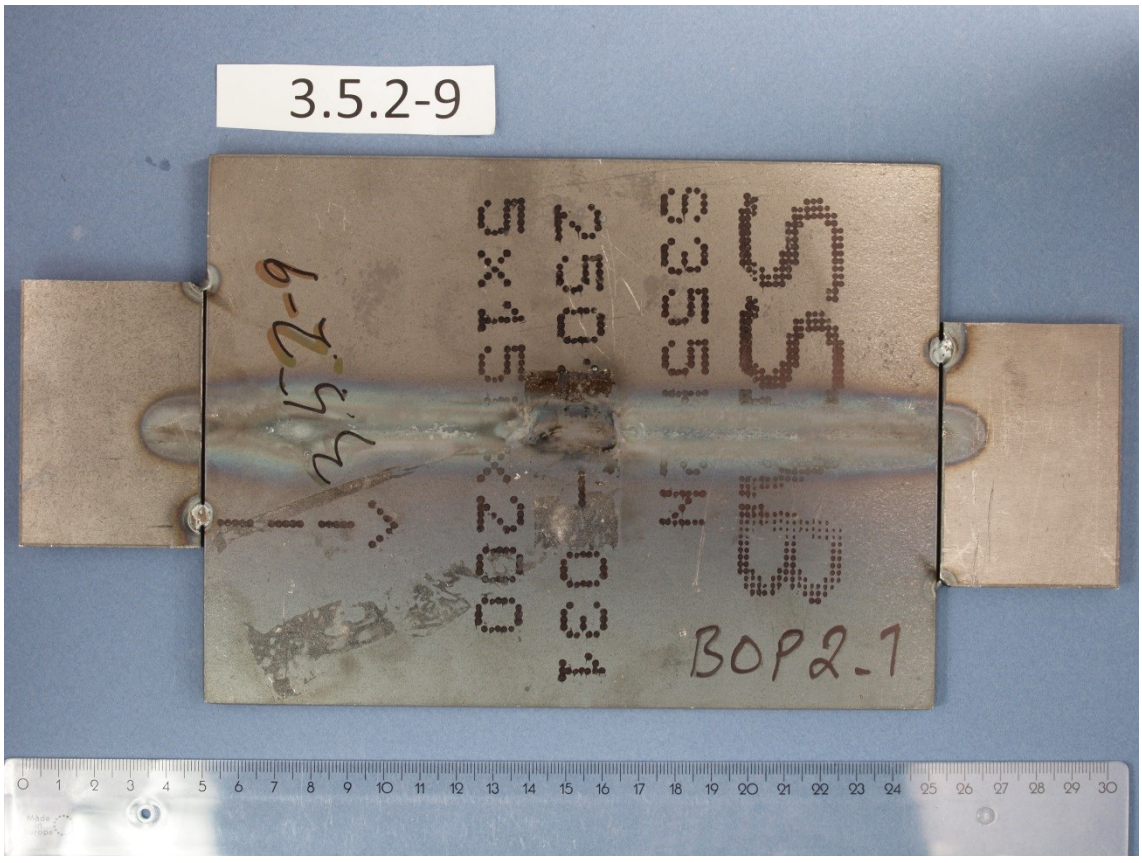

MAG 3.5.2-2

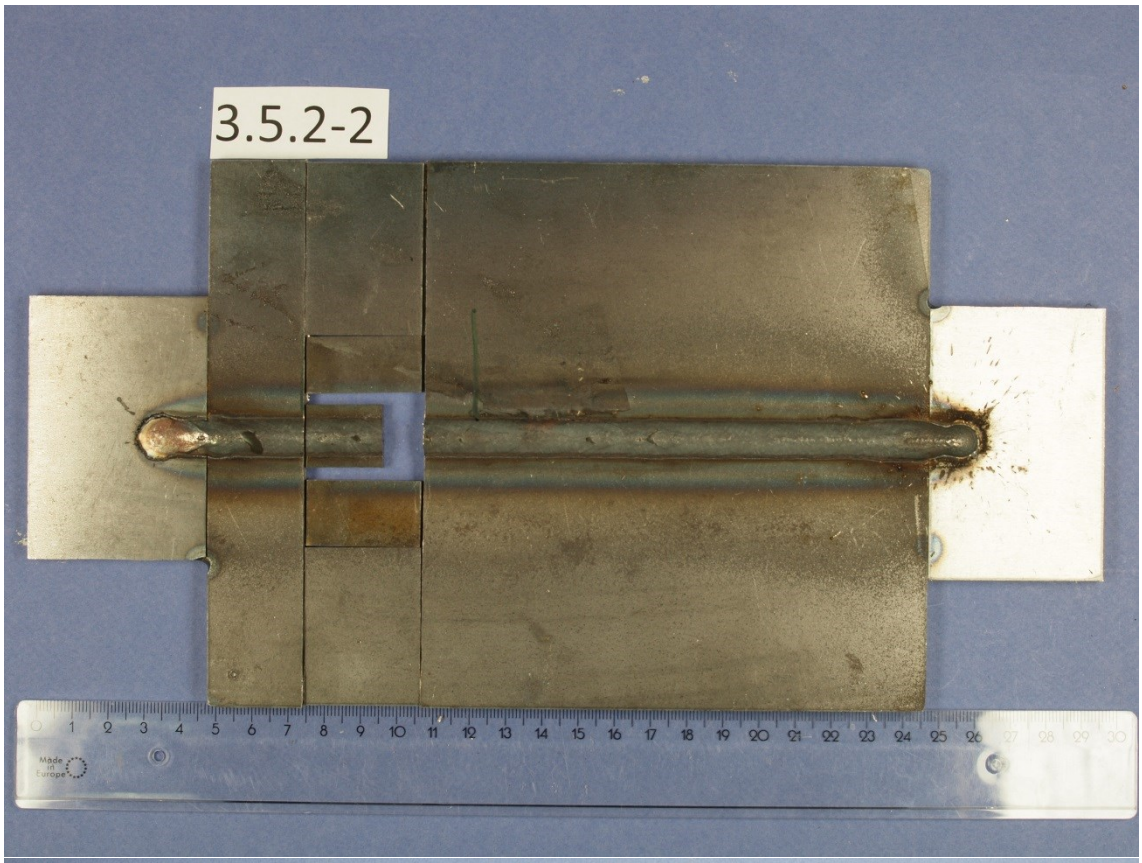

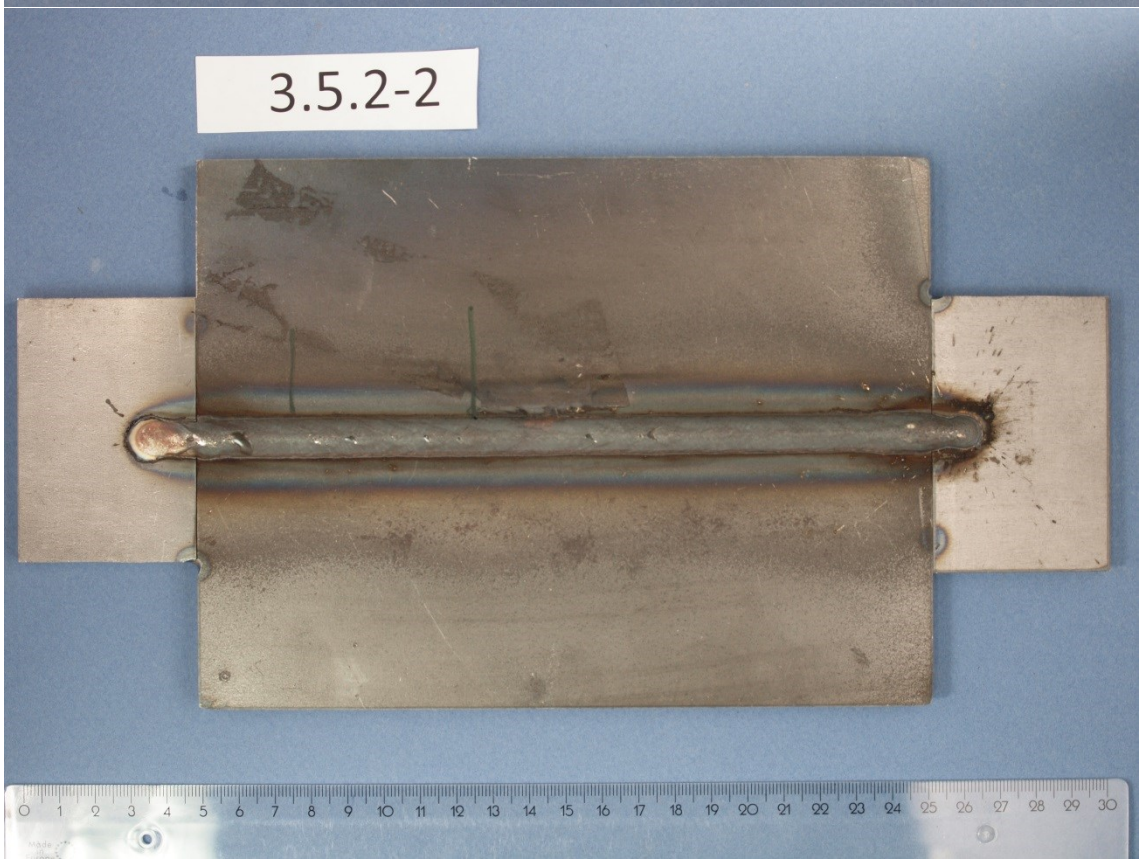

Appendix 3

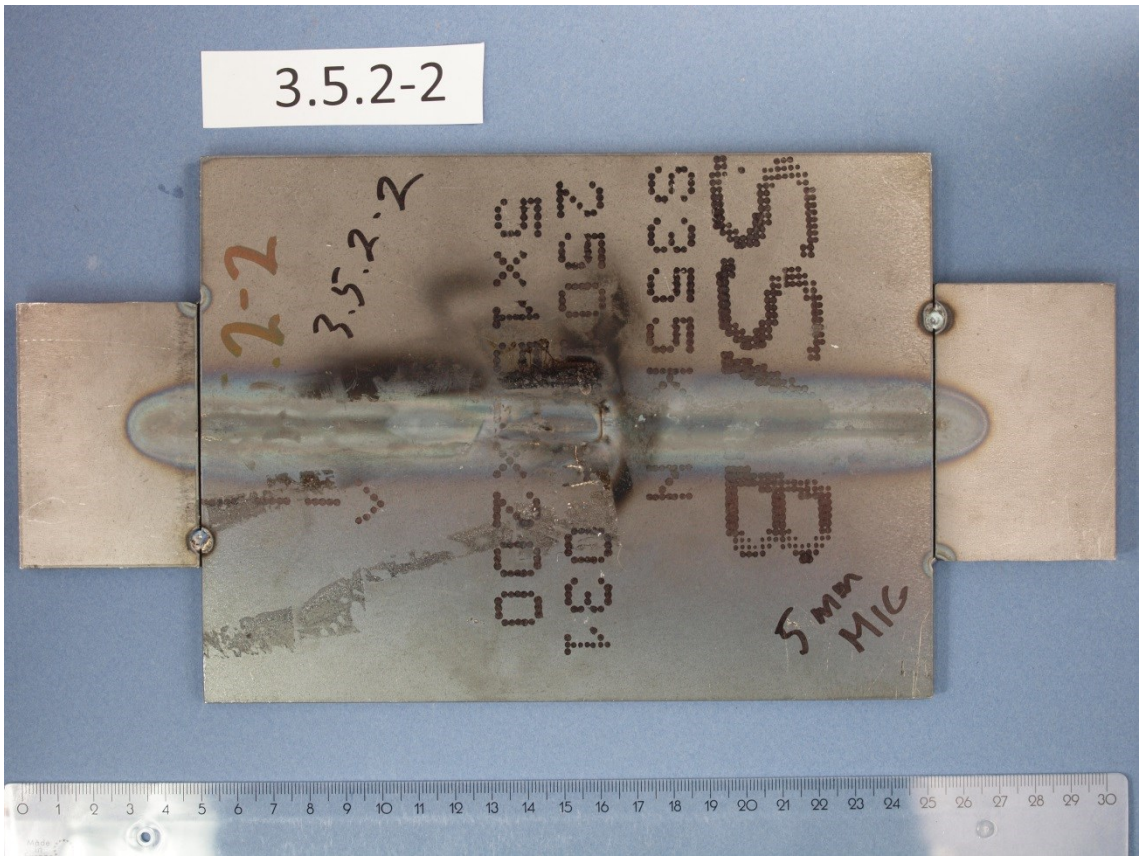

MAG 3.15.2-4

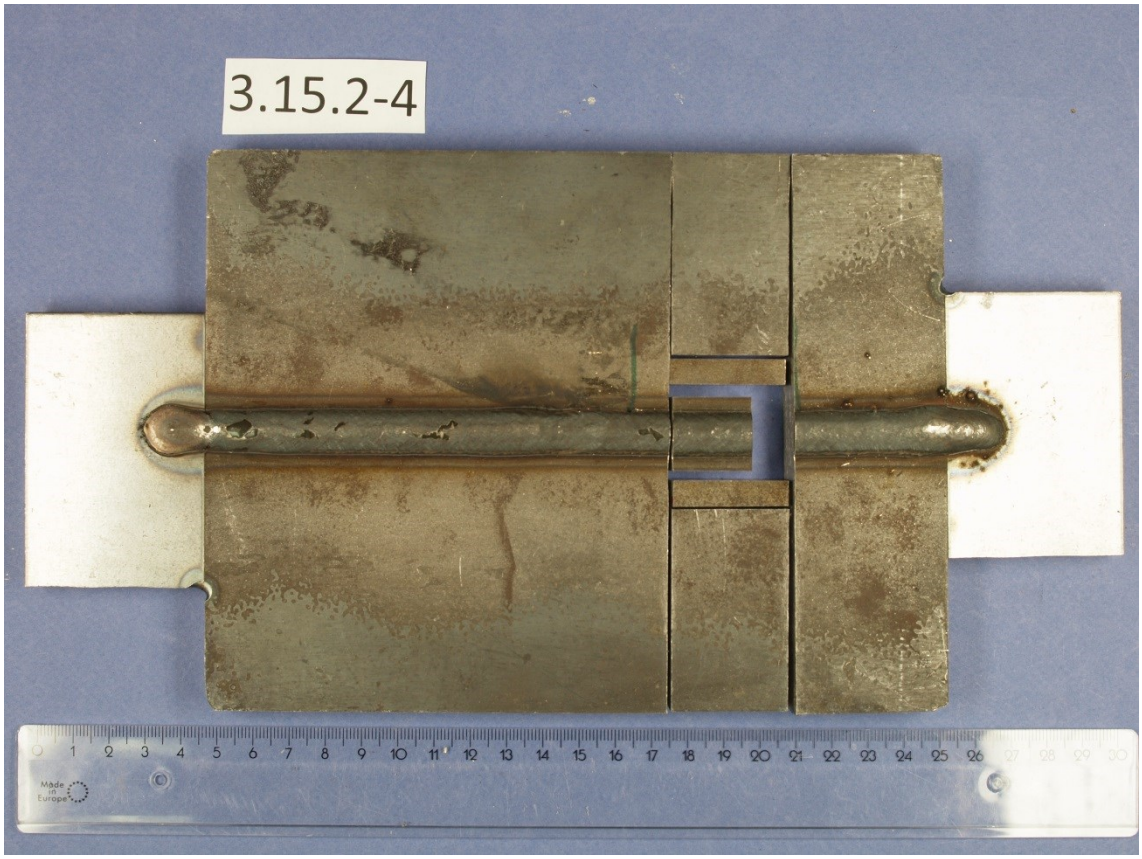

Appendix 3

Appendix 3

LAHW 3.5.2-3

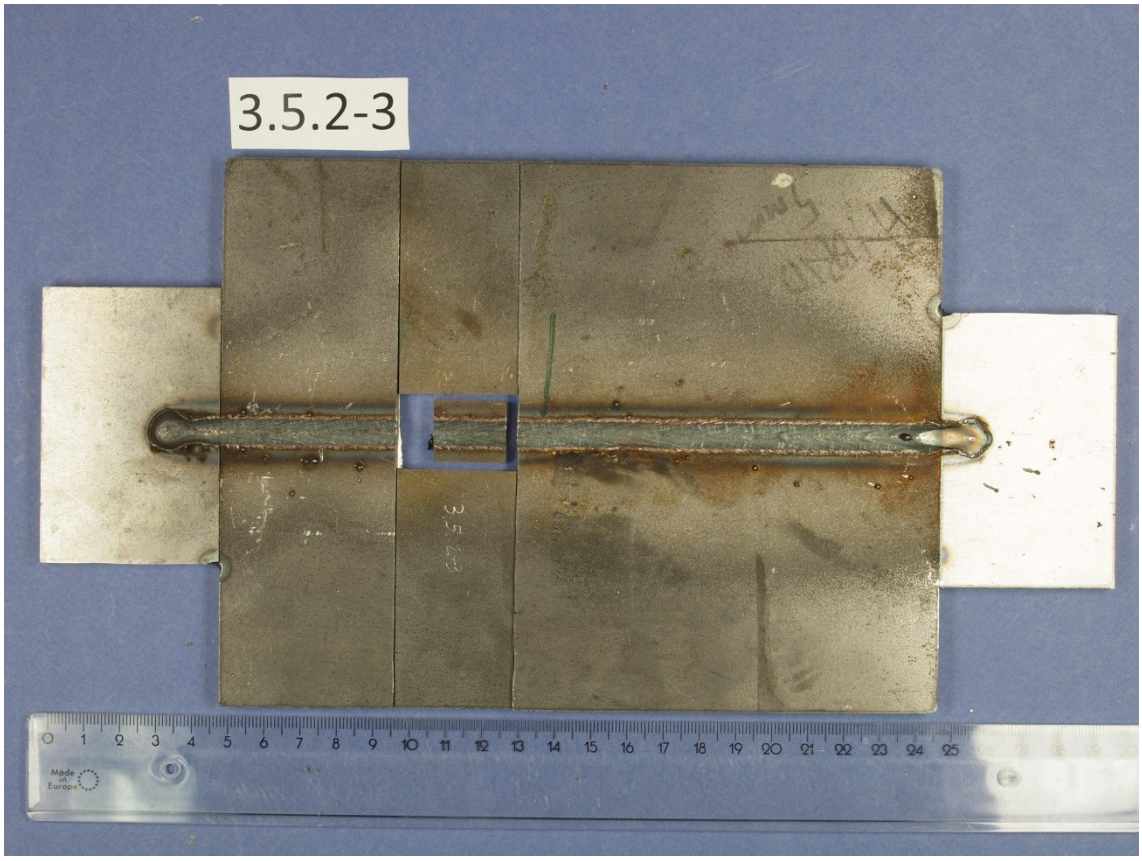

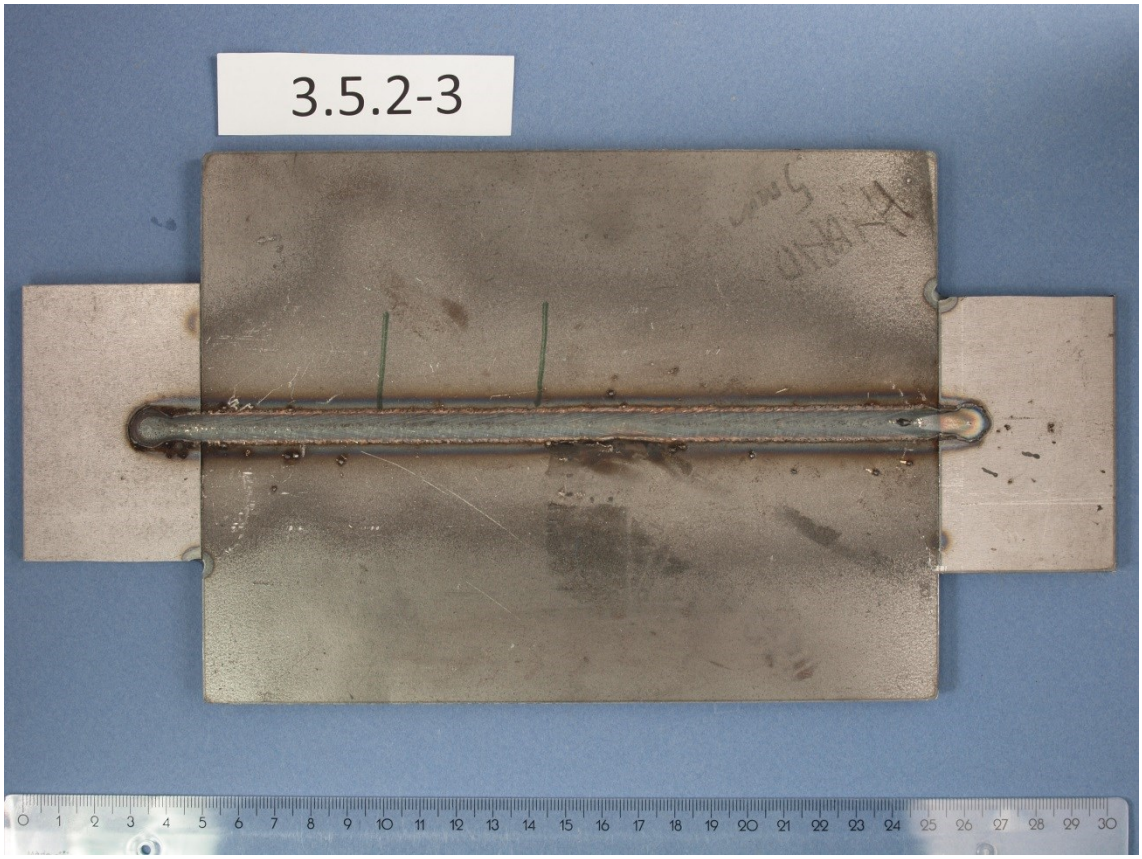

Appendix 3

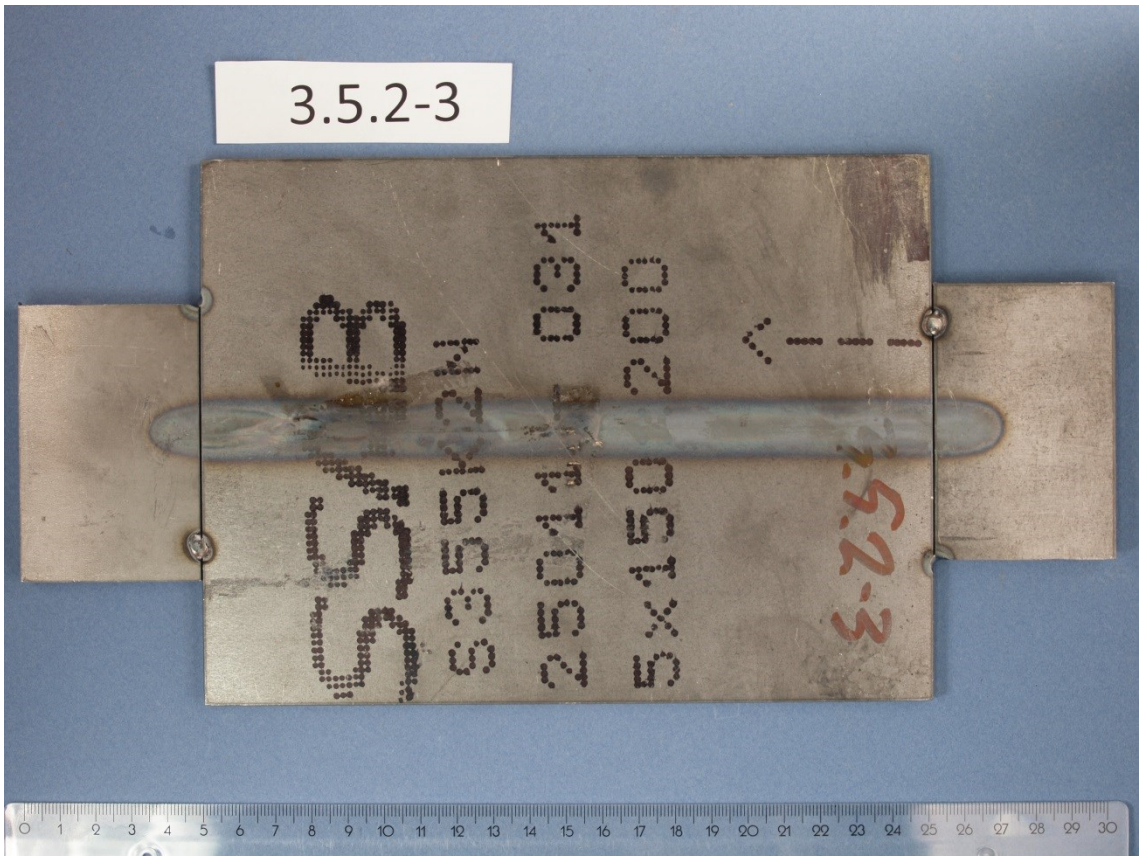

LAHW 3.15.2-9

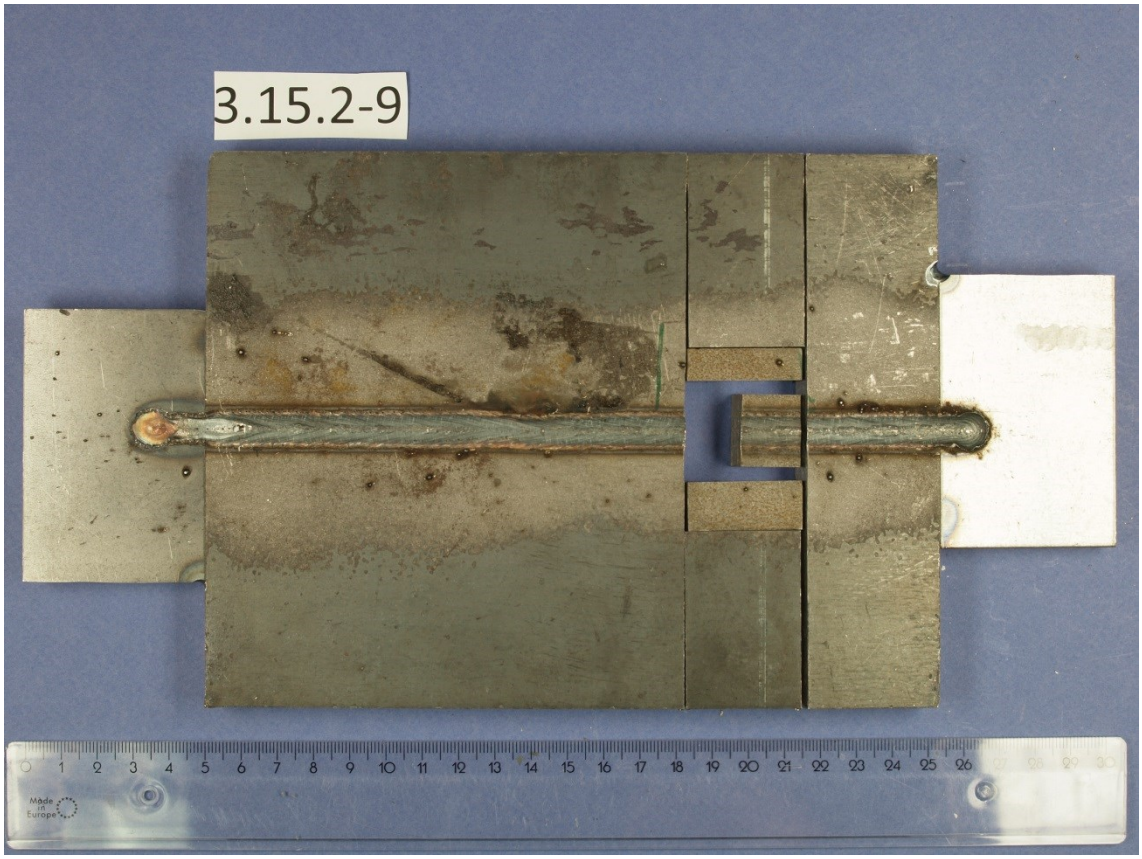

Appendix 3

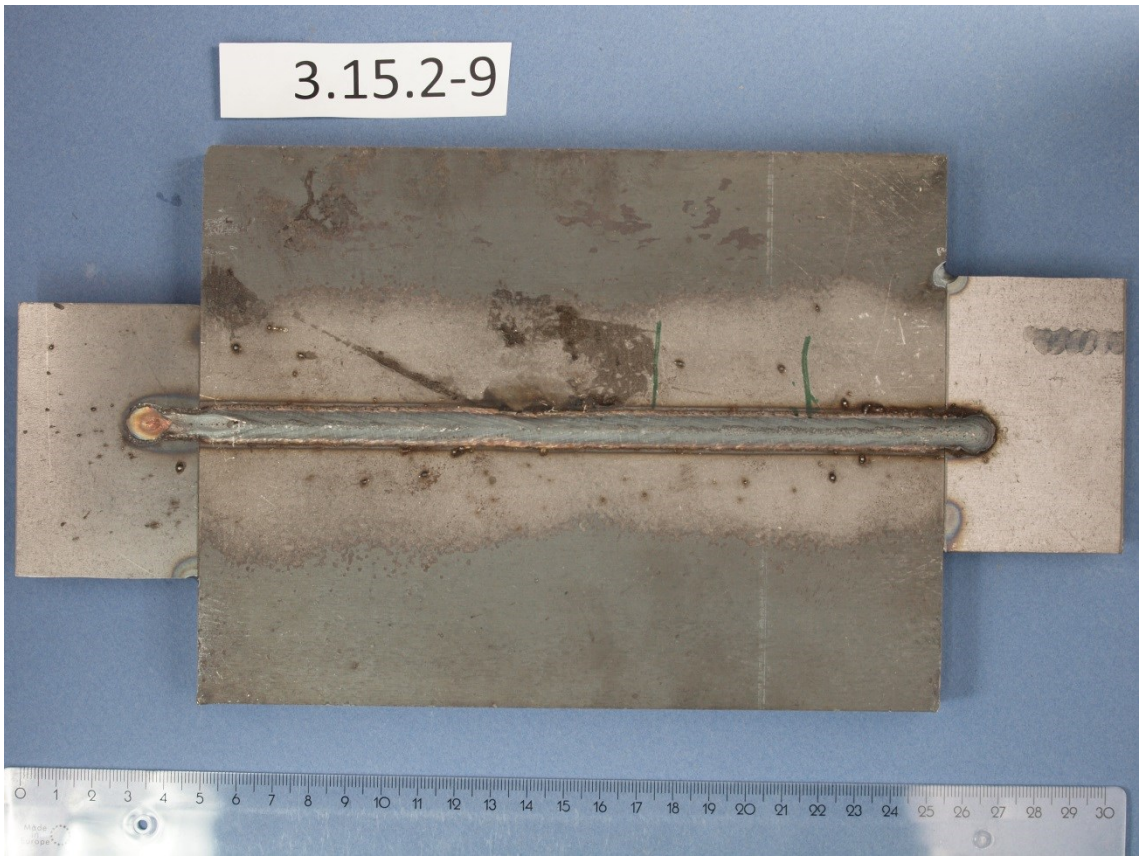

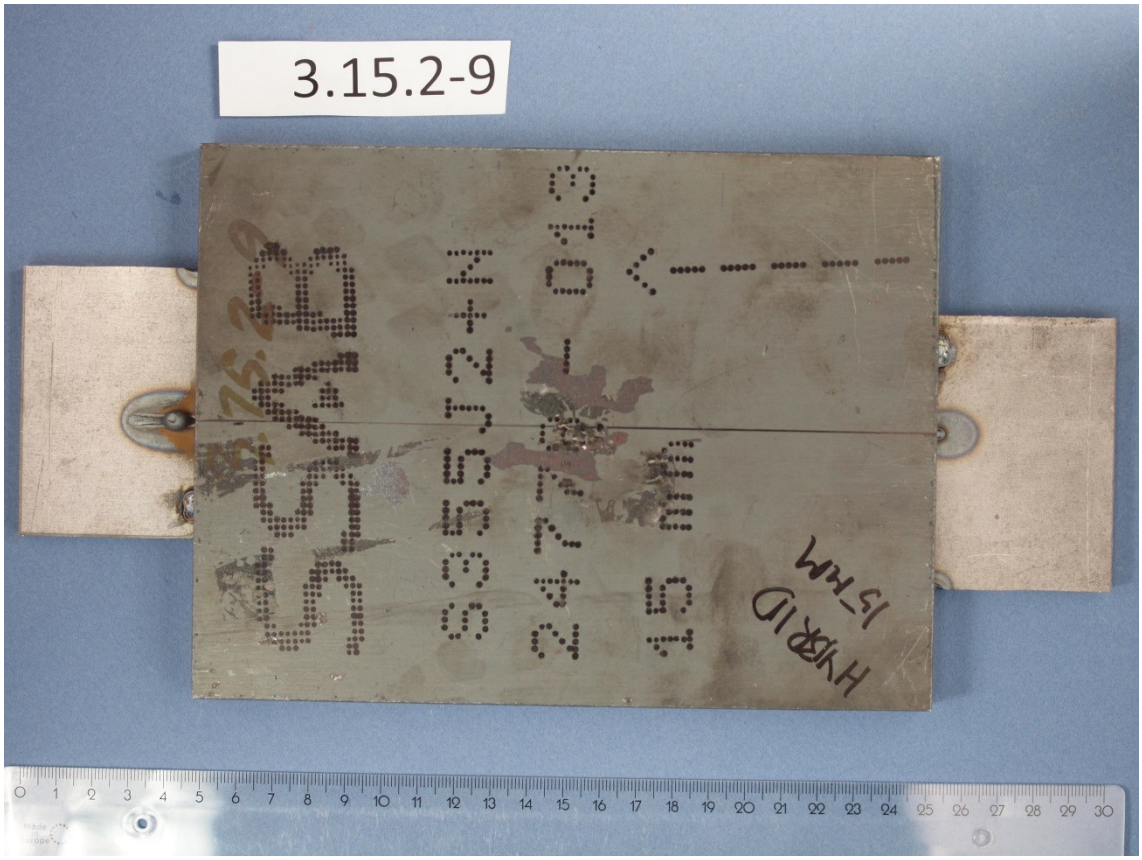

Appendix 3

LASER 3.5.2-1

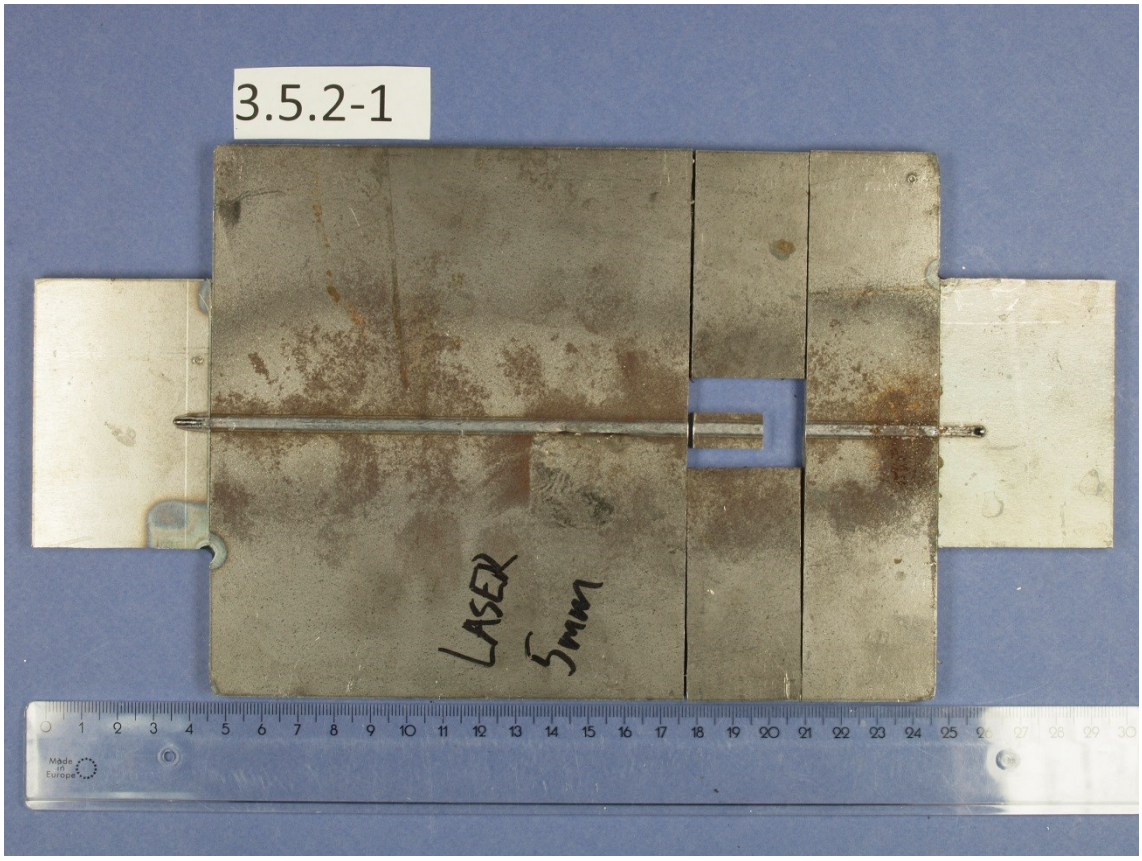

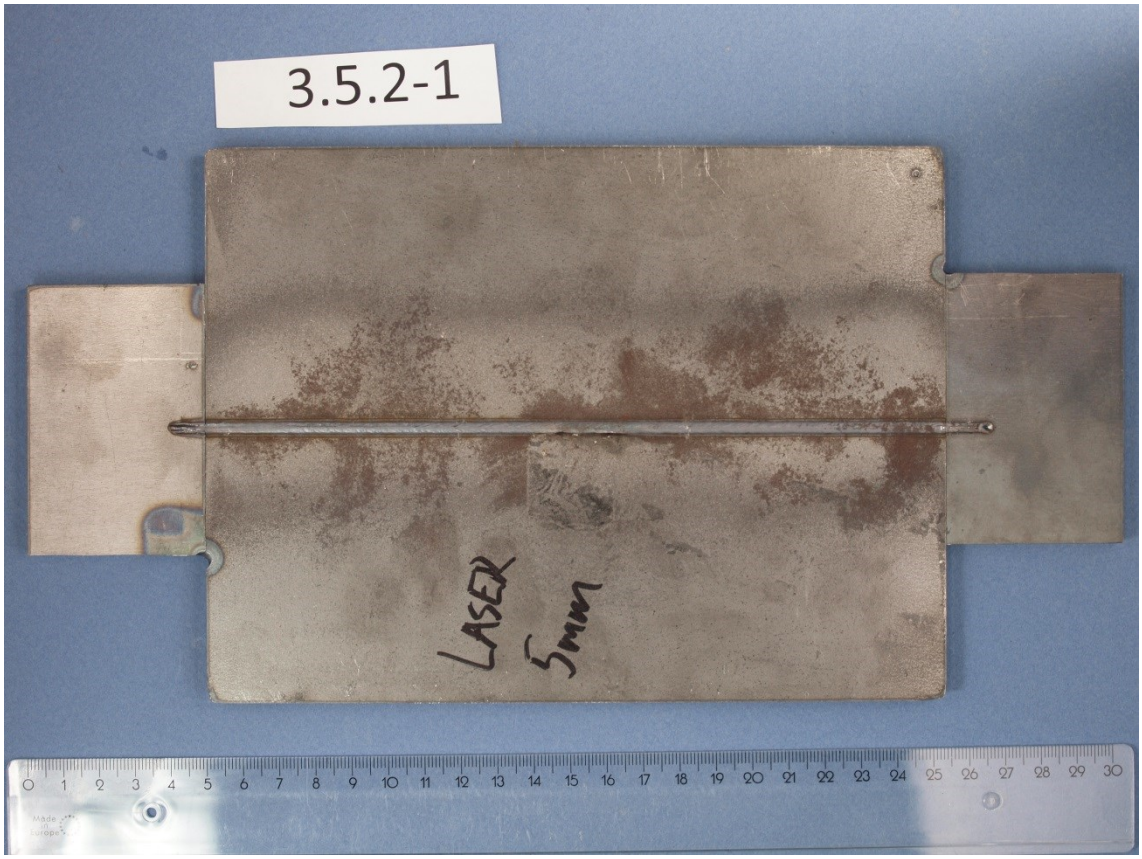

Appendix 3

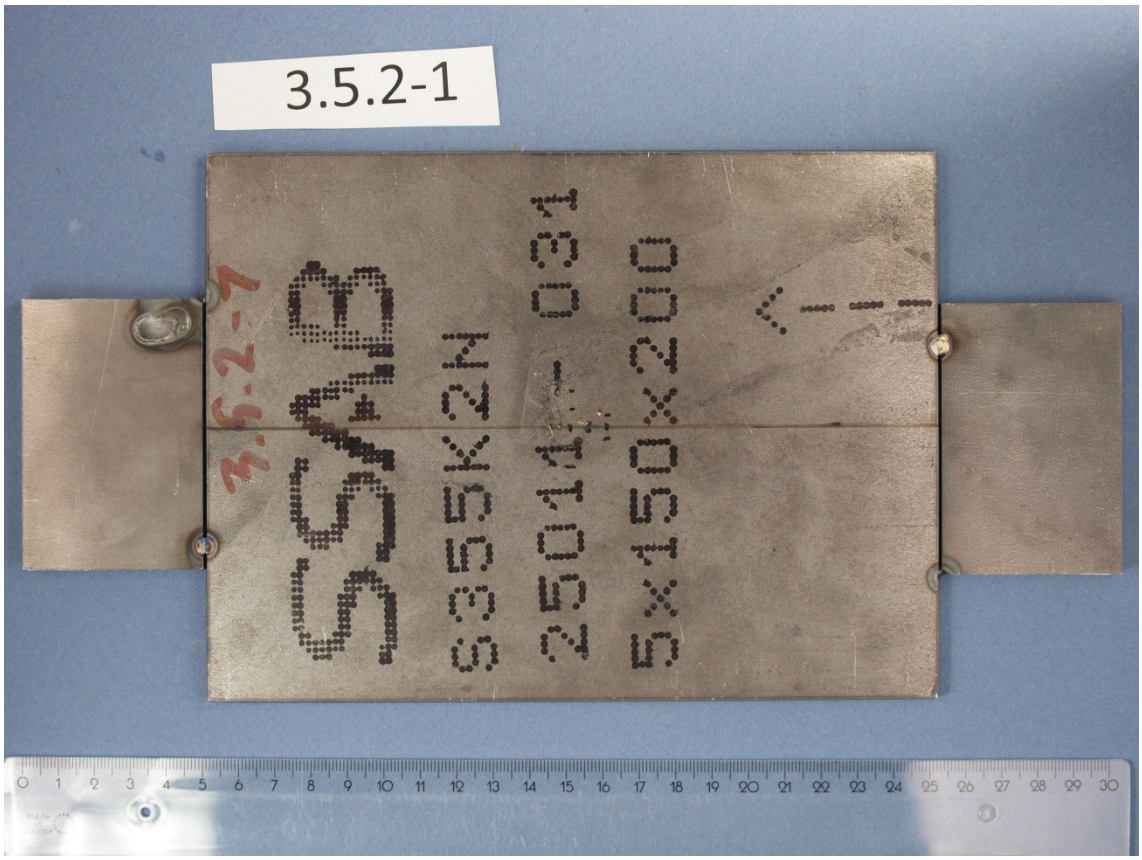

LASER 3.15.2-5

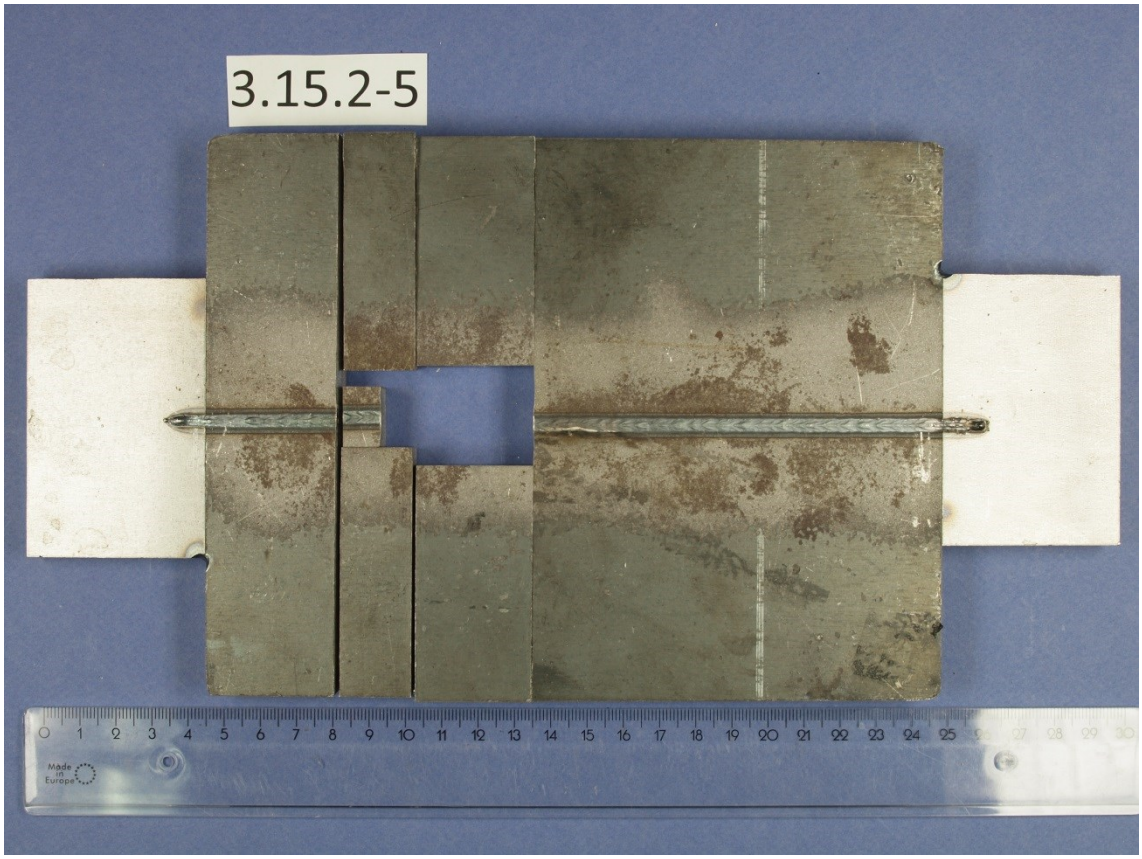

Appendix 3

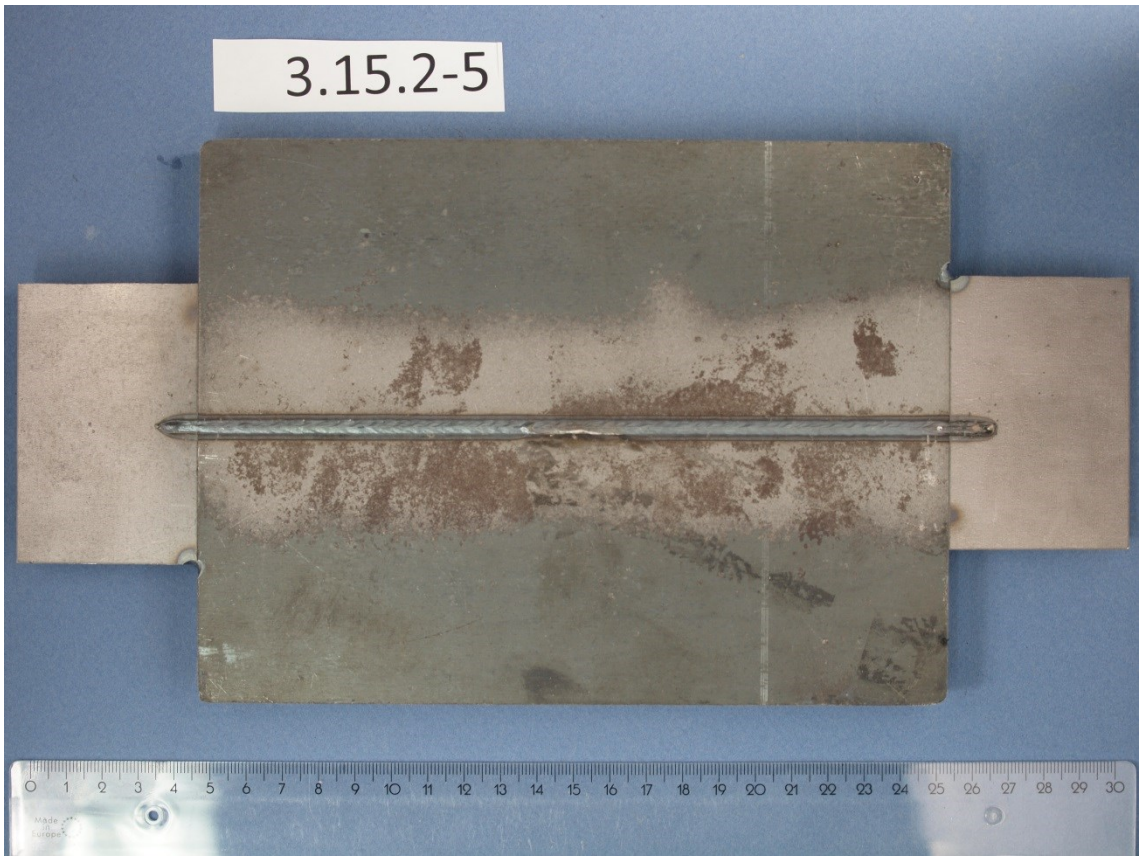

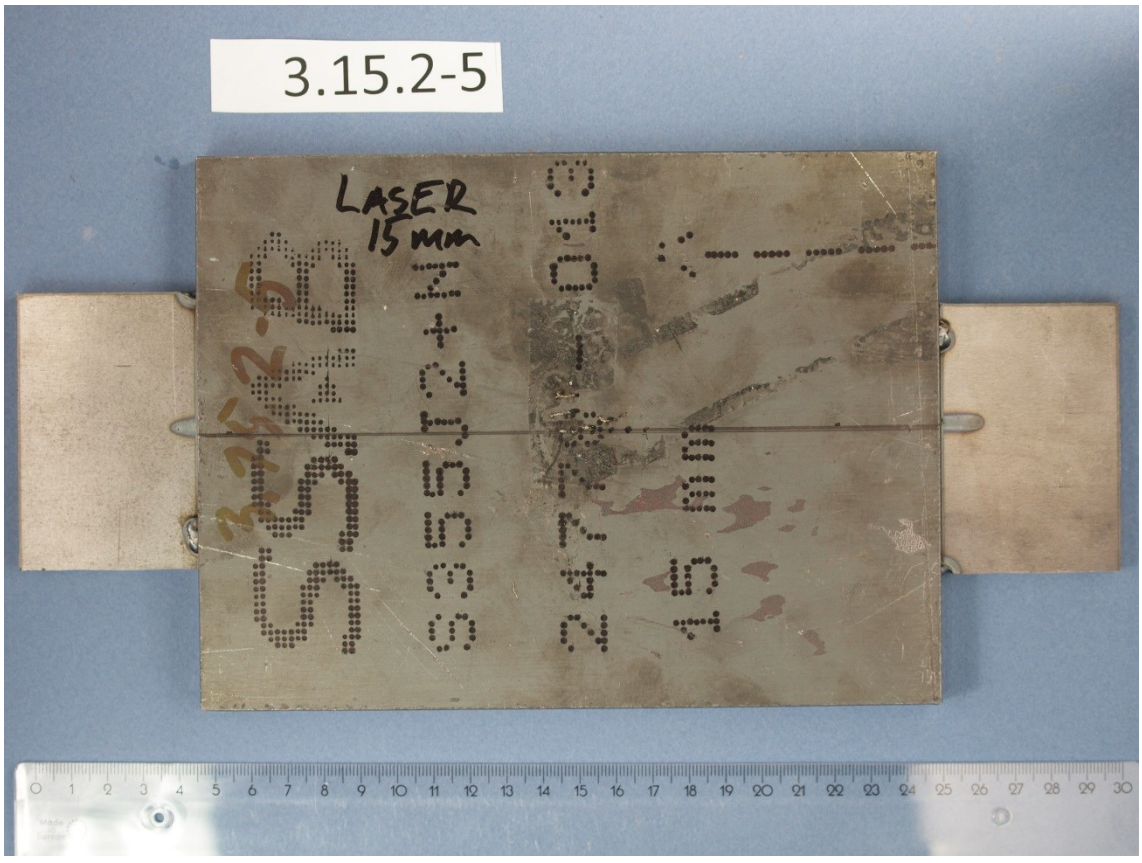

Appendix 4 / Photographs of butt welds and base material, position of their microsections and cut parts

Contents

Sample 1 / MAG

Figure 1 Top side of MAG 1.

Figure 2 Bottom side of MAG 1.

Figure 3 Top side of MAG 1.

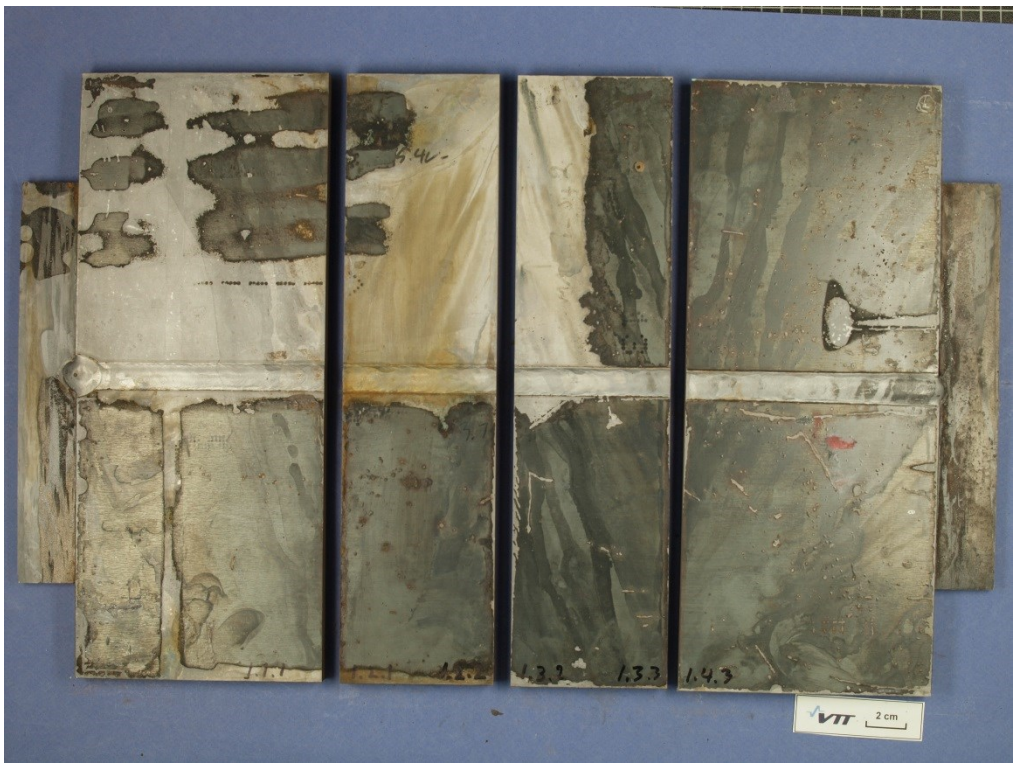

Figure 4 Bottom side of MAG 1.

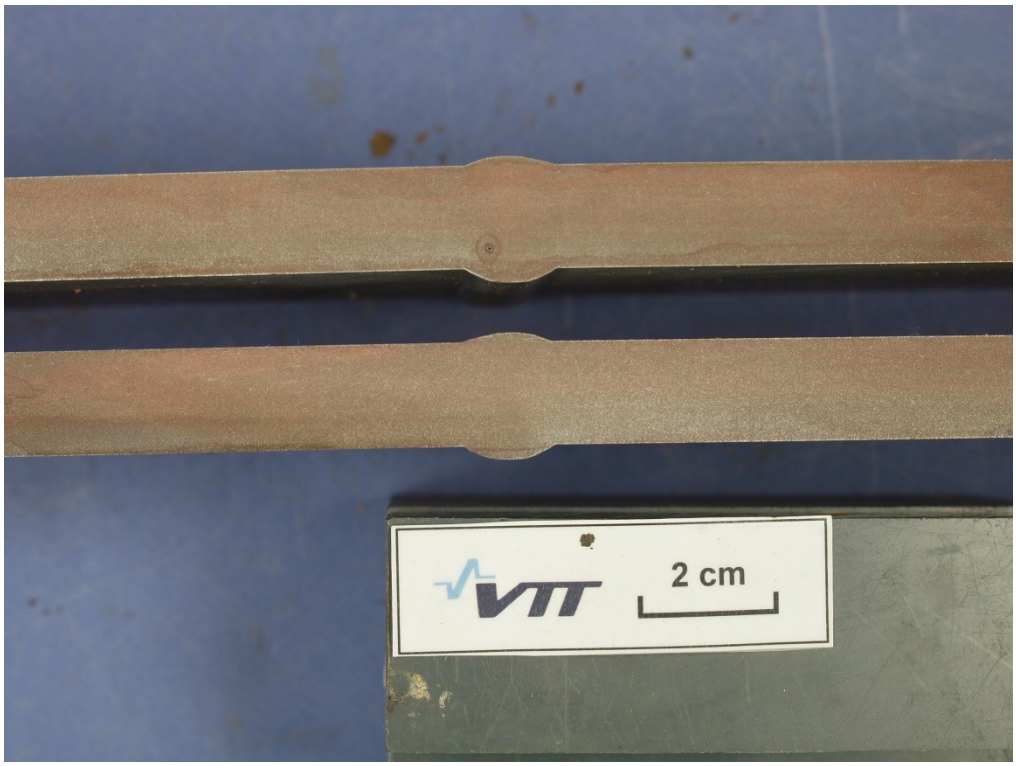

Figure 5 Cross-section in the middle of MAG 2.

Sample 2 / MAG

Figure 6 Top side of MAG 2.

Figure 7 Bottom side of MAG 2.

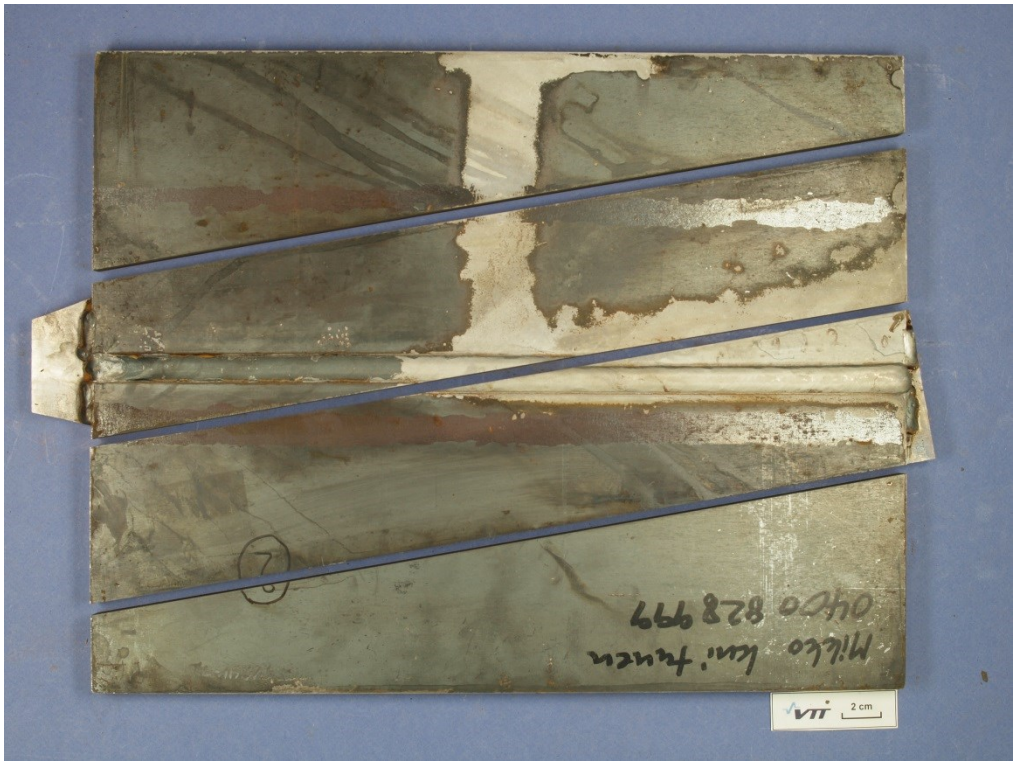

Figure 8 Top side of MAG 2.

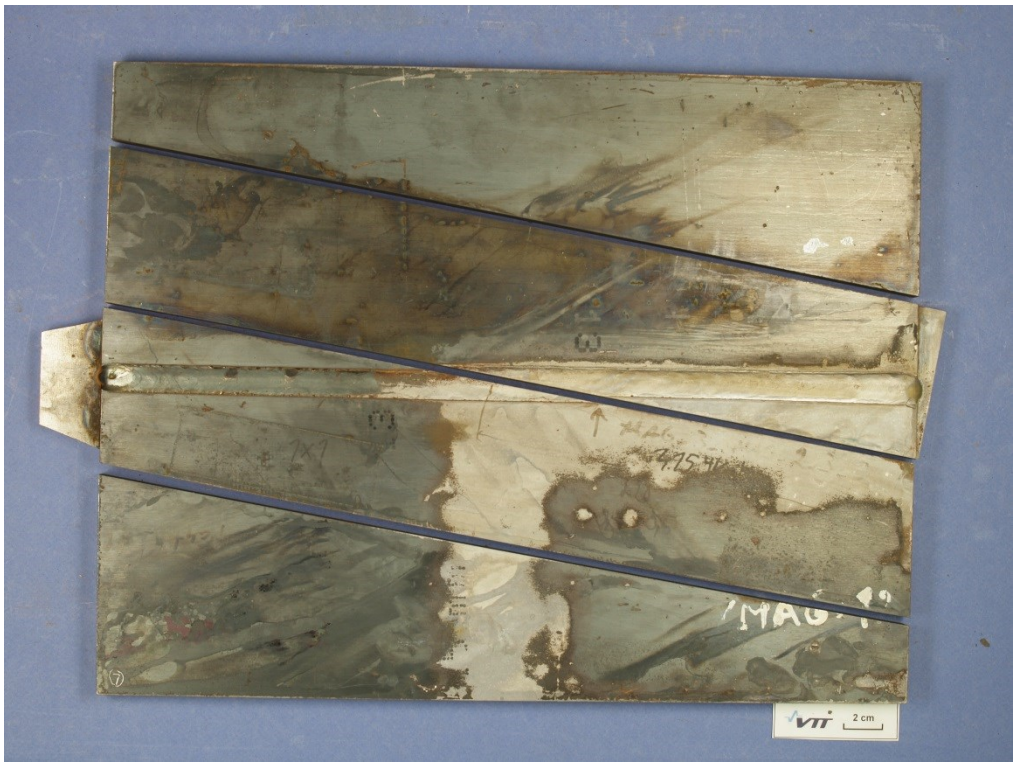

Figure 9 Bottom side of MAG 2.

Figure 10 Cross-section in the middle of MAG 2.

Sample 3 / Base material

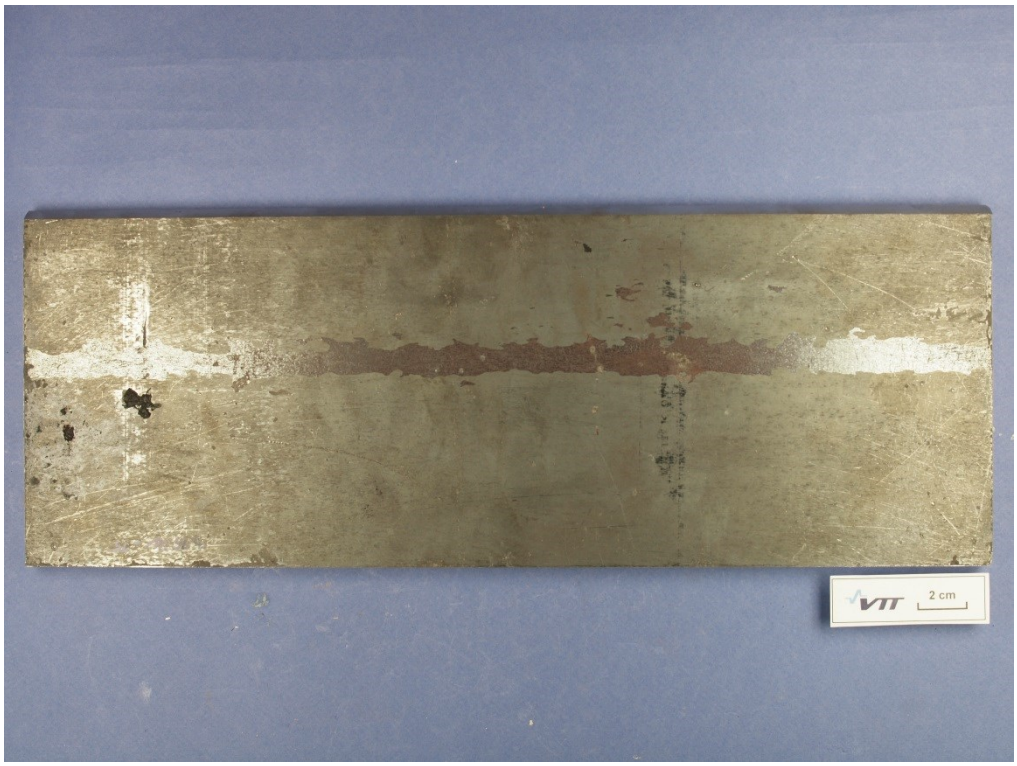

Figure 11 Top side of base material plate.

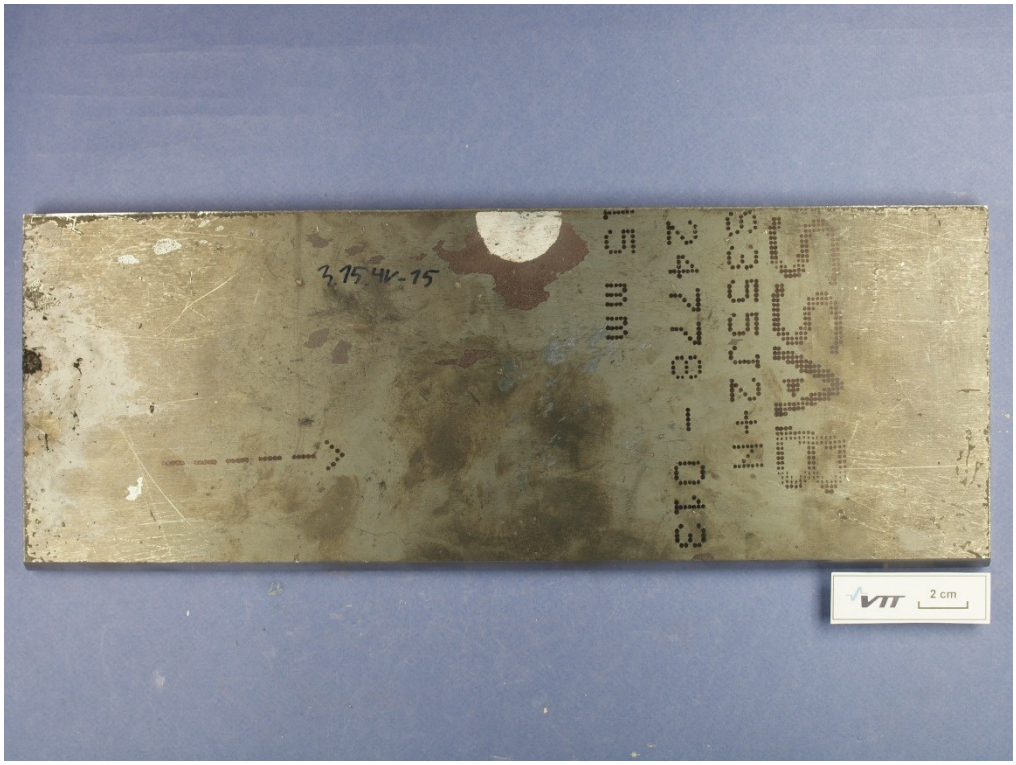

Figure 12 Bottom side of base material plate.

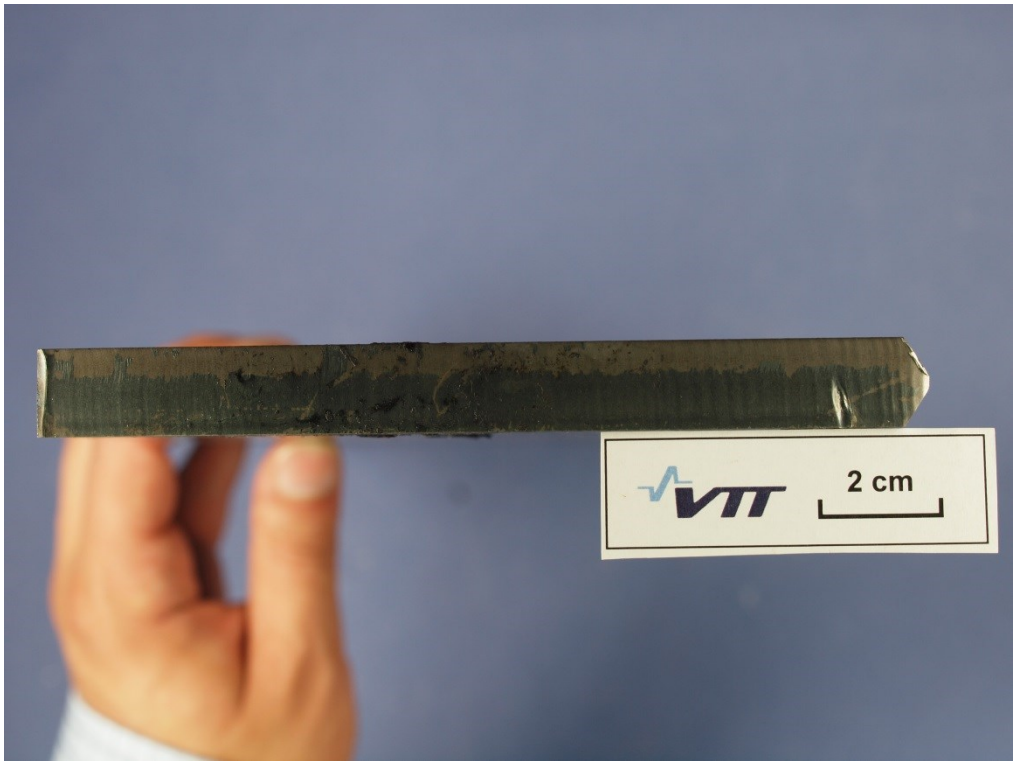

Figure 13 Front side of base material plate.

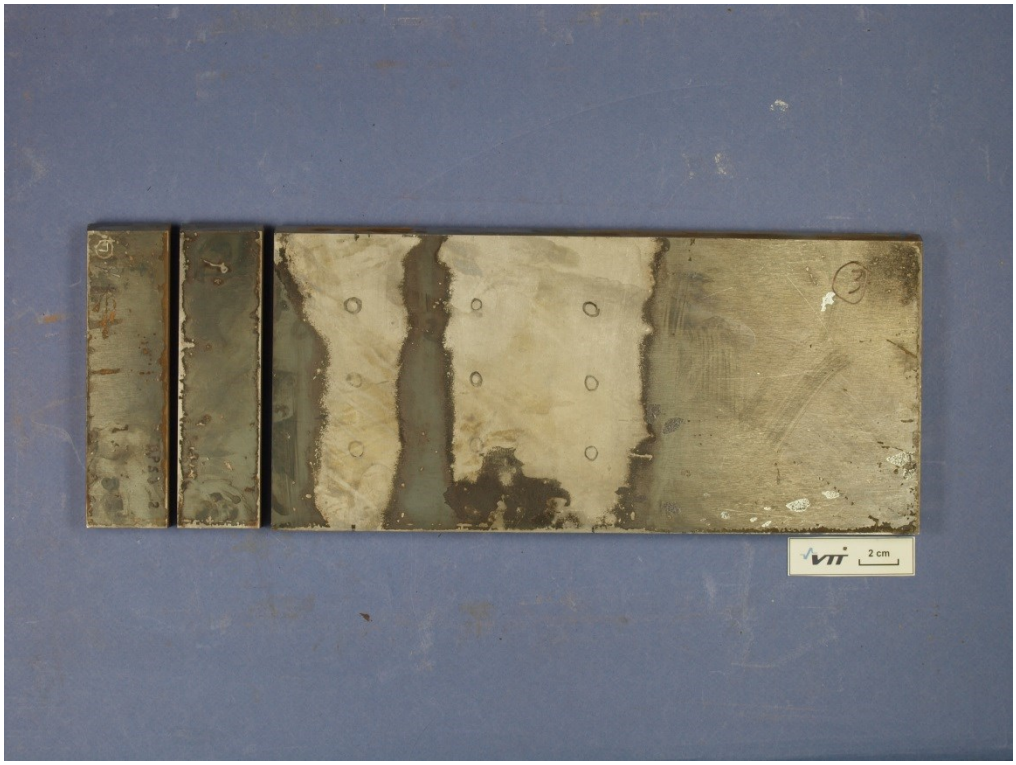

Figure 14 Front side of base material plate.

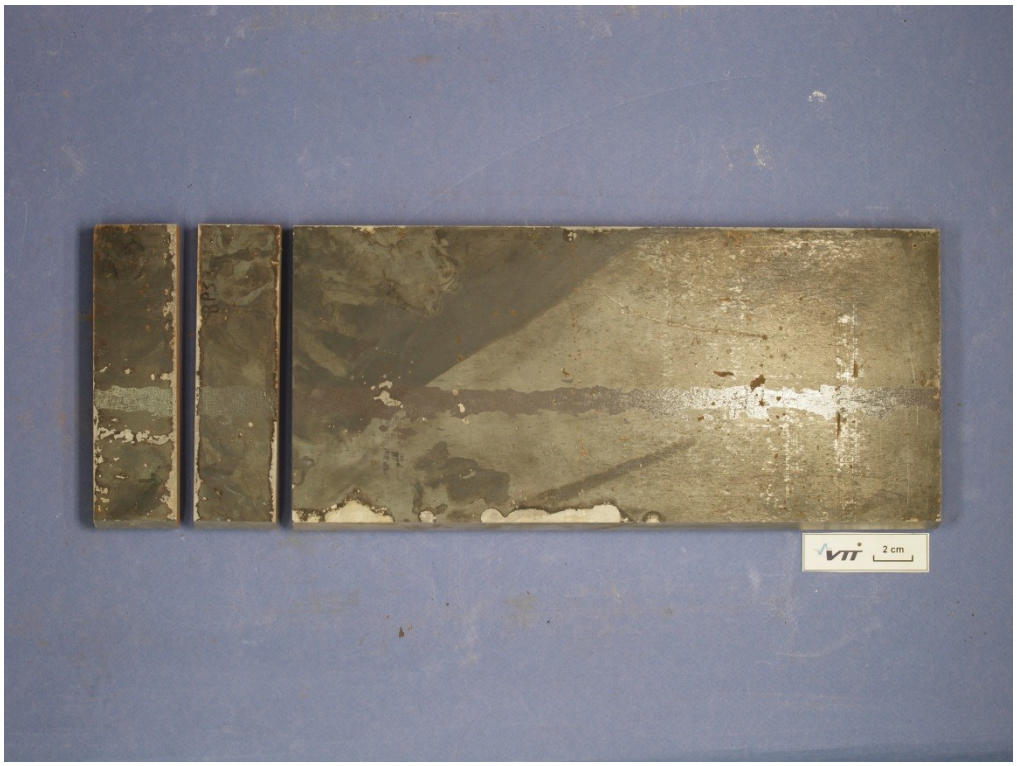

Figure 15 Bottom side of base material plate.

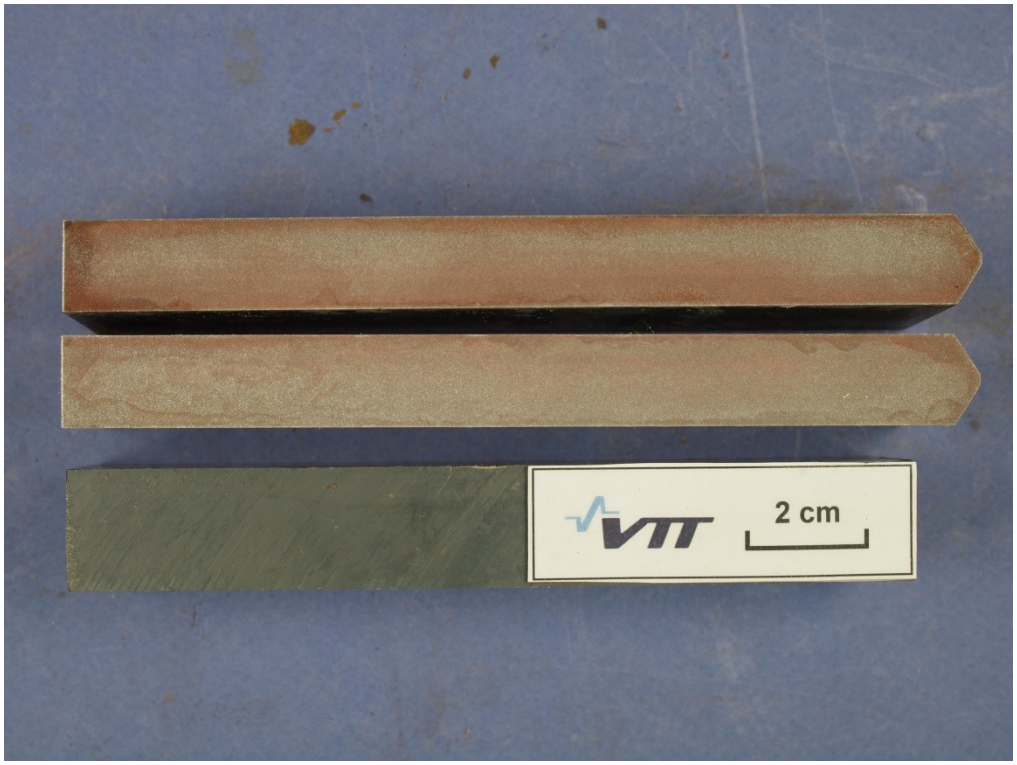

Figure 16 Cross-section of base material plate.

Sample 4 / MAG

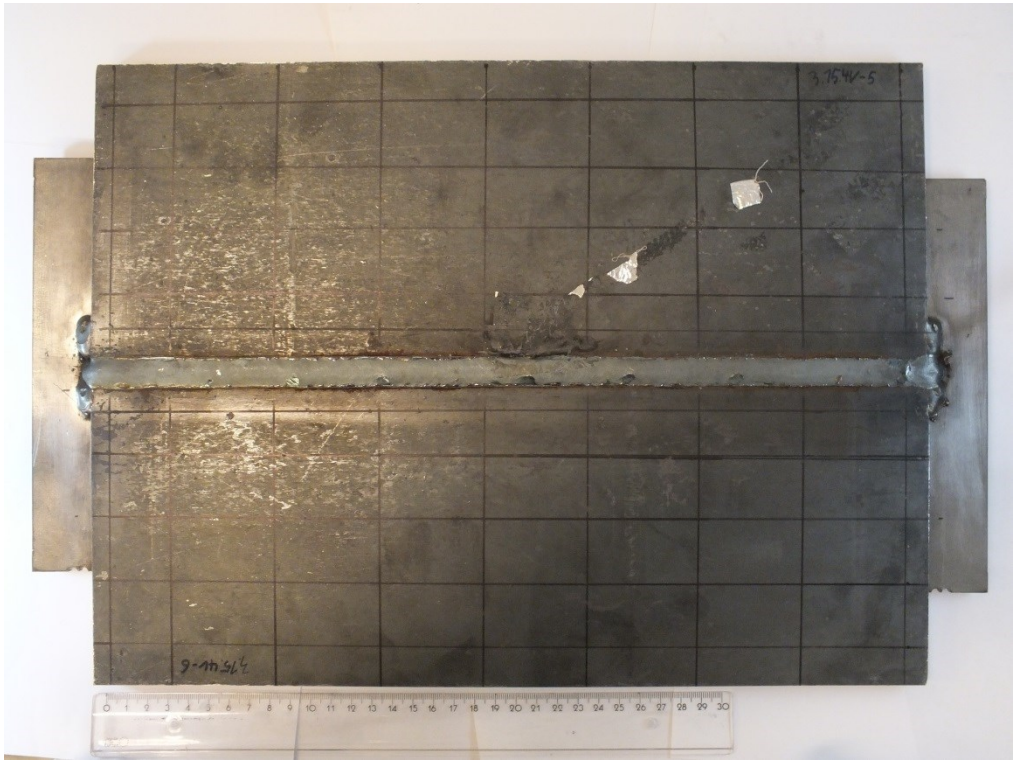

Figure 17 Front side of MAG 4.

Figure 18 Bottom side of MAG 4.

Sample 5 / LAHW

Appendix 4

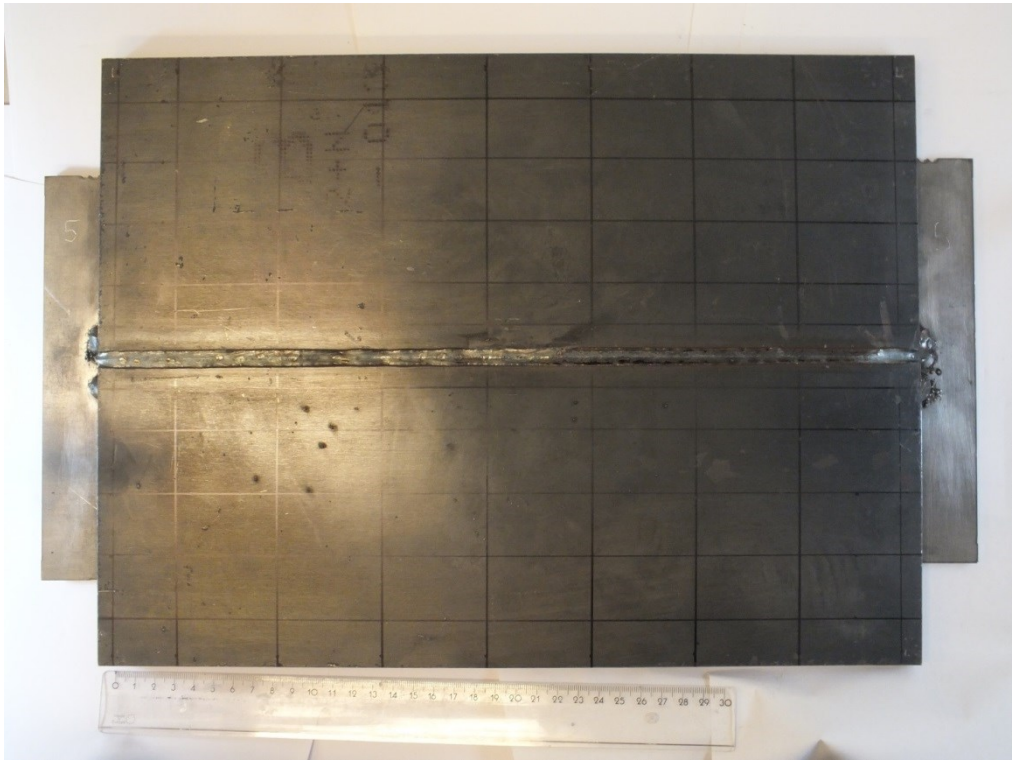

Figure 19 Front side of LAHW 5.

Figure 20 Bottom side of LAHW 5.

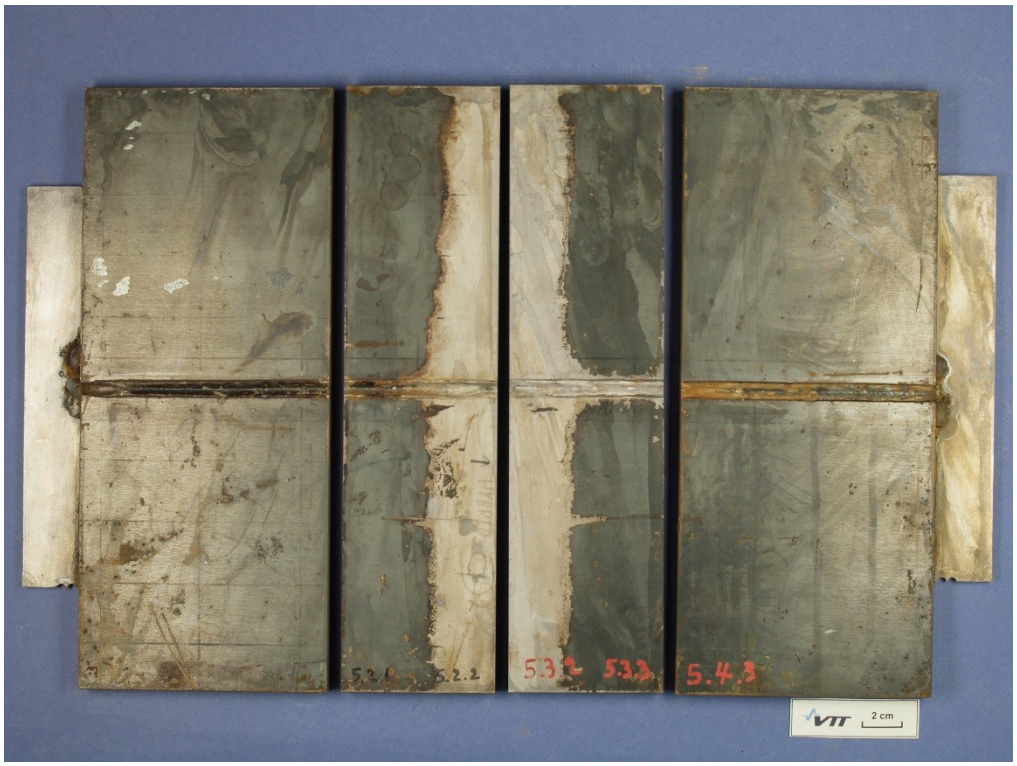

Figure 21 Front side of LAHW 5.

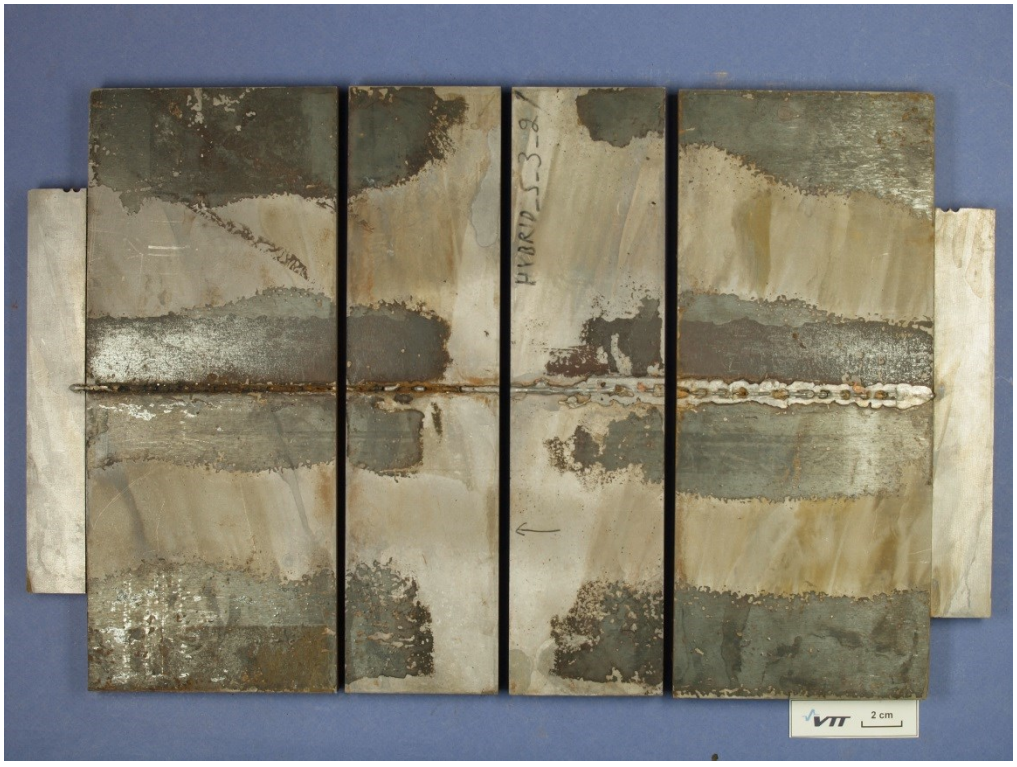

Figure 22 Bottom side of LAHW 5.

Appendix 4

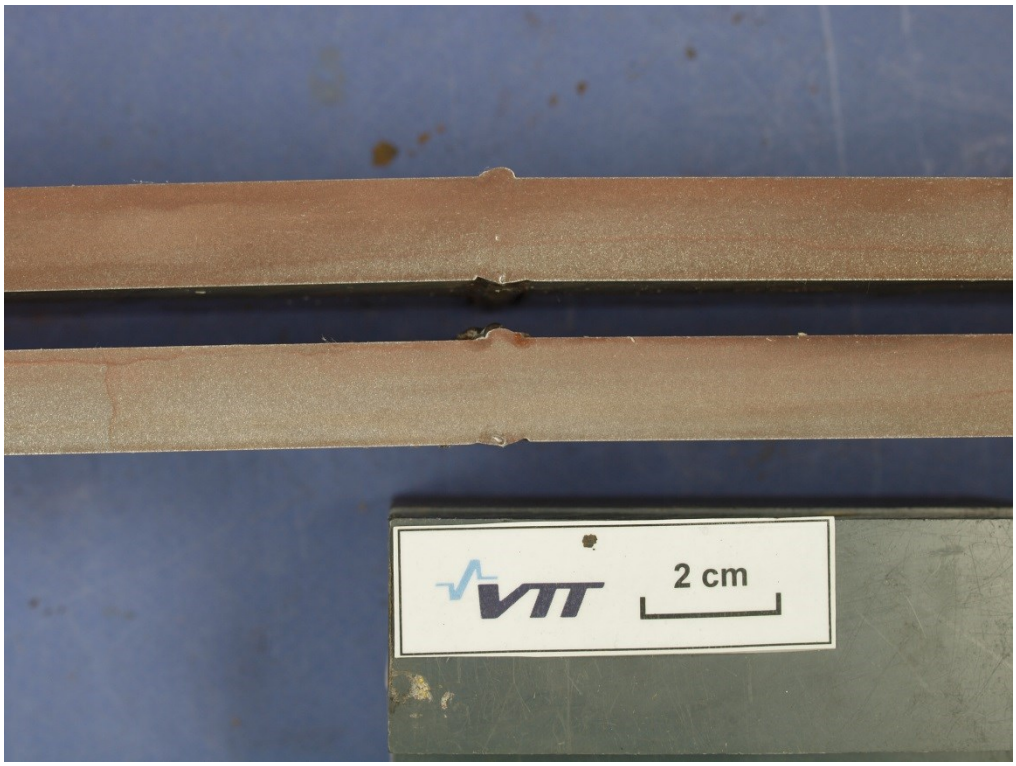

Figure 23 Cross-section in middle of LAHW 5.

Appendix 5 / Maximum dimensions of weld metal and HAZ

Table 1 Dimensions of HAZ and weld metal.

Welding process	Number of sample	Dimensions (mm)			
		Weld		HAZ	
		A	B	C	D
LAHW	3.15.2-9	10.1	5.9	11.2	5.9
LAHW	3.5.2-3	9.4	3.7	10.3	4
LASER	3.15.2-5	3.2	4.8	4.8	4.9
LASER	3.5.2-7	2.7	2.5	3.7	2.7
MAG	3.15.2-4	12.9	2.6	15.4	3.9
MAG	3.5.2-2	11.1	2.7	12.7	trough
TIG	3.15.2-6	9	3.3	12.5	5.2
TIG	3.15.2-7	8.1	2.5	10.8	3.8
TIG	3.15.2-8	7.2	1.4	9.5	2.7
TIG	3.5.2-4	7.6	1.7	9.6	3.7
TIG	3.5.2-8	10.6	3.2	19.3	trough
TIG	3.5.2-9	9.3	1.7	11.3	trough

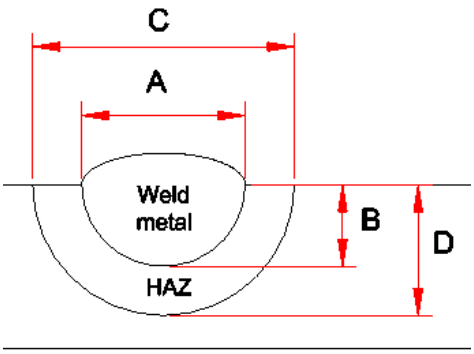

Figure 1 Dimensions of HAZ and weld metal.

- Macro photos of stereomicroscope were taken with 10x ocular, 0.8X objective lens and 0.4x extra lens.

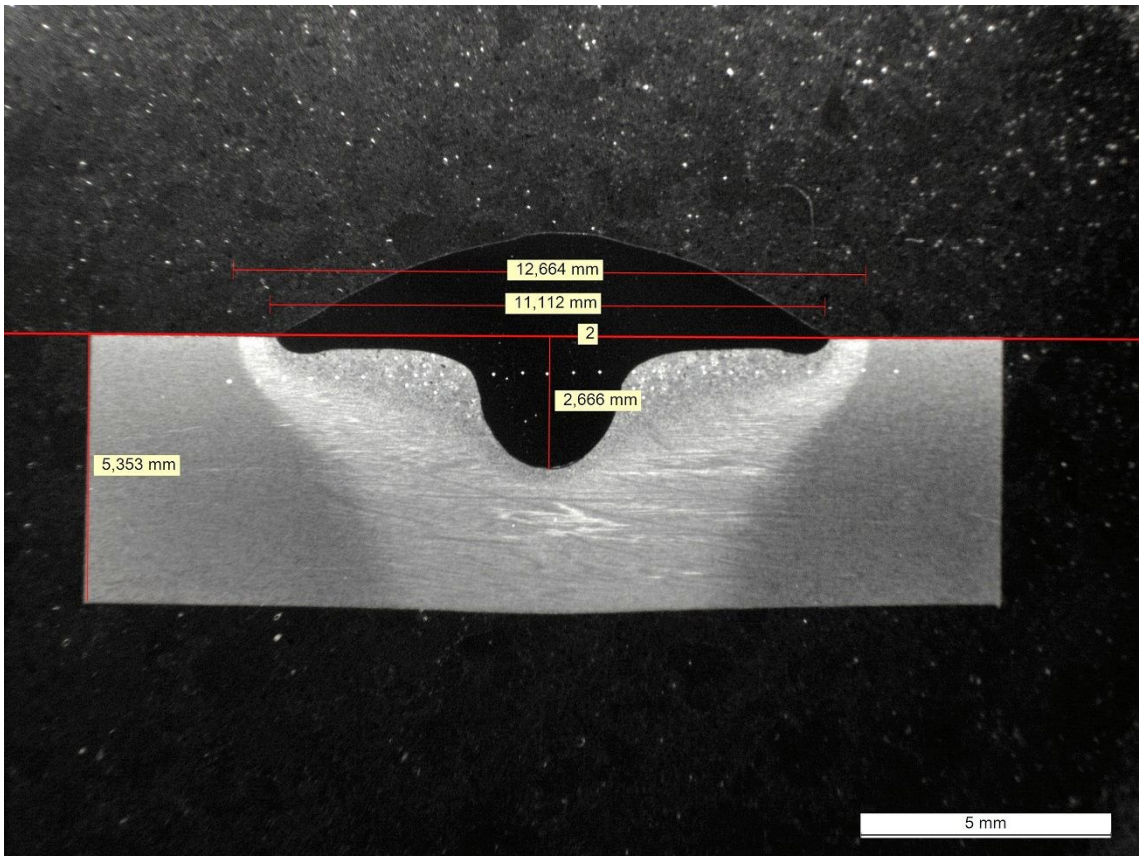

Figure 2: 3.5.2-2 MAG

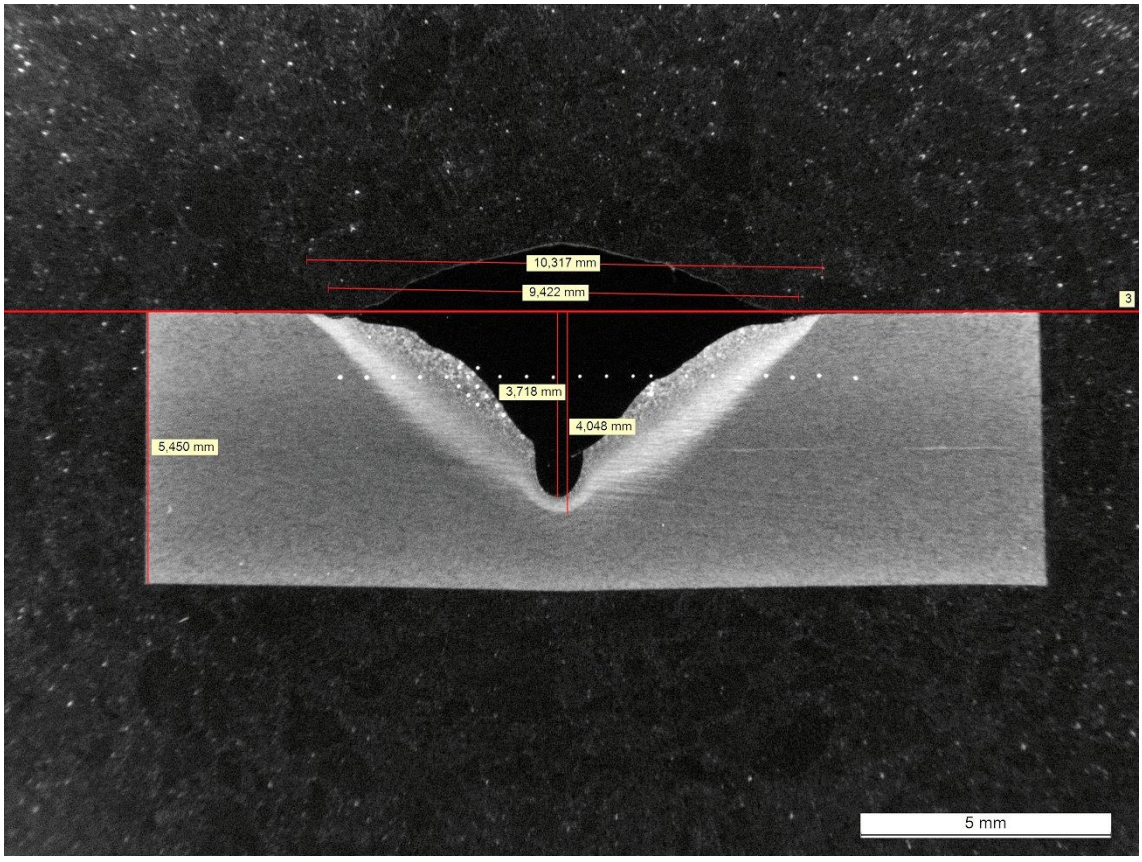

Figure 3: 3.5.2-3 LAHW

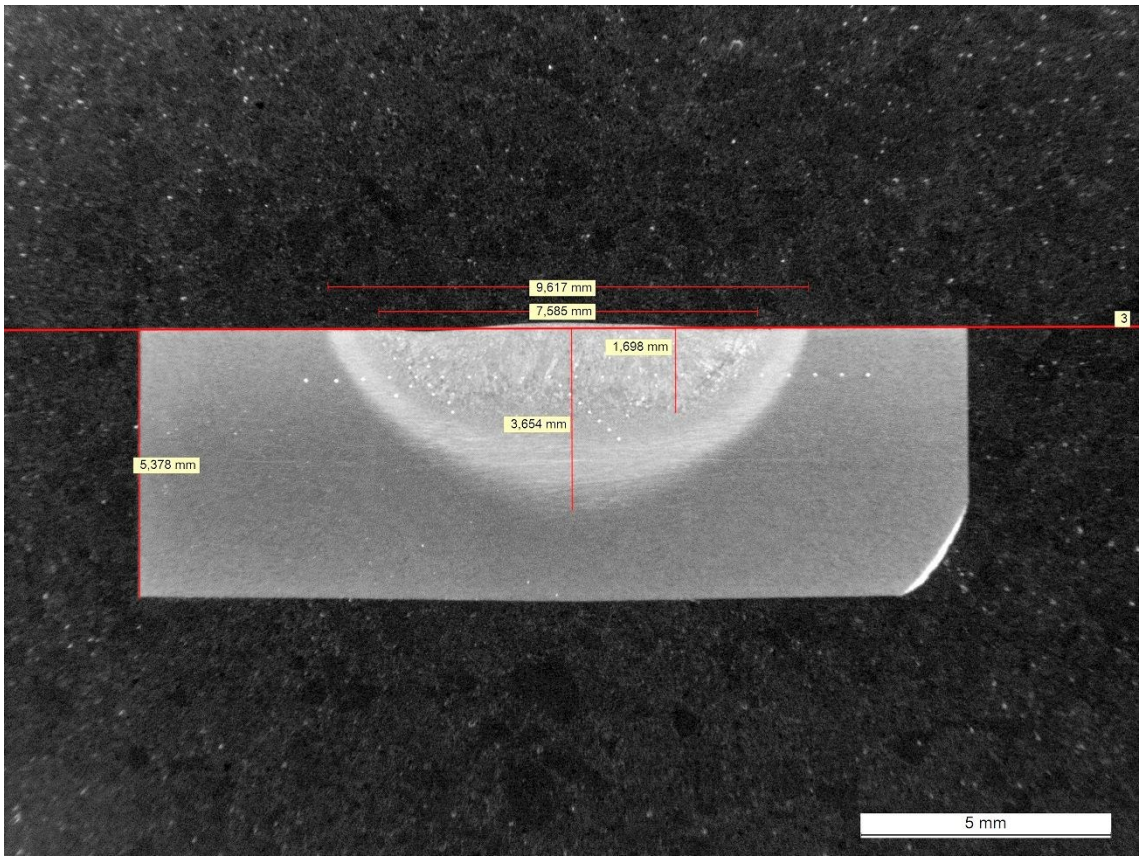

Figure 4: 3.5.2-4 LASER

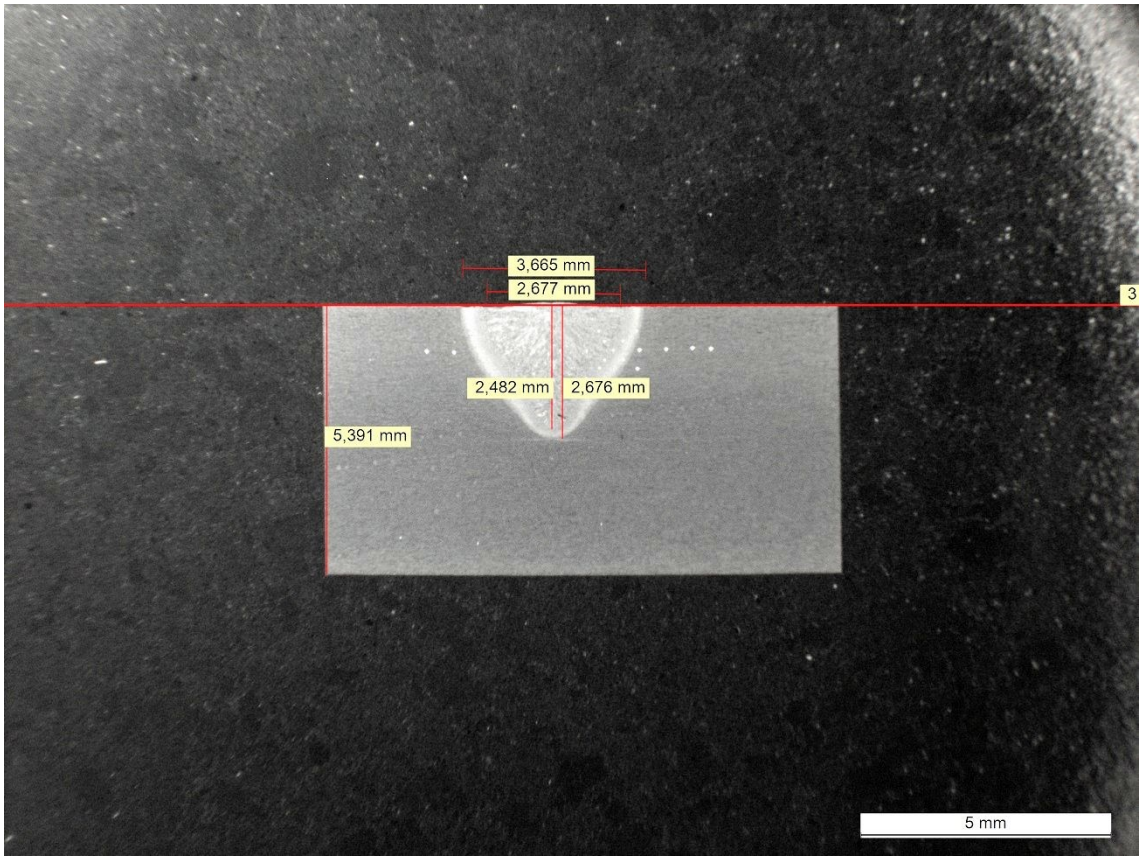

Figure 5: 3.5.2-7 LASER

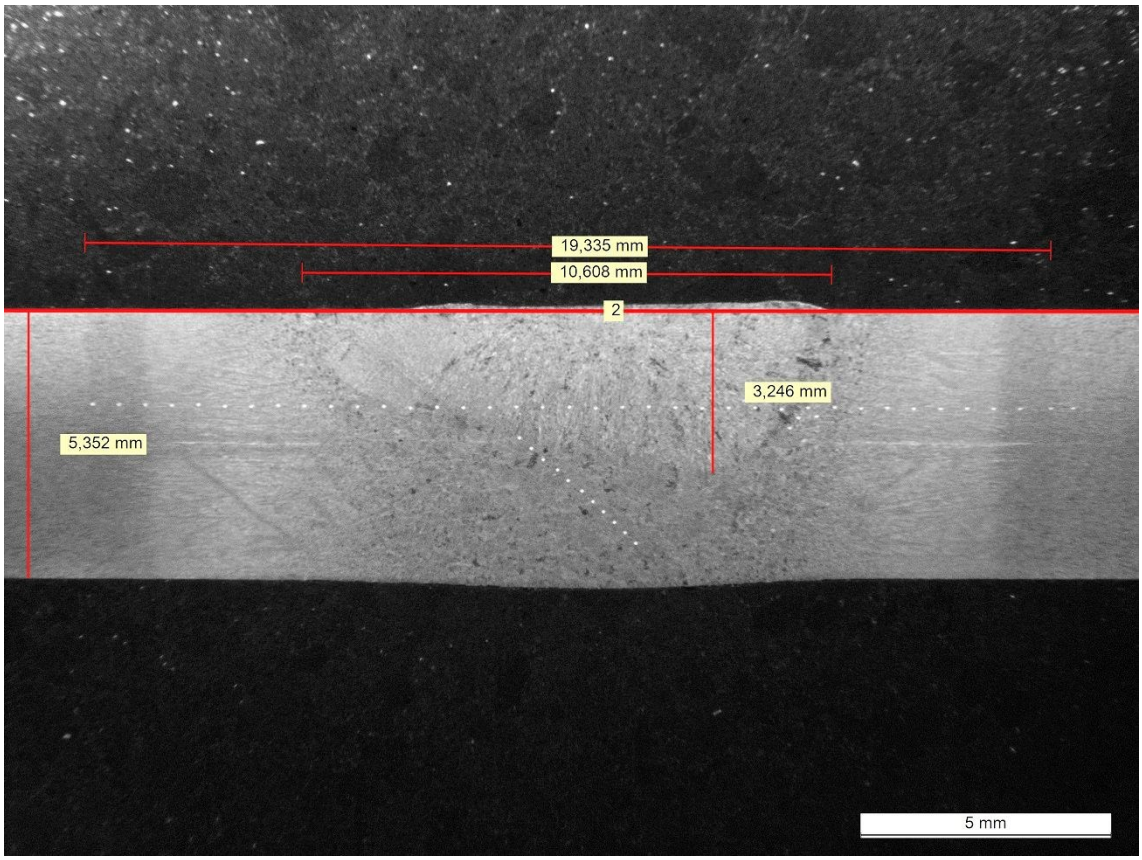

Figure 6: 3.5.2-8 TIG

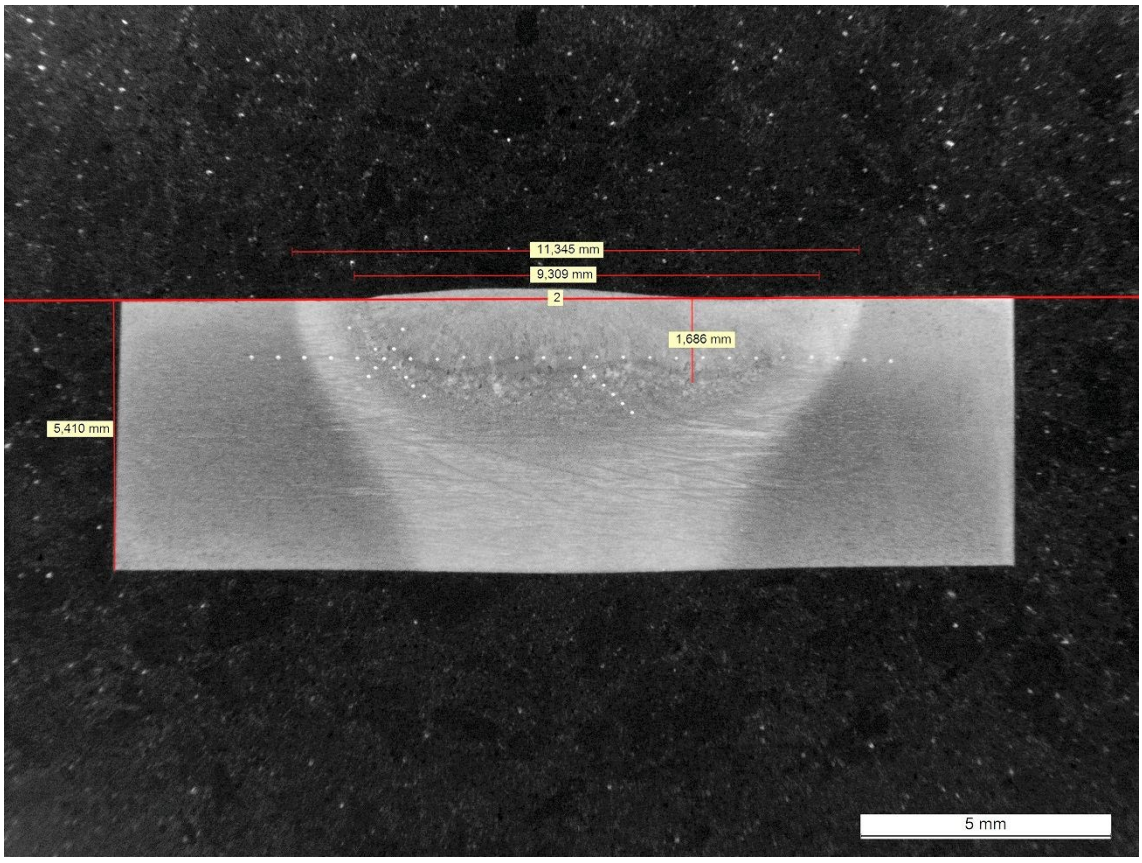

Figure 7: 3.5.2-9 TIG

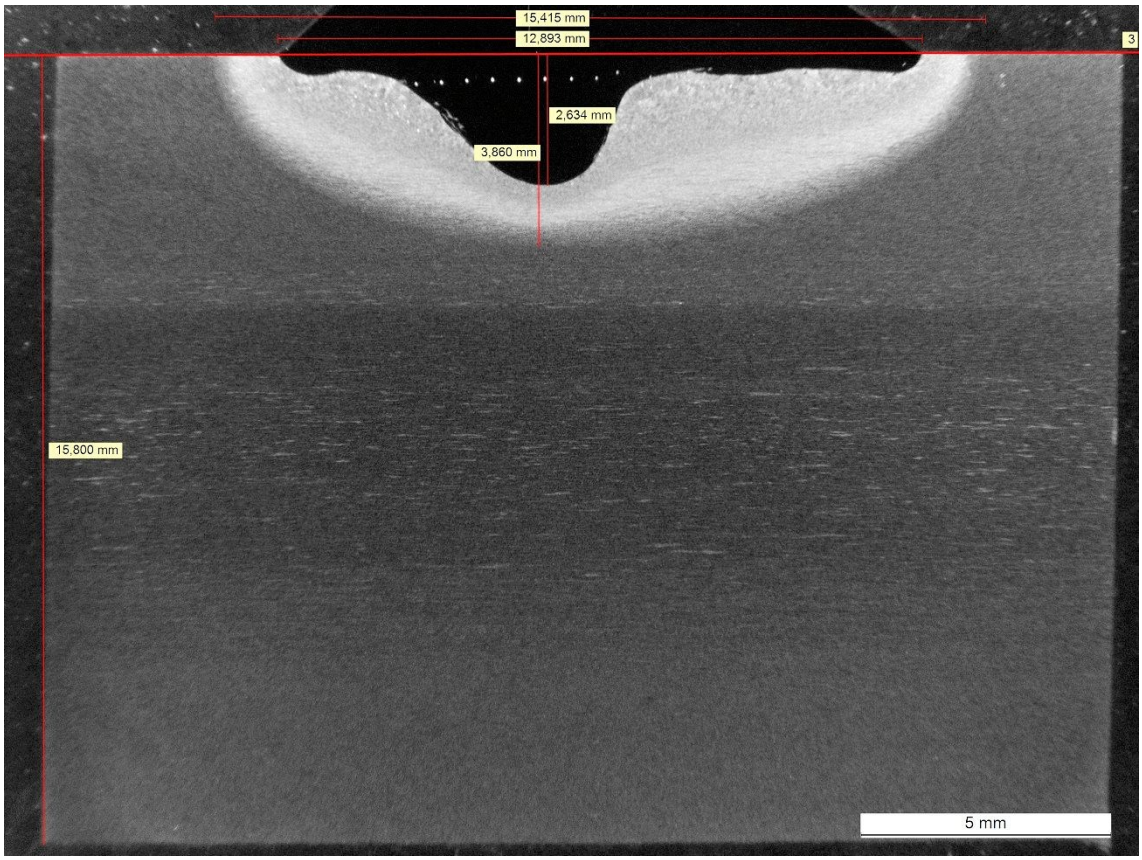

Figure 8: 3.15.2-4 MAG

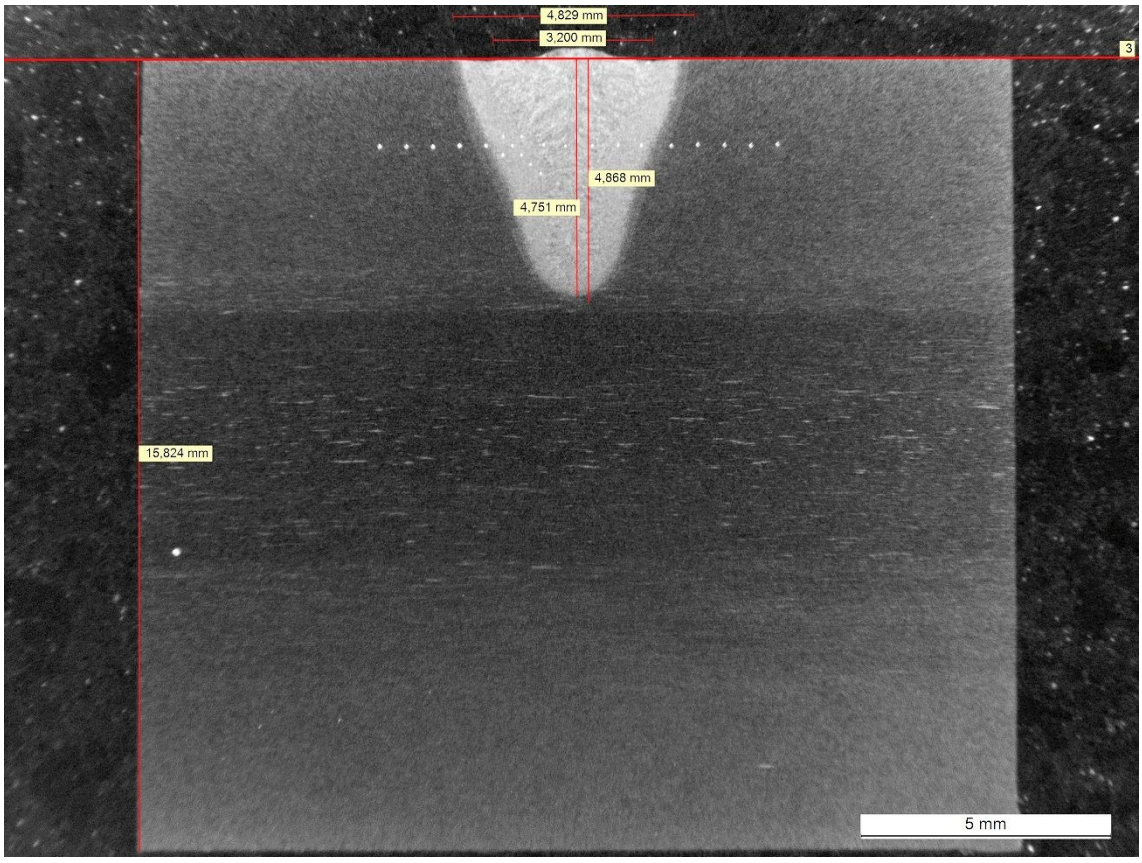

Figure 9: 3.15.2-5 LASER

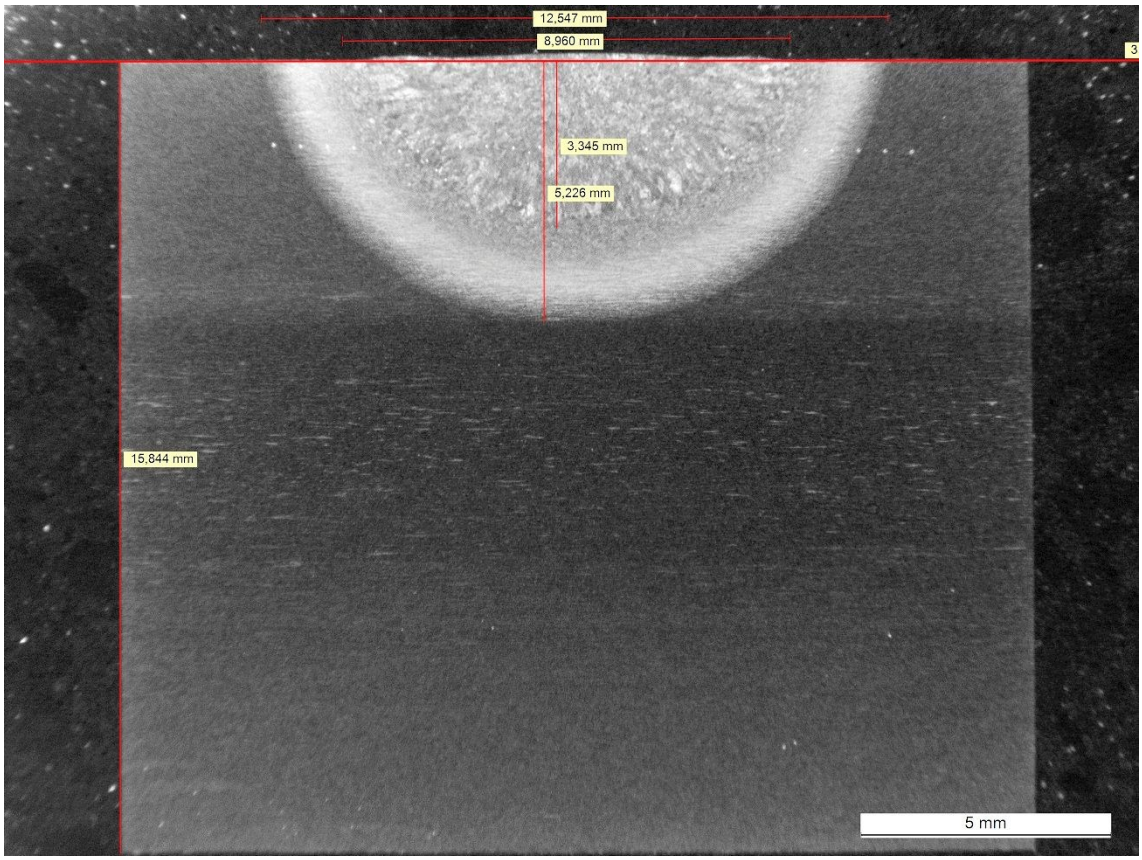

Figure 10: 3.15.2-6 TIG

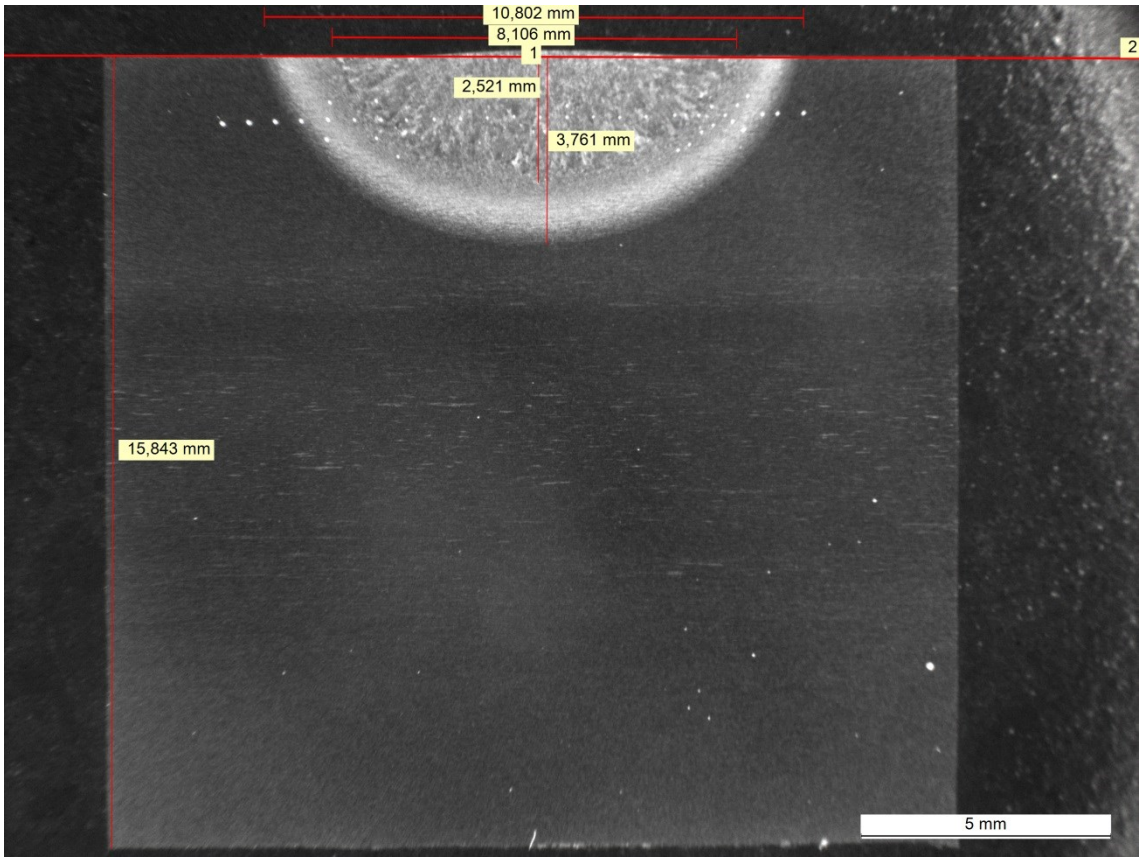

Figure 11: 3.15.2-7 TIG

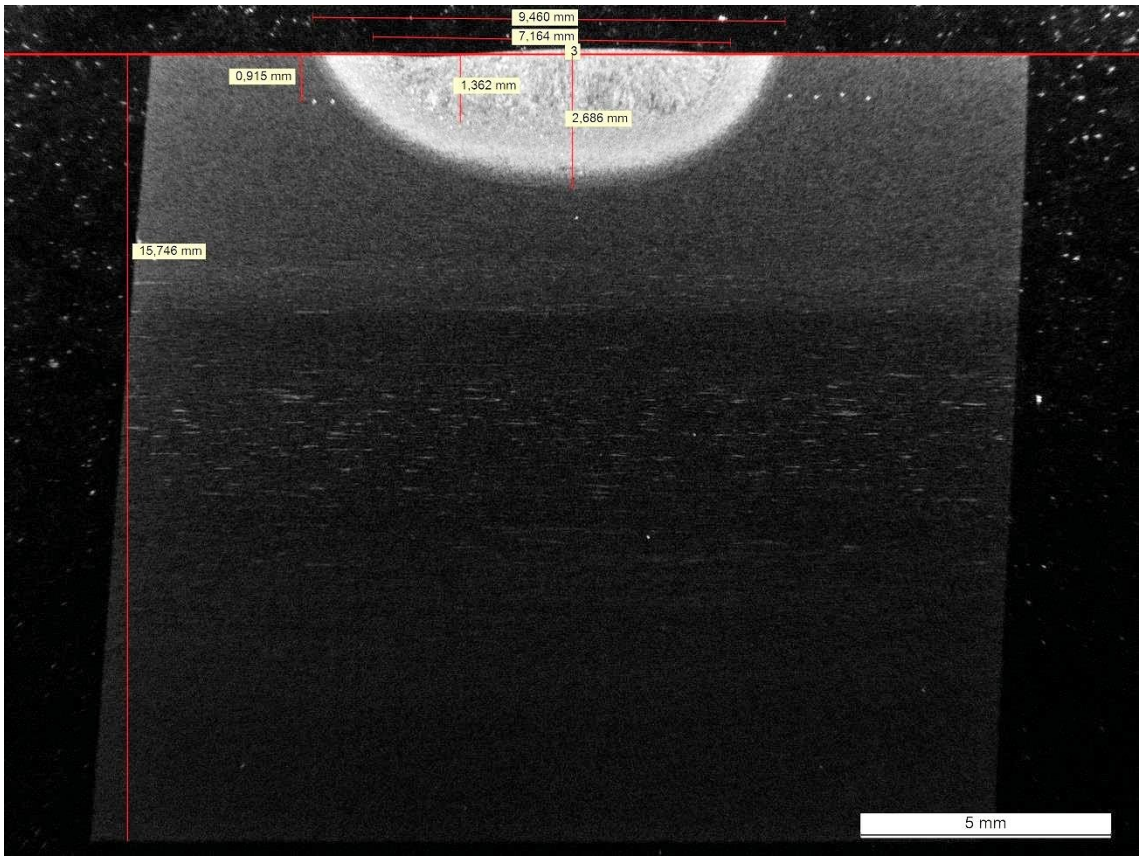

Figure 12: 3.15.2-8 TIG

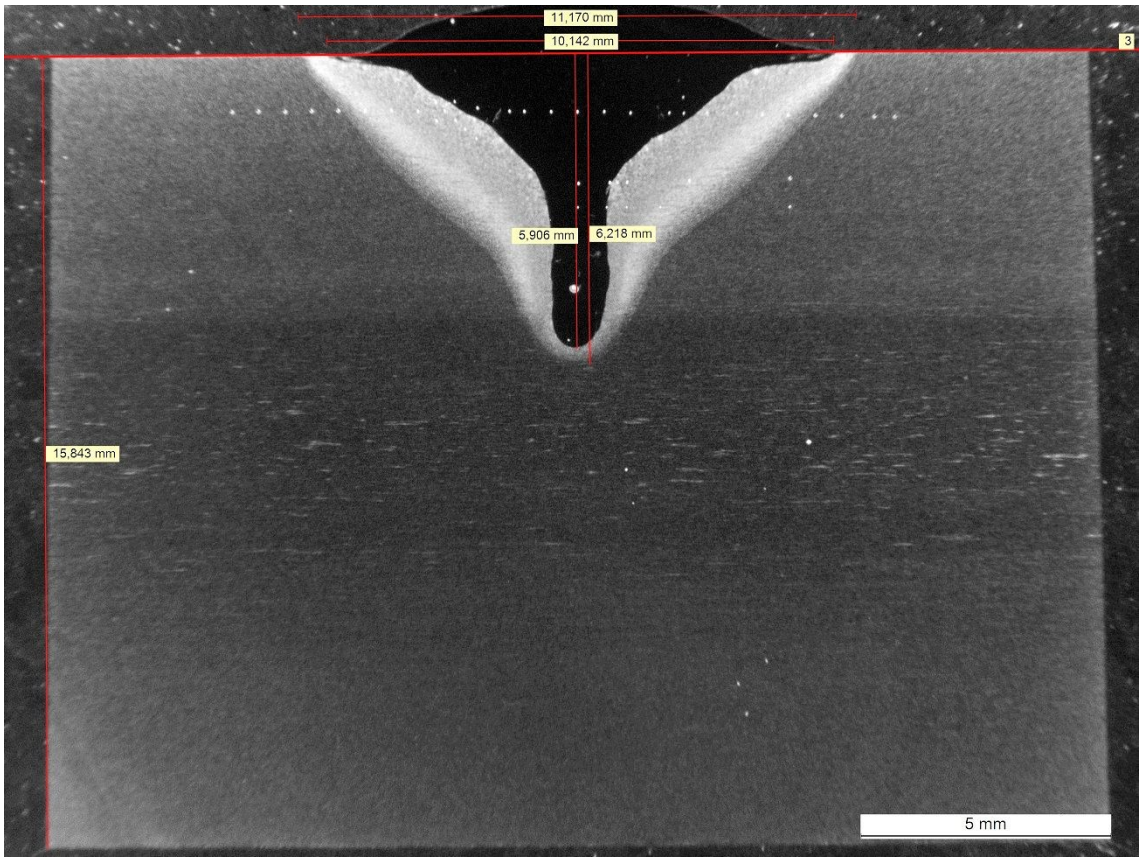

Figure 13: 3.15.2-9 LAHW

Appendix 6 / Hardness distributions of bead-on-plate welds

Contents

Appendix 6

LAHW 3.5.2-3

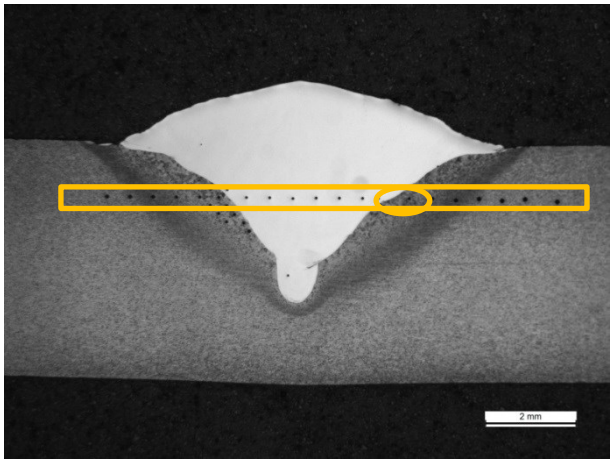

Figure 1 This micrograph of 3.5.2-3 was taken with Leica MEF 4M light microscope with 10X ocular and 1X objective. Distance between selected horizontal indentations of HV1 is 500 µm. Horizontal indentations were measured with automatic microhardness tester Zwick Roell BZ2.5 TS1P

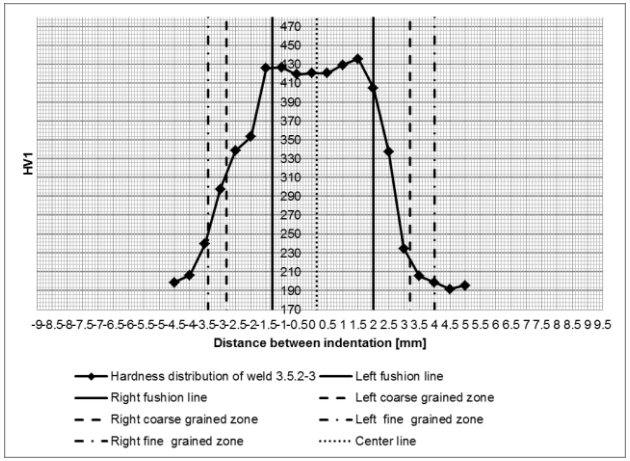

Figure 3 Measured distribution of HV1 hardness with distance of 500 µm. Measured hardnesses and distance between indentations are shown in Table 1.

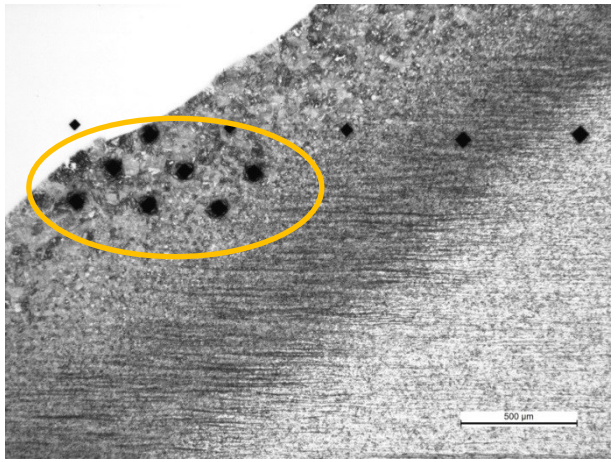

Figure 2 This micrograph of 3.5.2-3 was taken with Leica MEF 4M light microscope with 10X ocular and 5X objective. Maximum peak of hardness distribution was clarified with the help of additional HV1 measurements by HV1 microhardness tester Buehler 1600-6400.

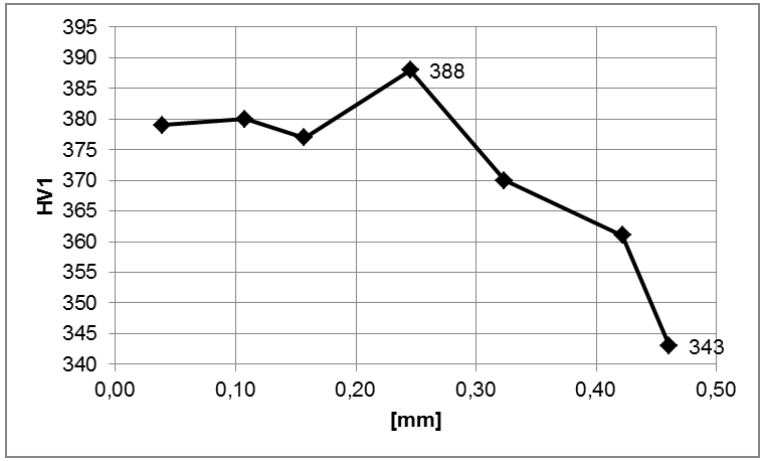

Figure 4 Additional hardness values were measured from coarse-grained zone from fusion line. Measured distribution of HV1 hardness is shown. Measured hardnesses and their distances from fusion line are shown in Table 2.

Appendix 6

Table 1 Measured HV1 hardnesses and distance between indentations.

Hardness distribution of weld 3.5.2-3		
Number	Distance [mm]	HV1
1	-4.5	199
2	-4.0	207
3	-3.5	240
4	-3.0	298
5	-2.5	339
6	-2.0	354
7	-1.5	426
8	-1.0	427
9	-0.5	420
10	0	421
11	0.5	421
12	1.0	430
13	1.5	436
14	2.0	405
15	2.5	338
16	3.0	235
17	3.5	206
18	4.0	199
19	4.5	192
20	5.0	196
	max	436

Table 2 Additional measured HV1 hardnesses and distance between indentations.

Hardness distribution of weld 3.5.2-3 from fusion line.		
Number	Distance [mm]	HV1
1	0.04	379
2	0.11	380
3	0.16	377
4	0.25	388
5	0.32	370
7	0.42	361
9	0.46	343
	max	377

Appendix 6

LAHW3.15.2-9

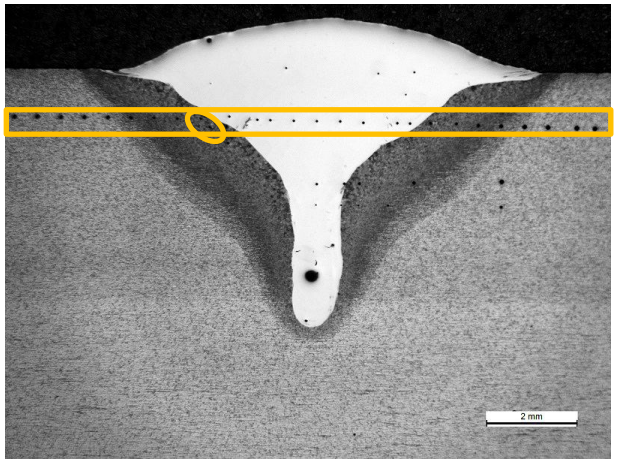

Figure 5 This micrograph of 3.15.2-9 was taken with Leica MEF 4M light microscope with 10X ocular and 1X objective. Distance between selected horizontal indentations of HV1 is 500 µm. Horizontal indentations were measured with automatic microhardness tester Zwick Roell BZ2.5 TS1P

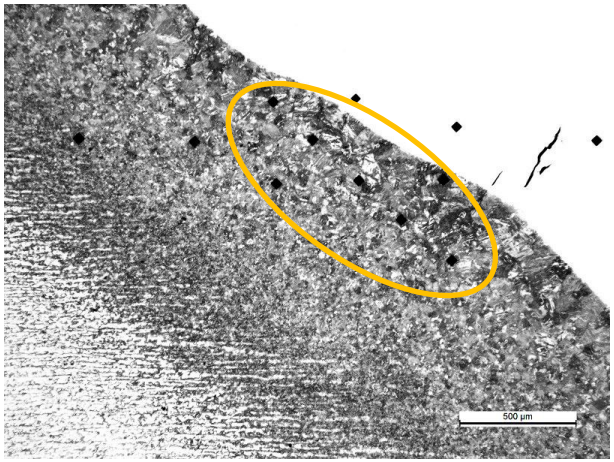

Figure 6 This micrograph of 3.15.2-9 was taken with Leica MEF 4M light microscope with 10X ocular and 5X objective. Maximum peak of hardness distribution was clarified with the help of additional HV1 measurements with HV1 microhardness tester Buehler 1600-6400.

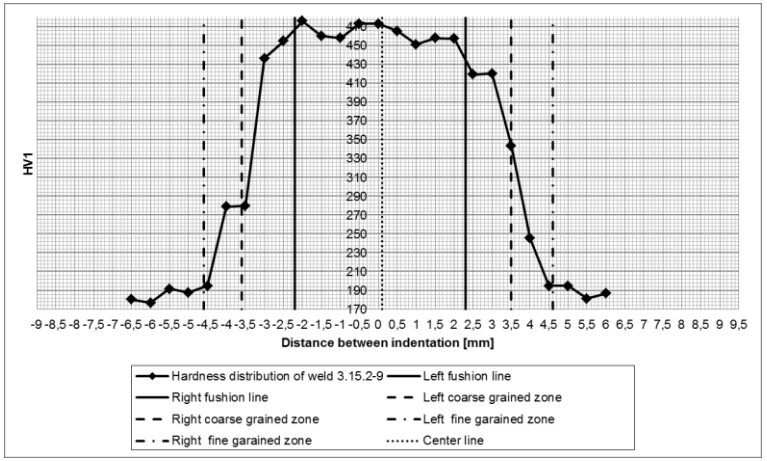

Figure 7 Measured distribution of HV1 hardness with distance of 500 µm. Measured hardnesses and distance between indentations are shown in Table 3.

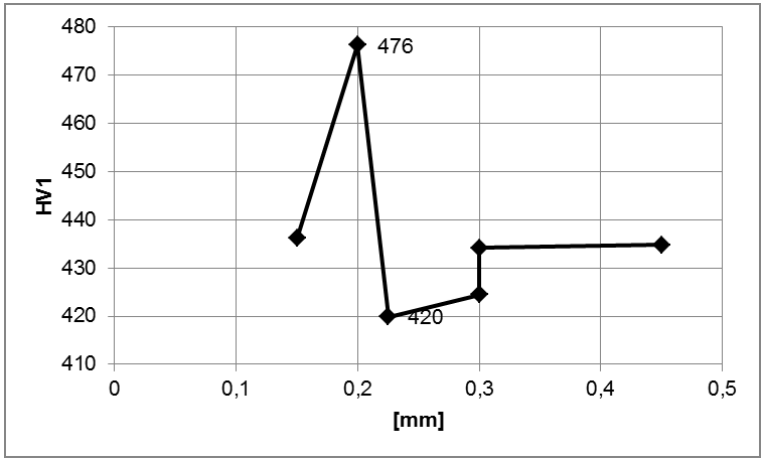

Figure 8 Additional hardness values were measured from coarse-grained zone from fusion line. Measured distribution of HV1 hardness is shown. Measured hardnesses and their distances from fusion line are shown in Table 4.

Appendix 6

Table 3 Measured HV1 hardnesses and distance between indentations.

Hardness distribution of weld 3.15.2-9					
Number	**Distance [mm]**	**HV1**	**Number**	**Distance [mm]**	**HV1**
1	-6.5	180	**15**	0.5	466
2	-6.0	177	**16**	1.0	451
3	-5.5	192	**17**	1.5	458
4	-5.0	188	**18**	2.0	458
5	-4.5	195	**19**	2.5	420
6	-4.0	279	**20**	3.0	420
7	-3.5	280	**21**	3.5	344
8	-3.0	436	**22**	4.0	246
9	-2.5	455	**23**	4.5	195
10	-2.0	476	**24**	5.0	195
11	-1.5	461	**25**	5.5	181
12	-1.0	458	**26**	6.0	187
13	-0.5	473		**max**	**476**
14	0	473			

Table 4 Additional measured HV1 hardnesses and distance between indentations.

Hardness distribution of weld 3.15.2-9 from fusion line.		
Number	**Distance [mm]**	**HV1**
1	0.15	436
2	0.20	476
3	0.23	420
4	0.30	424
5	0.30	434
6	0.45	435
	max	**476**

Appendix 6

LASER 3.5.2-7

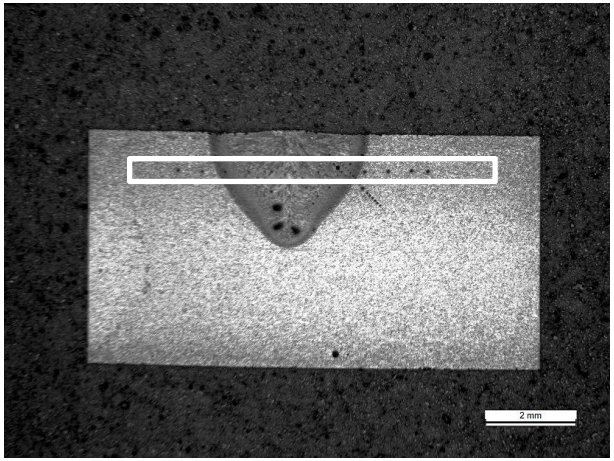

Figure 9 This micrograph of 3.5.2-7 was taken with Leica MEF 4M light microscope with 10X ocular and 1X objective. Distance between selected horizontal indentations of HV1 is 500 µm. Horizontal indentations were measured with automatic microhardness tester Zwick Roell BZ2.5 TS1P. Maximum peak of hardness distribution was measured with the help of additional measures. These measures were measured with HV01 microhardness tester Buehler 1600-6400.

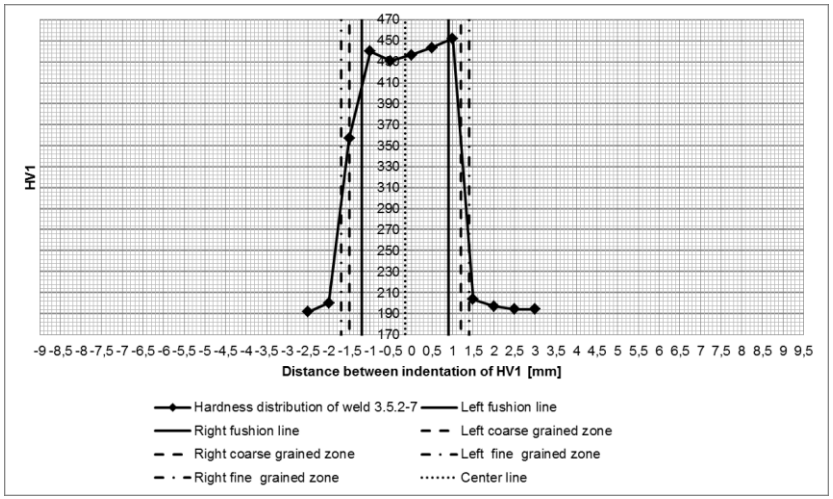

Figure 11 Measured distribution of HV1 hardness with distance of 500 µm.

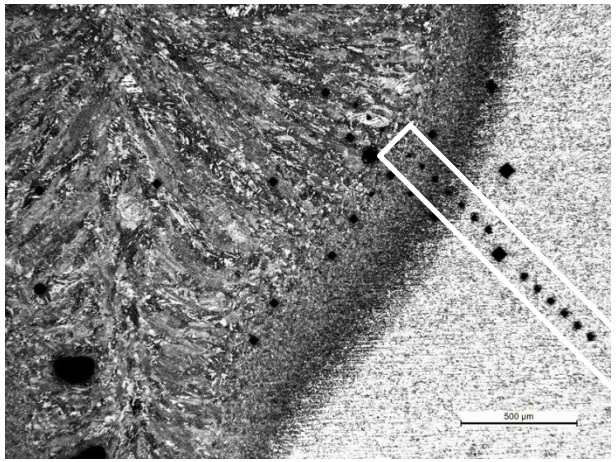

Figure 10 This micrograph of 3.5.2-7 was taken with Leica MEF 4M light microscope with 10X ocular and 5X objective. Maximum peak of hardness distribution was clarified with the help of HV01 because size of Laser weld was too small for minimum gab of HV1. The distance between centres of adjacent indentations must be at least three times the diagonal length of the indentation with steels according SFS-EN ISO 6507-2. Selected hardness distribution of HV01 was measured with microhardness tester Struers DuraScan from fusion line.

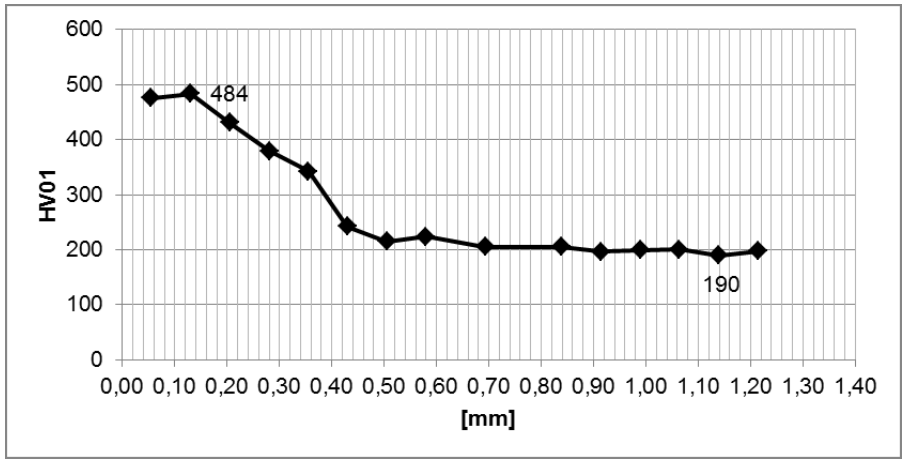

Figure 12 Additional hardness values were measured from fusion line. Measured distribution of HV01 hardness is shown. Measured hardnesses and their distances

Appendix 6

Measured hardnesses and distance between indentations are shown in Table 5. from fusion line are shown in Table 6.

Table 5 Measured HV1 hardnesses and distance between indentations.

Hardness distribution of weld 3.5.2-7 over weld.		
Number	Distance [mm]	HV1
1	-2.5	192
2	-2.0	200
3	-1.5	357
4	-1.0	440
5	-0.5	431
6	0	436
7	0.5	444
8	1.0	452
9	1.5	204
10	2.0	197
11	2.5	195
12	3.0	194
Maximum hardness		**452**

Table 6 Additional measured HV01 hardnesses and distance between indentations.

Hardness distribution of weld 3.5.2-7 from fusion line.					
Number	Distance [mm]	HV01	Number	Distance [mm]	HV01
1	0.06	476	9	0.69	205
2	0.13	484	10	0.84	205
3	0.21	431	11	0.91	196
4	0.28	379	12	0.99	199
5	0.36	342	13	1.06	200
6	0.43	242	14	1.14	190
7	0.51	215	15	1.21	197
8	0.58	224	**Maximum hardness**		**484**

Appendix 6

LASER 3.15.2-5

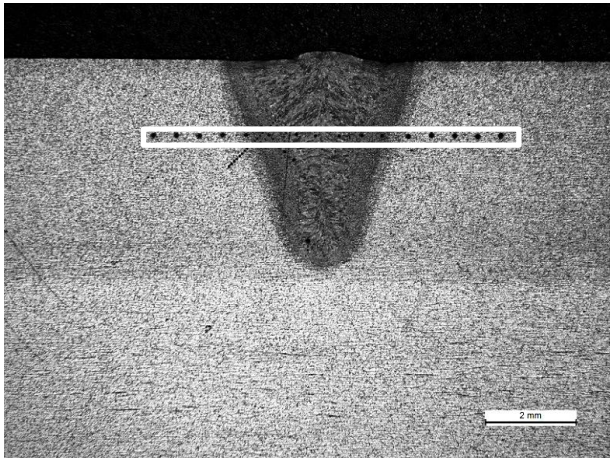

Figure 13 This micrograph of 3.15.2-5 was taken with Leica MEF 4M light microscope with 10X ocular and 1X objective. Distance between selected horizontal indentations of HV1 is 500 µm. Horizontal indentations were measured with automatic microhardness tester Zwick Roell BZ2.5 TS1P. Maximum peak of hardness distribution was measured with the help of additional measures. These measures were measured with HV01 microhardness tester Buehler 1600-6400.

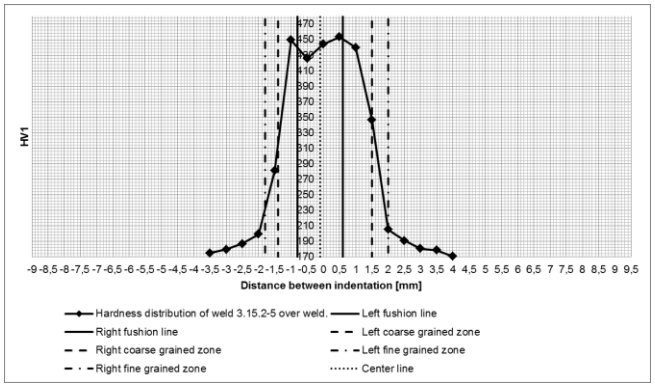

Figure 15 Measured distribution of HV1 hardness with distance of 500 µm. Measured hardnesses and distance between indentations are shown in Table 7.

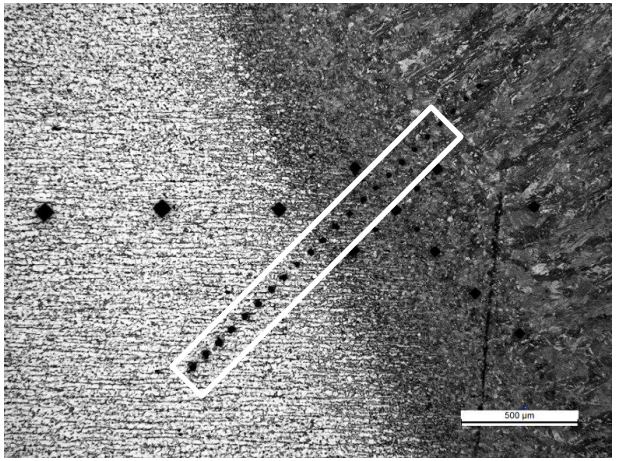

Figure 14 This micrograph of 3.15.2-5 was taken with Leica MEF 4M light microscope with 10X ocular and 5X objective. Maximum peak of hardness distribution was clarified with the help of HV01 because size of Laser weld was too small for minimum gab of HV1. The distance between centres of adjacent indentations must be at least three times the diagonal length of the indentation with steels according SFS-EN ISO 6507-2. Selected hardness distribution of HV01 was measured with microhardness tester Struers DuraScan from fusion line.

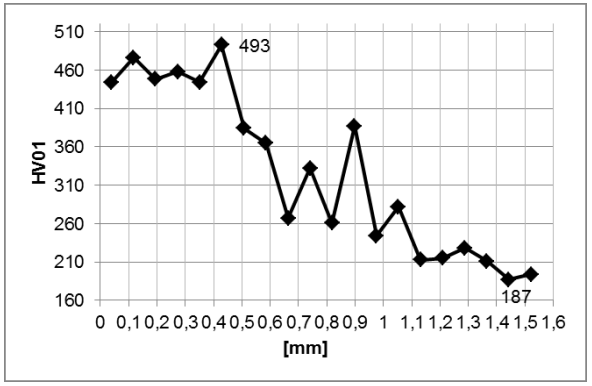

Figure 16 Additional hardness values were measured from fusion line. Measured distribution of HV01 hardness is shown. Measured hardnesses and their distances from fusion line are shown in Table 8.

Appendix 6

Table 7 Measured HV1 hardnesses and distance between indentations.

Hardness distribution of weld 3.15.2-5 over weld.					
Number	Distance [mm]	HV1	**Number**	Distance [mm]	HV1
1	-3.5	175	**9**	0.5	454
2	-3.0	180	**10**	1.0	440
3	-2.5	187	**11**	1.5	346
4	-2.0	199	**12**	2.0	205
5	-1.5	281	**13**	2.5	191
6	-1.0	450	**14**	3.0	181
7	-0.5	425	**15**	3.5	179
8	0	444	**16**	4.0	171
			Maximum hardness		**454**

Table 8 Additional measured HV01 hardnesses and distance between indentations.

Hardness distribution of weld 3.15.2-5 from fusion line.					
Number	[mm]	HV01	**Number**	[mm]	HV01
1	0.04	444	**11**	0.82	261
2	0.12	476	**12**	0.90	387
3	0.20	448	**13**	0.98	244
4	0.27	458	**14**	1.05	282
5	0.35	444	**15**	1.13	213
6	0.43	493	**16**	1.21	215
7	0.51	384	**17**	1.29	228
8	0.59	365	**18**	1.37	211
9	0.66	267	**19**	1.44	187
10	0.74	332	**20**	1.52	194
			Maximum hardness		**493**

Appendix 6

MAG 3.5.2-2

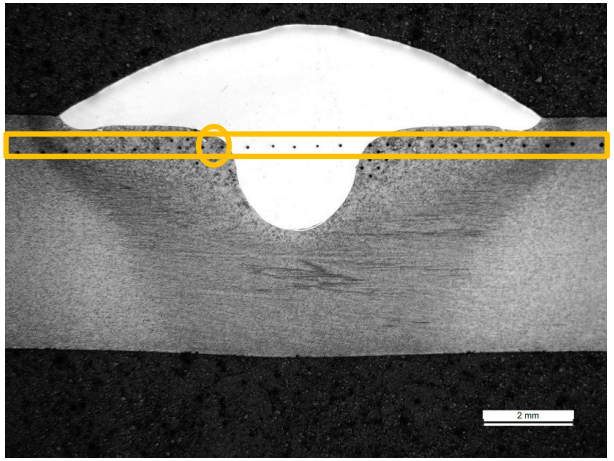

Figure 17 This micrograph of 3.5.2-2 was taken with Leica MEF 4M light microscope with 10X ocular and 1X objective. Distance between selected horizontal indentations of HV1 is 500 µm. Horizontal indentations were measured with automatic microhardness tester Zwick Roell BZ2.5 TS1P

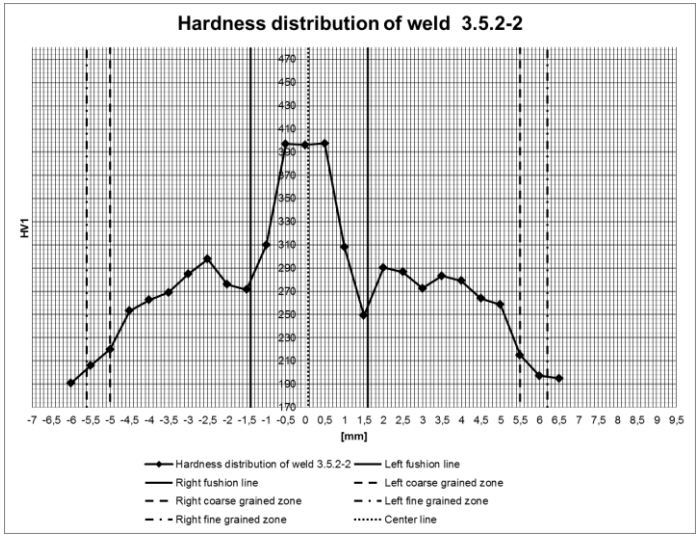

Figure 19 Measured distribution of HV1 hardness with distance of 500 µm. Measured hardnesses and distance between indentations are shown in Table 9.

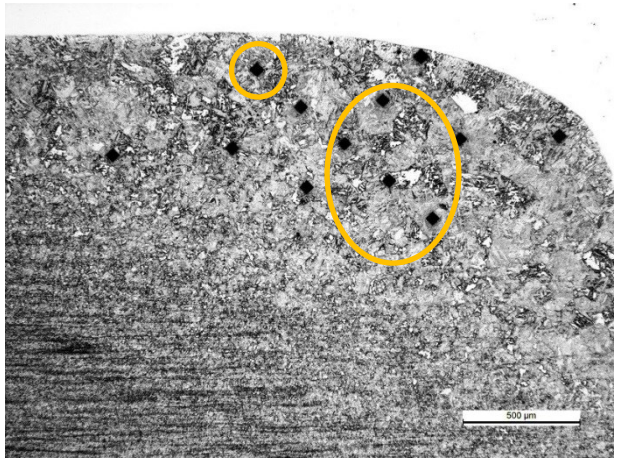

Figure 18 This micrograph of 3.5.2-2 was taken with Leica MEF 4M light microscope with 10X ocular and 5X objective. Maximum peak of hardness distribution was clarified with the help of additional HV1 measurements with HV1 microhardness tester Buehler 1600-6400.

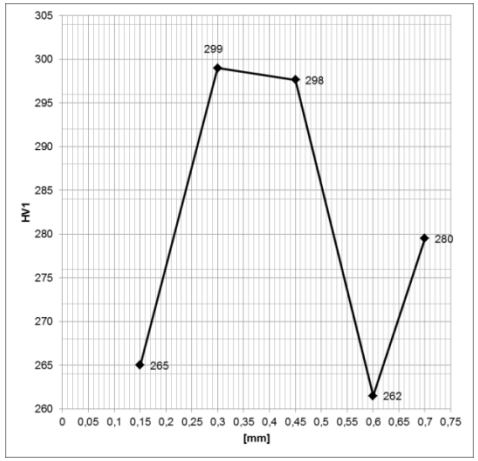

Figure 20 Additional hardness values were measured from coarse-grained zone from fusion line. Measured distribution of HV1 hardness is shown. Measured hardnesses and their distances from fusion line are shown in Table 10.

Table 9 Measured HV1 hardnesses and distance between indentations.

Hardness distribution of weld 3.5.2-2					
Number	distance from a middle of weld [mm]	HV1	Number	distance from a middle of weld [mm]	HV1
1	-6	191	14	0.5	397
2	-5.5	206	15	1.0	308
3	-5.0	220	16	1.5	249
4	-4.5	253	17	2.0	290
5	-4.0	262	18	2.5	287
6	-3.5	269	19	3.0	272
7	-3.0	285	20	3.5	283
8	-2.5	298	21	4.0	279
9	-2.0	276	22	4.5	264
10	-1.5	271	23	5.0	258
11	-1.0	310	24	5.5	215
12	-0.5	397	25	6.0	197
13	0	396	26	6.5	195
			Maximum hardness		**397**

Table 10 Additional measured HV01 hardnesses and distance between indentations.

Hardness distribution of weld 3.5.2-2 from fusion line.		
Number	distance from a middle of weld [mm]	HV1
1	0.15	265
2	0.30	299
3	0.45	298
4	0.60	262
5	0.70	280
Maximum hardness		**299**

Appendix 6

MAG 3.15.2-4

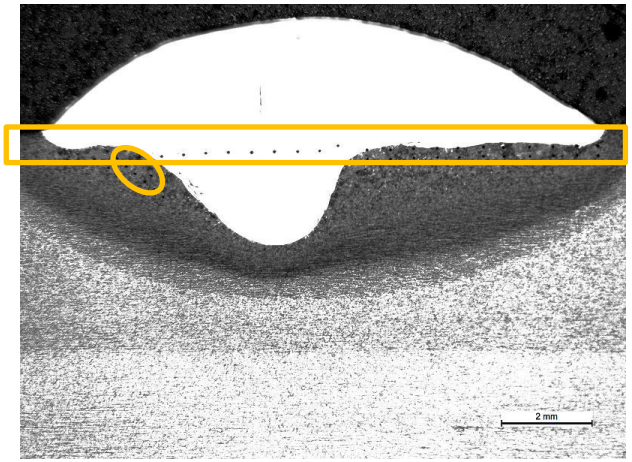

Figure 21 This micrograph of 3.15.2-4 was taken with Leica MEF 4M light microscope with 10X ocular and 1X objective. Distance between selected horizontal indentations of HV1 is 500 µm. Horizontal indentations were measured with automatic microhardness tester with Zwick Roell BZ2.5 TS1P.

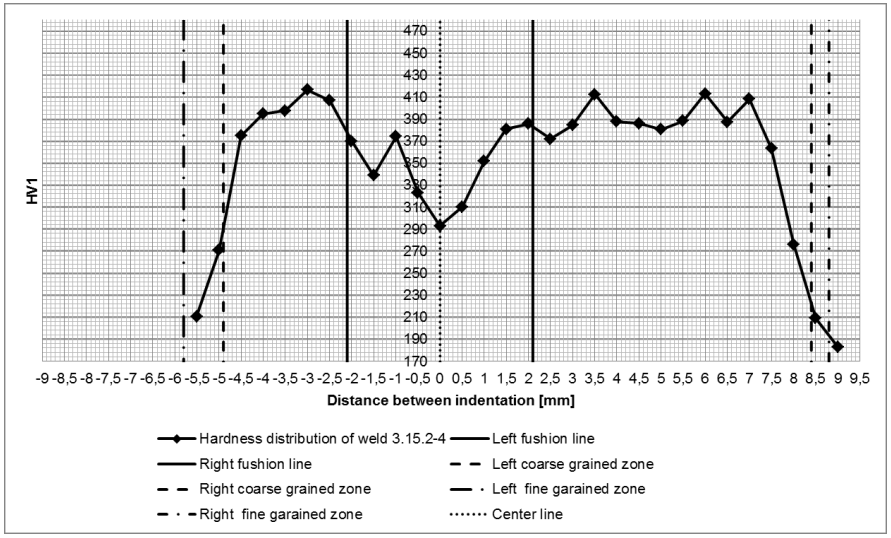

Figure 23 Measured distribution of HV1 hardness with distance of 500 µm. Measured hardnesses and distance between indentations are shown in Table 11.

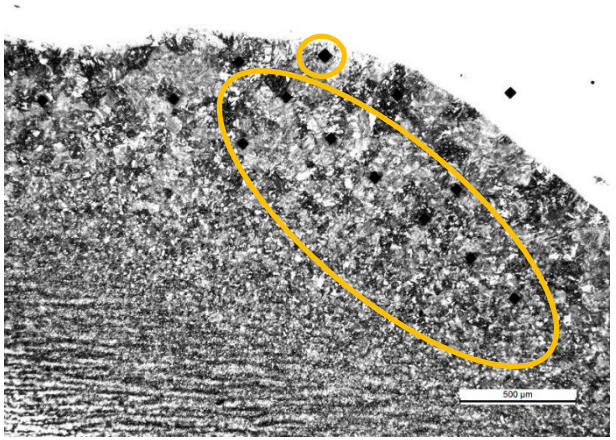

Figure 22 This micrograph of 3.15.2-4 was taken with Leica MEF 4M light microscope with 10X ocular and 5X objective. Maximum peak of hardness distribution was clarified with the help of additional HV1 measurements with HV1 microhardness tester Buehler 1600-6400.

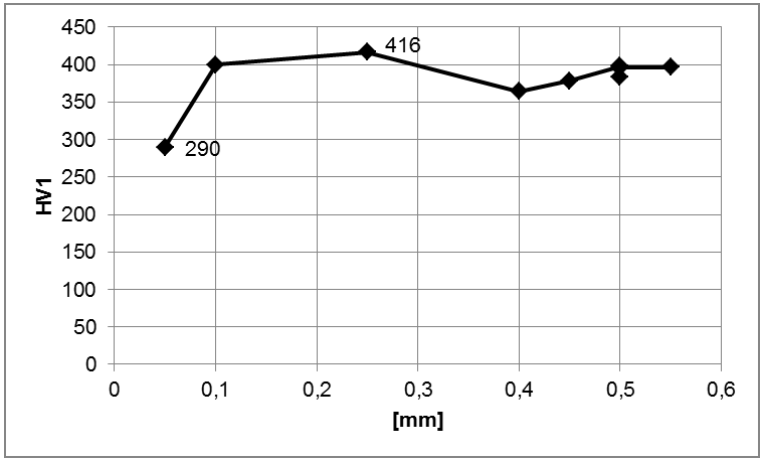

Figure 24 Additional hardness values were measured from coarse-grained zone from fusion line. Measured distribution of HV1 hardness is shown. Measured hardnesses and their distances from fusion line are shown in Table 12.

Table 11 Measured HV1 hardnesses and distance between indentations.

Hardness distribution of weld 3.15.2-4					
Number	Distance [mm]	HV1	Number	Distance [mm]	HV1
1	-5.5	211	16	2.0	386
2	-5.0	271	17	2.5	372
3	-4.5	375	18	3.0	384
4	-4.0	395	19	3.5	412
5	-3.5	398	20	4.0	388
6	-3.0	416	21	4.5	386
7	-2.5	407	22	5.0	381
8	-2.0	370	23	5.5	388
9	-1.5	339	24	6.0	413
10	-1.0	374	25	6.5	387
11	-0.5	323	26	7.0	408
12	0	293	27	7.5	363
13	0.5	310	28	8.0	276
14	1.0	352	29	8.5	209
15	1.5	381	30	9.0	183
				max	416

Table 12 Additional measured HV01 hardnesses and distance between indentations.

Hardness distribution of weld 3.15.2-4 from fusion line		
Number	Distance [mm]	HV1
1	0.05	290
2	0.10	400
3	0.25	416
4	0.40	364
5	0.45	378
6	0.50	398
7	0.50	383
8	0.50	396
9	0.55	396
	max	416

Appendix 6

TIG 3.5.2-4

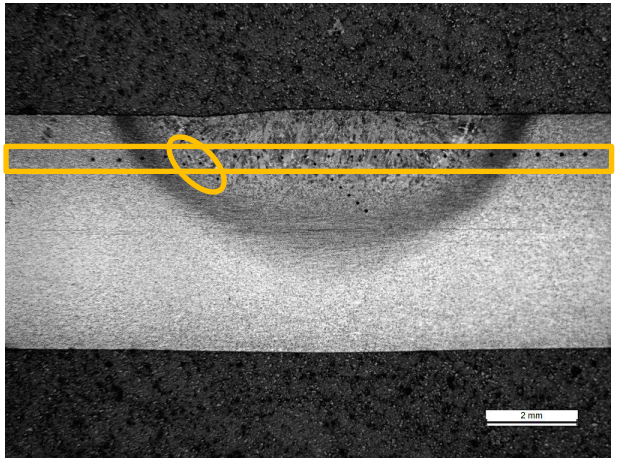

Figure 25 This micrograph of 3.5.2-4 was taken with Leica MEF 4M light microscope with 10X ocular and 1X objective. Distance between selected horizontal indentations of HV1 is 500 µm. Horizontal indentations were measured with automatic microhardness tester Zwick Roell BZ2.5 TS1P.

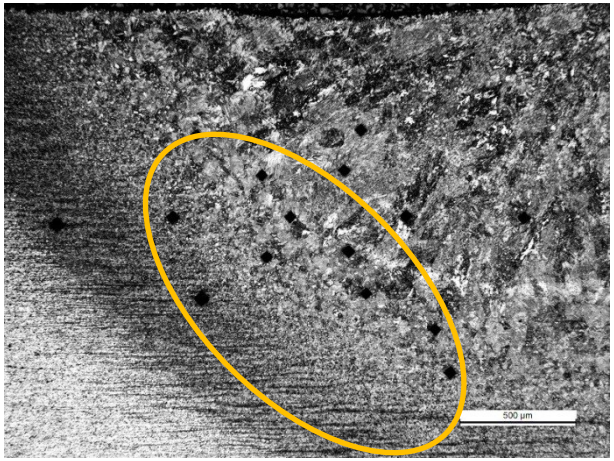

Figure 26 This micrograph of 3.5.2-4 was taken with Leica MEF 4M light microscope with 10X ocular and 5X objective. Maximum peak of hardness distribution was clarified with the help of additional HV1 measurements with HV1 microhardness tester Buehler 1600-6400.

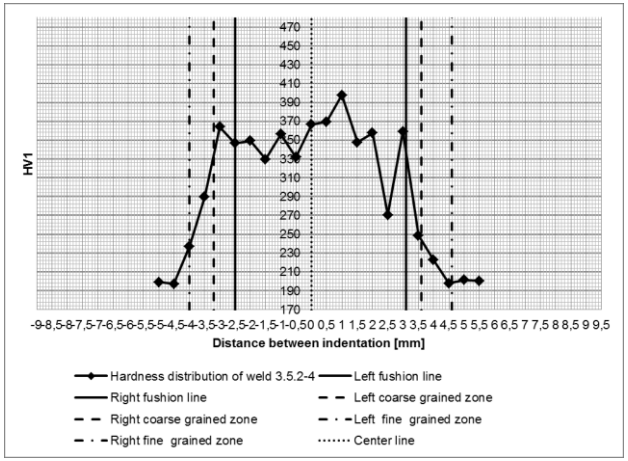

Figure 27 Measured distribution of HV1 hardness with distance of 500 µm. Measured hardnesses and distance between indentations are shown in Table 13.

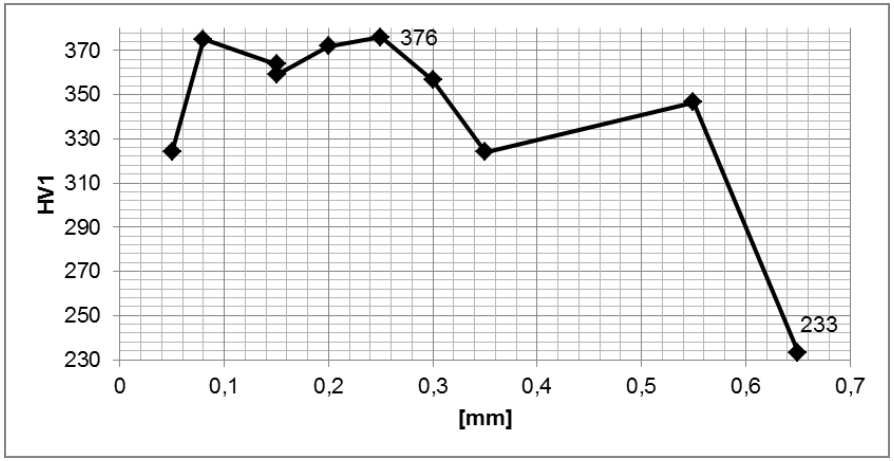

Figure 28 Additional hardness values were measured from coarse-grained zone from fusion line. Measured distribution of HV1 hardness is shown. Measured hardnesses and their distances from fusion line are shown in Table 14.

Appendix 6

Table 13 Measured HV1 hardnesses and distance between indentations.

Hardness distribution of weld 3.5.2-4					
Number	Distance [mm]	HV1	Number	Distance [mm]	HV1
1	-5.0	199	12	0.5	369
2	-4.5	197	13	1.0	398
3	-4.0	237	14	1.5	347
4	-3.5	289	15	2.0	357
5	-3.0	364	16	2.5	270
6	-2.5	347	17	3.0	359
7	-2.0	349	18	3.5	248
8	-1.5	330	19	4.0	222
9	-1.0	356	20	4.5	198
10	-0.5	332	21	5.0	201
11	0	367	22	5.5	200
				max	367

Table 14 Additional measured HV01 hardnesses and distance between indentations.

Hardness distribution of weld 3.5.2-4 from fusion line.		
Number	Distance [mm]	HV1
1	0.05	324
2	0.08	375
3	0.15	364
4	0.15	359
5	0.20	372
6	0.25	376
7	0.30	357
8	0.35	324
9	0.55	347
10	0.65	233
	max	376

Appendix 6

TIG 3.5.2-8

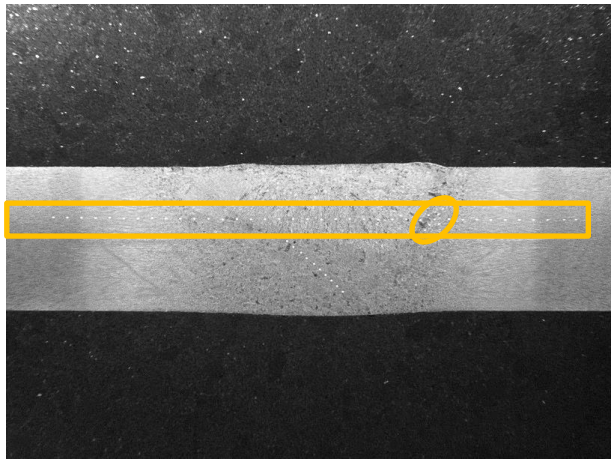

Figure 29 This micrograph of 3.5.2-8 has taken with Leica MZ12 microscope with 10X ocular and 0.8X objective. Distance between selected horizontal indentations of HV1 is 500 µm. Horizontal indentations were measured with automatic microhardness tester Zwick Roell BZ2.5 TS1P

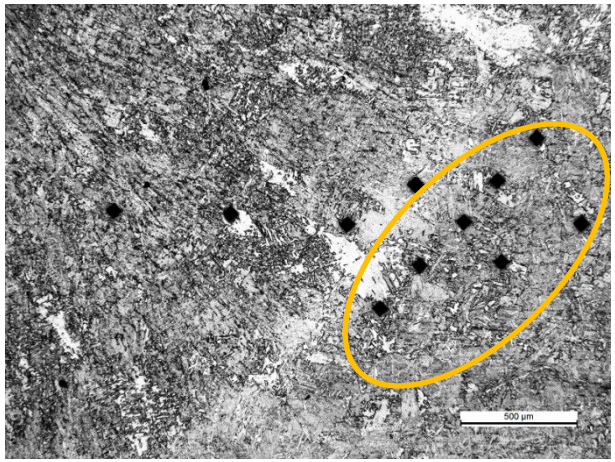

Figure 30 This micrograph of 3.5.2-8 was taken with Leica MEF 4M light microscope with 10X ocular and 5X objective. Maximum peak of hardness distribution was clarified with the help of additional HV1 measurements with HV1 microhardness tester Buehler 1600-6400.

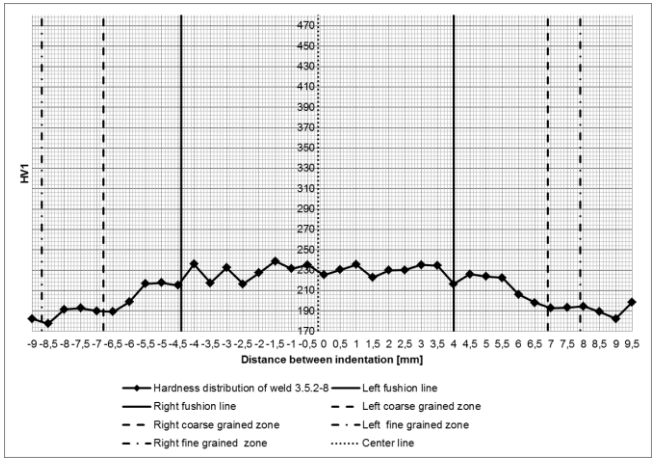

Figure 31 Measured distribution of HV1 hardness with distance of 500 µm. Measured hardnesses and distance between indentations are shown in Table 15.

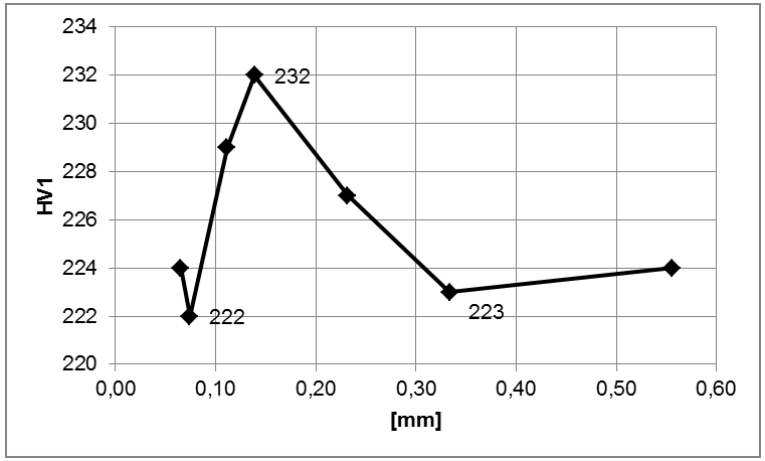

Figure 32 Additional hardness values were measured from coarse-grained zone from fusion line. Measured distribution of HV1 hardness is shown. Measured hardnesses and their distances from fusion line are shown in Table 16.

Appendix 6

Table 15 Measured HV1 hardnesses and distance between indentations.

Hardness distribution of weld 3.5.2-8					
Number	Distance [mm]	HV1	Number	Distance [mm]	HV1
1	-9.0	182	20	0.5	230
2	-8.5	177	21	1.0	235
3	-8.0	191	22	1.5	223
4	-7.5	193	23	2.0	230
5	-7.0	190	24	2.5	230
6	-6.5	189	25	3.0	235
7	-6.0	199	26	3.5	234
8	-5.5	216	27	4.0	216
9	-5.0	218	28	4.5	226
10	-4.5	215	29	5.0	224
11	-4.0	236	30	5.5	222
12	-3.5	217	31	6.0	206
13	-3.0	232	32	6.5	198
14	-2.5	216	33	7.0	193
15	-2.0	227	34	7.5	193
16	-1.5	239	35	8.0	194
17	-1.0	231	36	8.5	189
18	-0.5	235	37	9.0	182
19	0	225	38	9.5	198
				max	239

Table 16 Additional measured HV01 hardnesses and distance between indentations.

Hardness distribution of weld 3.5.2-8 from fusion line.		
Number	Distance [mm]	HV1
1	0.06	224
2	0.07	222
3	0.11	229
4	0.14	232
5	0.23	227
6	0.33	223
7	0.56	224
	max	232

Appendix 6

TIG 3.5.2-9

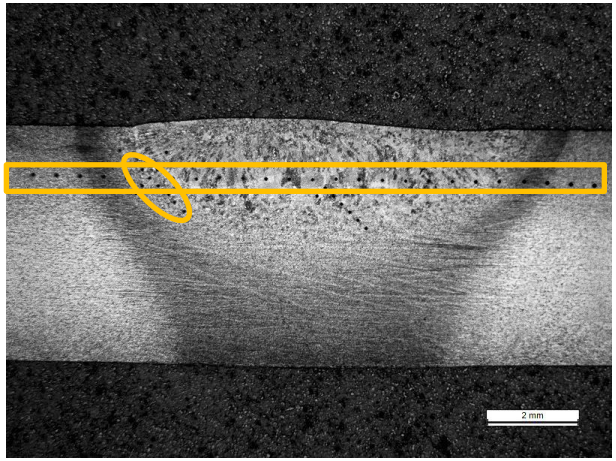

Figure 33 This micrograph of 3.5.2-9 was taken with Leica MEF 4M light microscope with 10X ocular and 1X objective. Distance between selected horizontal indentations of HV1 is 500 µm. Horizontal indentations were measured with automatic microhardness tester by Zwick Roell BZ2.5 TS1P.

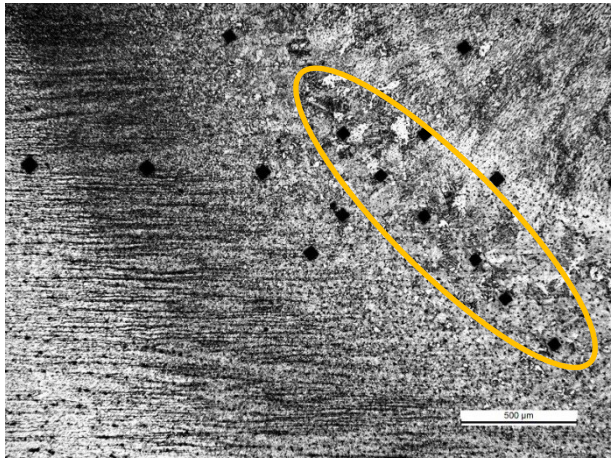

Figure 34 This micrograph of 3.5.2-9 was taken with Leica MEF 4M light microscope with 10X ocular and 5X objective. Maximum peak of hardness distribution was clarified with the help of additional HV1 measurements with HV1 microhardness tester Buehler 1600-6400.

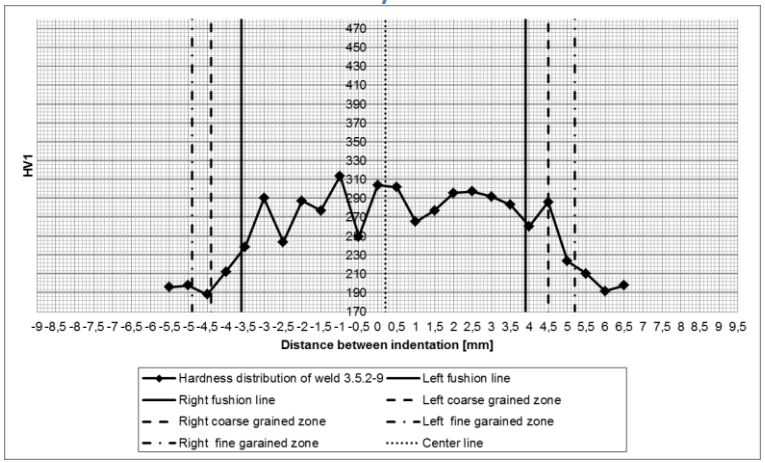

Figure 35 Measured distribution of HV1 hardness with distance of 500 µm. Measured hardnesses and distance between indentations are shown in Table 17.

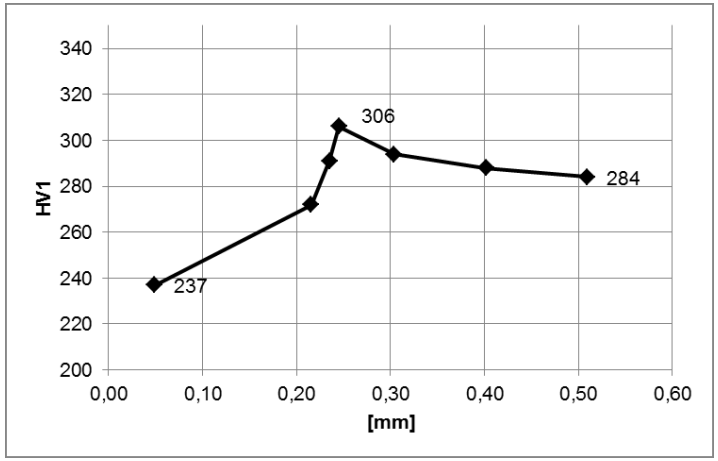

Figure 36 Additional hardness values were measured from coarse-grained zone from fusion line. Measured distribution of HV1 hardness is shown. Measured hardnesses and their distances from fusion line are shown in Table 18.

Appendix 6

Table 17 Measured HV1 hardnesses and distance between indentations.

Hardness distribution of weld 3.5.2-9					
Number	Distance [mm]	HV1	Number	Distance [mm]	HV1
1	-5.5	196	14	1	266
2	-5.0	198	15	1.5	278
3	-4.5	189	16	2	296
4	-4.0	213	17	2.5	298
5	-3.5	239	18	3	292
6	-3.0	291	19	3.5	284
7	-2.5	244	20	4	261
8	-2.0	288	21	4.5	287
9	-1.5	278	22	5	224
10	-1.0	314	23	5.5	211
11	-0.5	250	24	6	192
12	0	304	25	6.5	198
13	0.5	302		max	314

Table 18 Additional measured HV01 hardnesses and distance between indentations.

Hardness distribution of weld 3.5.2-9 from fusion line		
Number	Distance [mm]	HV1
1	0.05	237
2	0.22	272
3	0.24	291
4	0.25	306
5	0.30	294
6	0.40	288
7	0.51	284
	max	306

Appendix 6

TIG 3.15.2-6

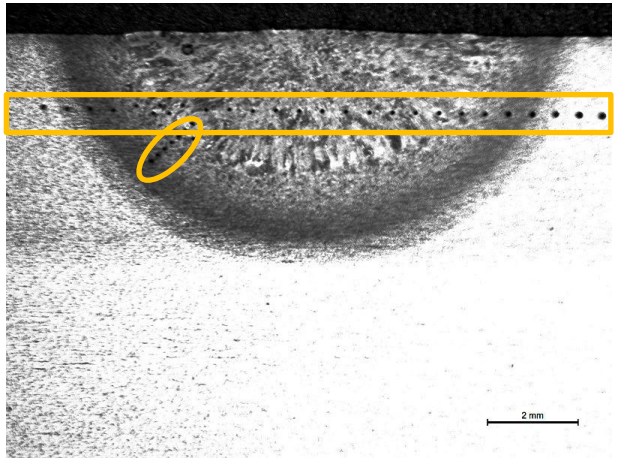

Figure 37 This micrograph of 3.15.2-6 was taken with Leica MEF 4M light microscope with 10X ocular and 1X objective. Distance between selected horizontal indentations of HV1 is 500 µm. Horizontal indentations were measured with automatic microhardness tester Zwick Roell BZ2.5 TS1P

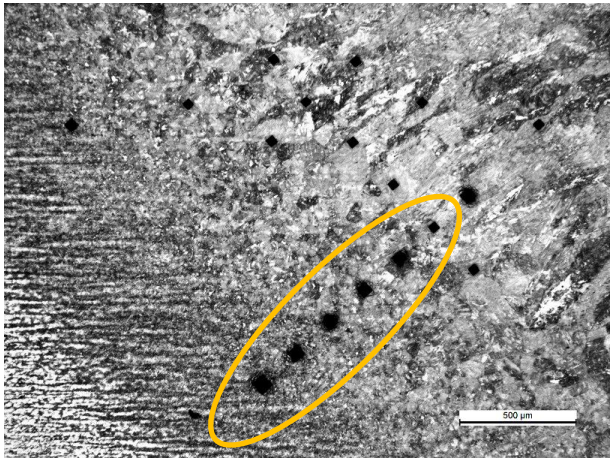

Figure 38 This micrograph of 3.15.2-6 was taken with Leica MEF 4M light microscope with 10X ocular and 5X objective. Maximum peak of hardness distribution was clarified with the help of additional HV1 measurements with HV1 microhardness tester Buehler 1600-6400.

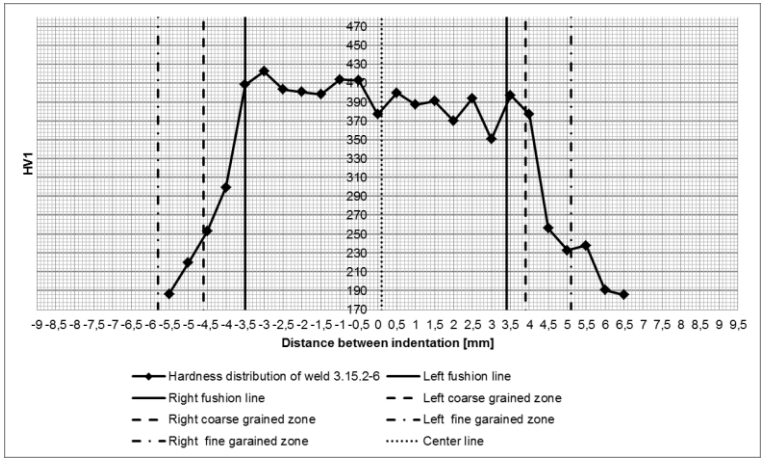

Figure 39 Measured distribution of HV1 hardness with distance of 500 µm. Measured hardnesses and distance between indentations are shown in Table 19.

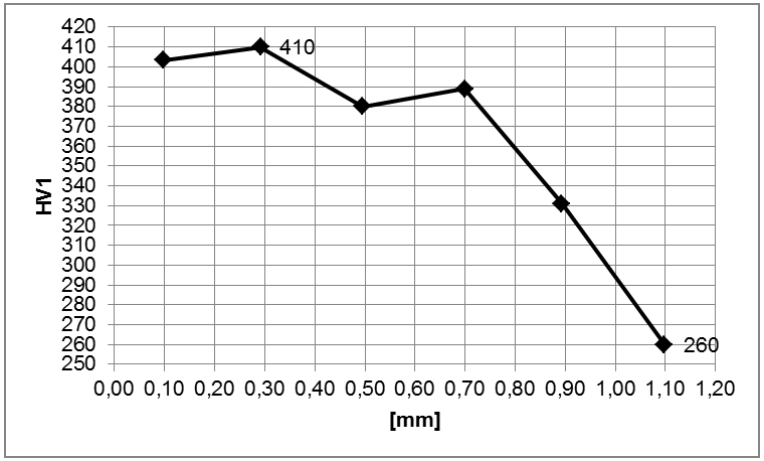

Figure 40 Additional hardness values were measured from coarse-grained zone from fusion line. Measured distribution of HV1 hardness is shown. Measured hardnesses and their distances from fusion line are shown in Table 20.

Appendix 6

Table 19 Measured HV1 hardnesses and distance between indentations.

Hardness distribution of weld 3.15.2-6					
Number	Distance [mm]	HV1	Number	Distance [mm]	HV1
1	-5.5	187	14	1.0	387
2	-5.0	220	15	1.5	391
3	-4.5	253	16	2.0	370
4	-4.0	300	17	2.5	394
5	-3.5	409	18	3.0	351
6	-3.0	423	19	3.5	398
7	-2.5	404	20	4.0	377
8	-2.0	401	21	4.5	257
9	-1.5	398	22	5.0	233
10	-1.0	414	23	5.5	238
11	-0.5	413	24	6.0	191
12	0	377	25	6.5	186
13	0.5	400		max	423

Table 20 Additional measured HV1 hardnesses and distance between indentations.

Hardness distribution of weld 3.15.2-6 from fusion line.		
Number	Distance [mm]	HV1
1	0.10	403
2	0.29	410
3	0.50	380
4	0.70	389
5	0.89	331
6	1.10	260
	max	410

Appendix 6

TIG 3.15.2-7

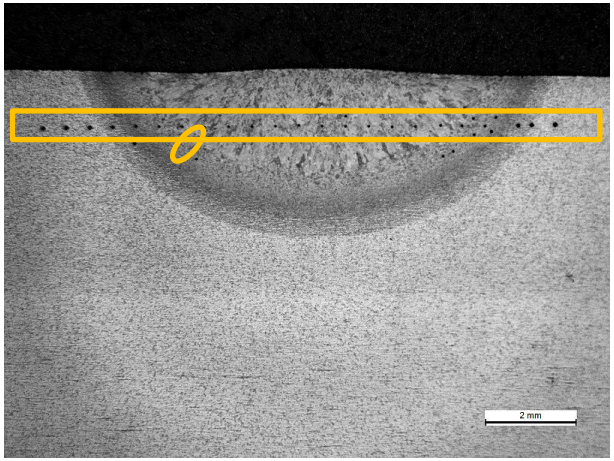

Figure 41 This micrograph of 3.15.2-7 was taken Leica MEF 4M light microscope with 10X ocular and 1X objective. Distance between selected horizontal indentations of HV1 is 500 µm. Horizontal indentations were measured with automatic microhardness tester Zwick Roell BZ2.5 TS1P.

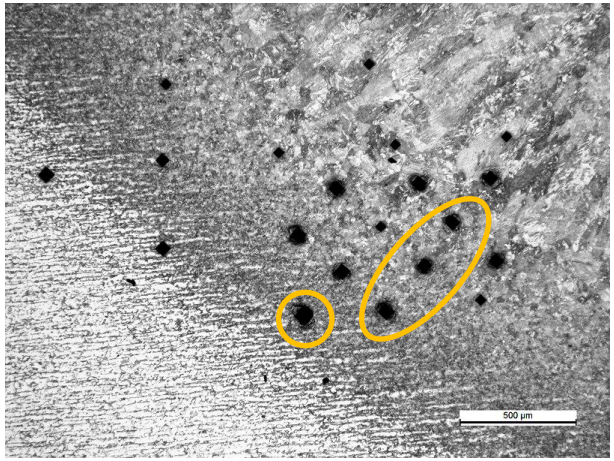

Figure 42 This micrograph of 3.15.2-7 was taken with Leica MEF 4M light microscope with 10X ocular and 5X objective. Maximum peak of hardness distribution was clarified with the help of additional HV1 measurements with HV1 microhardness tester Buehler 1600-6400.

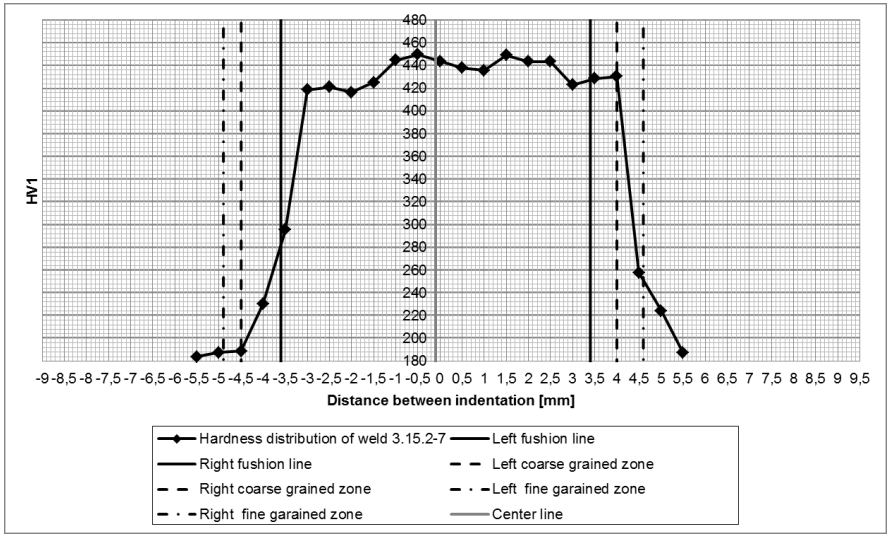

Figure 43 Measured distribution of HV1 hardness with distance of 500 µm. Measured hardnesses and distance between indentations are shown in Table 21.

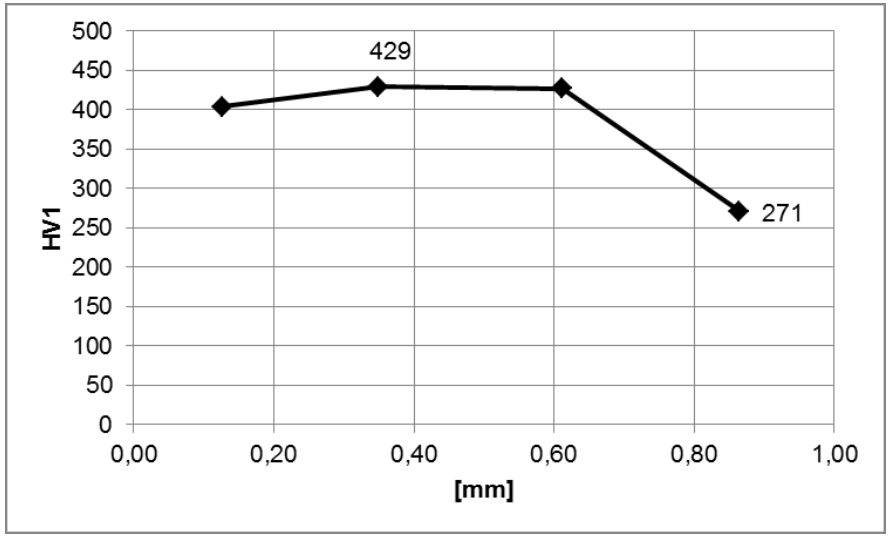

Figure 44 Additional hardness values were measured from coarse-grained zone from fusion line. Measured distribution of HV1 hardness is shown. Measured

hardnesses and their distances from fusion line are shown in Table 22.

Table 21 Measured HV1 hardnesses and distance between indentations.

Hardness distribution of weld 3.15.2-7					
Number	Distance [mm]	HV1	Number	Distance [mm]	HV1
1	-5.5	184	13	0.5	438
2	-5.0	188	14	1.0	436
3	-4.5	189	15	1.5	449
4	-4.0	230	16	2.0	443
5	-3.5	295	17	2.5	443
6	-3.0	419	18	3.0	423
7	-2.5	421	19	3.5	429
8	-2.0	416	20	4.0	430
9	-1.5	425	21	4.5	258
10	-1.0	445	22	5.0	224
11	-0.5	450	23	5.5	187
12	0	444		max	449

Table 22 Additional measured HV1 hardnesses and distance between indentations.

Hardness distribution of weld 3.15.2-7 from fusion line.		
Number	Distance [mm]	HV1
1	0.13	404
2	0.35	429
3	0.61	427
4	0.86	271
	max	429

Appendix 6

TIG 3.15.2-8

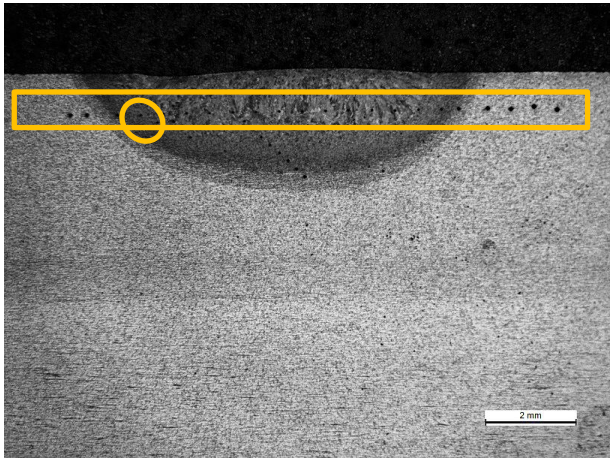

Figure 45 This micrograph of 3.15.2-8 was taken with Leica MEF 4M light microscope with 10X ocular and 1X objective. Distance between selected horizontal indentations of HV1 is 500 µm. Horizontal indentations were measured with automatic microhardness tester Zwick Roell BZ2.5 TS1P

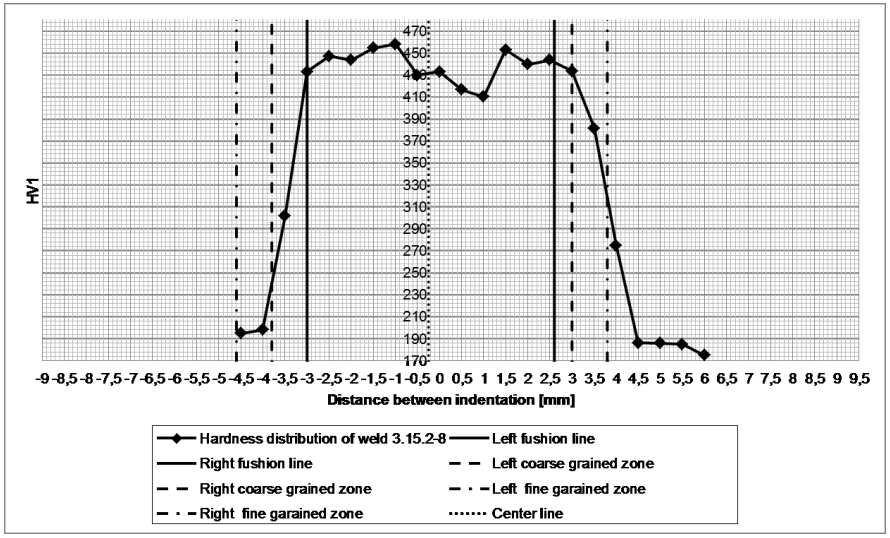

Figure 47 Measured distribution of HV1 hardness with distance of 500 µm. Measured hardnesses and distance between indentations are shown in Table 23.

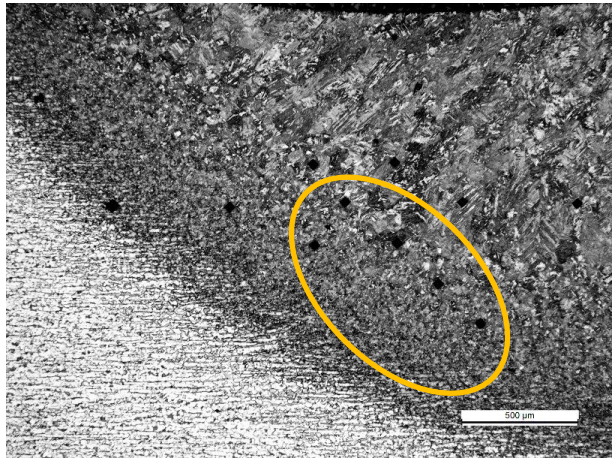

Figure 46 This micrograph of 3.15.2-8 was taken with Leica MEF 4M light microscope with 10X ocular and 5X objective. Maximum peak of hardness distribution was clarified with the help of additional HV1 measurements with HV1 microhardness tester Buehler 1600-6400.

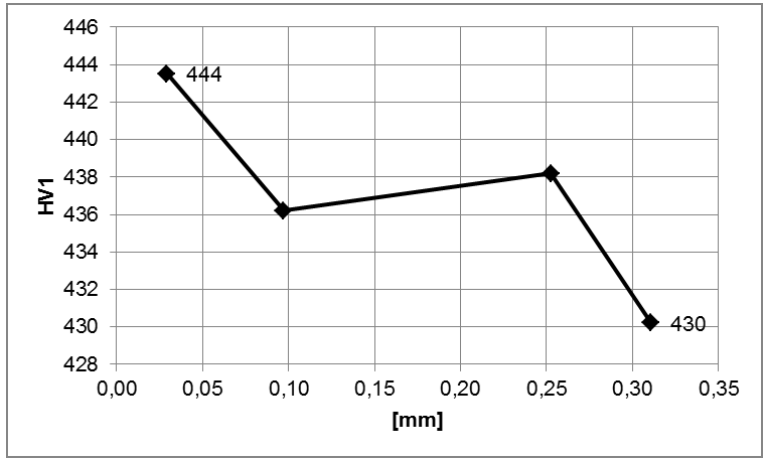

Figure 48 Additional hardness values were measured from coarse-grained zone from fusion line. Measured distribution of HV1 hardness is shown. Measured hardnesses and their distances from fusion line are shown in Table 24.

Table 23 Measured HV1 hardnesses and distance between indentations.

Hardness distribution of weld 3.15.2-8					
Number	Distance [mm]	HV1	Number	Distance [mm]	HV1
1	-4.5	195	13	1.5	453
2	-4.0	198	14	2.0	440
3	-3.5	302	15	2.5	444
4	-3.0	433	16	3.0	434
5	-2.5	447	17	3.5	381
6	-2.0	444	18	4.0	275
7	-1.5	454	19	4.5	186
8	-1.0	458	20	5.0	186
9	-0.5	430	21	5.5	185
10	0	433	22	6.0	175
11	0.5	416		max	458
12	1.0	410			

Table 24 Additional measured HV1 hardnesses and distance between indentations.

Hardness distribution of weld 3.15.2-8 from fusion line.		
Number	Distance [mm]	HV1
1	0.03	444
2	0.10	436
3	0.25	438
4	0.31	430
max		444

Appendix 7 / Micrographs of bead-on-plate weld sample

Contents

Appendix 7

LAHW 3.15.2-9

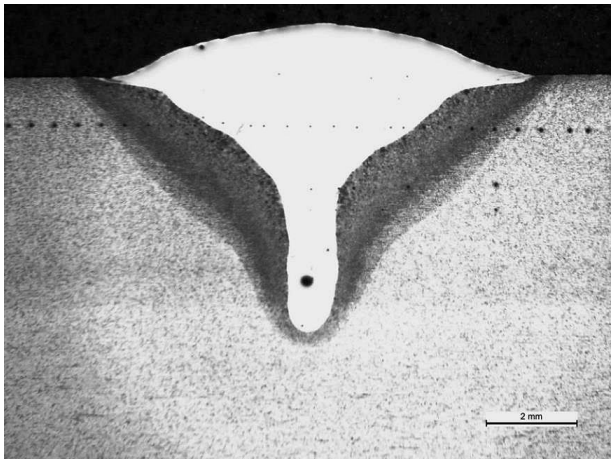

Figure 1 This micrograph of LAHW welded sample 3.15.2-9 is taken with 10X ocular and 1X objective with Leica MEF 4M light microscope.

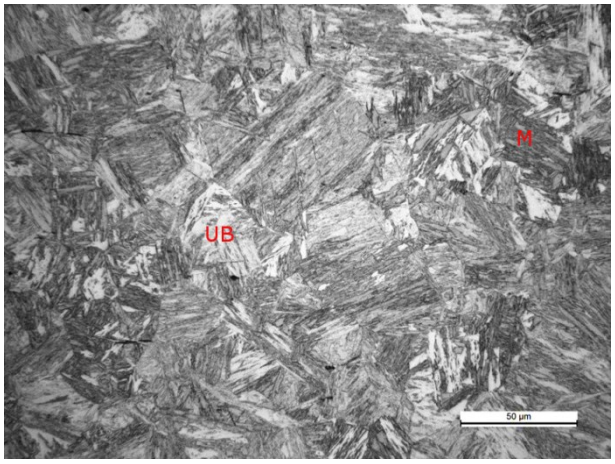

Figure 2 This micrograph of LAHW welded sample 3.15.2-9 is taken with 10X ocular and 50X objective from coarse-grained zone with Leica MEF 4M light microscope. Measured maximum hardness of this microstructure is 476 HV1. Phases of this microstructure are martensite (M) and lower bainite (UB).

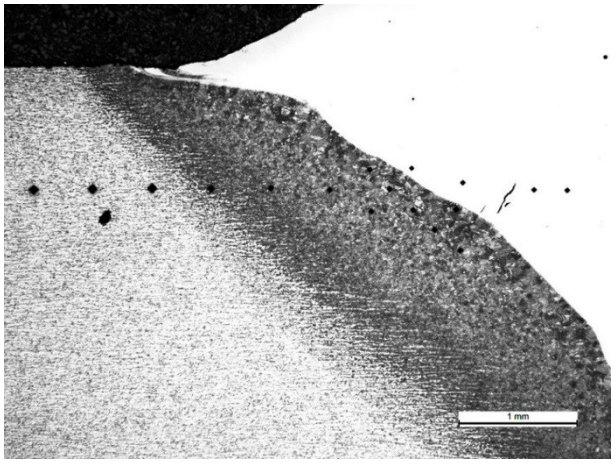

Figure 3 This micrograph of LAHW welded sample of 3.15.2-9 is taken with 10X ocular and 2.5X objective with Leica MEF 4M light microscope.

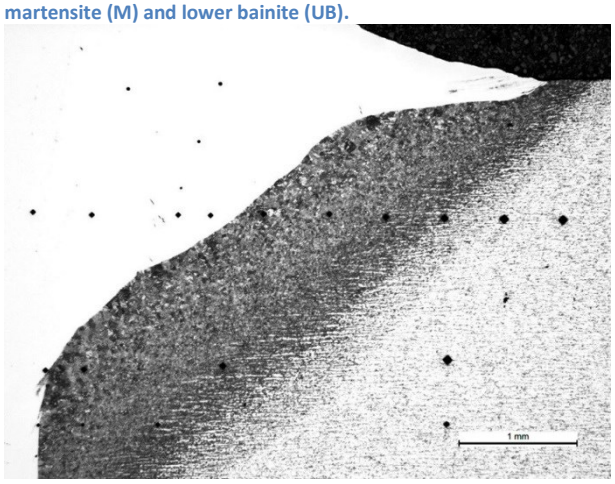

Figure 4 This micrograph of LAHW welded sample of 3.15.2-9 is taken with 10X ocular and 2.5X objective with Leica MEF 4M light microscope.

Figure 5 This micrograph of LAHW welded sample of 3.15.2-9 is taken with 10X ocular and 10X objective with Leica MEF 4M light microscope.

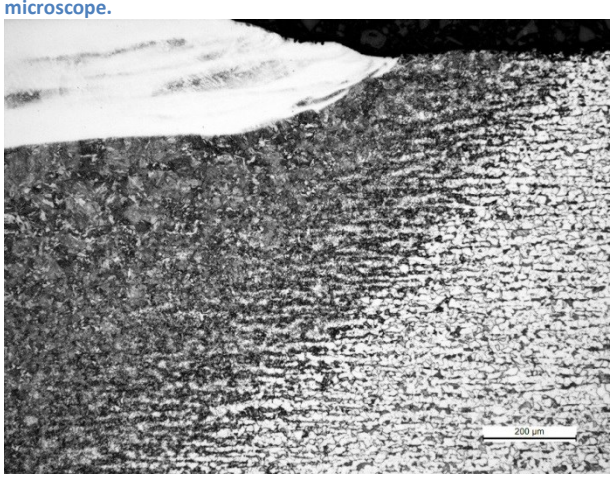

Figure 6 This micrograph of LAHW welded sample of 3.15.2-9 is taken with 10X ocular and 10X objective with Leica MEF 4M light microscope.

Appendix 7

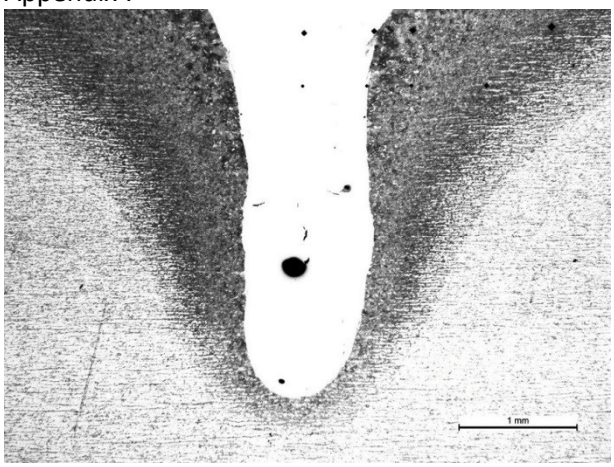

Figure 7 This micrograph of LAHW welded sample of 3.15.2-9 is taken with 10X ocular and 2.5X objective with Leica MEF 4M light microscope.

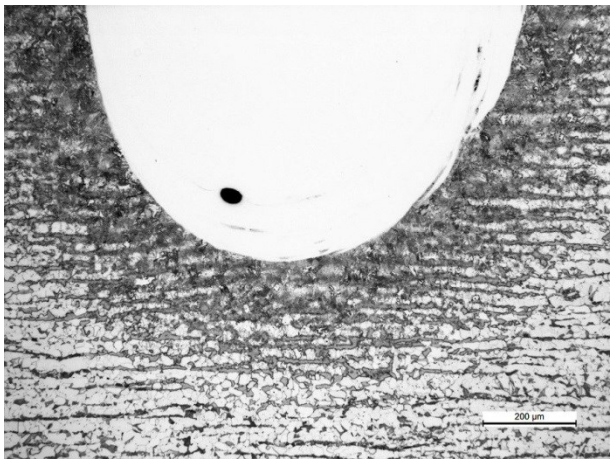

Figure 8 This micrograph of LAHW welded sample of 3.15.2-9 is taken with 10X ocular and 10X objective with Leica MEF 4M light microscope.

LAHW 3.5.2-3

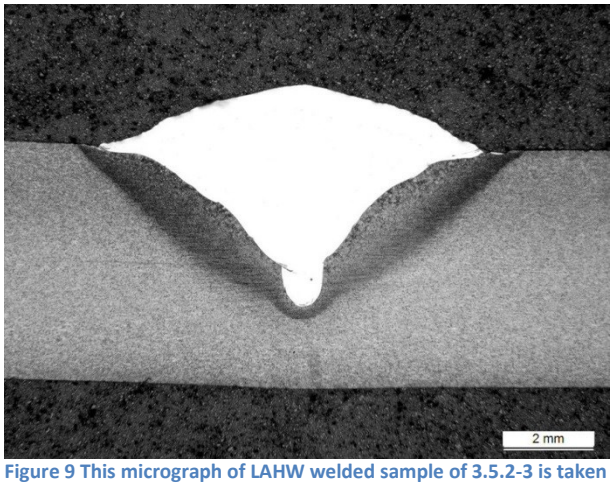

Figure 9 This micrograph of LAHW welded sample of 3.5.2-3 is taken with 10X ocular and 1X objective with Leica MEF 4M light microscope.

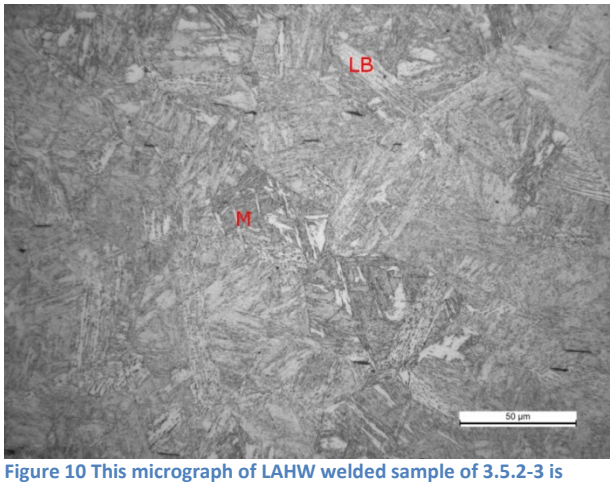

Figure 10 This micrograph of LAHW welded sample of 3.5.2-3 is taken with 10X ocular and 50X objective from coarse-grained zone with Leica MEF 4M light microscope. Measured maximum hardness of this microstructure is 388 HV1. Phases of this microstructure are martensite (M), lower bainite (LB) and upper bainite (HB).

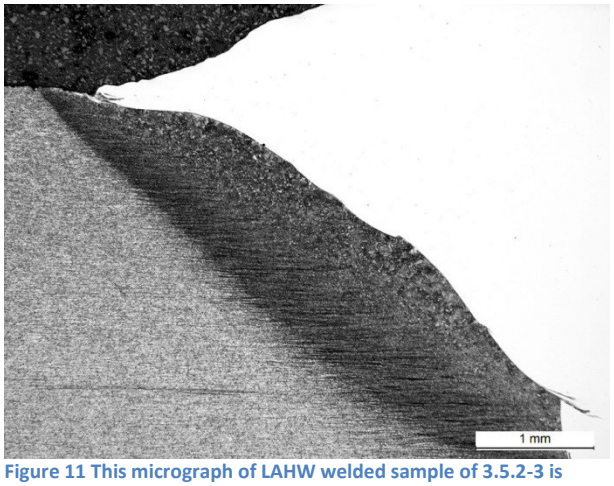

Figure 11 This micrograph of LAHW welded sample of 3.5.2-3 is taken with 10X ocular and 2.5X objective with Leica MEF 4M light microscope.

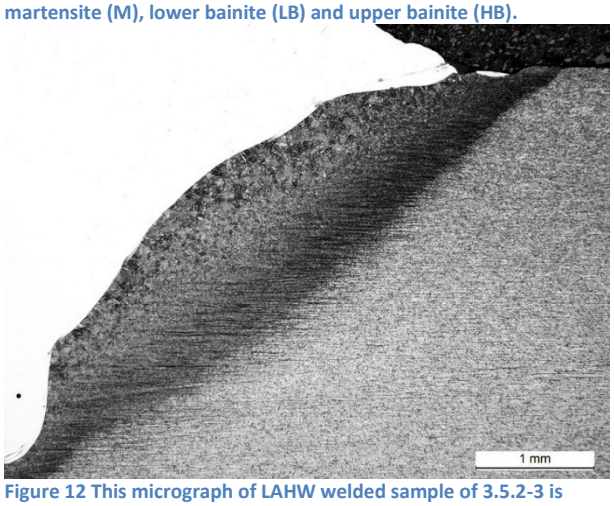

Figure 12 This micrograph of LAHW welded sample of 3.5.2-3 is taken with 10X ocular and 2.5X objective with Leica MEF 4M light microscope.

Appendix 7

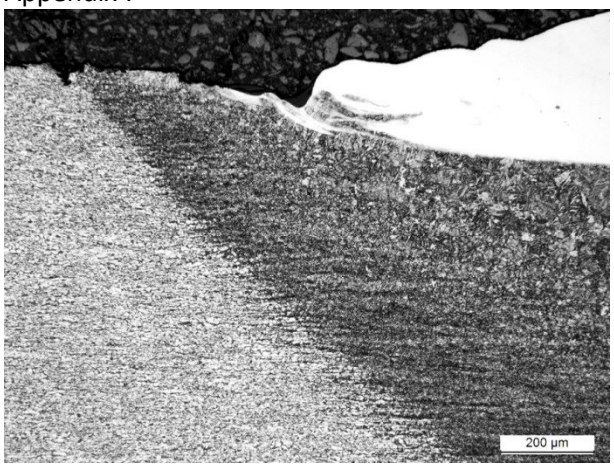

Figure 13 This micrograph of LAHW welded sample of 3.5.2-3 is taken with 10X ocular and 10X objective with Leica MEF 4M light microscope.

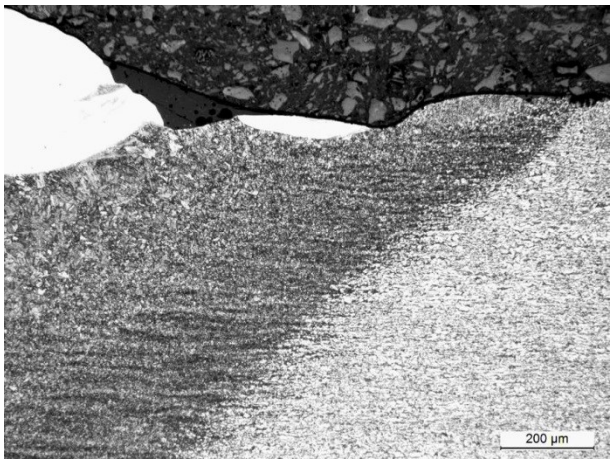

Figure 14 This micrograph of LAHW welded sample of 3.5.2-3 is taken with 10X ocular and 10X objective with Leica MEF 4M light microscope.

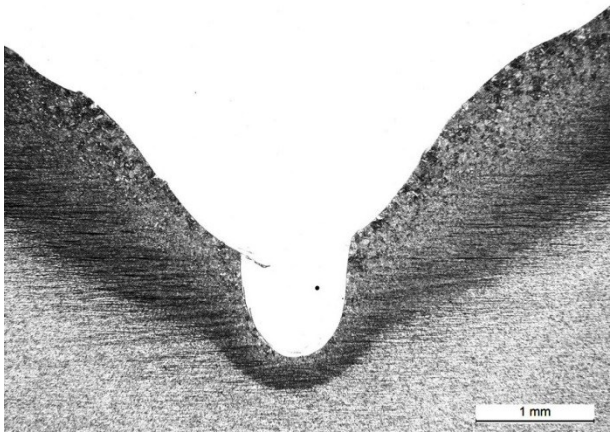

Figure 15 This micrograph of LAHW welded sample of 3.5.2-3 is taken with 10X ocular and 2.5X objective with Leica MEF 4M light microscope.

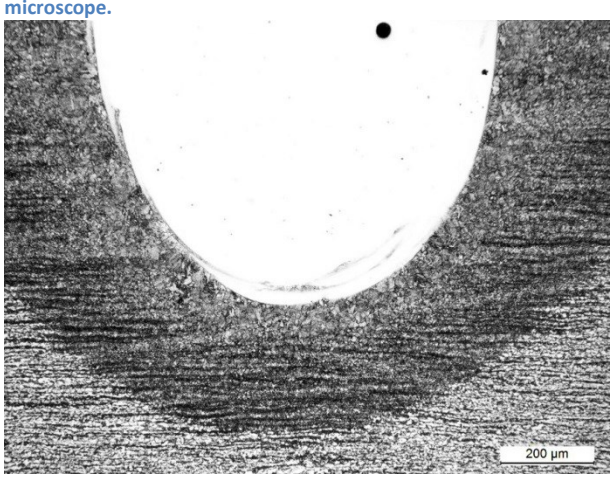

Figure 16 This micrograph of LAHW welded sample of 3.5.2-3 is taken with 10X ocular and 10X objective with Leica MEF 4M light microscope.

LASER 3.15.2-5

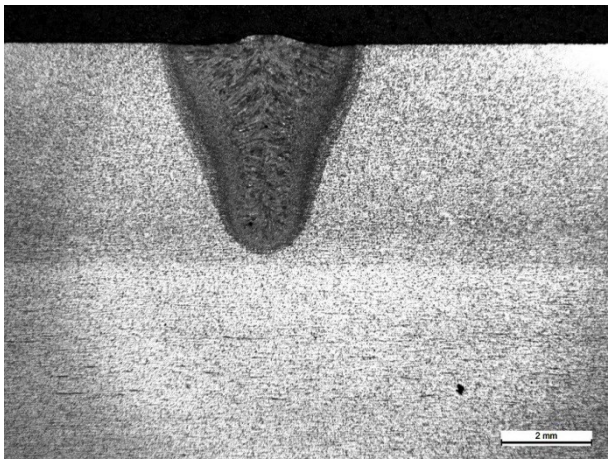

Figure 17 This micrograph of LASER welded sample 3.15.2-5 is taken with 10X ocular and 1X objective with Leica MEF 4M light microscope.

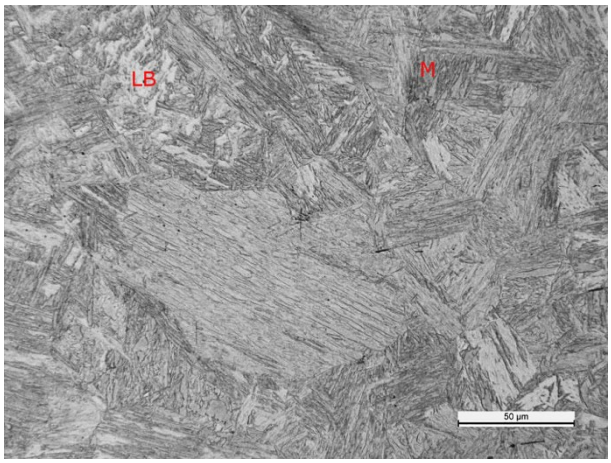

Figure 18 This micrograph of LASER welded sample 3.15.2-5 is taken with 10X ocular and 50X objective from coarse-grained zone with Leica MEF 4M light microscope. Measured maximum hardness of this microstructure is 493 HV01. Phases of this microstructure are martensite (M) and lower bainite (LB).

Appendix 7

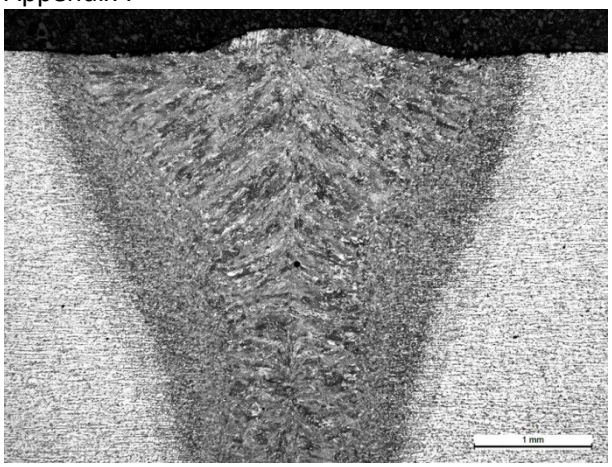

Figure 19 This micrograph of LASER welded sample 3.15.2-5 is taken with 10X ocular and 2.5X objective with Leica MEF 4M light microscope.

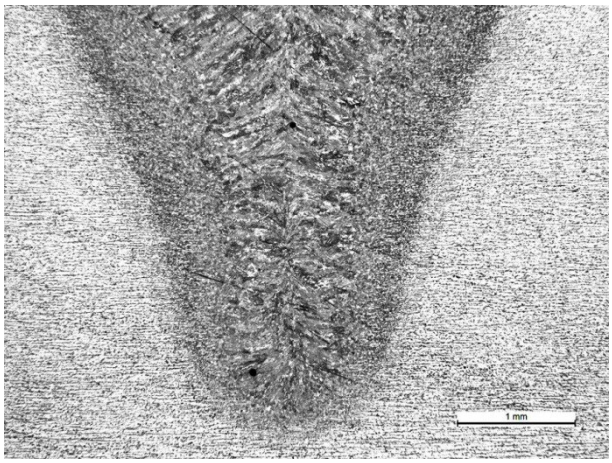

Figure 20 This micrograph of LASER welded sample 3.15.2-5 is taken with 10X ocular and 2.5X objective with Leica MEF 4M light microscope.

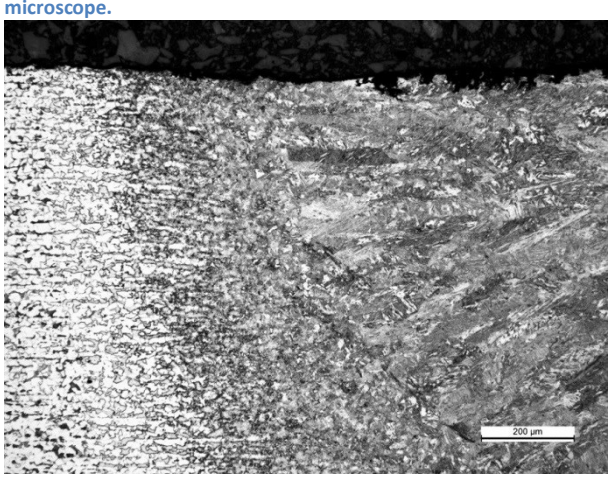

Figure 21 This micrograph of LASER welded sample 3.15.2-5 is taken with 10X ocular and 10X objective with Leica MEF 4M light microscope.

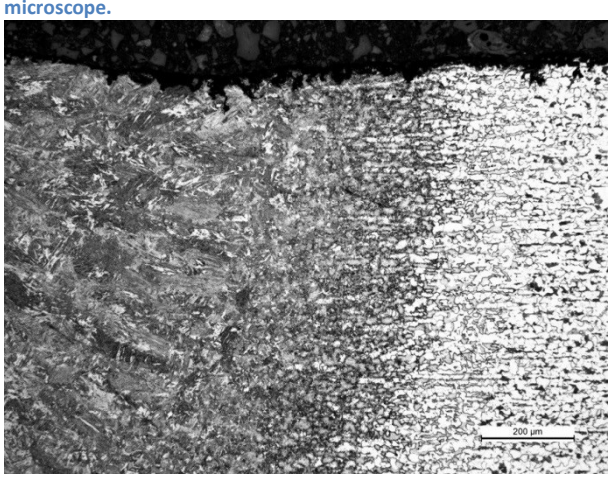

Figure 22 This micrograph of LASER welded sample 3.15.2-5 is taken with 10X ocular and 10X objective with Leica MEF 4M light microscope. Porosity was found in weld metal.

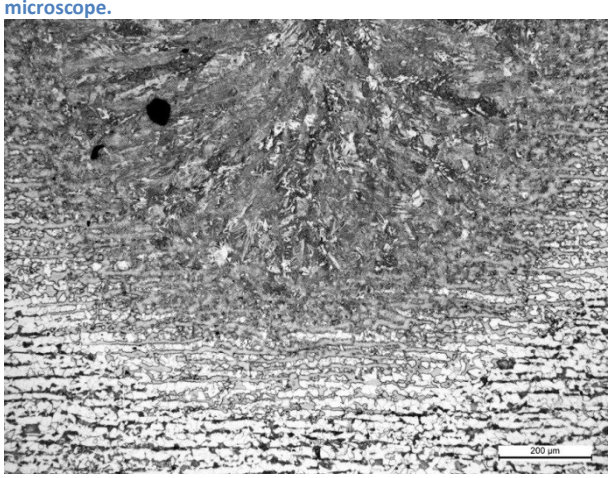

Figure 23 This micrograph of LASER welded sample 3.15.2-5 is taken with 10X ocular and 2.5X objective with Leica MEF 4M light microscope. A gas pore was found in weld metal.

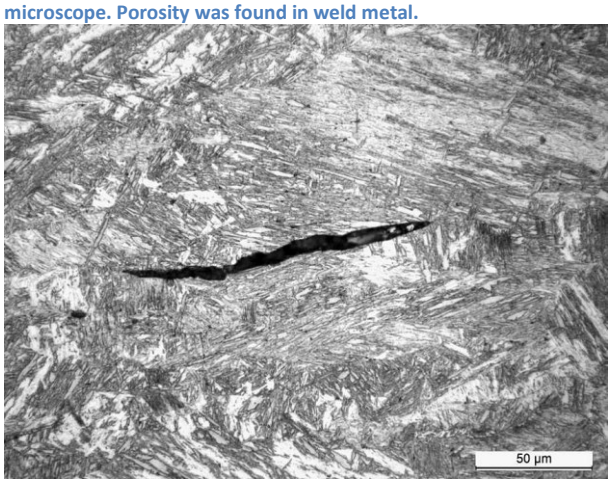

Figure 24 This micrograph of weld metal of LASER welded sample 3.15.2-5 is taken with 50X ocular and 10X objective with Leica MEF 4M light microscope. A crack was found in weld metal.

Appendix 7

LASER 3.5.2-7

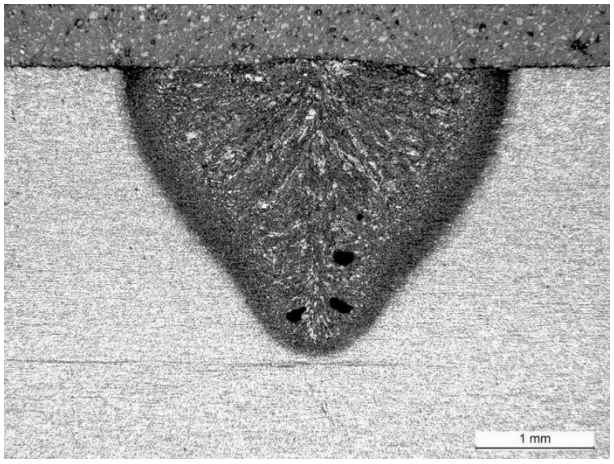

Figure 25 This micrograph of LASER welded sample 3.5.2-7 is taken with 10X ocular and 2.5X objective with Leica MEF 4M light microscope.

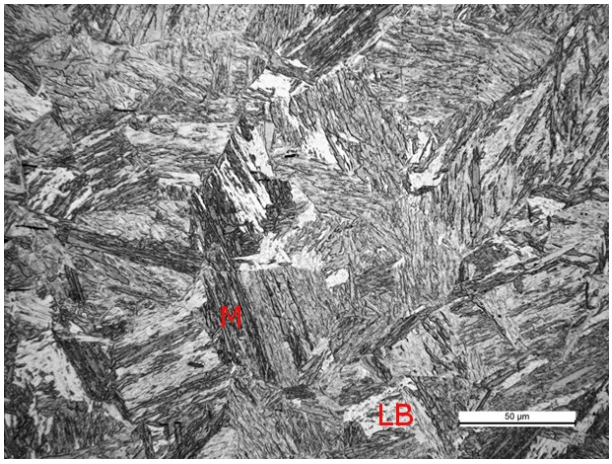

Figure 26 This micrograph of LASER welded sample 3.5.2-7 is taken with 10X ocular and 50X objective from coarse-grained zone with Leica MEF 4M light microscope. Measured maximum hardness of this microstructure is 484 HV01. Phases of this microstructure are martensite (M) and lower bainite (LB).

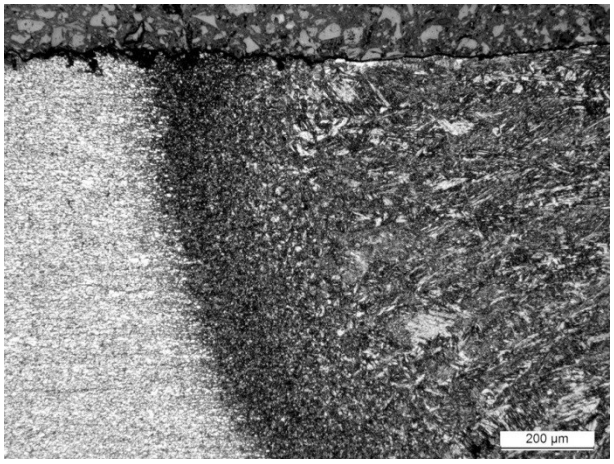

Figure 27 This micrograph of LASER welded sample 3.5.2-7 is taken with 10X ocular and 10X objective with Leica MEF 4M light microscope.

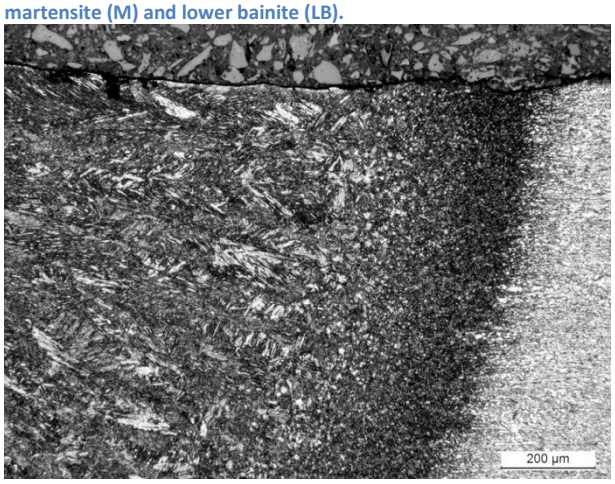

Figure 28 This micrograph of LASER welded sample 3.5.2-7 is taken with 10X ocular and 10X objective with Leica MEF 4M light microscope.

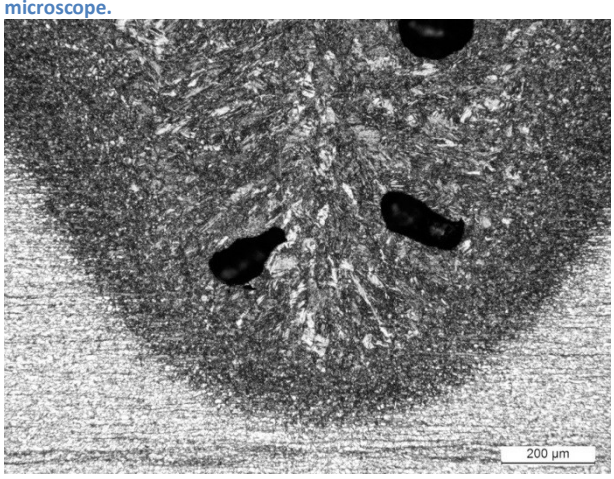

Figure 29 This micrograph of LASER welded sample 3.5.2-7 is taken with 10X ocular and 10X objective with Leica MEF 4M light microscope.

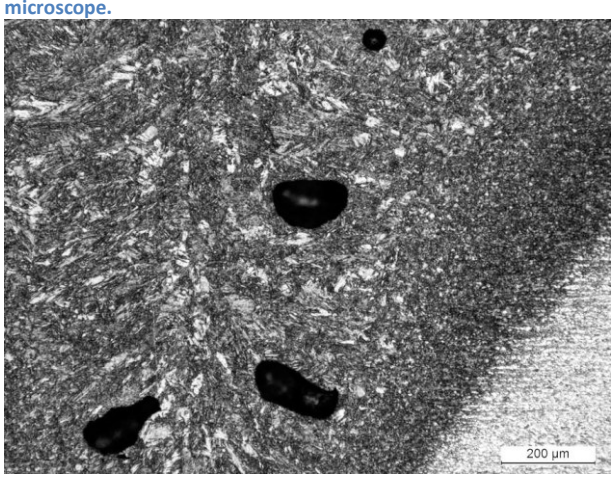

Figure 30 This micrograph of LASER welded sample 3.5.2-7 is taken with 10X ocular and 10X objective with Leica MEF 4M light microscope. Porosity was found in weld metal.

Appendix 7

MAG 3.15.2-4

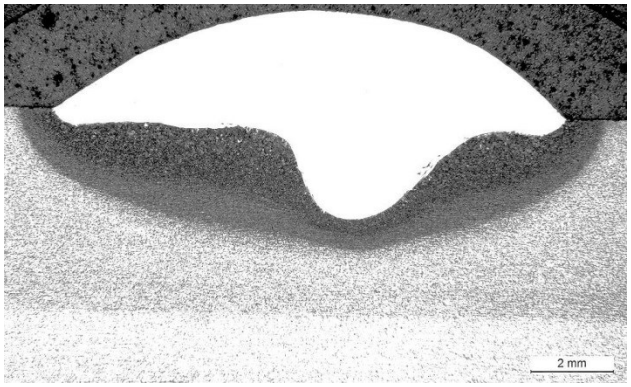

Figure 31 This combined micrograph of MAG welded sample 3.15.2-4 is taken with 10X ocular and 0.8X objective with Leica MEF 4M light microscope. The micrograph is combination of 2 macro photos which are combined with the help of the Image J.

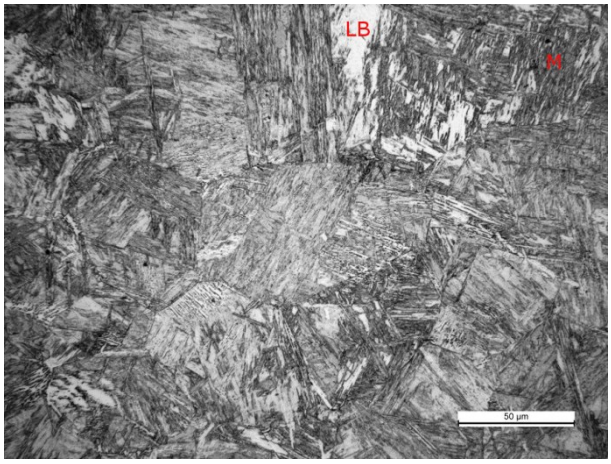

Figure 32 This micrograph of MAG welded sample 3.15.2-4 is taken with 10X ocular and 50X objective from coarse-grained zone with Leica MEF 4M light microscope. Measured maximum hardness of this microstructure is 416 HV1. Phases of this microstructure are lower bainite (LB) and martensite (M).

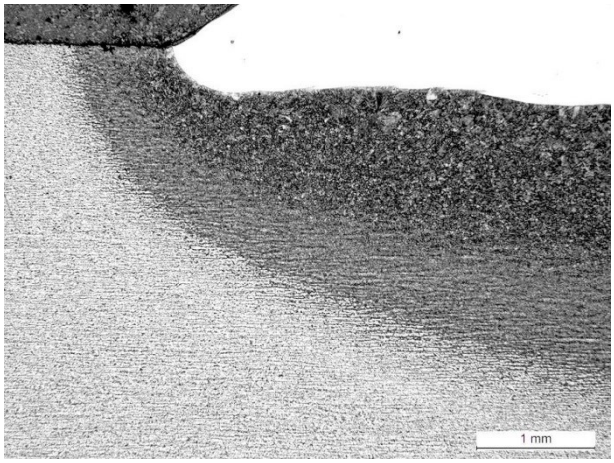

Figure 33 This micrograph of MAG welded sample 3.15.2-4 is taken with 10X ocular and 2.5X objective with Leica MEF 4M light microscope.

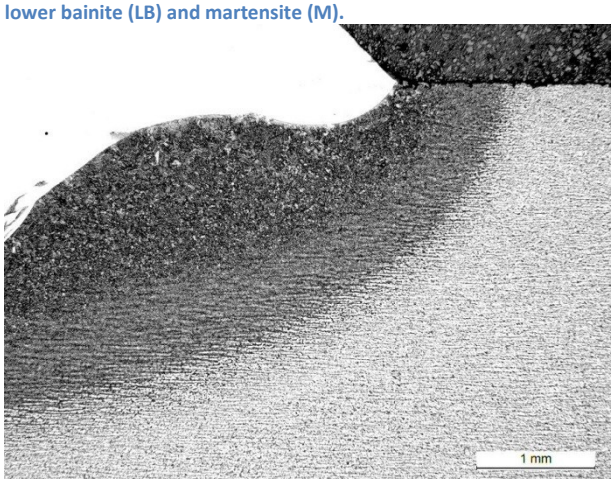

Figure 34 This micrograph of MAG welded sample 3.15.2-4 is taken with 10X ocular and 2.5X objective with Leica MEF 4M light microscope.

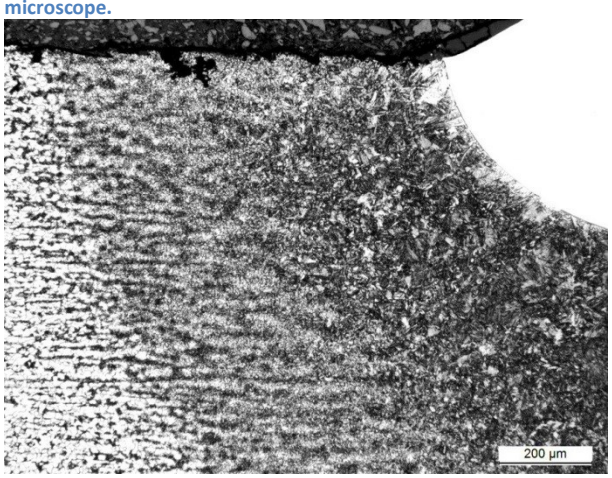

Figure 35 This micrograph of MAG welded sample 3.15.2-4 is taken with 10X ocular and 10X objective with Leica MEF 4M light microscope.

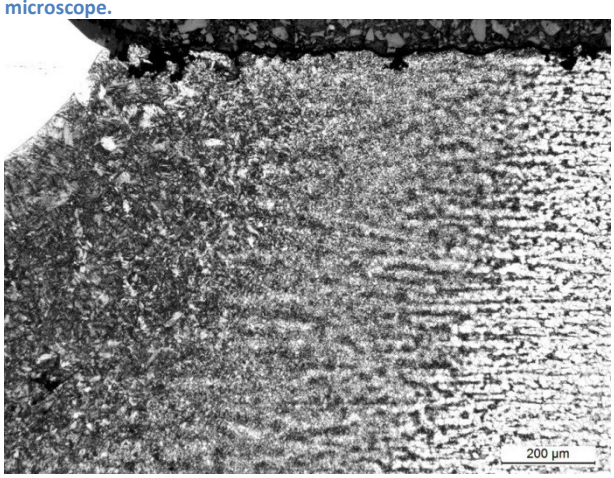

Figure 36 This micrograph of MAG welded sample 3.15.2-4 is taken with 10X ocular and 10X objective with Leica MEF 4M light microscope.

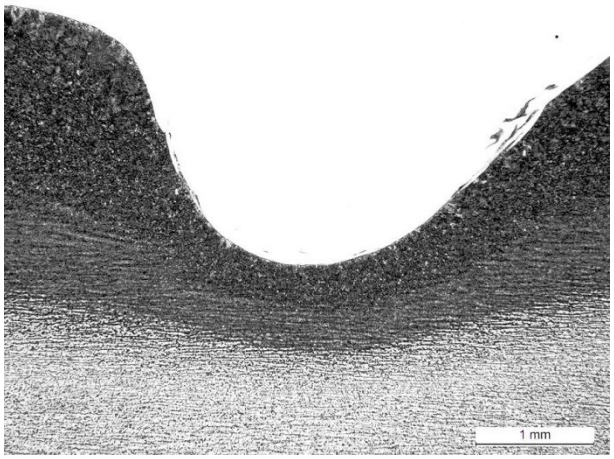

Figure 37 This micrograph of MAG welded sample 3.15.2-4 is taken with 10X ocular and 2.5X objective with Leica MEF 4M light microscope.

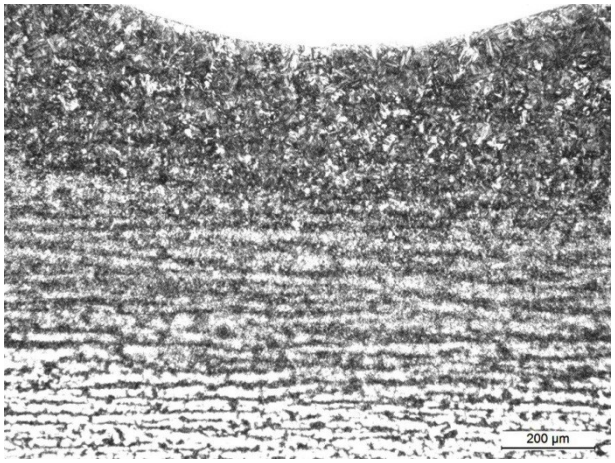

Figure 38 This micrograph of MAG welded sample 3.15.2-4 is taken with 10X ocular and 10X objective with Leica MEF 4M light microscope.

MAG 3.5.2-2

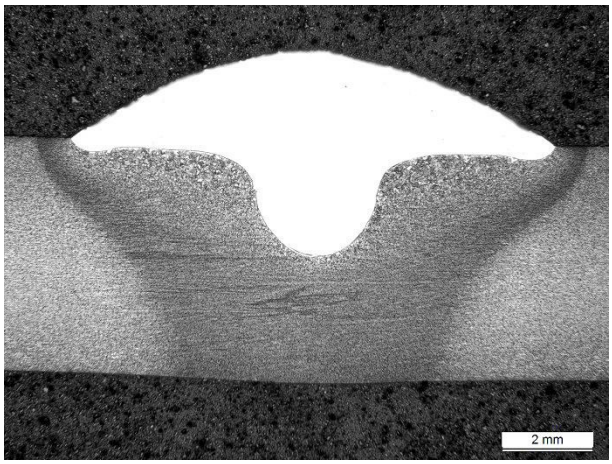

Figure 39 This micrograph of MAG welded sample 3.5.2-2 is taken with 10X ocular and 1X objective with Leica MEF 4M light microscope.

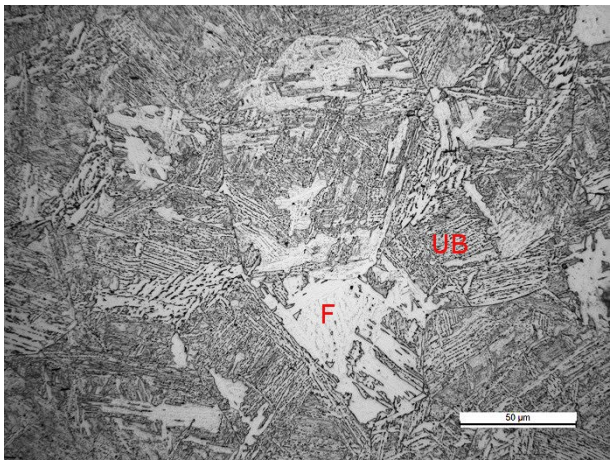

Figure 40 This micrograph of MAG welded sample 3.5.2-2 is taken with 10X ocular and 50X objective from coarse-grained zone with Leica MEF 4M light microscope. Measured maximum hardness of this microstructure is 299 HV1. Phases of this microstructure are ferrite (F) and upper bainite (HB).

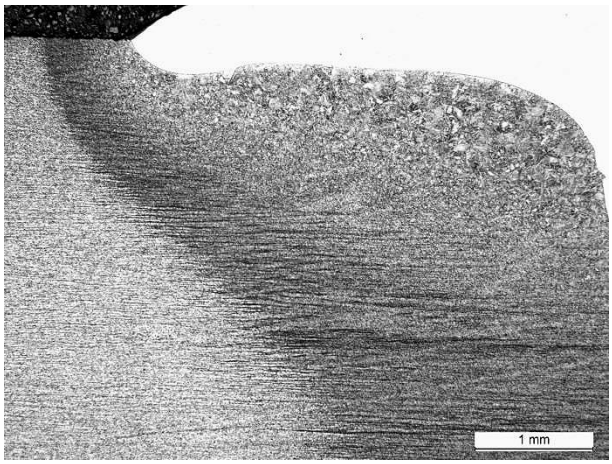

Figure 41 This micrograph of MAG welded sample 3.5.2-2 is taken with 10X ocular and 2.5X objective with Leica MEF 4M light microscope.

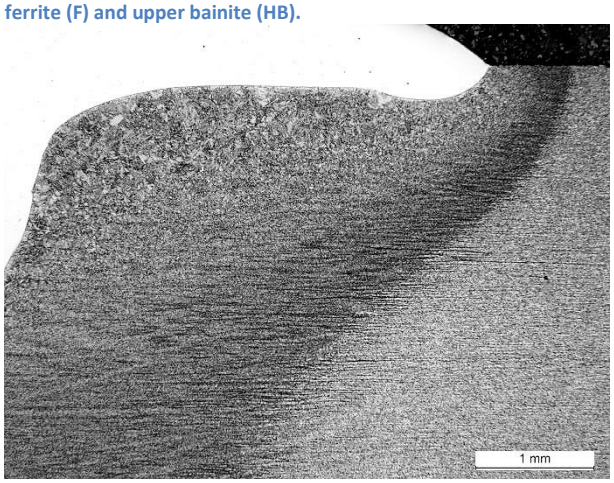

Figure 42 This micrograph of MAG welded sample 3.5.2-2 is taken with 10X ocular and 2.5X objective with Leica MEF 4M light microscope.

Appendix 7

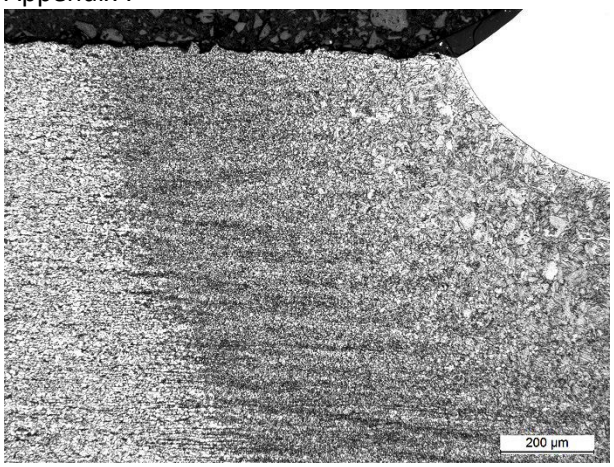

Figure 43 This micrograph of MAG welded sample 3.5.2-2 is taken with 10X ocular and 10X objective with Leica MEF 4M light microscope.

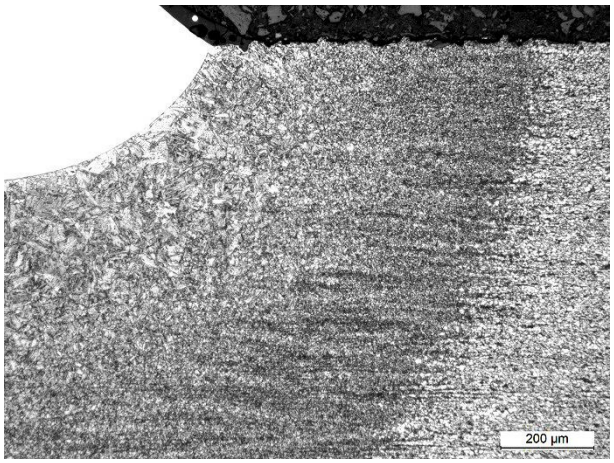

Figure 44 This micrograph of MAG welded sample 3.5.2-2 is taken with 10X ocular and 10X objective with Leica MEF 4M light microscope.

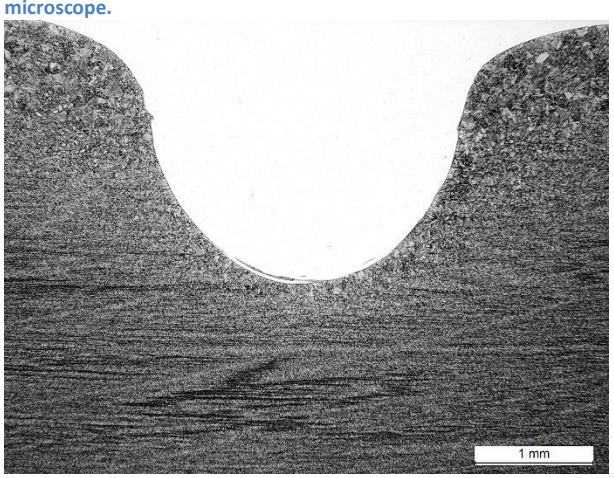

Figure 45 This micrograph of MAG welded sample 3.5.2-2 is taken with 10X ocular and 2.5X objective with Leica MEF 4M light microscope.

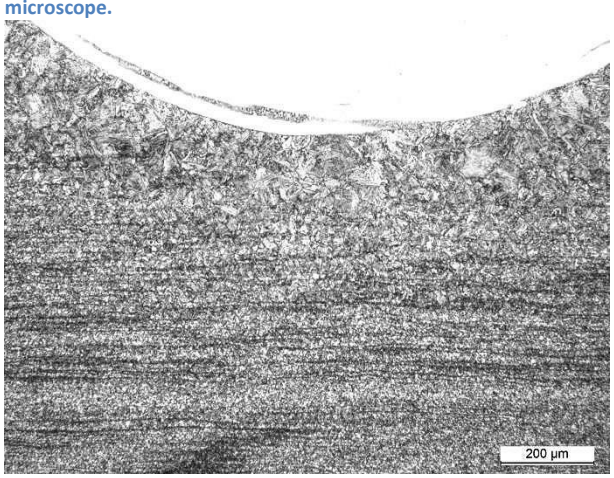

Figure 46 This micrograph of MAG welded sample 3.5.2-2 is taken with 10X ocular and 10X objective with Leica MEF 4M light microscope.

TIG 3.15.2-7

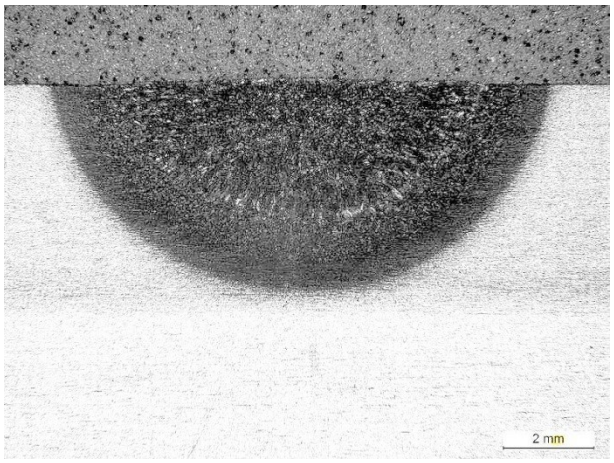

Figure 47 This micrograph of TIG welded sample 3.15.2-7 is taken with 10X ocular and 1X objective with Leica MEF 4M light microscope.

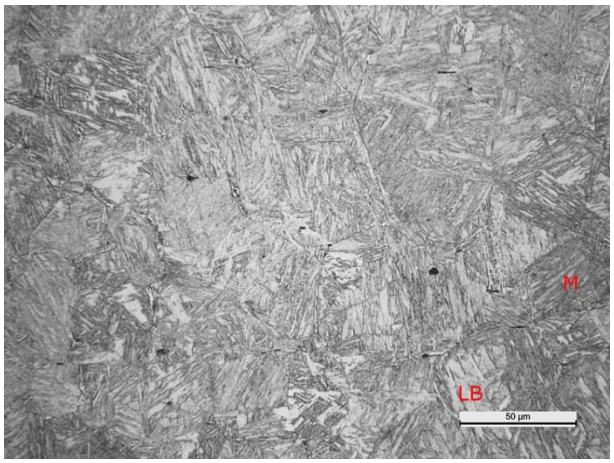

Figure 48 This micrograph of TIG welded sample 3.15.2-7 is taken with 10X ocular and 50X objective from coarse-grained zone with Leica MEF 4M light microscope. Measured maximum hardness of this microstructure is 410 HV1. Phases of this microstructure are lower bainite (LB) and martensite (M).

Appendix 7

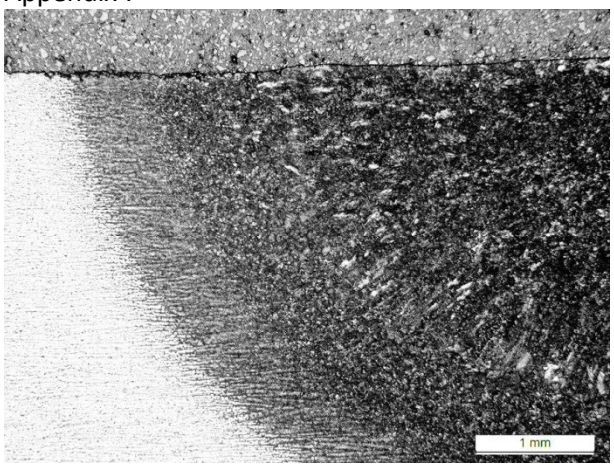

Figure 49 This micrograph of TIG welded sample 3.15.2-7 is taken with 10X ocular and 2.5X objective with Leica MEF 4M light microscope.

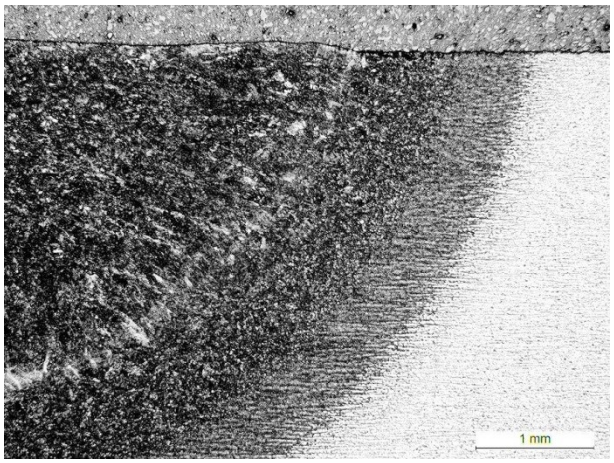

Figure 50 This micrograph of TIG welded sample 3.15.2-7 is taken with 10X ocular and 2.5X objective with Leica MEF 4M light microscope.

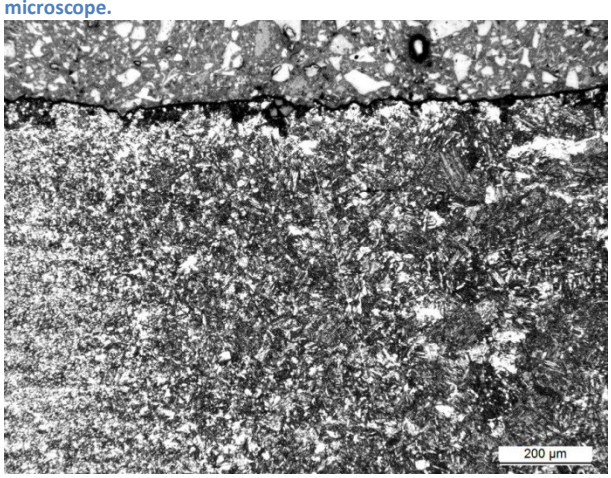

Figure 51 This micrograph of TIG welded sample 3.15.2-7 is taken with 10X ocular and 10X objective with Leica MEF 4M light microscope.

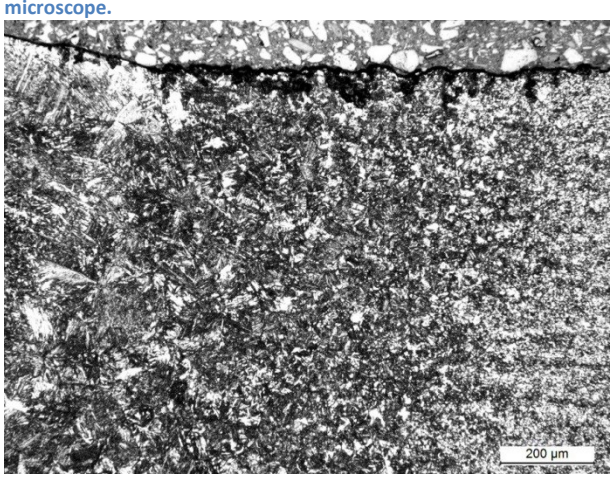

Figure 52 This micrograph of TIG welded sample 3.15.2-7 is taken with 10X ocular and 10X objective with Leica MEF 4M light microscope.

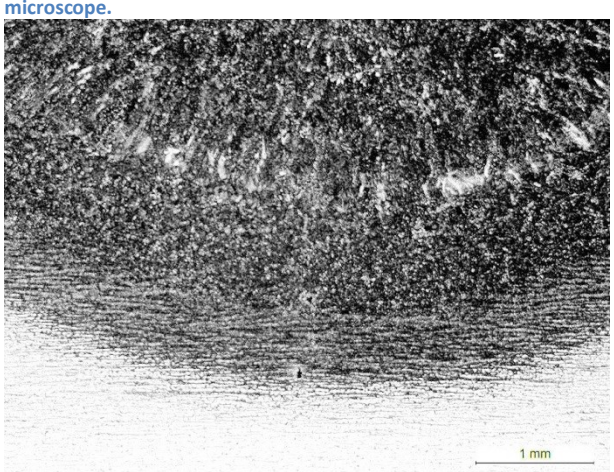

Figure 53 This micrograph of root side of TIG welded sample 3.15.2-7 is taken from fine grained zone with 10X ocular and 2.5X objective with Leica MEF 4M light microscope. Oriented base material can be seen below.

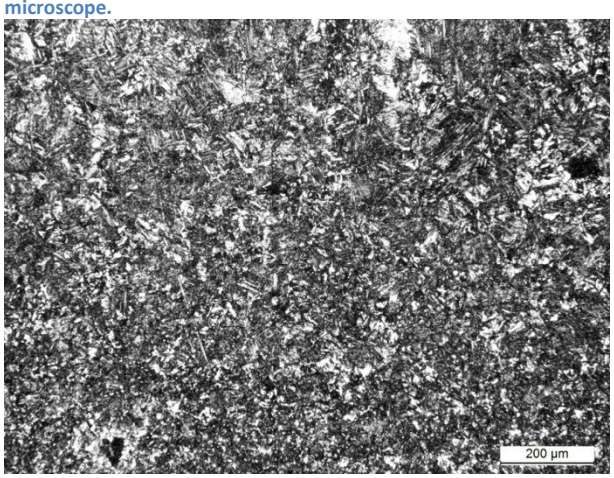

Figure 54 This micrograph of TIG welded sample 3.15.2-7 is taken on root side from coarse-grained zone near fusion line with 10X ocular and 10X objective with Leica MEF 4M light microscope.

Appendix 7

TIG 3.15.2-6

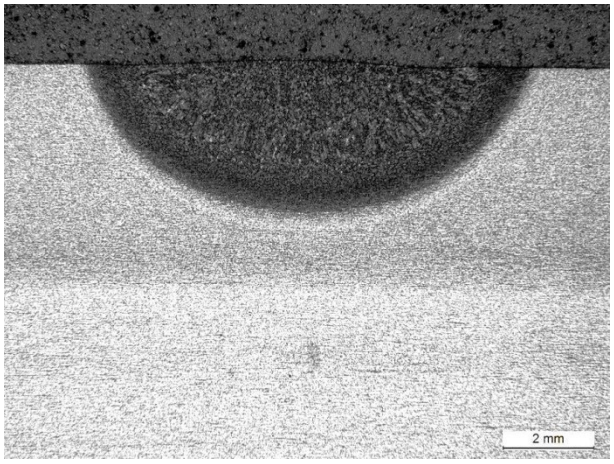

Figure 55 This micrograph of TIG welded sample 3.15.2-6 is taken with 10X ocular and 1X objective with Leica MEF 4M light microscope.

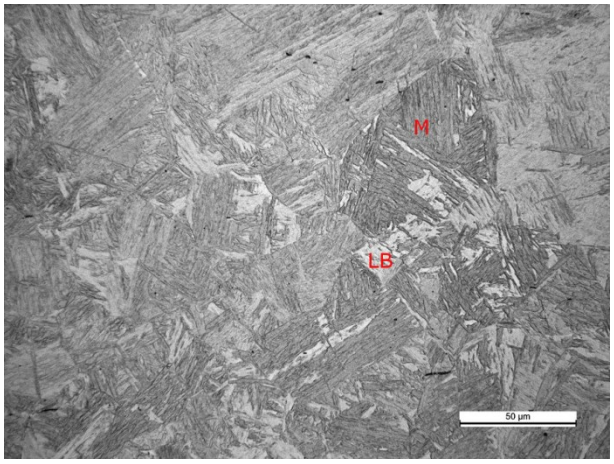

Figure 56 This micrograph of TIG welded sample 3.15.2-6 is taken with 10X ocular and 50X objective from coarse-grained zone with Leica MEF 4M light microscope. Measured maximum hardness of this microstructure is 429 HV1. Phases of this microstructure are lower bainite (DB) and martensite (M).

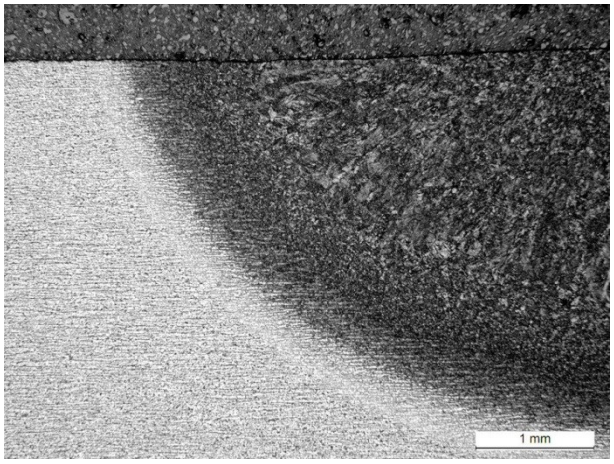

Figure 57 This micrograph of TIG welded sample 3.15.2-6 is taken with 10X ocular and 2.5X objective with Leica MEF 4M light microscope.

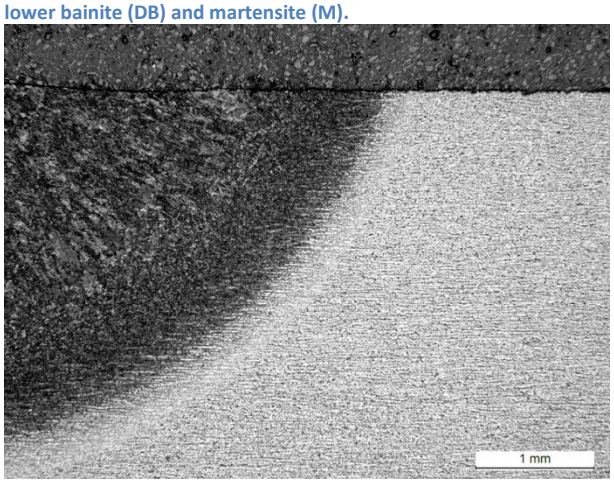

Figure 58 This micrograph of TIG welded sample 3.15.2-6 is taken with 10X ocular and 2.5X objective with Leica MEF 4M light microscope.

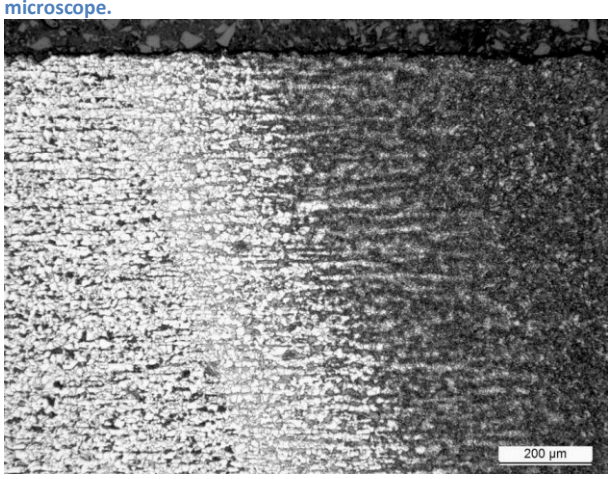

Figure 59 This micrograph of TIG welded sample 3.15.2-6 is taken with 10X ocular and 10X objective with Leica MEF 4M light microscope.

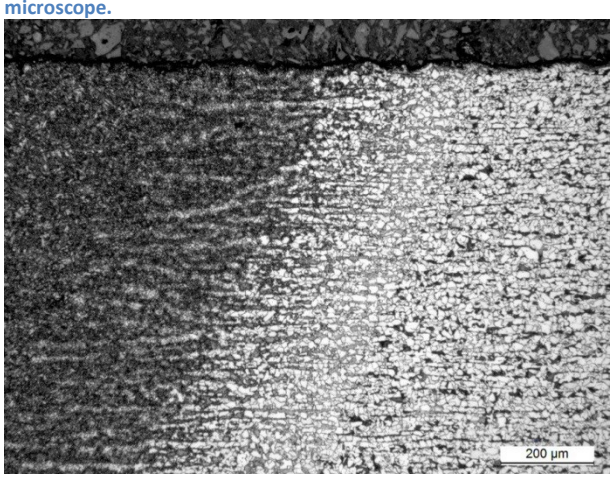

Figure 60 This micrograph of TIG welded sample 3.15.2-6 is taken with 10X ocular and 10X objective with Leica MEF 4M light microscope.

Appendix 7

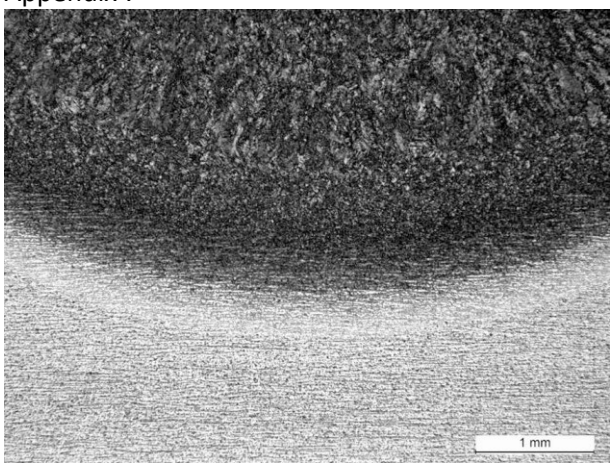

Figure 61 This micrograph of TIG welded sample 3.15.2-6 is taken from root side with 10X ocular and 2.5X objective with Leica MEF 4M light microscope.

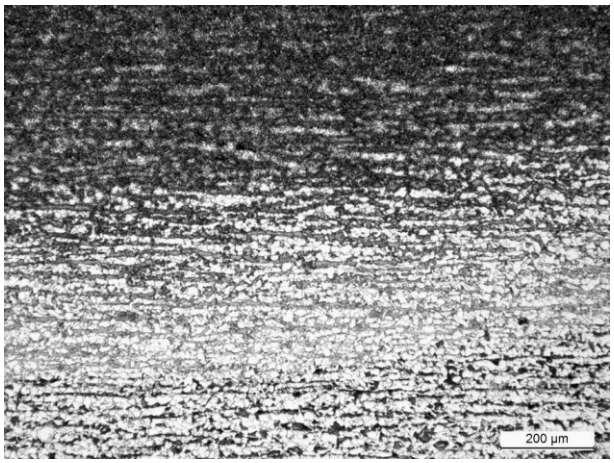

Figure 62 This micrograph of TIG welded sample 3.15.2-6 is taken from root side with 10X ocular and 10X objective with Leica MEF 4M light microscope.

TIG 3.15.2-8

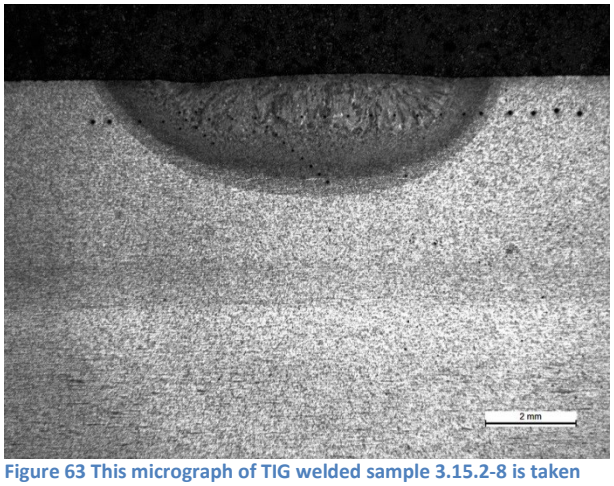

Figure 63 This micrograph of TIG welded sample 3.15.2-8 is taken with 10X ocular and 1X objective with Leica MEF 4M light microscope.

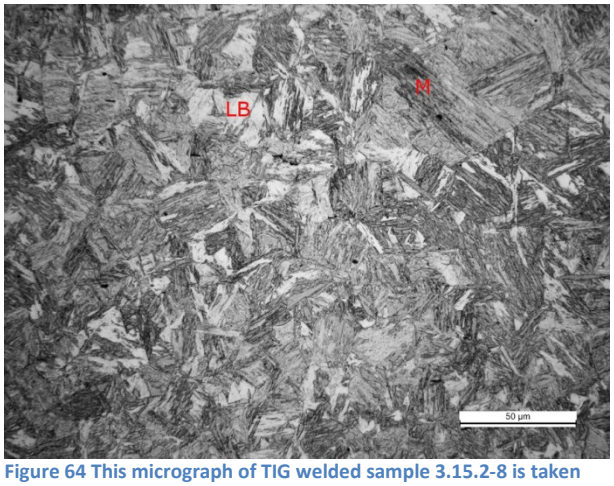

Figure 64 This micrograph of TIG welded sample 3.15.2-8 is taken with 10X ocular and 50X objective from coarse-grained zone with Leica MEF 4M light microscope. Measured maximum hardness of this microstructure is 444 HV1. Phases of this microstructure are martensite (M) and lower bainite (DB).

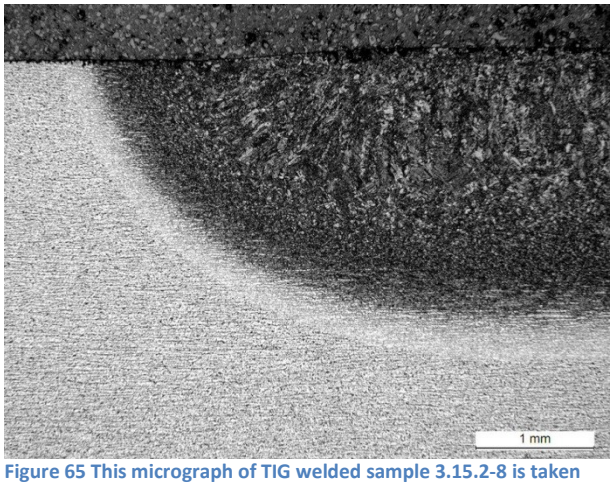

Figure 65 This micrograph of TIG welded sample 3.15.2-8 is taken with 10X ocular and 2.5X objective with Leica MEF 4M light microscope.

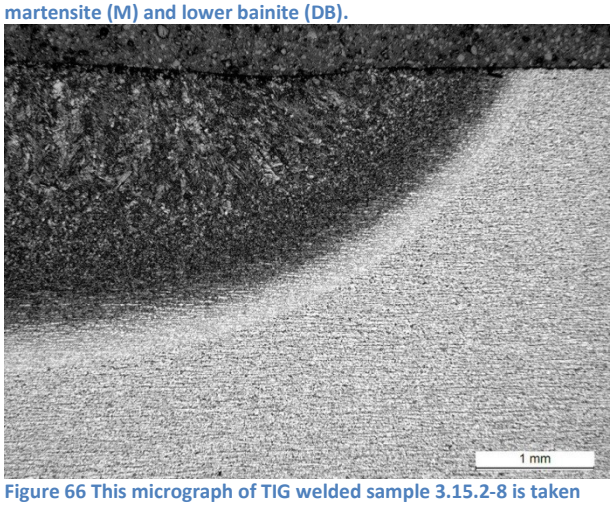

Figure 66 This micrograph of TIG welded sample 3.15.2-8 is taken with 10X ocular and 2.5X objective with Leica MEF 4M light microscope.

Appendix 7

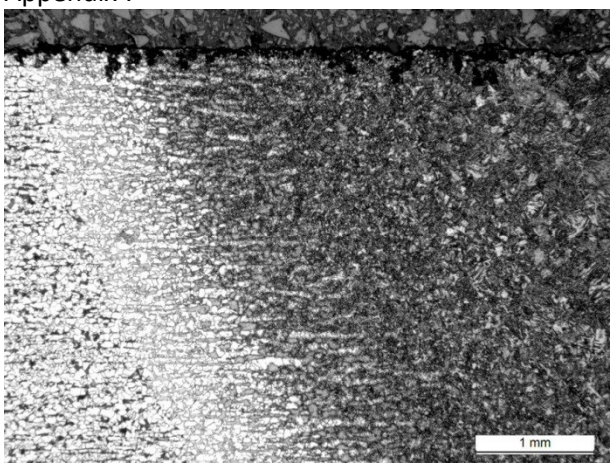

Figure 67 This micrograph of TIG welded sample 3.15.2-8 is taken with 10X ocular and 10X objective with Leica MEF 4M light microscope.

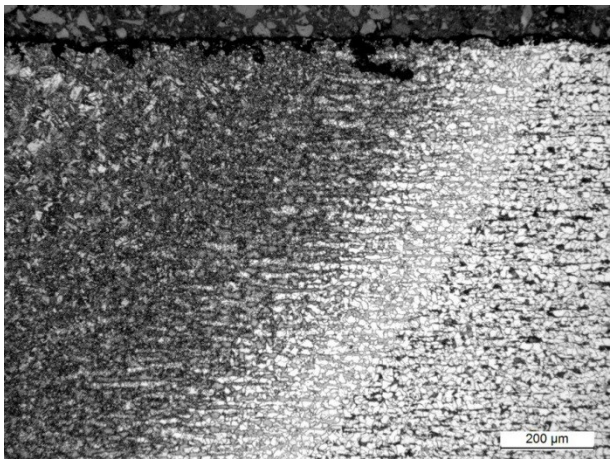

Figure 68 This micrograph of TIG welded sample 3.15.2-8 is taken with 10X ocular and 10X objective with Leica MEF 4M light microscope.

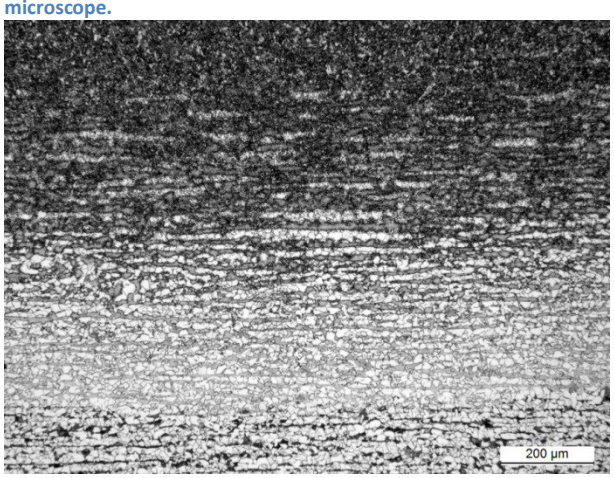

Figure 69 This micrograph of root side of TIG welded sample 3.15.2-8 is taken from fine grained zone with 10X ocular and 10X objective with Leica MEF 4M light microscope. Oriented base material can be seen below.

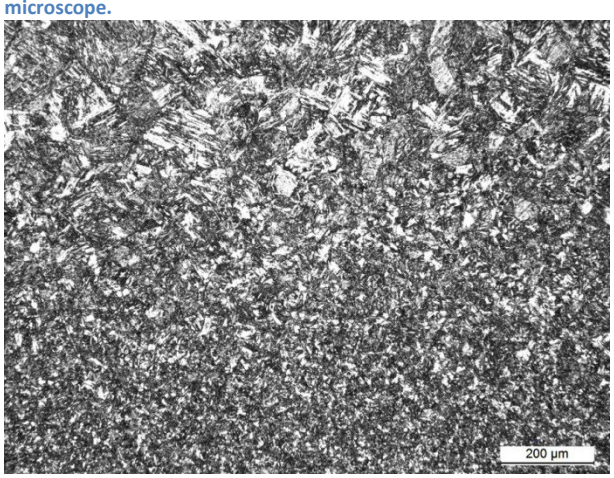

Figure 70 This micrograph of TIG welded sample 3.15.2-8 is taken on root side from coarse-grained zone near fusion line with 10X ocular and 10X objective with Leica MEF 4M light microscope.

TIG 3.5.2-4

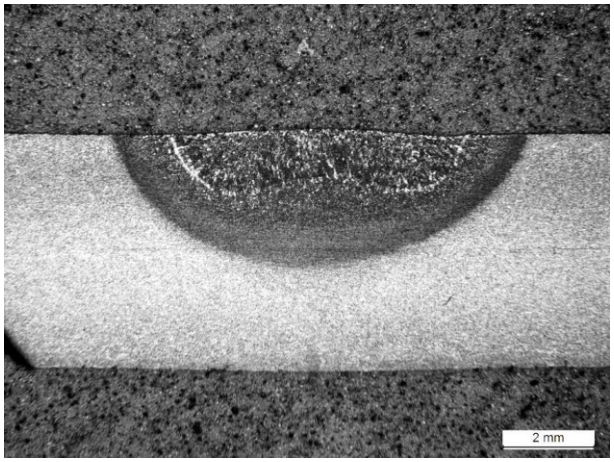

Figure 71 This micrograph of TIG welded sample 3.5.2-4 is taken with 10X ocular and 1X objective with Leica MEF 4M light microscope.

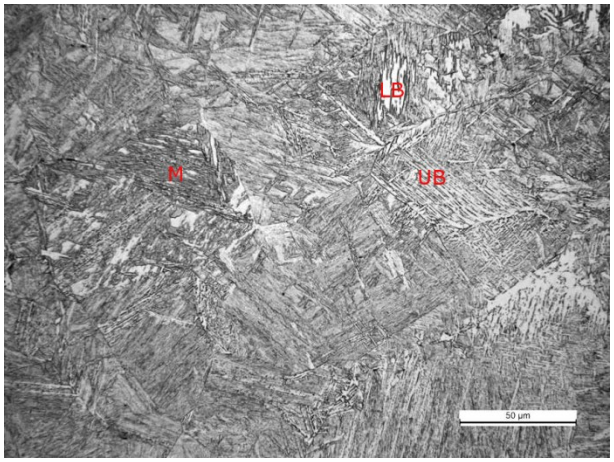

Figure 72 This micrograph of TIG welded sample 3.5.2-4 is taken with 10X ocular and 50X objective from coarse-grained zone with Leica MEF 4M light microscope. Measured maximum hardness of this microstructure is 376 HV1. Phases of this microstructure are martensite (M), lower bainite (DB) and upper bainite (HB).

Appendix 7

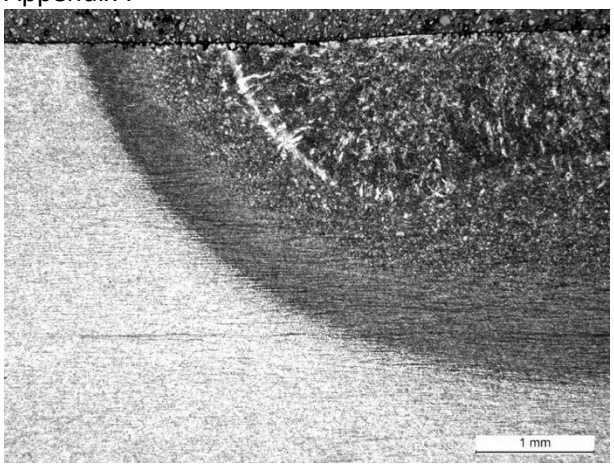

Figure 73 This micrograph of TIG welded sample 3.5.2-4 is taken with 10X ocular and 2.5X objective with Leica MEF 4M light microscope.

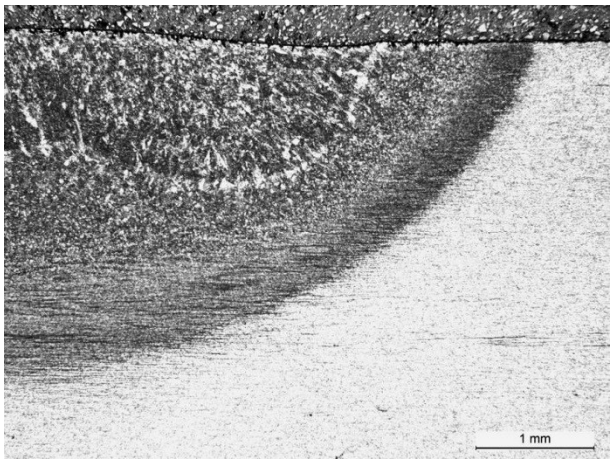

Figure 74 This micrograph of TIG welded sample 3.5.2-4 is taken with 10X ocular and 2.5X objective with Leica MEF 4M light microscope.

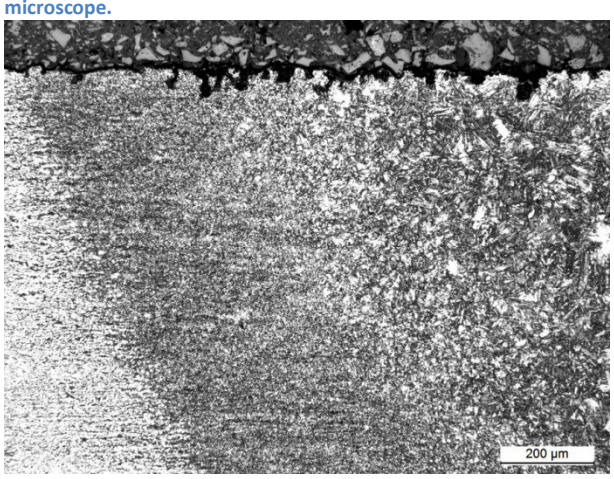

Figure 75 This micrograph of TIG welded sample 3.5.2-4 is taken with 10X ocular and 10X objective with Leica MEF 4M light microscope.

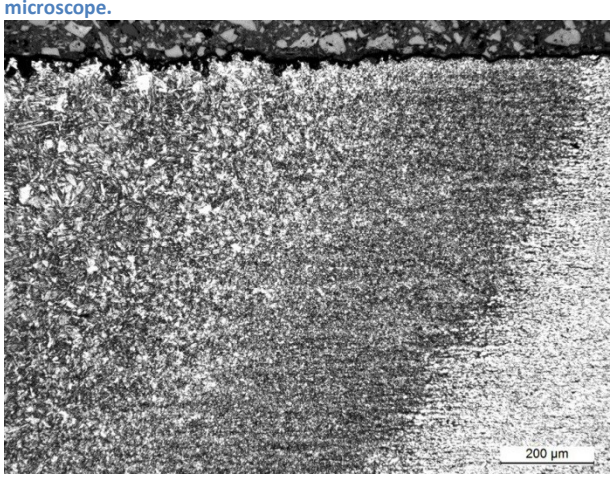

Figure 76 This micrograph of TIG welded sample 3.5.2-4 is taken with 10X ocular and 10X objective with Leica MEF 4M light microscope.

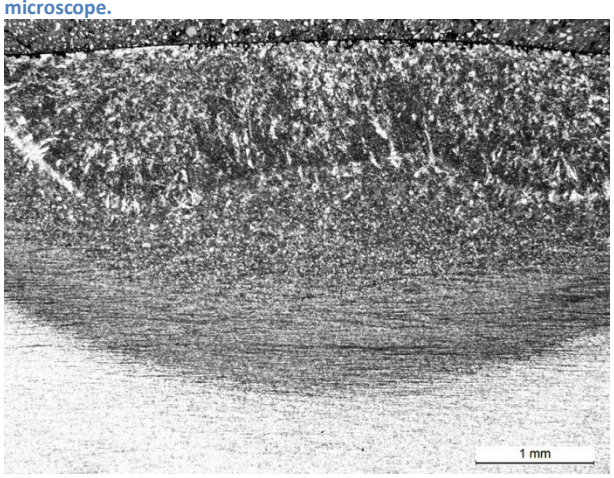

Figure 77 This micrograph of root side of TIG welded sample 3.5.2-4 is taken with 10X ocular and 2.5X objective with Leica MEF 4M light microscope.

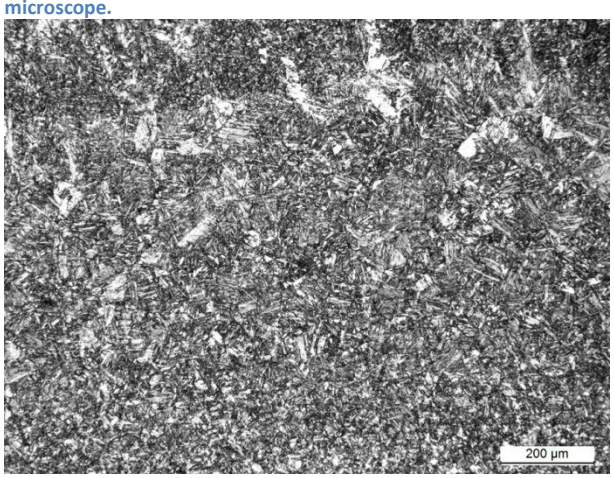

Figure 78 This micrograph of TIG welded sample 3.5.2-4 is taken on root side near fusion line with 10X ocular and 10X objective with Leica MEF 4M light microscope.

Appendix 7

TIG 3.5.2-8

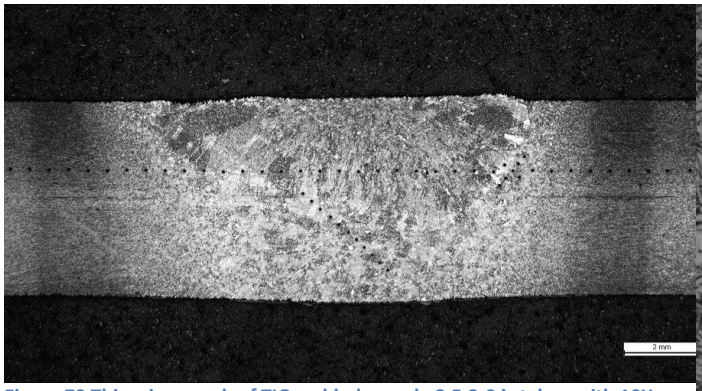

Figure 79 This micrograph of TIG welded sample 3.5.2-9 is taken with 10X ocular and 1X objective with Leica MEF 4M light microscope. The micrograph is combination of 2 macro photos which are combined with the help of the Image J.

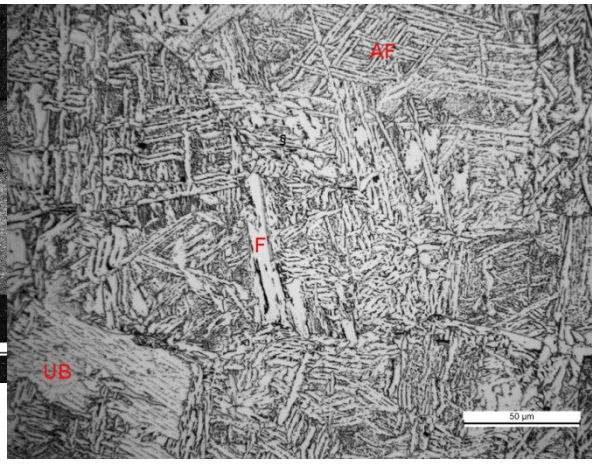

Figure 80 This micrograph of TIG welded sample 3.5.2-9 is taken with 10X ocular and 50X objective from coarse-grained zone with Leica MEF 4M light microscope. Measured maximum hardness of this microstructure is 232 HV1. Phases of this microstructure are acicular ferrite (AF) ferrite (F) and upper bainite (UB).

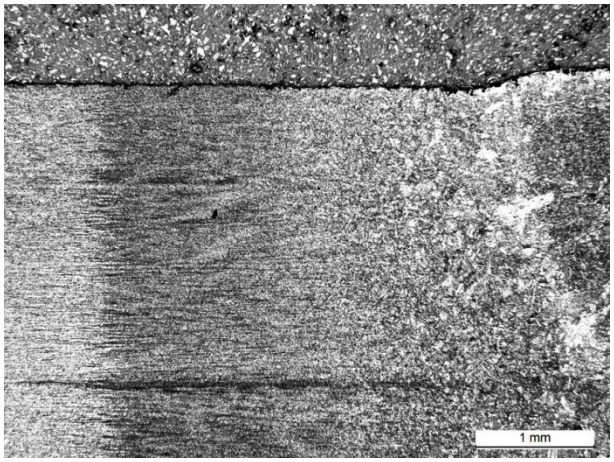

Figure 81 This micrograph of TIG welded sample 3.5.2-9 is taken with 10X ocular and 2.5X objective with Leica MEF 4M light microscope.

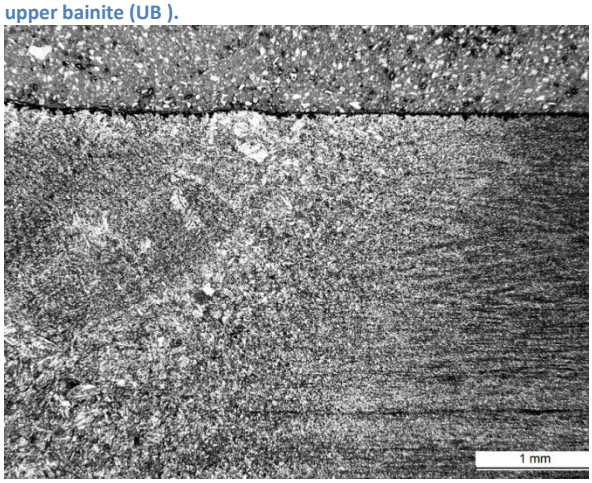

Figure 82 This micrograph of TIG welded sample 3.5.2-9 is taken with 10X ocular and 2.5X objective with Leica MEF 4M light microscope.

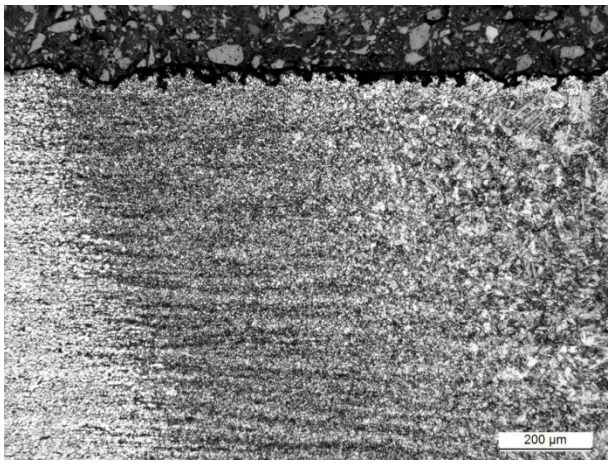

Figure 83 This micrograph of TIG welded sample 3.5.2-9 is taken with 10X ocular and 10X objective with Leica MEF 4M light microscope.

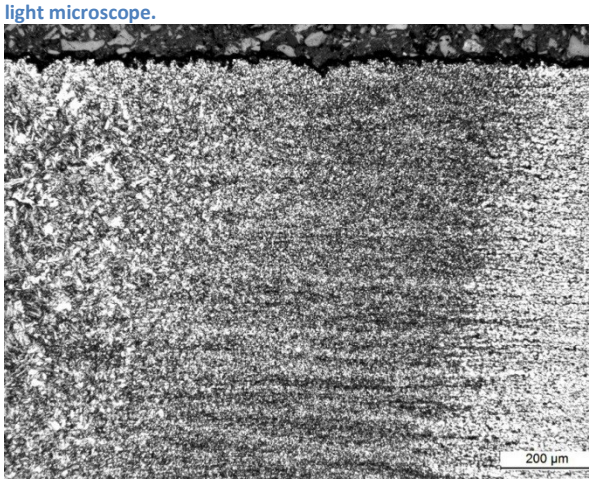

Figure 84 This micrograph of TIG welded sample 3.5.2-9 is taken with 10X ocular and 10X objective with Leica MEF 4M light microscope.

Appendix 7

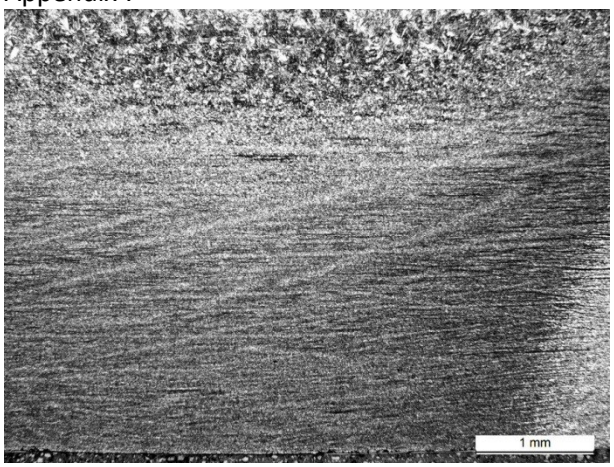

Figure 85 This micrograph of root side of TIG welded sample 3.5.2-9 is taken with 10X ocular and 2.5X objective with Leica MEF 4M light microscope.

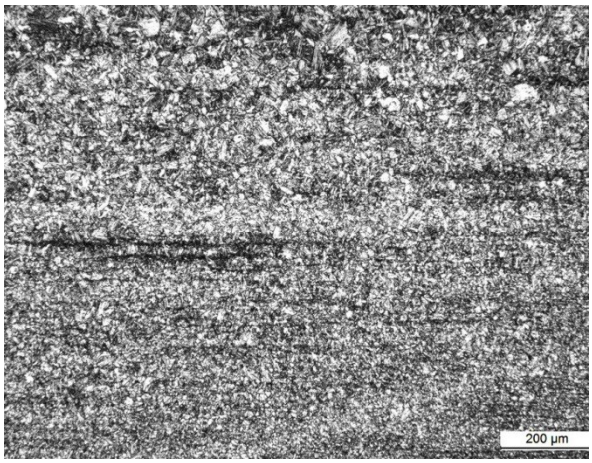

Figure 86 This micrograph of TIG welded sample root side of 3.5.2-9 is taken with 10X ocular and 10X objective with Leica MEF 4M light microscope.

TIG 3.5.2-9

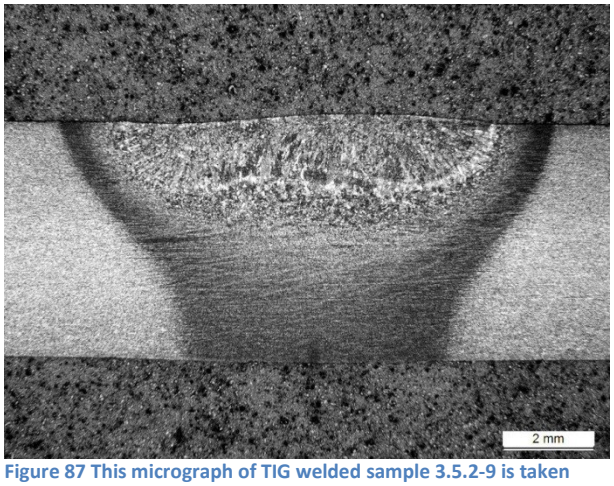

Figure 87 This micrograph of TIG welded sample 3.5.2-9 is taken with 10X ocular and 1X objective with Leica MEF 4M light microscope.

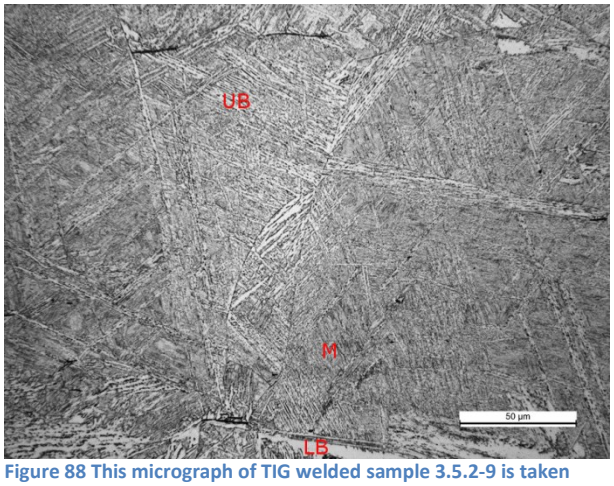

Figure 88 This micrograph of TIG welded sample 3.5.2-9 is taken with 10X ocular and 50X objective from coarse-grained zone with Leica MEF 4M light microscope. Measured maximum hardness of this microstructure is 306 HV1. Phases of this microstructure are martensite (M) lower bainite (LB) and upper bainite (UB).

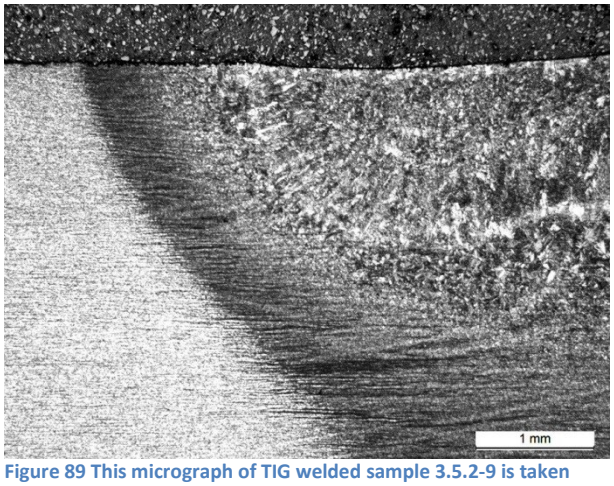

Figure 89 This micrograph of TIG welded sample 3.5.2-9 is taken with 10X ocular and 2.5X objective with Leica MEF 4M light microscope.

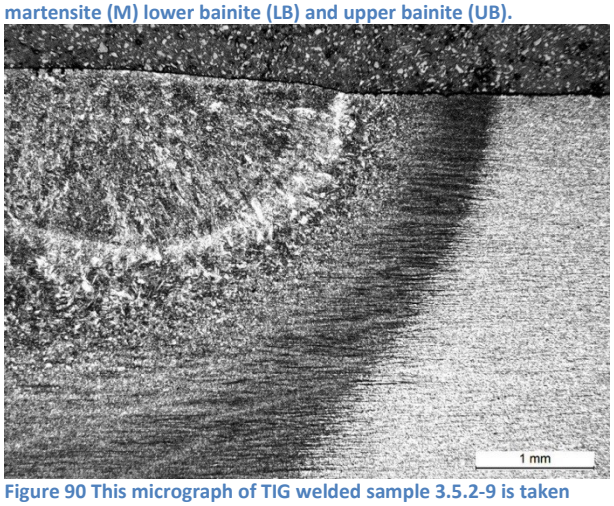

Figure 90 This micrograph of TIG welded sample 3.5.2-9 is taken with 10X ocular and 2.5X objective with Leica MEF 4M light microscope.

Appendix 7

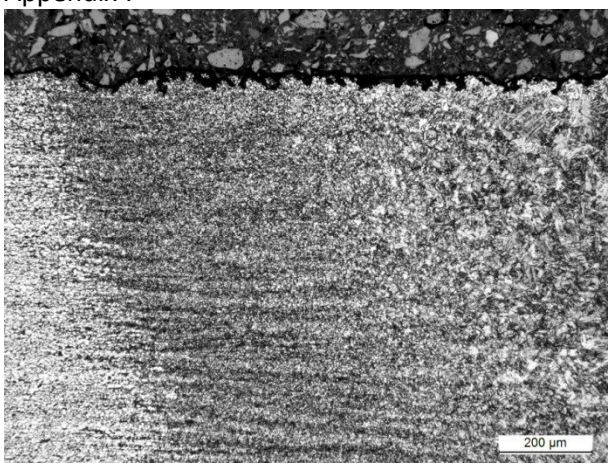

Figure 91 This micrograph of TIG welded sample 3.5.2-9 is taken with 10X ocular and 10X objective with Leica MEF 4M light microscope.

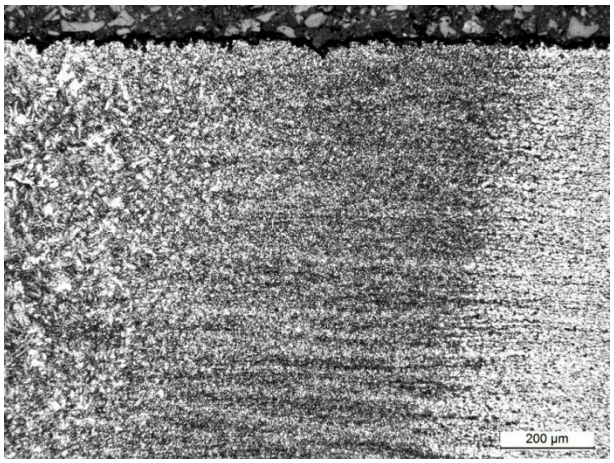

Figure 92 This micrograph of TIG welded sample 3.5.2-9 is taken with 10X ocular and 10X objective with Leica MEF 4M light microscope.

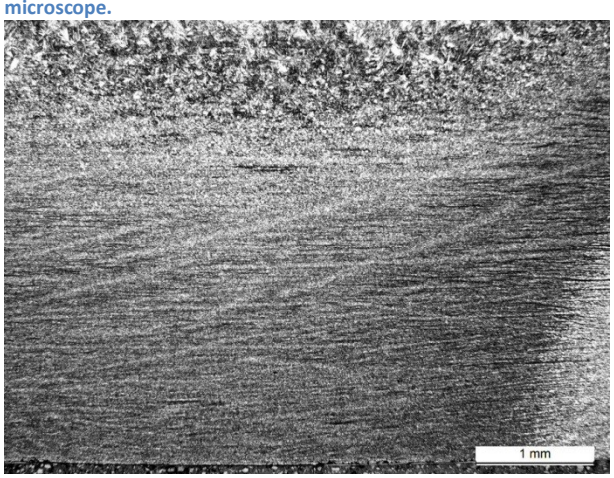

Figure 93 This micrograph of root side of TIG welded sample 3.5.2-9 is taken with 10X ocular and 2.5X objective with Leica MEF 4M light microscope.

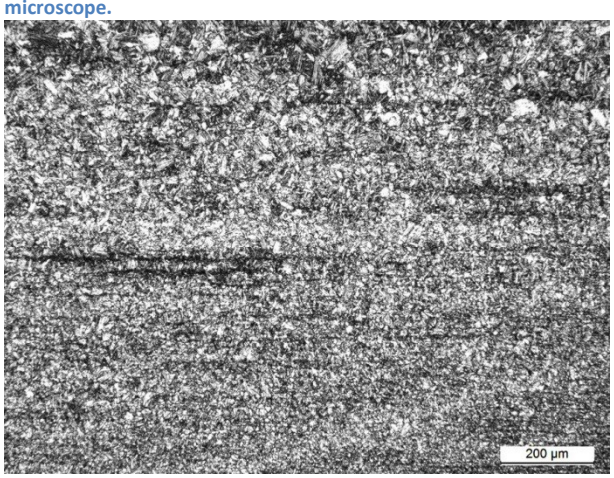

Figure 94 This micrograph of TIG welded sample root side of 3.5.2-9 is taken with 10X ocular and 10X objective with Leica MEF 4M light microscope.

Appendix 8 / EDS analysis / Cr, Ni and Fe distributions of samples 3.5.2-2, 3.5.2-3, 3.15.2-4 and 3.15.2-9

Contents

MAG 3.5.2-2

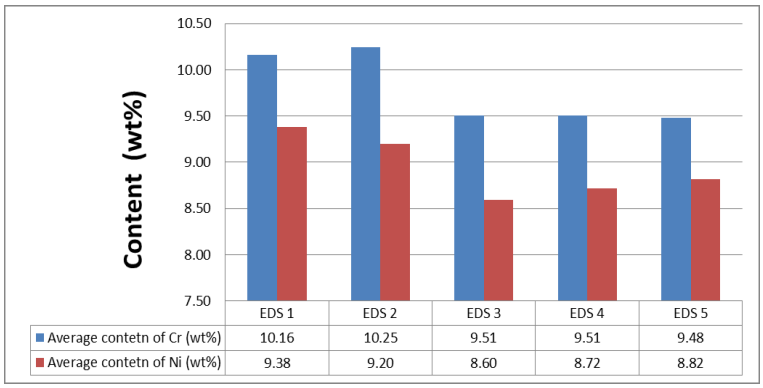

Figure 1 Average of Cr- and Ni-contents from weld metal of MAG welded sample 3.5.2-2.

Table 1 Statistical values of measuring lines of sample 3.5.2-2.

Method	(n)	stdev Cr	stdev Ni
EDS 1	128	1.16	1.36
EDS 2	233	0.92	1.22
EDS 3	47	0.87	1.19
EDS 4	78	1.05	1.31
EDS 5	38	0.85	1.39

MAG 3.5.2-2 / Measuring line 1 (EDS 1)

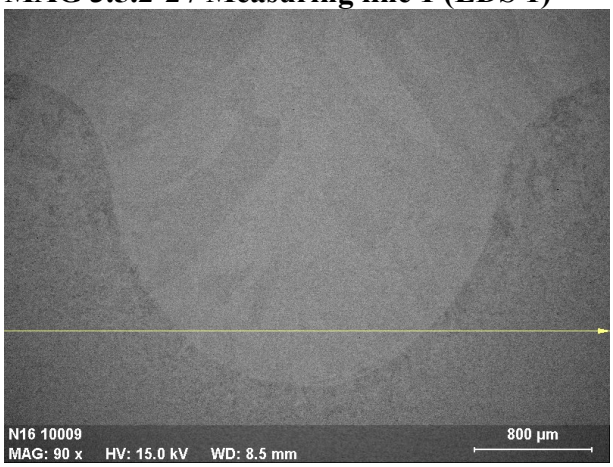

Figure 2 Position and direction of measuring line 1 (EDS 1) for MAG welded sample 3.5.2-2.

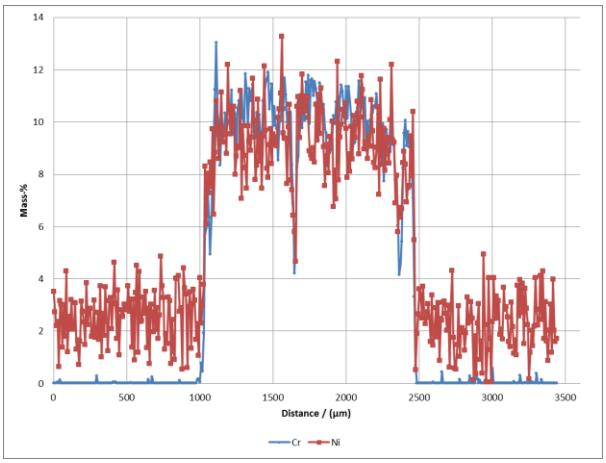

Figure 3 Measured Cr and Ni distribution of measuring line 1.

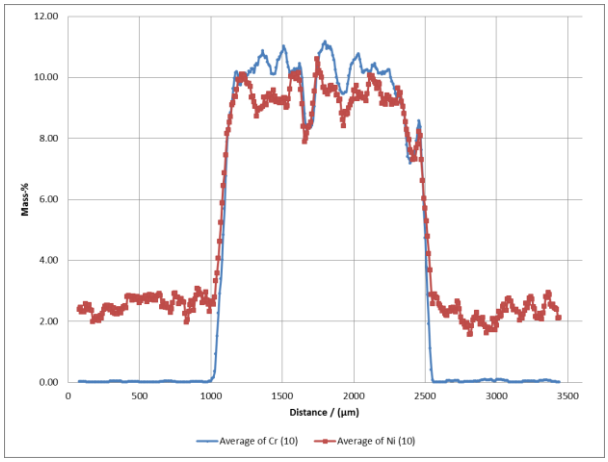

Figure 4 Moving average of Cr and Ni distribution of measuring line 1(n=10).

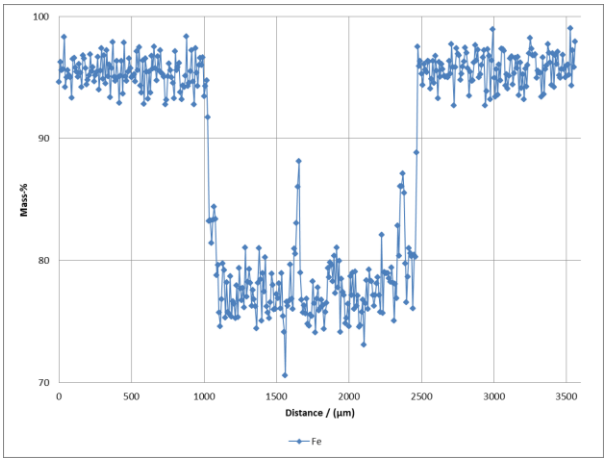

Figure 5 Measured Fe distribution of measuring line 1.

MAG 3.5.2-2 / Measuring line 2 (EDS 2)

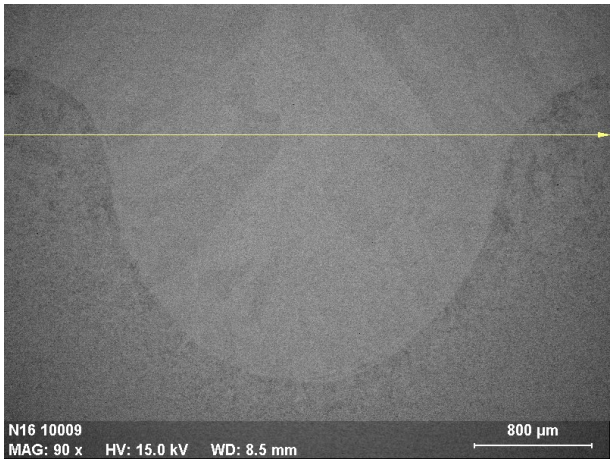

Figure 6 Position and direction of measuring line 2 (EDS 2) for MAG welded sample 3.5.2-2.

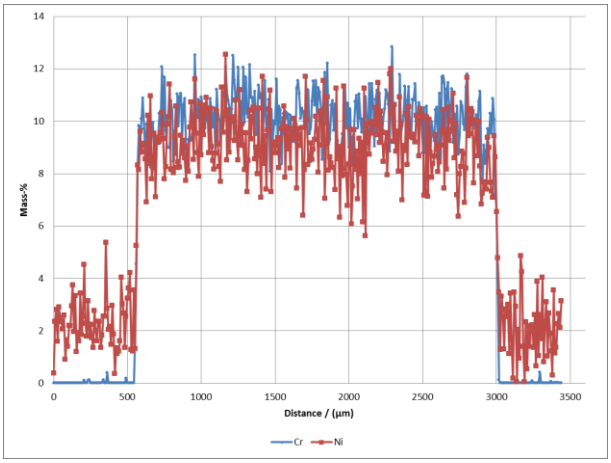

Figure 7 Measured Cr and Ni distribution of measuring line 2.

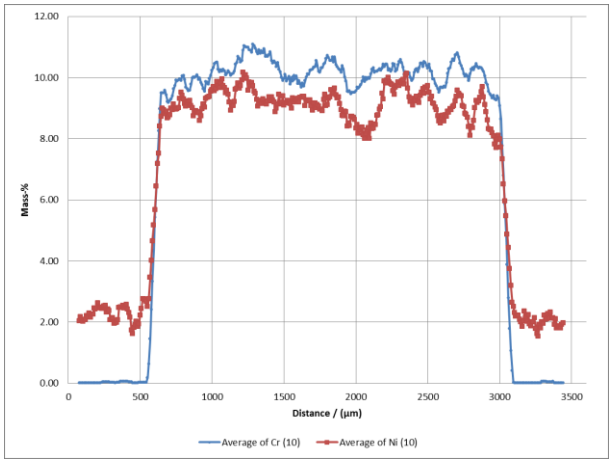

Figure 8 Moving average of Cr and Ni distribution of measuring line 2 (n=10).

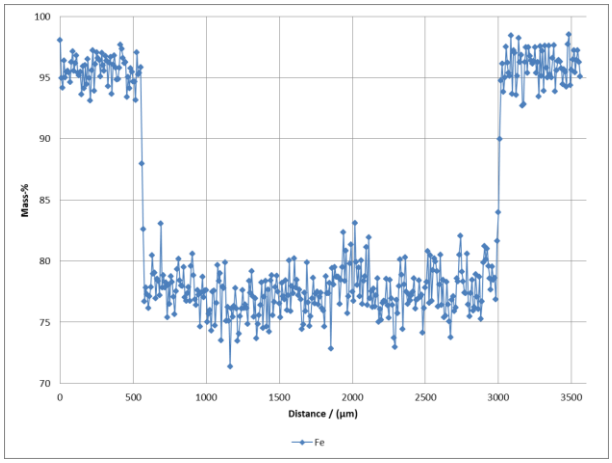

Figure 9 Measured Fe distribution of measuring line 2.

MAG 3.5.2-2 / Measuring line 3 (EDS 3)

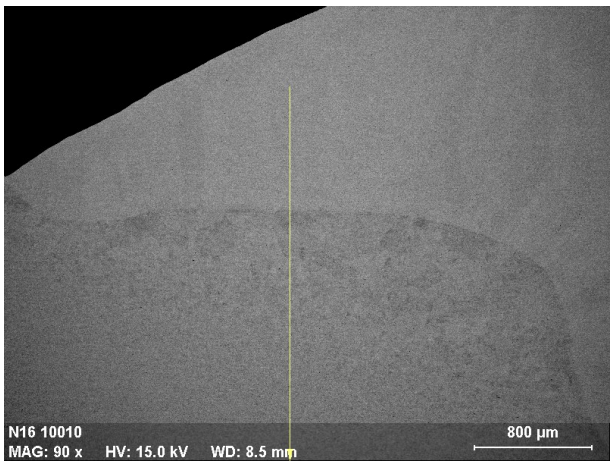

Figure 10 Position and direction of measuring line 3 (EDS 3) for MAG welded sample 3.5.2-2.

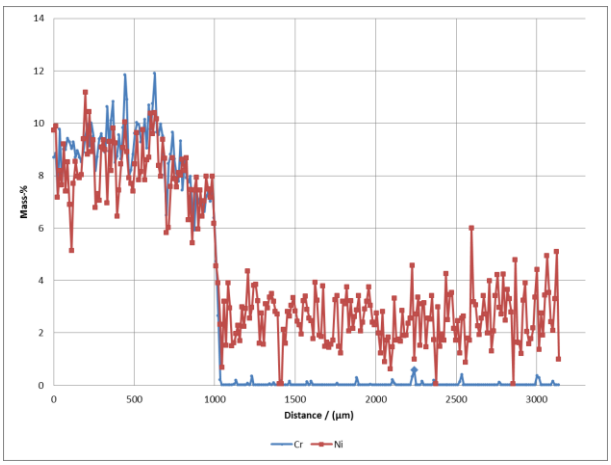

Figure 11 Measured Cr and Ni distribution of measuring line 3.

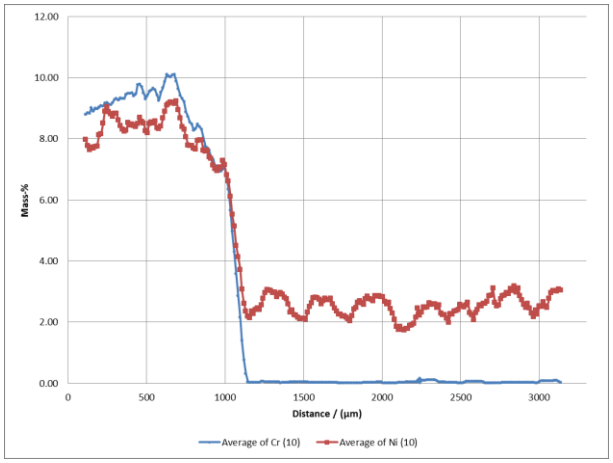

Figure 12 Moving average of Cr and Ni distribution of measuring line 3 (n=10).

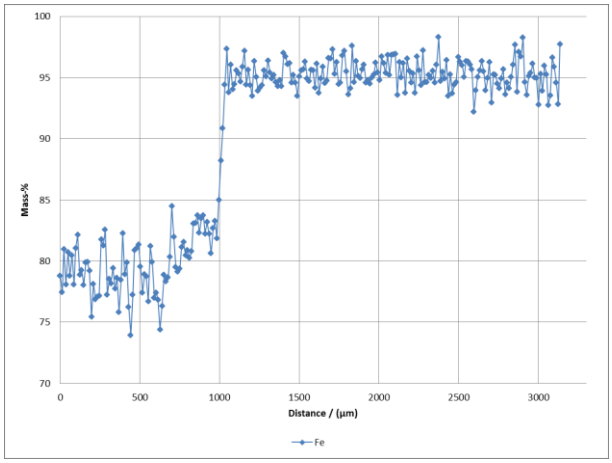

Figure 13 Measured Fe distribution of measuring line 3.

MAG 3.5.2-2 / Measuring line 4 (EDS 4)

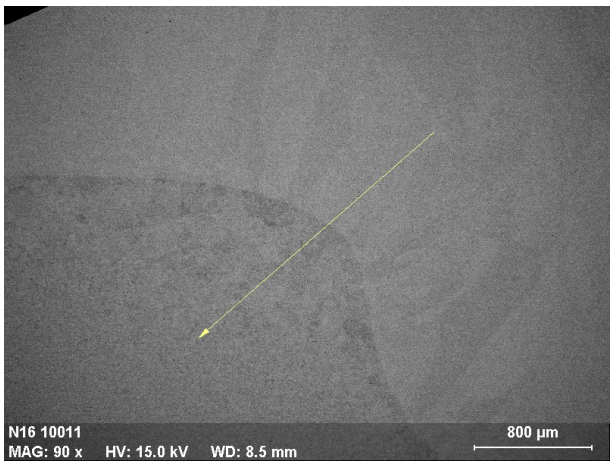

Figure 14 Position and direction of measuring line 4 (EDS 4) for MAG welded sample 3.5.2-2.

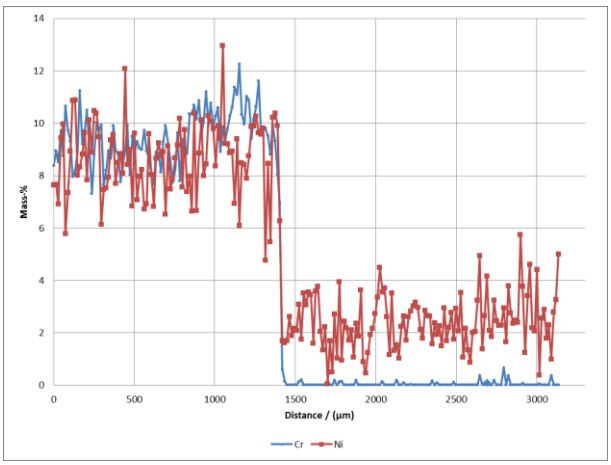

Figure 15 Measured Cr and Ni distribution of measuring line 4.

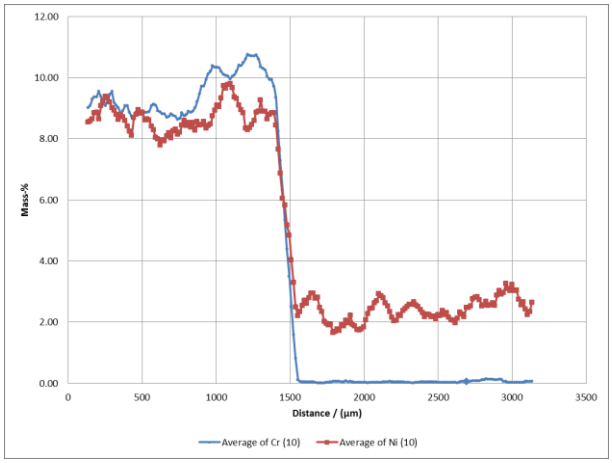

Figure 16 Moving average of Cr and Ni distribution of measuring line 4 (n=10).

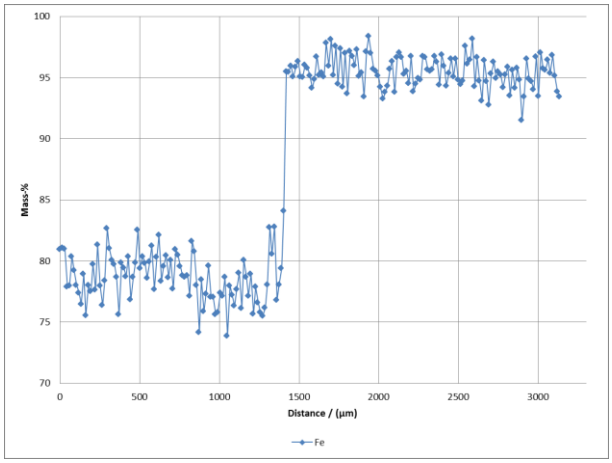

Figure 17 Measured Fe distribution of measuring line 4.

MAG 3.5.2-2 / Measuring line 5 (EDS 5)

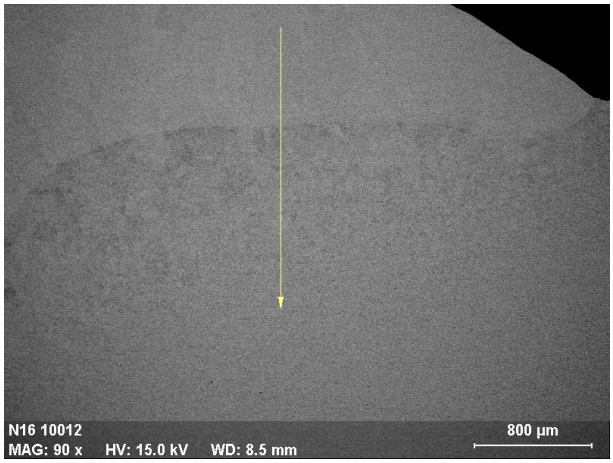

Figure 18 Position and direction of measuring line 5 (EDS 5) for MAG welded sample 3.5.2-2.

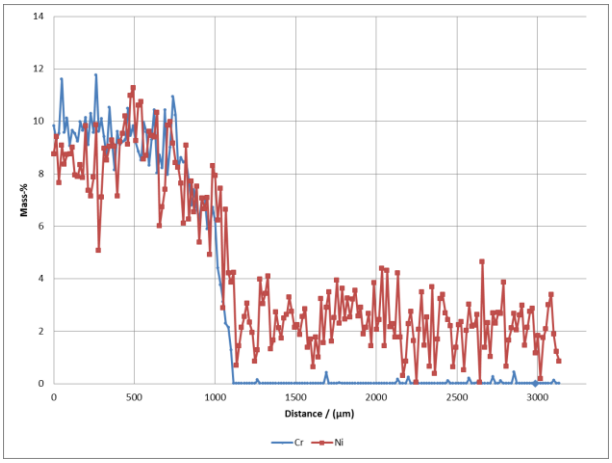

Figure 19 Measured Cr and Ni distribution of measuring line 5.

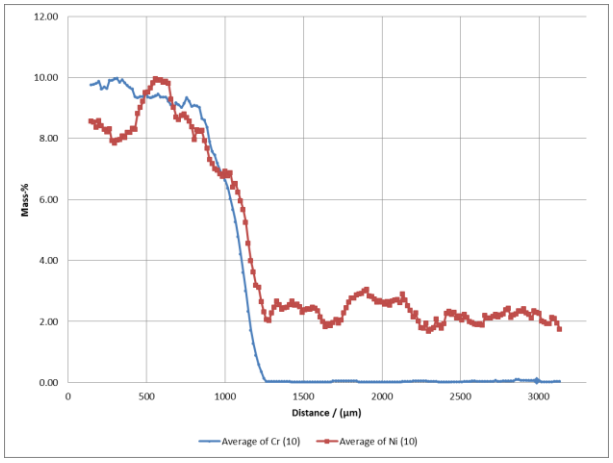

Figure 20 Moving average of Cr and Ni distribution of measuring line 5 (n=10).

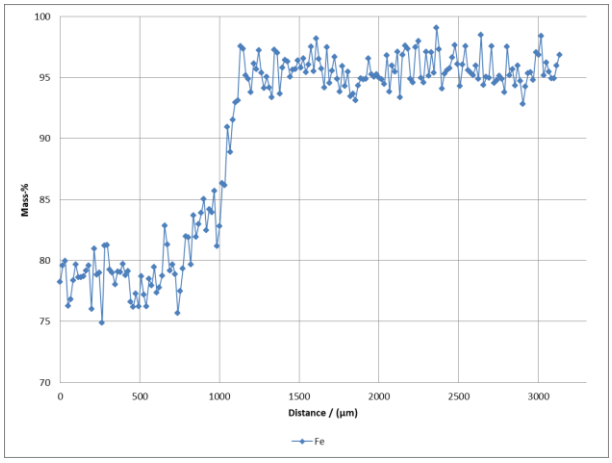

Figure 21 Measured Fe distribution of measuring line 5.

MAG 3.15.2-4

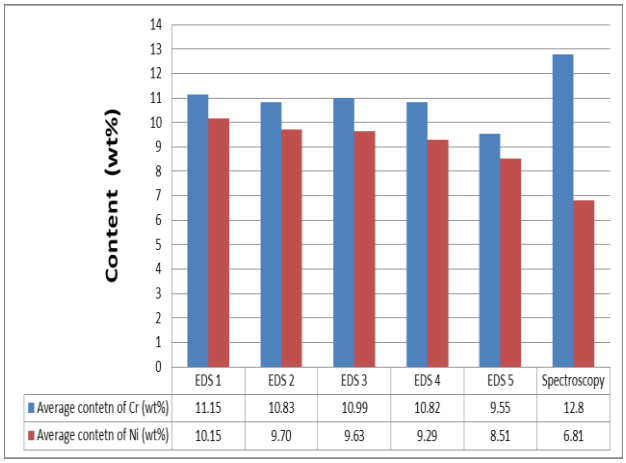

Figure 22 Average of Cr- and Ni-contents from weld metal of MAG welded sample 3.15.2-4.

Table 2 Statistical values of measuring lines of sample 3.15.2-4.

Method	(n)	Standard deviation Cr	Standard deviation Ni
EDS 1	154	0.91	1.20
EDS 2	222	0.92	1.32
EDS 3	54	0.82	1.16
EDS 4	92	0.88	1.19
EDS 5	54	0.91	1.19

MAG 3.15.2-4 / Measuring line 1 (EDS 1)

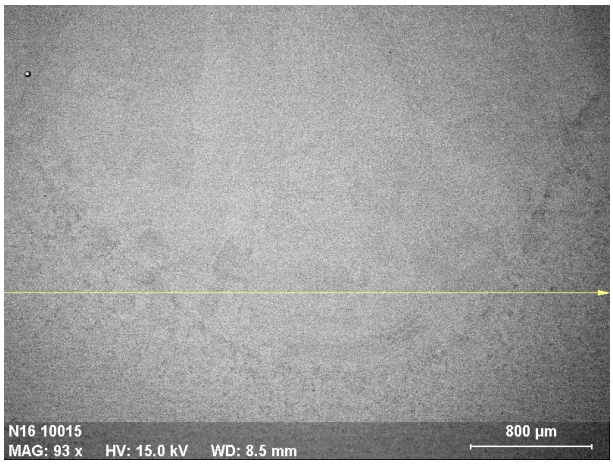

Figure 23 Position and direction of measuring line 1 (EDS 1) for MAG welded sample 3.15.2-4.

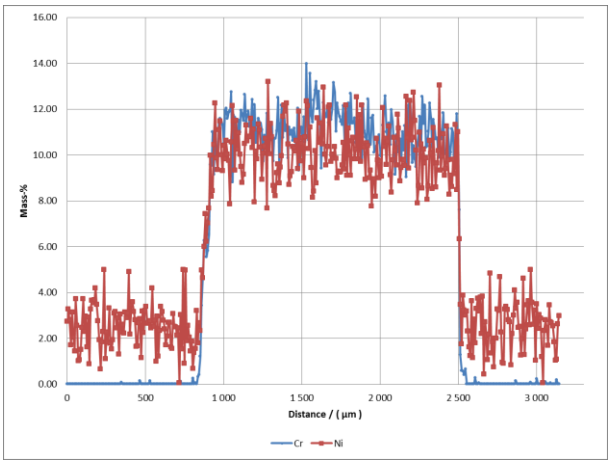

Figure 24 Measured Cr and Ni distribution of measuring line 1.

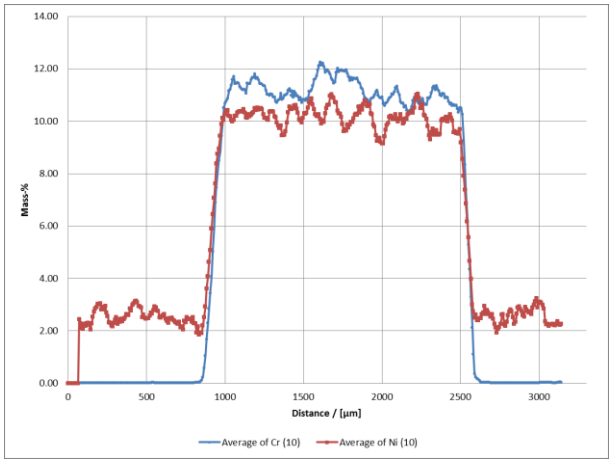

Figure 25 Moving average of Cr and Ni distribution of measuring line 1 (n=10).

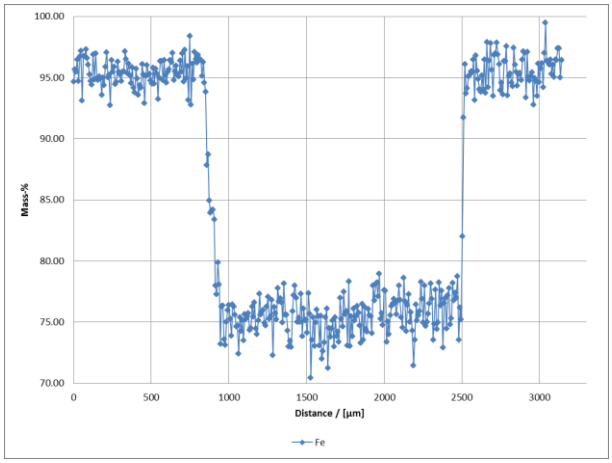

Figure 26 Measured Fe distribution of measuring line 1.

MAG 3.15.2-4 / Measuring line 2 (EDS 2)

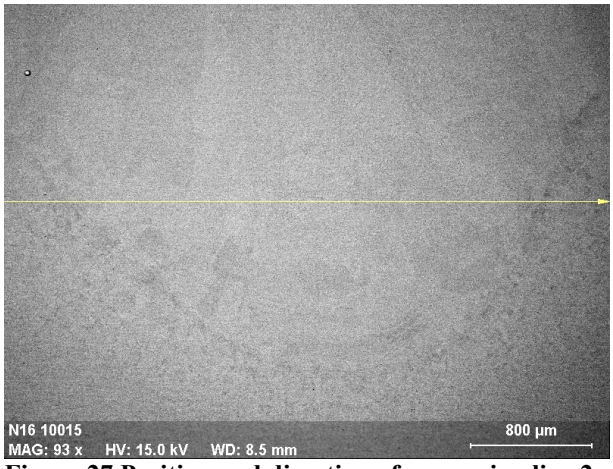

Figure 27 Position and direction of measuring line 2 (EDS 2) for MAG welded sample 3.15.2-4.

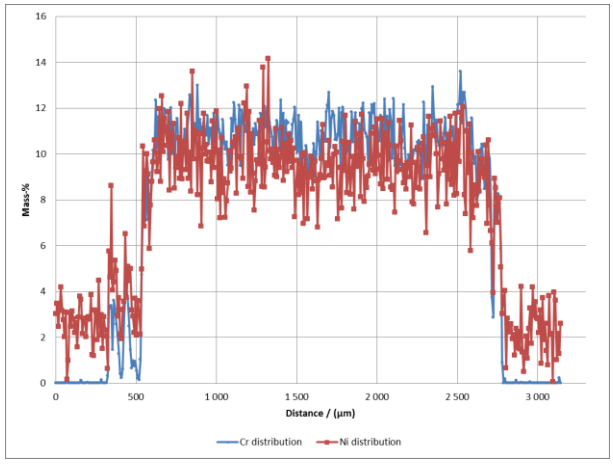

Figure 28 Measured Cr and Ni distribution of measuring line 2.

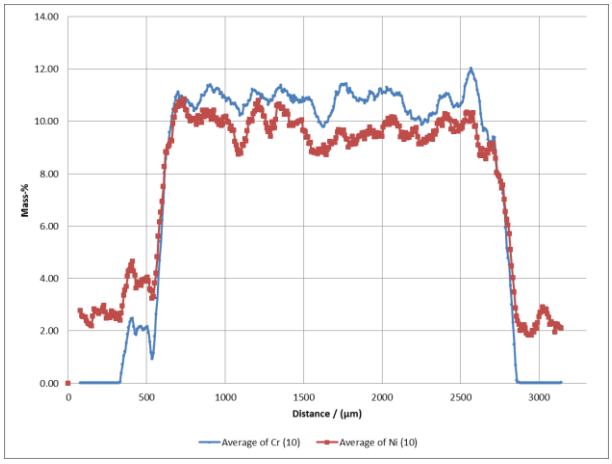

Figure 29 Moving average of Cr and Ni distribution of measuring line 2 (n=10).

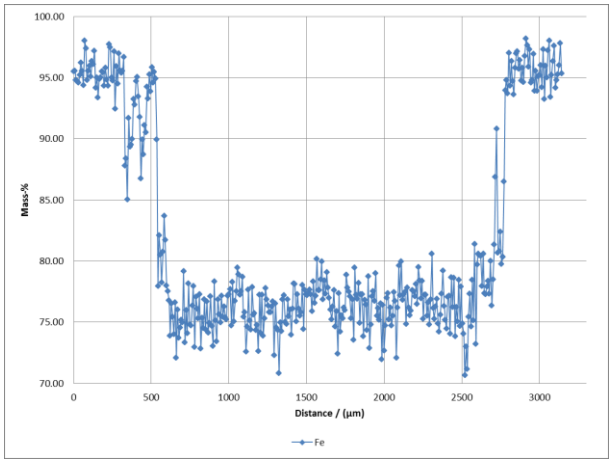

Figure 30 Measured Fe distribution of measuring line 2.

MAG 3.15.2-4 / Measuring line 3 (EDS 3)

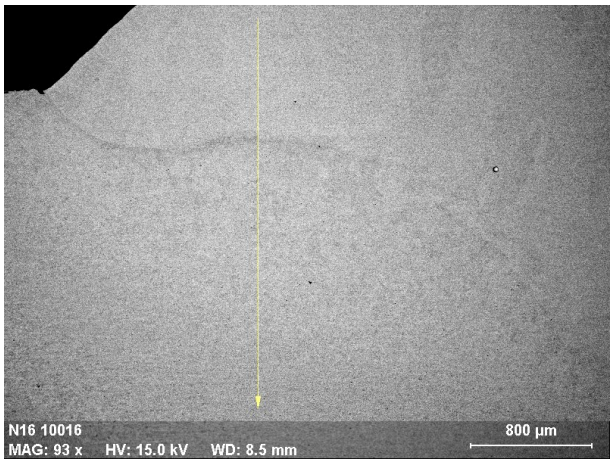

Figure 31 Position and direction of measuring line 3 (EDS 3) for MAG welded sample 3.15.2-4.

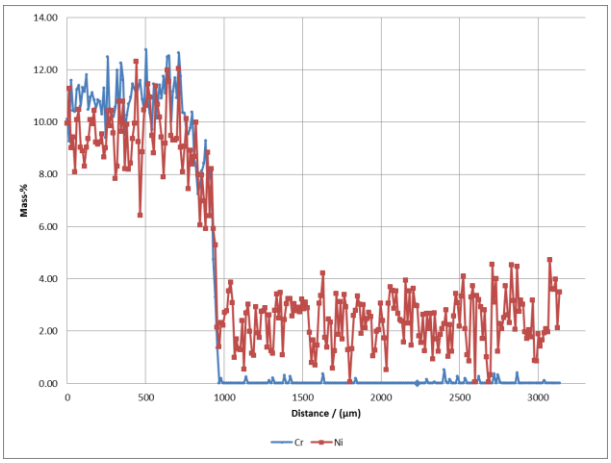

Figure 32 Measured Cr and Ni distribution of measuring line 3.

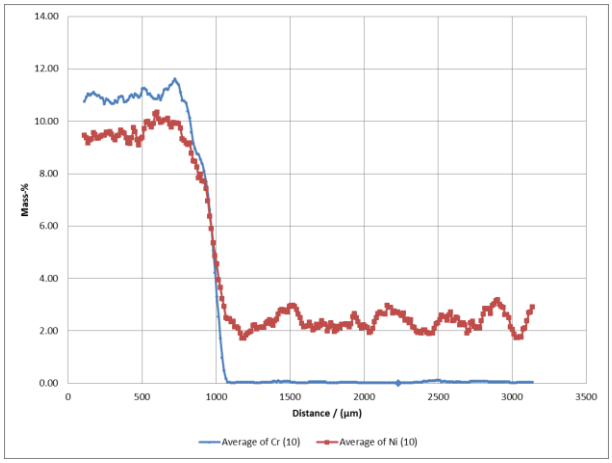

Figure 33 Moving average of Cr and Ni distribution of measuring line 3 (n=10).

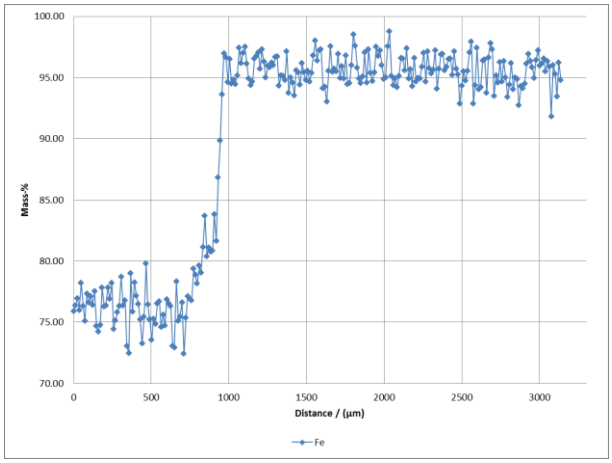

Figure 34 Measured Fe distribution of measuring line 3.

MAG 3.15.2-4 / Measuring line 4 (EDS 4)

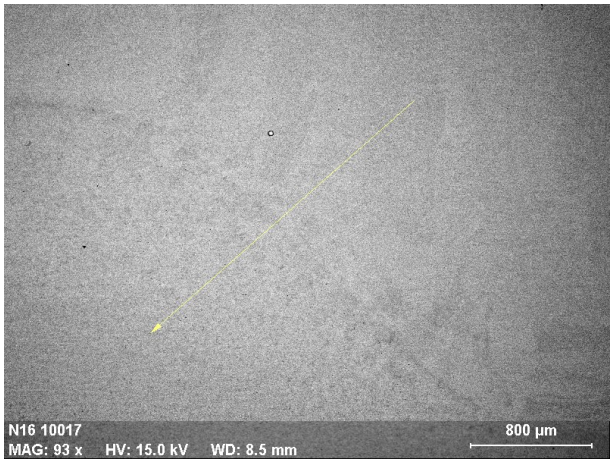

Figure 35 Position and direction of measuring line 4 (EDS 4) for MAG welded sample 3.15.2-4.

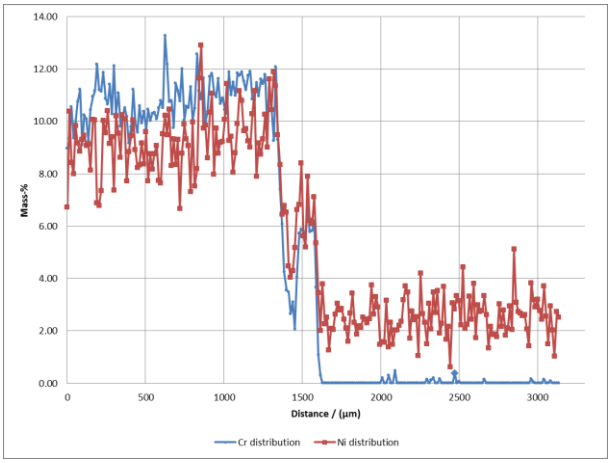

Figure 36 Measured Cr and Ni distribution of measuring line 4.

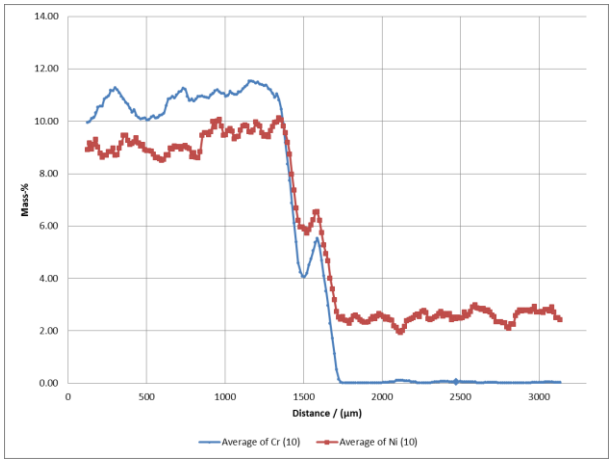

Figure 37Moving average of Cr and Ni distribution of measuring line 4 (n=10).

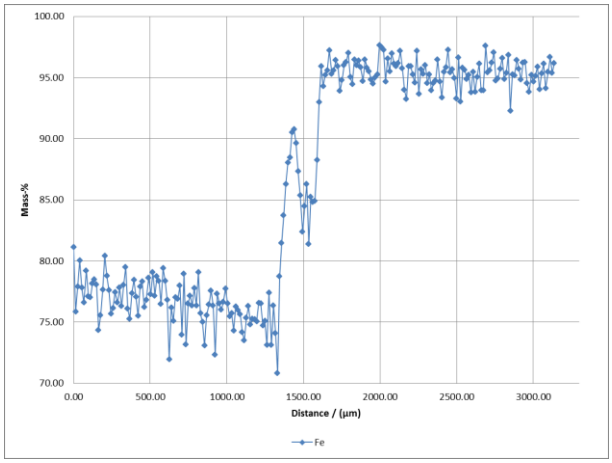

Figure 38 Measured Fe distribution of measuring line 4.

MAG 3.15.2-4 / Measuring line 5 (EDS 5)

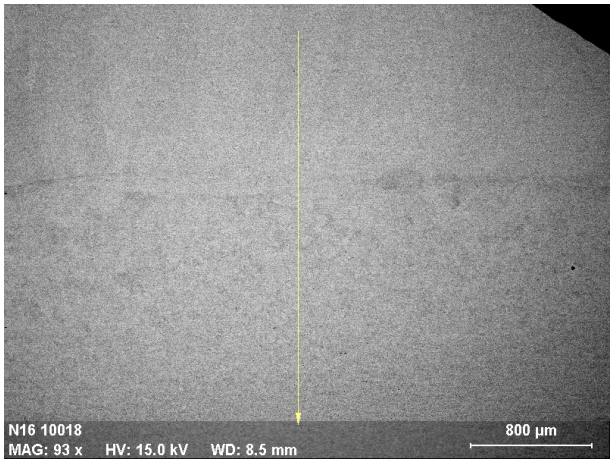

Figure 39 Position and direction of measuring line 5 (EDS 5) for MAG welded sample 3.15.2-4.

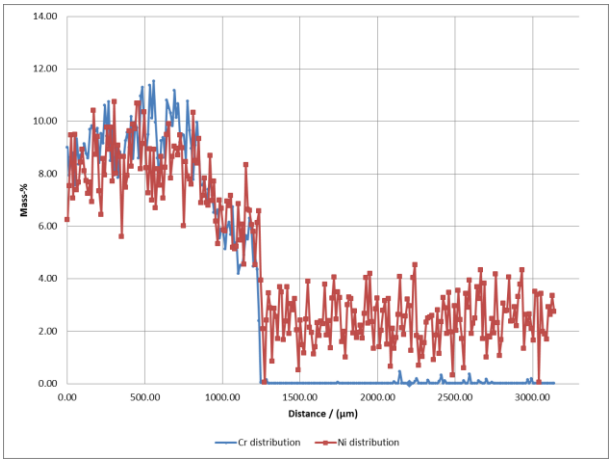

Figure 40 Measured Cr and Ni distribution of measuring line 5.

Figure 41 Moving average of Cr and Ni distribution of measuring line 5 (n=10).

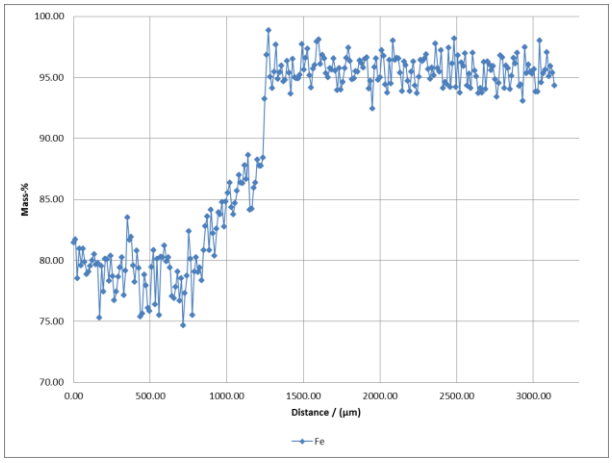

Figure 42 Measured Fe distribution of measuring line 5.

LAHW 3.5.2-3

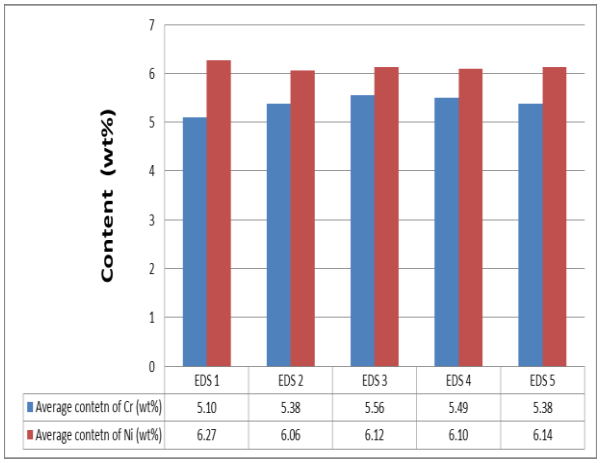

Figure 43 Average of Cr- and Ni-contents from weld metal of LAHW welded sample 3.5.2-3.

Table 3 Statistical values of measuring lines of sample 3.5.2-3.

Method	(n)	stdev Cr	stdev Ni
EDS 1	75	0.38	0.46
EDS 2	220	0.67	1.16
EDS 3	138	0.58	1.24
EDS 4	112	0.61	1.09
EDS 5	126	0.58	1.19

LAHW 3.5.2-3 / Measuring line 1 (EDS 1)

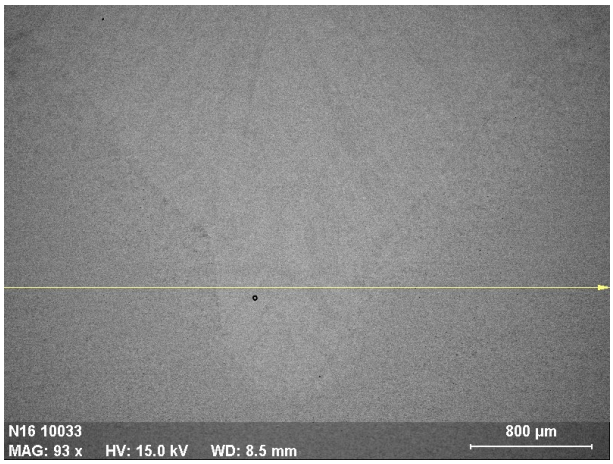

Figure 44 Position and direction of measuring line 1 (EDS 1) for LAHW welded sample 3.5.2-3.

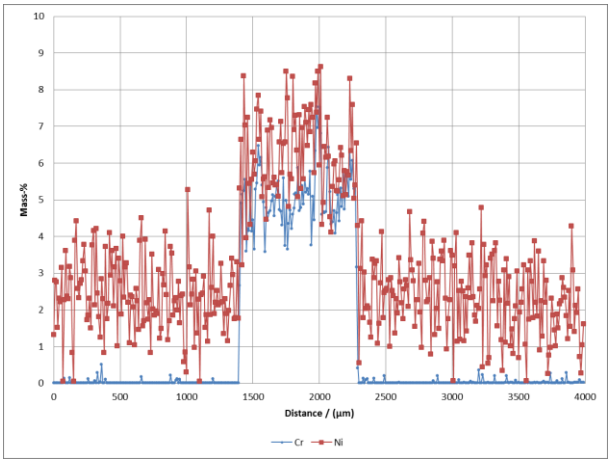

Figure 45 Measured Cr and Ni distribution of measuring line 1.

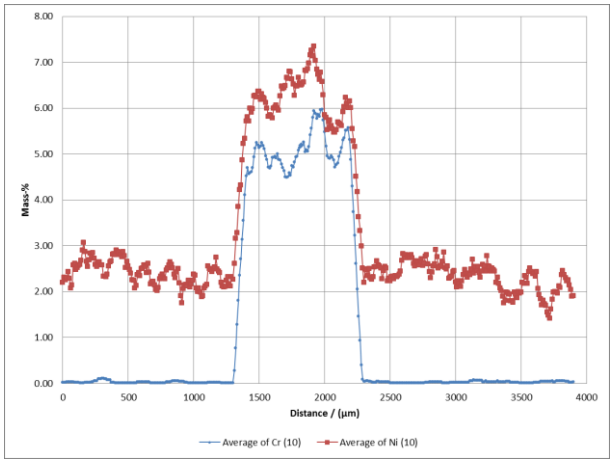

Figure 46 Moving average of Cr and Ni distribution of measuring line 1 (n=10).

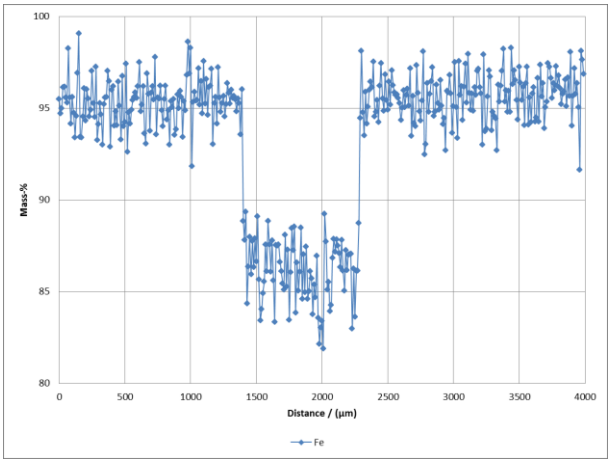

Figure 47 Measured Fe distribution of measuring line 1.

LAHW 3.5.2-3 / Measuring line 2 (EDS 2)

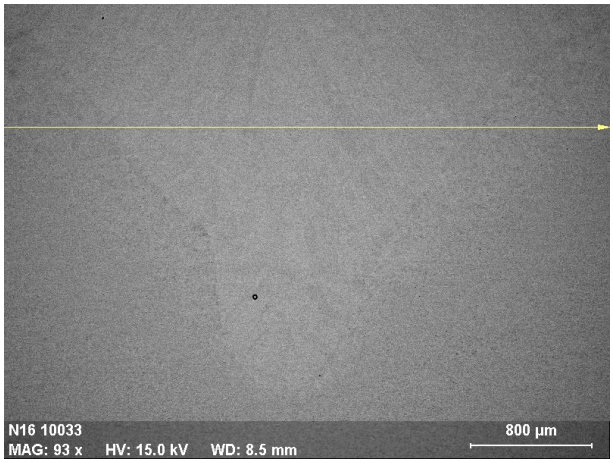

Figure 48 Position and direction of measuring line 2 (EDS 2) for LAHW welded sample 3.5.2-3.

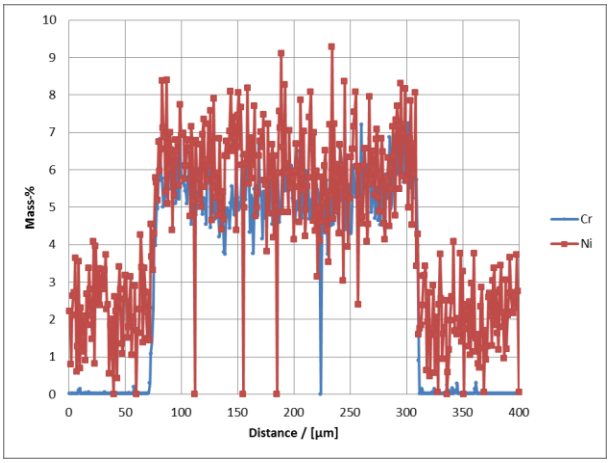

Figure 49 Measured Cr and Ni distribution of measuring line 2.

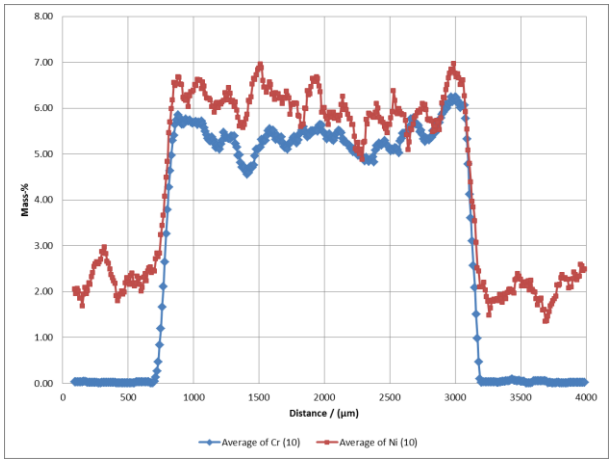

Figure 50 Moving average of Cr and Ni distribution of measuring line 2 (n=10).

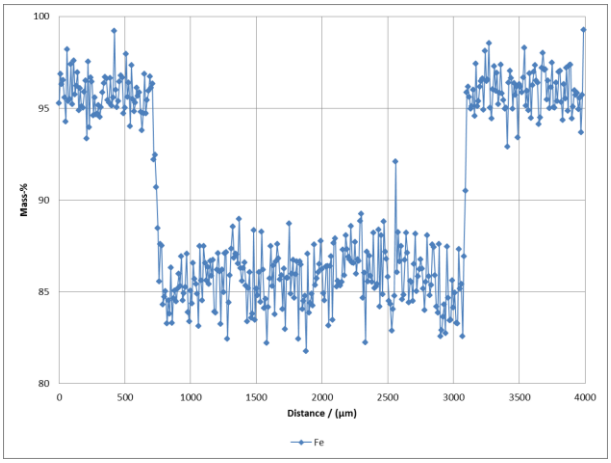

Figure 51 Measured Fe distribution of measuring line 2.

LAHW 3.5.2-3 / Measuring line 3 (EDS 3)

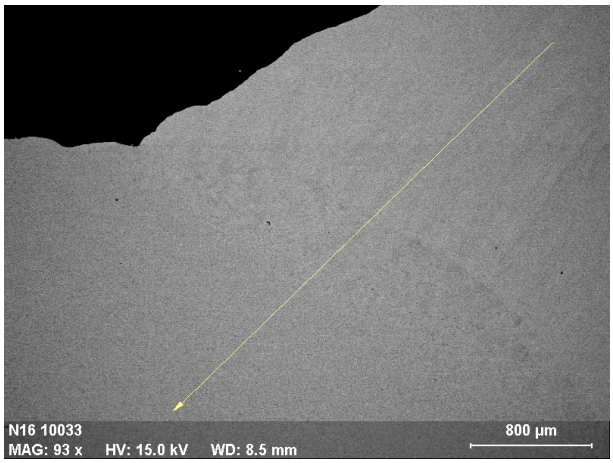

Figure 52 Position and direction of measuring line 3 (EDS 3) for LAHW welded sample 3.5.2-3.

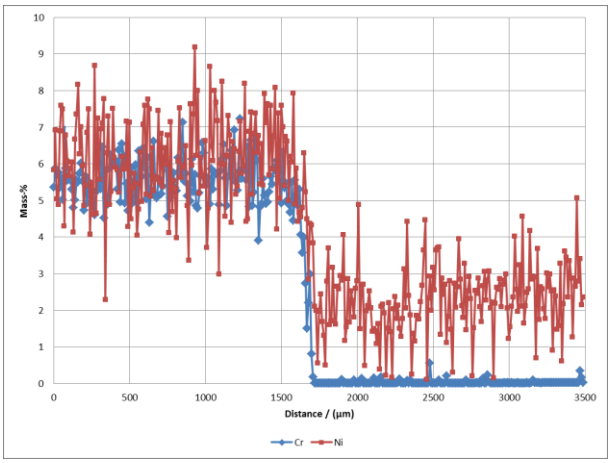

Figure 53 Measured Cr and Ni distribution of measuring line 3.

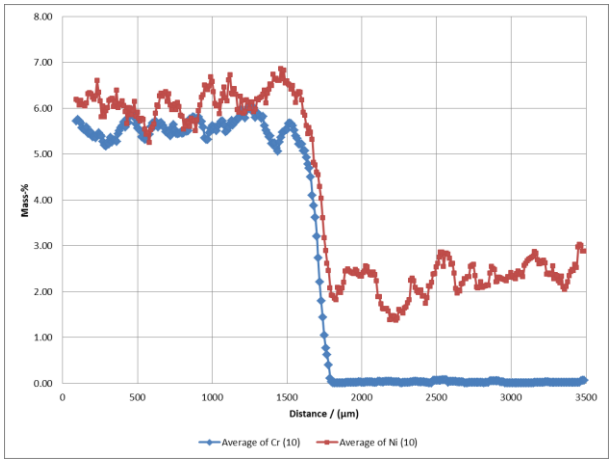

Figure 54 Moving average of Cr and Ni distribution of measuring line 3 (n=10).

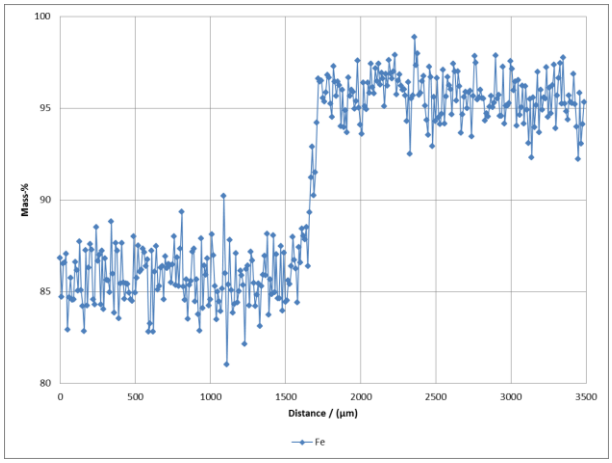

Figure 55 Measured Fe distribution of measuring line 3.

LAHW 3.5.2-3 / Measuring line 4 (EDS 4)

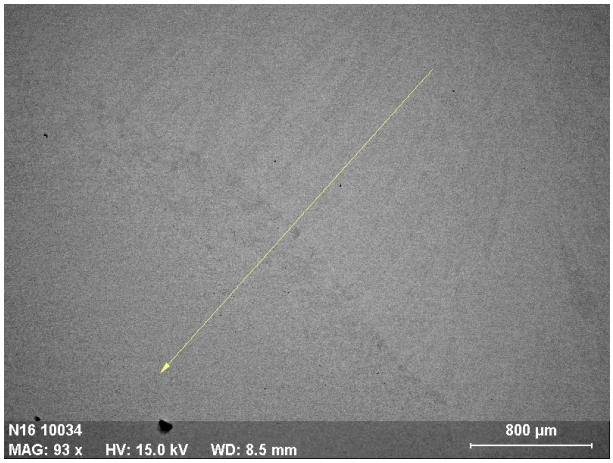

Figure 56 Position and direction of measuring line 4 (EDS 4) for LAHW welded sample 3.5.2-3.

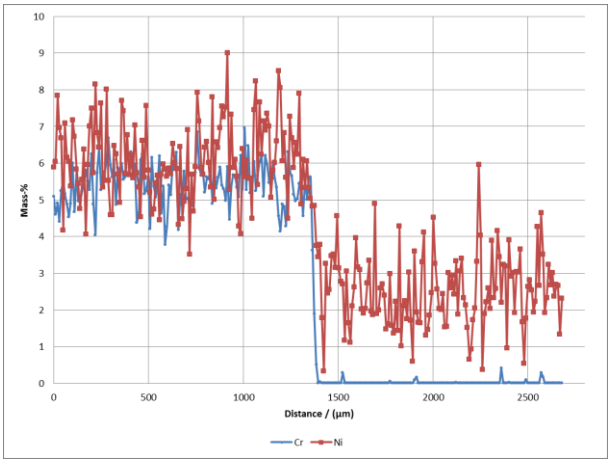

Figure 57 Measured Cr and Ni distribution of measuring line 4.

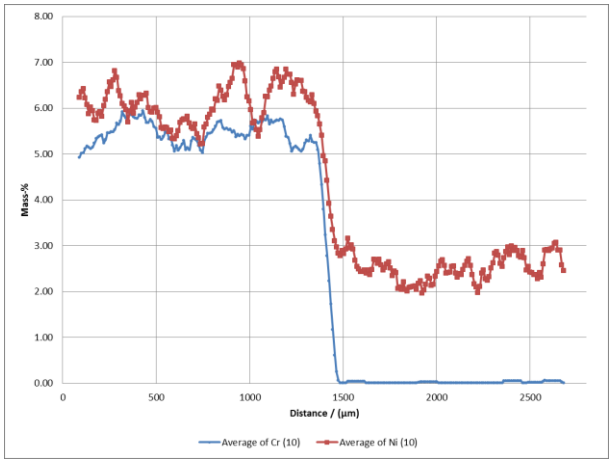

Figure 58 Moving average of Cr and Ni distribution of measuring line 4 (n=10).

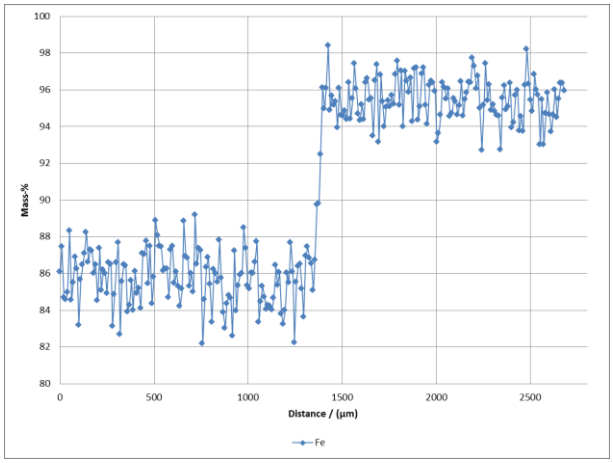

Figure 59 Measured Fe distribution of measuring line 4.

LAHW 3.5.2-3 / Measuring line 5 (EDS 5)

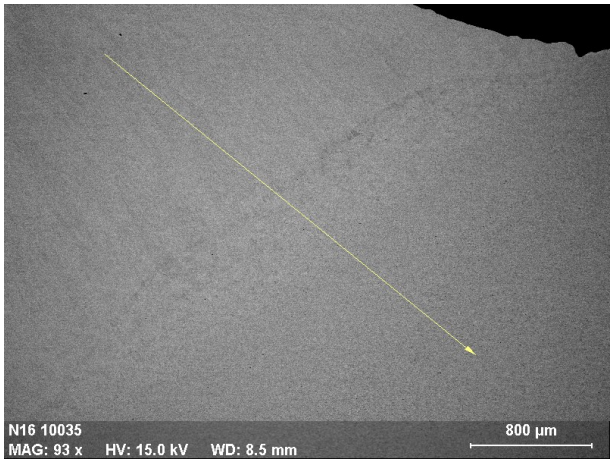

Figure 60 Position and direction of measuring line 5 (EDS 5) for LAHW welded sample 3.5.2-3.

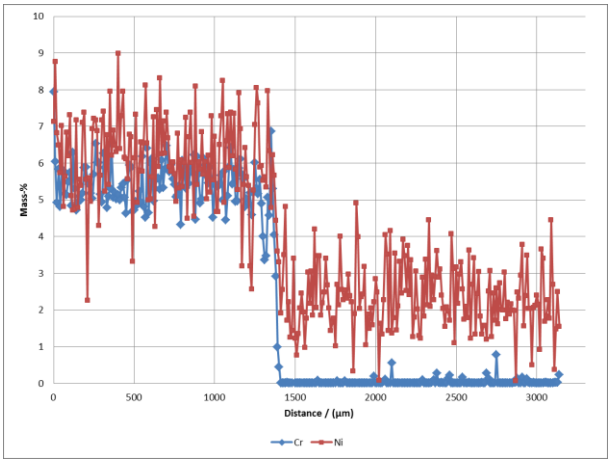

Figure 61 Measured Cr and Ni distribution of measuring line 5.

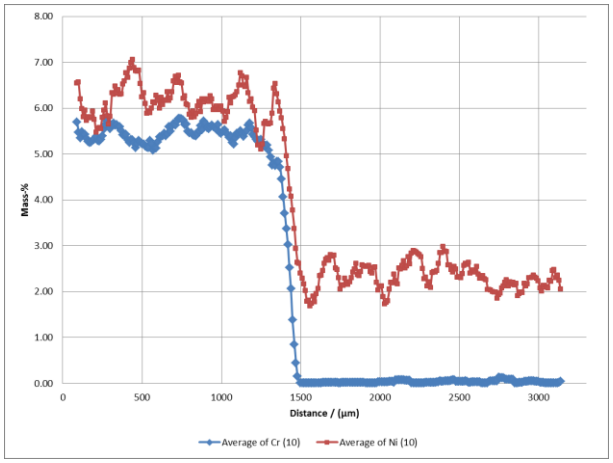

Figure 62 Moving average of Cr and Ni distribution of measuring line 5 (n=10).

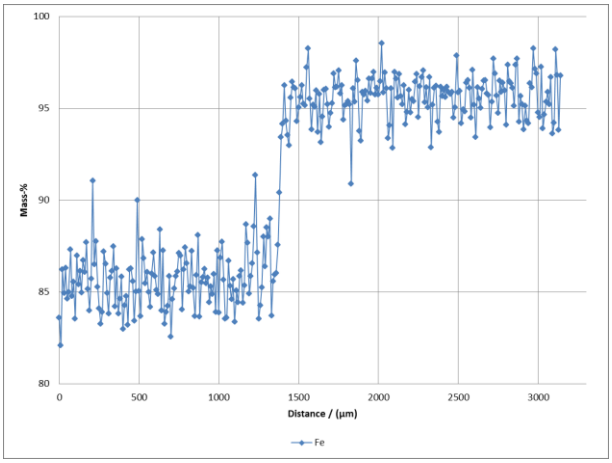

Figure 63 Measured Fe distribution of measuring line 5.

LAHW 3.15.2-9

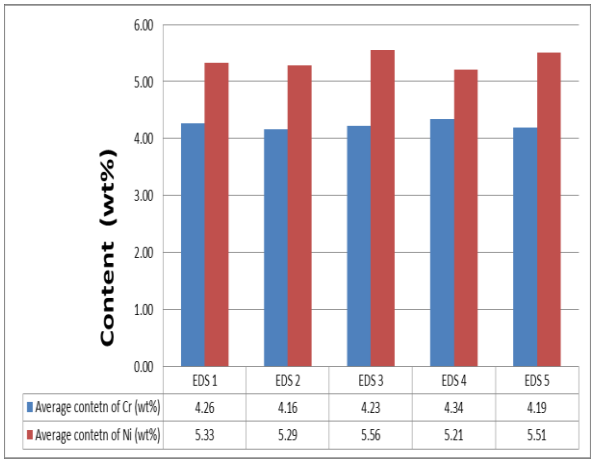

Figure 64 Average of Cr- and Ni-contents from weld metal of LAHW welded sample 3.15.2-9.

Table 4 Statistical values of measuring lines of sample 3.15.2-9.

Method	(n)	stdev Cr	stdev Ni
EDS 1	53	0.54	1.31
EDS 2	85	1.12	1.27
EDS 3	131	0.46	1.24
EDS 4	137	0.48	0.96
EDS 5	94	0.58	1.10

LAHW 3.15.2-9 / Measuring line 1 (EDS 1)

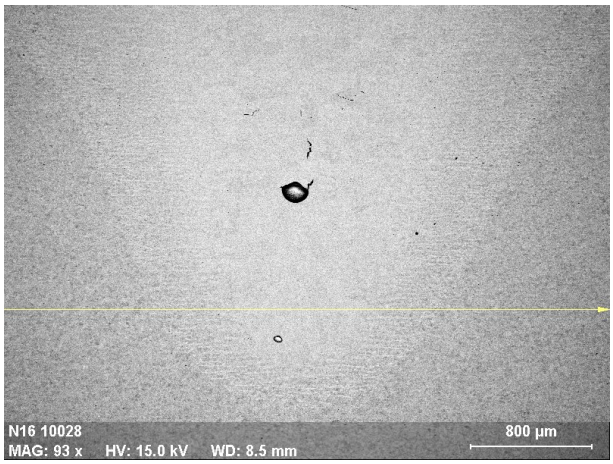

Figure 65 Position and direction of measuring line 1 (EDS 1) for LAHW welded sample 3.15.2-9.

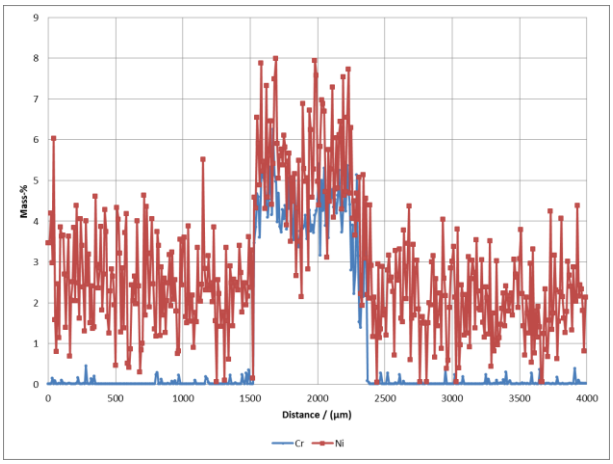

Figure 66 Measured Cr and Ni distribution of measuring line 1.

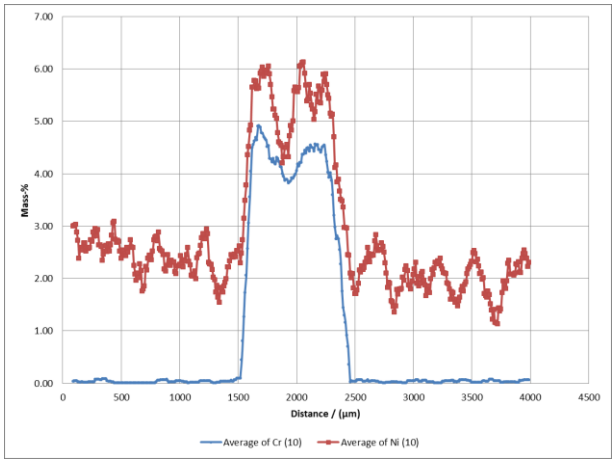

Figure 67 Moving average of Cr and Ni distribution of measuring line 1 (n=10).

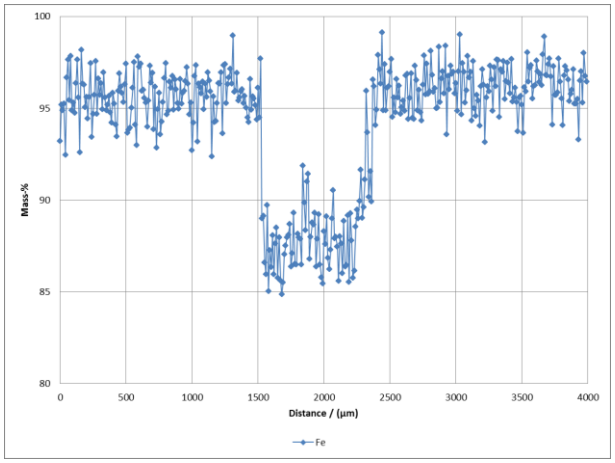

Figure 68 Measured Fe distribution of measuring line 1.

LAHW 3.15.2-9 / Measuring line 2 (EDS 2)

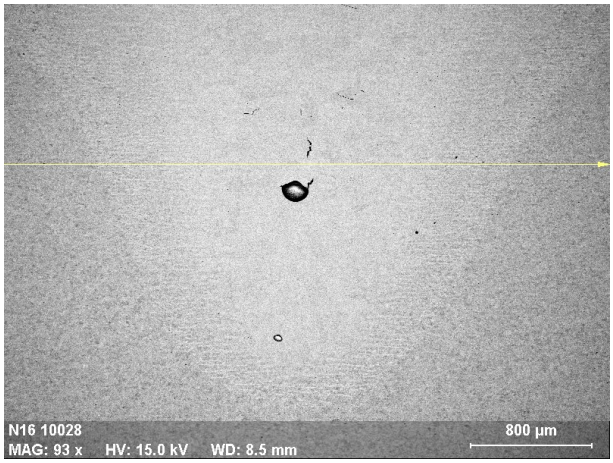

Figure 69 Position and direction of measuring line 2 (EDS 2) for LAHW welded sample 3.15.2-9.

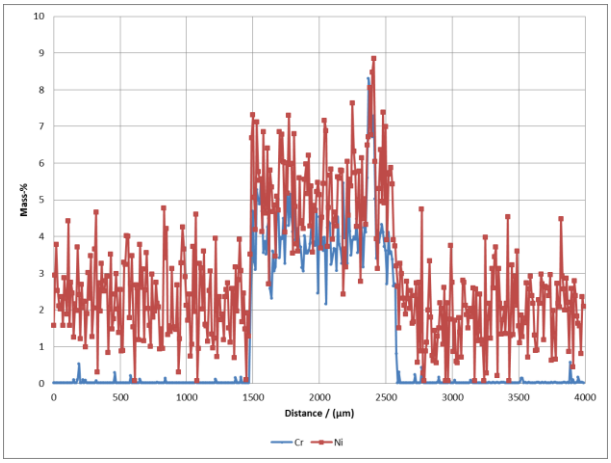

Figure 70 Measured Cr and Ni distribution of measuring line 2.

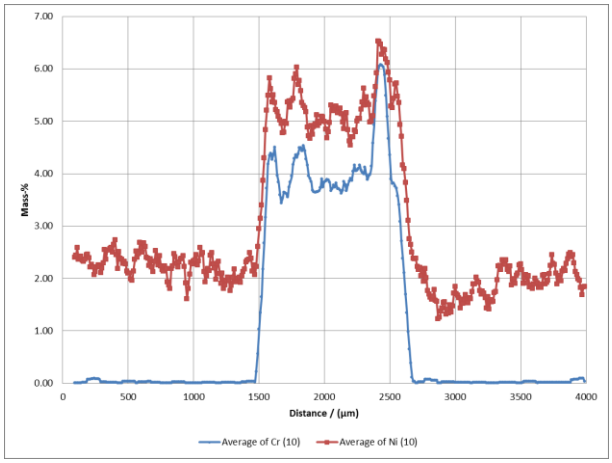

Figure 71 Moving average of Cr and Ni distribution of measuring line 2 (n=10).

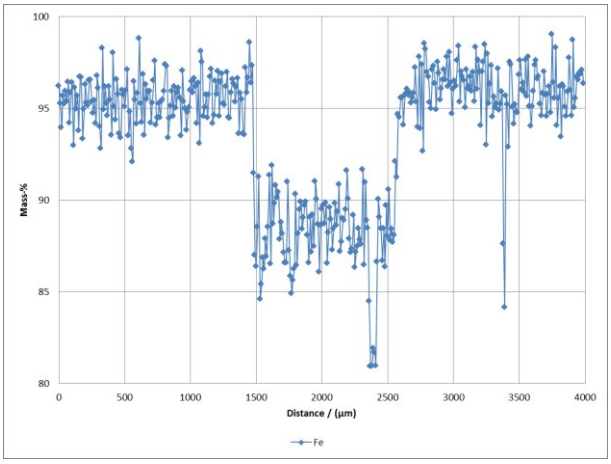

Figure 72 Measured Fe distribution of measuring line 2.

LAHW 3.15.2-9 / Measuring line 3 (EDS 3)

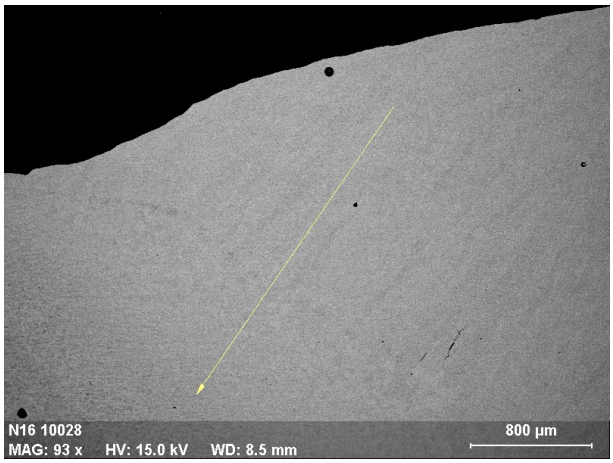

Figure 73 Position and direction of measuring line 3 (EDS 3) for LAHW welded sample 3.15.2-9.

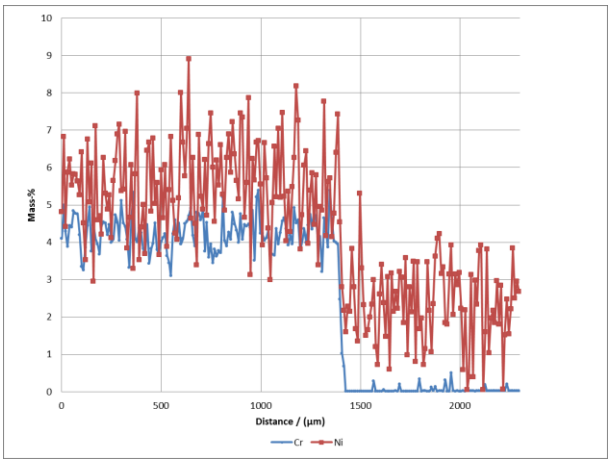

Figure 74 Measured Cr and Ni distribution of measuring line 3.

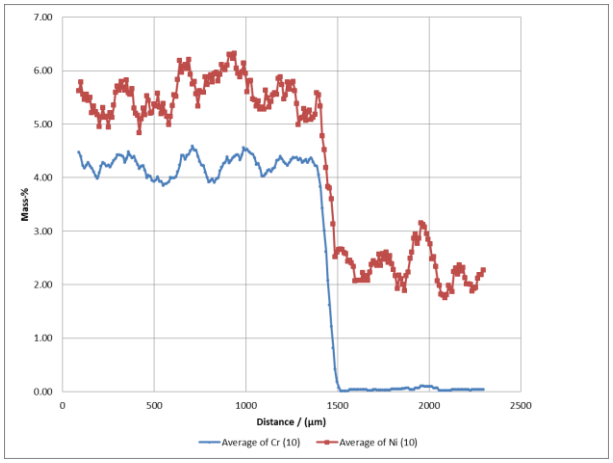

Figure 75 Moving average of Cr and Ni distribution of measuring line 3 (n=10).

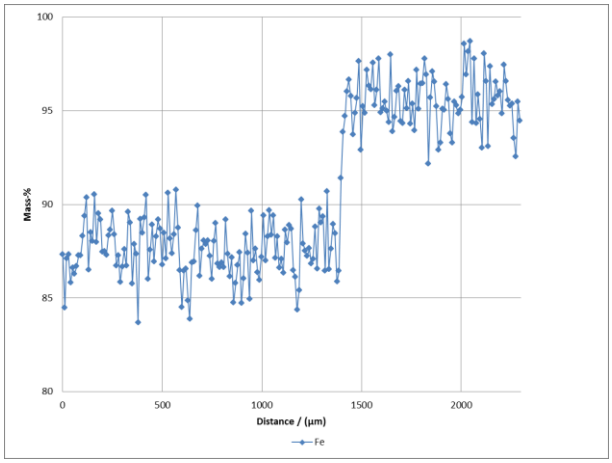

Figure 76 Measured Fe distribution of measuring line 3.

LAHW 3.15.2-9 / Measuring line 4 (EDS 4)

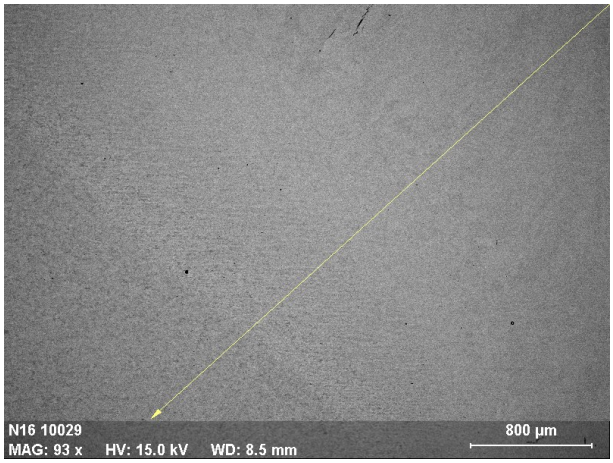

Figure 77 Position and direction of measuring line 4 (EDS 4) for LAHW welded sample 3.15.2-9.

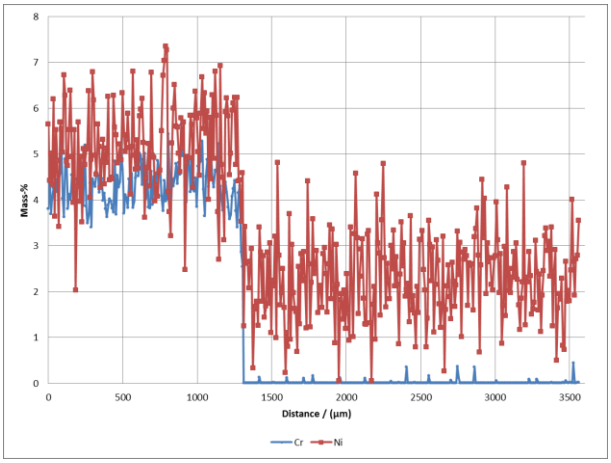

Figure 78 Measured Cr and Ni distribution of measuring line 4.

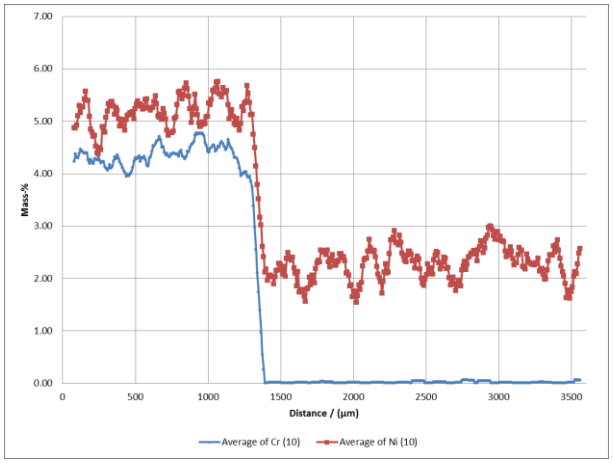

Figure 79 Moving average of Cr and Ni distribution of measuring line 4 (n=10).

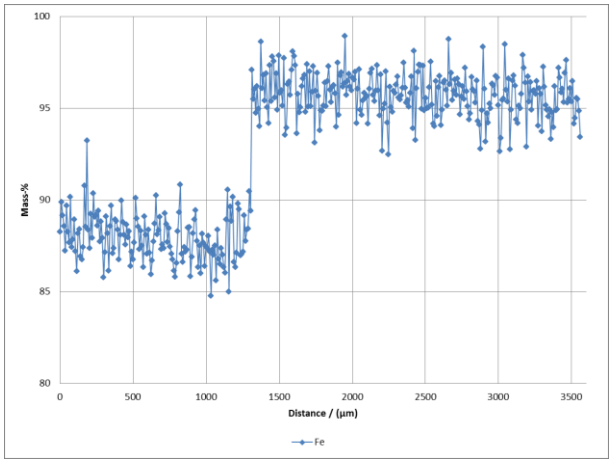

Figure 80 Measured Fe distribution of measuring line 4.

LAHW 3.15.2-9 / Measuring line 5 (EDS 5)

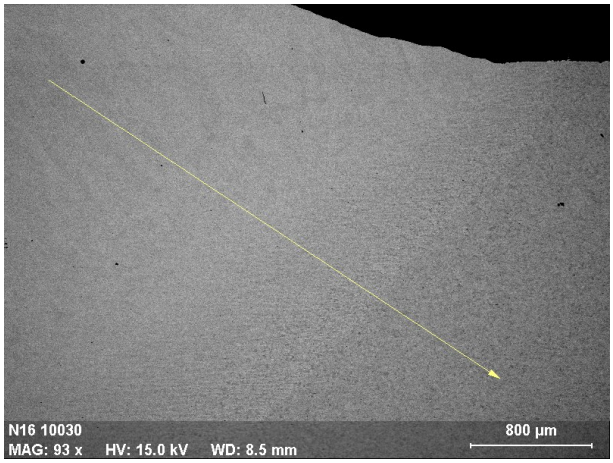

Figure 81 Position and direction of measuring line 5 (EDS 5) for LAHW welded sample 3.15.2-9.

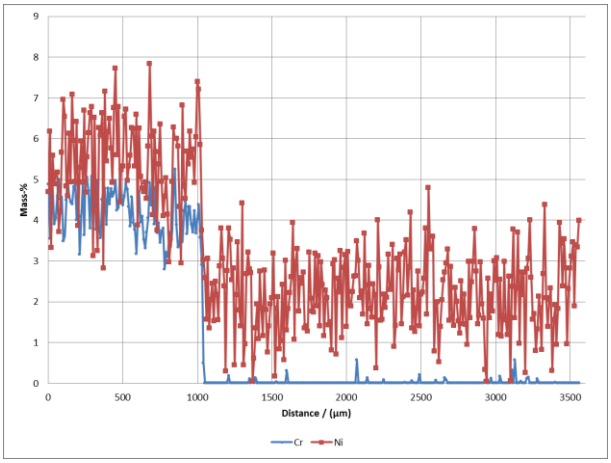

Figure 82 Measured Cr and Ni distribution of measuring line 5.

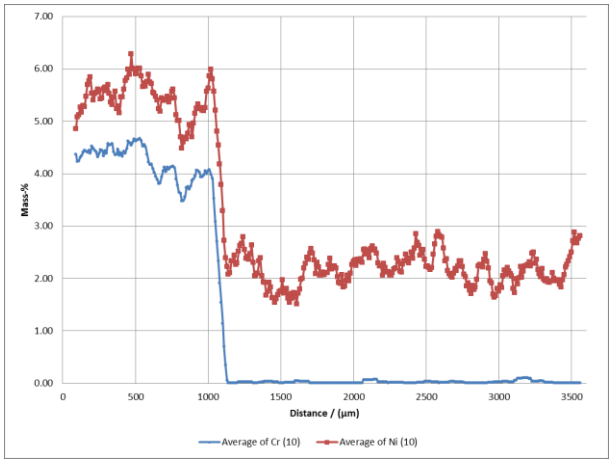

Figure 83 Moving average of Cr and Ni distribution of measuring line 5 (n=10).

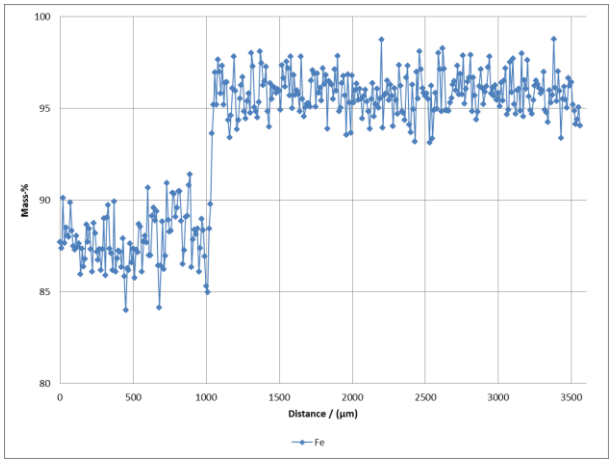

Figure 84 Figure 85 Measured Fe distribution of measuring line 5.

Appendix 9 - Analysis of optical emission spectrometer

VTT EXPERT SERVICES LTD

VTT Expert Services Ltd
P.O. Box 1001. FIN-02044 VTT. Finland
(Kemistintie 3. Espoo. Finland)
Tel. +358 20 722 111.

CERTIFICATE OF ANALYSES

Optical Emission Spectrometer. Spectrolab S
Carrier gas method (O_2 N_2). Leco TC-500
(Internal methods T001-021. T001-022. T001-023)

No. VTT-S-04647-15
OM 172235

Appendix 9

Pages 1/1

Requested by: VTT Mikko Kuitunen

Order: 6.10.2015

Date of reception: 6.10.2015

Date of analyses: 8.10.2015

Sample	Chemical composition %																Anal. No.
	C	Si	Mn	S	P	Cr	Ni	Mo	Cu	Al	W	V	Ti	Co	Nb	Fe	
MAG-welded sample # 3.15.2-4	0.067	0.60	1.59	n.a.	0.011	12.8	6.81	0.03	0.06	0.010	<0.01	0.03	<0.01	0.03	(0.04)	(rest)	311/15
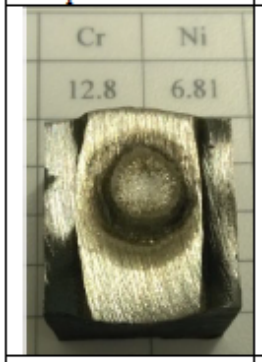																	

The sample was hot worked before the analyses.

Sulfur (S) n.a. = not analysed

Espoo 9.10.2015
VTT Expert Services Ltd

Senior Expert Pertti Koskinen

Senior Laboratory Technician Jouni Penttilä

The results are valid only for the tested samples
A table of the estimated uncertainty for this test method will be provided on request.

Appendix 10 / Measured distributions of residual stresses with X-ray diffraction

Contents

Appendix 10

Sample 1 / MAG

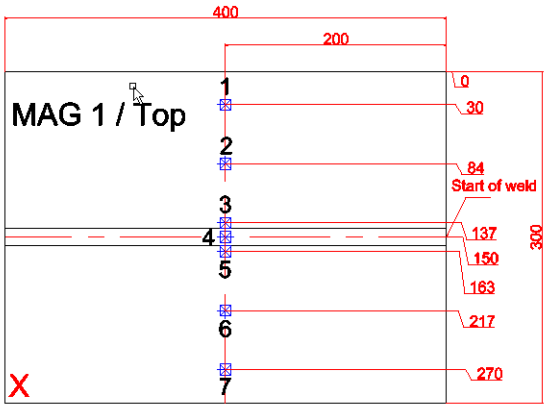

Figure 1 Positions of XRD measuring are introduced in this picture. Measured distributions of residual stresses are shown in Figure 2.

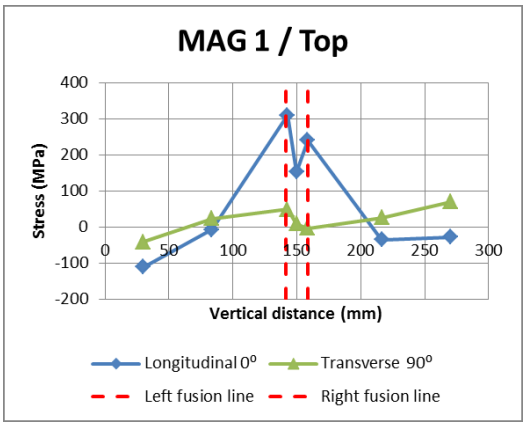

Figure 2 Distributions of residual stresses.

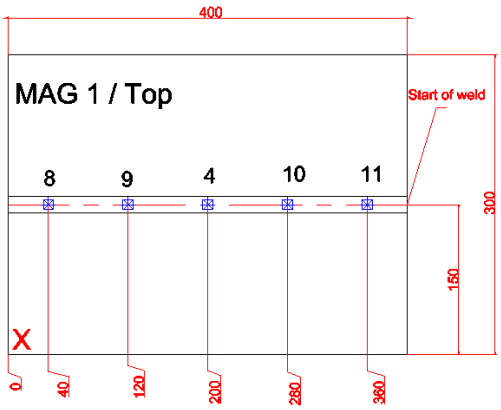

Figure 3 Positions of XRD measuring are introduced in this picture. Measured distributions of residual stresses are shown in Figure 4.

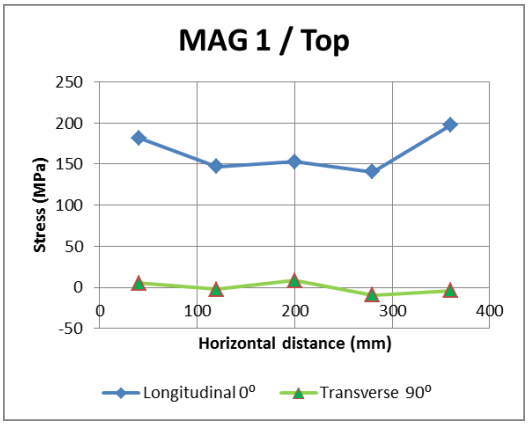

Figure 4 Distributions of residual stresses.

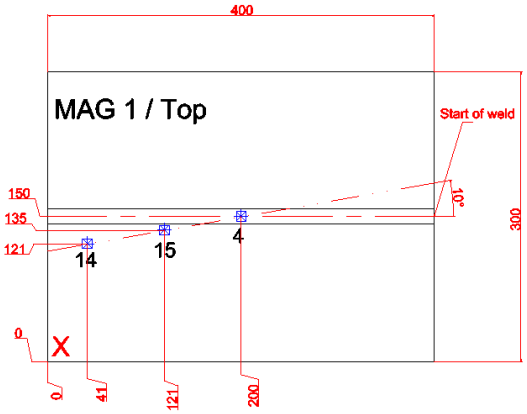

Figure 5 Positions of XRD measuring are introduced in this picture. Measured distributions of residual stresses are shown in Figure 6.

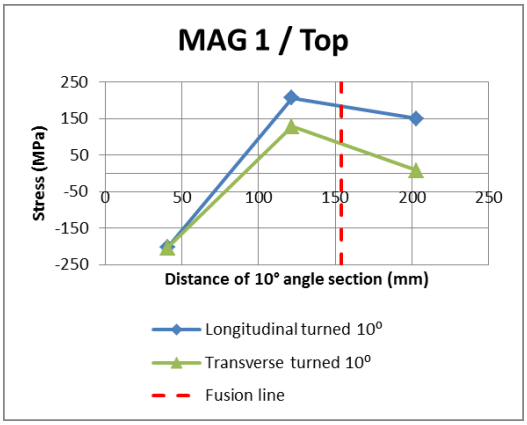

Figure 6 Distributions of residual stresses. Tensile stress which was measured from position 4 was too low. Tensile stress should be near yield strength.

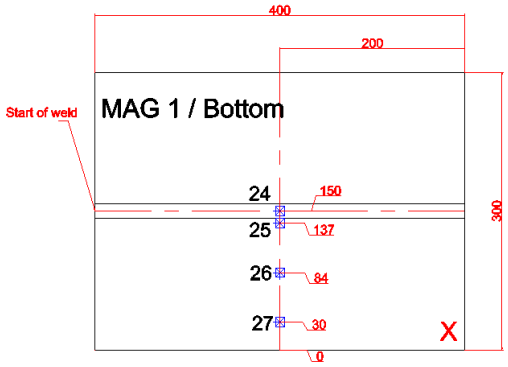

Figure 7 Positions of XRD measuring are introduced in this picture. Measured distributions of residual stresses are shown in Figure 8.

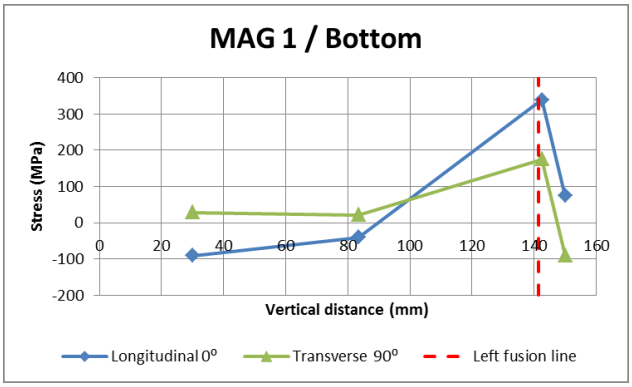

Figure 8 Distributions of residual stresses. Tensile stress which was measured from position 4 was too low.

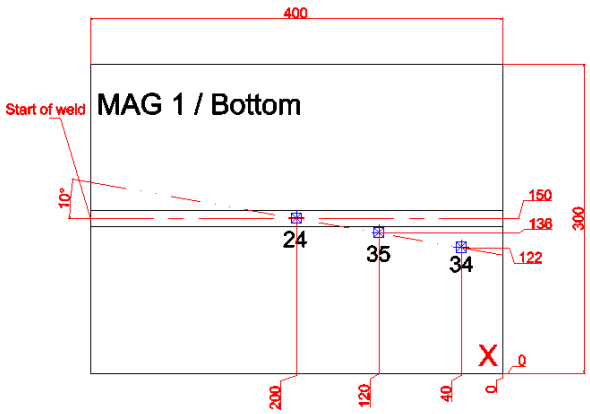

Figure 9 Positions of XRD measuring are introduced in this picture. Measured distributions of residual stresses are shown in

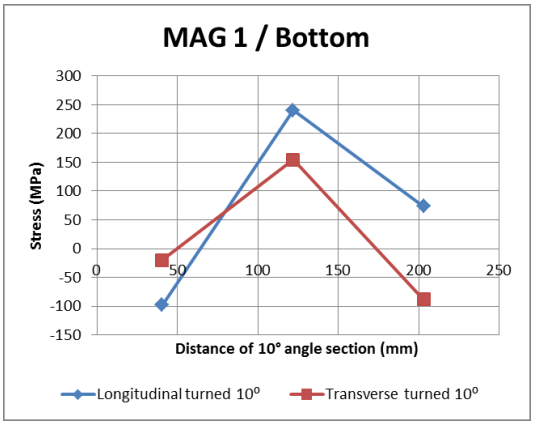

Figure 10 Distributions of residual stresses. Tensile stress which was measured from position 24 was too low.

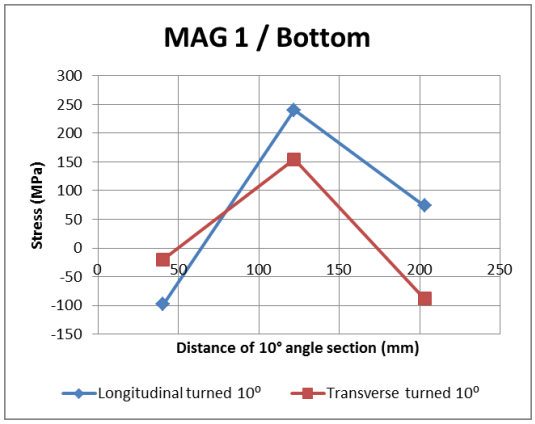

Figure 10.

Sample 2 / MAG

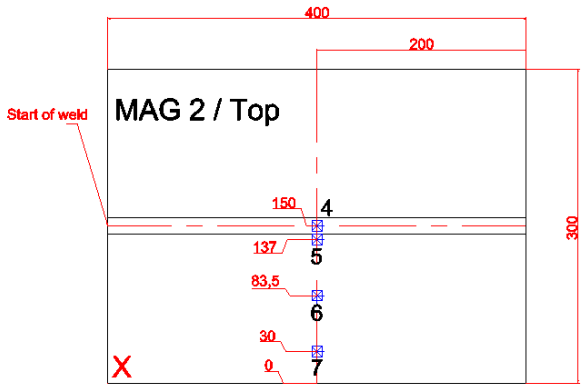

Figure 11 Positions of XRD measuring are introduced in this picture. Measured distributions of residual stresses are shown in Figure 12.

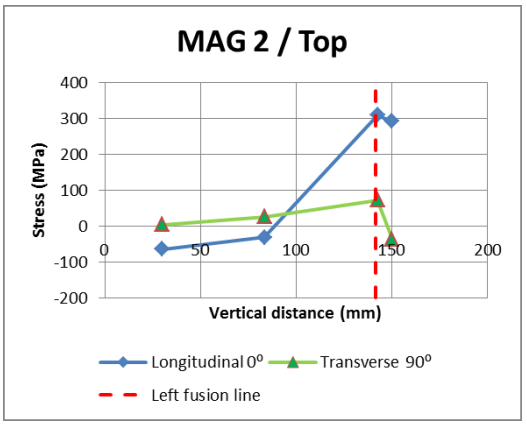

Figure 12 Distributions of residual stresses. Tensile stress which was measured from position 4 was too low.

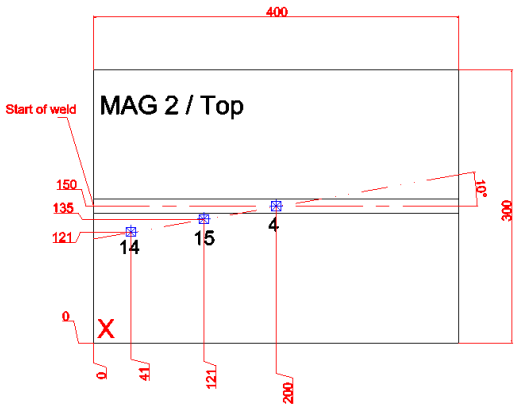

Figure 13 Positions of XRD measuring are introduced in this picture. Measured distributions of residual stresses are shown in Figure 14.

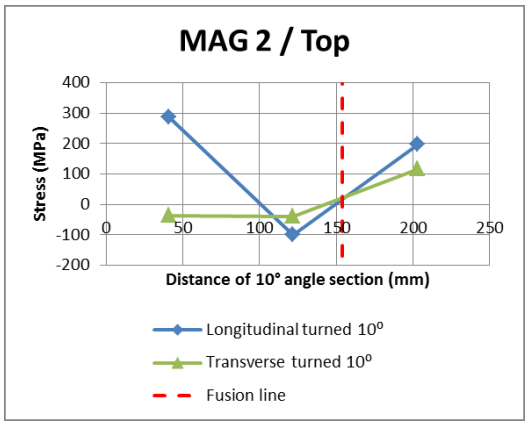

Figure 14 Distributions of residual stresses. Tensile stress which was measured from position 4 was too low.

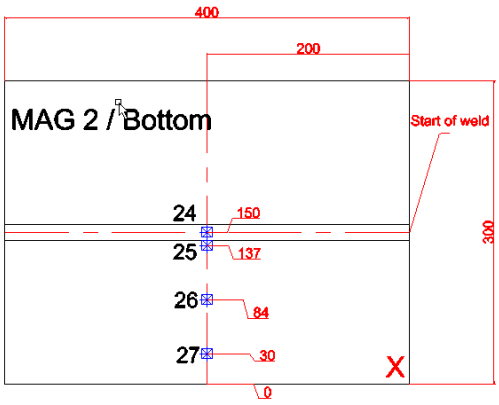

Figure 15 Positions of XRD measuring are introduced in this picture. Measured distributions of residual stresses are shown in Figure 16.

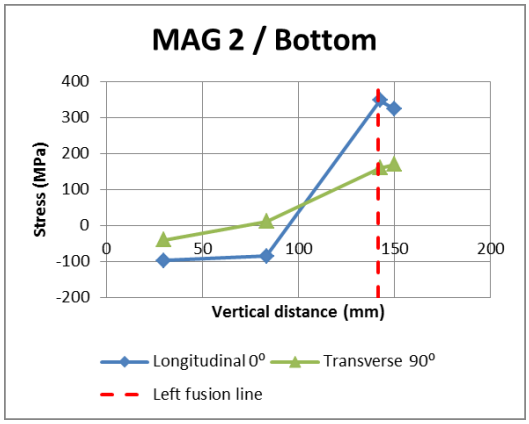

Figure 16 Distributions of residual stresses. Tensile stress which was measured from position 24 was too low.

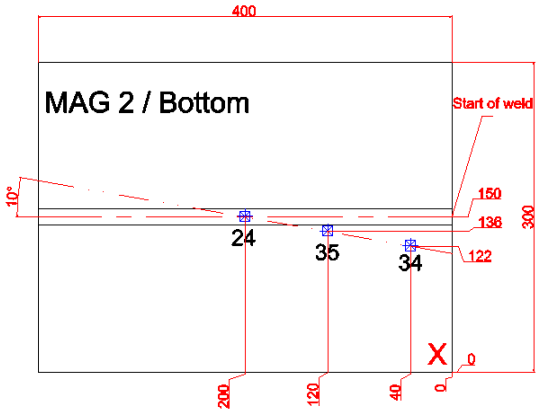

Figure 17 Positions of XRD measuring are introduced in this picture. Measured distributions of residual stresses are shown in Figure 18.

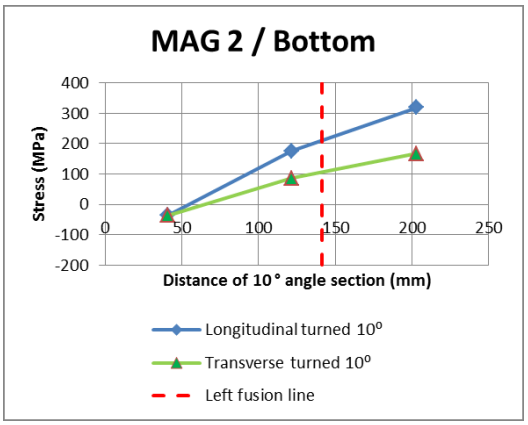

Figure 18 Distributions of residual stresses.

Sample 3 / Base material

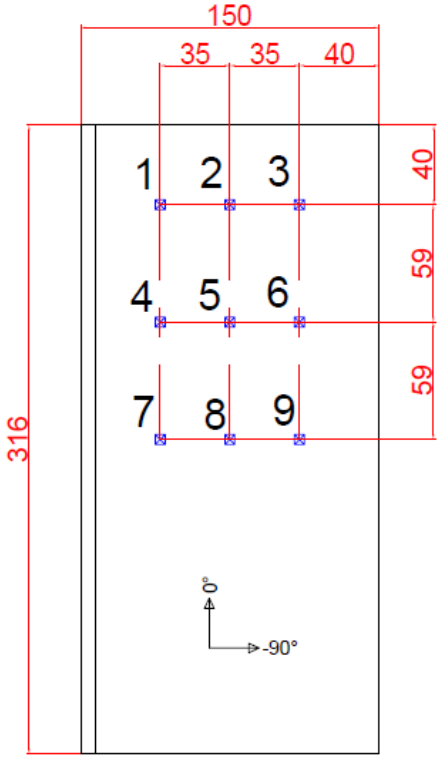

Figure 19 Positions of XRD measuring are introduced in this picture. Measured residual stresses are shown in Table 1.

Table 1 Measured residual stresses.

Sample 3 / Base material			
Sample 1	Stress (Mpa) with rotation(phi)		
Measuring point	0°	-45°	-90°
1	-22,9	-42,2	9,2
2	-6,4	-22,5	-25,7
3	-33,3	-0,3	-34,6
4	-25,2	-13,2	-4,8
5	-7,4	-20,2	-20,1
6	-8,6	2,1	3,1
7	-10,1	-8,6	13,4
8	-17,6	-5,7	7,2
8b	-3,4	-12,5	17,1
9	-41,4	-50,0	-10,9
9b	-33,8	-42,9	-3,8
Average	-19,1	-19,6	-4,5
min	-41,4	-50,0	-34,6
max	-3,4	2,1	17,1

Sample 5 / LAHW

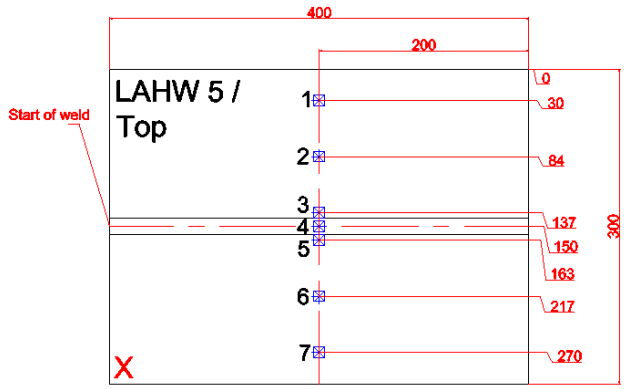

Figure 20 Positions of XRD measuring are introduced in this picture. Measured distributions of residual stresses are shown in Figure 21.

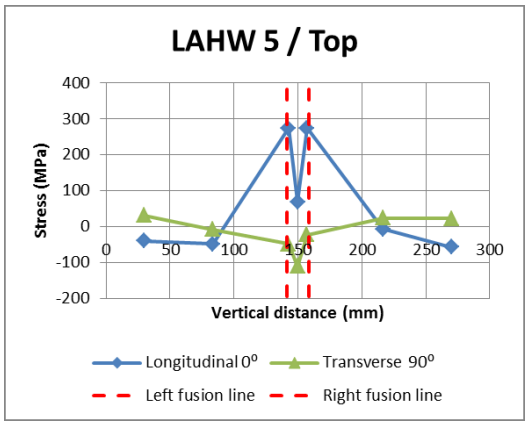

Figure 21 Distributions of residual stresses. Tensile stress which was measured from position 4 was too low.

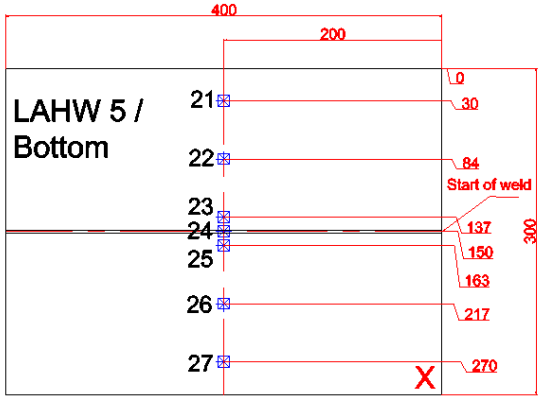

Figure 22 Positions of XRD measuring are introduced in this picture. Measured distributions of residual stresses are shown in Figure 23.

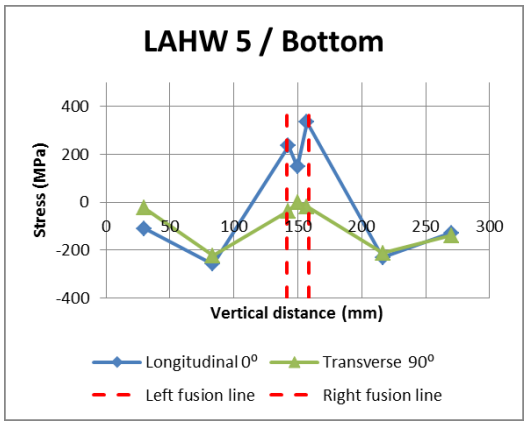

Figure 23 Distributions of residual stresses. Tensile stress which was measured from position 4 was too low.

Position of XRD measurings for weld samples

Table 2 Position of XRD measurings for weld samples. Positions are marked according the pictures of this document.

MAG welded sample 1					MAG welded sample 2					LAHW welded sample 5				
Measuring point	Stress (MPa) with		Position (mm)		Measuring point	Stress (MPa) with		Position (mm)		Measuring point	Stress (Mpa) with		Position (mm)	
	Longitudinal 0°	Transverse 90°	X	Y		Longitudinal 0°	Transverse 90°	X	Y		Longitudinal 0°	Transverse 90°	X	Y
1	-27.6	70.4	200	270	4	292.3	-36.2	200	150	1	-57.0	22.1	200	270
2	-35.3	26.1	200	217	5	309.2	72.8	200	143	2	-7.3	23.6	200	217
3	240.5	-3.3	200	159	6	-32.0	25.8	200	84	3	274.3	-22.8	200	157
4	152.8	8.3	200	150	7	-65.0	4.3	200	30	4	68.2	-110.7	200	150
5	310.1	49.6	200	143	14	-100.8	-40.1	120	150	5	274.0	-49.3	200	143
6	-7.4	22.9	200	84	15	200.1	119.2	200	150	6	-48.3	-8.9	200	84
7	-111.1	-41.5	200	30	24	324.1	169.8	200	150	7	-40.3	31.2	200	30
8	181.8	5.0	40	150	24	324.1	169.8	200	150	21	-129.3	-139.5	200	270
9	147	-2.5	120	150	25	348.6	159.9	200	143	22	-232.0	-212.7	200	217
10	140.7	-9.6	280	150	26	-85.0	11.2	200	84	23	334.2	-18.5	200	157
11	197.3	-4	360	150	27	-97.6	-40.1	200	30	24	147.4	-	200	150
14	-205.2	-207.3	40	122	34	-36.8	-36.4	40	150	25	236.1	-36.6	200	143
15	210.0	129.8	120	136	35	179.1	87.8	120	150	26	-259.4	-225.2	200	84
24	74.4	-89.5	200	150						27	-111.3	-24.3	200	30
24	74.4	-89.5	200	150										
25	339.2	174.9	200	143										
26	-40.8	22.0	200	84										
27	-90.6	28.9	200	30										
34	-99.7	-20.3	40	122										
35	244.1	157	120	136										

Appendix 11 / Results of contour method of samples 1, 2, 3 and 5

Contents

Sample 1 / MAG

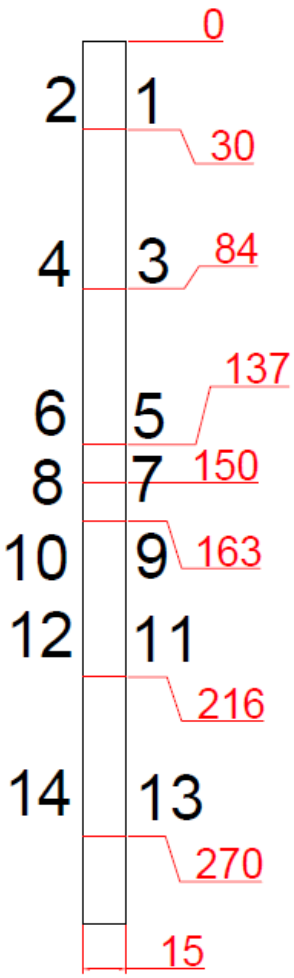

Figure 1 Dimensions for cross-section of sample 1.

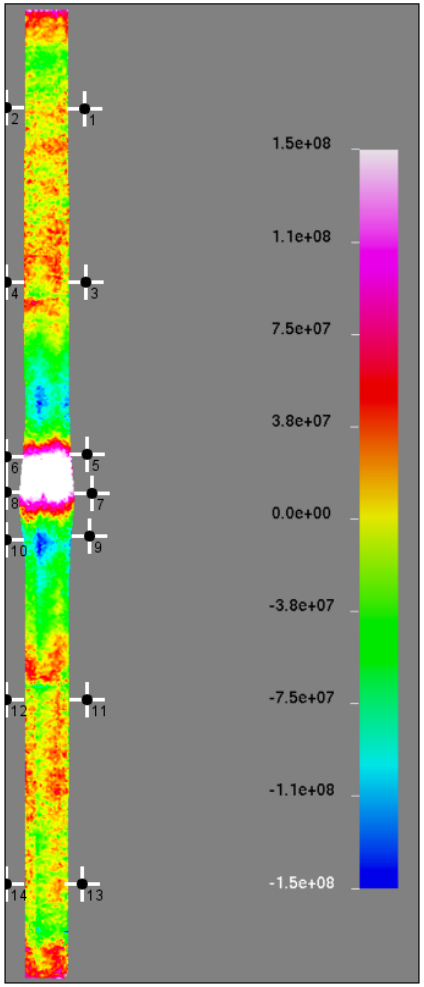

Figure 2 Normal stresses in cut surface 1 of sample 1.

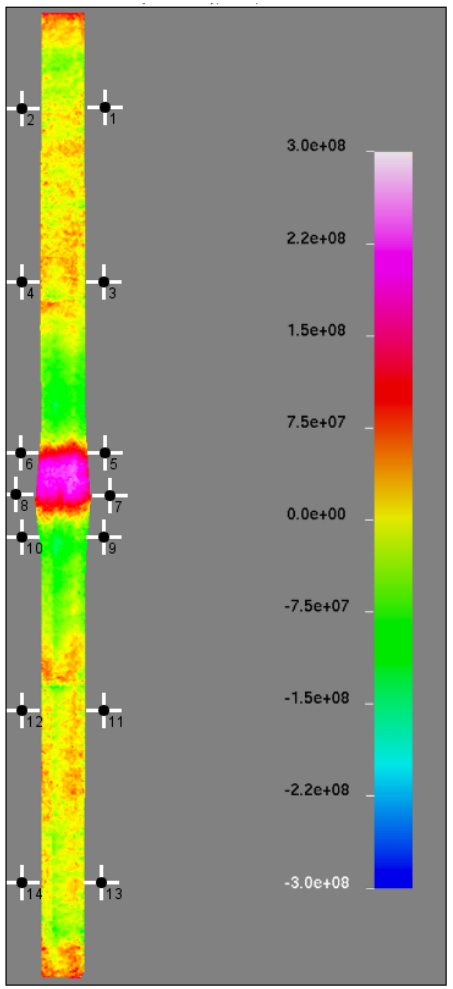

Figure 3 Normal stresses in cut surface 1 of sample 1.

Appendix 11

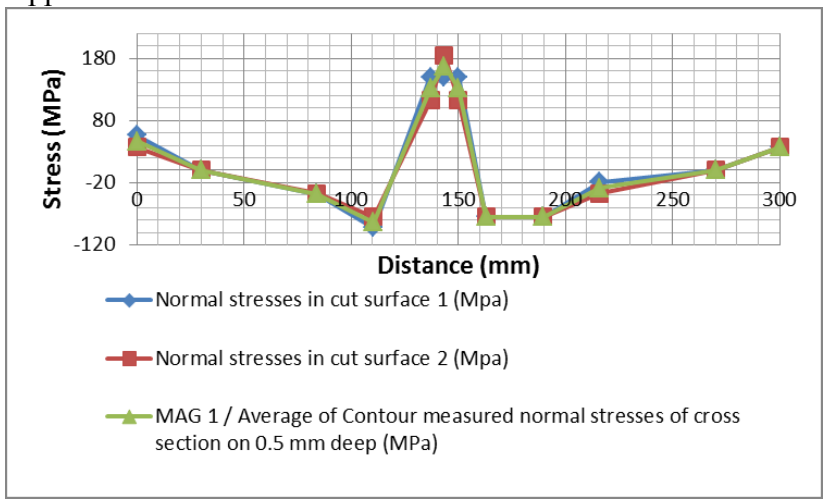

Figure 4 Stress distribution on top side of sample 1 from 0.5 mm deep.

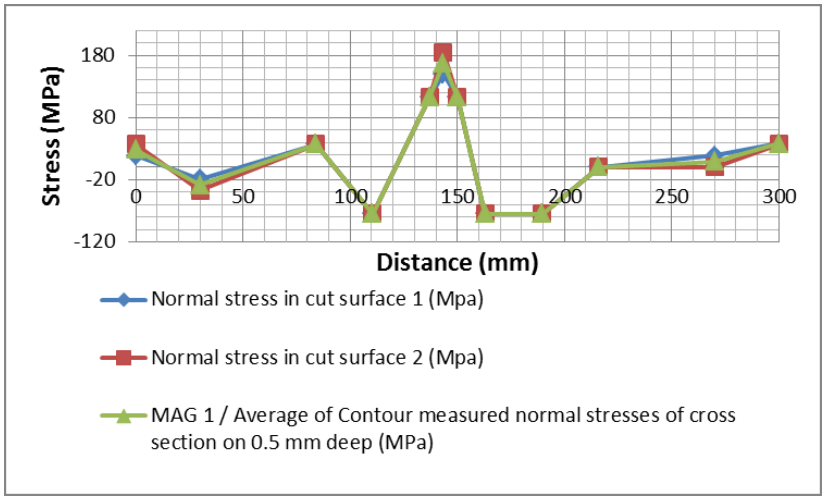

Figure 5 Stress distribution on bottom side of sample 1 from 0.5 mm deep.

Table 1 Determined stresses for top side of sample 1 from 0.5 mm deep..

Position	Distance from end of plate (mm)	Normal stresses in cut surface 1 (MPa)	Normal stresses in cut surface 2 (MPa)	Average of normal stresses (MPa)
End	0	56.5	37.5	47.0
1	30	0.0	0.0	0.0
3	84	-38.0	-37.5	-37.8
Extra	110.5	-92.5	-75.0	-83.8
5	137	150.0	112.5	131.3
Extra	143.5	150.0	185.0	167.5
7	150	150.0	112.5	131.3
9	163	-75.0	-75.0	-75.0
Extra	189.5	-75.0	-75.0	-75.0
11	216	-19.0	-37.5	-28.3
13	270	0.0	0.0	0.0
End	300	37.5	37.5	37.5

Table 2 Determined stresses for bottom side of sample 5 from 0.5 mm deep.

Position	Distance from end of plate (mm)	Normal stress in cut surface 1 (MPa)	Normal stress in cut surface 2 (MPa)	Average of normal stress (MPa)
End	0	19	37.5	28.3
2	30	-19.0	-37.5	-28.3
4	84	37.5	37.5	37.5
Extra	110.5	-75.0	-75.0	-75.0
6	137	112.5	112.5	112.5
Extra	143.5	150.0	185.0	167.5
8	150	112.5	112.5	112.5
10	163	-75.0	-75.0	-75.0
Extra	189.5	-75.0	-75.0	-75.0
12	216	0.0	0.0	0.0
14	270	19.0	0.0	9.5
End	300	38	37.5	37.8

Sample 2 / MAG

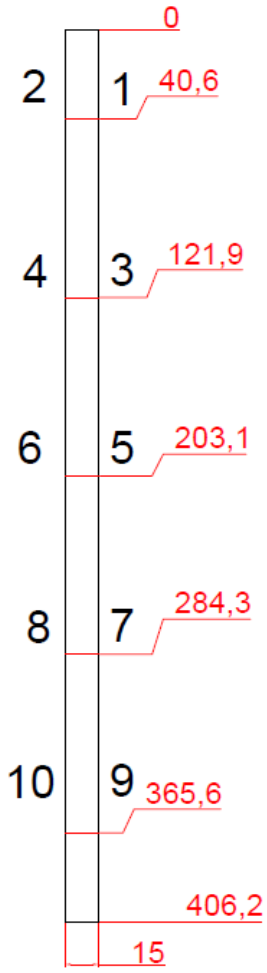

Figure Dimensions for cross-section of sample 2.

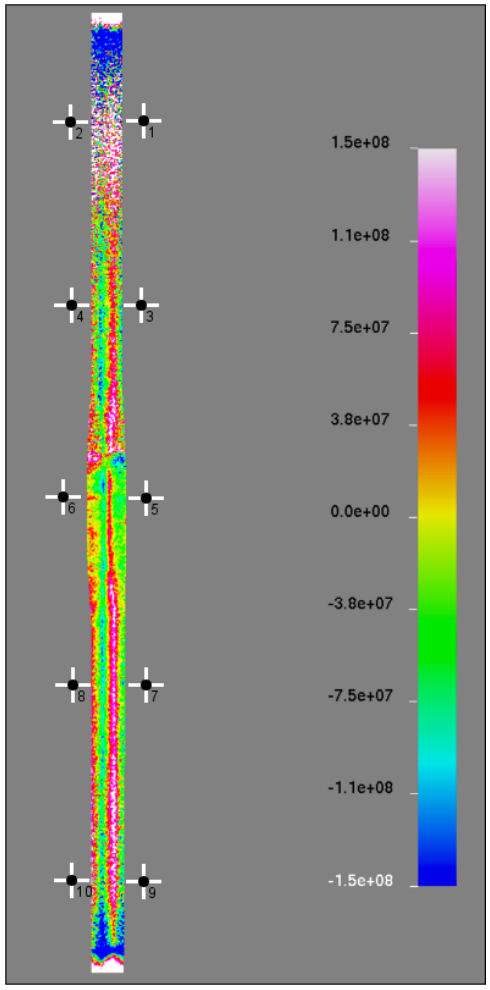

Figure 6 Normal stresses in cut surface 1 of sample 2.

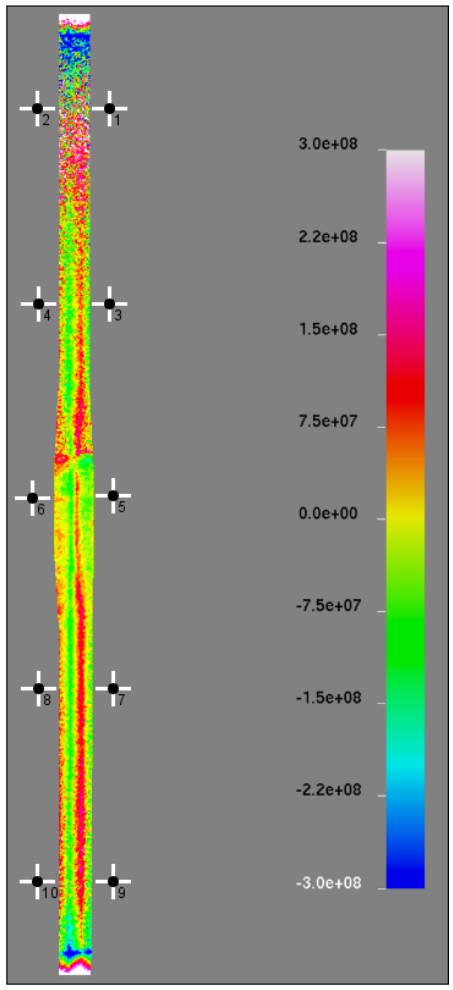

Figure 7 Normal stresses in cut surface 2 of sample 2.

Appendix 11

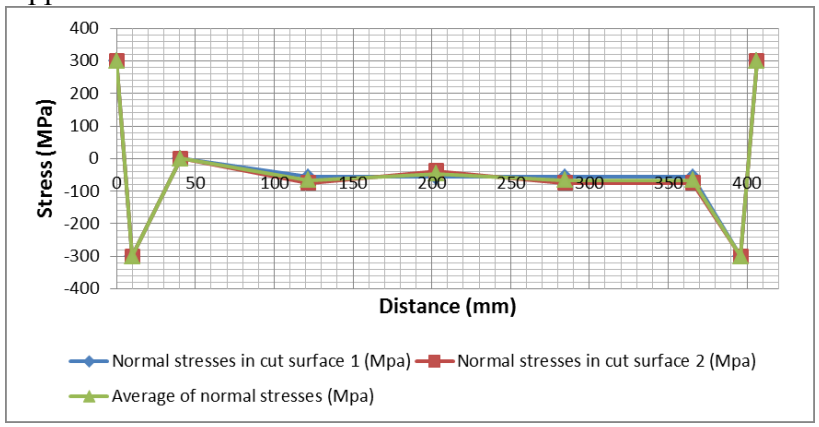

Figure 8 Stress distribution on top side of sample 2 from 0.5 mm deep.

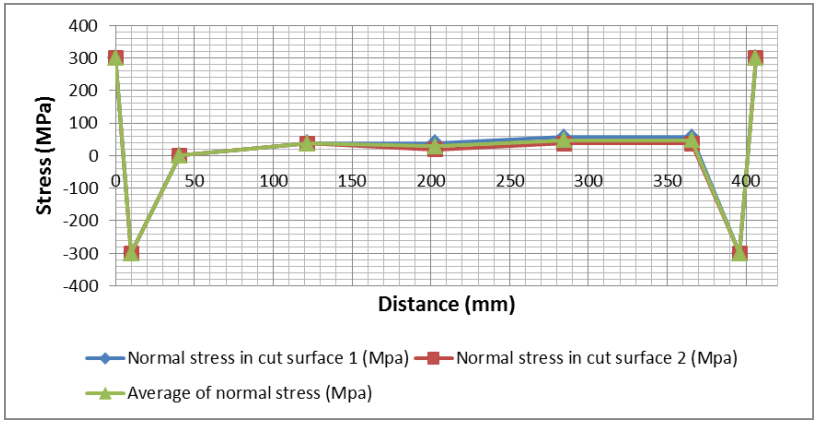

Figure 9 Stress distribution on bottom side of sample 2 from 0.5 mm deep.

Table 3 Determined stresses for top side of sample 2 from 0.5 mm deep.

Position	Distance from end of plate (mm)	Normal stresses in cut surface 1 (MPa)	Normal stresses in cut surface 2 (MPa)	Average of normal stresses (MPa)
End	0	300	300	300.0
Extra	10	-300	-300	-300.0
1	40.6	0.0	0.0	0.0
3	121.9	-56.5	-75.0	-65.8
5	203.1	-56.5	-37.5	-47.0
7	284.5	-56.5	-75.0	-65.8
9	365.6	-56.5	-75.0	-65.8
Extra	396	-300	-300	-300.0
End	406.2	300	300	300.0

Table 4 Determined stresses for bottom side of sample 2 from 0.5 mm deep.

Position	Distance from end of plate (mm)	normal stress in cut surface 1 (MPa)	normal stress in cut surface 2 (MPa)	Average of normal stress (MPa)
End	0	300	300	300.0
Extra	10	-300	-300	-300.0
2	40.6	0.0	0.0	0.0
4	121.9	38.0	37.5	37.8
6	203.1	38.0	19.0	28.5
8	284.5	56.5	37.5	47.0
10	365.6	56.5	37.5	47.0
Extra	396	-300	-300	-300.0
End	406.2	300	300	300.0

Sample 3 / Base material

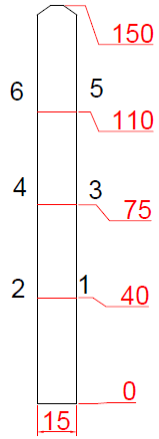

Figure 10 Dimensions for cross-section of sample 3.

Table 5 Stresses of sample 3.

Position	Normal stress in cut surface 1 (MPa)	Normal stress in cut surface 2 (MPa)	Average of normal stress (MPa)
1	0	0	0
2	19	38	28
3	19	38	28
4	-38	-38	-38
5	-38	-75	-57
6	-19	-38	-28
Average	-9	-13	-11.0

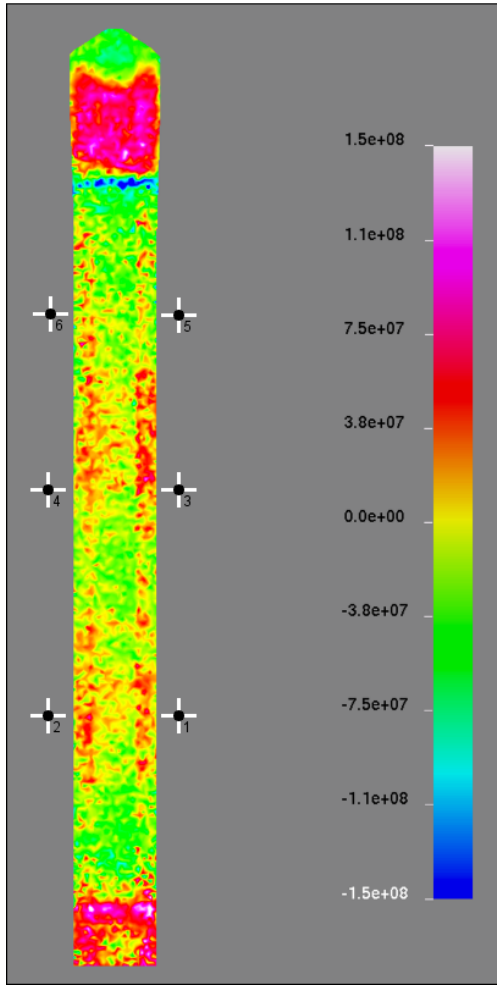

Figure 11 Normal stresses in cut surface 1 of sample 3.

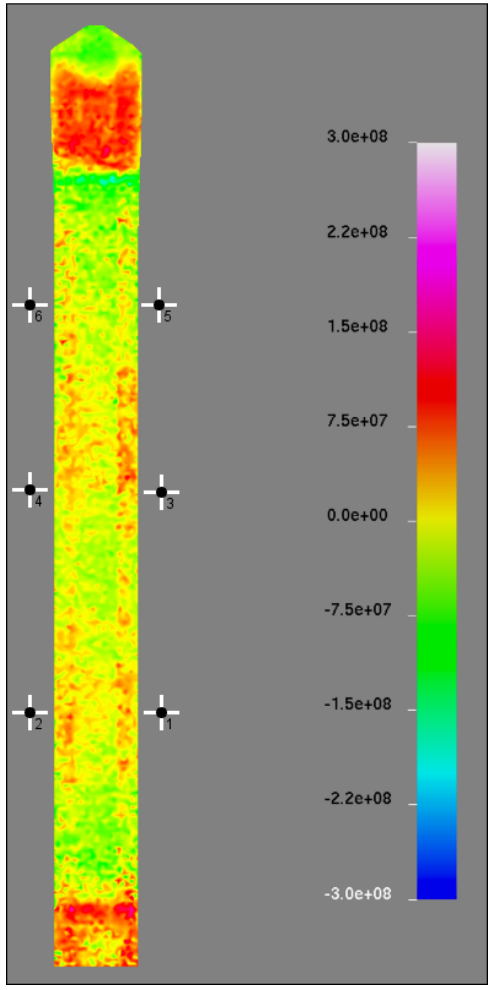

Figure 12 Normal stresses in cut surface 2 of sample 3.

Appendix 11

Sample 5 / LAHW

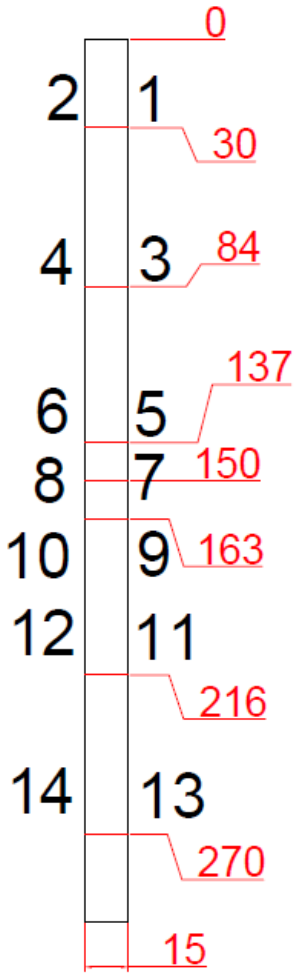

Figure 13 Dimensions for cross-section of sample 5.

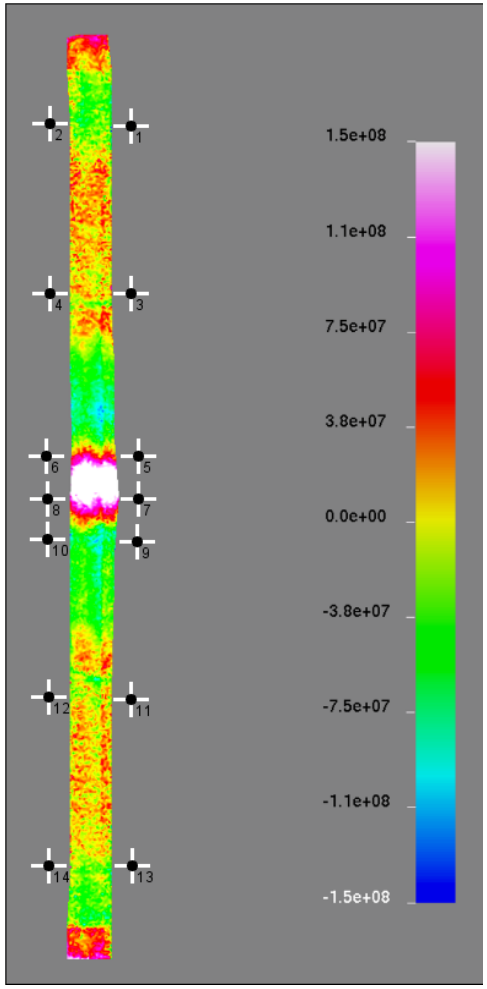

Figure 14 Normal stresses in cut surface 1 of sample 5.

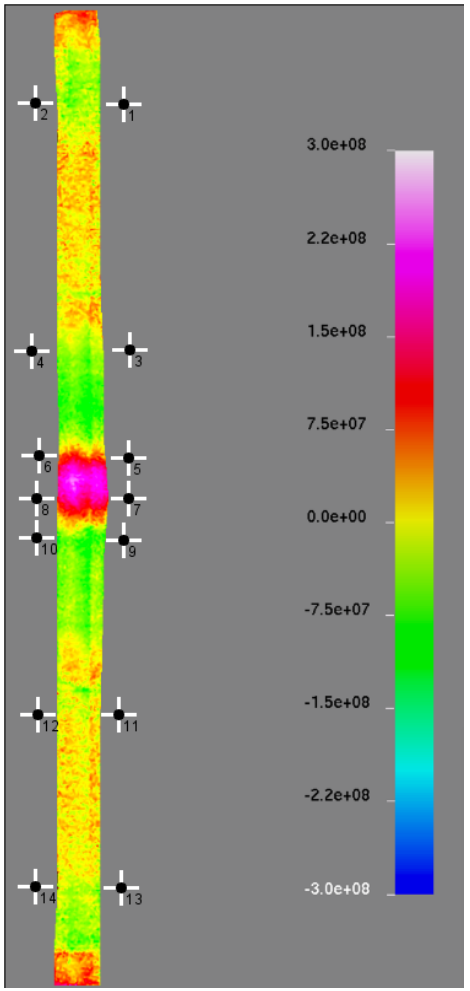

Figure 15 Normal stresses in cut surface 1 of sample 5.

Appendix 11

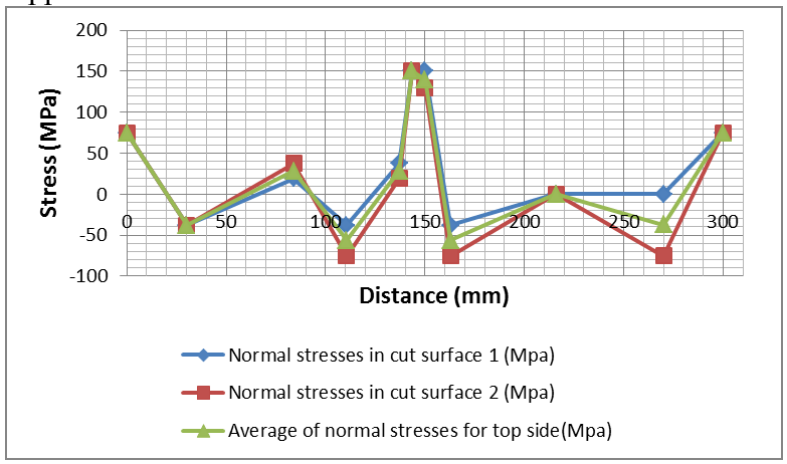

Figure 16 Stress distribution on top side of sample 5 from 0.5 mm deep.

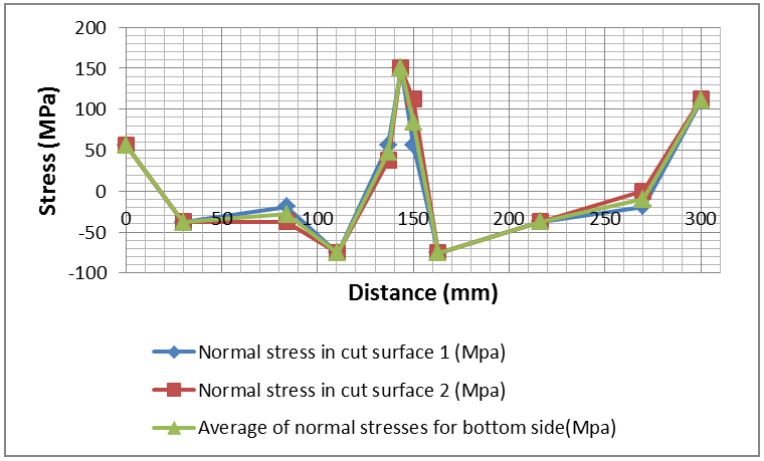

Figure 17 Stress distribution on bottom side of sample 5 from 0.5 mm deep.

Table 6 Determined stresses for top side of sample 5 from 0.5 mm deep.

Position	Distance from end of plate (mm)	Normal stresses in cut surface 1 (MPa)	Normal stresses in cut surface 2 (MPa)	Average of normal stresses (MPa)
End	0	75	75	75.0
1	30	-38.0	-38.0	-38.0
3	84	19.0	37.5	28.3
Extra	110.5	-38.0	-75.0	-56.5
5	137	37.5	19.0	28.3
Extra	143.5	150.0	150.0	150.0
7	150	150.0	130.0	140.0
9	163	-38.0	-75.0	-56.5
11	216	0.0	0.0	0.0
13	270	0.0	-75.0	-37.5
End	300	75.0	75.0	75.0

Table 7 Determined stresses for bottom side of sample 5 from 0.5 mm deep.

Position	Distance from end of plate (mm)	Normal stress in cut surface 1 (MPa)	Normal stress in cut surface 2 (MPa)	Average of normal stress (MPa)
End	0	56.5	56.5	56.5
2	30	-38.0	-37.5	-37.8
4	84	-19.0	-37.5	-28.3
Extra	110.5	-75.0	-75.0	-75.0
6	137	56.5	37.5	47.0
Extra	143.5	150.0	150.0	150.0
8	150	56.5	112.5	84.5
10	163	-75.0	-75.0	-75.0
12	216	-37.5	-37.5	-37.5
14	270	-19.0	0.0	-9.5
End	300	110.0	112.5	111.3

Appendix 12 / Measured cooling times of thermoelements and the determined $t_{8/5}$ cooling times

Contents

Appendix 12

Table 1 Comparison of $t_{8/5}$ between calculated and measured values.

Welding method	Number of sample	Thickness (mm)	Calculated $t_{8/5}$ (s)	Thermoelement number	Measured $t_{8/5}$ (s)
LAHW	3.5.2-3	5	2.0	0	4.9
				1	4.5
LAHW	3.15.2-9	15	1.2	0	4.9
				1	2.7
LASER	3.5.2-7	5	0.7	-	-
LASER	3.15.2-5	15	1.1	0	1.0
MAG	3.5.2-2	5	11.6	0	7.8
				1	5.4
MAG	3.15.2-4	15	4.2	0	4.3
TIG	3.5.2-4	5	2.5	0	3.7
				1	2.8
TIG	3.5.2-8	5	25.7	0	9.8
TIG	3.5.2-9	5	6.6	-	-
TIG	3.15.2-6	15	4.0	0	3.6
TIG	3.15.2-7	15	2.0	0	1.6
TIG	3.15.2-8	15	1.2	-	-

LAHW and MAG samples

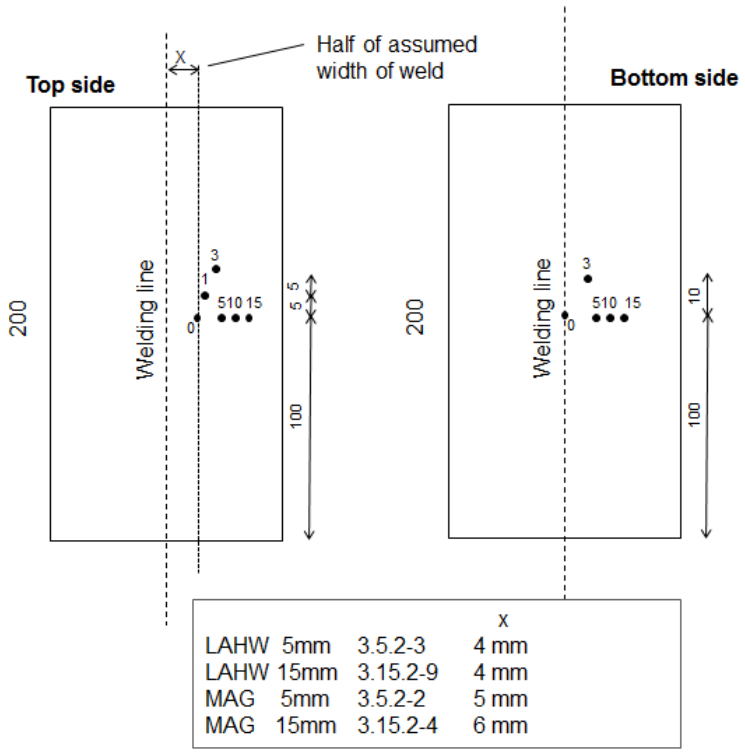

Figure 1 Positions of thermoelements of LAHW and MAG samples.

Appendix 12

LAHW 3.15.2-9

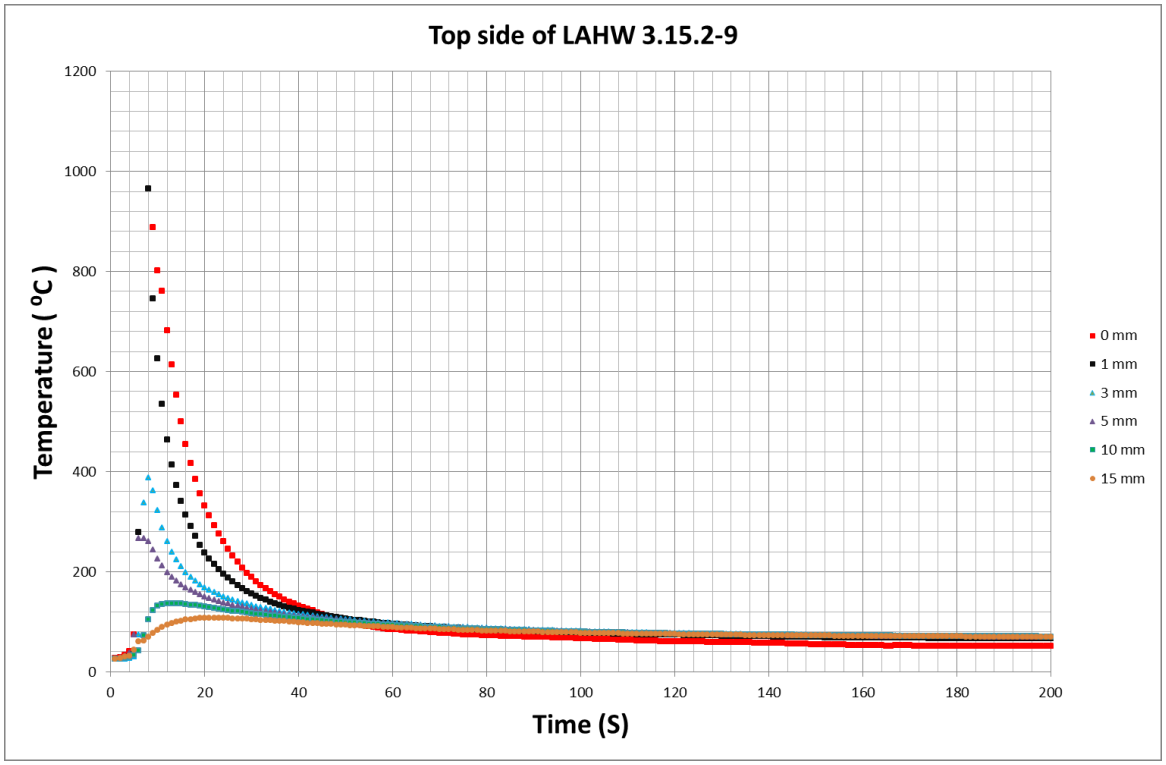

Figure 2 Top side of LAHW-weld sample 3.15.2-9.

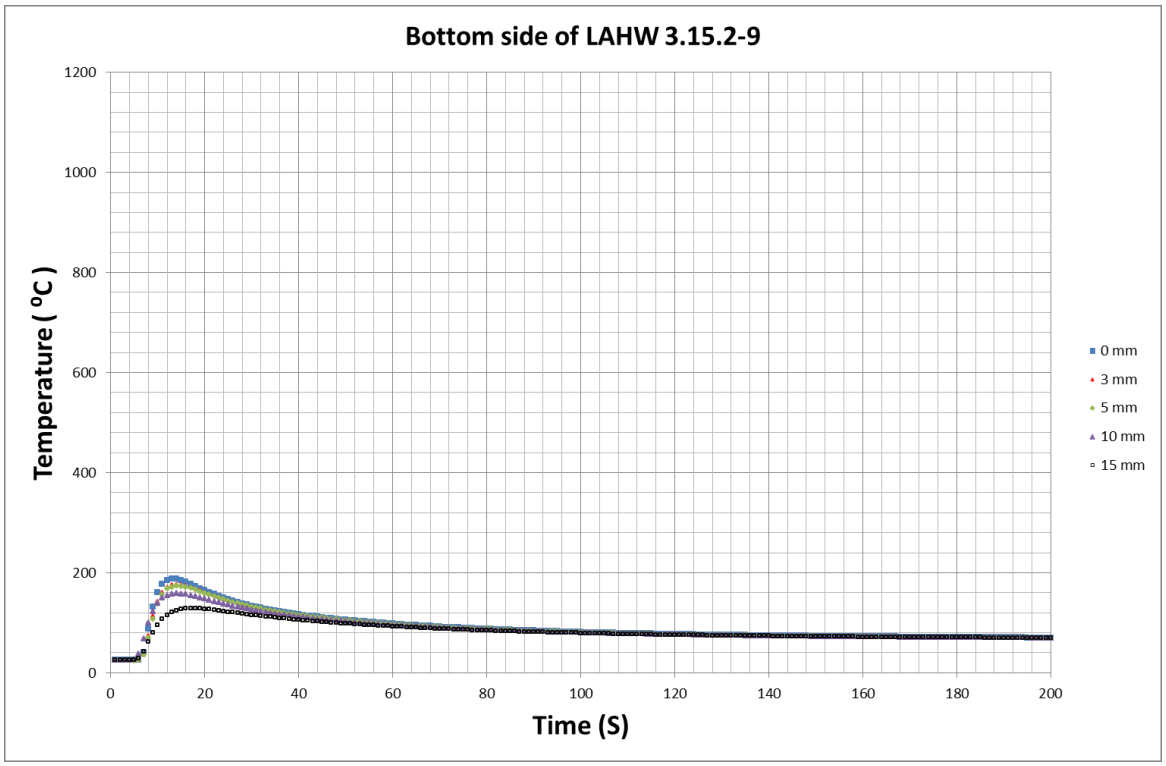

Figure 3 Bottom side of LAHW-weld sample 3.15.2-9.

Appendix 12

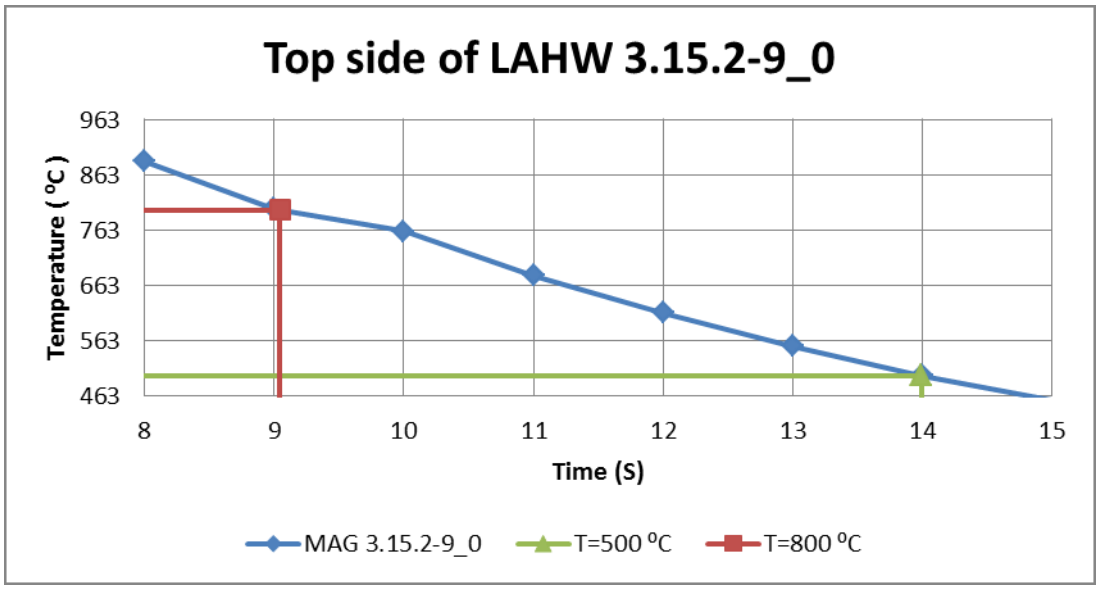

Figure 4 Interpolated $t_{8/5}$ value for thermoelements 0 of top side. $t_{8/5}$ value is 4.9 s.

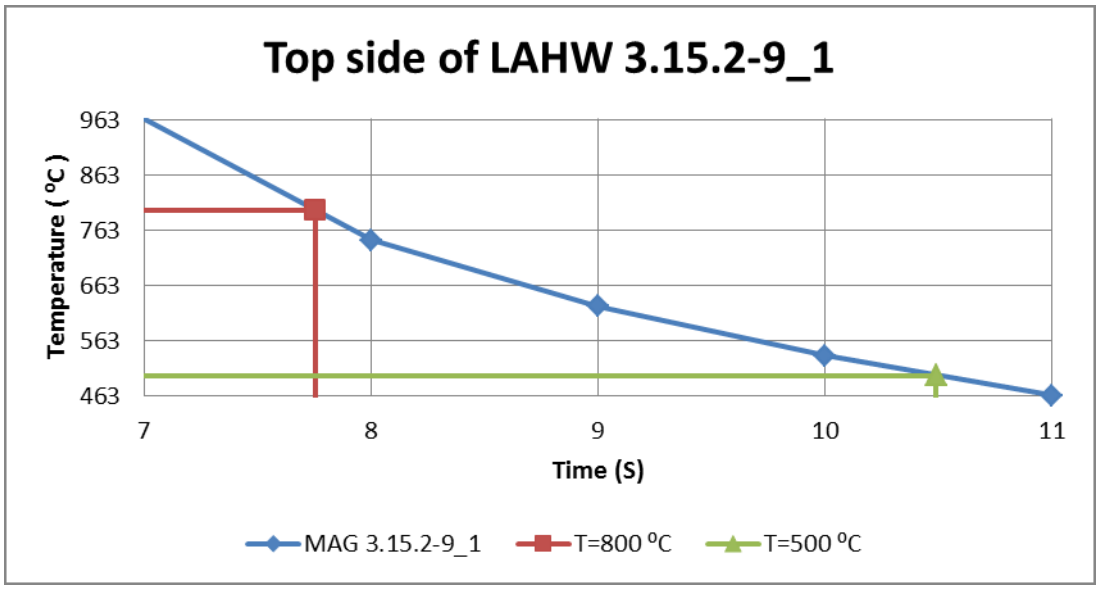

Figure 5 Interpolated $t_{8/5}$ value for thermoelements 0 of top side. $t_{8/5}$ value is 2.7 s.

Appendix 12

LAHW 3.5.2-3

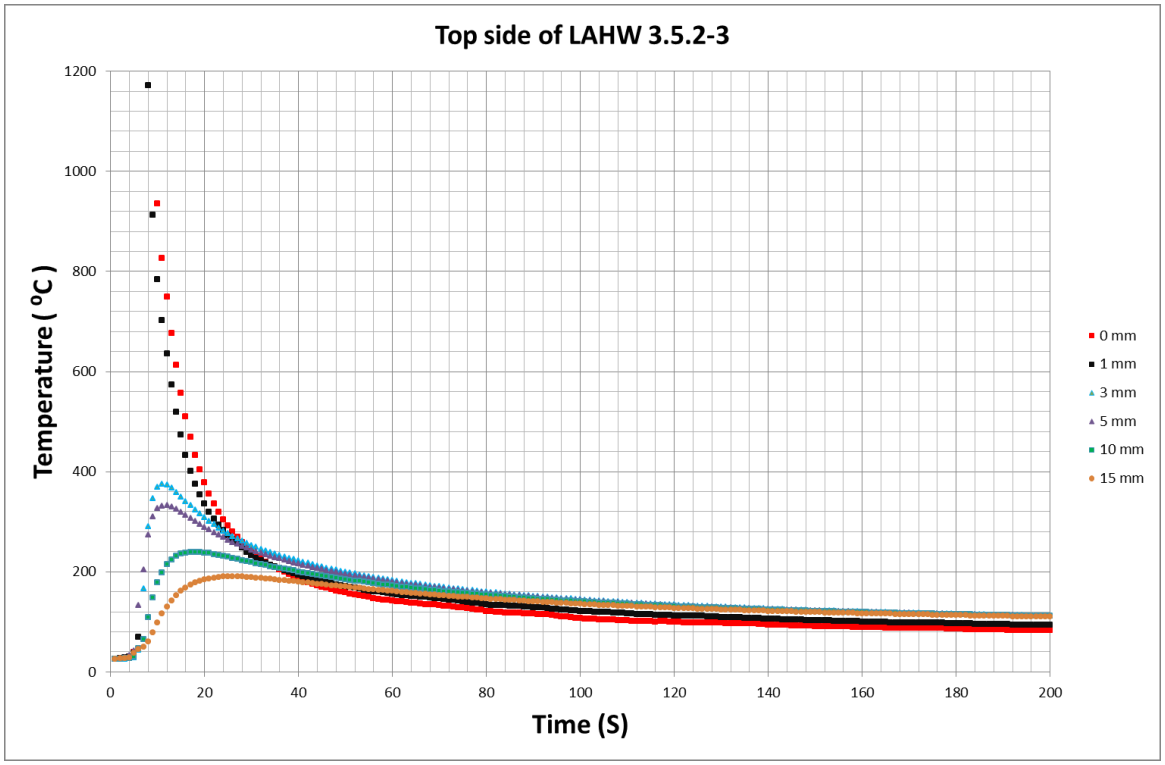

Figure 6 Top side of LAHW-weld sample 3.5.2-3.

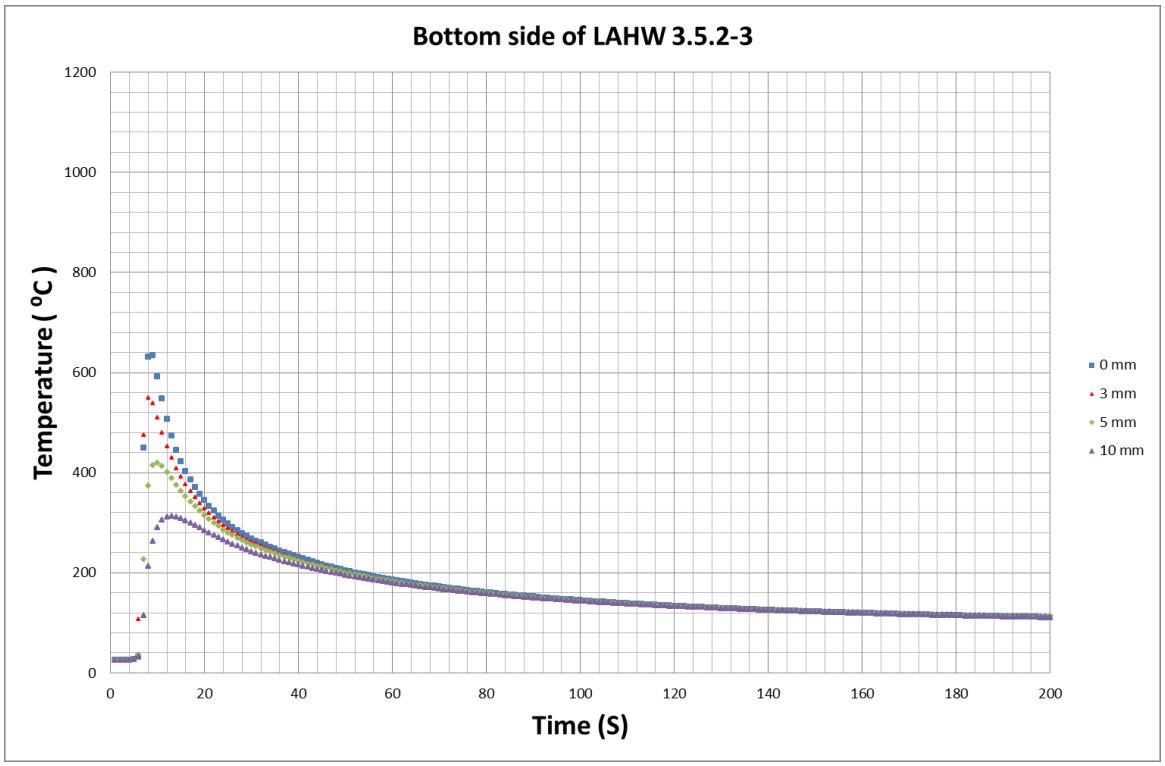

Figure 7 Bottom side of LAHW-weld sample 3.5.2-3.

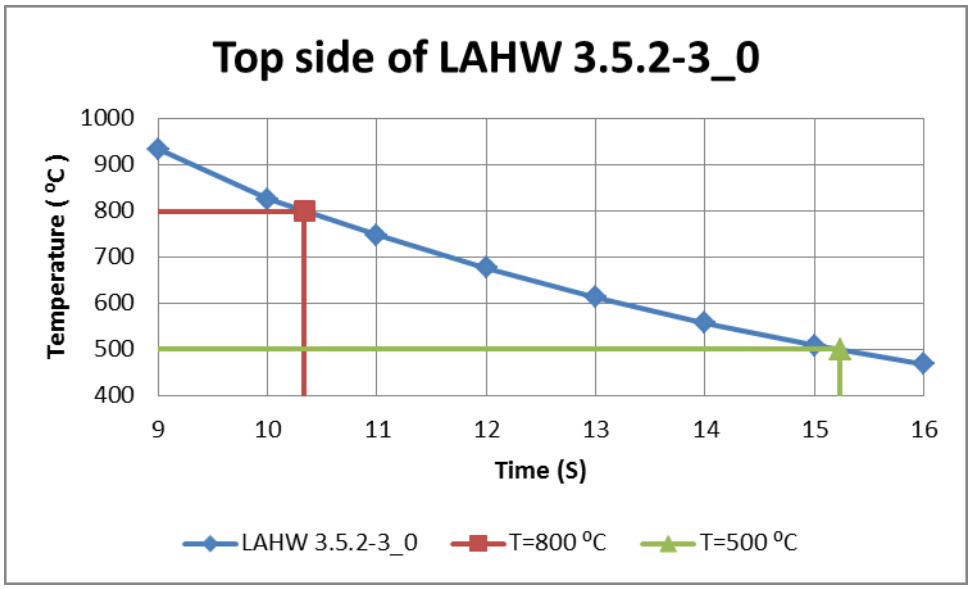

Figure 8 Interpolated $t_{8/5}$ value for thermoelements 0 of top side. $t_{8/5}$ value is 4.9 s.

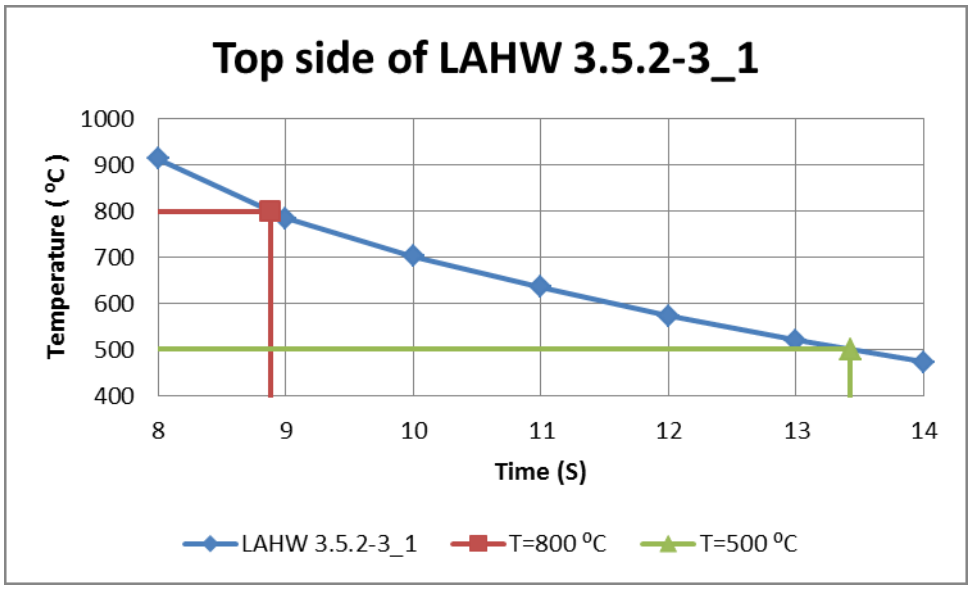

Figure 9 Interpolated $t_{8/5}$ value for thermoelements 0 of top side. $t_{8/5}$ value is 2.7 s.

Appendix 12

MAG 3.15.2-4

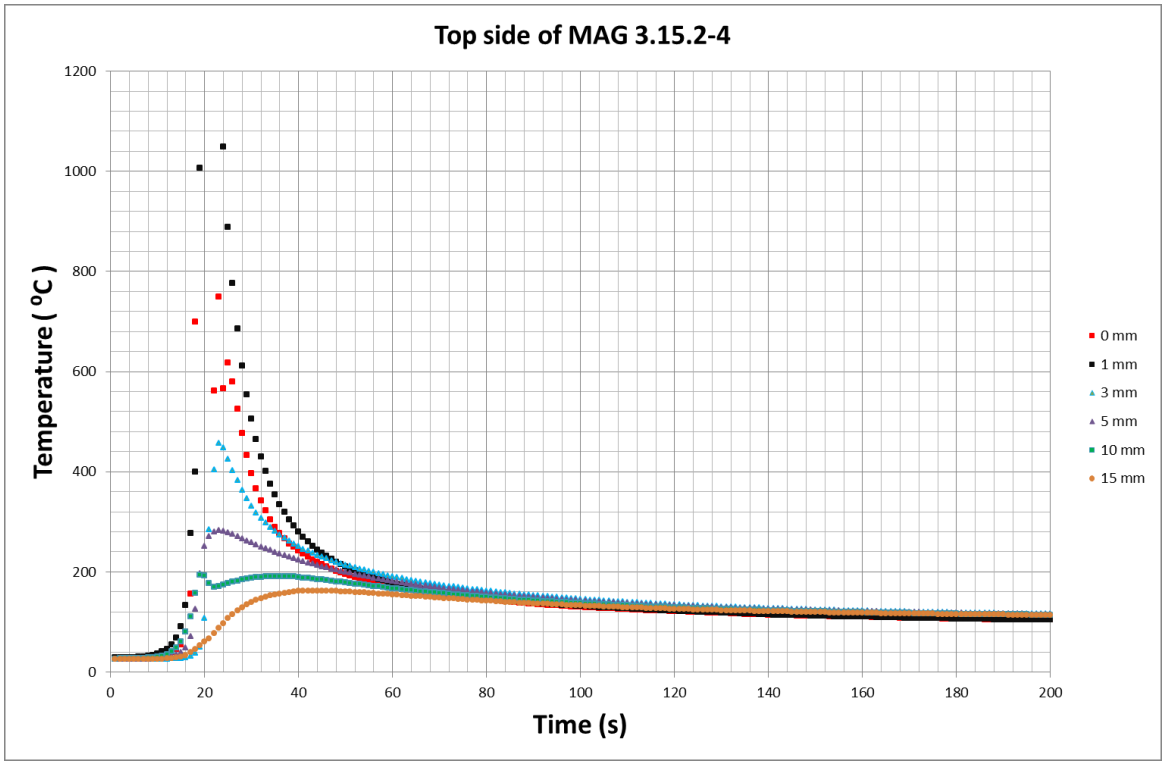

Figure 10 Top side of MAG-weld sample 3.15.2-4.

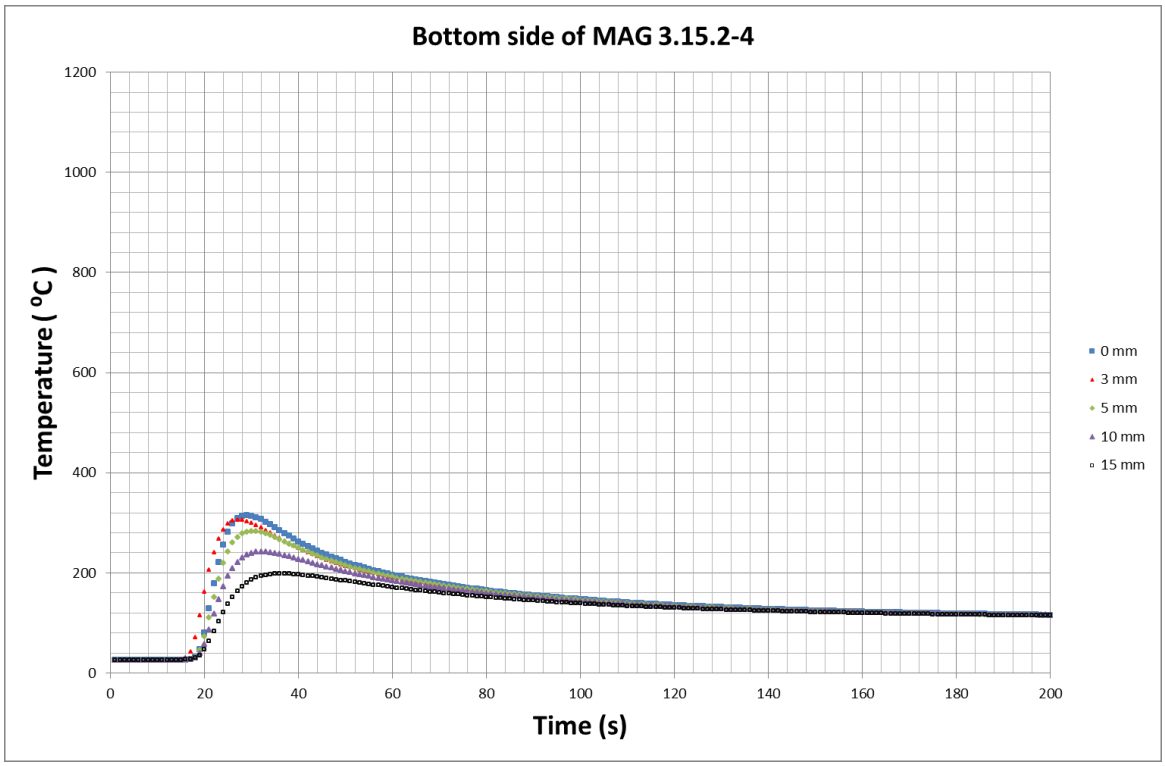

Figure 11 Bottom side of MAG-weld sample 3.15.2-4.

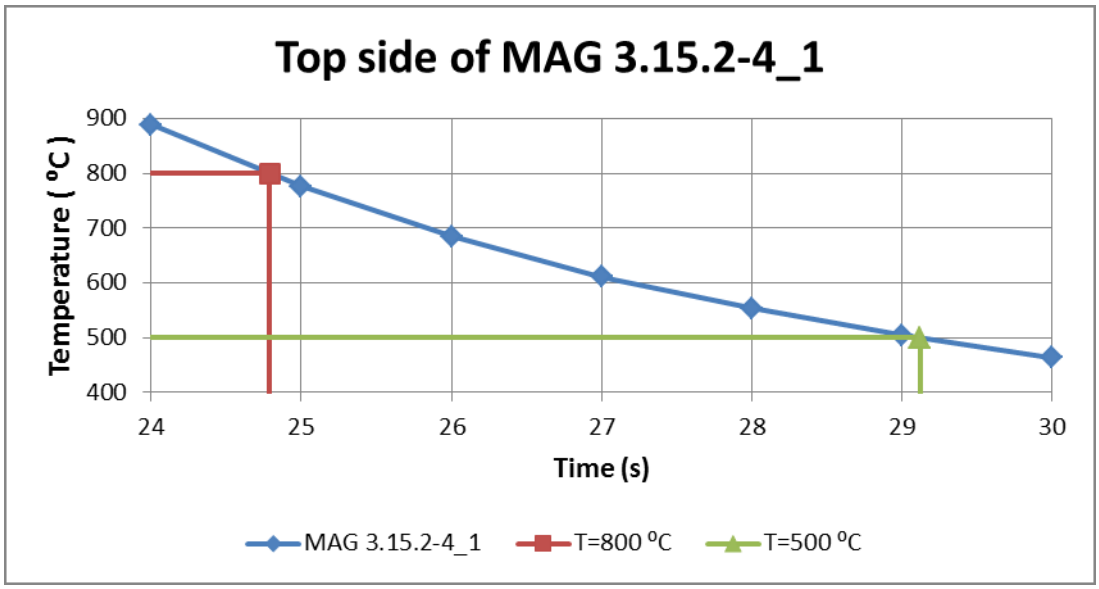

Figure 12 Interpolated $t_{8/5}$ value for thermoelements 0 of top side is 4.3 s.

MAG 3.5.2-2

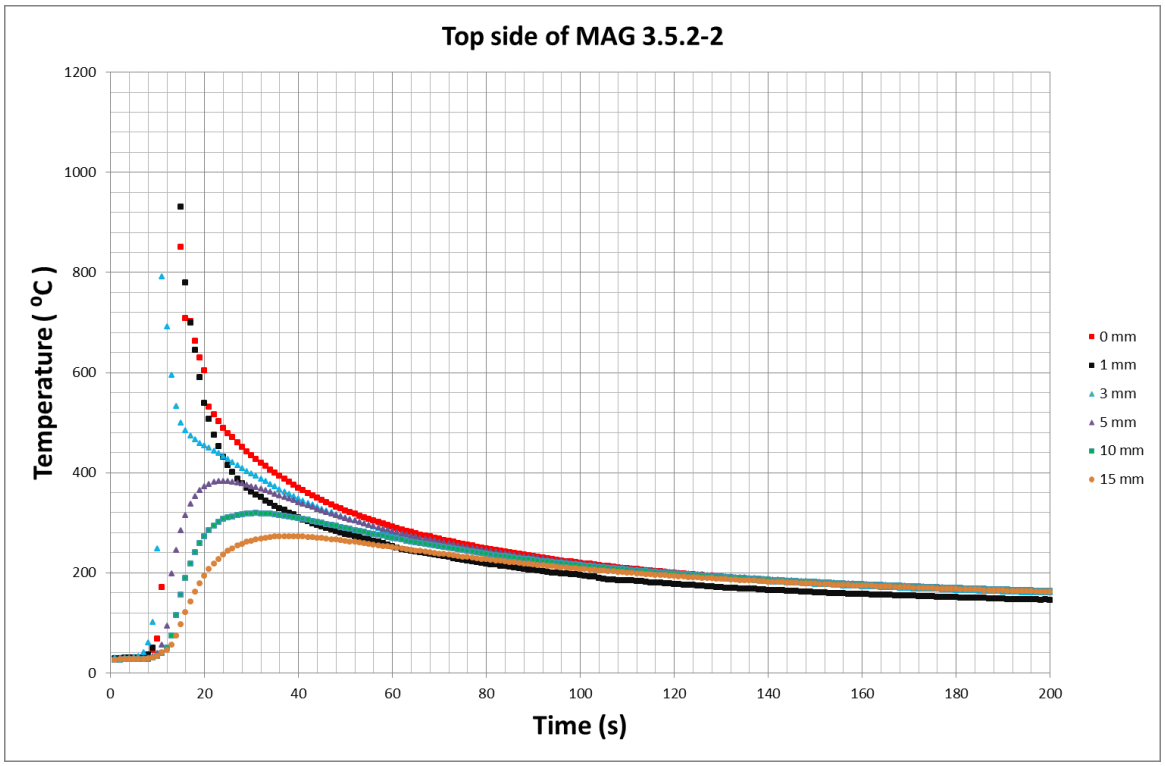

Figure 13 Top side of MAG-weld sample 3.5.2-2.

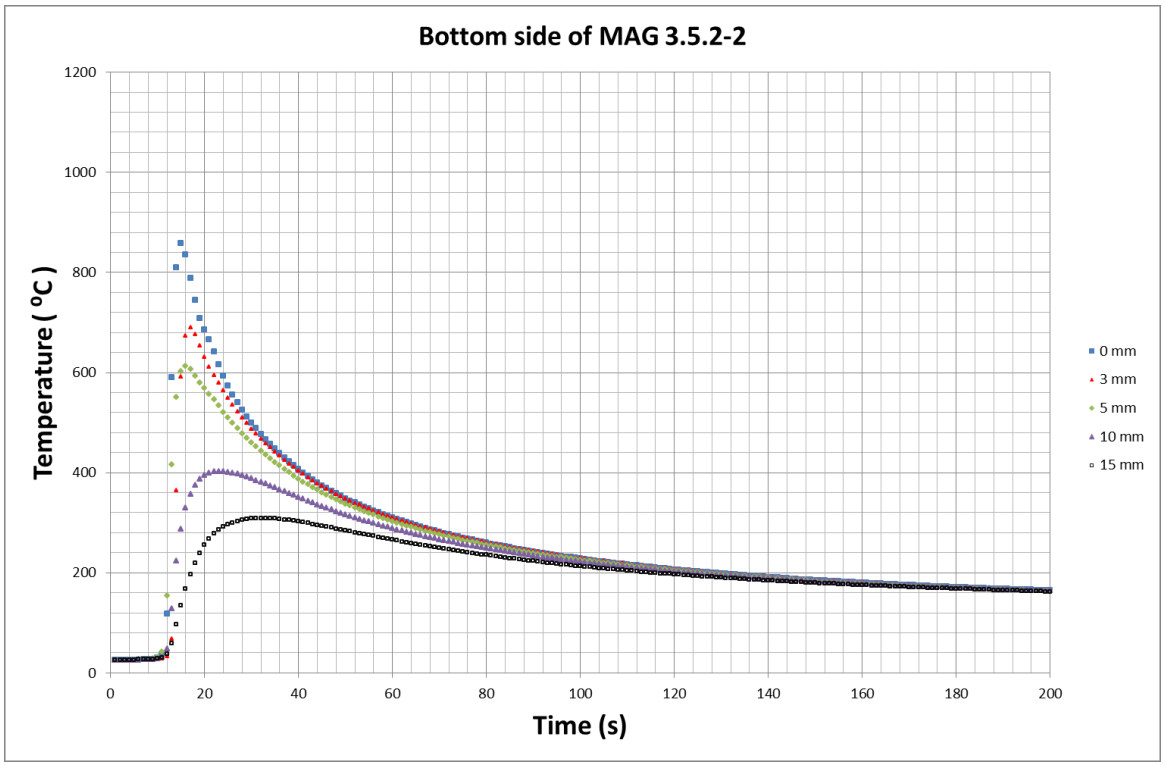

Figure 14 Bottom side of MAG-weld sample 3.5.2-2.

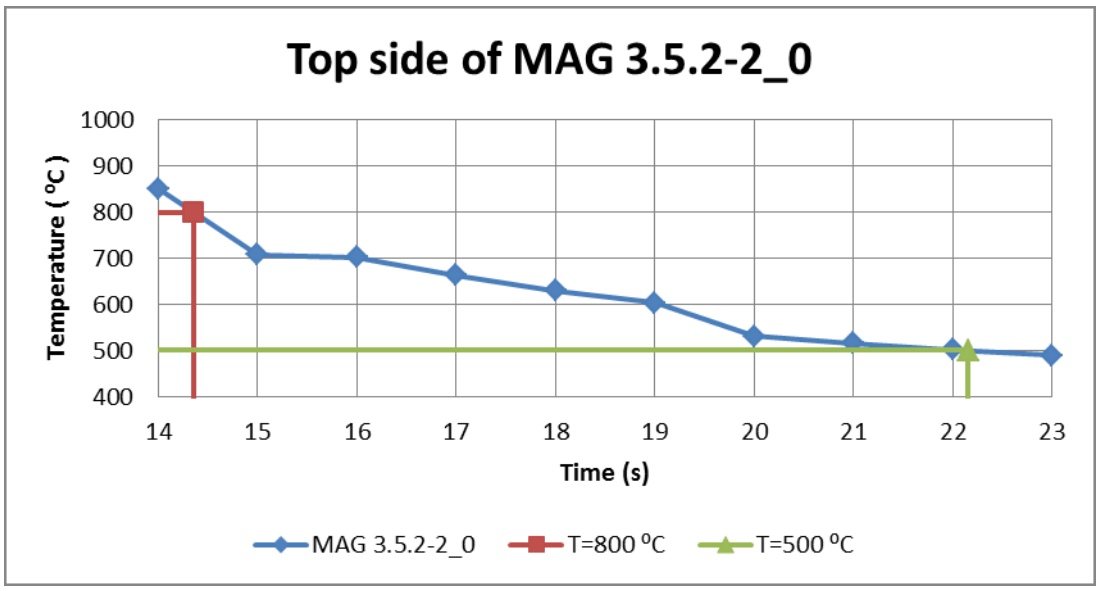

Figure 15 Interpolated $t_{8/5}$ value for thermoelements 0 of top side is 7.8 s.

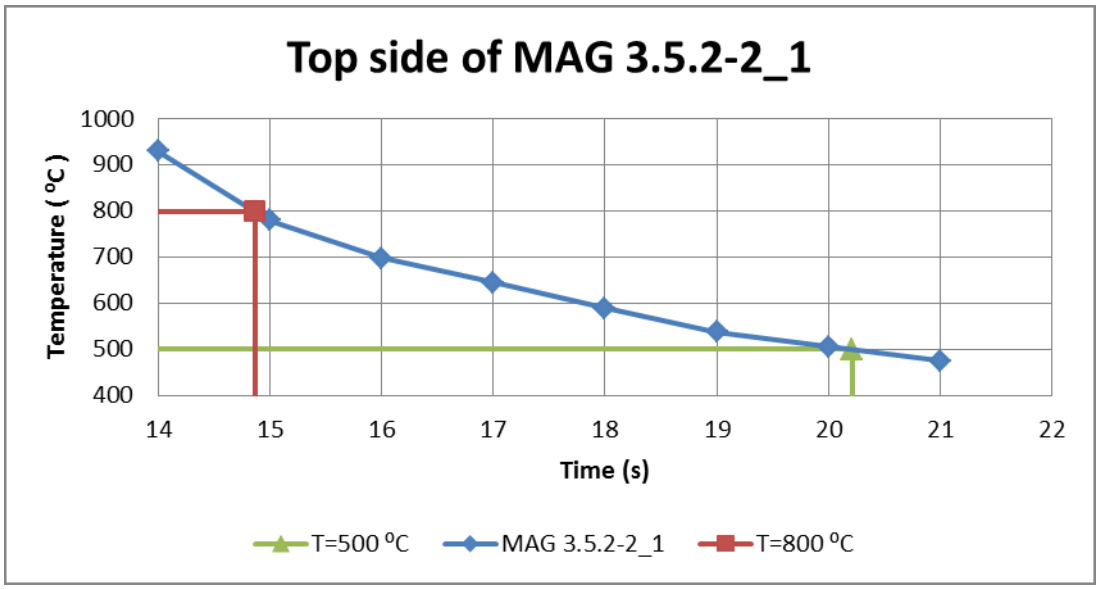

Figure 16 Interpolated $t_{8/5}$ value for thermoelements 1 of top side is 5.4 s.

LASER samples

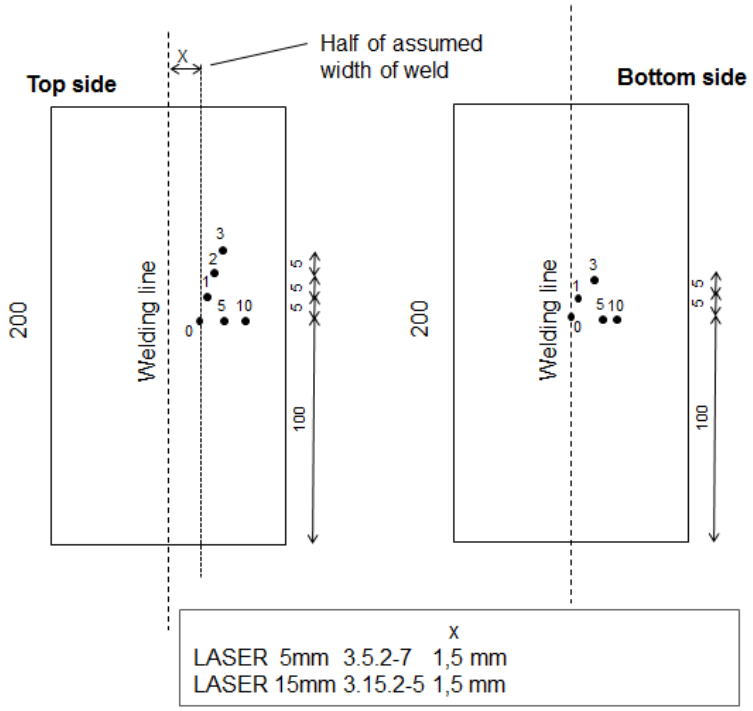

Figure 17 Positions of thermoelements of LASER samples.

LASER 3.15.2-5

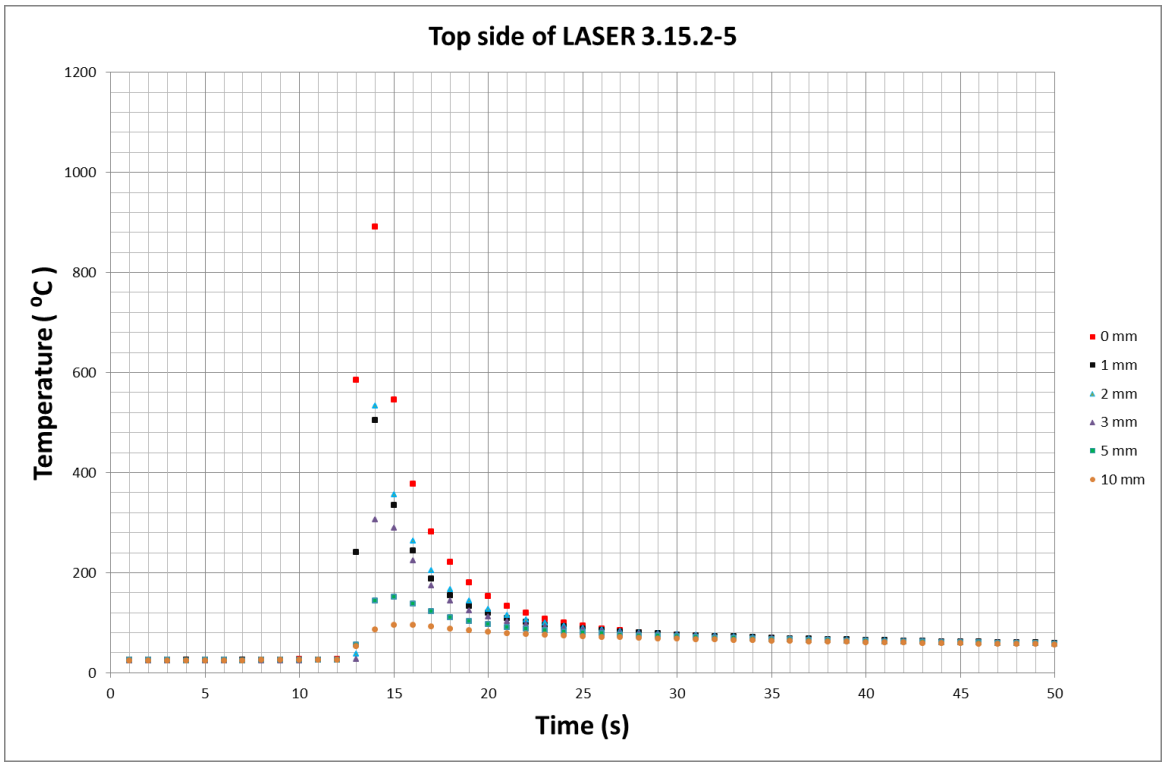

Figure 18 Top side of LASER-weld sample 3.15.2-5.

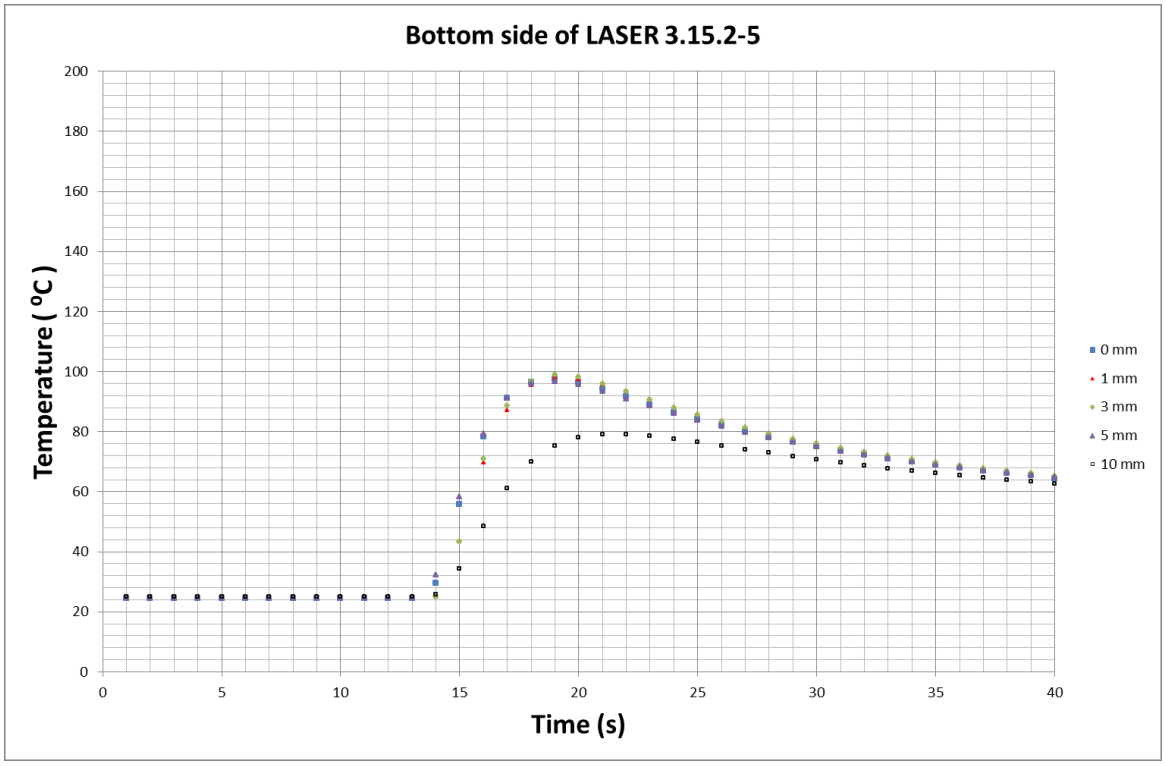

Figure 19 Bottom side of LASER-weld sample 3.15.2-5.

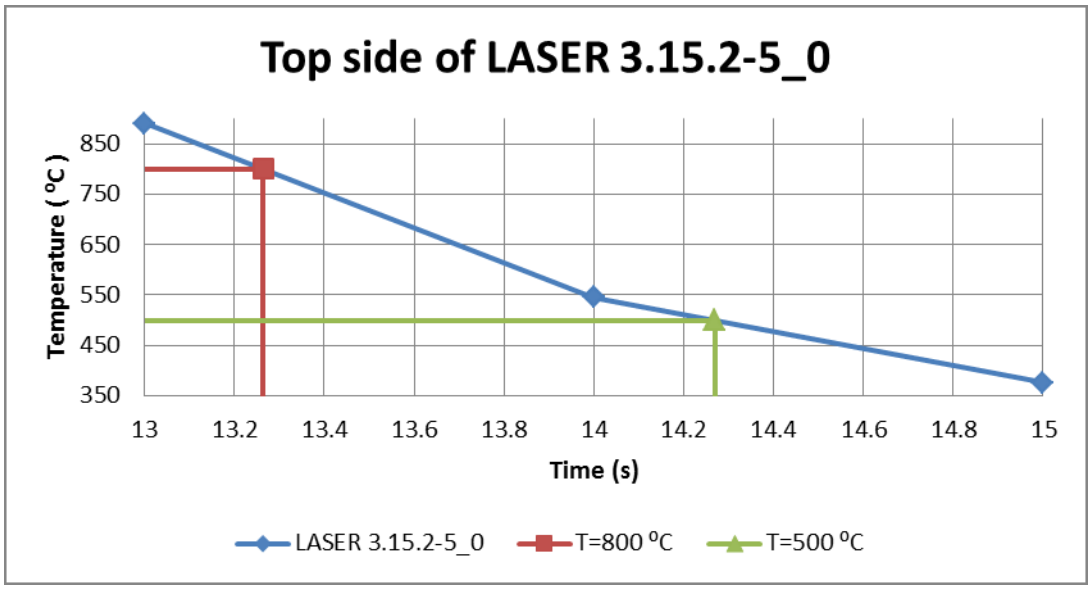

Figure 20 Interpolated $t_{8/5}$ value for thermoelements 0 of top side is 1.0 s.

LASER 3.5.2-7

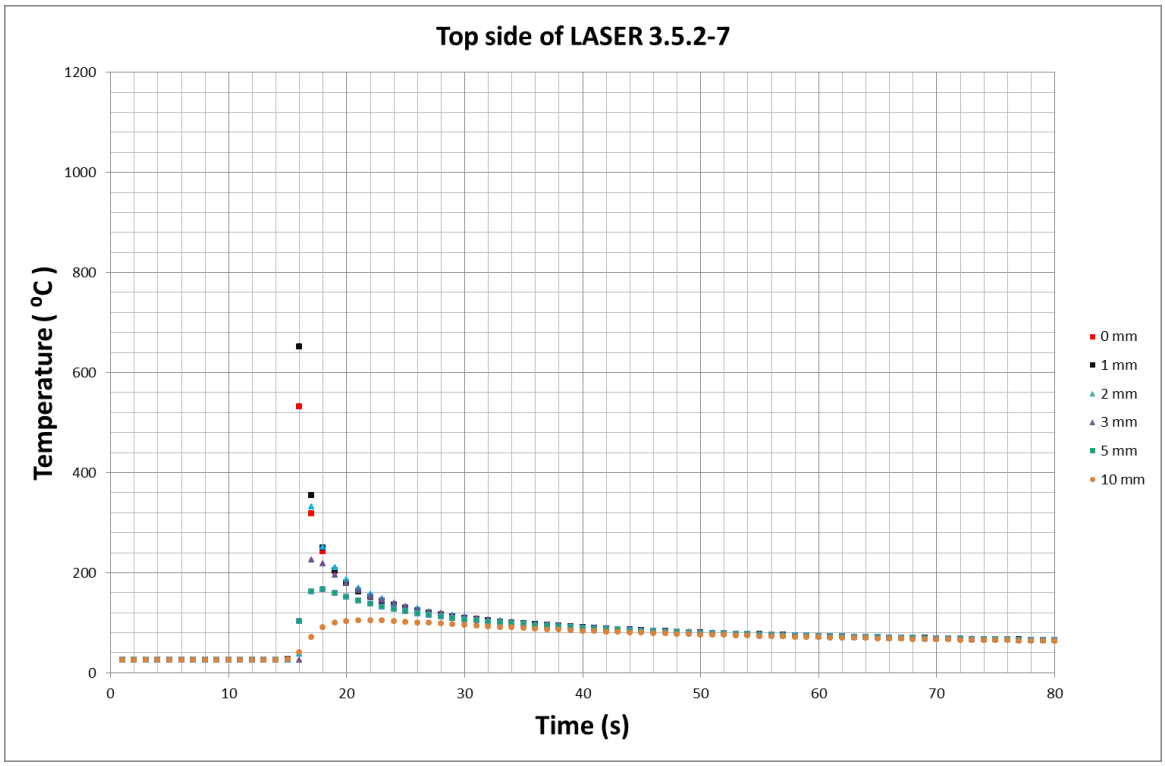

Figure 21 Top side of LASER-weld sample 3.5.2-7.

Appendix 12

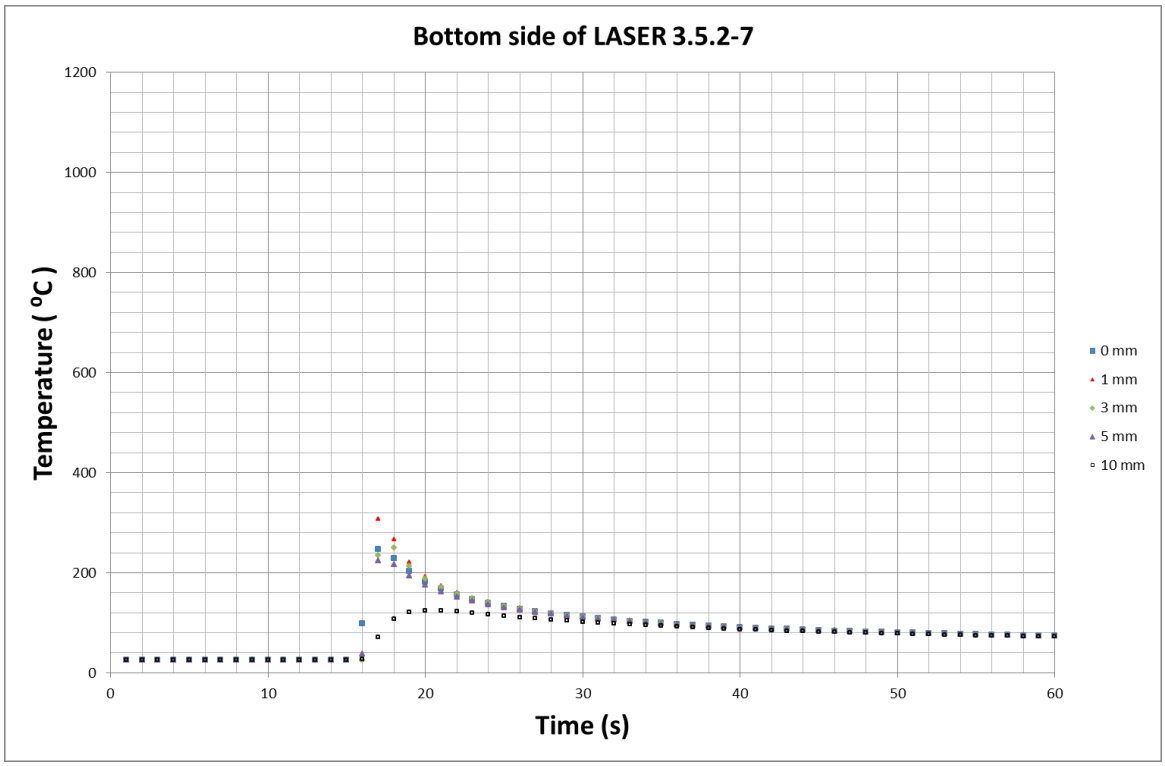

Figure 22 Bottom side of LASER-weld sample 3.5.2-7.

TIG samples

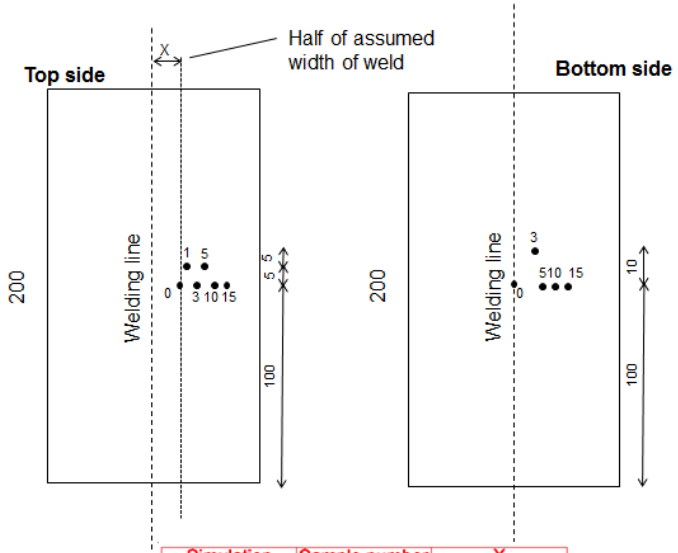

Simulation	Sample number	X
BOP-1.1	3.5.2-8	4
BOP-2.1	3.5.2-9	5
BOP-4.1	3.15.2-4	6
BOP-5.1	3.15.2-6	4
BOP-6.1	3.15.2-7	4
BOP-7.1	3.15.2-8	4

Figure 23 Positions of thermoelements of TIG samples.

Appendix 12

TIG 3.5.2-8 (BOP 1.1)

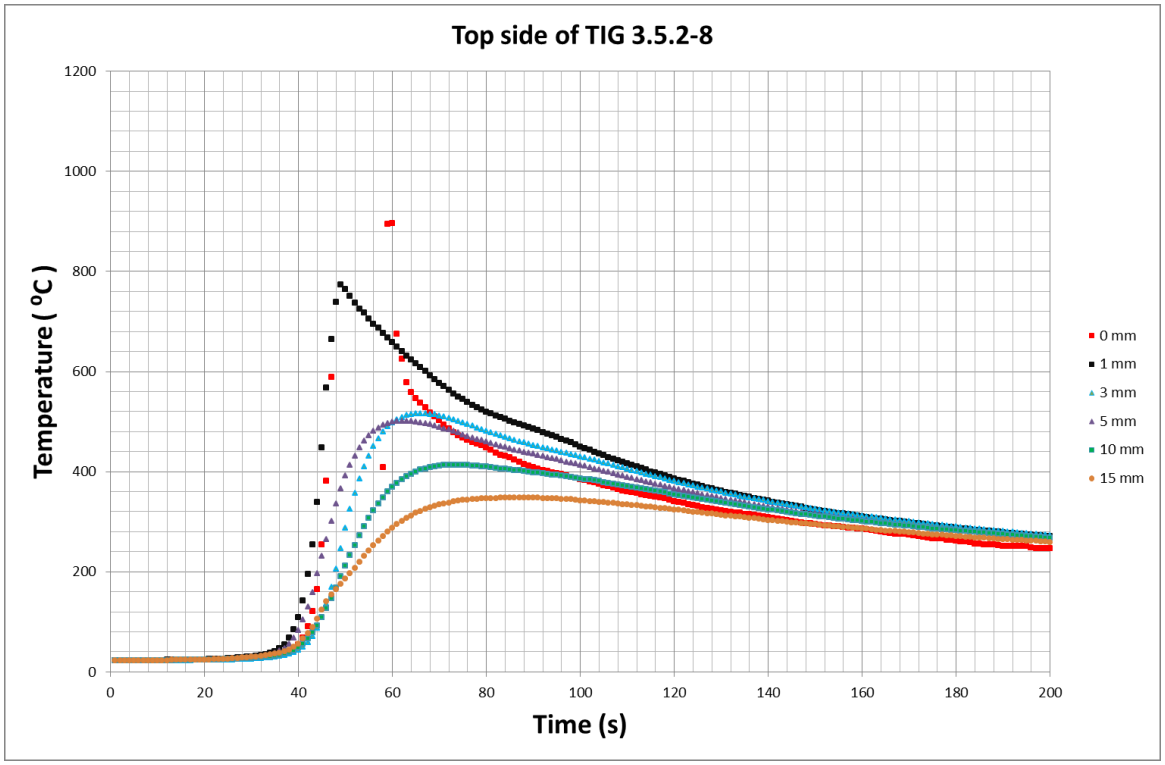

Figure 24 Top side of TIG-weld sample 3.5.2-8.

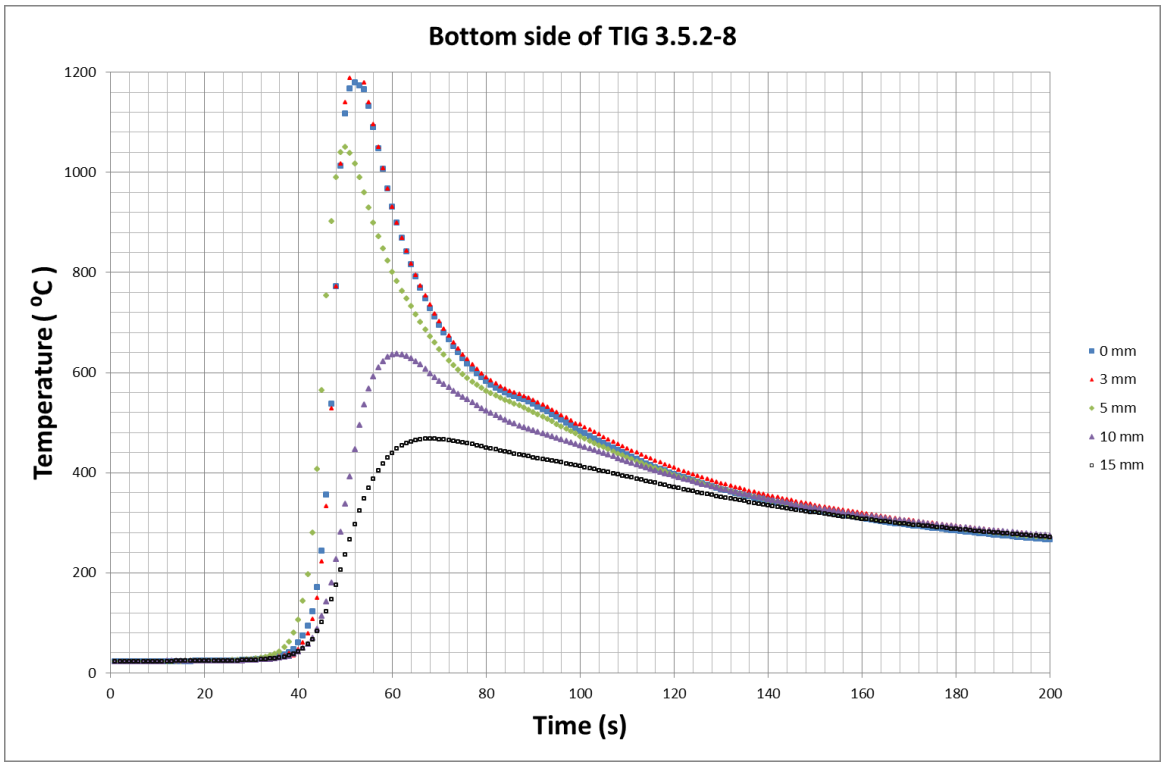

Figure 25 Bottom side of TIG-weld sample 3.5.2-8

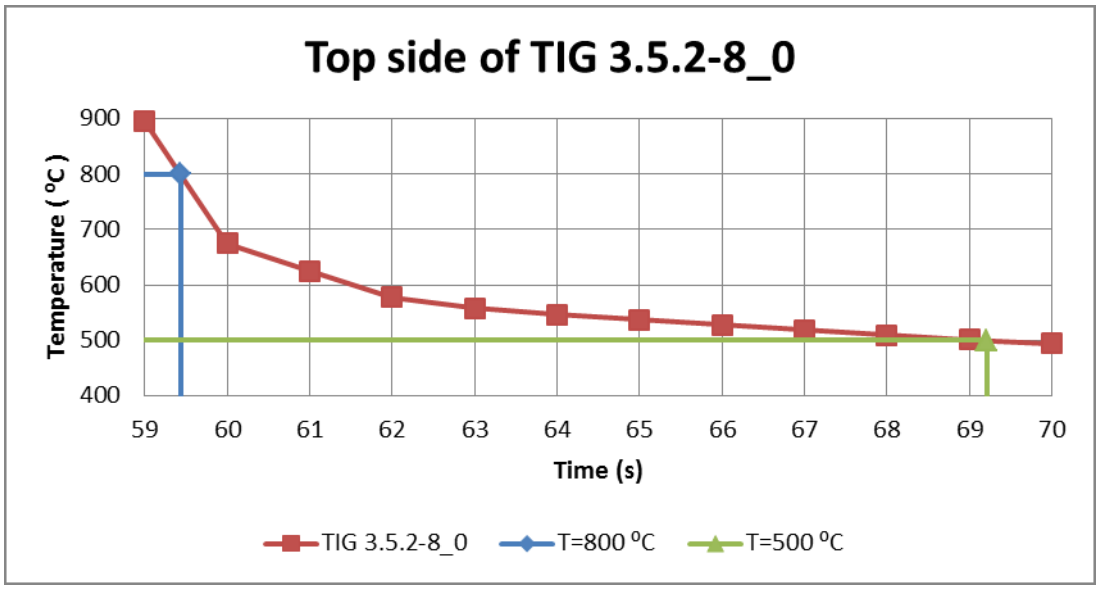

Figure 26 Interpolated $t_{8/5}$ value for thermoelements 0 of top side is 9.8 s.

TIG 3.5.2-9 (BOP 2.1)

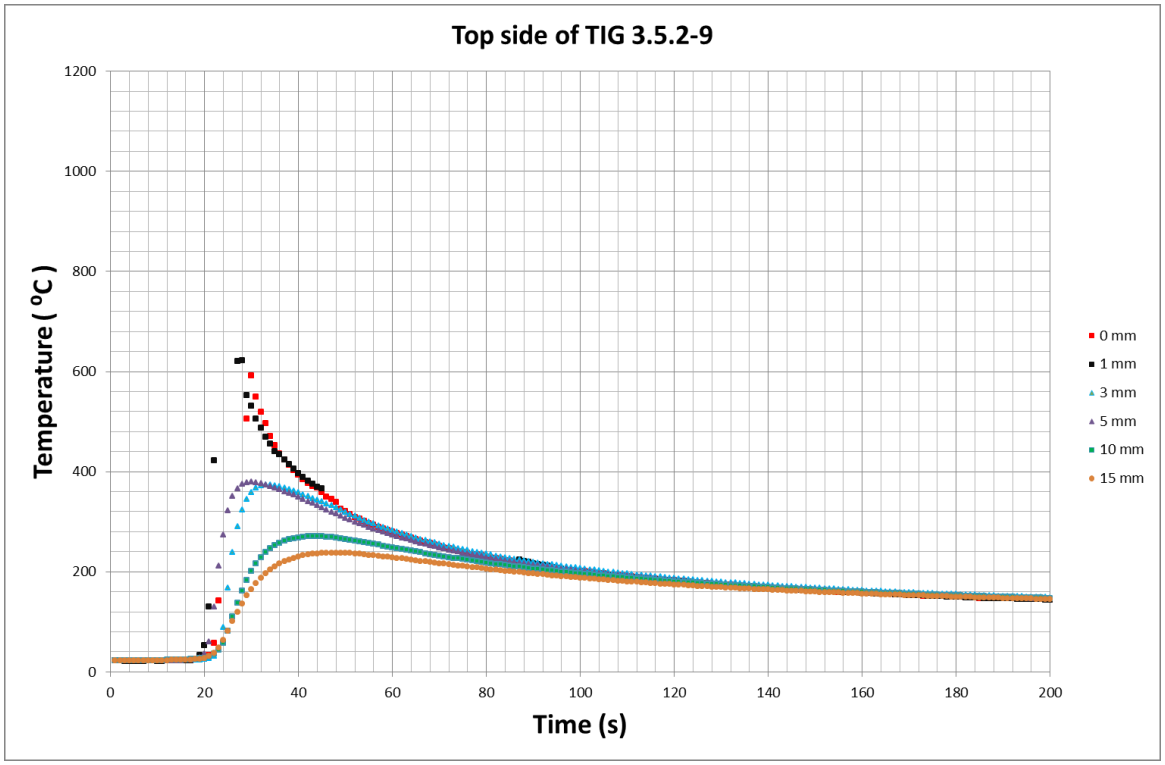

Figure 27 Top side of TIG-weld sample 3.5.2-9.

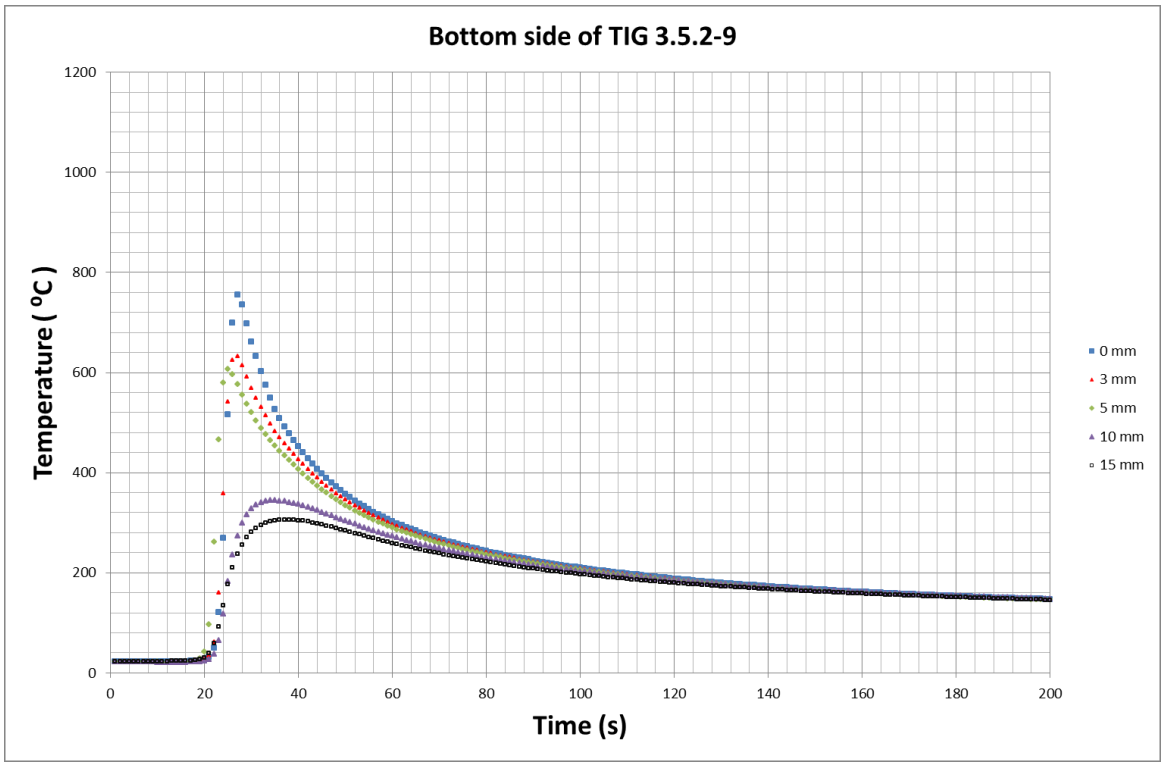

Figure 28 Bottom side of TIG-weld sample 3.5.2-9.

TIG 3.5.2-4 (BOP 4.1)

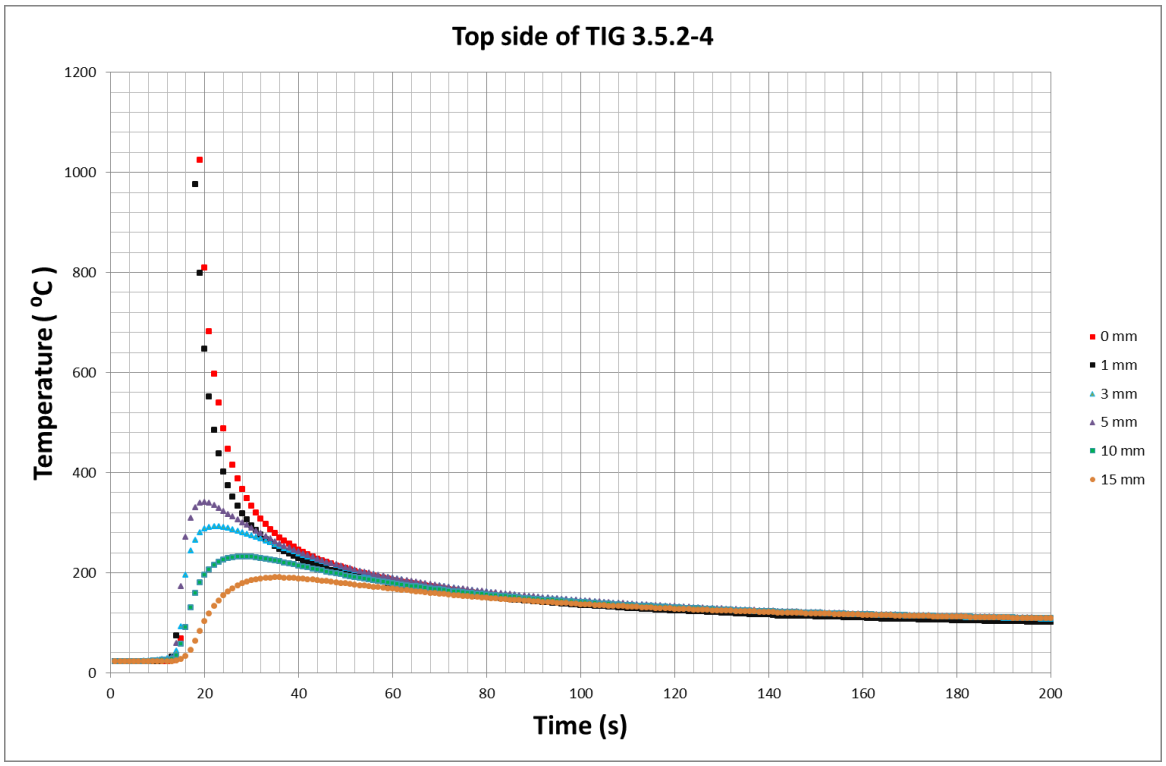

Figure 29 Top side of TIG-weld sample 3.15.2-4.

Appendix 12

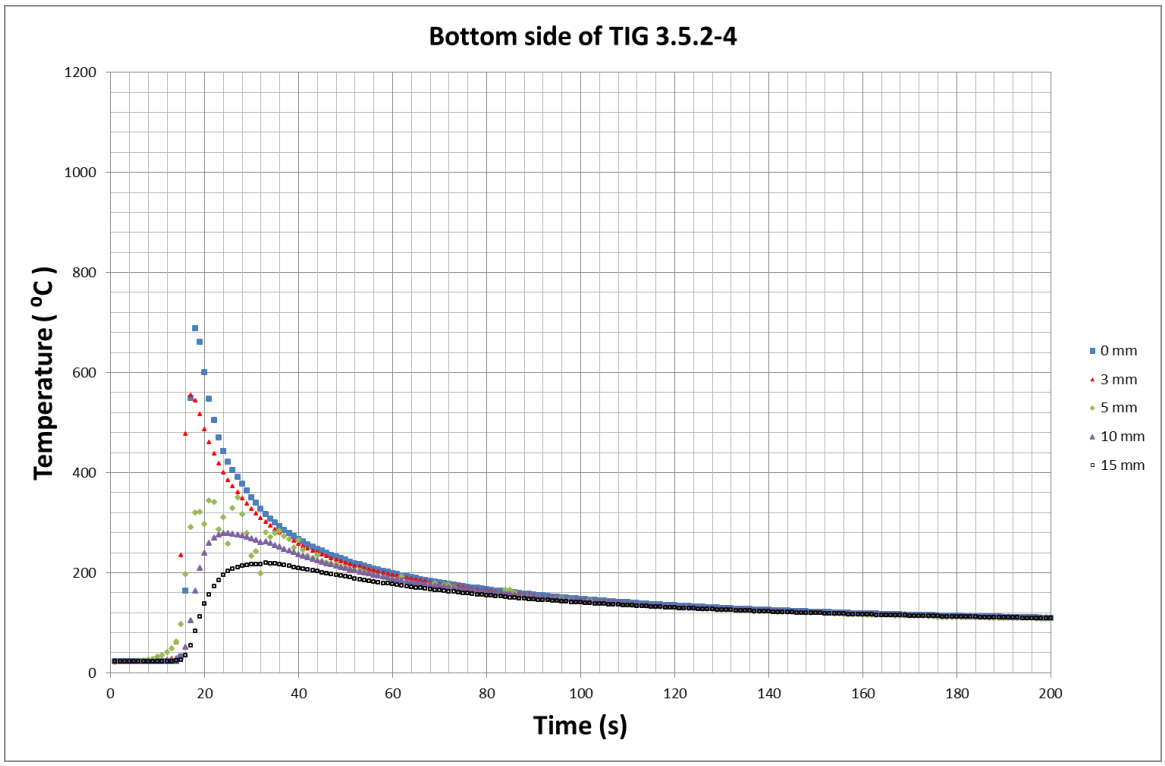

Figure 30 Bottom side of TIG-weld sample 3.15.2-4.

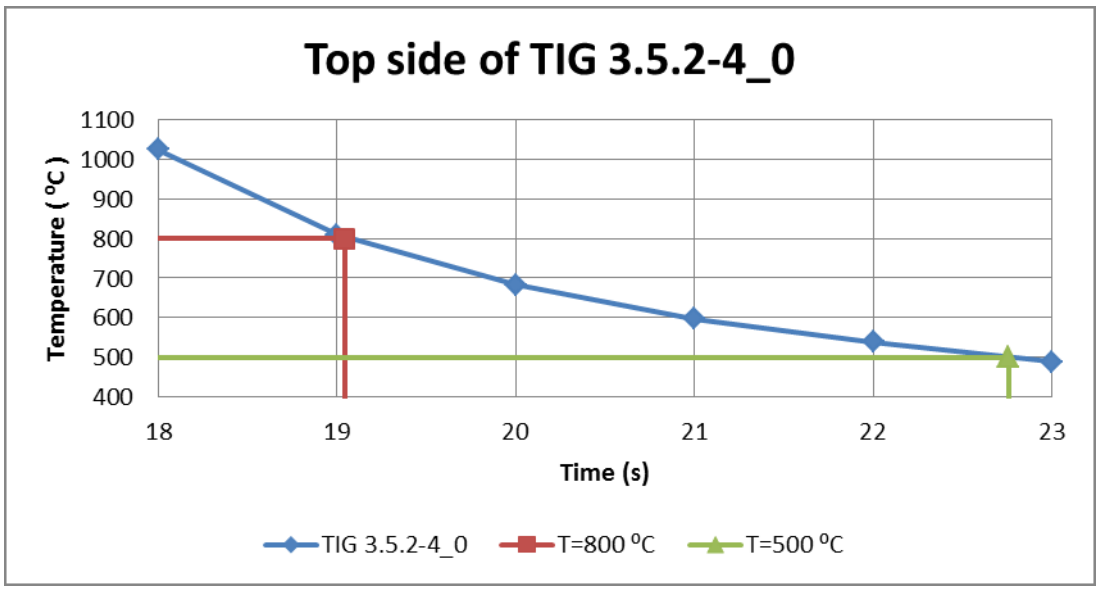

Figure 31 Interpolated $t_{8/5}$ value for thermoelements 0 of top side is 3.7 s.

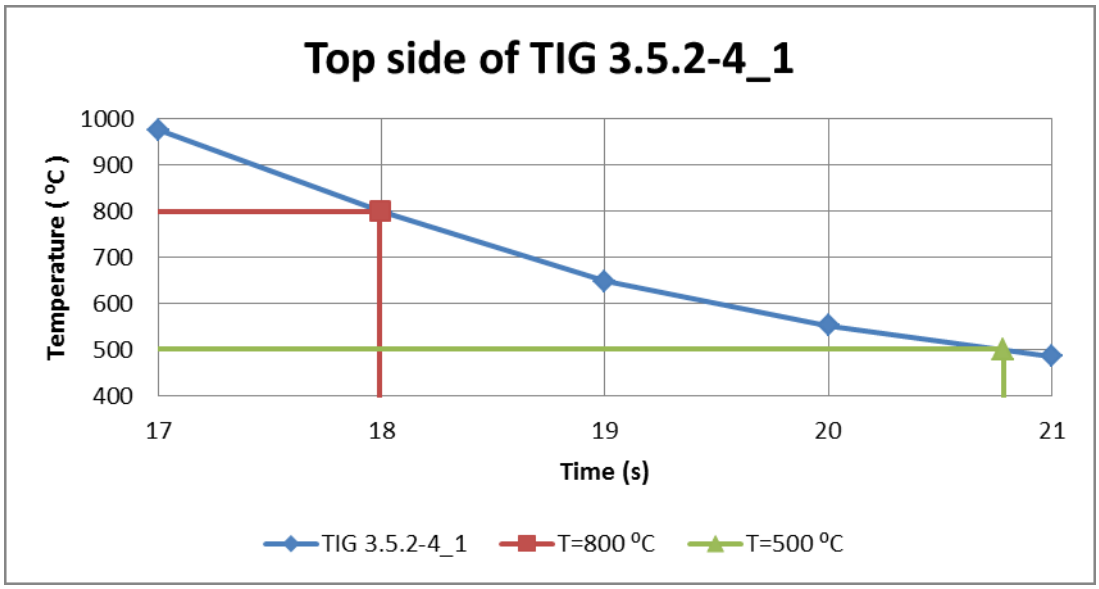

Figure 32 Interpolated $t_{8/5}$ value for thermoelements 0 of top side is 2.8 s.

TIG 3.15.2-6 (BOP 5.1)

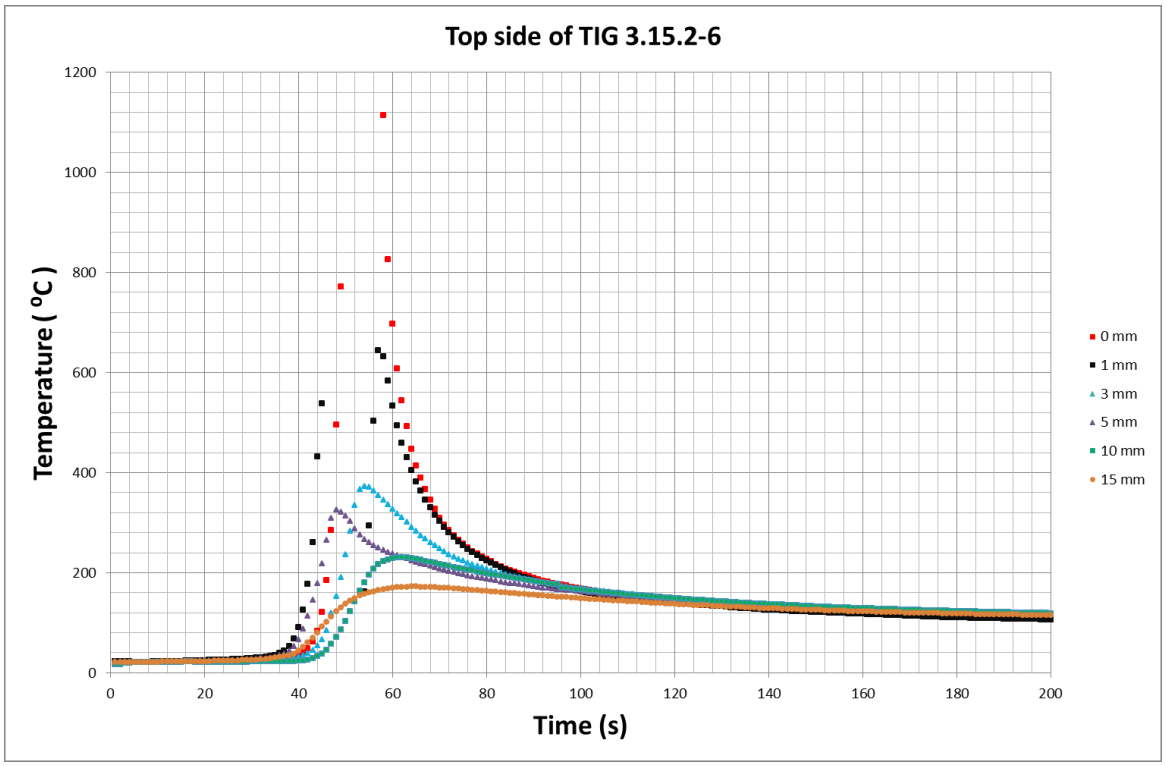

Figure 33 Top side of TIG-weld sample 3.15.2-6.

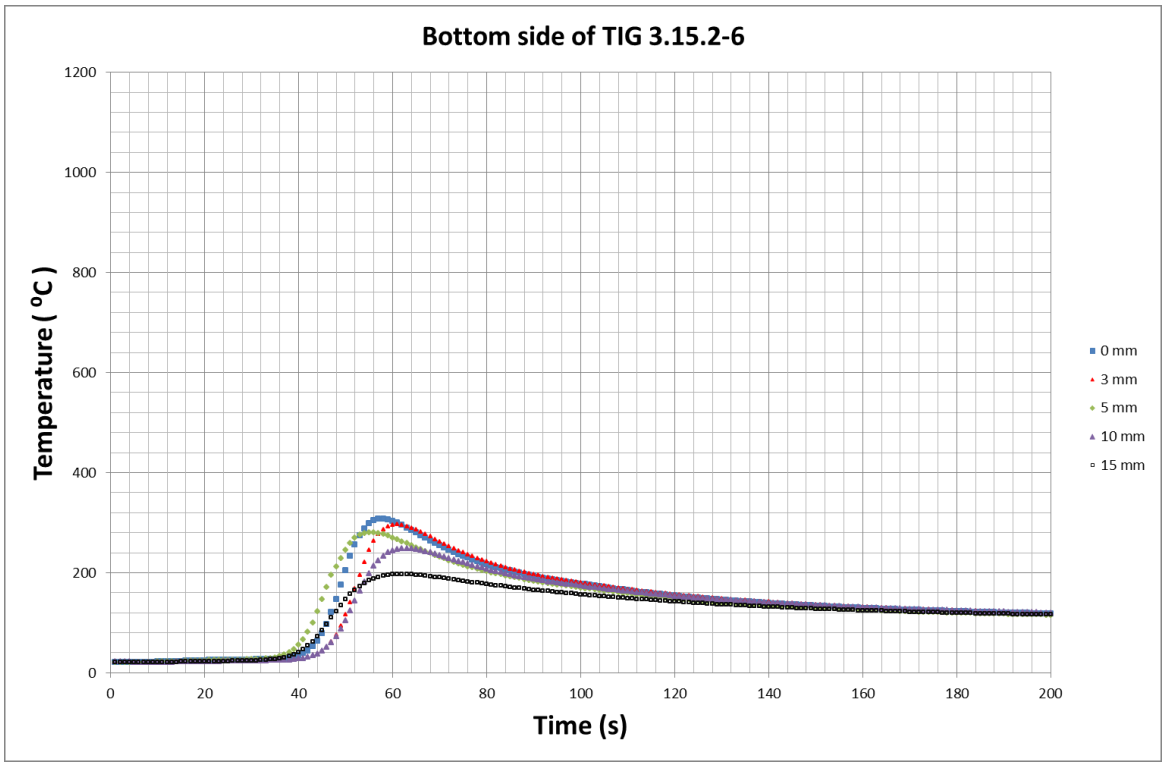

Figure 34 Bottom side of TIG-weld sample 3.15.2-6.

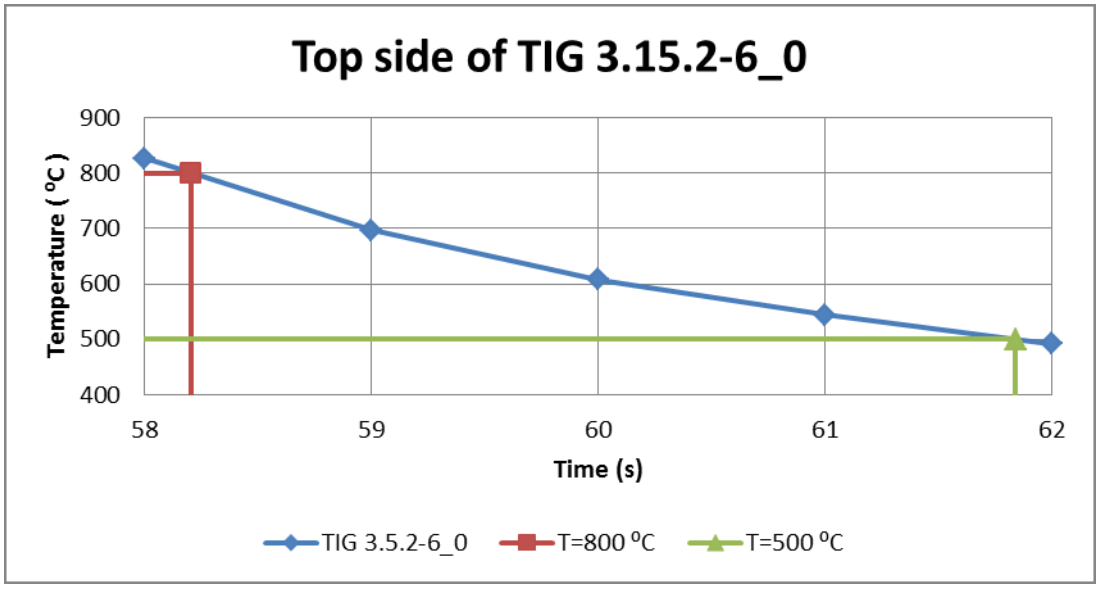

Figure 35 Interpolated $t_{8/5}$ value for thermoelements 0 of top side is 3.6 s.

Appendix 12

TIG 3.15.2-7 (BOP 6.1)

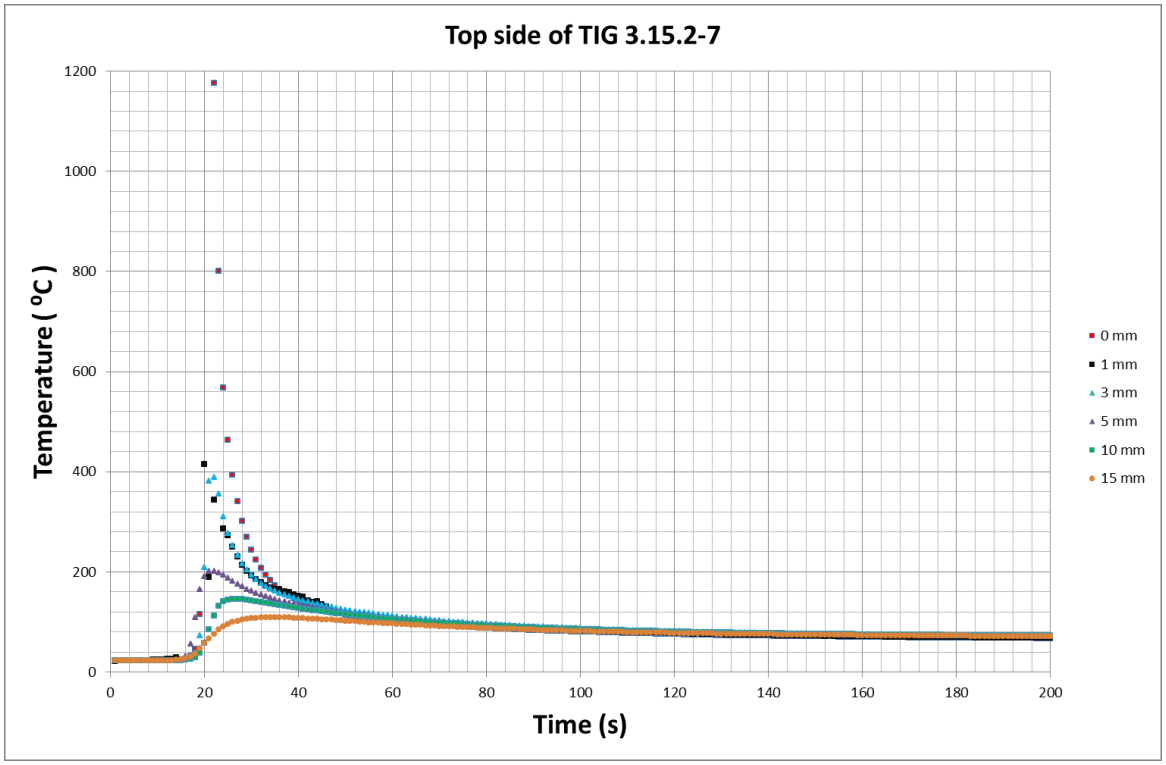

Figure 36 Top side of TIG weld sample 3.15.2-7.

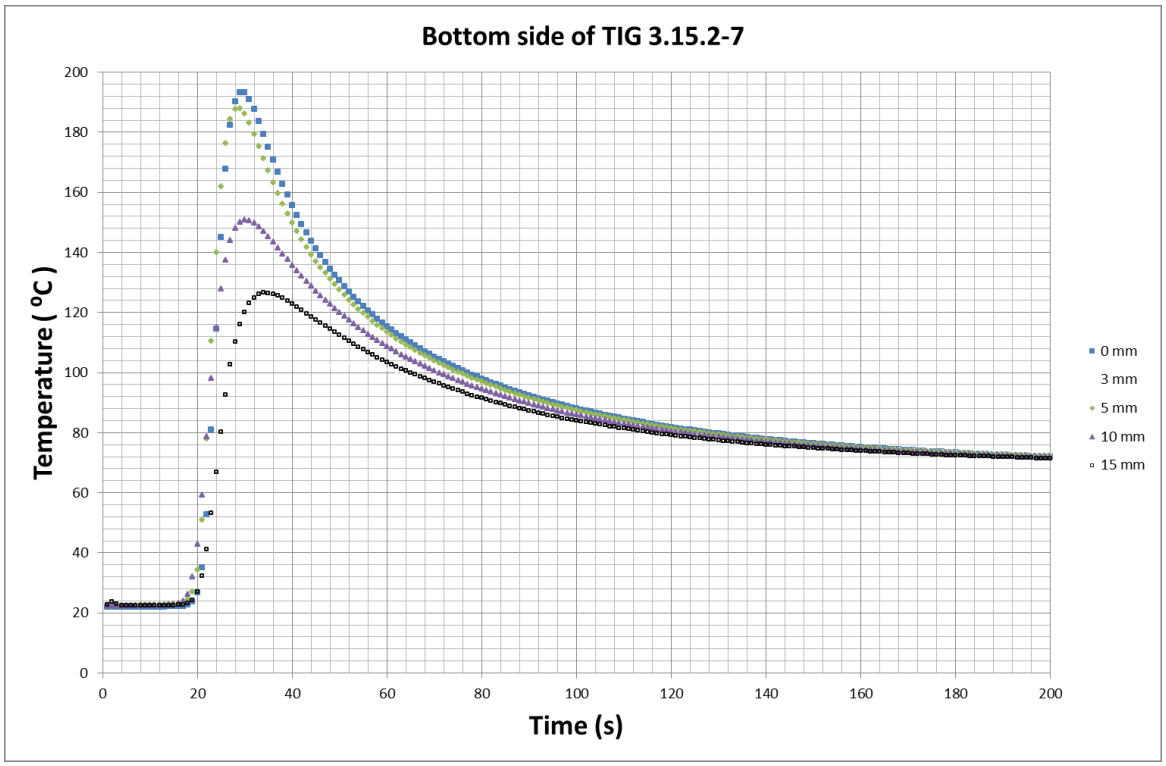

Figure 37 Bottom side of TIG weld sample 3.15.2-7.

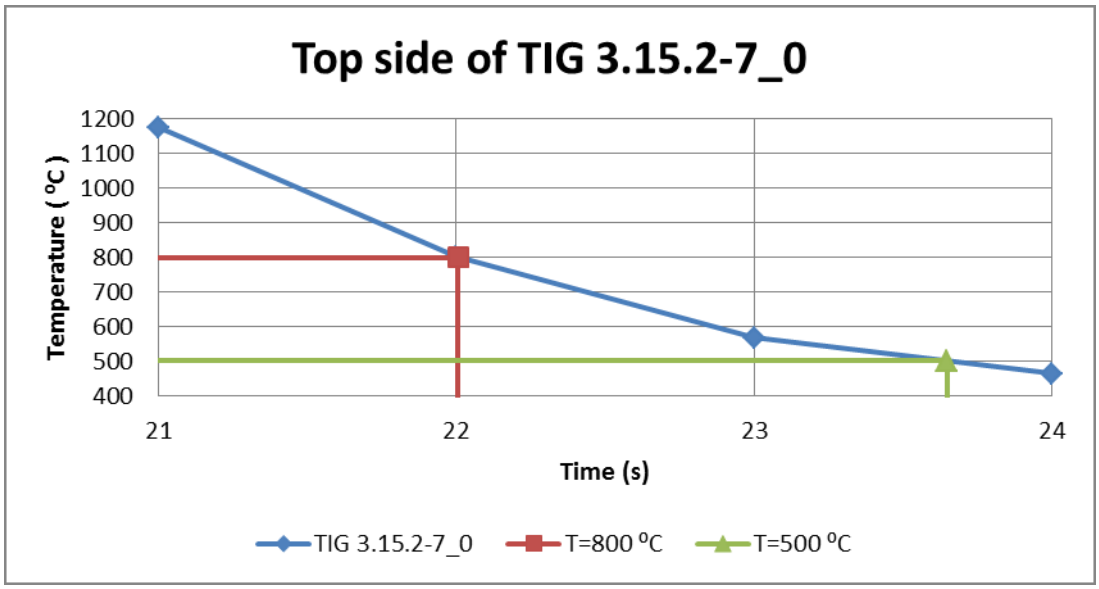

Figure 38 Interpolated $t_{8/5}$ value for thermoelements 0 of top side is 1.6 s.

TIG 3.15.2-8 (BOP 7.1)

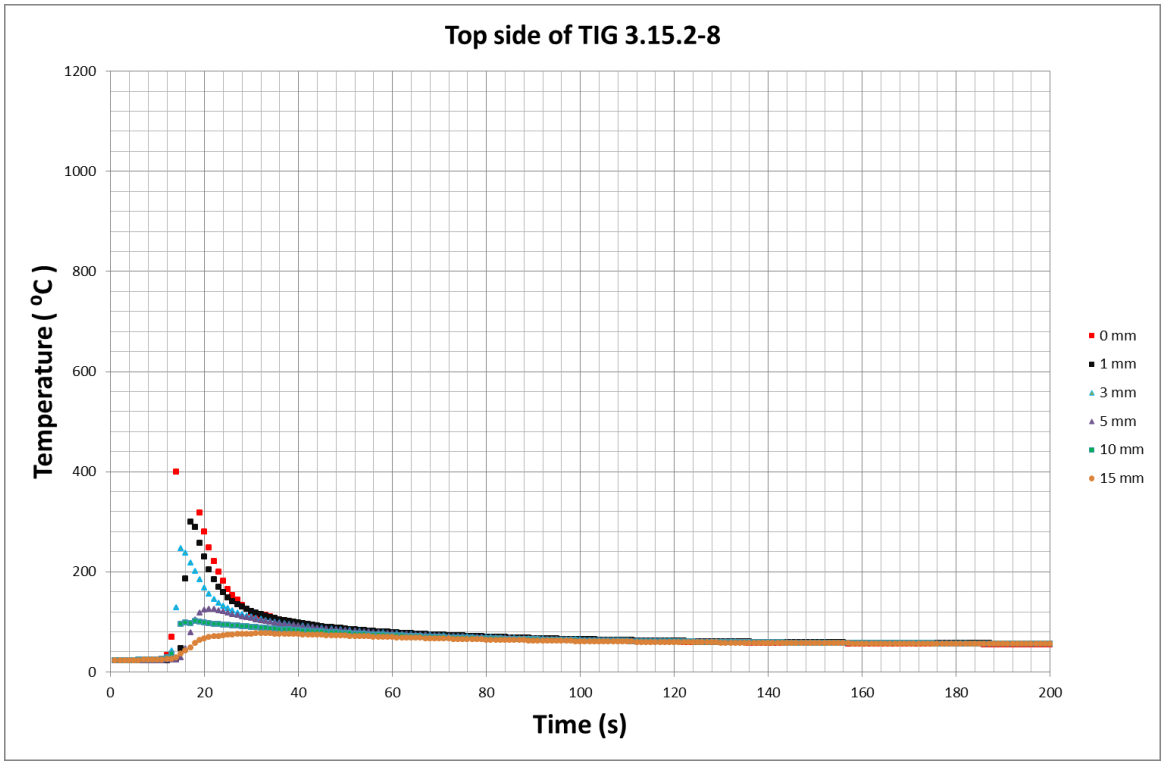

Figure 39 Top side of TIG weld sample 3.15.2-8.

Appendix 12

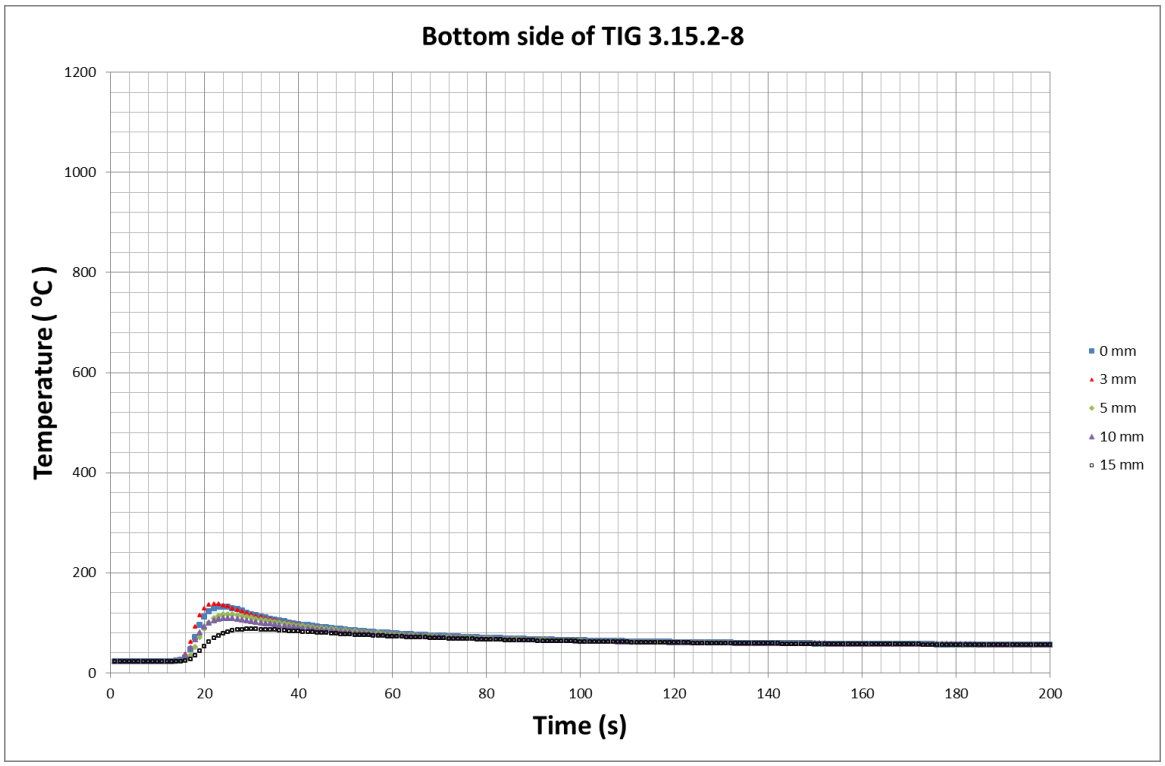

Figure 40 Bottom side of TIG-weld sample 3.15.2-8.

Appendix 13 / Cooling simulation of 3D-flow and the determined $t_{8/5}$ cooling times

Contents

Appendix 13

Table 1 $t_{8/5}$ values were determined with the help of 3D-flow simulation and Excel. N means no data awailable and - means too small temperature area to determine $t_{8/5}$ value.

Number of sample	Modelling code	Thickness (mm)	Simulated position (0) $t_{8/5}$ (s)	Simulated position (P) $t_{8/5}$ (s)
LAHW 3.5.2-3	-	5	-	-
LAHW 3.15.2-9	-	15	-	-
LASER 3.5.2-7	-	5	-	-
LASER 3.15.2-5	-	15	-	-
MAG 3.5.2-2	MIG 5 mm	5	10.6	9.7
MAG 3.15.2-4	MIG 15 mm	15	2.7	2.7
TIG 3.5.2-8	BOP-1.1	5	4.8	4.8
TIG 3.5.2-9	BOP-2.1	5	4.3	4.2
TIG 3.5.2-4	BOP-4.1	5	1.6	1.9
TIG 3.15.2-6	BOP-5.1	15	1.4	1.4
TIG 3.15.2-7	BOP-6.1	15	1.4	1.4
TIG 3.15.2-8	BOP-7.1	15	-	-

LAHW and MAG samples

LAHW 3.15.2-9

- No simulation

LAHW 3.5.2-3

- No simulation

Appendix 13

MAG 3.15.2-4

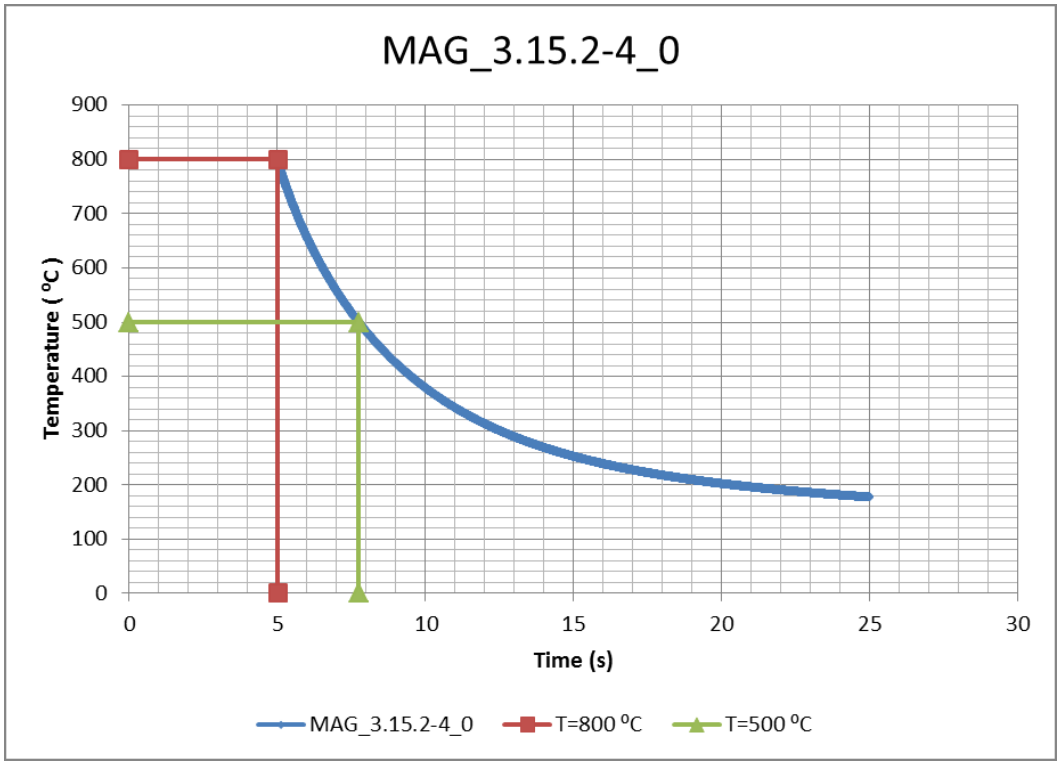

Figure 1 Interpolated $t_{8/5}$ value of fusion line is 2.7 s.

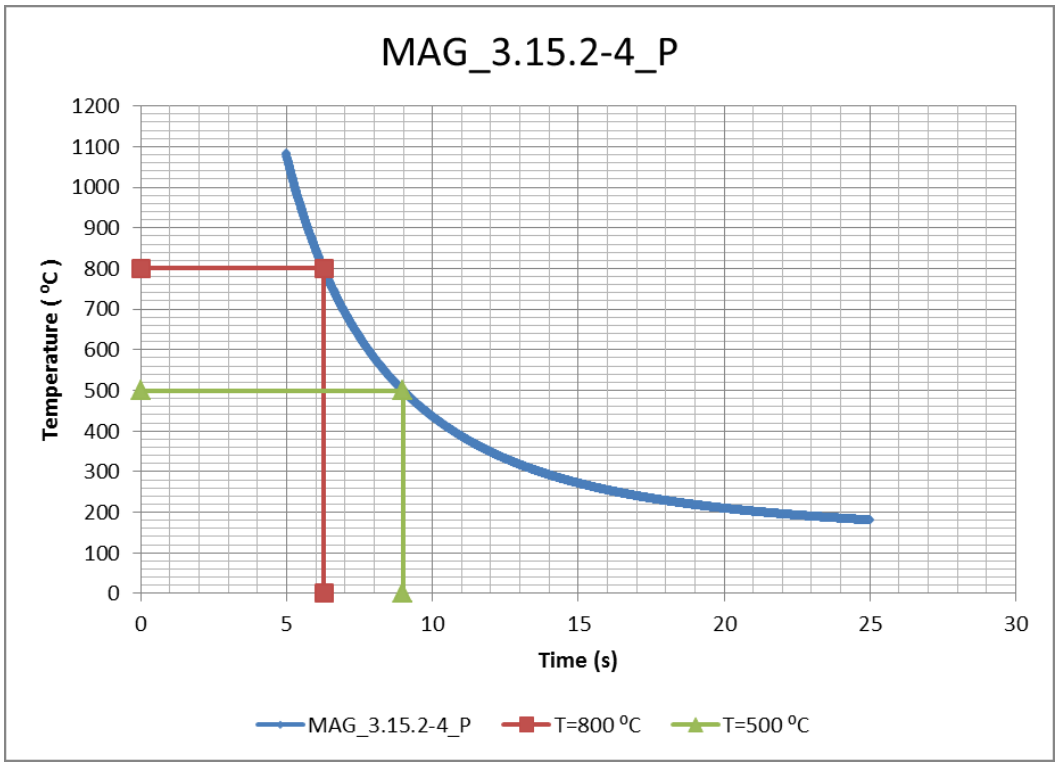

Figure 2 Interpolated $t_{8/5}$ value of hardest point of coarse-grained zone is 2.7 s.

MAG 3.5.2-2

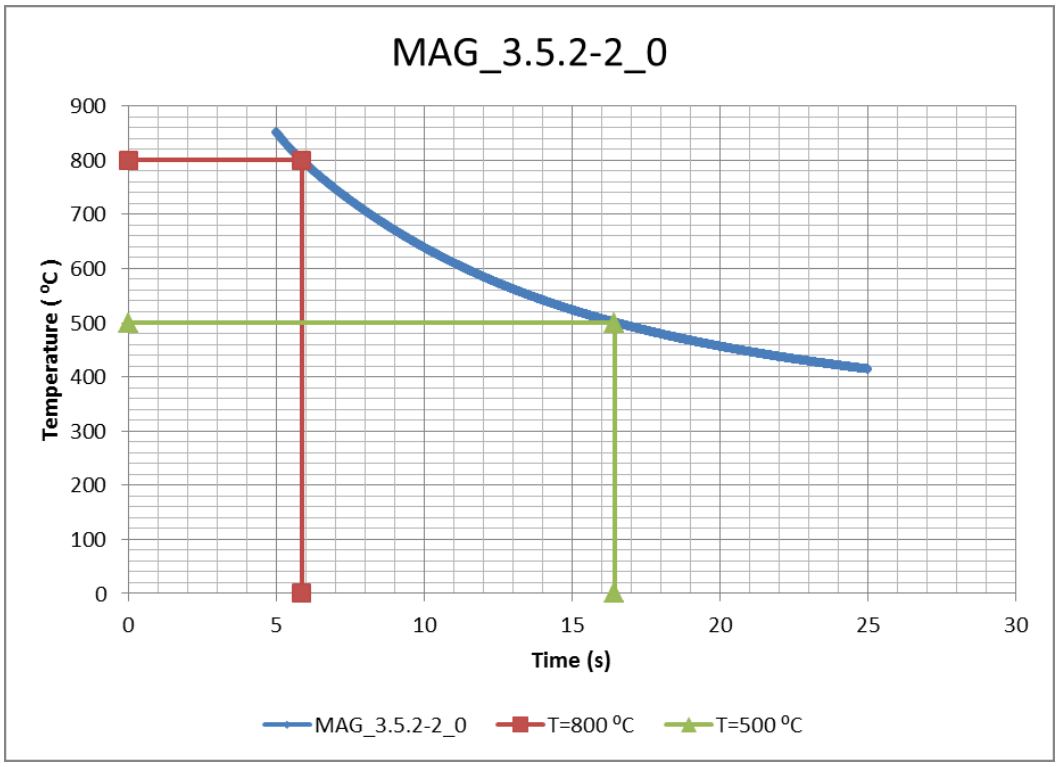

Figure 3 Interpolated $t_{8/5}$ value of fusion line is 10.6 s.

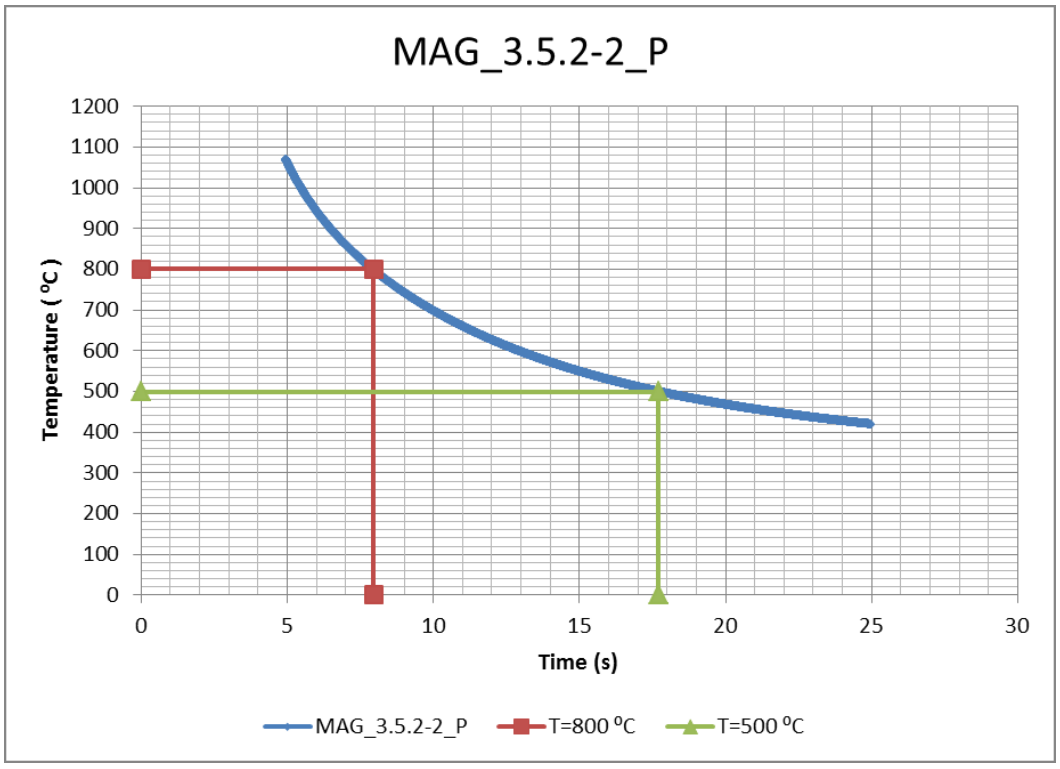

Figure 4 Interpolated $t_{8/5}$ value of hardest point of coarse-grained zone is 9.7 s.

Appendix 13

LASER samples

LASER 3.15.2-5

- No simulation

LASER 3.5.2-7

- No simulation

TIG samples

TIG 3.5.2-8 (BOP 1.1)

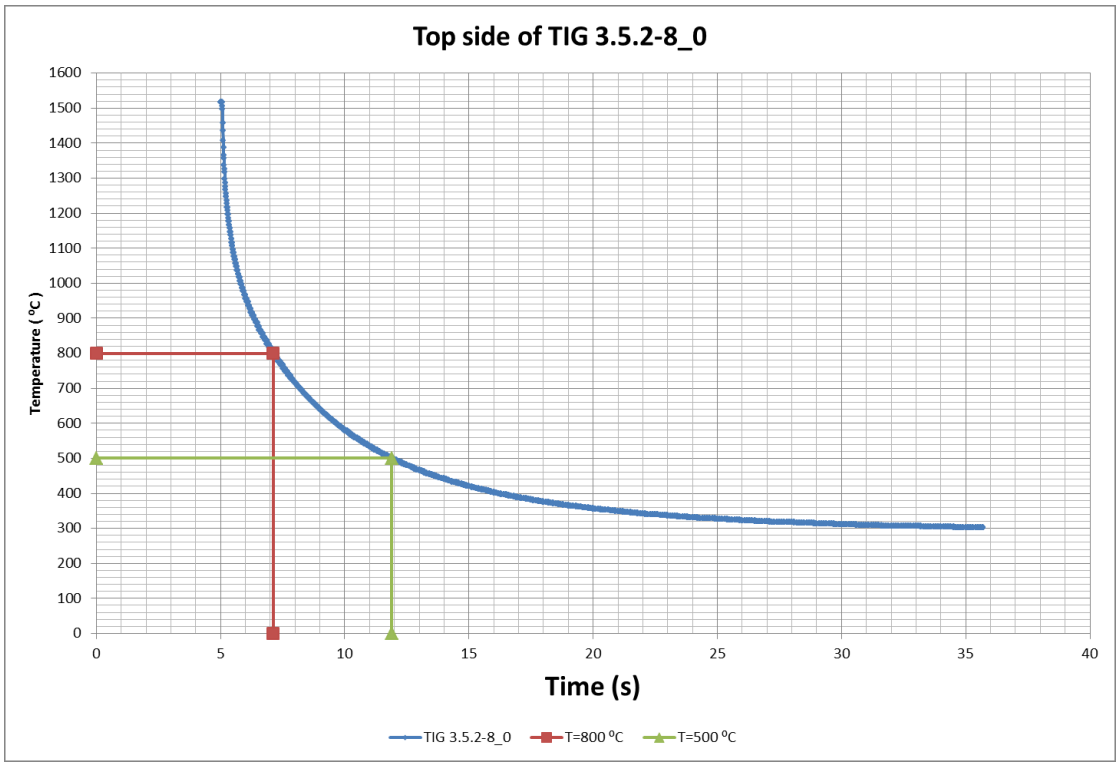

Figure 5 Interpolated $t_{8/5}$ value of fusion line is 4.8 s.

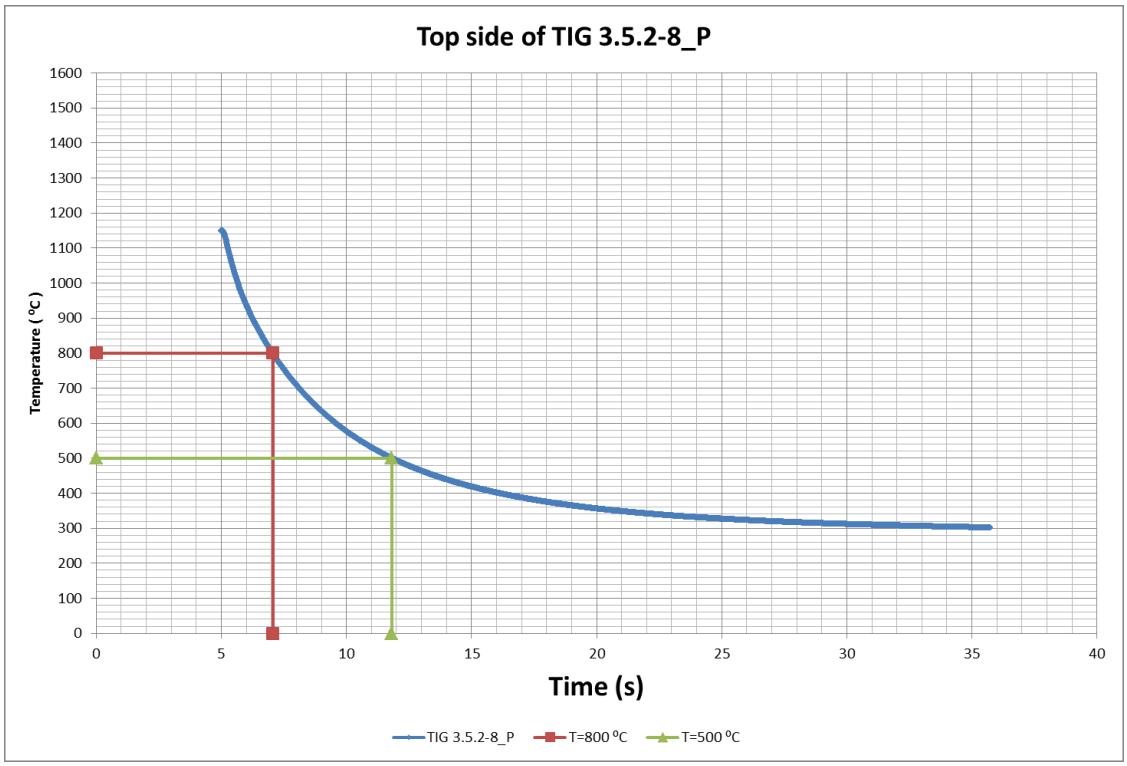

Figure 6 Interpolated $t_{8/5}$ value of hardest point of coarse-grained zone is 4.8 s.

TIG 3.5.2-9 (BOP 2.1)

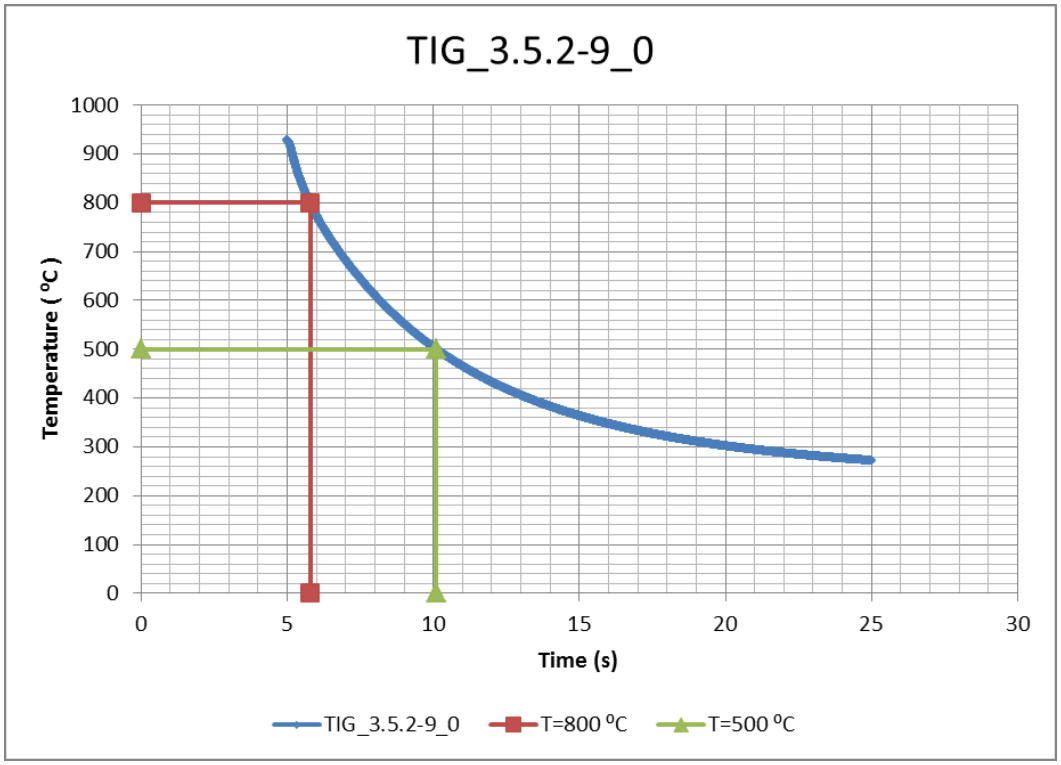

Figure 7 Interpolated $t_{8/5}$ value of fusion line is 4.3 s.

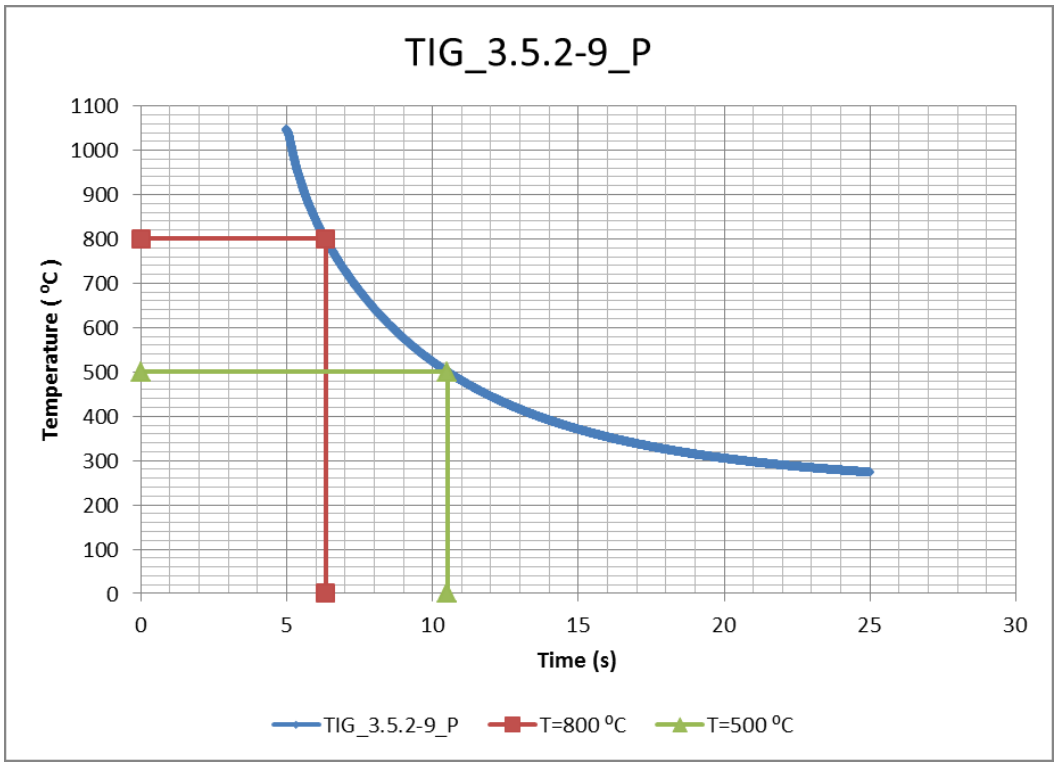

Figure 8 Interpolated $t_{8/5}$ value of hardest point of coarse-grained zone is 4.2 s.

TIG 3.5.2-4 (BOP 4.1)

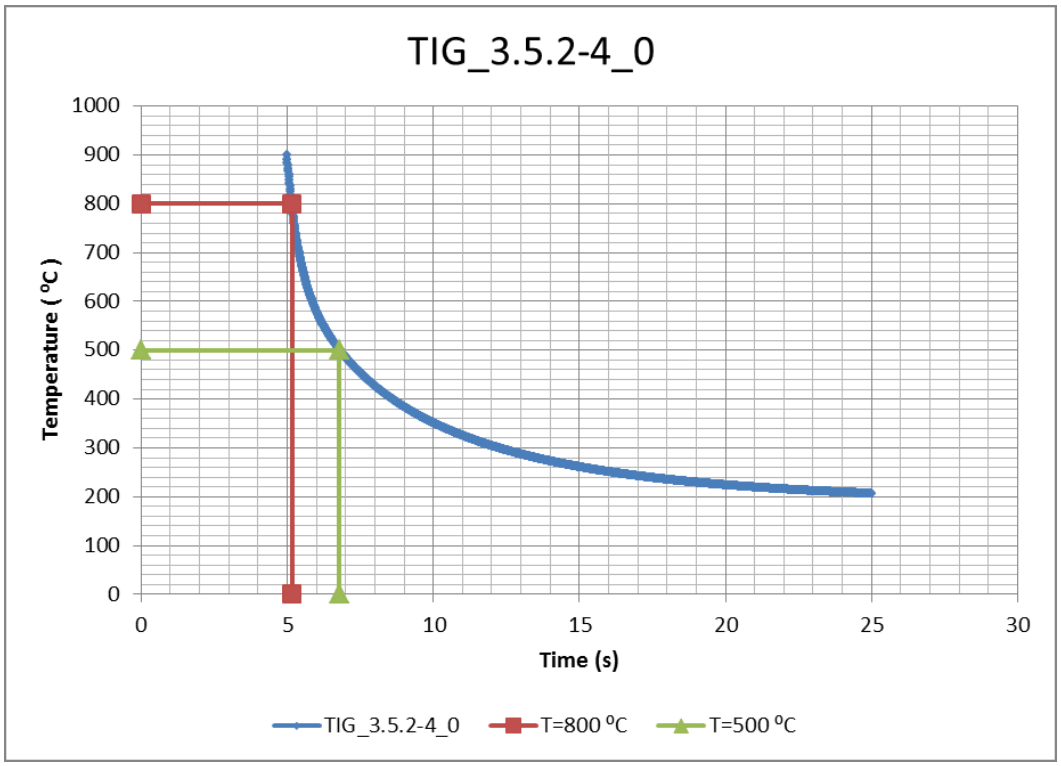

Figure 9 Interpolated $t_{8/5}$ value of fusion line is 1.6 s.

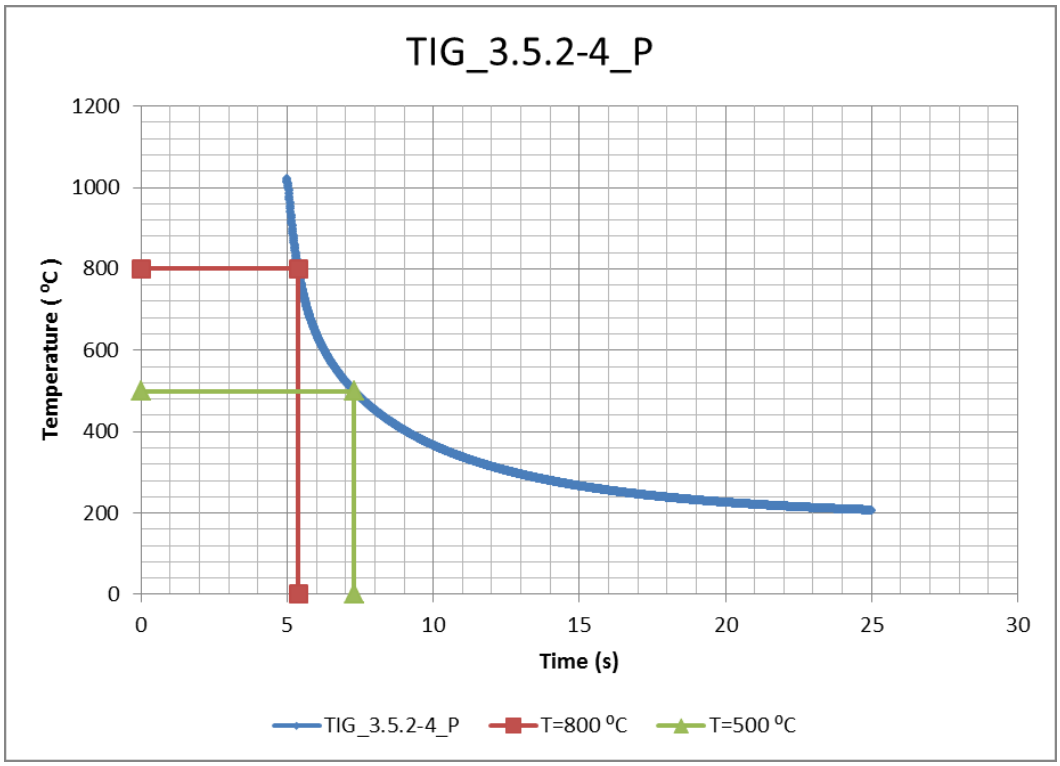

Figure 10 Interpolated $t_{8/5}$ value of hardest point of coarse-grained zone is 1.9 s.

TIG 3.15.2-6 (BOP 5.1)

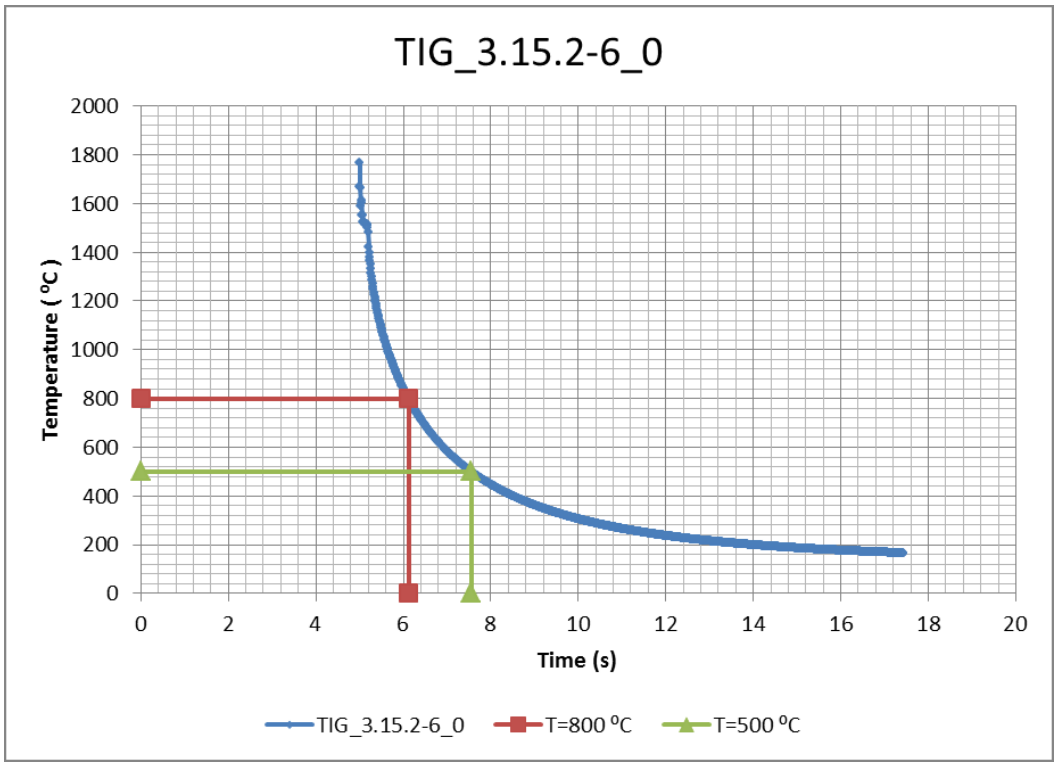

Figure 11 Interpolated $t_{8/5}$ value of fusion line is 1.4 s.

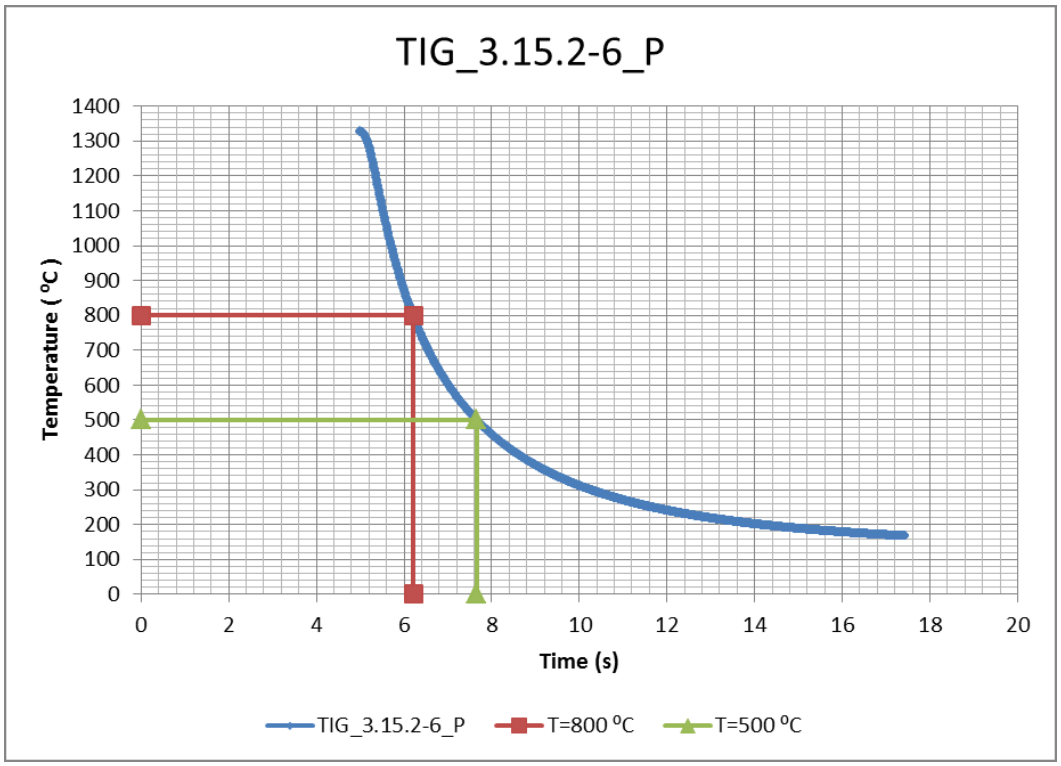

Figure 12 Interpolated $t_{8/5}$ value of hardest point of coarse-grained zone is 1.4 s.

TIG 3.15.2-7 (BOP 6.1)

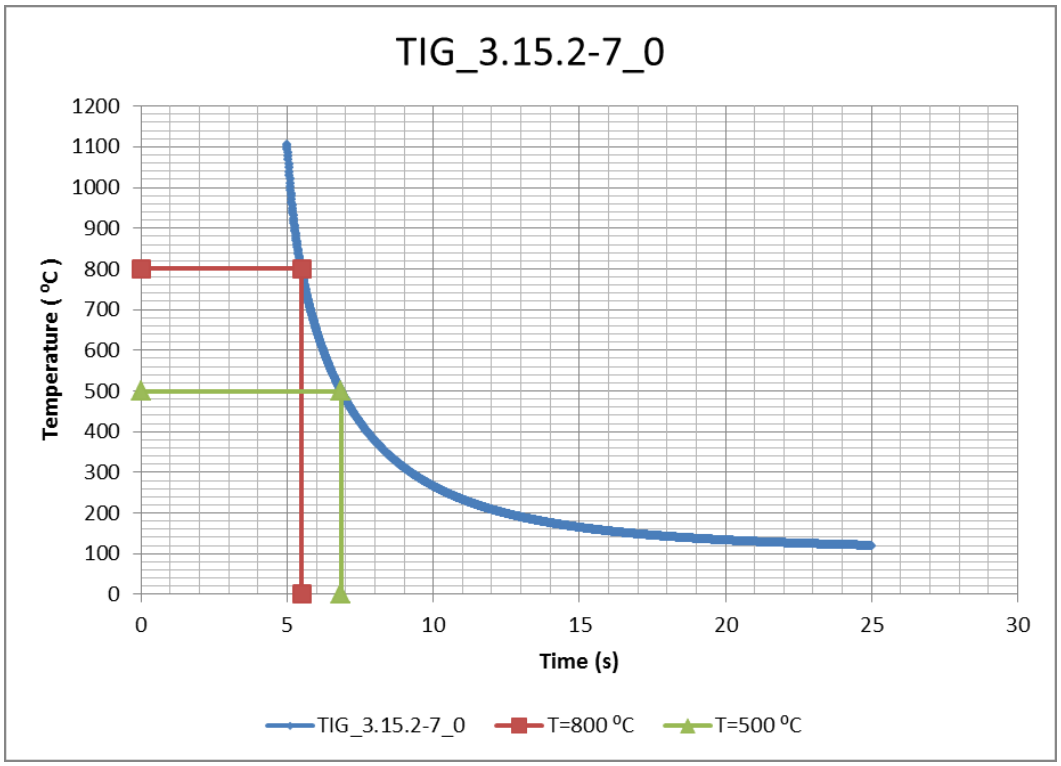

Figure 13 Interpolated $t_{8/5}$ value of fusion line is 1.4 s.

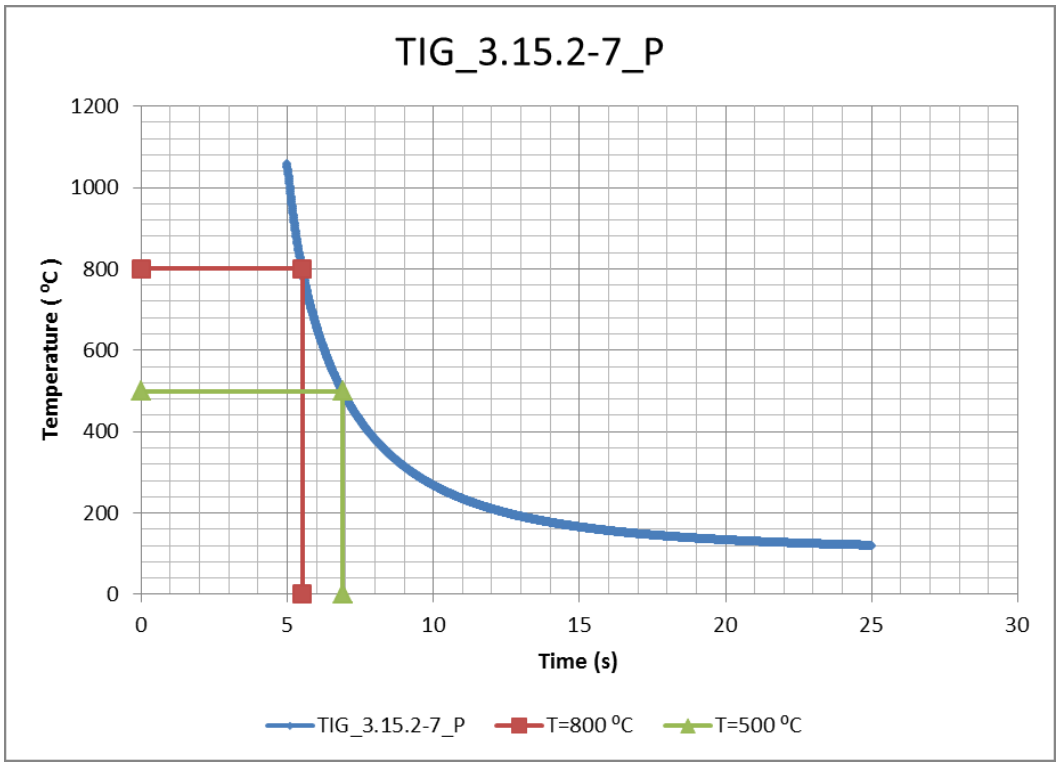

Figure 14 Interpolated $t_{8/5}$ value of hardest point of coarse-grained zone is 1.4 s.

TIG 3.15.2-8 (BOP 7.1)

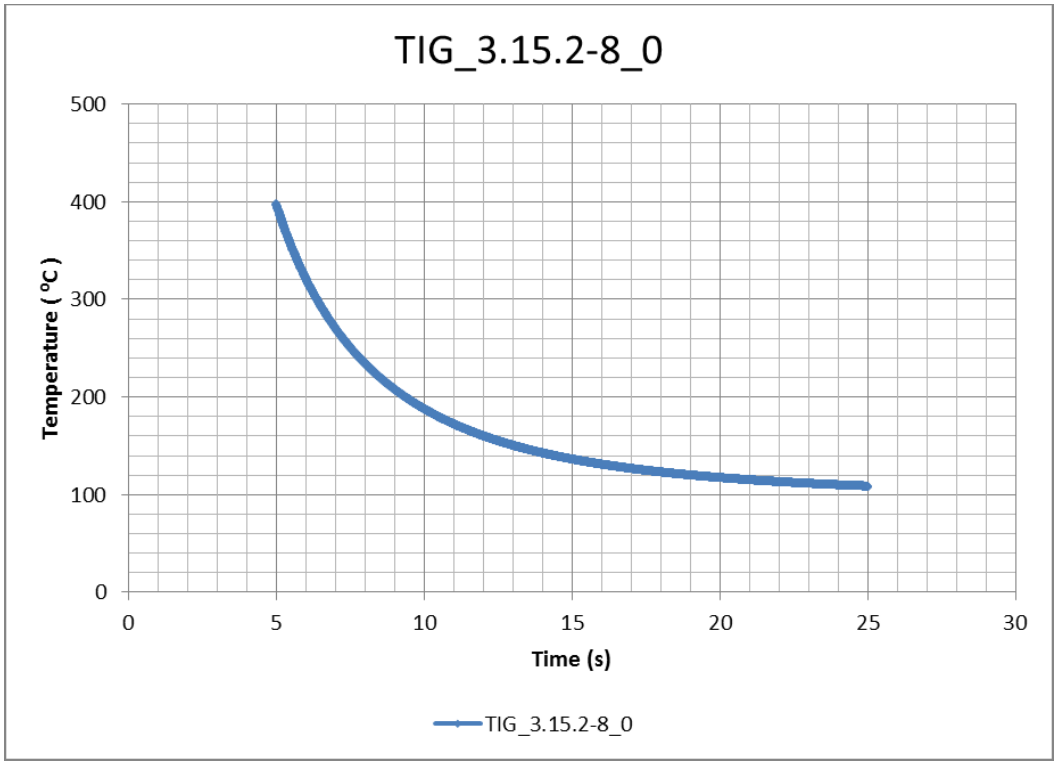

Figure 15 Value of $t_{8/5}$ was impossible to determine due to too small area of temperature.

Appendix 13

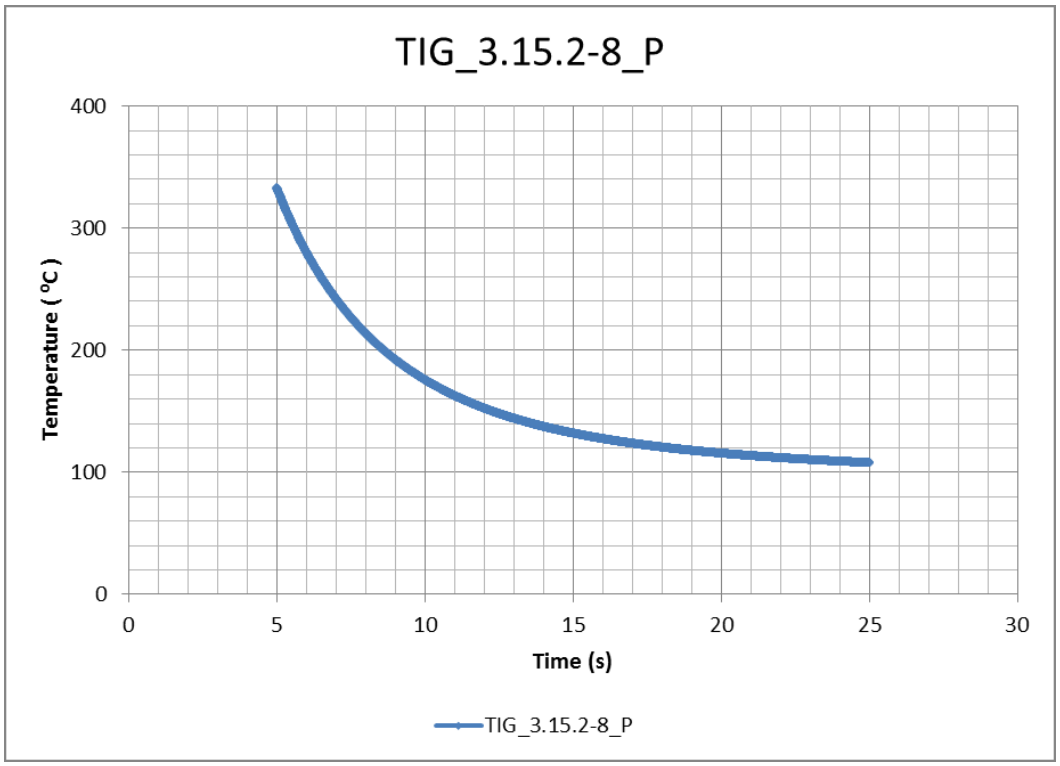

Figure 16 Value of $t_{8/5}$ was impossible to determine due to too small area of temperature.

Appendix 14 / Results of cooling times, dimensions of HAZ and hardness distributions of TIG welded bead-on-plate welds (According to Voss's doctoral thesis, ISBN 3-8265-9119-4)

Contents

3.5.2-8

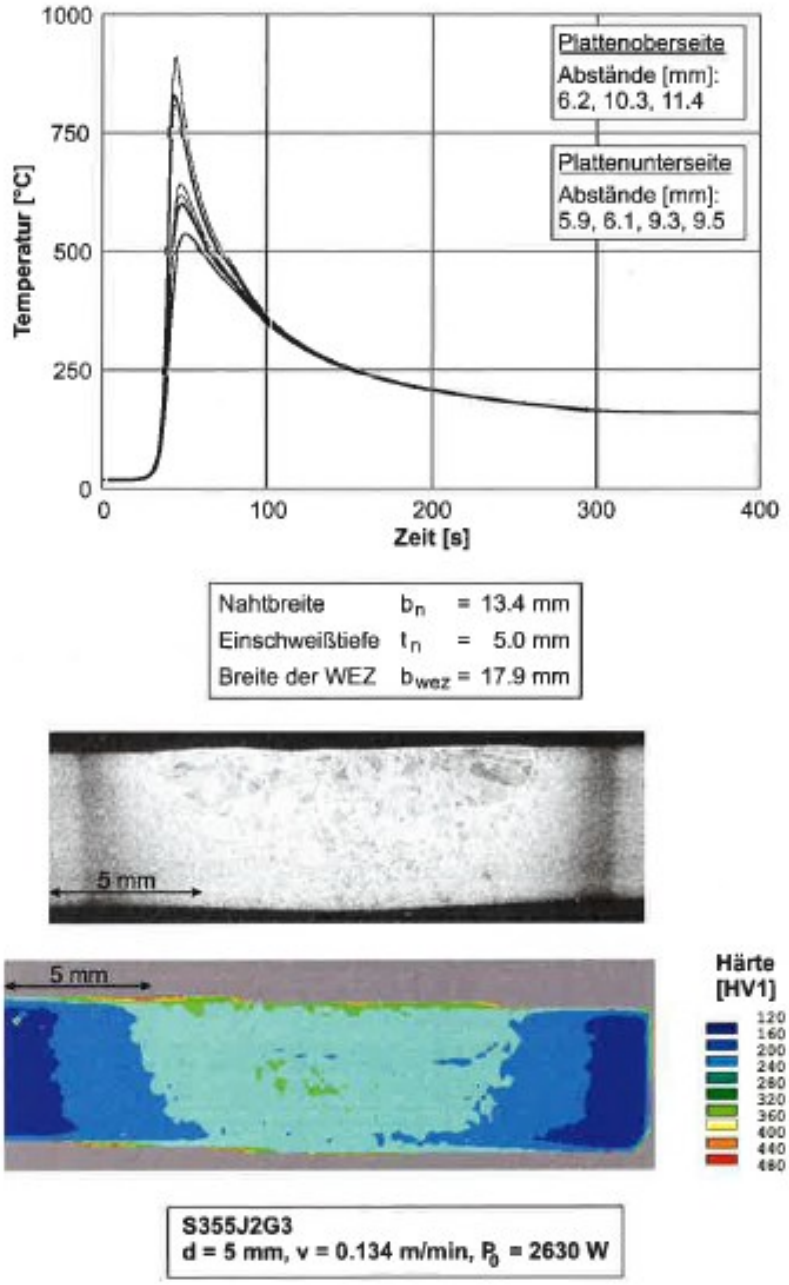

Abbildung B.54: Experimentell bestimmte Temperaturzyklen, Nahtausbildung und Härteverteilung an der Probe S355-5-13

Figure 1 Welding parameters, dimensions of HAZ, weld cooling and distribution of hardness for TIG welded sample 3.5.2-8.

Appendix 14

3.5.2-9

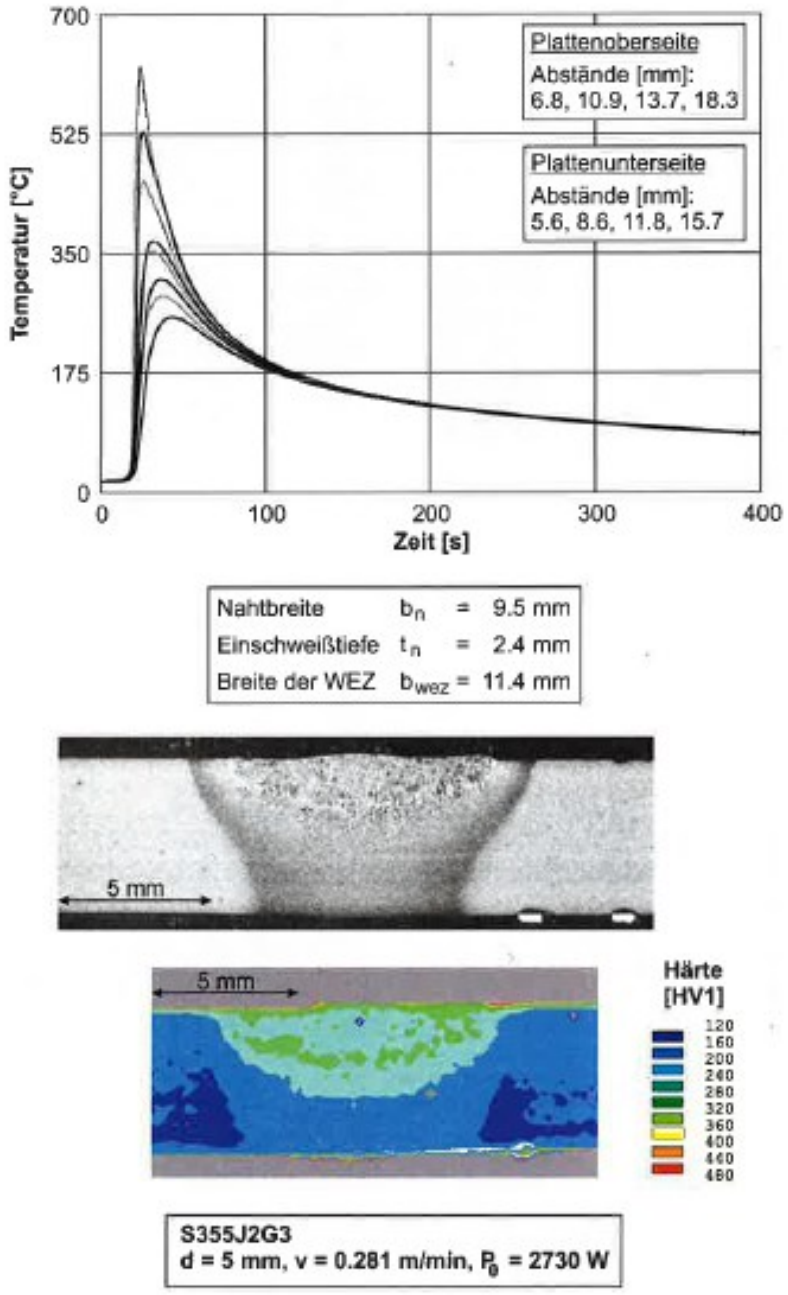

Abbildung B.57: Experimentell bestimmte Temperaturzyklen, Nahtausbildung und Härteverteilung an der Probe S355-5-28

Figure 2 Welding parameters, dimensions of HAZ, weld cooling and distribution of hardness for TIG welded sample 3.5.2-9.

Appendix 14

3.5.2-4

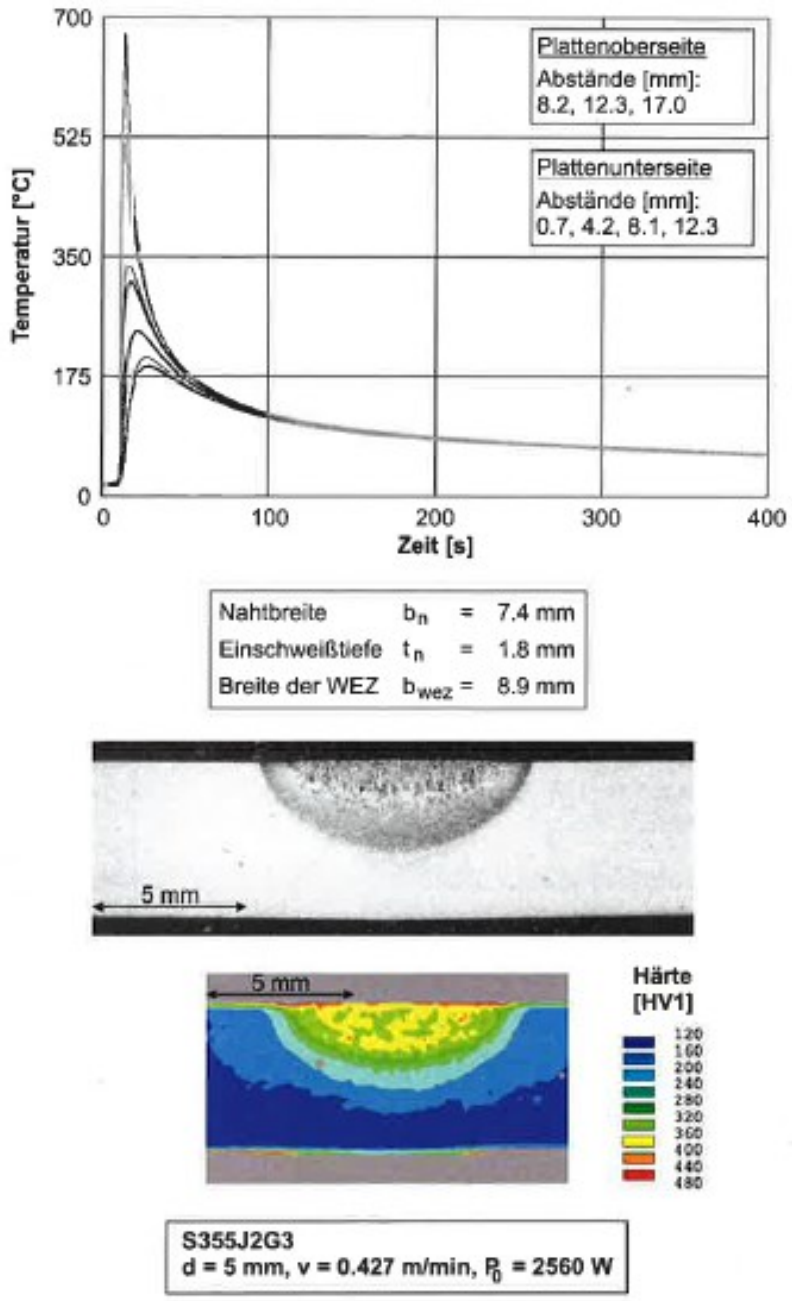

Abbildung B.60: Experimentell bestimmte Temperaturzyklen, Nahtausbildung und Härteverteilung an der Probe S355-5-42

Figure 3 Welding parameters, dimensions of HAZ, weld cooling and distribution of hardness for TIG welded sample 3.5.2-4.

Appendix 14

3.15.2-6

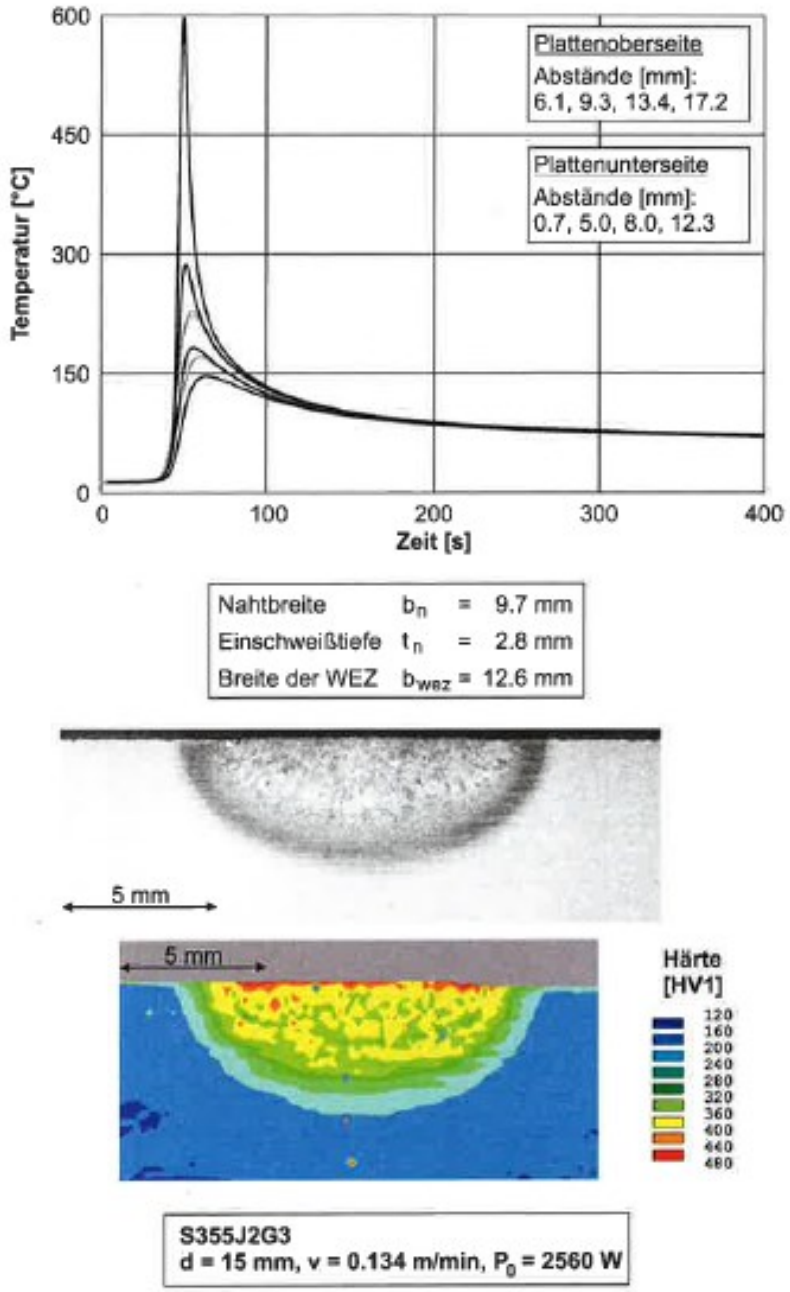

Abbildung B.72: Experimentell bestimmte Temperaturzyklen, Nahtausbildung und Härteverteilung an der Probe S355-15-13

Figure 4 Welding parameters, dimensions of HAZ, weld cooling and distribution of hardness for TIG welded sample 3.15.2-6.

Appendix 14

3.15.2-7

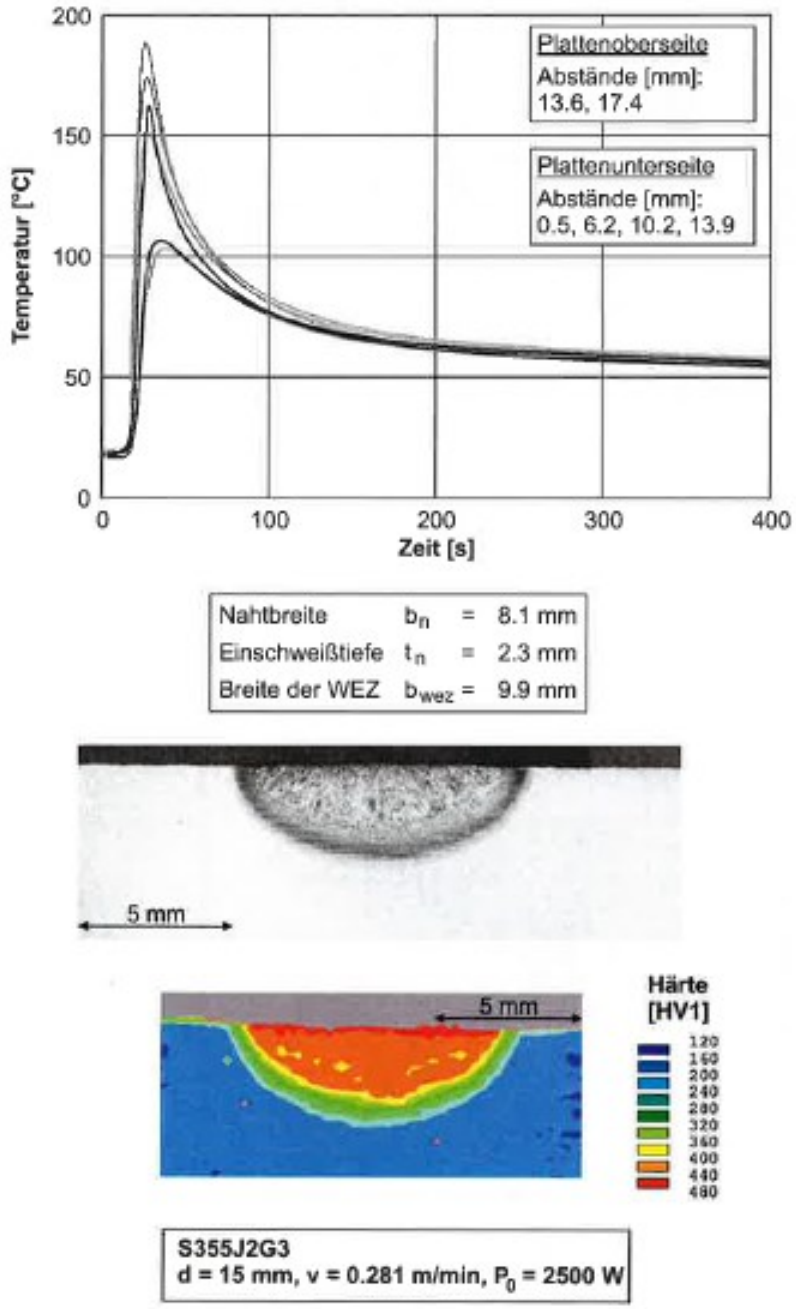

Abbildung B.75: Experimentell bestimmte Temperaturzyklen, Nahtausbildung und Härteverteilung an der Probe S355-15-28

Figure 5 Welding parameters, dimensions of HAZ, weld cooling and distribution of hardness for TIG welded sample 3.15.2-7.

Appendix 14

3.15.2-8

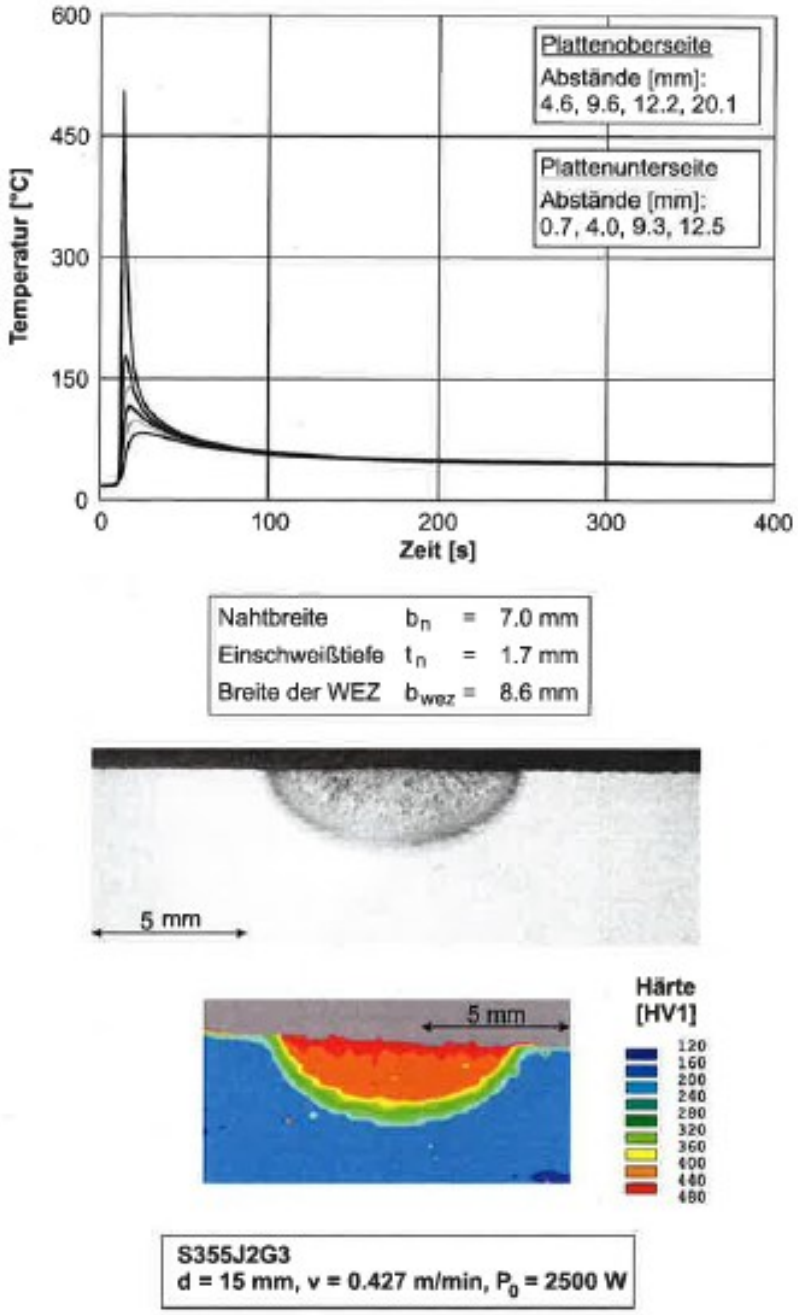

Abbildung B.78: Experimentell bestimmte Temperaturzyklen, Nahtausbildung und Härteverteilung an der Probe S355-15-42

Figure 6 Welding parameters, dimensions of HAZ, weld cooling and distribution of hardness for TIG welded sample 3.15.2-8.

Appendix 15 / Grain size distributions of bead-on-plate welds

Contents

Appendix 15

Table 1 Maximum grain size of base material, coarse-grained zone and weld metal for bead-on-plate welds.

Method and number of sample	Max distribution size from BM (µm)	Max distribution size from coarse-grained zone (µm)	Max distribution size from weld metal (µm)
LAHW 3.5.2-3	12	17	-
LAHW 3.15.2-9	28	15	-
LASER 3.5.2-7	69	38	55
LASER 3.15.2-5	31	19	14
MAG 3.5.2-2	12	32	-
MAG 3.15.2-4	20	12	-
TIG 3.5.2-4	12	19	13
TIG 3.5.2-8	13	19	18
TIG 3.5.2-9	9	8	13
TIG 3.15.2-6	17	9	10
TIG 3.15.2-7	29	10	14
TIG 3.15.2-8	23	12	17

Table 2 Properties of mosaic micrograph which are taken with Leica MEF 4M light optical microscope with DFC450 digital camera, computer aided table and software of LAS Core V4.6.1

sample	Image size			scale
	width	***height***	***megapixels***	
LAHW 3.5.2-3	21191	1903	40	9.8
LAHW 3.15.2-9	27965	1900	53	9.8
LASER 3.5.2-7	38176	1820	69	9.8
LASER 3.15.2-5	45748	1892	87	9.8
MAG 3.5.2-2	15994	632	10	3.27
MAG 3.15.2-4	63701	1876	120	9.8
TIG 3.5.2-4	48588	1892	92	9.8
TIG 3.5.2-8	79317	1734	138	9.8
TIG 3.5.2-9	61700	1883	116	9.8
TIG 3.15.2-6	62838	1881	118	9.8
TIG 3.15.2-7	53827	1883	101	9.8
TIG 3.15.2-8	45709	1892	86	9.8

LAHW 3.5.2-3

Figure 1 Original mosaic micrograph of LAHW welded 3.5.2-3.

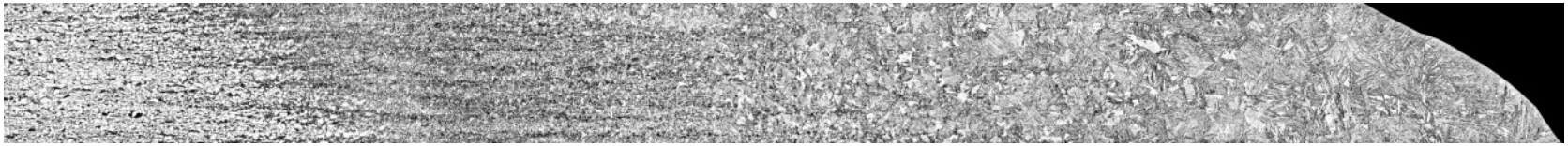

Figure 2 Micrograph of LAHW welded sample 3.5.2-3 which contrast and sharpness were enhanced.

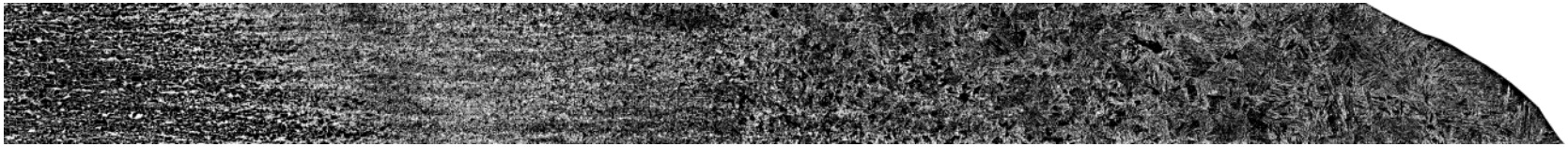

Figure 3 Grain boundary map of LAHW welded sample 3.5.2-3.

Appendix 15

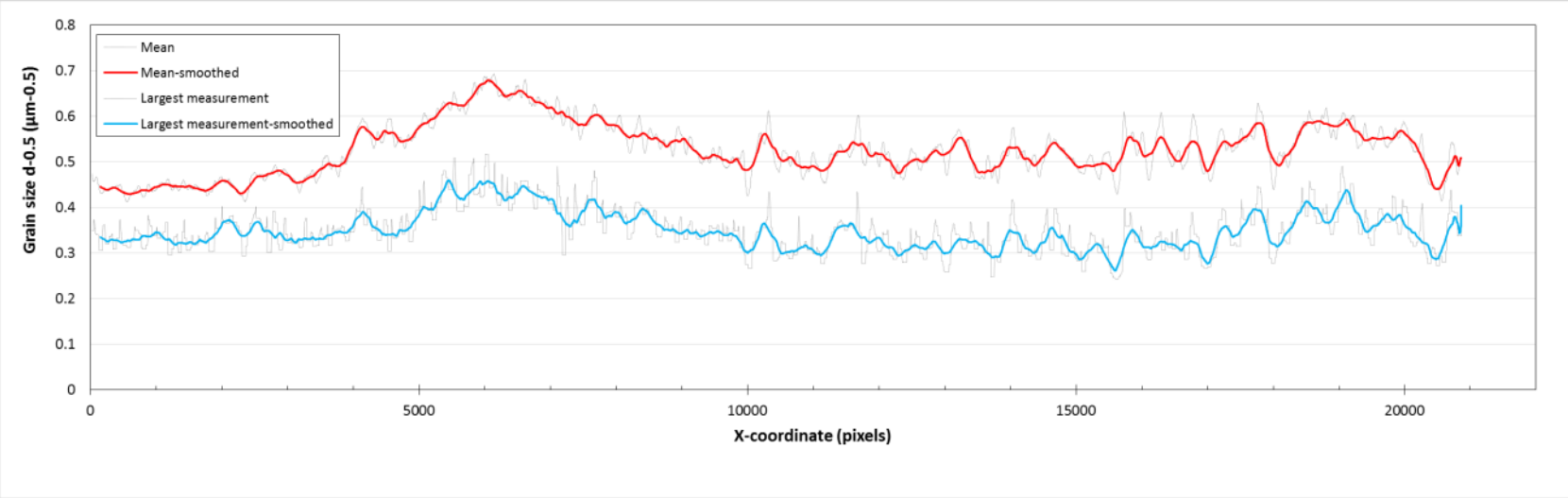

Figure 4 Grain size distributions of LAHW welded sample 3.5.2-3 were calculated by Matlab.

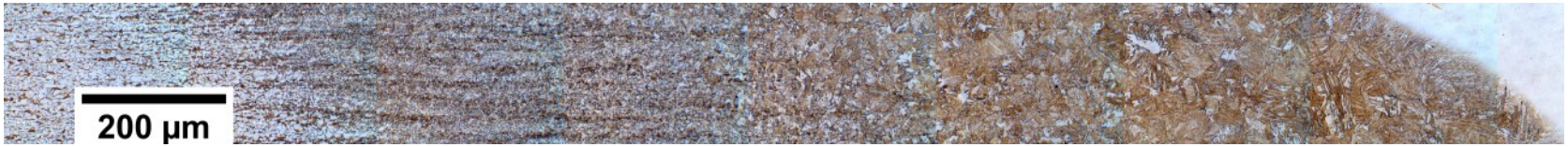

Figure 5 Enhanced micrograph of LAHW welded sample 3.5.2-3 in scale.

Appendix 15

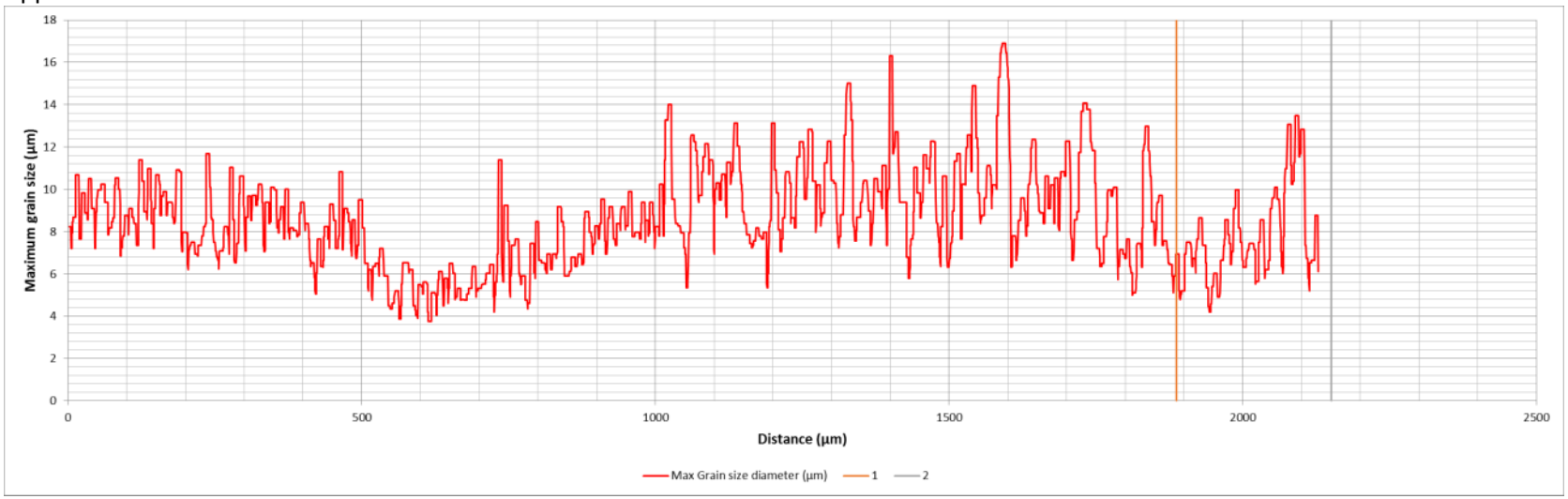

Figure 6 Grain size distribution of LAHW welded sample 3.5.2-3 between base material and weld metal. Fusion line of Figure 5 is between lines 1 and 2.

LAHW 3.15.2-9

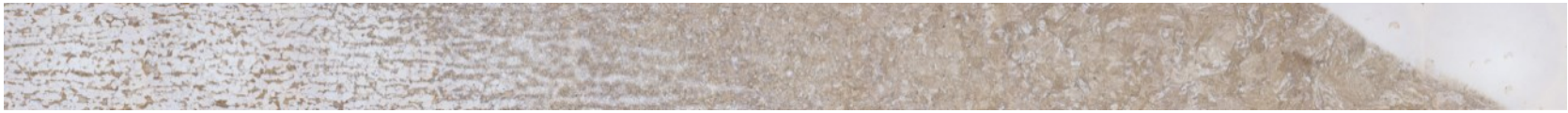

Figure 7 Original mosaic micrograph of LAHW welded 3.15.2-9.

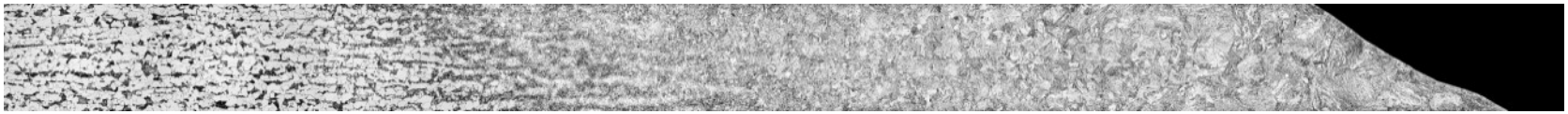

Figure 8 Micrograph of LAHW welded sample 3.15.2-9 which contrast and sharpness were enhanced.

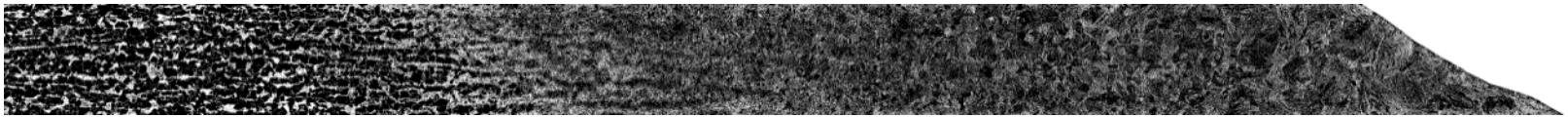

Figure 9 Grain boundary map of LAHW welded sample 3.15.2-9.

Appendix 15

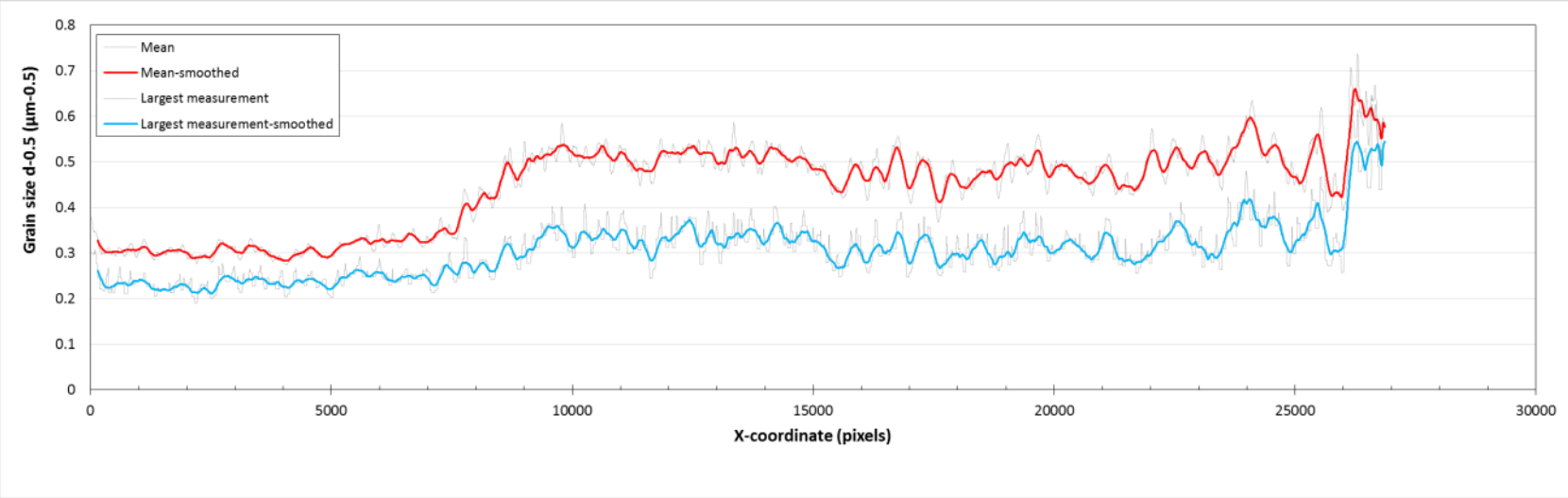

Figure 10 Grain size distributions of LAHW welded sample 3.15.2-9 were calculated by Matlab.

Figure 11 Enhanced micrograph of LAHW welded sample 3.15.2-9 in scale.

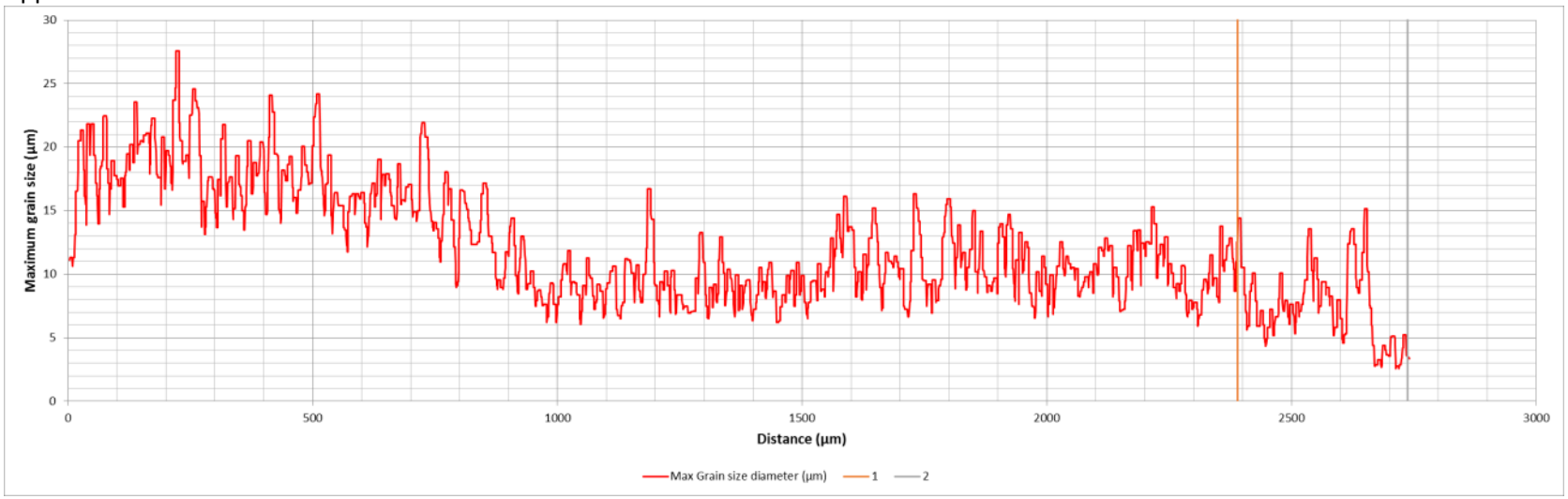

Figure 12 Grain size distribution of LAHW welded sample 3.15.2-9 between base material and weld metal. Fusion line of Figure 11 is between lines 1 and 2.

LASER 3.5.2-7

Figure 13 Original mosaic micrograph of LASER welded 3.5.2-7.

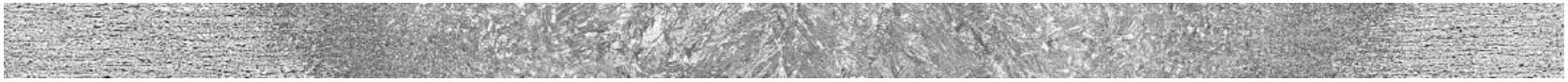

Figure 14 Micrograph of LASER welded sample 3.5.2-7 which contrast and sharpness were enhanced.

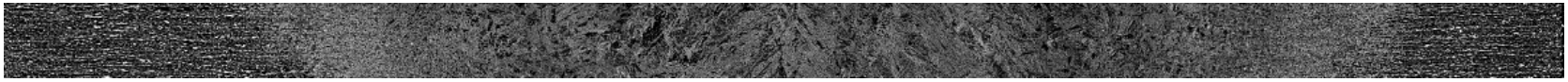

Figure 15 Grain boundary map of LASER welded sample 3.5.2-7.

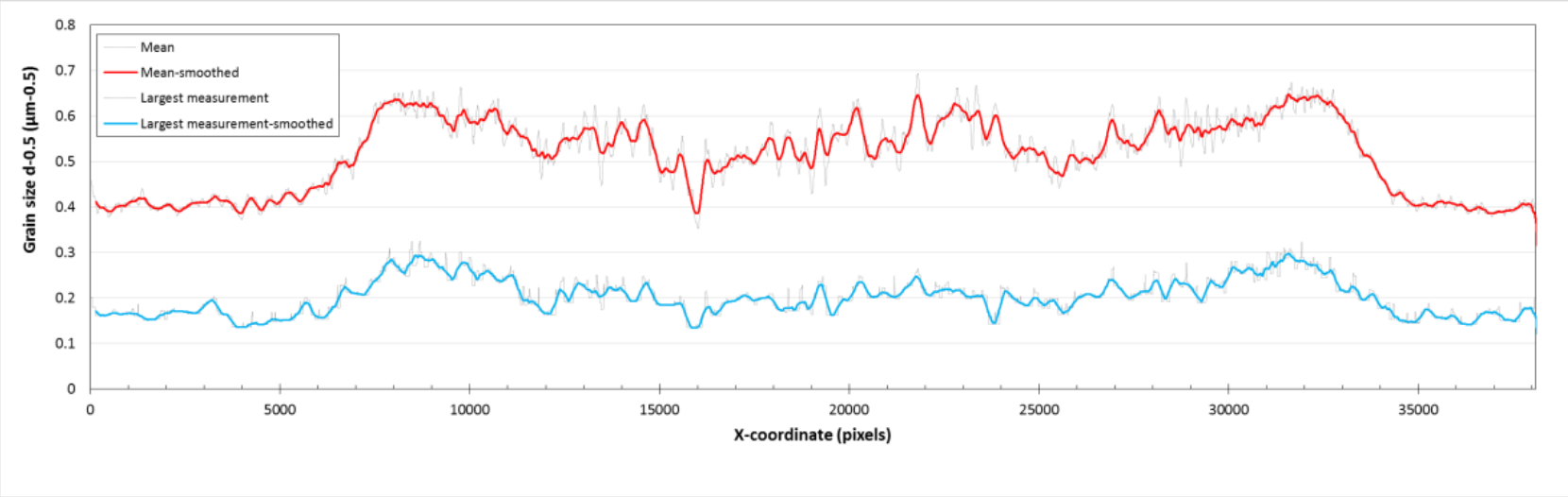

Figure 16 Grain size distributions of LASER welded sample 3.5.2-7 were calculated by Matlab.

Figure 17 Enhanced micrograph of LASER welded sample 3.5.2-7 in scale.

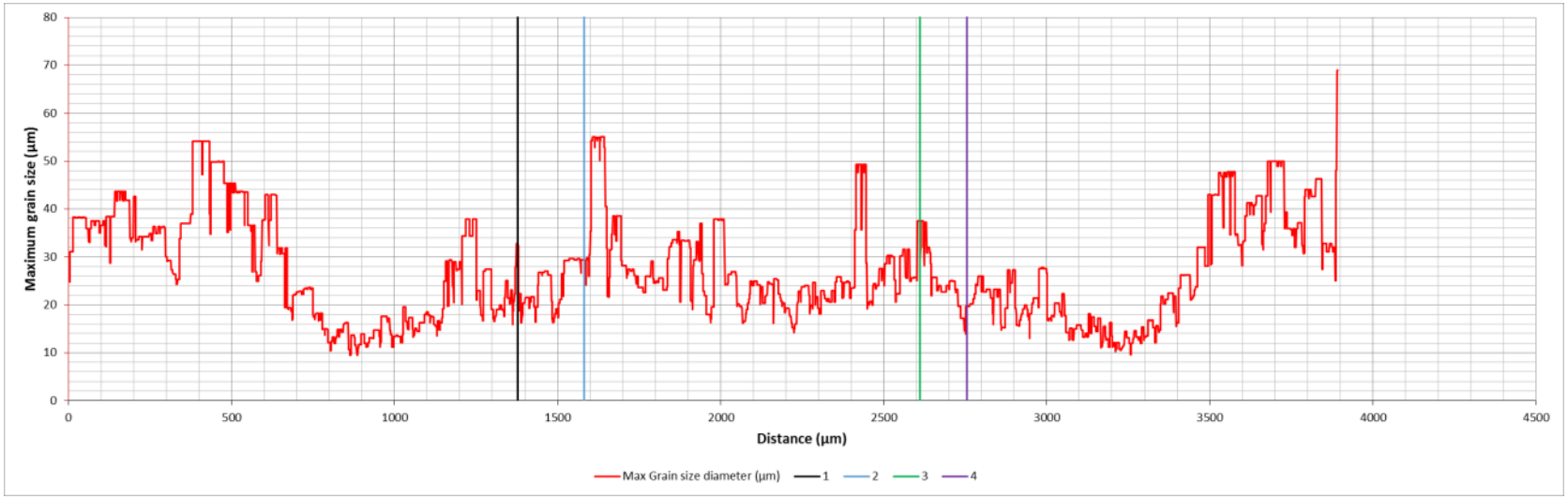

Figure 18 Grain size distribution over LASER welded sample 3.5.2-7. Left fusion line of Figure 17 is between lines 1 and 2. Right fusion line of Figure 17 is between lines 3 and 4.

LASER 3.15.2-5

Figure 19 Original mosaic micrograph of LASER welded 3.15.2-3.

Figure 20 Micrograph of LASER welded sample 3.15.2-5 which contrast and sharpness were enhanced.

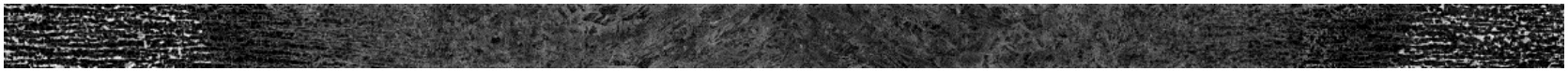

Figure 21 Grain boundary map of LASER welded sample 3.15.2-5.

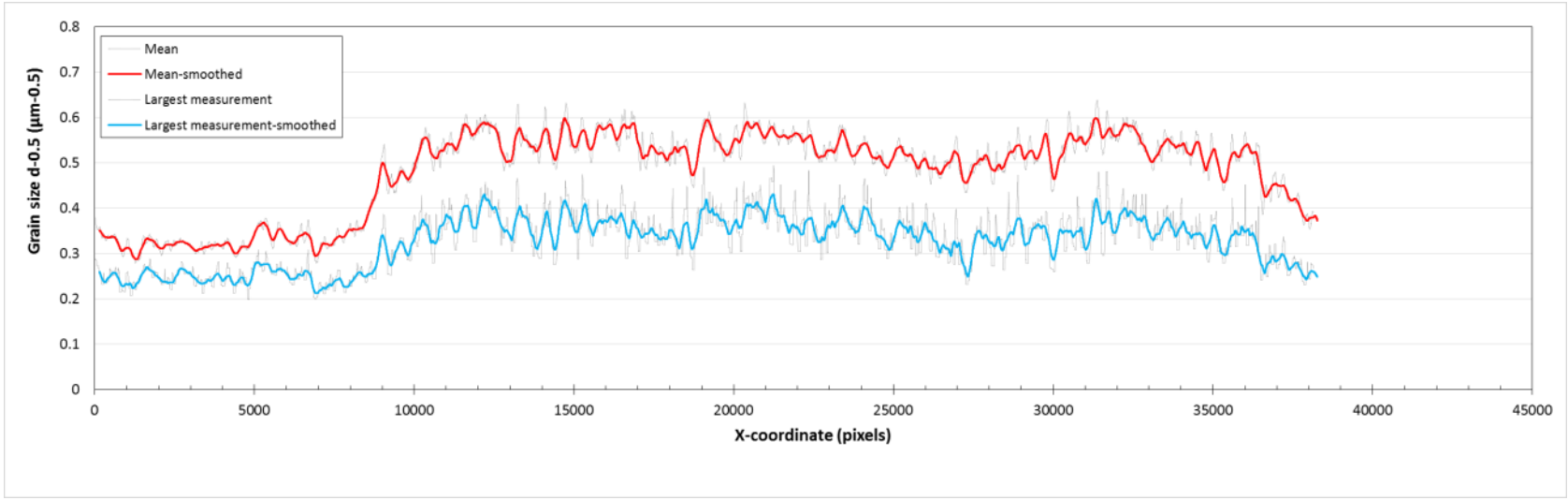

Figure 22 Grain size distributions of LASER welded sample 3.15.2-5 were calculated by Matlab.

Figure 23 Enhanced micrograph of LASER welded sample 3.15.2-5 in scale.

Appendix 15

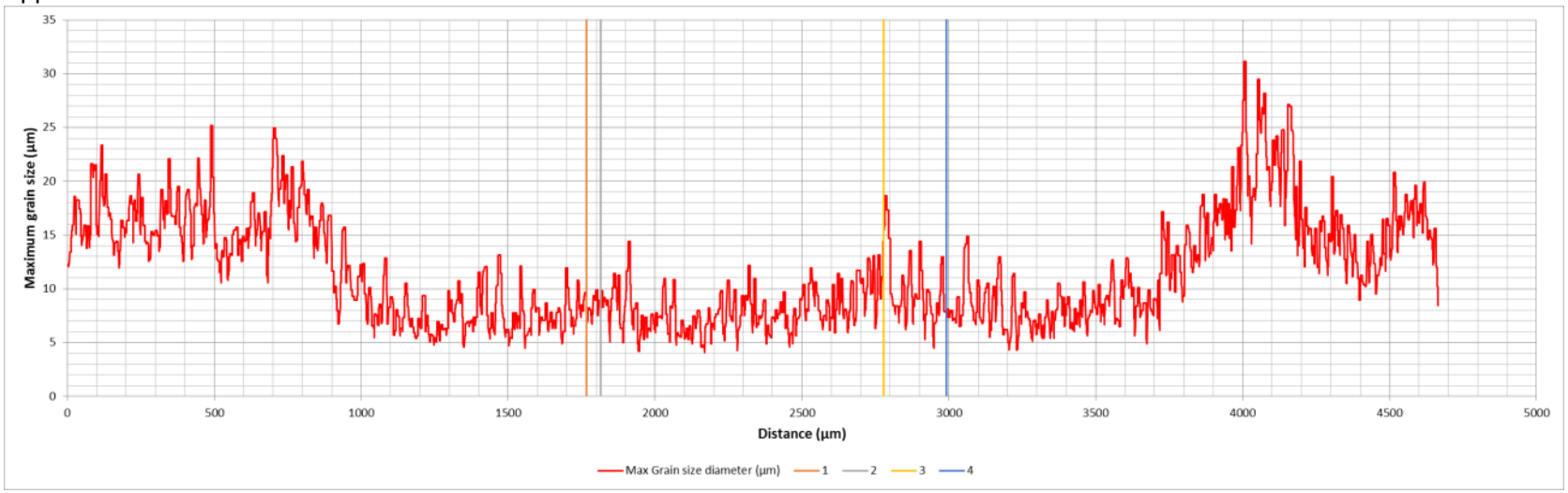

Figure 24 Grain size distribution over LASER welded sample 3.15.2-5. Left fusion line of Figure 23 is between lines 1 and 2. Right fusion line of Figure 23 is between lines 3 and 4.

MAG 3.5.2-2

Figure 25 Original mosaic micrograph of MAG welded 3.5.2-2.

Figure 26 Micrograph of MAG welded sample 3.5.2-2 which contrast and sharpness were enhanced.

Figure 27 Grain boundary map of MAG welded sample 3.5.2-2.

Appendix 15

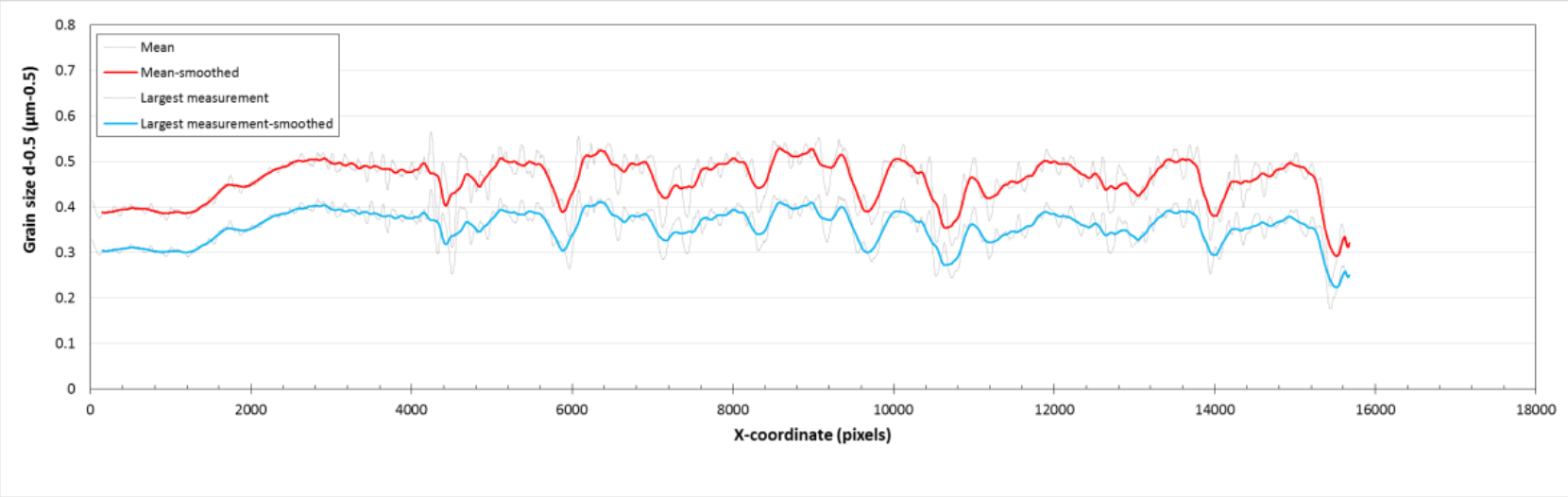

Figure 28 Grain size distributions of MAG welded sample 3.5.2-2 were calculated by Matlab.

Figure 29 Enhanced micrograph of MAG welded sample 3.5.2-2 in scale.

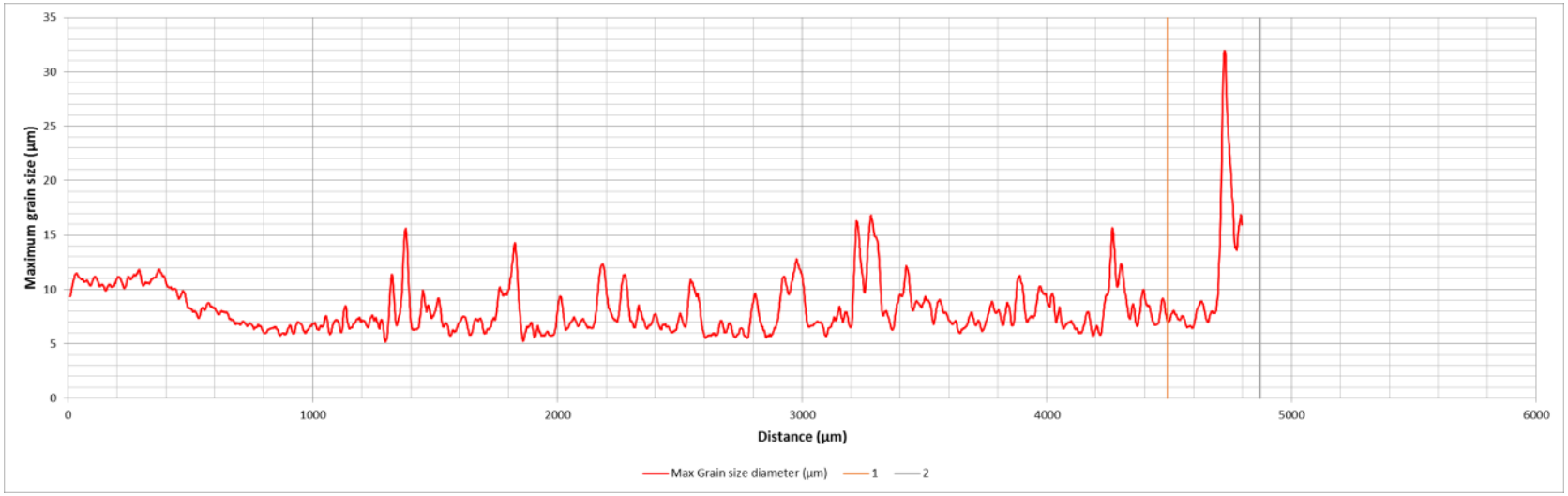

Figure 30 Grain size distribution of MAG welded sample 3.5.2-2 between base material and weld metal. Fusion line of Figure 29 is between lines 1 and 2.

MAG 3.15.2-4

Figure 31 Original mosaic micrograph of MAG welded 3.15.2-4.

Figure 32 Micrograph of MAG welded sample 3.15.2-4 which contrast and sharpness were enhanced.

Figure 33 Grain boundary map of MAG welded sample 3.15.2-4.

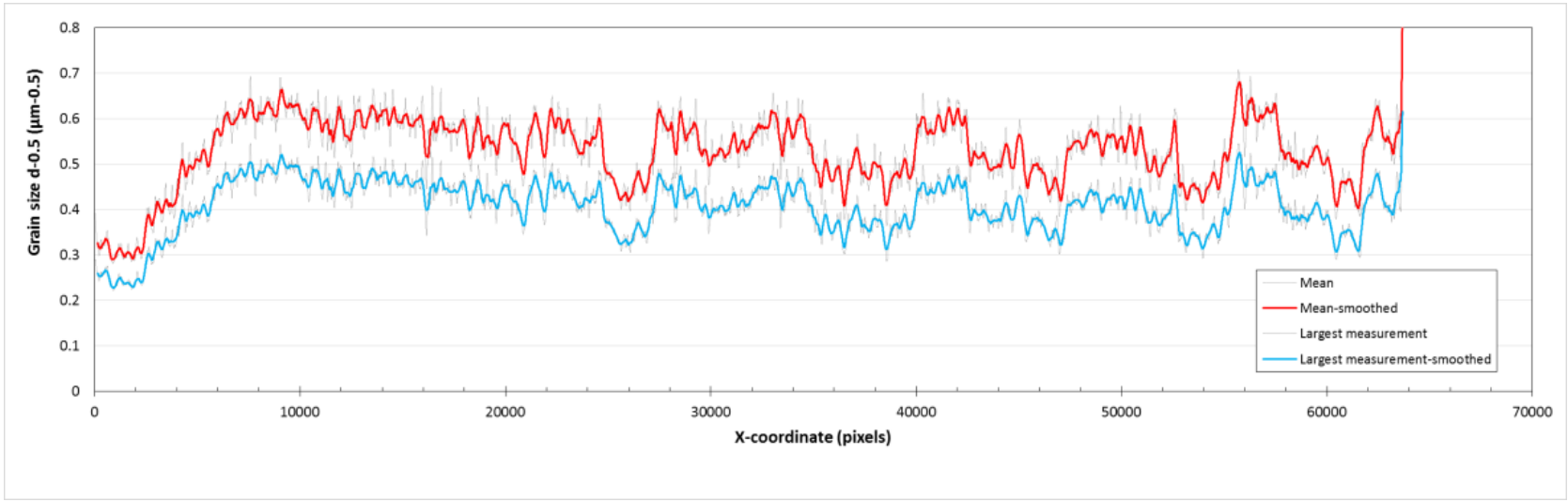

Figure 34 Grain size distributions of MAG welded sample 3.15.2-4 were calculated by Matlab.

Figure 35 Enhanced micrograph of MAG welded sample 3.15.2-4 in scale.

Appendix 15

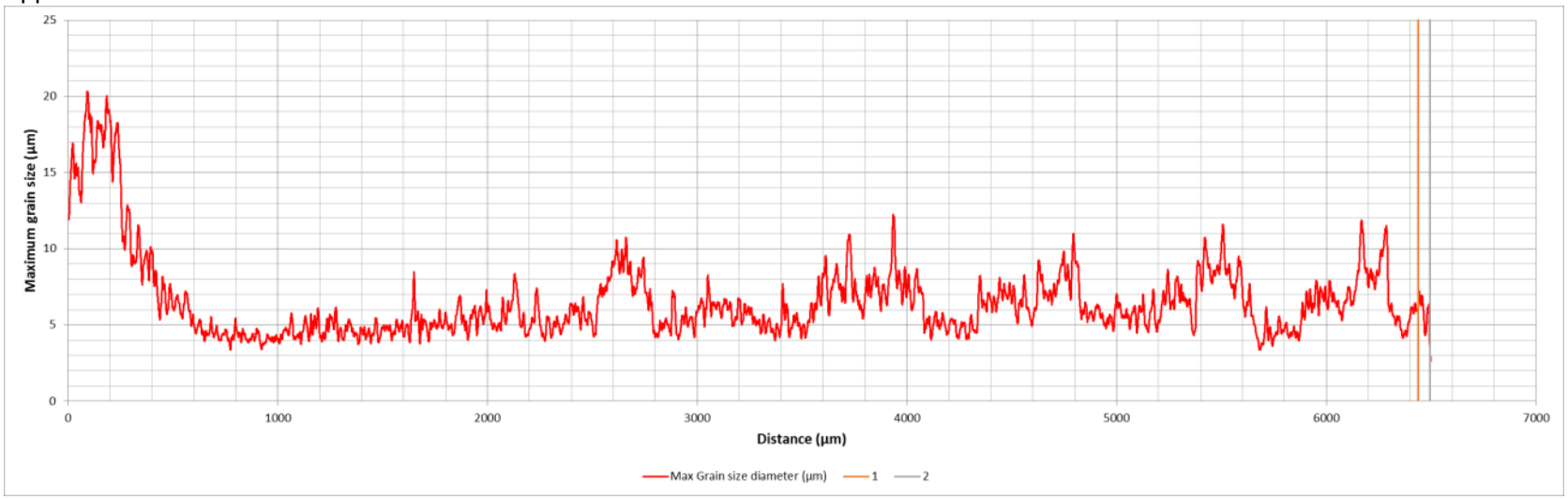

Figure 36 Grain size distribution of MAG welded sample 3.15.2-4 between base material and weld metal. Fusion line of Figure 35 is between lines 1 and 2.

TIG 3.5.2-4

Figure 37 Original mosaic micrograph of TIG welded 3.5.2-4.

Figure 38 Micrograph of TIG welded sample 3.5.2-4 which contrast and sharpness were enhanced.

Figure 39 Grain boundary map of TIG welded sample 3.5.2-4.

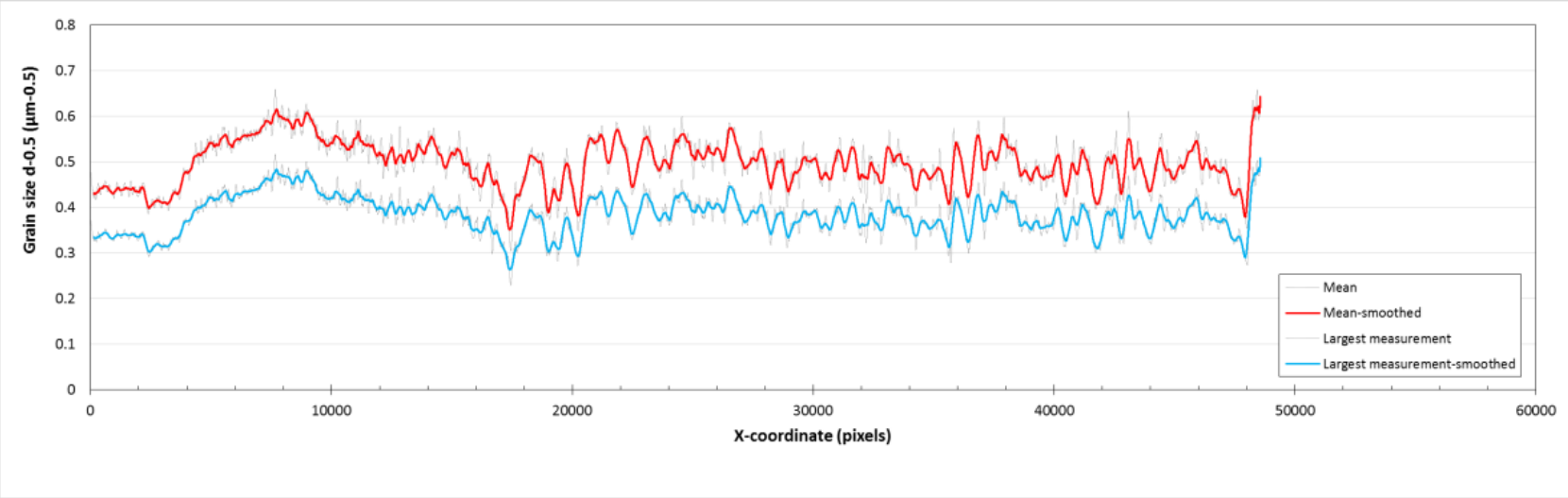

Figure 40 Grain size distributions of TIG welded sample 3.5.2-4 were calculated by Matlab.

Figure 41 Enhanced micrograph of TIG welded sample 3.5.2-4 in scale.

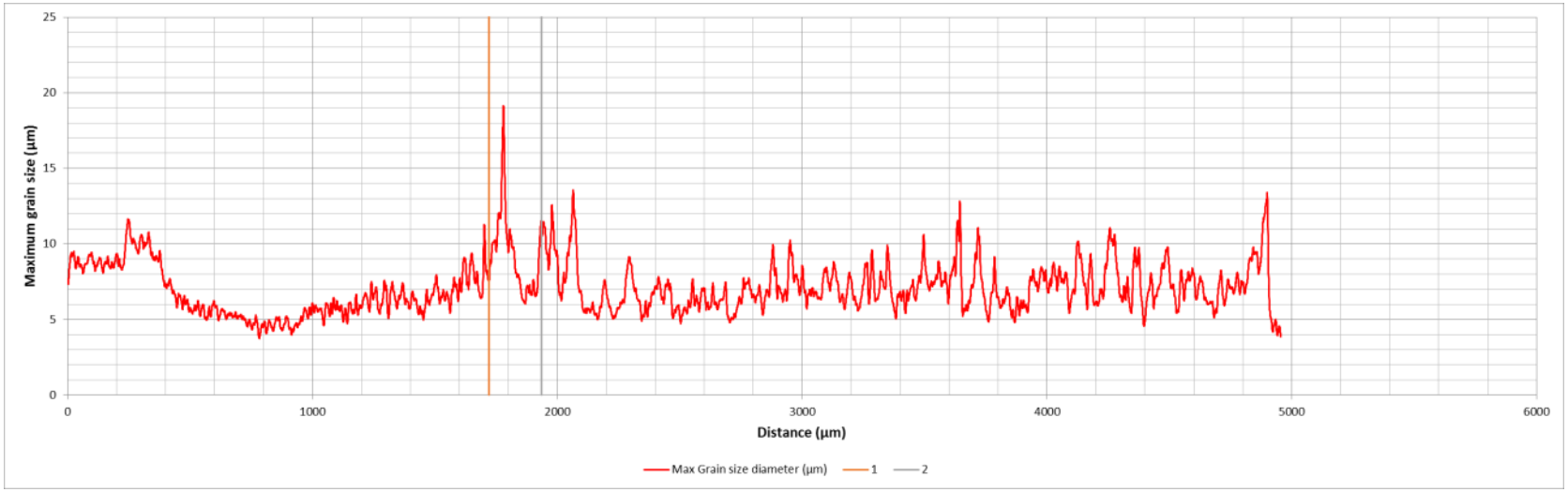

Figure 42 Grain size distribution of TIG welded sample 3.5.2-4 from base material to weld metal. Fusion line of Figure 41 is between lines 1 and 2.

Appendix 15

TIG 3.5.2-8

Figure 43 Original mosaic micrograph of TIG welded 3.5.2-4.

Figure 44 Original mosaic micrograph of TIG welded 3.5.2-4.

Figure 45 Micrograph of TIG welded sample 3.5.2-8 which contrast and sharpness were enhanced.

Figure 46 Micrograph of TIG welded sample 3.5.2-8 which contrast and sharpness were enhanced.

Figure 47 Grain boundary map of TIG welded sample 3.5.2-8.

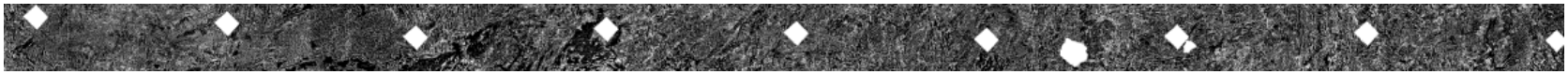

Figure 48 Grain boundary map of TIG welded sample 3.5.2-8.

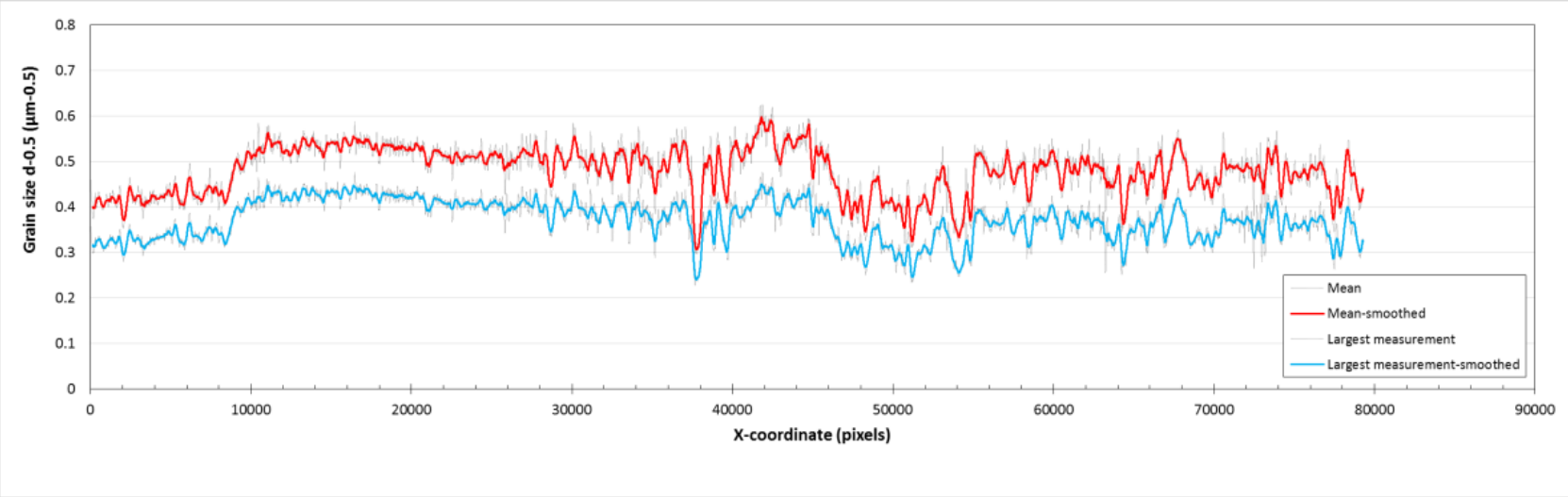

Figure 49 Grain size distributions of TIG welded sample 3.5.2-8 were calculated by Matlab.

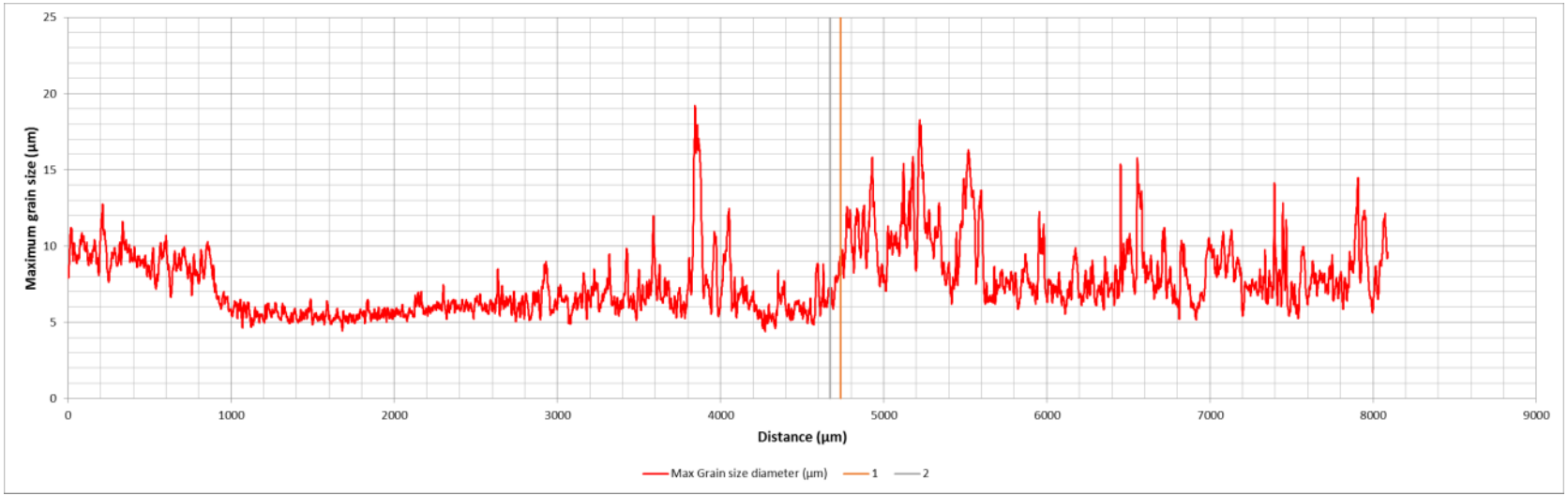

Figure 50 Grain size distribution of TIG welded sample 3.5.2-8 from base material to weld metal. Fusion line is between lines 1 and 2.

Appendix 15

TIG 3.5.2-9

Figure 51 Original mosaic micrograph of TIG welded 3.5.2-9.

Figure 52 Micrograph of TIG welded sample 3.5.2-9 which contrast and sharpness were enhanced.

Figure 53 Grain boundary map of TIG welded sample 3.5.2-9.

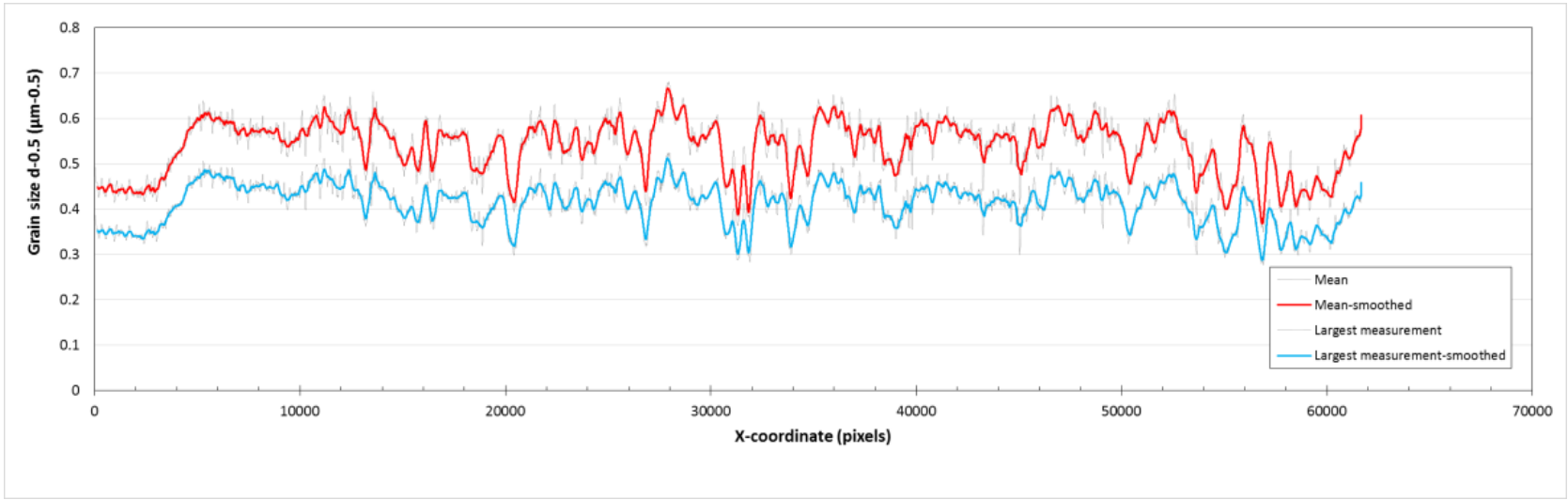

Figure 54 Grain size distributions of TIG welded sample 3.5.2-9 were calculated by Matlab.

Figure 55 Enhanced micrograph of TIG welded sample 3.5.2-9 in scale.

Appendix 15

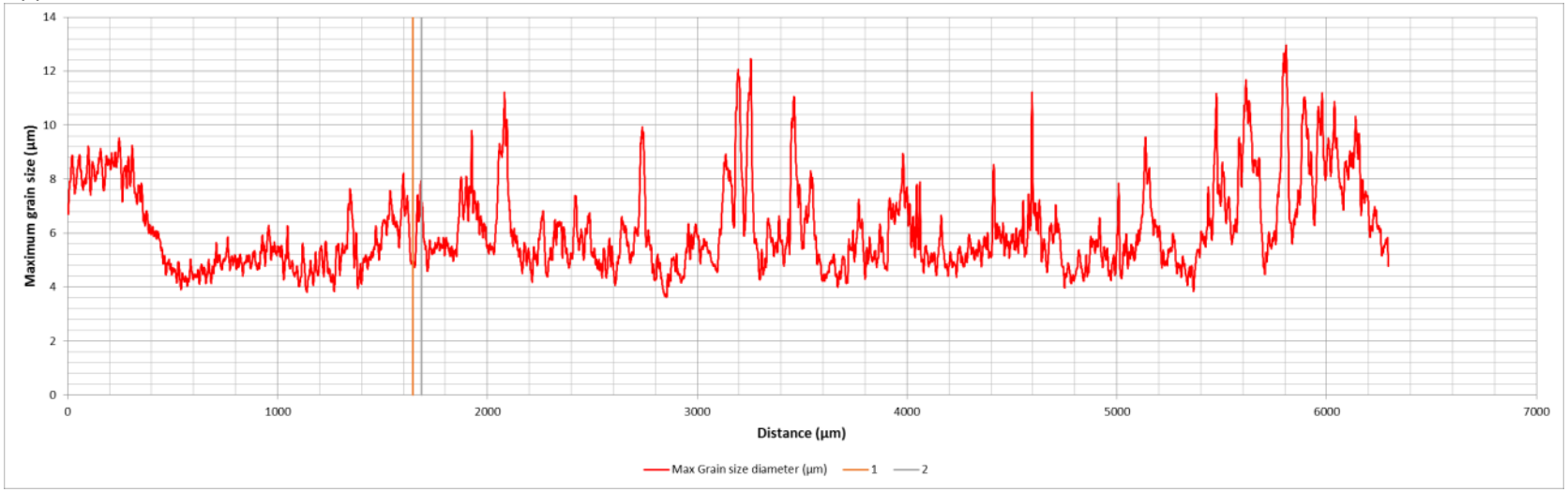

Figure 56 Grain size distribution of TIG welded sample 3.5.2-9 from base material to weld metal. Fusion line of Figure 55 is between lines 1 and 2.

TIG 3.15.2-6

Figure 57 Original mosaic micrograph of TIG welded 3.15.2-6.

Figure 58 Micrograph of TIG welded sample 3.15.2-6 which contrast and sharpness were enhanced.

Figure 59 Grain boundary map of TIG welded sample 3.15.2-6.

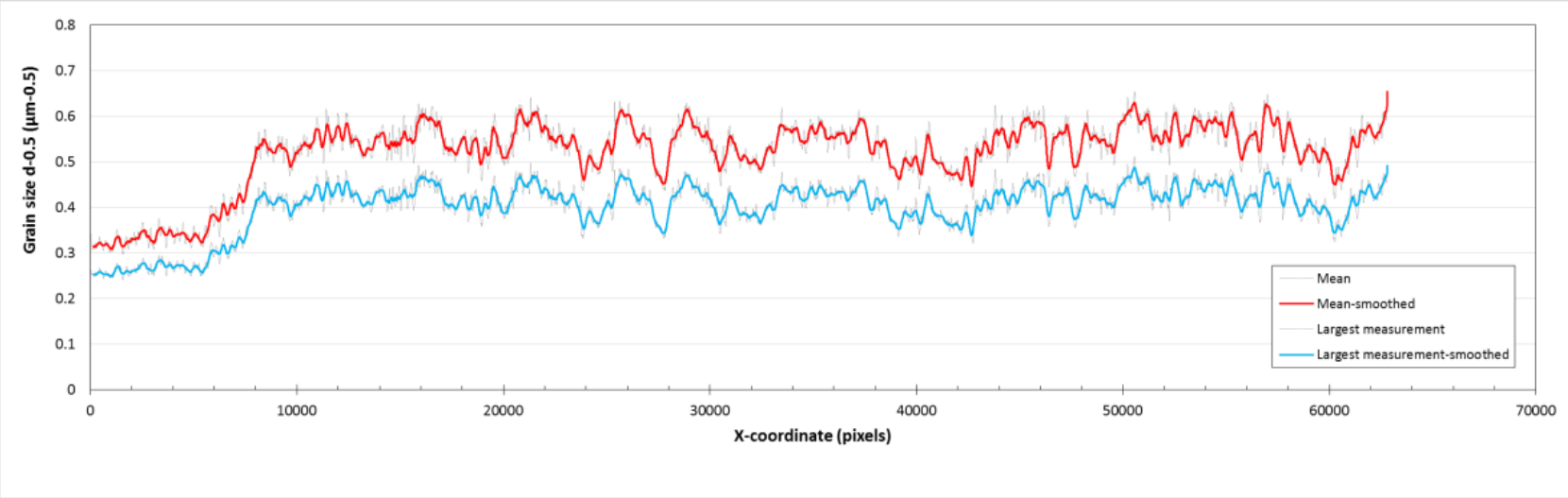

Figure 60 Grain size distributions of TIG welded sample 3.15.2-6 were calculated by Matlab.

Figure 61 Enhanced micrograph of TIG welded sample 3.15.2-6 in scale.

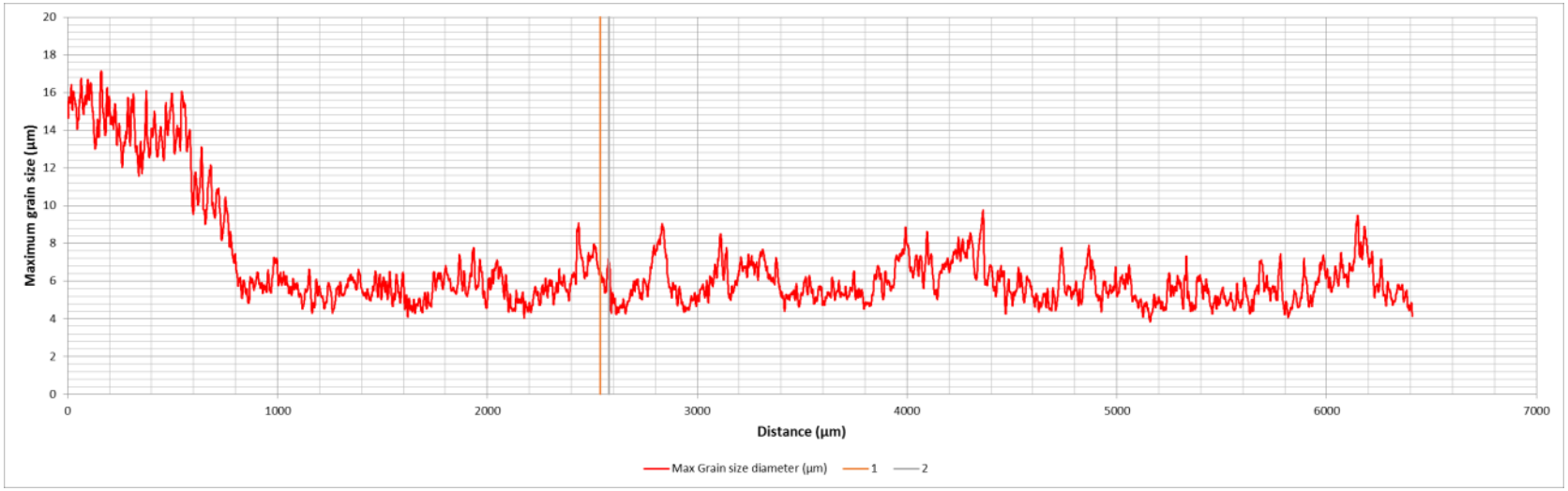

Figure 62 Grain size distribution of TIG welded sample 3.15.2-6 from base material to weld metal. Fusion line of Figure 61 is between lines 1 and 2.

Appendix 15

TIG 3.15.2-7

Figure 63 Original mosaic micrograph of TIG welded 3.15.2-7.

Figure 64 Micrograph of TIG welded sample 3.15.2-7 which contrast and sharpness were enhanced.

Figure 65 Grain boundary map of TIG welded sample 3.15.2-7.

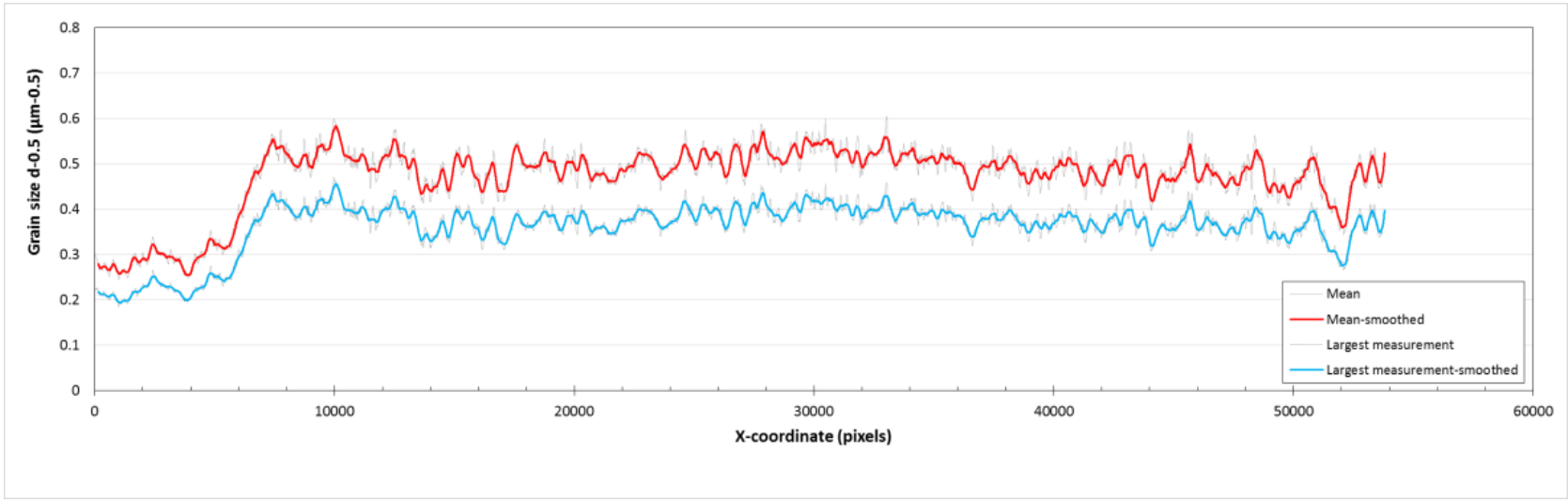

Figure 66 Grain size distributions of TIG welded sample 3.15.2-7 were calculated by Matlab.

Figure 67 Enhanced micrograph of TIG welded sample 3.15.2-7 in scale.

Appendix 15

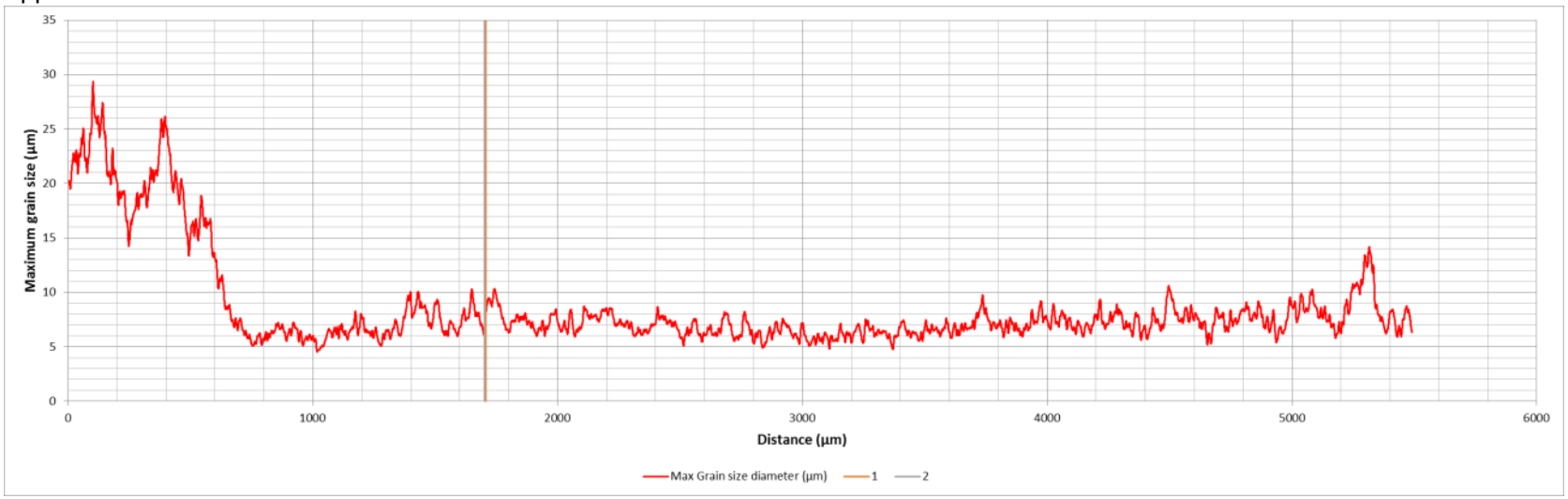

Figure 68 Grain size distribution of TIG welded sample 3.15.2-7 from base material to weld metal. Fusion line of Figure 67 is between lines 1 and 2.

TIG 3.15.2-8

Figure 69 Original mosaic micrograph of TIG welded 3.15.2-8.

Figure 70 Micrograph of TIG welded sample 3.15.2-8 which contrast and sharpness were enhanced.

Figure 71 Grain boundary map of TIG welded sample 3.15.2-8.

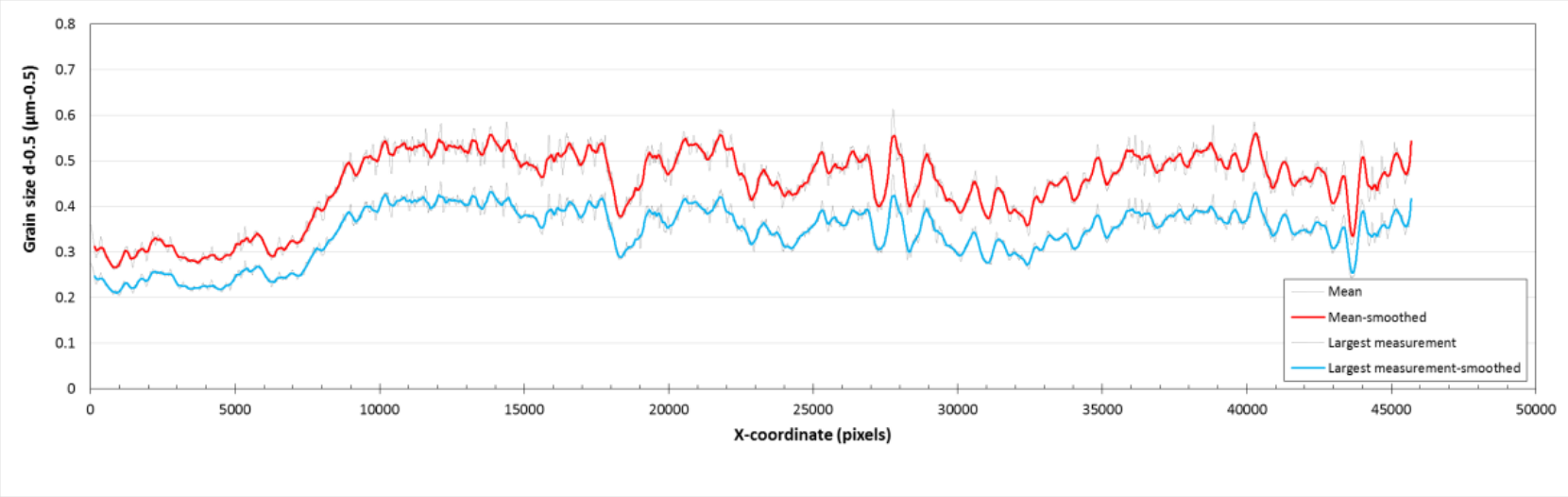

Figure 72 Grain size distributions of TIG welded sample 3.15.2-8 were calculated by Matlab.

Figure 73 Enhanced micrograph of TIG welded sample 3.15.2-8 in scale.

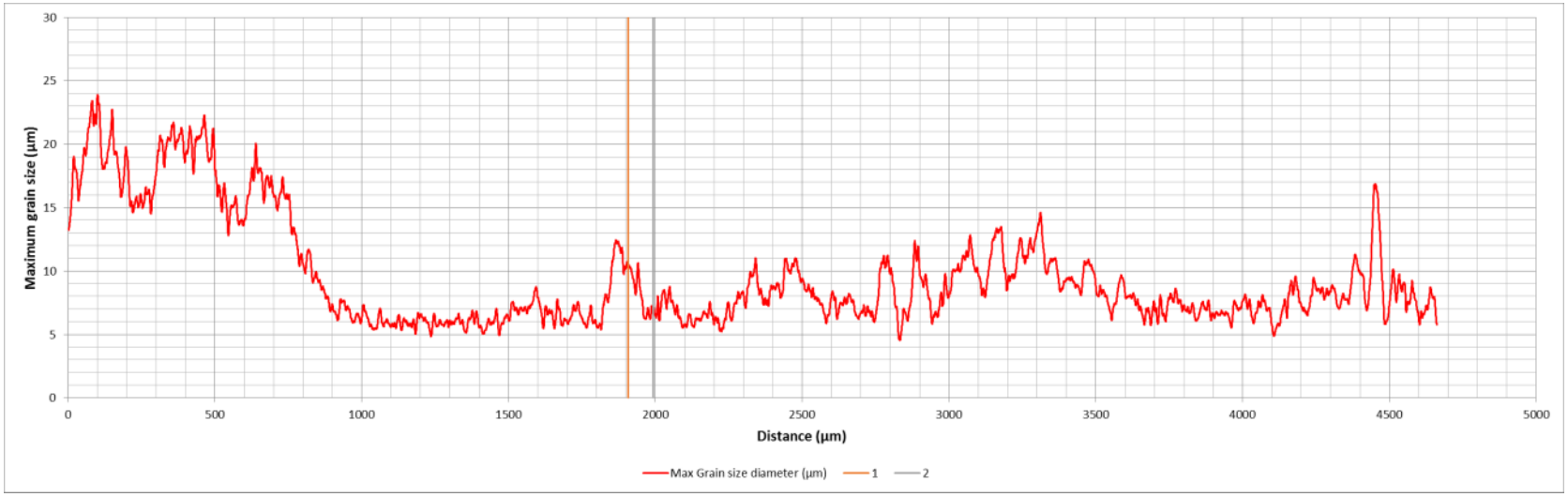

Figure 74 Grain size distribution of TIG welded sample 3.15.2-8 from base material to weld metal. Fusion line of is between lines 1 and 2.

Appendix 16 / Measured grain sizes from coarse-grained zone with optical microscope for bead-on-plate welds

Contents

Appendix 16

Table 1 Maximum measured grain sizes and amount of measured micrographs.

Number of sample	Amount of measured micrographs	*max measured size (µm)*
LAHW 3.5.2-3	5	102
LAHW 3.15.2-9	5	107
LASER 3.5.2-7	5	124
LASER 3.15.2-5	5	136
MAG 3.5.2-2	11	201
MAG 3.15.2-4	5	162
TIG 3.5.2-4	3	173
TIG 3.5.2-8	5	180
TIG 3.5.2-9	3	220
TIG 3.15.2-6	4	135
TIG 3.15.2-7	3	138
TIG 3.15.2-8	3	144

LAHW 3.5.2-3

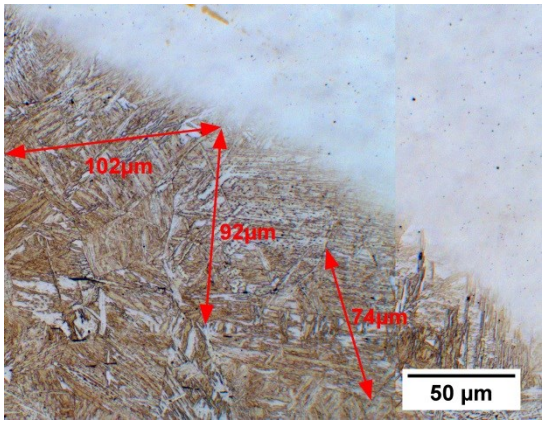

Figure 1 LAHW welded sample 3.5.2-3. Maximum diameter of grain is 102 µm.

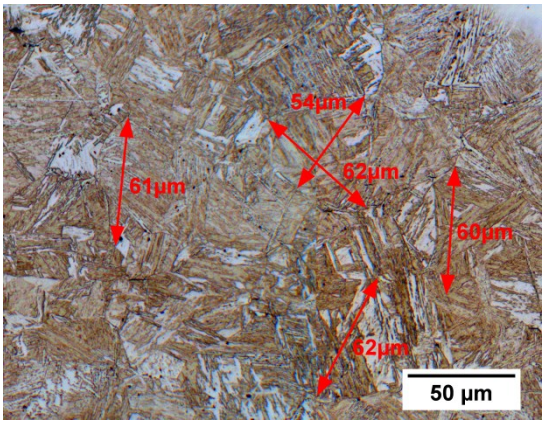

Figure 2 LAHW welded sample 3.5.2-3. Maximum diameter of grain is 62 µm.

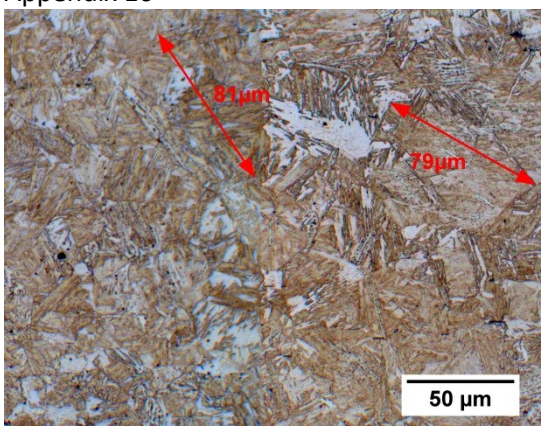

Figure 3 LAHW welded sample 3.5.2-3. Maximum diameter of grain is 81 µm.

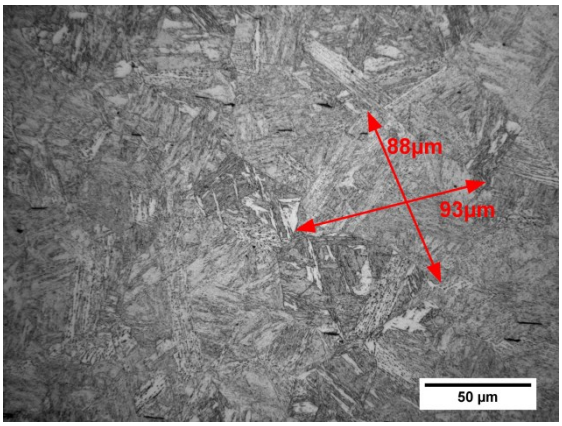

Figure 4 LAHW welded sample 3.5.2-3. Maximum diameter of grain is 93 µm.

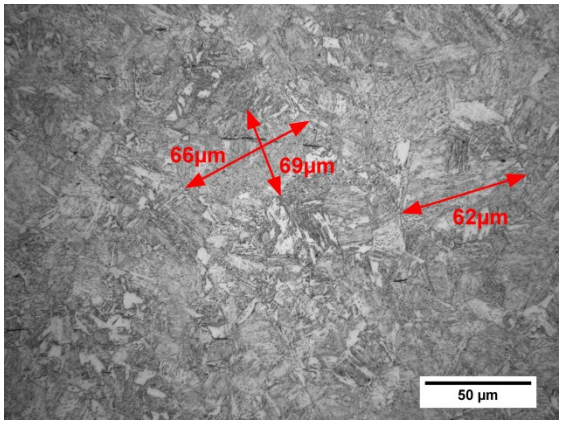

Figure 5 LAHW welded sample 3.5.2-3. Maximum diameter of grain is 69 µm.

LAHW 3.15.2-9

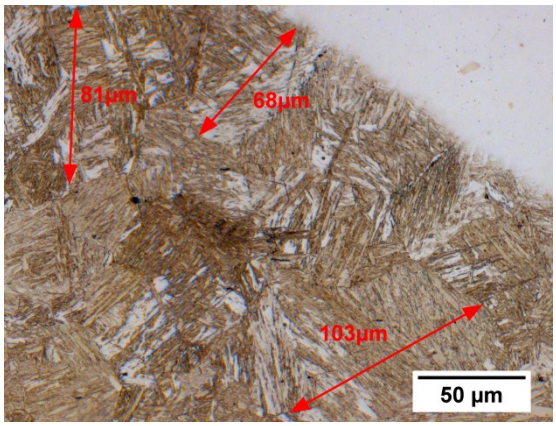

Figure 6 LAHW welded sample 3.15.2-9. Maximum diameter of grain is 103 µm.

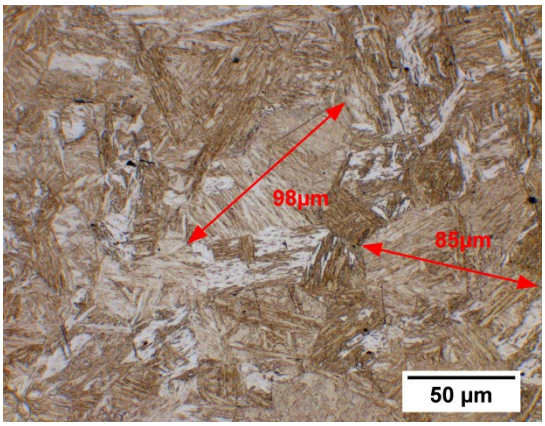

Figure 7 LAHW welded sample 3.15.2-9. Maximum diameter of grain is 98 µm.

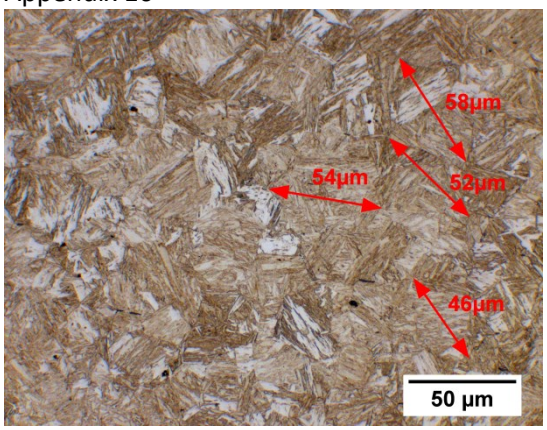

Figure 8 LAHW welded sample 3.15.2-9. Maximum diameter of grain is 58 µm.

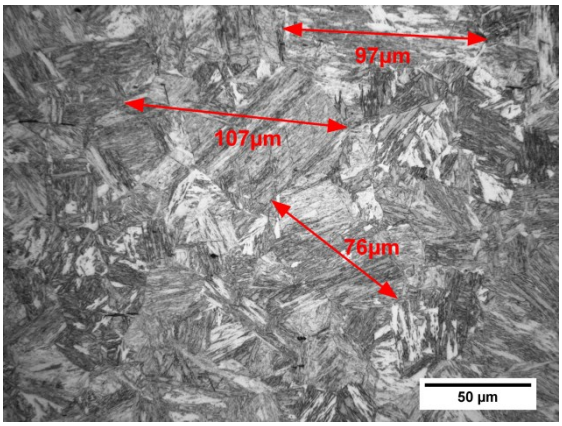

Figure 9 LAHW welded sample 3.15.2-9. Maximum diameter of grain is 107 µm.

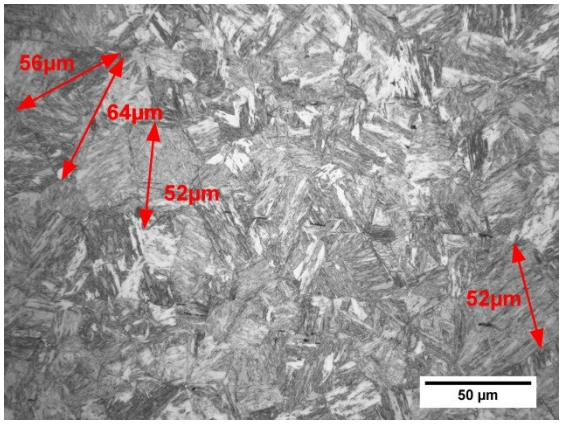

Figure 10 LAHW welded sample 3.15.2-9. Maximum diameter of grain is 56 µm.

LASER 3.5.2-7

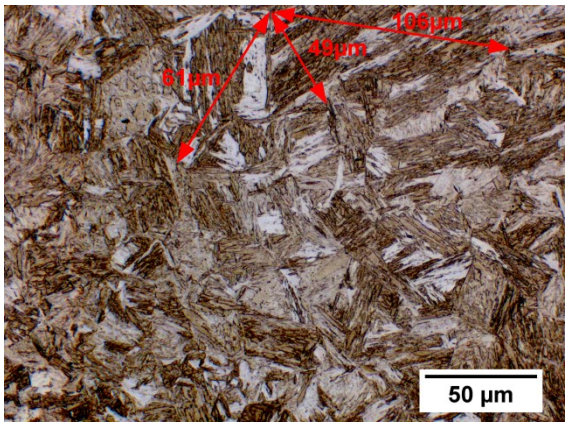

Figure 11 LASER welded sample 3.5.2-7. Maximum diameter of grain is 106 µm.

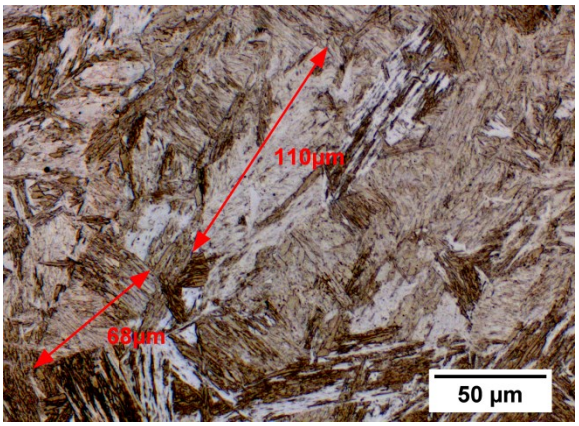

Figure 12 LASER welded sample 3.5.2-7. Maximum diameter of grain is 110 µm.

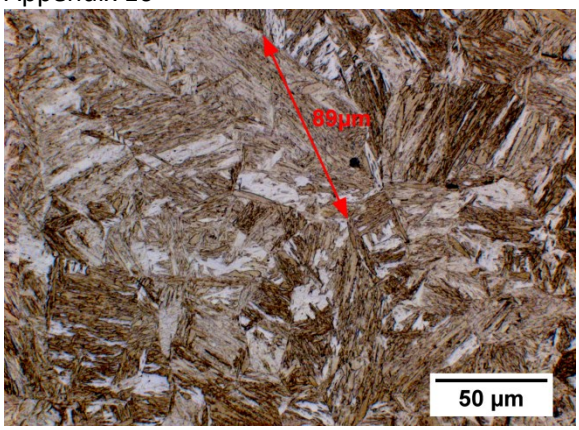

Figure 13 LASER welded sample 3.5.2-7. Maximum diameter of grain is 89 µm.

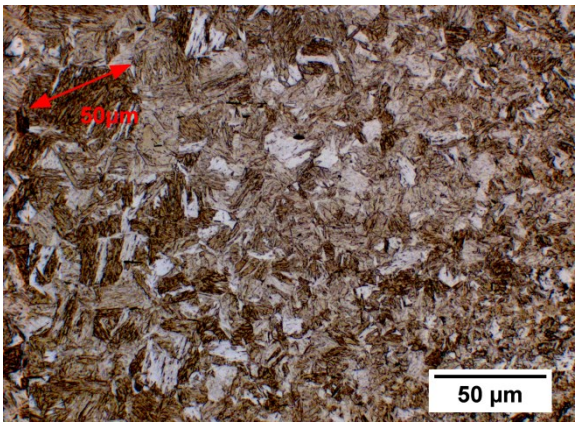

Figure 14 LASER welded sample 3.5.2-7. Maximum diameter of grain is 50 µm.

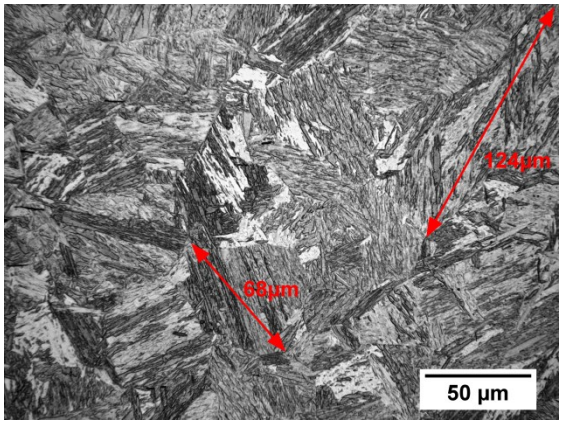

Figure 15 LASER welded sample 3.5.2-7. Maximum diameter of grain is 124 µm.

LASER 3.15.2-5

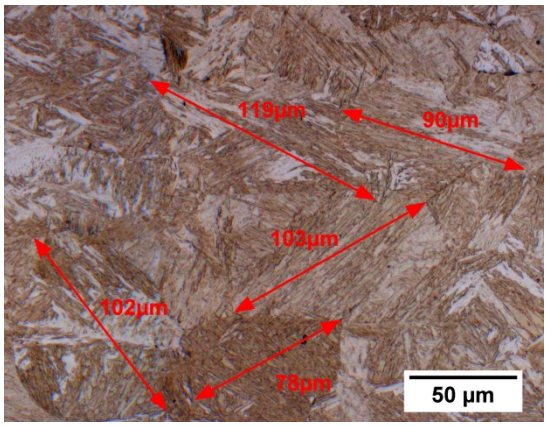

Figure 16 LASER welded sample 3.15.2-5. Maximum diameter of grain is 119 µm.

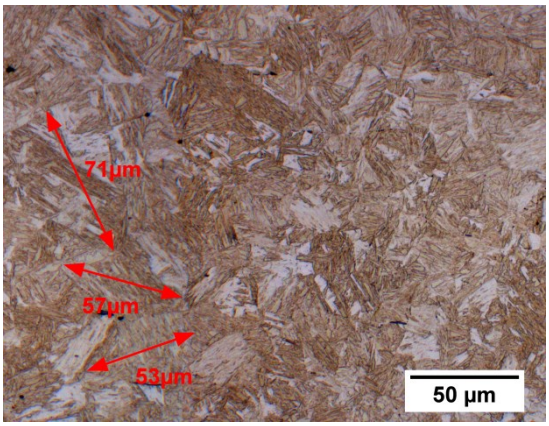

Figure 17LASER welded sample 3.15.2-5. Maximum diameter of grain is 71 µm.

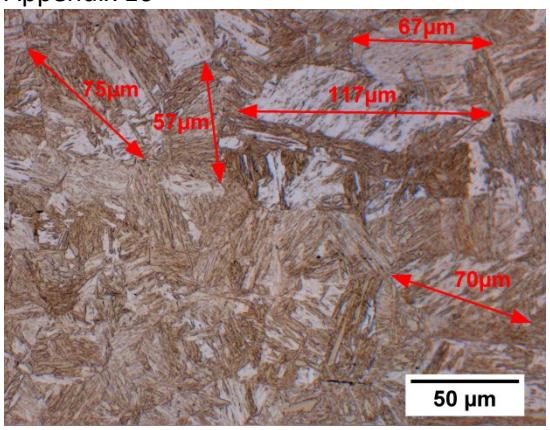

Figure 18 LASER welded sample 3.15.2-5. Maximum diameter of grain is 117 µm.

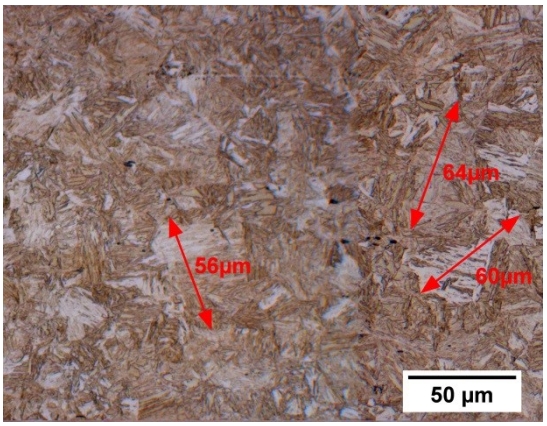

Figure 19 LASER welded sample 3.15.2-5. Maximum diameter of grain is 64 µm.

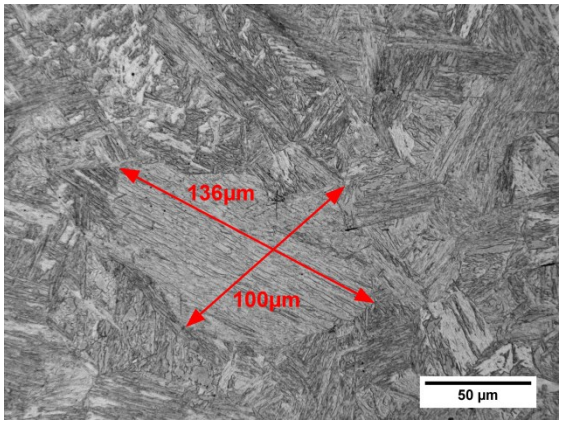

Figure 20 LASER welded sample 3.15.2-5. Maximum diameter of grain is 136 µm.

MAG 3.5.2-2

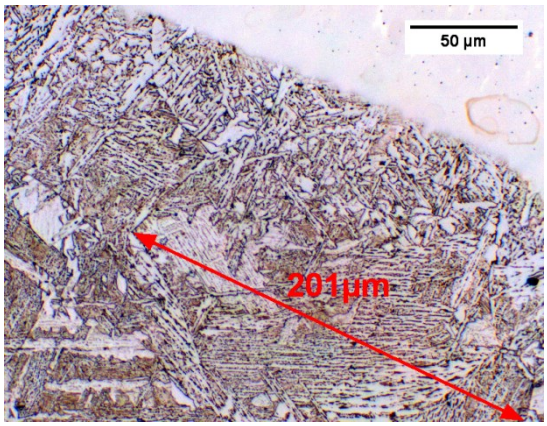

Figure 21 MAG welded sample 3.5.2-2. Maximum diameter of grain is 201 µm.

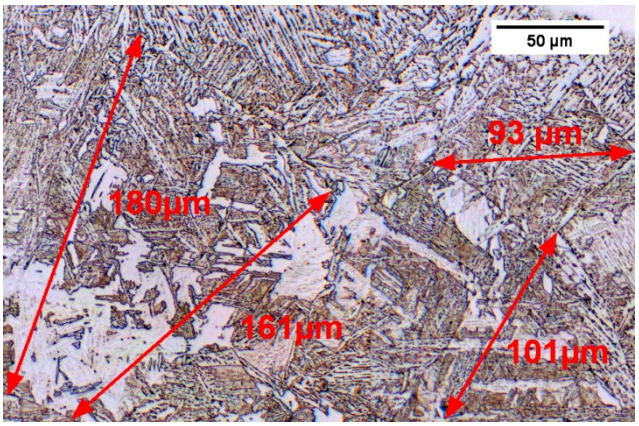

Figure 22 MAG welded sample 3.5.2-2. Maximum diameter of grain is 180 µm.

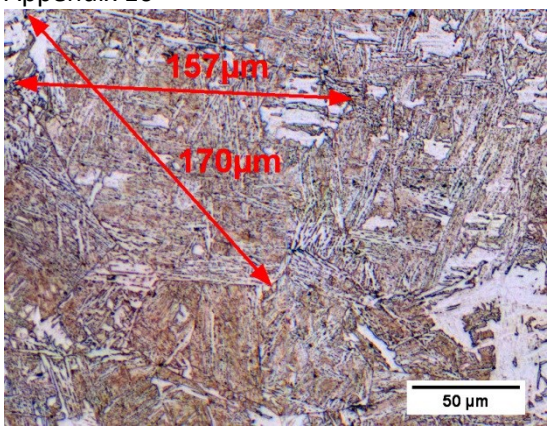

Figure 23 MAG welded sample 3.5.2-2. Maximum diameter of grain is 170 µm.

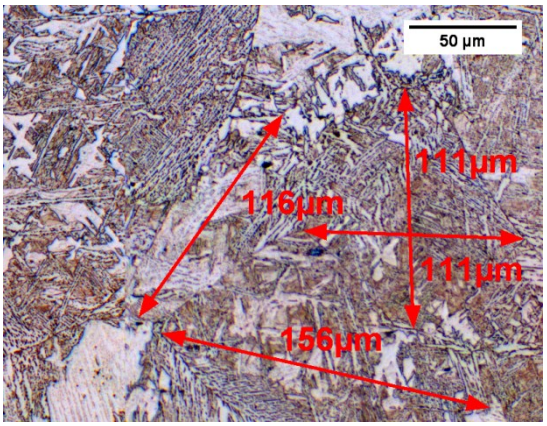

Figure 24 MAG welded sample 3.5.2-2. Maximum diameter of grain is 156 µm.

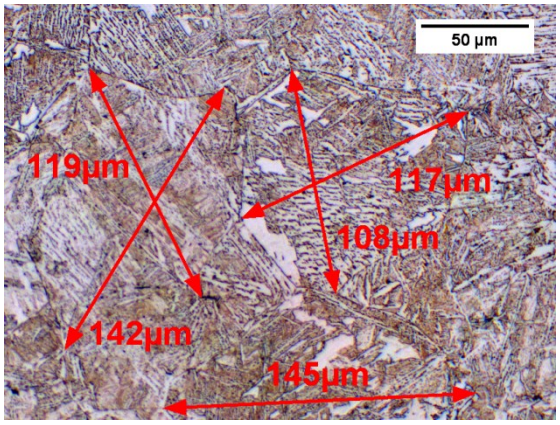

Figure 25 MAG welded sample 3.5.2-2. Maximum diameter of grain is 145 µm.

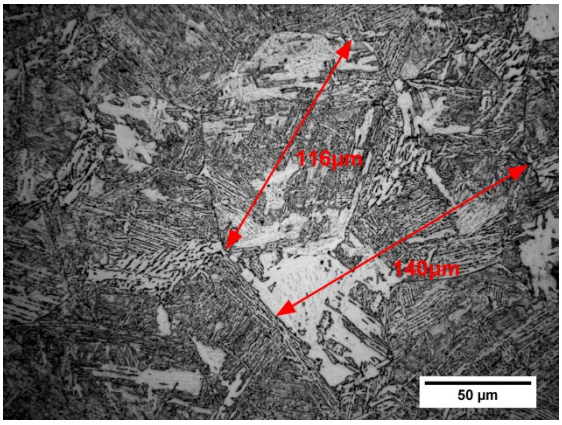

Figure 26 MAG welded sample 3.5.2-2. Maximum diameter of grain is 140 µm.

Appendix 16

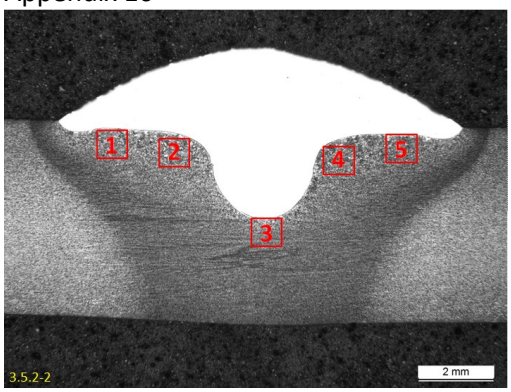

Figure 27 Positions of measured maximum grain size diameter of MAG welded sample 3.5.2-2 were numbered. (10X ocular & 1 objective)

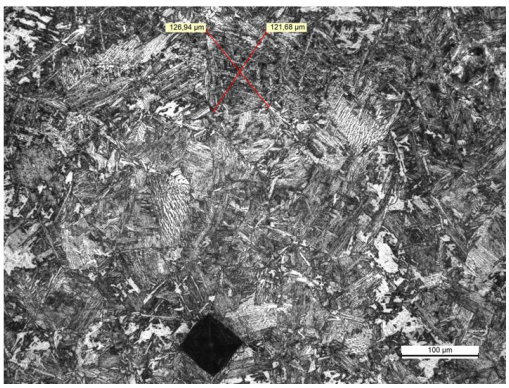

Figure 28 Measured maximum grain diameter of position 1 was 127 µm.

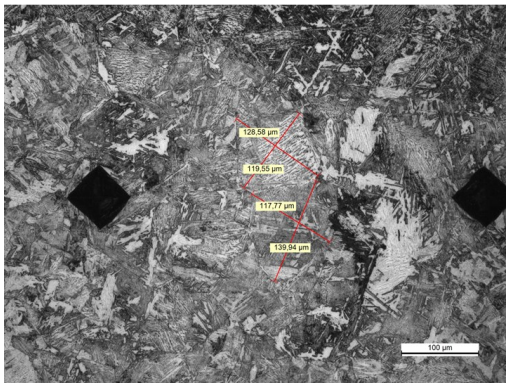

Figure 29 Measured maximum grain diameter of position 2 was 140 µm.

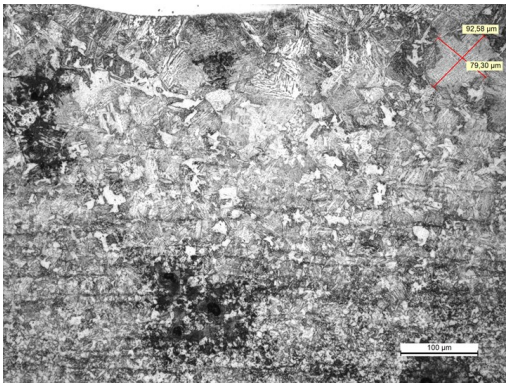

Figure 30 Measured maximum grain diameter of position 3 was 93 µm.

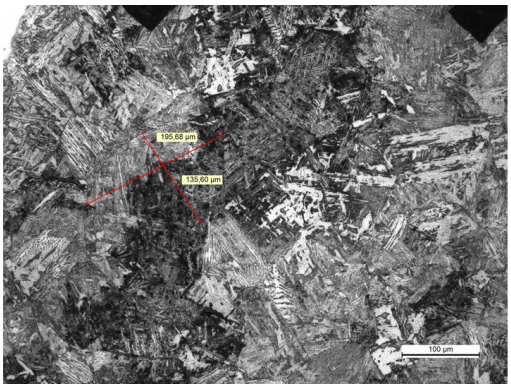

Figure 31 Measured maximum grain diameter of position 4 was 196 µm.

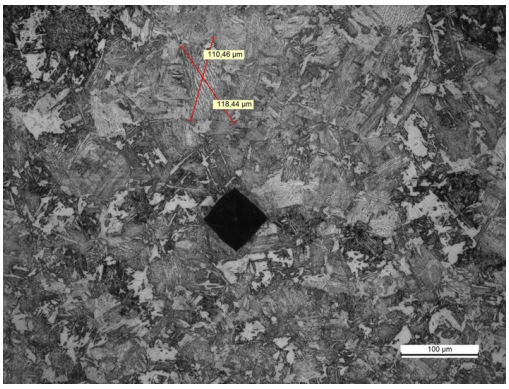

Figure 32 Measured maximum grain diameter of position 5 was 118 µm.

Appendix 16

MAG 3.15.2-4

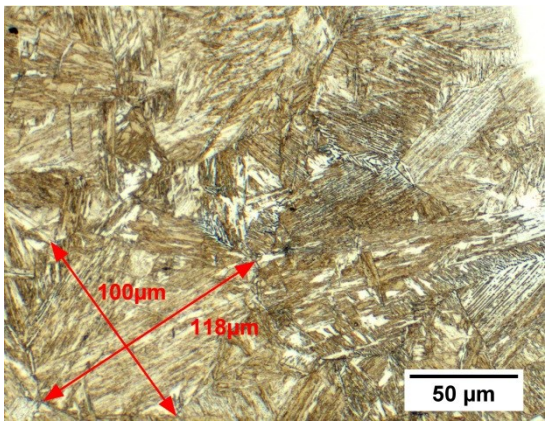

Figure 33 MAG welded sample 3.15.2-4. Maximum diameter of grain is 118 µm.

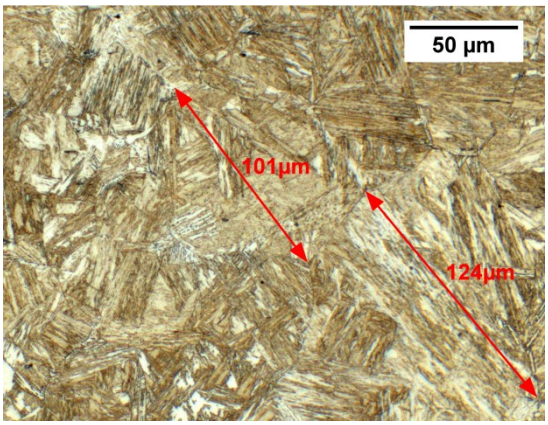

Figure 34MAG welded sample 3.15.2-4. Maximum diameter of grain is 124 µm.

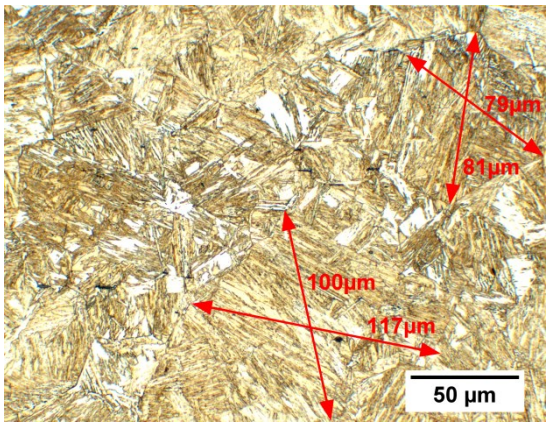

Figure 35 MAG welded sample 3.15.2-4. Maximum diameter of grain is 117 µm.

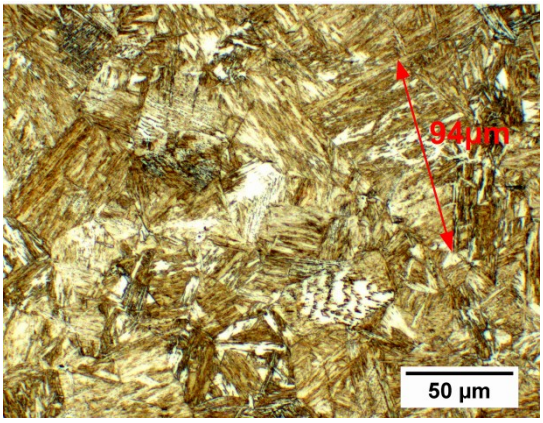

Figure 36 MAG welded sample 3.15.2-4. Maximum diameter of grain is 94 µm.

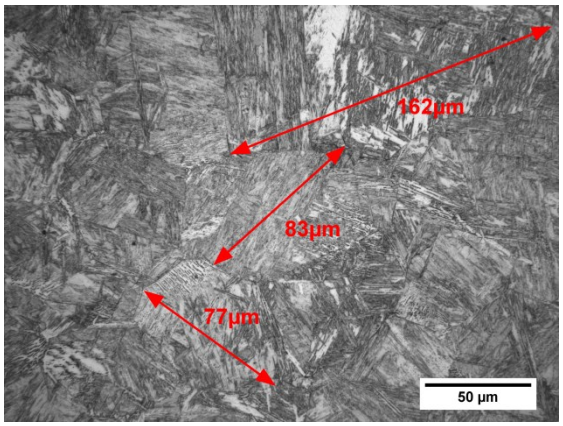

Figure 37 MAG welded sample 3.15.2-4. Maximum diameter of grain is 162 µm.

TIG 3.5.2-4

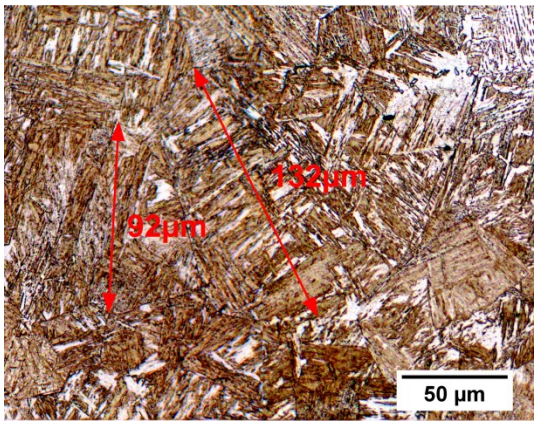

Figure 38 TIG welded sample 3.5.2-4. Maximum diameter of grain is 132 µm.

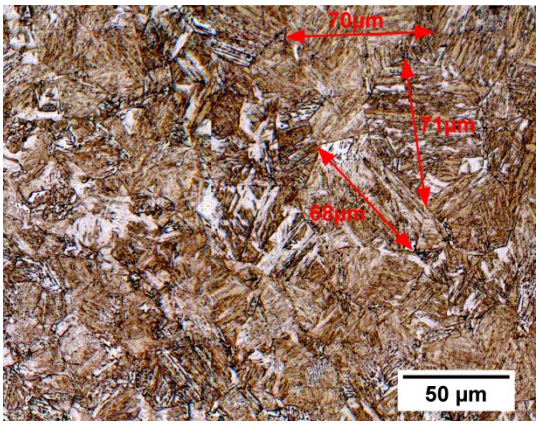

Figure 39 TIG welded sample 3.5.2-4. Maximum diameter of grain is 71 µm.

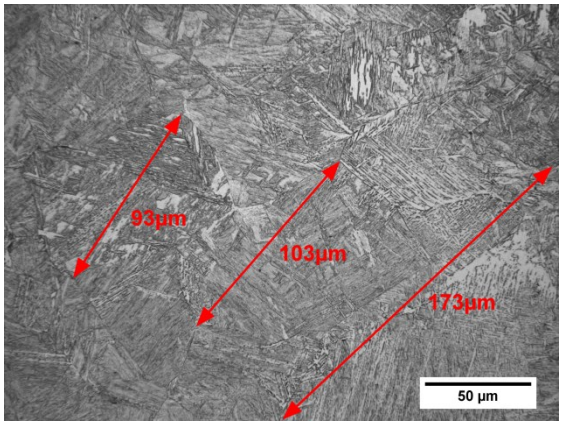

Figure 40 TIG welded sample 3.5.2-4. Maximum diameter of grain is 173 µm.

TIG 3.5.2-8

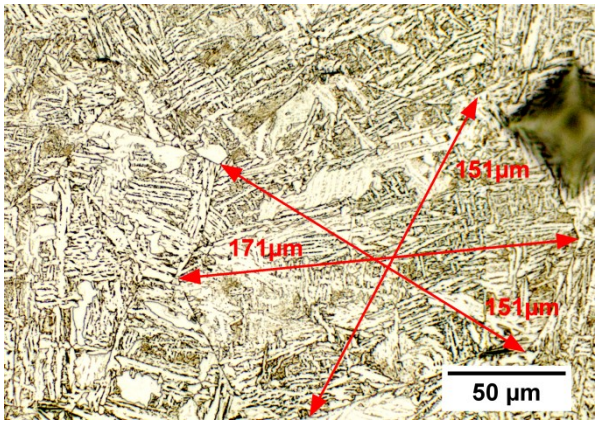

Figure 41 TIG welded sample 3.5.2-8. Maximum diameter of grain is 171 µm.

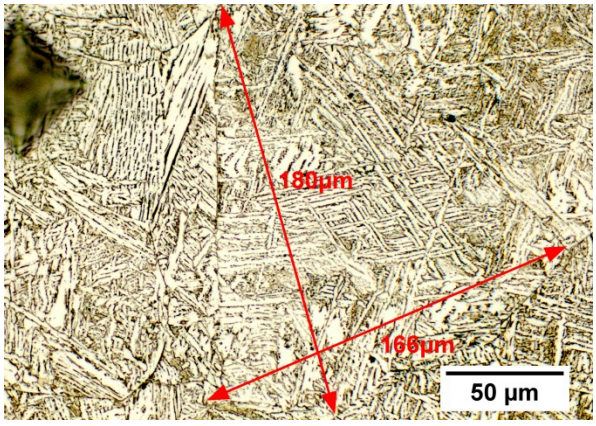

Figure 42 TIG welded sample 3.5.2-8. Maximum diameter of grain is 180 µm.

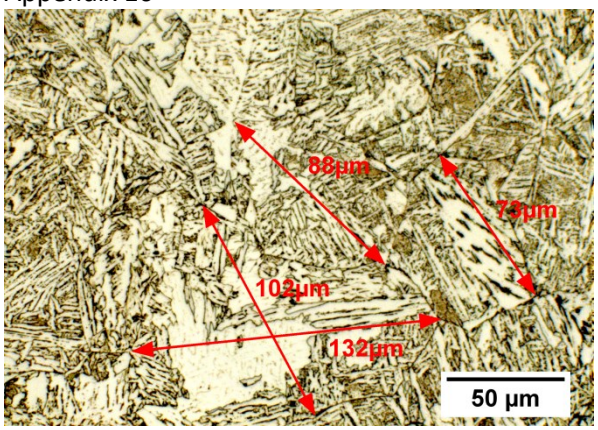

Figure 43 TIG welded sample 3.5.2-8. Maximum diameter of grain is 132 µm.

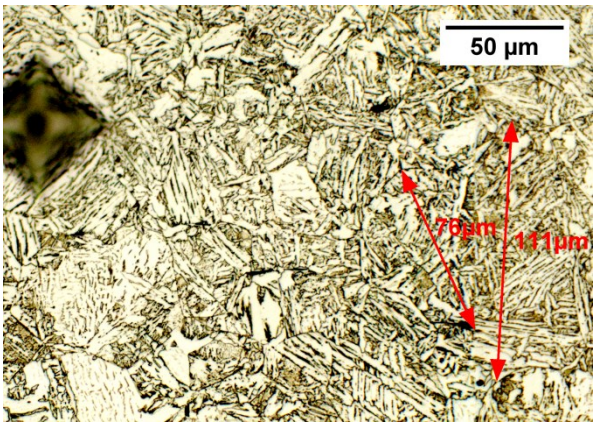

Figure 44 TIG welded sample 3.5.2-8. Maximum diameter of grain is 111 µm.

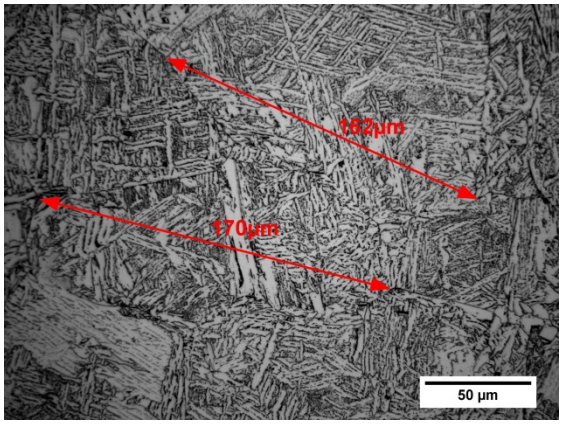

Figure 45 TIG welded sample 3.5.2-8. Maximum diameter of grain is 170 µm.

TIG 3.5.2-9

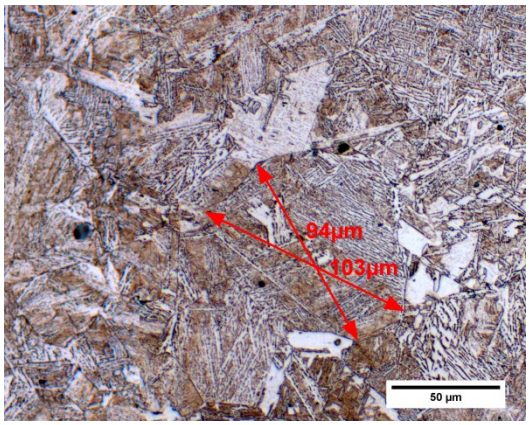

Figure 46 TIG welded sample 3.5.2-9. Maximum diameter of grain is 103 µm.

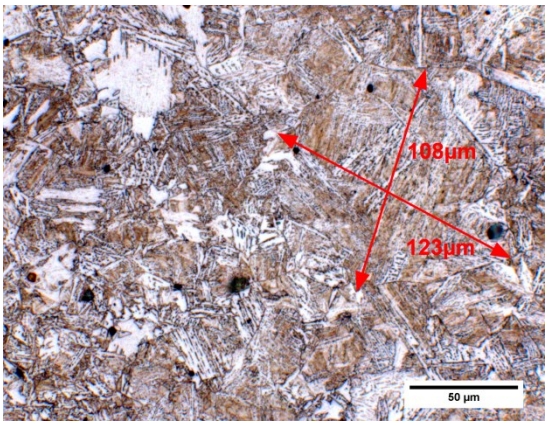

Figure 47 TIG welded sample 3.5.2-9. Maximum diameter of grain is 123 µm.

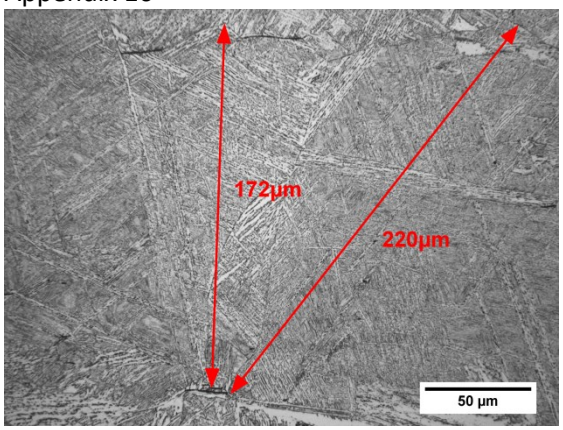

Figure 48 TIG welded sample 3.5.2-9. Maximum diameter of grain is 220 µm.

TIG 3.15.2-6

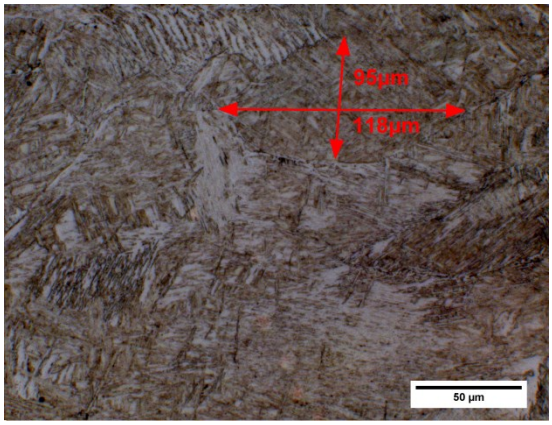

Figure 49 TIG welded sample 3.15.2-6. Maximum diameter of grain is 118 µm.

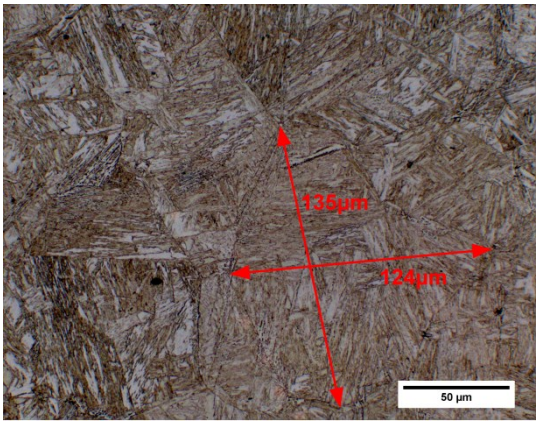

Figure 50 TIG welded sample 3.15.2-6. Maximum diameter of grain is 135 µm.

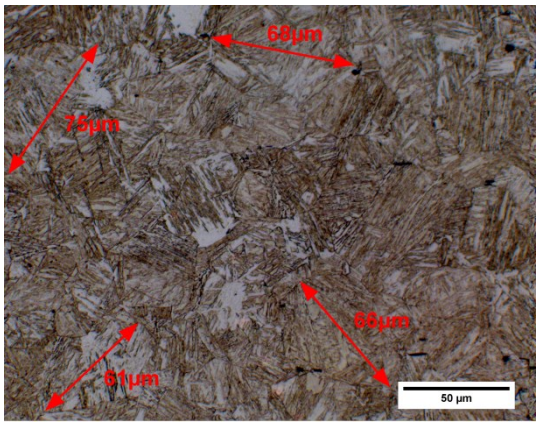

Figure 51 TIG welded sample 3.15.2-6. Maximum diameter of grain is 75 µm.

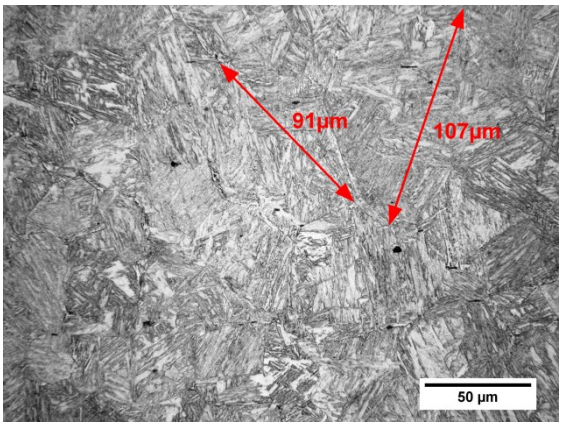

Figure 52 TIG welded sample 3.15.2-6. Maximum diameter of grain is 107 µm.

TIG 3.15.2-7

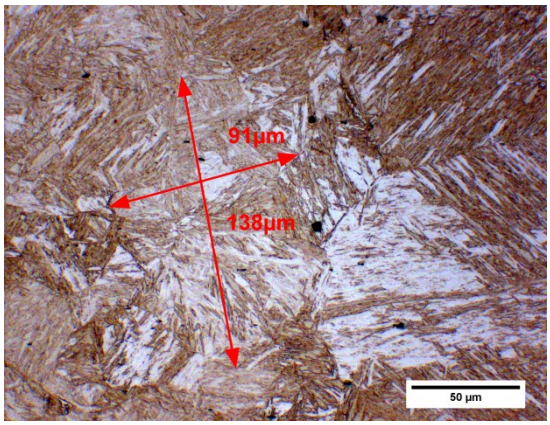

Figure 53 TIG welded sample 3.15.2-7. Maximum diameter of grain is 138 µm.

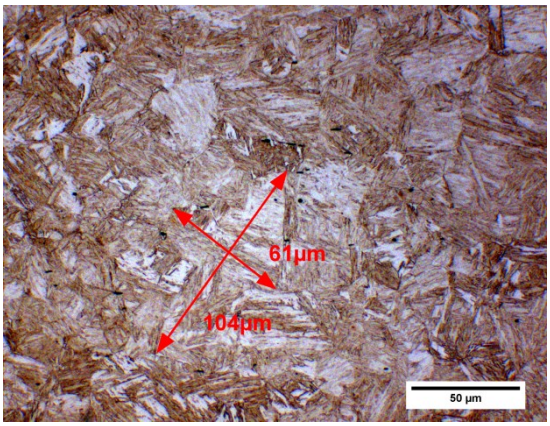

Figure 54 TIG welded sample 3.15.2-7. Maximum diameter of grain is 104 µm.

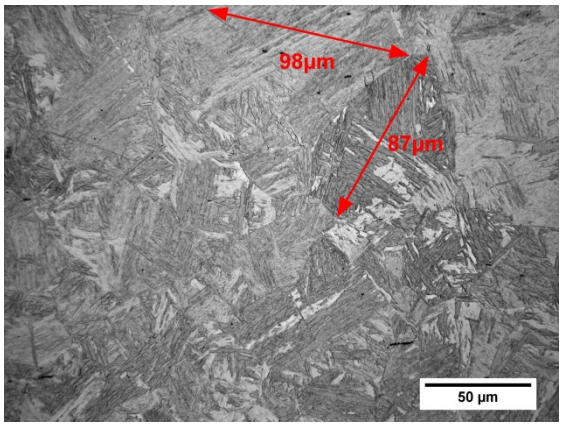

Figure 55 TIG welded sample 3.15.2-7. Maximum diameter of grain is 98 µm.

TIG 3.15.2-8

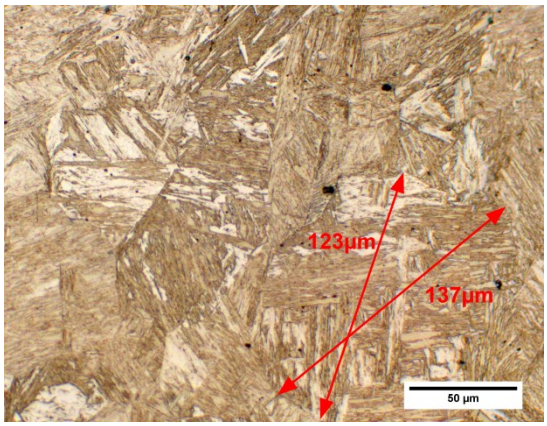

Figure 56 TIG welded sample 3.15.2-8. Maximum diameter of grain is 137 µm.

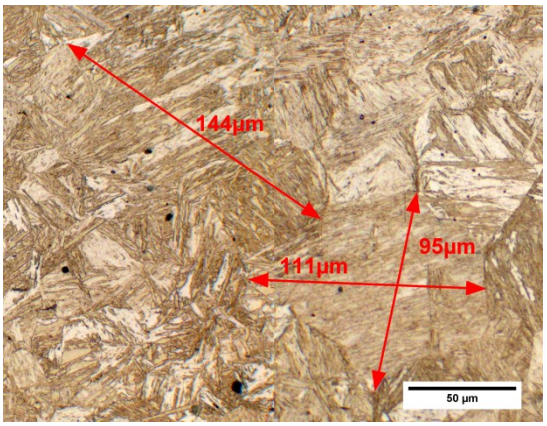

Figure 57 TIG welded sample 3.15.2-8. Maximum diameter of grain is 144 µm.

Appendix 16

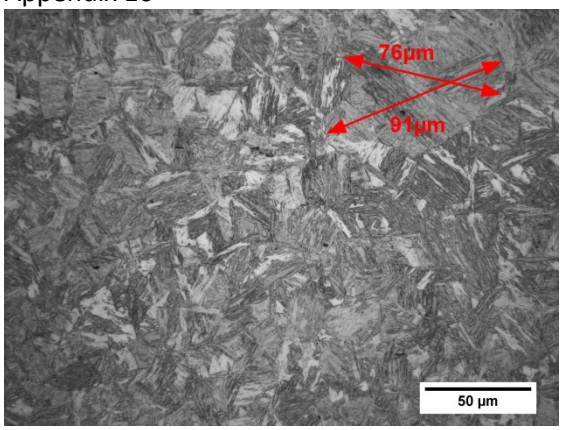

Figure 58 TIG welded sample 3.15.2-8. Maximum diameter of grain is 91 µm.

Appendix 17 / HV1 hardness distributions of butt welds

Contents

Appendix 17

MAG welded sample 1

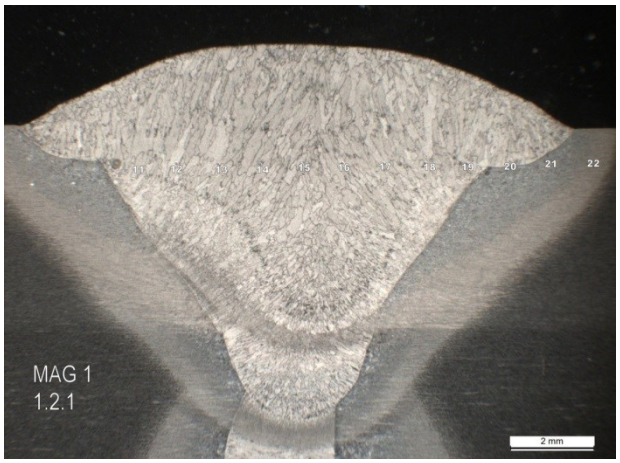

Figure 1 Measuring points of MAG welded sample 1.

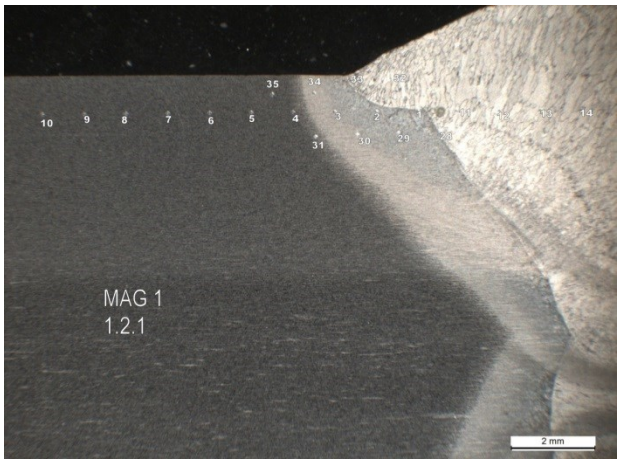

Figure 2 Measuring points of MAG welded sample 1.

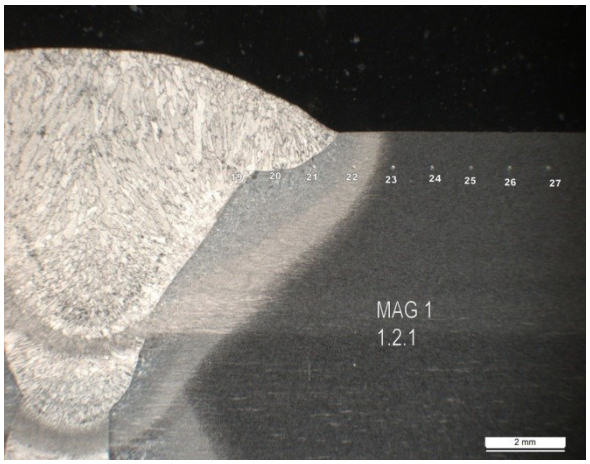

Figure 3 Measuring points of MAG welded sample 1.

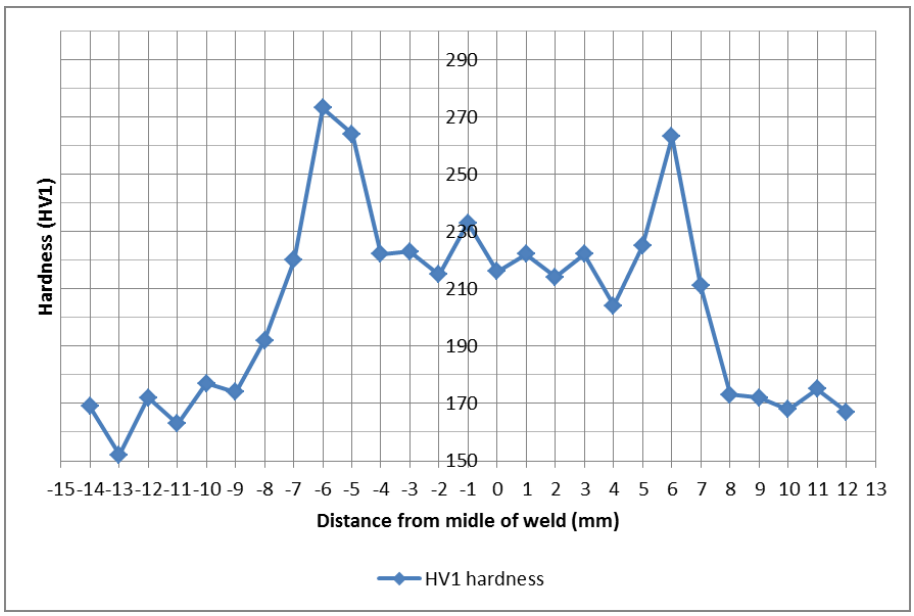

Figure 4 Hardness distribution of MAG welded sample 1 was measured over weld from 0.9 mm depth.

Appendix 17

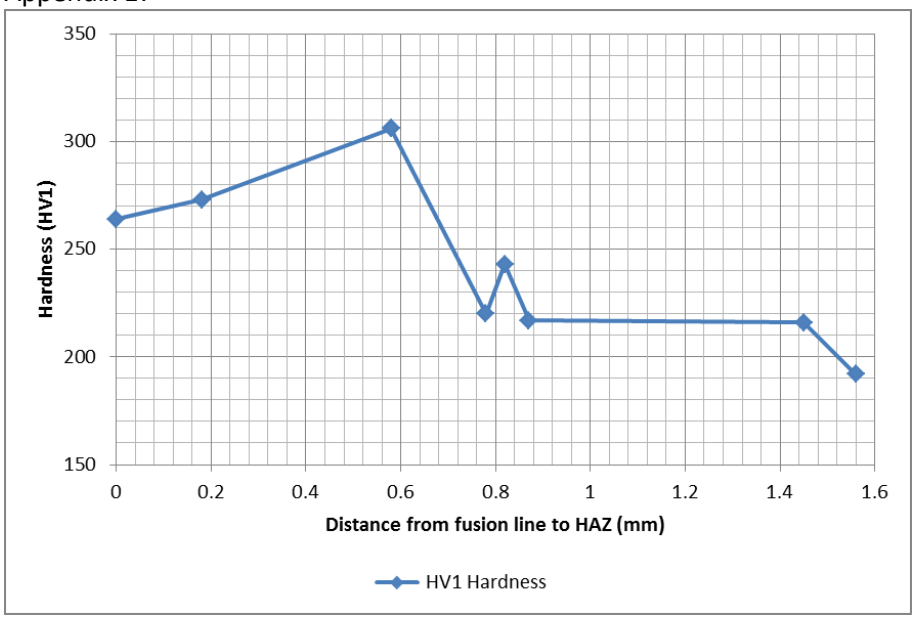

Figure 5 Hardness distribution from fusion line to HAZ for MAG welded sample 1.

Table 1 Measuring points of HV1 hardnesses for MAG welded samples 1.

Measuring points	Hardness (HV1)	Measuring points	Hardness (HV1)
1	264	19	204
2	273	20	225
3	220	21	263
4	192	22	211
5	174	23	173
6	177	24	172
7	163	25	168
8	172	26	175
9	152	27	167
10	169	28	235
11	222	29	306
12	223	30	243
13	215	31	216
14	233	32	223
15	216	33	261
16	222	34	217
17	214	35	183
18	222		

Appendix 17

LAHW welded sample 5

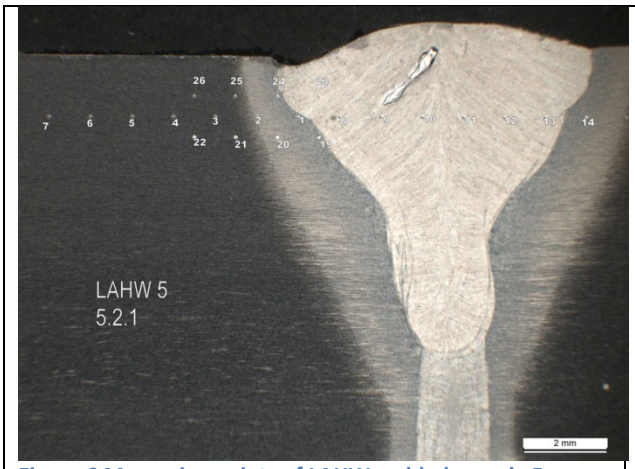

Figure 6 Measuring points of LAHW welded sample 5.

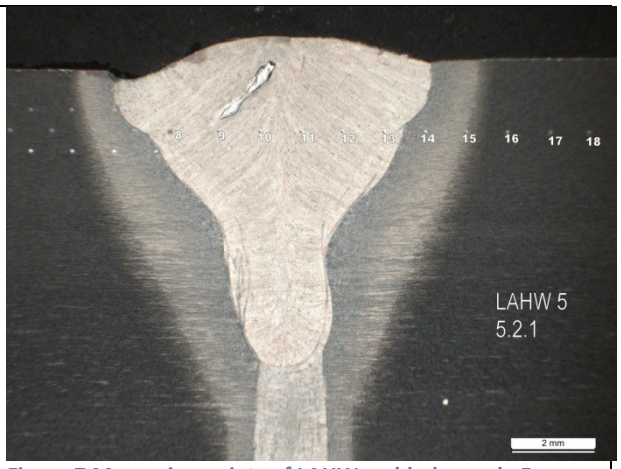

Figure 7 Measuring points of LAHW welded sample 5.

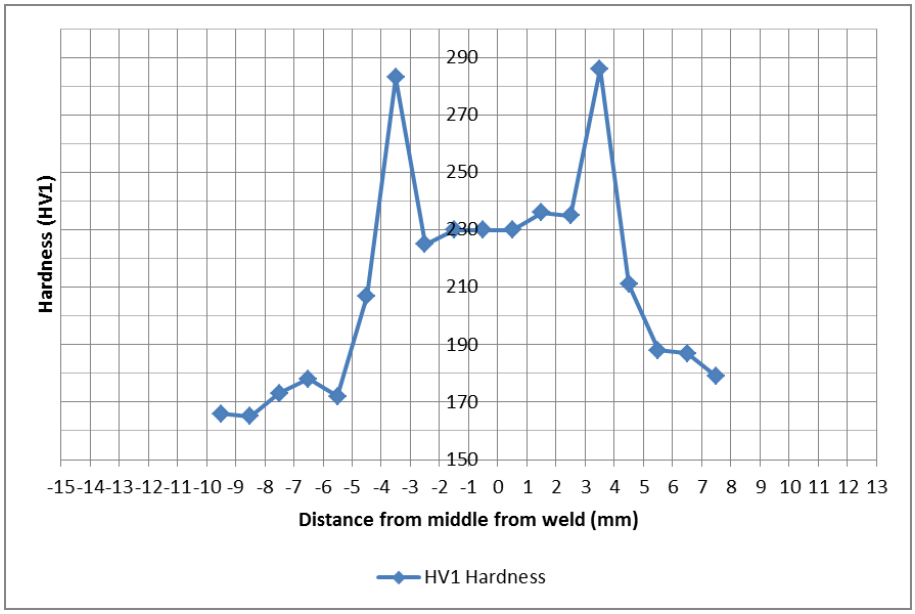

Figure 8 Hardness distribution of LAHW welded sample 5 was measured over weld from 1.5 mm depth.

Appendix 17

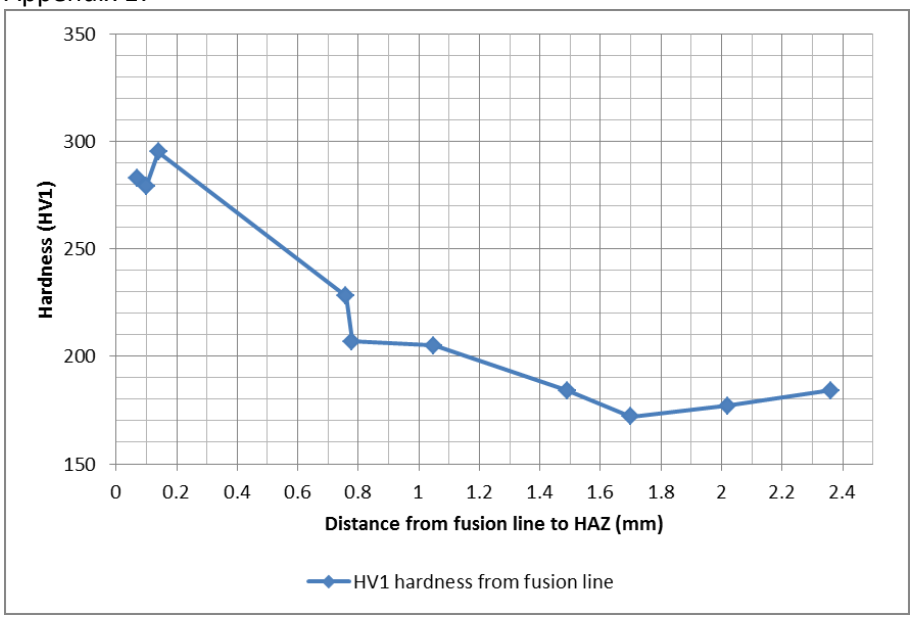

Figure 9 Hardness distribution from fusion line to HAZ for LAHW welded sample 5.

Table 2 Measuring points of HV1 hardnesses for LAHW welded samples 5.

Measuring points	Hardness (HV1)	Measuring points	Hardness (HV1)
1	283	14	286
2	207	15	211
3	172	16	188
4	178	17	187
5	173	18	179
6	165	19	279
7	166	20	228
8	225	21	184
9	230	22	184
10	230	23	227
11	230	24	295
12	236	25	205
13	235	26	177

Appendix 18 / Micrographs of butt weld samples

Contents

MAG welded sample 1

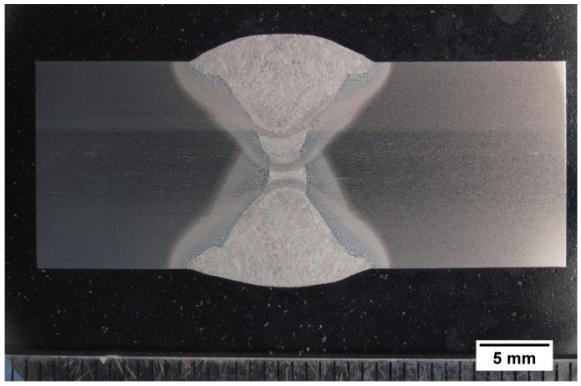

Figure 1 Macrograph of MAG welded sample 1 was taken with Leica MZ12 stereo microscope.

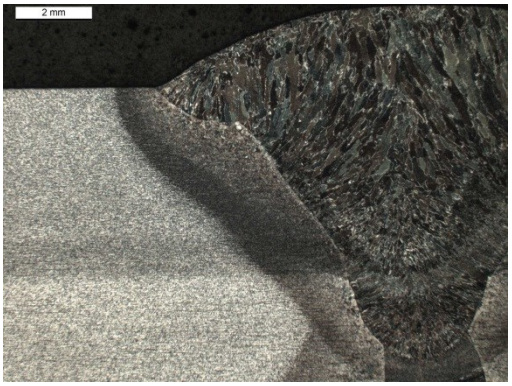

Figure 2 Micrograph of MAG welded sample 1 was taken with Leica MEF 4M light optical microscope.

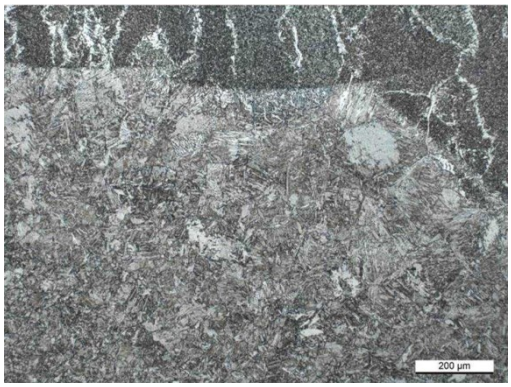

Figure 3 Micrograph of MAG welded sample 1 was taken with Leica MEF 4M light optical microscope from area of Figure 2.

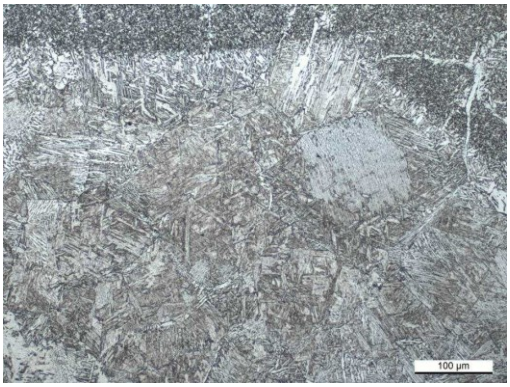

Figure 4 Micrograph of MAG welded sample 1 was taken with Leica MEF 4M light optical microscope from area of Figure 2.

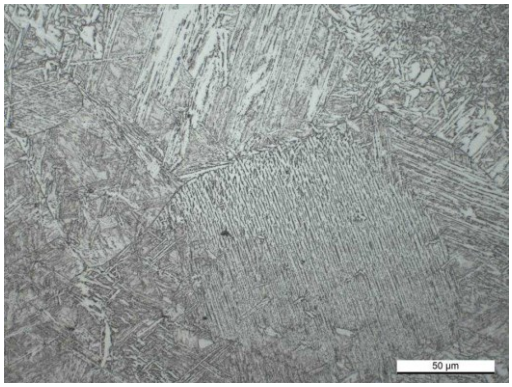

Figure 5 Micrograph of MAG welded sample 1 was taken with Leica MEF 4M light optical microscope from area of Figure 2.

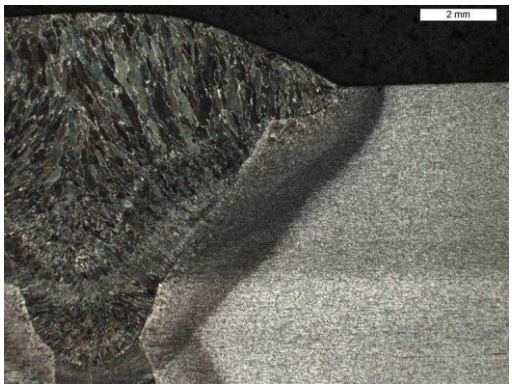

Figure 6 Micrograph of MAG welded sample 1 was taken with Leica MEF 4M light optical microscope.

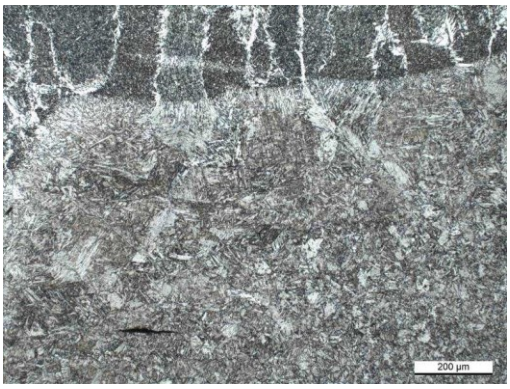

Figure 7 Micrograph of MAG welded sample 1 was taken with Leica MEF 4M light optical microscope from area of Figure 6.

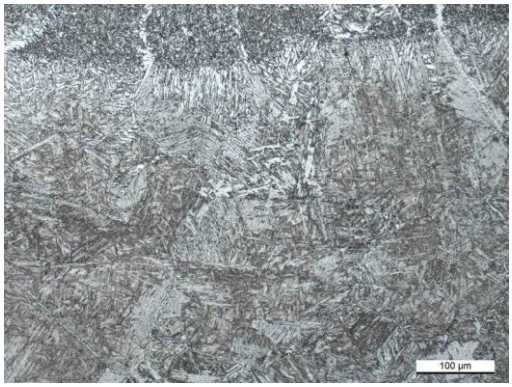

Figure 8 Micrograph of MAG welded sample 1 was taken with Leica MEF 4M light optical microscope from area of Figure 6.

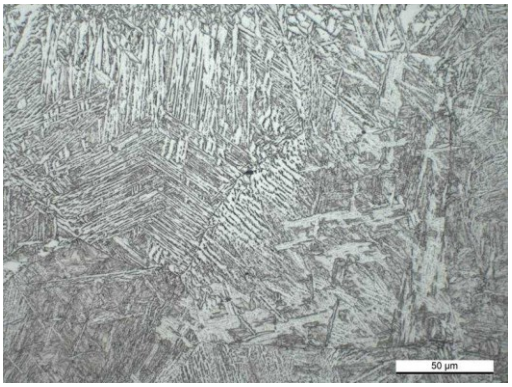

Figure 9 Micrograph of MAG welded sample 1 was taken with Leica MEF 4M light optical microscope from area of Figure 6.

LAHW welded sample 5

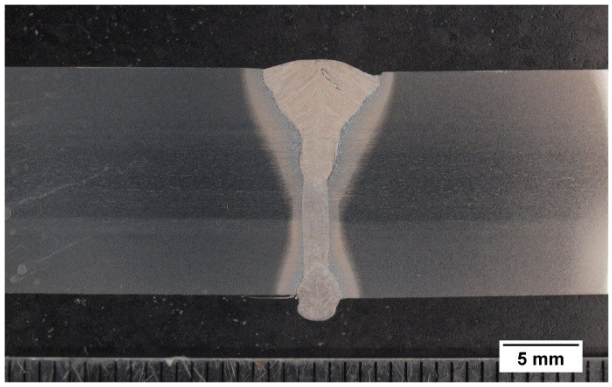

Figure 10 Macrograph of LAHW welded sample 5 was taken with Leica MZ12 stereo microscope.

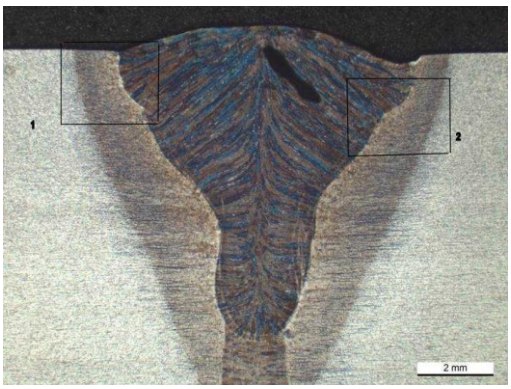

Figure 11 Micrograph of LAHW welded sample 5 was taken with Leica MEF 4M light optical microscope.

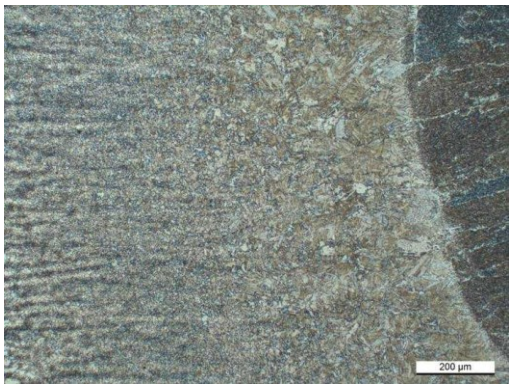

Figure 12 Micrograph of LAHW welded sample 5 was taken with Leica MEF 4M light optical microscope from area of 1 from Figure 11.

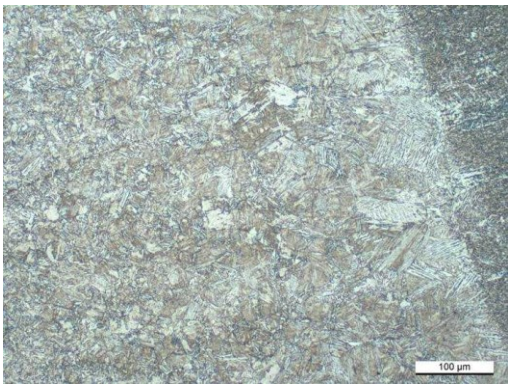

Figure 13 Micrograph of LAHW welded sample 5 was taken with Leica MEF 4M light optical microscope from area of 1 from Figure 11.

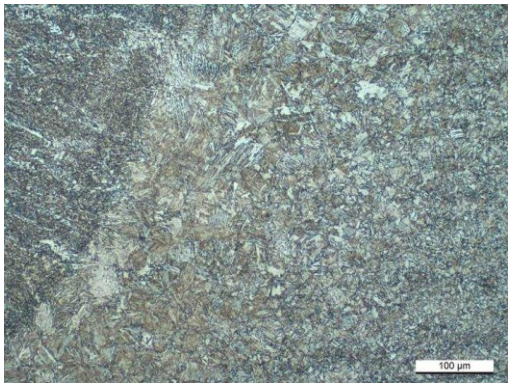

Figure 14 Micrograph of LAHW welded sample 5 was taken with Leica MEF 4M light optical microscope from area of 1 from Figure 11.

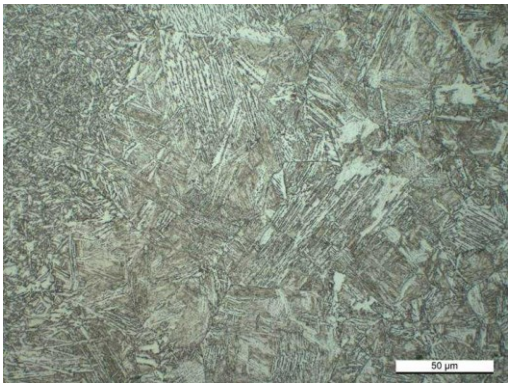

Figure 15 Micrograph of LAHW welded sample 5 was taken with Leica MEF 4M light optical microscope from area of 1 from Figure 11.

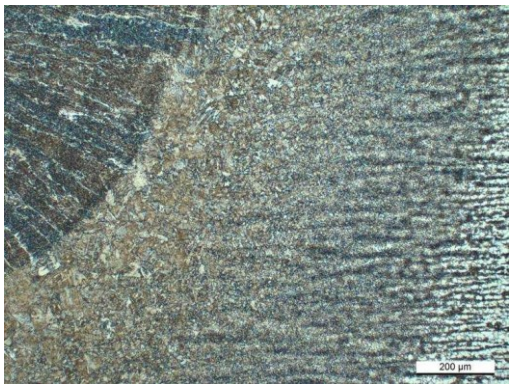

Figure 16 Micrograph of LAHW welded sample 5 was taken with Leica MEF 4M light optical microscope from area of 2 from Figure 10.

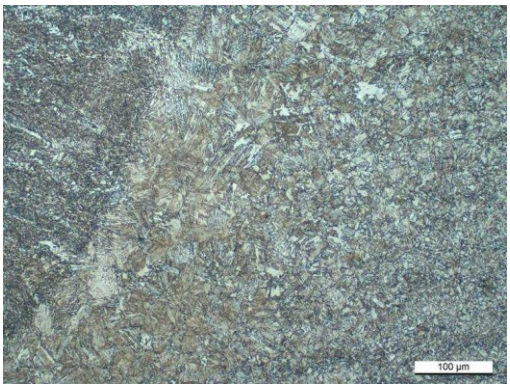

Figure 17 Micrograph of LAHW welded sample 5 was taken with Leica MEF 4M light optical microscope from area of 2 from Figure 10.

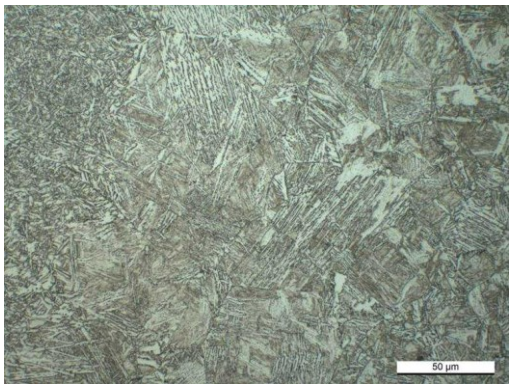

Figure 18 Micrograph of LAHW welded sample 5 was taken with Leica MEF 4M light optical microscope from area of 2 from Figure 10.